Government of Western Australia

Department of
Mines and Petroleum

REPORT 172

PETROGENESIS OF THE MAFIC-ULTRAMAFIC INTRUSIONS OF THE MESOPROTEROZOIC GILES EVENT, MUSGRAVE PROVINCE, CENTRAL AUSTRALIA

by REB Seubert

MONASH University

NGAANYATJARRA COUNCIL (Aboriginal Corporation)

Geological Survey of Western Australia

Government of Western Australia
Department of Mines and Petroleum

REPORT 172

PETROGENESIS OF THE MAFIC-ULTRAMAFIC INTRUSIONS OF THE MESOPROTEROZOIC GILES EVENT, MUSGRAVE PROVINCE, CENTRAL AUSTRALIA

by
REB Seubert

School of Earth, Atmosphere and Environment, Faculty of Science, Monash University, Melbourne, Australia

Perth 2017

Geological Survey of Western Australia

REFERENCE
The recommended reference for this publication is:
Seubert, REB 2017, Petrogenesis of the mafic-ultramafic intrusions of the Mesoproterozoic Giles Event, Musgrave Province, central Australia: Geological Survey of Western Australia, Report 172, 409p.

National Library of Australia Cataloguing-in-Publication entry

Creator:	Seubert, Roland E. B., author
Title:	Petrogenesis of the mafic-ultramafic intrusions of the mesoproterozoic Giles Event, Musgrave Province, Central Australia / Roland E.B. Seubert
ISBN:	9781741687538 (ebook)
Subjects:	Petrogenesis. Ultrabasic rocks. Igneous rocks. Geology. Musgrave Province.

Grid references in this publication refer to the Geocentric Datum of Australia 1994 (GDA94). Locations mentioned in the text are referenced using Map Grid Australia (MGA) coordinates, Zone 52. All locations are quoted to at least the nearest 100 m.

MONASH University NGAANYATJARRA COUNCIL (Aboriginal Corporation)

Notice to the reader
This Report is an accepted PhD research thesis submitted by the author to the School of Geosciences, Monash University, Melbourne and was partially funded by the Geological Survey of Western Australia (GSWA). The scientific content of the Report, and the drafting of figures, has been the responsibility of the author and has not been modified by GSWA. No editing has been undertaken by GSWA. All work carried out in the west Musgrave region was done so within the framework of a collaborative project involving GSWA, the traditional owners of the region and the Ngaanyatjarra Council. The considerable effort of the traditional owners and of the Ngaanyatjarra Council in facilitating this work, is gratefully acknowledged.

Published 2017 by Geological Survey of Western Australia
This Report is published in digital format (PDF) and is available online at <www.dmp.wa.gov.au/GSWApublications>.

Further details of geological publications and maps produced by the Geological Survey of Western Australia are available from:
Information Centre
Department of Mines and Petroleum
100 Plain Street | EAST PERTH WESTERN AUSTRALIA 6004
Telephone: +61 8 9222 3459 Facsimile: +61 8 9222 3444
www.dmp.wa.gov.au/GSWApublications

Cover photograph: Magnetite banding in troctolite of the Blackstone intrusion

Petrogenesis of the mafic-ultramafic intrusions of the Mesoproterozoic Giles Event, Musgrave Province, central Australia

Dipl.-Geol. Roland E. B. Seubert

A thesis submitted in fulfilment of the requirements
for the degree of Doctor of Philosophy

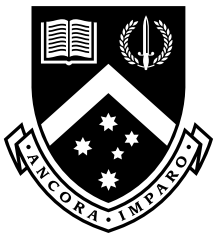

School of Earth, Atmosphere and Environment
Faculty of Science
Monash University
Melbourne, Australia

February, 2016

Sometimes I guess there just aren't enough rocks.
—Forrest Gump

Abstract

The 1090–1040 Ma Giles Event in the Musgrave Province, central Australia, led to the formation of the Ngaanyatjarra Rift. Mafic-ultramafic layered intrusions formed contemporaneously with massive gabbroic intrusions within this tectonic setting. The Bell Rock Range, Latitude Hill and Wingellina Hills intrusions represent three of the main different types of the 'G1' layered intrusions in this region, and were sampled as representative examples covering much of the compositional spectrum of layered intrusive bodies in this area. The Bell Rock Range olivine gabbronoritic-troctolitic intrusion forms a large segment of the Mantamaru intrusion that was rapidly emplaced into the crust at a maximum depth of c. 10 km. In comparison, the Latitude Hill and Wingellina Hills gabbronoritic-ultramafic intrusions are smaller intrusive bodies containing large proportions of websterite cumulates and gabbronorites with intercumulus plagioclase.

Several of the G1 layered intrusions are associated with massive 'G2' gabbroic intrusions that were locally contaminated by felsic magmas. Evidence for the previously proposed chronological order of emplacement in which G1 was followed by G2 is ambiguous: the boundary between G1 and G2 was revisited during this study. Hierarchical cluster analysis enabled the extraction of chemical elements that vary most between the G1 and G2 intrusions, with principle component analysis outlining natural clusters within the data. The clustering within the G1 and G2 compositions can be readily explained by simple cumulate effects, where the G1 layered intrusions lost late-stage melts and as a result became incompatible element depleted, whereas the G2 gabbros have compositions that closely represent original liquid compositions. This indicates that the G2 intrusions may have formed from the same parental magmas as the gabbronoritic-ultramafic G1 intrusions. In addition, this study indicates that linear discriminant analysis can be used to determine exploration vectors for Nebo-Babel style Ni-Cu-PGE targets in the area.

Although initial rifting in this region was most likely passive (i.e. driven by plate dynamics) it is still unclear whether the parental magmas for these intrusions were derived from the asthenospheric mantle (potentially plume-related) or from the subcontinental lithospheric mantle. Derivations from a likely enriched mantle reservoir as well as a maximum melting depth of c. 75 km permit both interpretations. Partial mantle melting generated magmas that then underwent moderate crustal contamination before being rapidly emplaced at mid-crustal levels to form the intrusions in the study area. Recent advances in the classification of rift settings indicate that active and passive processes can occur together in the same setting. Thus, the involvement of mantle dynamics, at least

for later stages of the Giles Event (potentially generating the Warakurna Large Igneous Province), cannot be ruled out.

Most magmatic sulphides within these intrusions are Cu-rich, are located in interstitial spaces and formed by extensive fractionation rather than by assimilation of crustal S, indicating that G1 intrusions may be prospective for smaller but PGE-rich deposits. This is supported by the presence of Ni-rich olivine and pyroxene, indicating an early major sulphide segregation event at depth is unlikely; hence, the G1 intrusions are likely to be unprospective for large orthomagmatic Ni-Cu ore deposits.

Declaration

This thesis contains no material which has been accepted for the award of any other degree or diploma at any university or equivalent institution and that, to the best of my knowledge and belief, this thesis contains no material previously published or written by another person, except where due reference is made in the text of the thesis.

Roland E. B. Seubert (candidate) Date

Acknowledgements

First of all I would like to thank my supervisors Prof. Reid Keays, Dr Simon Jowitt and Dr Andrew Tomkins for giving me this opportunity, as well as advice and guidance over the last six years. Comments and suggestions from both, Prof. Reid Keays as well as Dr Simon Jowitt, were invaluable during the preparation of this thesis.

I am also grateful to the Geological Survey of Western Australia (GSWA) and in particular to Dr Hugh Smithies, Dr Heather Howard and all field technicians for logistical and financial support as well as invaluable advice on planning and organising the field campaign. I am especially indebted to Dr Mario Werner and Dr Carmen Krapf for hosting me during my stays in Perth and also to Dr C. Cleghorne Medlin for his help in the field.

I would also like to respectfully acknowledge the Ngaanyatjarra People as the Traditional Owners of the land on which I carried out the field work to this study. I am grateful to all members and Elders, both past and present, of the Mantamaru (Jameson), Papulankutja (Blackstone) and Irrunytju (Wingellina) communities for granting me access to their land.

This PhD project would not have been possible without the financial support that was provided to me by Monash University through the Faculty of Science Dean's International Postgraduate Research Scholarship as well as the School of Geosciences Departmental Research Scholarship. I am also grateful for research funding from the Society of Economic Geologists (SEG) through the Hugh E. McKinstry Fund in 2011 and 2012, from the Institute of Materials, Minerals and Mining (IOM3) through the G Vernon Hobson Bequest in 2011 and from the Australasian Institute of Mining and Metallurgy (AusIMM) through the Bicentennial Gold Endowment '88 in 2010. Furthermore, several industry organisations supported this project in various ways and I would like to acknowledge especially Anglo American Exploration (Australia) Pty Ltd., in particular Dr Paul Polito, for financial and logistical support with the chemical analyses, as well as Metals X Limited, and here in particular Mr Max Maczurad, for giving me access to drill cores as well as providing me with accommodation and catering in their Wingellina exploration camp.

This research benefited greatly from many people that provided excellent technical support during laboratory work. From Monash University I would like to thank Dr Massimo Raveggi for running trace element analyses as well as Mr Robert Douglass and Mr Junnel Alegado for making countless thin sections and providing assistance during sample preparation. From the University of Melbourne I would like to express my gratitude to Mr Graham Hutchinson for running the microprobe analyses and to Dr Roland Maas for

running the isotope analyses and for being very helpful during data interpretation. Finally, I would like to thank Dr Daryl Howard from the Australian Synchrotron for his assistance during the element mapping on the X-ray fluorescence microprobe (even though the results did unfortunately not make it into the final thesis, after all).

Various administrative tasks are to be dealt with during a PhD project and I would like to thank especially Ms Tien Chin Chen, Ms Silvana Cifaratti, Ms Florita Henricus and Mr Robert Oakley for handling so many of them.

Many members of the academic staff of the School of Earth, Atmosphere and Environment gave me invaluable advice and suggestions that were helpful along the way. For this, I am particularly grateful to Prof. Sandy Cruden, Prof. Roberto Weinberg, Dr Oliver Nebel as well as Dr Ian Nicholls. I am also indebted to Prof. Franco Pirajno from the University of Western Australia and Prof. Mei-Fu Zhou from the University of Hong Kong for their helpful examiner comments that greatly improved the quality of this thesis.

Finally, I would like to say thank you to all postgraduate students and staff members of the School of Earth, Atmosphere and Environment, past and present, for friendship, advice, encouragement and for making these past years a great experience. Also, the entire intercontinental Millsbert family has always supported and encouraged me during these past years, and for this I am very grateful.

Mein ganz besonderer Dank gilt meiner Familie zu Hause, für deren ständige Unterstützung einmal quer über den ganzen Globus und dafür, dass sie immer Verständnis dafür aufgebracht haben, dass der Auslandsaufenthalt letztlich etwas länger geworden als ursprünglich geplant war.

Nicht zuletzt gilt mein größter Dank Dir Steph, für all die moralische Unterstützung und dafür, dass Du diese Arbeit damit und mit unablässiger Geduld am Ende überhaupt erst möglich gemacht hast.

Contents

List of figures

List of tables

List of acronyms

alr	additive log-ratio.
clr	centered log-ratio.
ilr	isometric log-ratio.
Ab	albite.
AFC	assimilation and fractional crystallisation.
Afs	alkali-feldspar.
AGSO	Australian Geological Survey Organisation.
An	anorthite.
ANO	anorthosite.
BABI	basaltic achondrite best initial.
BDL	below detection limit.
C	common component.
CGG	coarse-grained gabbronorite.
CHUR	chondritic uniform reservoir.
CIPW	Cross, Iddings, Pirsson, Washington.
D-MORB	depleted mid-ocean ridge basalt.
DM	depleted mantle.
DMM	depleted mid-ocean ridge basalt mantle.
EM	enriched mantle.
EMPA	electron beam microprobe analysis.
EM 1	enriched mantle 1.
EM 2	enriched mantle 2.
FOZO	focal zone.

GFC	Gifford Creek Ferrocarbonatite Complex.
GSSA	Geological Survey of South Australia.
GSWA	Geological Survey of Western Australia.
HCA	hierarchical cluster analysis.
HFSE	high field strength element.
HIMU	high-μ mantle.
HREE	heavy rare earth element.
ICP-MS	inductively coupled plasma mass spectrometry.
ICP-OES	inductively coupled plasma optical emission spectrometry.
IQR	inter-quartile range.
LDA	linear discriminant analysis.
LIP	large igneous province.
LOD	limit of detection.
LREE	light rare earth element.
MCAR	missing completely at random.
MCG	microgabbronorite.
MLG	melagabbronorite.
MORB	mid-ocean ridge basalt.
MPG	microporphyritic gabbronorite.
N-MORB	normal mid-ocean ridge basalt.
NaN	Not a Number.
NT	Northern Territory.
NTGS	Northern Territory Geological Survey.
OGA	olivine gabbronorite adcumulate.
OGT	olivine gabbronorite and troctolite.
OIB	ocean island basalt.
Or	orthoclase.
PC	principal component.
PCA	principal component analysis.
PGE	platinum-group element.

PHEM	primitive helium mantle.
Pl	plagioclase.
PM	primitive mantle.
PREMA	prevalent mantle.
PYR	pyroxenite.
REE	rare earth element.
ROC	receiver operating characteristic.
SA	South Australia.
SCLM	subcontinental lithospheric mantle.
SVD	singular value decomposition.
UHT	ultra-high temperature.
UTM	universal transverse mercator.
VTG	variably-textured gabbronorite.
WA	Western Australia.
WDS	wavelength-dispersive spectroscopy.
XRF	X-ray fluorescence.

Chapter 1

Introduction

The Musgrave Province in central Australia hosts what might arguably be one of the world's largest mafic-ultramafic igneous complexes. It comprises the layered intrusions, massive gabbros and associated felsic rocks of the Giles Suite that formed during the Mesoproterozoic Giles Event. But it is also located in one of the most remote and underexplored areas of the Australian continent, despite its high prospectivity for nickel, copper, platinum-group element (PGE), vanadium and titanium deposits, amongst others. Even though the mafic-ultramafic intrusions of the Giles Event have been subject to geological studies for more than 100 years, their petrogenesis and economic potential are still not fully understood; thus, they continue to inspire both basic and applied research.

1.1 History of exploration

The scientific exploration of the Musgrave Province is an ongoing effort that ultimately goes back to Ernest Giles (1835–1897) and William Christie Gosse (1842–1881), the first European explorers to traverse the region during expeditions in 1873 and 1874. Ernest Giles was also the first non-Indigenous Australian to discover the Bell Rock Range. While on his second expedition, from August 1873 to July 1874, he found and named the prominent range of hills on the 30 September 1873 upon entering Western Australia from South Australia:

> The summit of this hill I found to consist of great masses of rifted stone, which were either solid iron or stone coated thickly with it. The blocks rang with the sound of my iron-shod boots, while moving over them, with such a musical intonation and bell-like clang, that I called this the Bell Rock. (Giles 1889, p. 200)

Shortly before, during late August and early September 1873, Gosse (1874) discovered and named several of the other intrusions in the Musgrave Province, such as Mt Hinckley, Mt Davis and the Cavenagh Range. Giles and Gosse were succeeded by a number of explorers and prospectors in the following decades of the late 19th century. Some of

the first geological research was done by Streich (1893) as part of the 1891–1892 Elder Exploring Expedition and shortly after by Basedow (1905). Talbot et al. (1917) provided a comprehensive geological study of the region between Laverton, Western Australia and the South Australian border, including the Musgrave Province. Their work was based on an extensive mapping campaign initiated by the Geological Survey of Western Australia (GSWA) and included an assessment of the prospectivity of this area for copper and gold deposits.

The minerals exploration industry began to target the Musgrave Province for the first time on a large scale in 1954, when the Southwestern Mining Company began to lease extensive land and map the mafic intrusions and surroundings, in an attempt to discover nickel and copper deposits (e.g. Aborigines Protection Board 1957; Nesbitt and Talbot 1966). This was also the time when Sprigg and Wilson (1959, p. 535) coined the term 'Giles Complex' for the mafic intrusions.

Driven by the economic potential of the Musgrave Province in general and the mafic-ultramafic Giles intrusions in particular the various geological surveys of Australia carried out multiple mapping programmes and geophysical surveys over the following decades. In South Australia the field campaigns began in 1963 (Nesbitt and Talbot 1966) and led to many publications on the Ewarara, Kalka and Gosse Pile intrusions (e.g. Nesbitt and Kleeman 1964; Moore 1971a, 1973; Goode 1975; Goode and Moore 1975; Goode 1977b). The GSWA executed their programme in 1966–1968. Four geological map sheets on a scale of 1:250 000, which cover the entire Western Australian part of the Musgrave Province, were produced and Daniels (1974) gave a detailed petrological account of the Musgrave Province. In 1987 the Australian Geological Survey Organisation (AGSO, now Geoscience Australia) began to reinvestigate the Musgrave Province with particular focus on the Giles Complex (e.g. Ballhaus and Glikson 1989; Ballhaus and Berry 1991; Ballhaus 1993; Ballhaus and Glikson 1995; Glikson et al. 1996). Their petrological study focused heavily on mapping of the mafic-ultramafic layered intrusions as well as on their petrography, mineralogy and mineral chemistry. The same year the Northern Territory Geological Survey (NTGS) commenced a programme to cover the part of the Musgrave Province that is located in the Northern Territory on 1:250 000-scale geological maps. Edgoose et al. (2004) published a comprehensive report on the findings of the NTGS, giving the term 'Giles Event' preference over 'Giles Complex' to underline the prolonged bimodal intrusive and extrusive magmatic activity recorded in this region.

The discovery of the Ni-Cu-Co deposit at Voisey's Bay (Canada) in 1993 by Diamond Fields Resources (e.g. Amelin et al. 1999; Li and Naldrett 1999; Li et al. 2000; Naldrett et al. 2000a,b) stimulated exploration in the Musgrave Province from 1995 onwards, because Voisey's Bay is hosted by troctolitic rocks which are abundant in some of the largest layered intrusions that formed during the Giles Event. This led to the discovery of the Nebo-Babel deposit in 2000 by WMC Resources Limited (later acquired by BHP Billiton; Baker and Waugh 2005; Seat et al. 2007; Seat 2008). With interest in the Musgrave Province thus renewed, the GSWA commenced field work in 2004, this time mapping on a scale of 1:100 000 (e.g. Smithies et al. 2009a; Howard et al. 2011a,b). The accompanying research lead to the unravelling of the Giles Event (Evins et al. 2010b,c), the redefinition

of the Musgrave Orogeny as a (largely) extensional event (Smithies et al. 2010, 2011), investigations into potential supervolcanoes and -eruptions in the Musgrave Province (Smithies et al. 2013; Medlin 2014) and a major petrological and geochemical review of the mafic-ultramafic intrusions (Maier et al. 2014, 2015). The field work of this study was carried out as part of the mapping campaign of the GSWA. The Geological Survey of South Australia (GSSA) started a similar programme in 2011. Mapping on a scale of 1:100 000 began from the very east of the South Australian part of the Musgrave Province. No results for the Giles intrusions in South Australia that tie-in with the work of the GSWA were available at the time of this writing.

All of the above programmes had or have the intrusive bodies formed by the Giles Event as one of their main focuses. The various Giles intrusions have previously been divided into several compositional groups (see section 1.2 for details). This work uses the three intrusions of the Bell Rock Range (chapters 2 and 3) as well as Latitude Hill and Wingellina Hills (chapter 4) as proxies for the multitude of intrusive bodies, because together they account for most major lithologies within the Giles intrusions.

1.2 Geological history of the Musgrave Province

The Mesoproterozoic Musgrave Province is located between the North, South and West Australian Cratons and extends c. 800 km east-west and 350 km north-south (figure 1.1). It is bounded to the north, east, south and west by the Neoproterozoic/Palaeozoic Amadeus, Eromanga, Officer and Canning Basins, respectively. The south dipping Woodroffe Thrust, a major east-west trending structure, was active during most of the c. 580–520 Ma Petermann Orogeny (Camacho and Fanning 1995; Camacho 1997; Scrimgeour and Close 1999; Gregory et al. 2009; Raimondo et al. 2010) and divides the Musgrave Province into two tectonic domains with different metamorphic grade: the northern amphibolite-facies Mulga Park Domain and the southern granulite-facies Fregon Domain (Camacho and Fanning 1995), the latter of which hosts the intrusions of the Giles Event. The Fregon Domain itself can be further divided into at least two subdomains with high-pressure metamorphism from the Petermann Orogeny in the north (Scrimgeour and Close 1999; Gregory et al. 2009; Raimondo et al. 2010) and a markedly weaker Petermann-aged metamorphic overprint in the southern subdomain (Clarke et al. 1995), that enabled the preservation of Metaproterozoic high-temperature metamorphism (Howard et al. 2011b). The boundary between those two subdomains is thought to be the Mann fault (Edgoose et al. 2004).

1.2.1 Geological evolution prior to the Giles Event

The basement rocks as well as the Papulankutja, Wankanki and Pitjantjatjara Supersuites in the west and the Birksgate Complex and Olia Gneiss in the centre and east outcrop extensively across the Musgrave Province (figures 1.1 and 1.2). Contamination with crustal material is thought to be an important factor that drives mafic melts to sulphur saturation and the formation of magmatic sulphide ore deposits in many parts of the world (e.g. Lightfoot and Keays 2005; Keays and Lightfoot 2007, 2010; Ihlenfeld and Keays 2011; Ripley

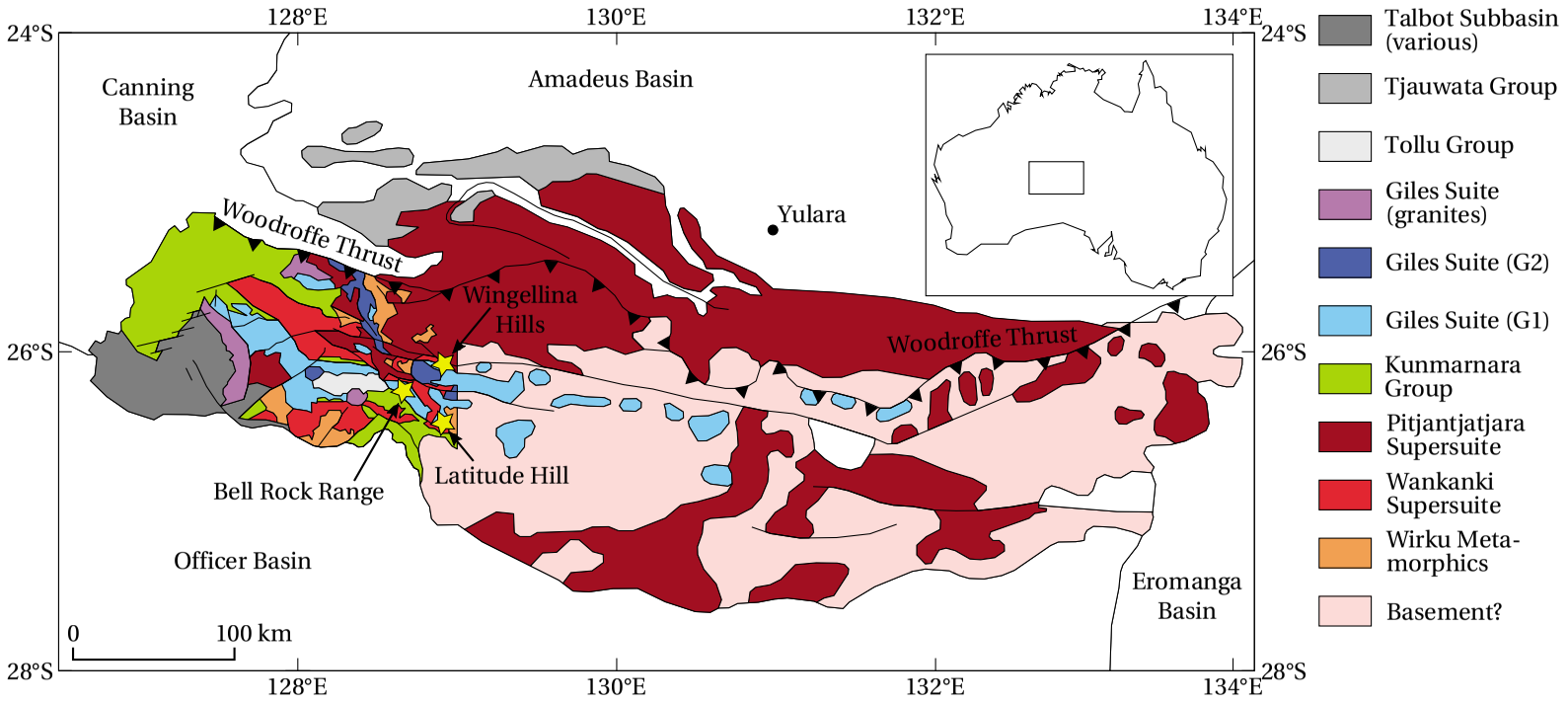

Figure 1.1 Geological map of the Musgrave Province, showing the locations of the Bell Rock Range, Latitude Hill and Wingellina Hills intrusions (modified after Howard et al. 2011a, 2015, the apparent higher degree of known detail in the west is an artefact that results from the progress of recent field mapping campaigns and does not necessarily reflect the true geology). The mafic-ultramafic layered and massive intrusions of the Giles Event are concentrated in the western part of the Musgrave Province. The inset map shows the location of the Musgrave Province within central Australia.

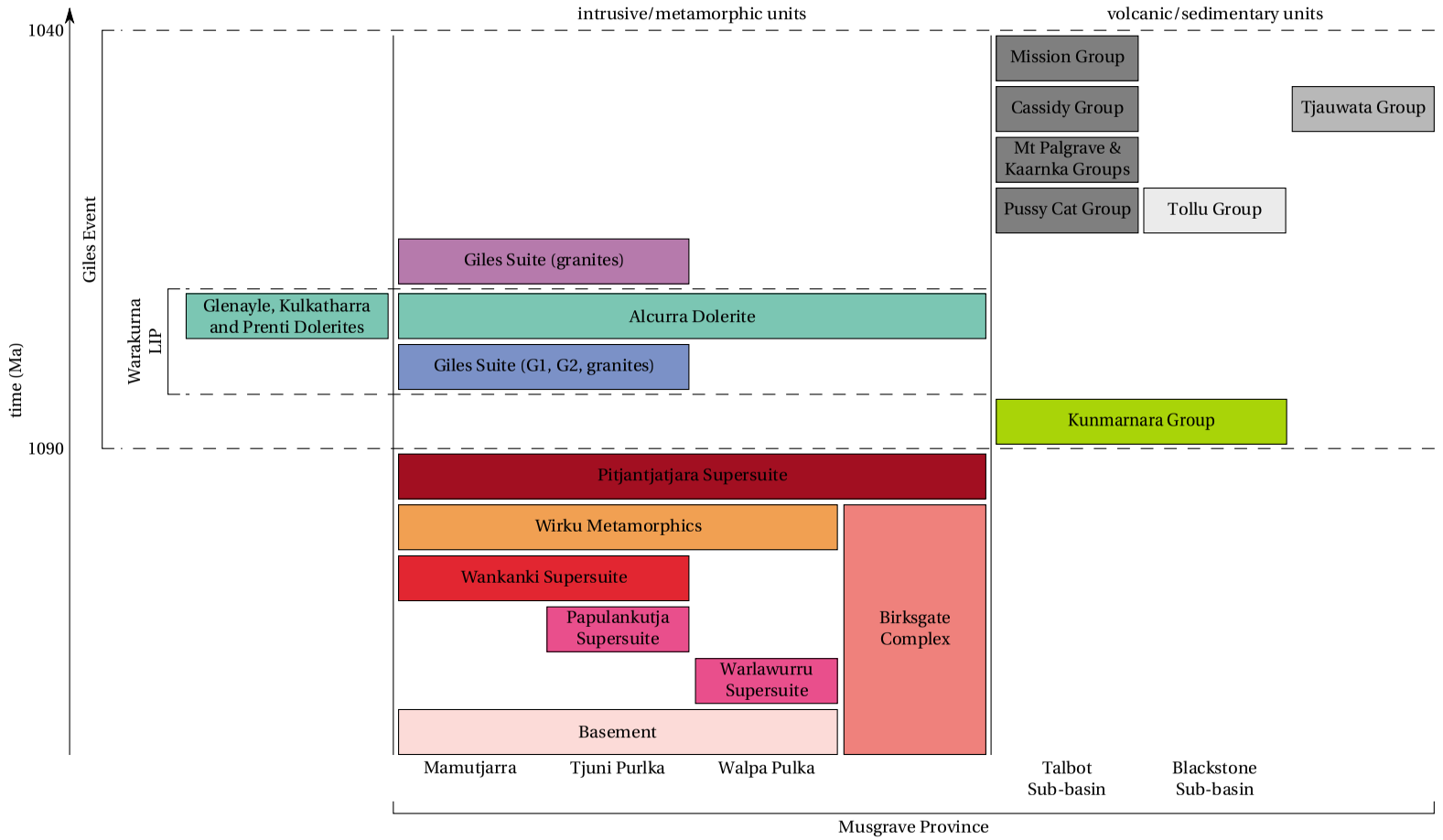

Figure 1.2 Stratigraphic chart of the Musgrave Province. The vertical axis illustrates the chronology of events with particular reference to the Giles Event and the emplacement of the Warakurna large igneous province (LIP). The horizontal axis separates the stratigraphic members into logical units, thus, showing the major volcanic/sedimentary as well as intrusive/metamorphic rocks in the Musgrave Province (stratigraphic table compiled after the *Australian Stratigraphic Units Database* at `http://www.ga.gov.au/data-pubs/data-standards/reference-databases/stratigraphic-units/` as well as Edgoose et al. 2004; Morris et al. 2005; Schmidt et al. 2006; Evins et al. 2010c; Quentin De Gromard et al. 2016).

and Li 2013). The significance of these pre-Giles stratigraphic units is that they represent likely contaminants that could have been assimilated by the parental magmas of the Giles intrusions.

Basement

The ages of the basement rocks in the Musgrave Province are still poorly constrained because outcrop is sparse. Earlier studies reported Rb-Sr ages of c. 1550 Ma for felsic granulite-facies gneisses that were interpreted to represent primary depositional ages of the clastic, volcaniclastic or volcanic protoliths (Gray 1971, 1978; Gray and Compston 1978). More recent studies confirmed these ages via U-Pb dating of gneisses, suggesting early crustal formation between c. 1600 and 1540 Ma (e.g. Maboko et al. 1991; Camacho and Fanning 1995; Edgoose et al. 2004). However, unambiguous crystallisation ages of protoliths of gneisses older than 1500 Ma are rare in the Musgrave Province. A granitic protolith at 1591 Ma was reported by Camacho and Fanning (1995) and Edgoose et al. (2004). In their study, Evins et al. (2012) investigated the provenance of the metasedimentary Wirku Metamorphics (section 1.2.1) and found several distinct detrital zircon age peaks of 1570, 1520 and 1330 Ma, as well as c. 1500–1400 Ma at younger stratigraphic levels. In the same study, Evins et al. (2012) report a component within the basement of the Musgrave Province that yields multiple Archaean age peaks, one as old as 2900 Ma; a finding that supports the discussion of Nd and Hf model ages in Smithies et al. (2010) and Kirkland et al. (2012a, 2013) who suggested reworking of small amounts of Archaean material in rocks of the Pitjantjatjara Supersuite (see section 1.2.1) on the Musgrave Orogeny).

The above mentioned ages largely describe the provenance of metamorphic rocks, thus, they are not necessarily instructive with regard to the basement's formation. Kirkland et al. (2012a, 2013) carried out isotope studies that confirmed two crust-formation events at 1950–1900 Ma and at 1600–1550 Ma, involving juvenile material and Archaean crust. The younger one of the two events is interpreted to represent an arc setting (Glikson et al. 1996; Wade 2006; Wade et al. 2006, 2008). The nature of the older crust formation event is still largely unconstrained, but is thought to have involved oceanic crust (Kirkland et al. 2013; Howard et al. 2015).

Oldest exposed lithologies

The basement lithologies are primarily inferred, for instance from isotopic studies of the provenance of metasedimentary gneisses and model ages (section 1.2.1). The oldest currently known igneous rocks that are actually exposed are 1600–1550 Ma old (Camacho and Fanning 1995; Edgoose et al. 2004). The granitic protoliths of members of this suite in Western Australia yielded an age of 1575 Ma and were recently grouped into the Warlawurru Supersuite (Howard et al. 2015). The Papulankutja Supersuite is another relatively old stratrgraphic unit and consists of c. 1400 Ma old granites whose origin is still unknown but the mineralogical and geochemical composition may suggest an arc setting (Howard et al. 2011b, 2015).

Mount West Orogeny—formation of the Wankanki Supersuite and the Wirku Metamorphics

The Wankanki Supersuite was defined by Howard et al. (2007b) and contains all rocks formed during the 1345–1293 Ma Mount West Orogeny (White et al. 1999; Smithies et al. 2009a, 2010). The unit consists of granulite-facies calcic to calc-alkaline, metaluminous I-type granitoid gneisses and associated volcanic rocks (Smithies et al. 2009a, 2010). Isotope data suggest moderately evolved melts (initial ϵ_{Nd} between –0.56 and –2.39; Smithies et al. 2010) that have formed in a continental arc setting (Giles et al. 2004; Betts and Giles 2006; Smithies et al. 2010; Evins et al. 2012; Kirkland et al. 2012a, 2013).

The quartzofeldspathic, peraluminous paragneisses of the Wirku Metamorphics (Howard et al. 2009a,b) are exposed over large areas of the western Musgrave Province. The protoliths are mainly pelitic to psammitic sedimentary rocks with depositional ages of c. 1340–1300 Ma that were deposited in the Ramarama Basin (see also section 1.2.1 on the basement). In addition, felsic volcanic protoliths and granitic leucosomes occur together with the metasedimentary rocks (Evins et al. 2012). The ages of the Wirku Metamorphics and the Wankanki Supersuite largely overlap. For this reason, the Wirku Metamorphics are interpreted to have formed by supracrustal reworking of the Wankanki Supersuite and therefore formed within the same tectonic setting during the Mount West Orogeny (Evins et al. 2012).

Stratigraphy of the pre-Musgravian South Australia and Northern Territory

In the central and eastern parts of the Musgrave Province all rocks that formed prior to and were later metamorphosed during the Musgrave Orogeny are grouped into the Olia Gneisses in the Mulga Park Domain and into the Birksgate Complex in the Fregon Domain, respectively (Major and Conor 1993, see also figure 1.2). Occasionally, these units are collectively termed the Musgravian gneisses (e.g. by Edgoose et al. 2004). No effort has been made so far to further subdivide the Olia Gneisses and the Birksgate Complex in order to align the stratigraphy of the central and eastern parts of the Musgrave Province with the western parts.

Musgrave Orogeny—formation of the Pitjantjatjara Supersuite

The granulite-facies gneisses of the Pitjantjatjara Supersuite formed during the Musgravian Orogeny between 1220 and 1150 Ma (White et al. 1999; Edgoose et al. 2004; Smithies et al. 2009a). The rocks of the Pitjantjatjara Supersuite broadly fall into three different lithologic groups, namely monzodiorites to alkali-feldspar granites and charnockites, leucocratic monzogranites and syenogranites as well as locally leucocratic anatectic melts (Smithies et al. 2010). The rocks are similar to the Wankanki Supersuite in that they yield moderate initial ϵ_{Nd} values in the range of –2.2–-4.0 (Smithies et al. 2011).

The granitic gneisses of the Pitjantjatjara Supersuite crystallised under ultra-high temperature (UHT) metamorphic conditions (≤1000 °C) and exhibit an intracrustal A-type signature (Smithies et al. 2010, 2011). The UHT conditions lasted at least until

1120 Ma and suggest that the rocks of the Pitjantjatjara Supersuite formed by intracratonic crustal reworking in an extensional setting involving crustal thinning to ≈35 km (Wade et al. 2008; Smithies et al. 2010, 2011; Gorczyk et al. 2014; Smithies et al. 2015). Smithies et al. (2011) and Kirkland et al. (2012a, 2013) identified mantle-derived material in the parental magma of the Pitjantjatjara granites, a finding that is in agreement with an extensional setting.

1.2.2 Giles Event

The Giles Event was a multi-phase magmatic event associated with the extensive emplacement and eruption of mafic to felsic magmas (Smithies et al. 2009a; Evins et al. 2010b,c; Aitken et al. 2013). The mafic-ultramafic layered intrusions and gabbroic plutons formed during the Giles Event were in the past referred to as the 'Giles Complex' (section 1.1), a term that does not reflect the multitude of stages during the event and the spectrum of intrusions that were emplaced at different crustal levels. More recently, Evins et al. (2010b,c) provided a detailed summary of the succession of the approximately eight stages of the Giles Event that occurred between c. 1090 and 1040 Ma. The Warakurna Supersuite was defined to comprise all igneous rocks formed during this event (Howard et al. 2011a). The tectonic processes accompanying this sequence of events are thought to have generated the failed intracontinental Ngaanyatjarra Rift (Evins et al. 2010b,c; Aitken et al. 2013) and it has further been speculated that the Musgrave Orogeny and the Giles Event may have formed during a single long-lived series of events (Howard et al. 2015; Smithies et al. 2015).

Bentley Supergroup

The Bentley Supergroup is a sequence of clastic, volcaniclastic and volcanic rocks. Deposited within the Bentley Basin, it is thought to represent the supracrustal equivalent to the Warakurna Supersuite. As such, the Bentley Supergroup stratigraphically envelopes the Warakurna Supersuite and its deposition represents the first and last stages of the Giles Event (Daniels 1974; Smithies et al. 2009a; Evins et al. 2010b,c, see also figure 1.2). The Bentley Supergroup mainly outcrops in the western Musgrave Province, which is also where the bulk of the mafic intrusions are located. This supracrustal succession therefore constrains the timing of the emplacement of the mafic-ultramafic intrusions.

Phase one of the Giles Event is marked by the deposition of the Kunmarnara Group (lower Bentley Supergroup), which comprises the deformed sandstones and conglomerates of the MacDougall Formation and amygdaloidal basalts of the Mummawarrawarra Basalt (Daniels 1974; Smithies et al. 2009a). Equivalents to the MacDougall Formation and the Mummawarrawarra Basalt in the Northern Territory are the Karukali Quartzite and the Mount Harris Basalt of the Tjauwata Group, respectively (Close et al. 2003a). The age of the Kunmarnara Group is ill-defined. It stratigraphically overlies the Pitjantjatjara Supergroup of the Musgrave Orogeny, thus, the maximum deposition age is constrained by the end of the Musgravian metamorphism at c. 1120 Ma (Howard et al. 2015); the minimum age is constrained by the formation of the Tjauwata Group (c. 1090 Ma; Edgoose et al. 2004) as well as the emplacement age of the Giles Suite in the west Musgrave Province (1078 Ma;

Sun et al. 1996; Howard et al. 2011b). The latter age was interpreted by Evins et al. (2010b,c) to postdate the Kunmarnara Group.

The upper bracket for the intrusive magmatic activities during the Giles Event is provided by the formation of the Tollu Group (upper Bentley Supergroup), which comprises the rhyolitic and dacitic Smoke Hill Volcanics and the intermediate lavas of the Hogarth Formation (Daniels 1974; Evins et al. 2010b,c). A correlation between the Puntitjata Rhyolite and the Wankari Volcanics of the Tjauwata Group (Northern Territory) with the Smoke Hill Volcanics and the Hogarth Formation of the Tollu Group was established by Close et al. (2003a). Deposition of the Smoke Hill Volcanics began as early as c. 1073 Ma, with the Hogarth Formation emplaced at c. 1068 Ma (Howard et al. 2011a, 2015). In the Talbot Subbasin, volcanic activity ended at c. 1047 Ma (Smithies et al. 2013).

Early Giles Suite

The Giles Suite comprises all igneous rocks that were formed during the Giles Event. Of particular interest for this study are the mafic-ultramafic layered and massive intrusive rocks (e.g. Nesbitt and Kleeman 1964; Nesbitt and Talbot 1966; Daniels 1974; Ballhaus and Berry 1991; Ballhaus 1993; Ballhaus and Glikson 1995; Glikson et al. 1996; Maier et al. 2014, 2015) that were emplaced within the age brackets defined by the Bentley Supergroup (section 1.2.2). The mafic-ultramafic layered intrusions were referred to as G1 and the massive gabbroic intrusion as G2 (Evins et al. 2010b,c), and their emplacement represents the phases two and three of the Giles Event, respectively.

Phase two of the Giles Event followed the deposition of the lower Bentley Supergroup and resulted in the emplacement of mafic-ultramafic layered intrusions (G1; see above as well as Evins et al. 2010b,c; Maier et al. 2014). They are a group of c. 20 intrusive bodies that were emplaced over an area that extends c. 550 km from east to west (figure 1.1). The layered intrusions have been broadly categorised as either troctolitic, gabbroic or ultramafic by previous authors (Ballhaus and Glikson 1995; Glikson et al. 1996; Maier et al. 2014, 2015), although the membership of individual intrusive bodies in one group or another is not always consistent between different authors due to the qualitative nature of this classification. Exposed wall-rock contacts are rare and mostly between the G1 intrusions and the greenschist-facies Kunmarnara Group (Howard et al. 2011b, 2015), but an intrusive contact with felsic granulites has been reported at Latitude Hill (Ballhaus and Glikson 1995; Glikson et al. 1996). Few geochronological data exist for the G1 intrusions. Sun et al. (1996) dated a leucocratic dyke that was interpreted to be comagmatic with the Bell Rock Range intrusion and obtained an age of 1078 ± 3 Ma. More recently, Kirkland et al. (2011) obtained another age from a G1-related intrusive body of 1076 ± 7 Ma, thus, an age bracket of c. 1078–1076 Ma was proposed for the G1 members of the Giles Suite (Howard et al. 2011a).

The massive G2 gabbros were emplaced along large shear zones during phase three of the Giles Event. They are commonly associated with the layered G1 intrusions as well as A-type granites, leucogranitic veins and dykes, and there is extensive mixing and mingling between the mafic and the felsic units (Evins et al. 2010b,c; Howard et al. 2011a, 2015). The age brackets for the emplacement of the G2 intrusions ranges from 1078 to 1074 Ma

with an average of c. 1075 Ma. The Musgrave Province was also subject to large-scale deformation and folding during this phase (Evins et al. 2010b,c; Howard et al. 2011a, 2015).

There has been much debate around the depth of emplacement of the mafic-ultramafic intrusions of the Giles Event. Goode and Moore (1975) interpreted the Ewarara, Kalka and Gosse Pile intrusions (South Australia) to have formed at pressures of 1–1.2 GPa, corresponding to a depth of c. 35–45 km. Ballhaus and Berry (1991) estimated the pressure and temperature during crystallisation of the Wingellina Hills intrusion (Western Australia) and obtained results indicating isobaric cooling at lithostatic pressures of 0.62–0.65 GPa, which is in agreement with emplacement at low- to mid-crustal levels (c. 24 km). In contrast, Evins et al. (2010b,c) used the field relationships around the Blackstone Range intrusion (Western Australia) to suggest a maximum emplacement depth of c. 15 km, while Maier et al. (2014) suggested that the Blackstone Range intrusion formed at a lithostatic pressure of 0.1 GPa, corresponding to an even shallower depth of c. 3.5–4 km. On a regional scale, the different pressure estimates suggest a shallowing trend from east to west, potentially indicating emplacement at different crustal levels (e.g. Daniels 1967; Nesbitt et al. 1970; Glikson et al. 1996; Maier et al. 2014).

Alcurra Dolerite

The Alcurra Dolerite (previously called G3) is a series of mafic dykes and sills that outcrop in several parts of the Musgrave Province (Edgoose et al. 1993; Scrimgeour et al. 1999; Howard et al. 2009c). The suite was initially reported from the eastern part of the Musgrave Province in the Northern Territory and South Australia, and was interpreted to be a c. 1080 Ma old (e.g. Edgoose et al. 1993; Scrimgeour et al. 1999; Edgoose et al. 2004). Howard et al. (2009c) correlated a series of olivine gabbros and norites as well as ferronorites and -diorites from the western Musgrave Province (including for instance the host intrusion of the Nebo-Babel Ni-Cu-PGE deposit; section 1.3.1) with the Alcurra Dolerite based on geochemical similarities, such as increased incompatible element concentrations caused by crustal contamination. These authors also showed that members of the Alcurra Dolerite can be as young as 1068 Ma and initially termed them the G3 member of the Giles Suite (Evins et al. 2010b,c). However, since then Howard et al. (2015) reported volcanic equivalents of the Alcurra Dolerite that cross-cut and mingle with clastic rocks of the upper Bentley Supergroup. Thus, the Alcurra Dolerite is now seen as the result of prolonged magmatic activity that might have lasted for c. 30 Ma or more, and involved mantle- as well as crust-derived melts resulting in evolved mafic lithologies. The term G3 has subsequently been considered obsolete (Howard et al. 2015). The Alcurra Dolerite is also host to some of the most significant magmatic sulphide mineralisation that has been found so far in the Musgrave Province (section 1.3.1).

Late Giles Event

The magmatic activities of the remaining phases of the Giles Event cluster around c. 1062 and 1048 Ma. The earlier phase comprises mingled gabbroic and granitic magmas as well

as felsic dykes and volcanics, while the intrusive and extrusive magmatic activities during the later phase are restricted to felsic compositions (Evins et al. 2010b,c).

1.2.3 Warakurna large igneous province

The Warakurna large igneous province (LIP) extends over an area of c. 1.5×10^6 km^2 in central and western Australia (Wingate et al. 2004; Morris et al. 2005). Magmatic activity lasted between 1078 1070Ma and peak magmatism occured around c. 1075 Ma—well within the temporal extent of the Giles Event. The Giles intrusions are located roughly in the centre of the LIP. It is for these reasons that the Giles intrusions (including G1, G2 and Alcurra Dolerite) were classified as members of the Warakurna LIP (Wingate et al. 2004; Morris et al. 2005; Evins et al. 2010b,c), although recent reinterpretations of the significance of the Warakurna LIP (Howard et al. 2015; Smithies et al. 2015) suggest it may represent a short-lived episode during which the longer lasting magmatic activity in the Musgrave Province began to spread over central and western Australia. Apart from the Giles Suite, further members of the Warakurna Supersuite are the Glenayle, Kulkatharra and Prenti Dolerites (Wingate et al. 2004; Morris et al. 2005, see also the *Australian Stratigraphic Units Database* at `http://www.ga.gov.au/data-pubs/data-standards/reference-databases/stratigraphic-units/`).

1.3 Mineralisation in the Musgrave Province

Despite some exploration in the Musgrave Province over the past few decades (section 1.1) only few prospects hosting economic Ni, Cu or PGE mineralisation have been discovered so far, and the area is still underexplored compared to other regions of Australia. The most notable discoveries are arguably the Nebo-Babel Ni-Cu-PGE deposit (Baker and Waugh 2005; Seat et al. 2007; Seat 2008; Seat et al. 2009; Godel et al. 2011; Seat et al. 2011) and (although nonmagmatic) the Wingellina Ni-laterite deposit (Goode 2002; Metals X Limited n.d.).

1.3.1 Mineralisation within the Alcurra Dolerite

Members of the Alcurra Dolerite (section 1.2.2) are known to contain magmatic sulphide mineralisation (Howard et al. 2009c). For instance, localised malachite and chrysocolla were identified in an olivine gabbroic dyke in the north-western part of the troctolitic Jameson intrusion, that yielded an age of 1067 Ma and is considered to be a member of the Alcurra Dolerite (Howard et al. 2009c). A mineralised sample of the dyke (GSWA sample no. 194 405) contained 0.4 wt% Cu, 133 ppb Pd and 116 ppb Pt. The dyke is enriched in incompatible elements and has initial ϵ_{Nd} values between –3.03 and +1.23; Howard et al. (2009c) concluded that these values indicated that the parental magma of the dyke had been derived from a depleted mantle source and had undergone minor crustal contamination. The Halleys intrusion, which is thought to be a member of the Alcurra Dolerite, also contains some Cu-Ni-PGE-Au mineralisation (Maier et al. 2014, 2015), but no data is available from this prospect.

The Nebo-Babel Ni-Cu-PGE deposit

The Nebo-Babel deposit (Baker and Waugh 2005; Seat et al. 2007; Seat 2008; Seat et al. 2009; Godel et al. 2011; Seat et al. 2011) is hosted by a gabbronoritic intrusion that was emplaced into late-Musgravian felsic amphibolite-facies orthogneisses (c. 1150 Ma; Seat et al. 2011). The host intrusion is tube-shaped with a cross section of c. 1×0.5 km and is c. 5 km long. It trends approximately east-west and is separated by a fault into the eastern Nebo and the western Babel sections. Both sections are very similar and their main lithologies are barren and mineralised gabbronorites as well as leucogabbronorites. A barren gabbronorite of the Nebo-Babel host intrusion yielded an age of 1068 ± 4 Ma (Seat 2008; Seat et al. 2011). Therefore, Nebo-Babel cannot be directly associated with the layered G1 intrusions or the massive G2 gabbros as it is c. 10 Ma younger. Instead, Howard et al. (2009c) correlated the Nebo-Babel sulphide deposit with the Alcurra Dolerite (section 1.2.2).

According to Seat et al. (2007), Seat (2008) and Seat et al. (2011), the host intrusion was formed by three distinct pulses of a low-MgO tholeiitic parental magma that intruded along pre-existing faults or shear zones at a depth of c. 10–12 km. The sulphides that formed the mineralisation were carried into the magma chamber by the earlier and more primitive pulses. Seat et al. (2009), Godel et al. (2011) and Seat et al. (2011) provided evidence for the assimilation of country rocks of the Nebo-Babel host intrusion; however, no S-bearing country rocks have been reported by these authors. Seat et al. (2009) and Godel et al. (2011) favour a genetic model in which S-saturation was reached by felsification that was caused by the assimilation of gneissic country rocks and lead to a subsequent decrease in the S-solubility, as opposed to the addition of external S—a view that is not even-handedly shared by Maier et al. (2014, 2015), who provide an alternative model that includes the addition of external S.

Most mineralisation at Nebo-Babel (described in detail by Seat et al. 2007) occurs as disseminated blebs within gabbronorites with only minor massive sulphides that are located near hanging-wall contacts to the felsic orthogneisses. Nevertheless, the sulphide mineral assemblage can form up to 30 vol% in mineralised rocks and comprises pyrrhotite, pentlandite, chalcopyrite and some pyrite. The main host phases for PGE are the tellurides moncheite ($PtTe_2$), merenskyite ($PdTe_2$) and michenerite (PdBiTe). The tellurides are mainly hosted within silicates rather than sulphides (Seat et al. 2009).

1.3.2 Miscellaneous magmatic and nonmagmatic mineralisation

Cassini Resources Limited, who acquired the Nebo-Babel prospect (section 1.3.1) from BHP Billiton in 2014, confirmed several zones of high-grade mineralisation at the Succoth Cu-PGE prospect, which is located near Nebo-Babel. The reported ore grades of the intersected zones are 148 m at 0.94 % Cu, 0.09 % Ni and 0.24 g/t PGE as well as 42 m at 1.38 % Cu, 0.13 % Ni and 0.32 g/t PGE, respectively (Cassini Resources Limited 2014, see also `http://www.cassiniresources.com.au/west-musgrave-project/exploration/succoth-wa/`). Further prospects in the area surrounding Nebo-Babel, such as Yappsu, Esagila and Handpump, are currently being explored. Several other localities of the Musgrave

Province contain mineralisation, although none of them are currently economic. Maier et al. (2014, 2015) reported a PGE reef at Wingellina Hills although this study does not examine this finding. Furthermore, the top sections of the olivine gabbronoritic-troctolitic intrusions at the Bell Rock, Blackstone and Jameson Ranges exhibit an increase in magnetite abundance, occasionally forming magnetitite layers (e.g. Ballhaus and Glikson 1995; Glikson et al. 1996). At the Jameson Range intrusion these magnetite seams also contain increased levels of V and the PGEs (Maier et al. 2014, 2015).

The most prominent example of nonmagmatic mineralisation in the Musgrave Province are the Ni-laterite deposits near the Wingellina Hills and Claude Hills localities. The deposits were first discovered by the Southwestern Mining Company during their exploration activities in the 1950s (section 1.1). Metals X Limited currently holds the mineral rights to both deposits (Goode 2002; see also `http://www.metalsx.com.au/nickel/`). The deposit near Wingellina contains 167.5 Mt of mineralisation with 1 % Ni and 0.08 % Co, whereas the deposit at Claude Hills contains 33 Mt of mineralisation with 0.81 % Ni and 0.07 % Co (`http://www.metalsx.com.au/nickel/`).

1.4 Research objectives

This thesis discusses the petrogenesis and emplacement of the Giles Suite and its prospectivity for orthomagmatic Ni-Cu-PGE sulphide ore deposits, by studying three intrusive bodies in greater detail, namely the Bell Rock Range, Latitude Hill and Wingellina Hills intrusions. A combination of both traditional knowledge-driven methods of data analysis and interpretation are used as well as modern data-driven multivariate statistical techniques, that have become popular in many areas of science and technology, such as astronomy (Ball and Brunner 2010), quantum chemistry (Ramakrishnan et al. 2015), genomics (Huber et al. 2015), medical diagnosis (Kononenko 2001), energy systems engineering (Rudin et al. 2012) and many more.

One of the most striking features of the mafic-ultramafic intrusive magmatic activity during the Giles Event is the size of the earliest members of the Giles Suite (termed G1 and G2, respectively by Evins et al. 2010b,c). Important petrogenetic aspects that are studied here are the sourcing of the magmas within the Earth's mantle as well as subsequent assimilation and fractional crystallisation (AFC) processes. Previous studies identified multiple parental magmas for the different members of the Giles Suite (e.g. Ballhaus 1993; Ballhaus and Glikson 1995; Glikson et al. 1996; Evins et al. 2010b,c; Maier et al. 2014, 2015) and this thesis evaluates the potential relationships between those members. Geochemical and petrological methods restrict the focus of this study mainly on chemical dynamics, but wherever possible the emplacement of the above intrusions is also constrained. Particular aspects of the emplacement that are examined are the number of magma pulses and what petrogenetic changes, if any, occurred between them, as well as the overall timing of emplacement.

The mafic-ultramafic intrusions of the Giles Event are also interesting from an economic point of view because orthomagmatic Ni-Cu-PGE sulphide mineralisation is known to be associated with similar cumulate-textured rocks, such as at the Voisey's Bay Ni-Cu-

Co deposit in Canada (e.g. Li and Naldrett 1999; Ryan 2000; Scoates and Mitchell 2000). The petrography of sulphide minerals, the above petrogenetic constraints as well as chalcophile element signatures are used to discuss the economic potential of the intrusions for such deposits. Further, mineralised and unmineralised lithologies from the Nebo-Babel Ni-Cu-PGE deposit, the most significant discovery in the Musgrave Province so far, are used to extract a set of geochemical indicators for such mineralisation.

The combined results of this study are used to constrain the tectonic setting of the Musgrave Province during the Giles Event. Particularly, the relative importance of plate- and mantle-dynamics as the cause for the Giles Event is still a matter of debate (cf. Wingate et al. 2004; Evins et al. 2010b; Pirajno and Hoatson 2012; Smithies et al. 2015).

Several of the above research objectives are addressed with multivariate statistical methods. This choice was made to address the problem that the detection of petrogentic processes or subgroups within a population of rock samples can often be accomplished in multiple ways at the same time. For instance, testing for crustal contamination can be done using many different ratios of chemical concentrations, such as Ce/Nb, Ce/Yb, Cu/Zr, Pd/Zr and Th/Yb (e.g. Lightfoot and Keays 2005; Keays and Lightfoot 2010; Ihlenfeld and Keays 2011; Maier et al. 2015). Attempting to use several tests in a study can sometimes yield conflicting results and the choice is often made in favour of the set of variables that exhibits the 'clearest' trend and therefore appears most accessible for an interpretation, although cryptic variations can also carry relevant information. This study attempts to avoid the dangers of such subjective choices by approaching some of the research questions with multivariate techniques of dimensionality reduction and clustering. Straight-forward linear and hierarchical models are preferred over complex nonlinear models, such as neural networks, to retain the highest-possible interpretability.

1.5 Thesis structure

The thesis contains six chapters in total. This introduction into the subject as well as the geology and geography of the Musgrave Province is followed by chapters 2–5 which address the actual research questions outlined above (section 1.4). Each of these chapters is structured similar to a journal article to allow them to be read independently. While this approach entails some repetitions between chapters, they were kept to a minimum by describing much of the geological history in this introduction (section 1.2) and many methods in appendix A.

Chapters 2 and 3 cover the troctolitic and olivine gabbronoritic Bell Rock Range intrusion. Chapter 2 ('The Bell Rock Range intrusion I: petrography and mineral chemistry') contains the petrography and mineral chemistry in order to elucidate the petrogenesis and emplacement of the intrusive body. An attempt is made to subdivide of the intrusive body into smaller units. Chapter 3 ('The Bell Rock Range intrusion II: isotope and trace element geochemistry') contains an in-depth discussion of the whole-rock lithogeochemistry of the Bell Rock Range intrusion, including Sr-Nd-isotopes. The chapter adds constraints on magma sourcing and crustal contamination.

Chapter 4 ('Latitude Hill and Wingellina Hills layered intrusions and massive gabbros')

covers the layered intrusions at the Latitude Hill and Wingellina Hills localities using a similar approach to chapters 2 and 3. This chapter further revisits the boundary between the early stages of the Giles Event that led to the formation of the G1 and G2 members of the Giles Suite (as suggested by Evins et al. 2010b,c) and proposes a new petrogenetic model.

Chapter 5 ('Generation of exploration vectors with discriminant analysis') devises a set of geochemical indicator variables for Ni-Cu-PGE sulphide mineralisation from the chemical compositions of mineralised and barren rocks from the Nebo-Babel deposit. The Nebo-Babel deposit is a member of the Alcurra Dolerite, which hosts most of the known orthomagmatic sulphide mineralisation in the Musgrave Province. The results of this study may provide exploration vectors for such mineralisation in the mafic lithologies of the Giles Event.

The final chapter (6) summarises the results of chapters 2–5 and places them into the context of the research objectives outlined in section 1.4. Further, the results of the previous chapters are used to constrain the tectonic setting of the Musgrave Province during the Giles Event and suggestions for future research are made.

This thesis uses evidence from three different intrusions to discuss some important aspects of the petrogenesis of mafic-ultramafic layered and massive intrusions as well as their prospectivity for orthomagmatic Ni-Cu-PGE sulphide deposits (see section 1.4 above). For each research objective the most appropriate data for the purpose is used which causes an apparent imbalance in the subdivision of the thesis into individual chapters, devoting two chapters to one intrusion (chapters 2 and 3) and only one chapter to the other two intrusions (chapter 4).

1.6 Geography of the field area

The Bell Rock Range, Latitude Hill and Wingellina Hills intrusions are located on the map sheets *Cooper, WA sheet SG 52-10* (Daniels et al. 1971) of the 1:250 000 geological series and *Bell Rock, WA sheet 4645, 2nd edition* (Howard et al. 2009b) of the newer 1:100 000 geological series, respectively. Figure 1.3 shows a satellite image of the area containing the three intrusions. The field area is in a very remote region of central Australia, c. 550 km south-west of Alice Springs near the so called 'Surveyor Generals Corner' (26°S, 129°E). The closest communities are the Irrunytju (Wingellina) and Papulankutja (Blackstone) communities in Western Australia and the Pipalyatjara and Kalka communities in South Australia. The sampling sites of this study are all within c. 60 km or less of at least one of these communities.

This part of central Australia has a desert climate with annual mean temperatures of 15.9–29.3 °C. The lowest recorded temperature was –1.6 °C (June 1981) and the highest was 45.7 °C (January 2013). Rainfall is highly variable with some heavy rain events in the summer and dry spells over the winter months. The annual mean rainfall is 286.3 mm, but has ranged in the last 58 years from 38.0 mm (1961) to 843.4 mm (2001; all climate data is from the Bureau of Meteorology at `http://www.bom.gov.au/climate/averages/tables/cw_013017_All.shtml`). Due to the climate, the few waterbodies and streams

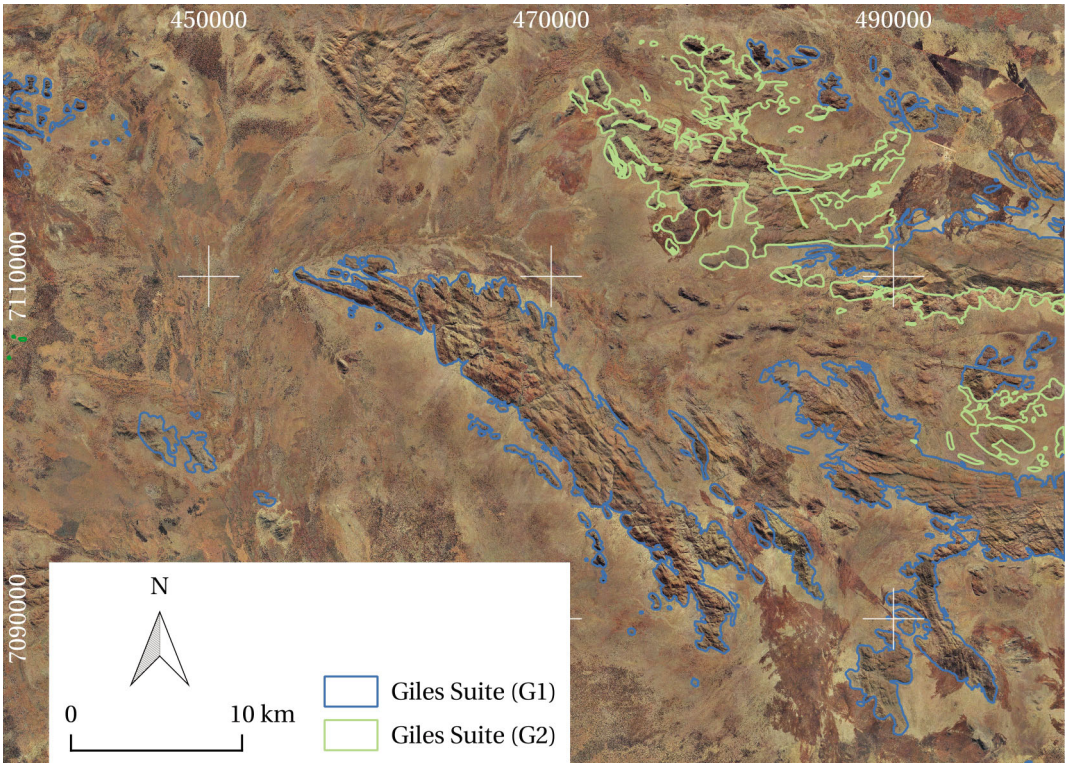

Figure 1.3 Orthophotograph of the field area showing the Bell Rock Range, Latitude Hill and Wingellina Hills intrusions. The blue and green outlines highlight outcrop of intrusions of the layered (G1) and massive (G2) suites, respectively. The shown section of the Musgrave Province is located entirely on the map sheet Bell Rock, WA sheet 4645 of the 1:100 000 Geological Series (Howard et al. 2009b, see figure 1.1 for the location of the intrusions within the Musgrave Province). All data are from Geological Survey of Western Australia (2011).

in the field area are ephemeral. The region borders the Australian bioregions of the Great Victoria Desert and the Central Ranges, hence, the flora consists mainly of acacia trees and shrubs, such as mulga trees, as well as spinifex grasses (`http://www.environment.gov.au/topics/land/national-reserve-system/science-maps-and-data/australias-bioregions-ibra/`).

Figures 1.4 and 1.5 show photographs of selected localities in the field area. Outcrop conditions can vary greatly from one field season to another due to changes in annual rainfall and vegetation (see above). Rock exposure is generally good for the intrusive bodies because they tend to form prominent elevations above the plains (figure 1.3). However, as seen on the photographs, sampling the intrusions can be made difficult in places by the patchy distribution of outcrops, vegetation and heavy weathering in-between. Country rocks surrounding the intrusions are commonly not exposed and covered with regolith.

Figure 1.4 Photographs of the field area and outcrop at the Bell Rock Range: **A**—view from the Bell Rock Range towards the parallel-running ridges (visible in the centre of the photograph) in the south-west; **B**—large-scale layering of the intrusion defined by several outcrops aligned along a competent layer with heavy weathering in-between; **C.1**—dolerite dyke (472 899 m E, 7 101 959 m N); **C.2**—chilled margin of dolerite dyke in photograph C.1; **D**—typical outcrop conditions showing common spheroidal weathering of coarse-grained massive rocks.

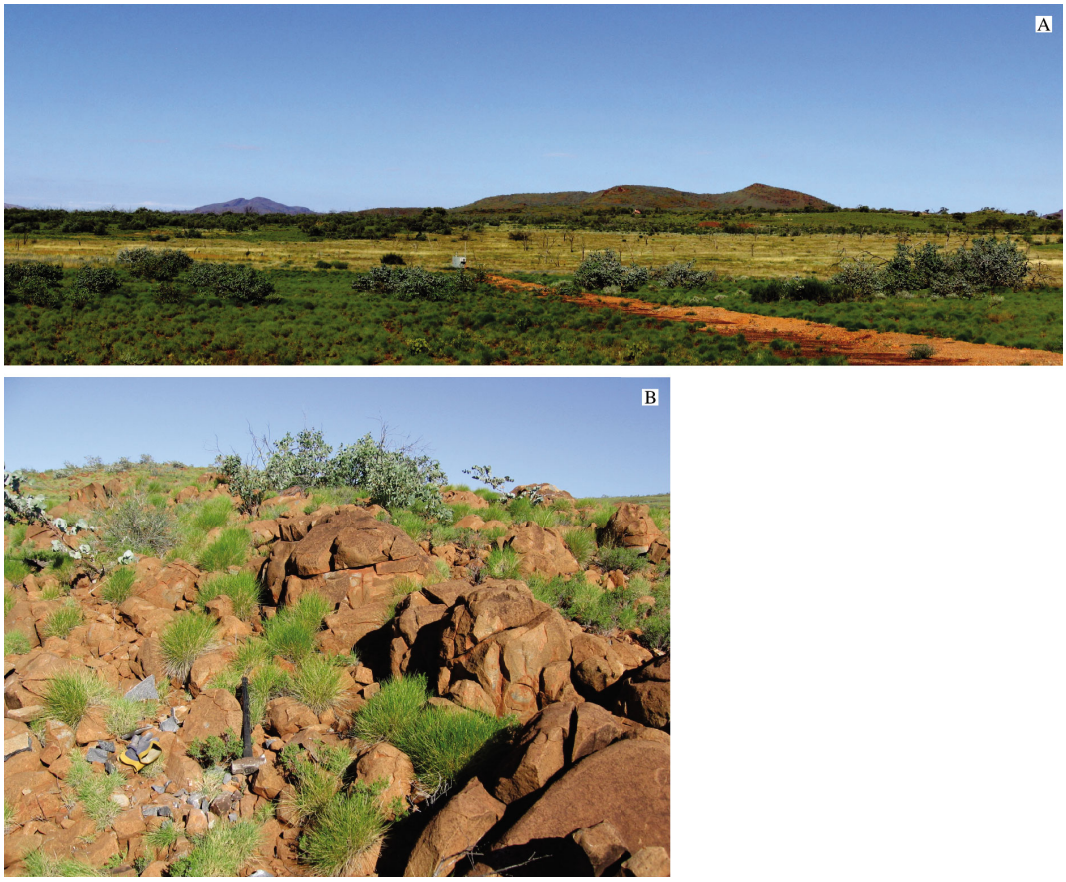

Figure 1.5 Photographs of the field area and outcrop at Latitude Hill and Wingellina Hills: **A**—view from the Metals X Limited exploration camp site towards east with the Wingellina Hills intrusion in thedistance. Layering of the intrusion falls towards south; **B**—typical outcrop conditions at Latitude Hill (498 973 m E, 7 116 416 m N) showing spheroidal to blocky weathering of coarse-grained massive rocks.

Chapter 2

The Bell Rock Range intrusion I: petrography and mineral chemistry

2.1 Introduction

The Giles Event in central Australia caused extensive melting of the Earth's mantle and lead to the formation of one of the largest known, yet underexplored, mafic-ultramafic igneous complexes that comprises c. 20 intrusions. The Bell Rock Range is one of the largest intrusive bodies that formed during this event and is part of a group of troctolitic and olivine gabbronoritic layered intrusions. Moreover, many previous studies have suggested that the Bell Rock Range may represent a segment of what might originally have been one of the largest known layered intrusive bodies (e.g. Nesbitt and Talbot 1966; Daniels 1974; Ballhaus and Glikson 1995; Glikson et al. 1996; Evins et al. 2010b,c; Aitken et al. 2013; Maier et al. 2014, 2015). The discovery of the Voisey's Bay Ni-Cu-Co deposit (e.g. Amelin et al. 1999; Li and Naldrett 1999) showed that large troctolitic intrusions can also host significant orthomagmatic sulphide ore deposits, which makes the Bell Rock Range intrusion an interesting exploration target for this deposit type.

Recent advances in the detailed textural analysis of cumulate rocks (e.g. Holness et al. 2007a,b, 2011), the study of processes within magma chambers (e.g. Marsh 2004; Marsh 2006; Egorova and Latypov 2012) and mineral-melt phase relationships between cumulus and intercumulus minerals (e.g. Boudreau 1999; Humphreys 2011; Matzen et al. 2012) provided new insights into the formation of layered intrusions, and thus, highlighted the importance and usefulness of petrography and mineral chemistry. Part of what makes the study of layered intrusions through the analysis of minerals instead of whole-rock samples so successful is that whole-rock compositions of cumulate rocks are often difficult to interpret, because they rarely represent liquid compositions. This chapter therefore constrains the petrogenesis of the lithologies at the Bell Rock Range, the emplacement of the intrusive body into the felsic country rocks as well as its prospectivity for the above type of sulphide ore deposits using petrographic and mineral chemical methods.

2.2 Geological setting

The Bell Rock Range intrusion is a gabbronoritic-olivine gabbronoritic-troctolitic layered intrusive body located in the Mesoproterozoic Musgrave Province, central Australia. The Musgrave Province (figure 2.1) is located between the North, South and West Australian Cratons and extends c. 800 km east-west and 350 km north-south. It is bounded to the north, east, south and west by the Neoproterozoic/Palaeozoic Amadeus, Eromanga, Officer and Canning basins, respectively. The south dipping Woodroffe Thrust, a major east-west trending structure, was active during the c. 570–530 Ma Petermann Orogeny (Camacho and Fanning 1995; Camacho 1997; Scrimgeour and Close 1999; Gregory et al. 2009; Raimondo et al. 2010) and divides the Musgrave Province into the northern amphibolite-facies Mulga Park Domain and the southern granulite-facies Fregon Domain (Camacho and Fanning 1995). Section 1.2.1 provides a detailed review of the basement lithologies and geological history prior to the Giles Event.

The Warakurna Supersuite comprises all igneous rocks formed during the Giles Event, a multi-phase magmatic event that lasted from c. 1090 to 1040 Ma and caused extensive intrusion and extrusion of mafic and felsic magmas in the failed Ngaanyatjarra Rift (Smithies et al. 2009a; Evins et al. 2010b,c; Aitken et al. 2013). Evins et al. (2010b,c) provided a detailed summary of the succession of the (at least) eight stages of the Giles Event. The extensive mafic-ultramafic layered intrusions and gabbroic plutons that formed during the Giles Event (Nesbitt and Kleeman 1964; Nesbitt and Talbot 1966; Daniels 1974; Ballhaus and Berry 1991; Ballhaus 1993; Ballhaus and Glikson 1995; Glikson et al. 1996; Maier et al. 2014) were in the past referred to as the 'Giles Complex' (section 1.1).

The intrusives were emplaced within age brackets defined by the Bentley Supergroup, the lower member of which defines phase one of the Giles Event (Evins et al. 2010b,c). Three major suites of extensive mafic-ultramafic rocks were identified by Evins et al. (2010b,c), constitute the main intrusive bodies in the complex and are referred to as G1, G2 and the Alcurra Dolerite, respectively. Some members of the Alcurra Dolerite were previously referred to as the G3 suite by Evins et al. (2010b,c) but Howard et al. (2015) pointed out the larger age bracket for the Alcurra Dolerite and geochemically similar rocks that cross-cut the upper Bentley Supergroup. The relationship of the Alcurra Dolerite to the Giles Suite is therefore currently somewhat ambiguous.

Phase two of the Giles Event involved the emplacement of the mafic-ultramafic layered G1 intrusions after the deposition of the lower Bentley Supergroup (Daniels 1974; Ballhaus and Glikson 1995; Glikson et al. 1996; Evins et al. 2010b,c). The G1 intrusions are a group of c. 20 intrusive bodies that were emplaced over an area that extends c. 550 km from east to west. A major review on the intrusions of the Giles Event was undertaken by Ballhaus and Glikson (1995) and Glikson et al. (1996), who broadly categorised the layered intrusions into either troctolitic, gabbroic or ultramafic intrusive bodies. The three types of intrusions are thus dominated by olivine gabbronoritic-troctolitic, (leuco-)gabbronoritic or pyroxenitic-peridotitic lithologies, respectively. In a more recent review, Maier et al. (2014) referred to the intrusions more generally as either mafic, mixed mafic-ultramafic or ultramafic.

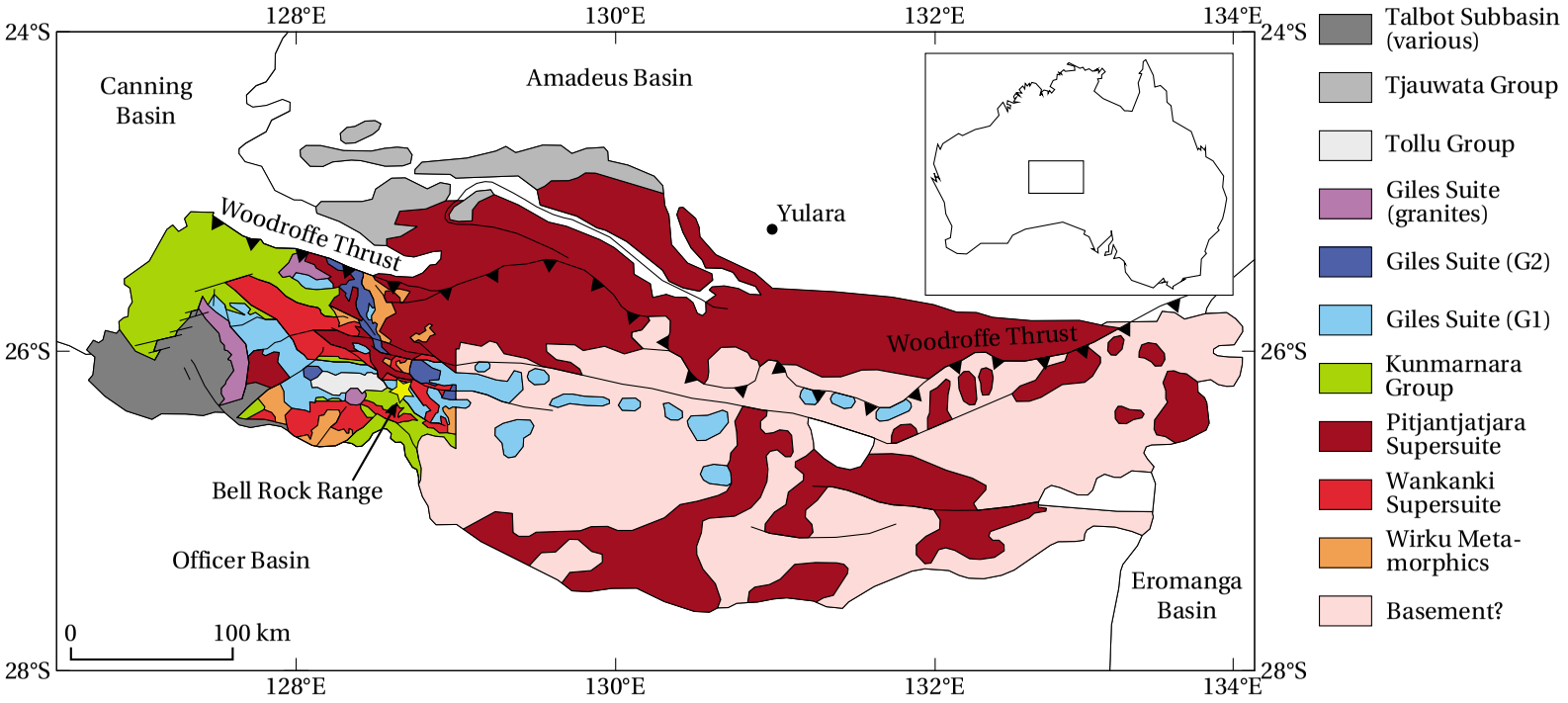

Figure 2.1 Geological map of the Musgrave Province, showing the location of the Bell Rock Range intrusion (modified after Howard et al. 2011a, 2015). The mafic-ultramafic layered and massive intrusions of the Giles Event are concentrated in the western parts of the Musgrave Province. The Bell Rock Range intrusion is located within a north-west to south-east trending chain of potentially genetically linked intrusive bodies (e.g. Daniels 1974; Glikson et al. 1996; Evins et al. 2010c; Maier et al. 2014). The inset map shows the location of the Musgrave Province in central Australia.

In rare cases where wall-rock contacts are exposed, they are mostly between the G1 intrusions and the greenschist-facies Kunmarnara Group (Howard et al. 2011b, 2015). An intrusive contact with felsic granulite at Latitude Hill (chapter 4) was reported by Ballhaus and Glikson (1995) and Glikson et al. (1996).

There has been much debate around the emplacement depths of the Giles intrusions because they appear to have intruded at different crustal levels. Goode and Moore (1975) for instance interpreted the Ewarara, Kalka and Gosse Pile intrusions in South Australia to have been emplaced at high pressures of 1–1.2 GPa, corresponding to a depth of c. 38–45 km. In contrast, Ballhaus and Berry (1991) estimated the pressure during crystallisation of the Wingellina Hills intrusion in Western Australia was 0.62–0.65 GPa, which is in agreement with emplacement at low- to mid-crustal levels (c. 24 km). And yet Evins et al. (2010b,c) propose the maximum emplacement depth to be c. 15 km mainly based on field relationships around the Blackstone Range and combined Jameson and Finlayson Ranges intrusion in Western Australia. Shallow crustal levels, at least for the Blackstone Range intrusion, are supported by an even more recent estimate of 0.1 GPa (<4 km; Maier et al. 2014). In summary, most studies agree on a broad shallowing trend from east to west (e.g. Daniels 1967; Nesbitt et al. 1970; Glikson et al. 1996; Maier et al. 2014). This is due to high-pressure crystallisation textures having been reported mainly from eastern intrusions (Moore 1971b; Goode and Moore 1975; Ballhaus and Berry 1991) and field relationships around some of the western intrusions suggesting shallow emplacement into the lower Bentley Supergroup (Evins et al. 2010b,c).

Geochronological data are still very sparse for the Giles intrusions. Sun et al. (1996) obtained an age of 1078 ± 3 Ma for a leucocratic dyke that was interpreted to be comagmatic with the Bell Rock Range intrusion. From field evidence, Howard et al. (2011a, 2015) concluded that the rock sample of Sun et al. (1996) was collected from a localised sill in the Kunmarnara Group and that the age therefore represents a minimum age for the Giles Event. More recently, Kirkland et al. (2011) obtained an age of 1076 ± 7 Ma for the Finlayson Range intrusion, which is a member of the G1 suite. Hence, an age bracket of c. 1078–1076 Ma has been proposed for phase two of the Giles Event (Howard et al. 2011a, 2015).

2.2.1 Bell Rock Range intrusion

The Bell Rock Range intrusion (figure 2.2) is a large northwest-southeast trending intrusive body with an exposed length of c. 35 km and width of c. 6 km (Daniels 1974; Ballhaus and Glikson 1995; Glikson et al. 1996; Maier et al. 2014). Several separate ridges run parallel directly southwest of the intrusive body and are separated from the latter by an up to c. 1 km wide plain without any outcrop, although the bedrock geology of the main intrusion and the ridges has been interpreted to be connected (Geological Survey of Western Australia 2011). Several legacy studies did not suggest a genetic relationship (e.g. Daniels 1974; Ballhaus and Glikson 1995; Glikson et al. 1996); this aspect is discussed in more depth in section 2.6.2. The intrusion is crosscut by microgabbroic dykes, predominantly along the base towards the northwestern margin (figure 2.2; see also descriptions in section 2.4.1). Maier et al. (2014) also report microgabbro sills around the top, a finding that was not

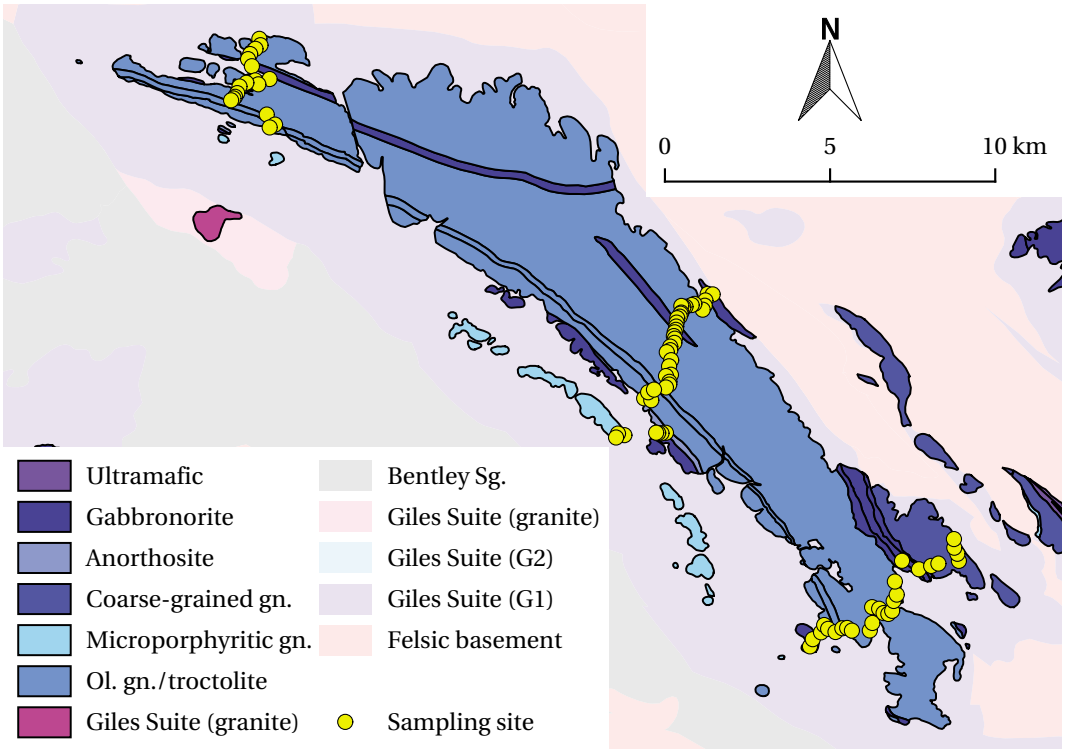

Figure 2.2 Geological map of the Bell Rock Range intrusion, indicating the locations of the sampling sites along the three sampling traverses in the northwest, centre and southeast of the intrusive body. Bold coloured areas show the surface outcrop with lithologies simplified from Howard et al. (2009b); light shaded areas show the interpreted bedrock geology (simplified from Howard et al. 2009b). The felsic basement includes the Wirku Metamorphics and the Wankanki and Pitjantjatjara Supersuites. Abbreviations are gn.—gabbronorite, Ol.—olivine, Sg.—supergroup.

observed during this study.

Country rock contacts are not exposed at the margins of the Bell Rock Range. The neighbouring and potentially genetically linked Blackstone Range intrusion is overlain by units of the Bentley Supergroup, thus, Maier et al. (2014) suggested the same would be true at the Bell Rock Range with the top contact being either eroded or fault-bound.

The Bell Rock Range intrusion is one of the most fractionated members of the Giles intrusions. The layered sequence of the intrusive body without the separate ridges is c. 4.4 km thick (see method of thickness/depth estimation in appendix A.1) and consists of magnetite-bearing olivine gabbronorites and troctolites with minor anorthosite. The intrusive body contains laterally continuous units that can be up to several hundreds of m thick, although there is occasional modal layering on a cm- to m-scale (figure 2.3). The cyclicity of layers on a large scale, however, is poorly developed. Magnetite occurs as a minor but common cumulus phase towards the top of the intrusive body. Glikson et al. (1996) and Maier et al. (2014) reported layers of magnetite in this part of the intrusion, but these layers were not observed during this study.

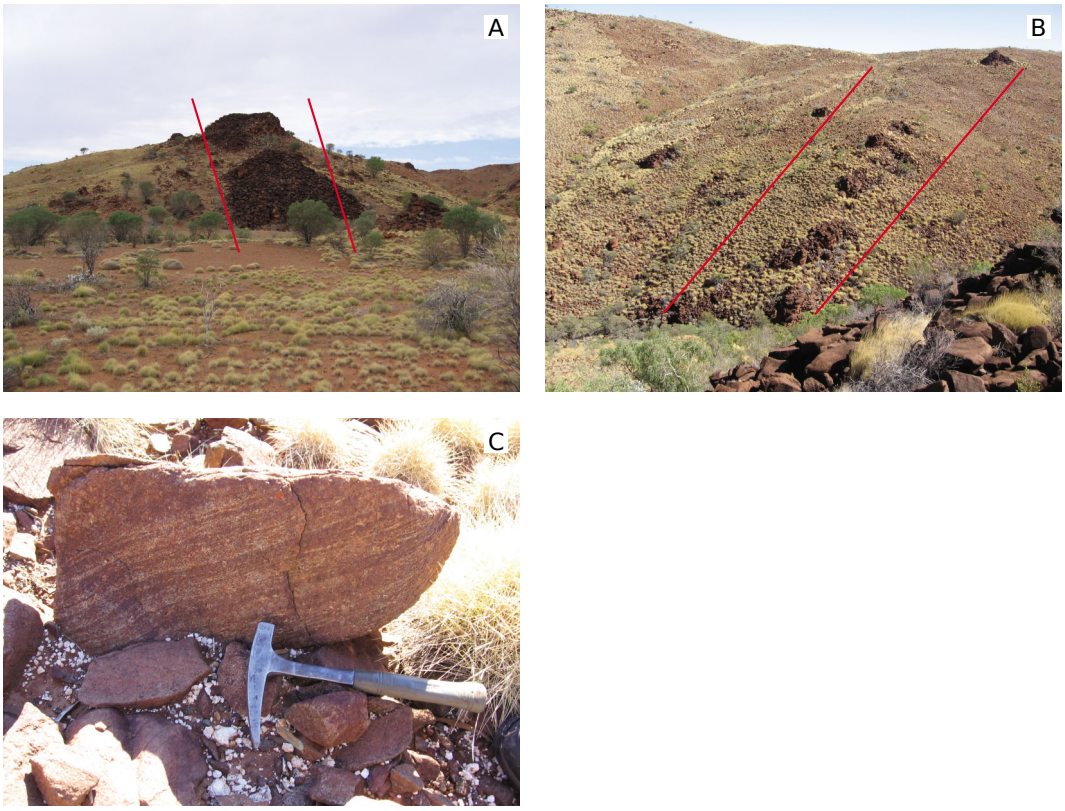

Figure 2.3 Photographs of igneous layering on different scales in the Bell Rock Range intrusion. Many lithologic units appear massive on a typical outcrop scale: **A**—several tens of metres thick layer at the south-eastern sampling traverse (view from 480 484 m E, 7 094 346 m N towards south-east; red lines indicate direction of layering); **B**—several tens of metres thick layer at the centre sampling traverse (view from 471 756 m E, 7 099 804 m N towards north-west; red lines indicate direction of layering); **C**—cm-scale layering defined by modal variations between olivine and plagioclase at an outcrop at the centre sampling traverse (471 582 m E, 7 099 466 m N).

Most previous authors assumed that the Bell Rock Range intrusion represents a segment of an originally much larger intrusive body (recently called the 'Mantamaru intrusion' by Maier et al. 2014, 2015), as suggested by the petrographically striking similarities between the Bell Rock and the Blackstone Ranges (Daniels 1974; Ballhaus and Glikson 1995; Glikson et al. 1996). Subsequent studies mentioned the gabbronoritic-troctolitic Jameson and Finlayson Ranges as well as the gabbroic Michael Hills and Cavenagh Range intrusions as potential members, forming an intrusive body that would have been over 170 km long, 25 km wide and 10 km thick (Evins et al. 2010b,c; Maier et al. 2014, 2015). The displacement of the individual members of this intrusion was suggested to have happened during the Petermann Orogeny.

Traverse	n	$\bar{\mathbf{a}}$	$d_{\max}$ (m)
South-east	27	241/09	5487
Centre	42	226/06	5410
North-west	18	017/04	2743

Table 2.1 Metadata for the three sampling traverses across the Bell Rock Range intrusion, along which samples were collected during the 2010 field season. Data include the total number of samples per traverse n, average values for the attitude $\bar{\mathbf{a}}$ of the poles of igneous layering planes and an estimate of the thickness of the intrusive body along the traverse d_{max} in metres (i.e. the estimated depth of the lowermost sample; see appendix A.1 for the estimation method).

2.3 Sampling and analytical procedures

A total of 87 samples were collected between March and April 2010 along three sampling traverses across the Bell Rock Range intrusion. The traverses ran approximately orthogonal to the direction of igneous layering (table 2.1 and figure 2.2). The collected rock samples can be broadly subdivided into three groups: (1) 77 samples from the main body of the intrusion, (2) seven micrograbbros and (3) three samples collected from the separate, parallel-running ridges (see description of the Bell Rock Range intrusion in section 2.2.1).

Petrographic descriptions (section 2.4) were undertaken on the same polished thin-sections that were used to determine the chemical compositions of mineral phases via electron beam microprobe analysis (EMPA) (section 2.5). Analyses were done via wavelength-dispersive spectroscopy (WDS) at the School of Earth Sciences of the University of Melbourne, Australia, using a Cameca SX 50 microprobe. The analyses were carried out in several batches operating under beam currents of 35.1–35.77 kV and an accelerating current of 14.92 kV. The take off angle was 40° and the tilt and azimuth angles were 0°. The results of the mineral chemical analyses are in appendix B.

The stratigraphic depth for individual samples was estimated according to the procedure described in appendix A.1; unless stated otherwise, the conversions between lithostatic pressure and depth were calculated assuming an average density of felsic continental crust $\rho = 2.7\,\mathrm{g/cm^3}$ and a gravitational acceleration $g = 9.81\,\mathrm{m/s^2}$.

2.4 Petrographic descriptions of the lithologies

The different lithologic units that are identified in the Bell Rock Range intrusion in this study are anorthosite (ANO), olivine gabbronorite and troctolite (OGT), olivine gabbronorite adcumulate (OGA) and coarse-grained gabbronorite (CGG) within the main body of the intrusion. Furthermore, late-intrusive dykes composed of microgabbronorite (MCG) are present as well as rocks in the parallel-running ridges, which are classified as microporphyritic gabbronorite (MPG). Figure 2.4 shows micrographs of all lithologies.

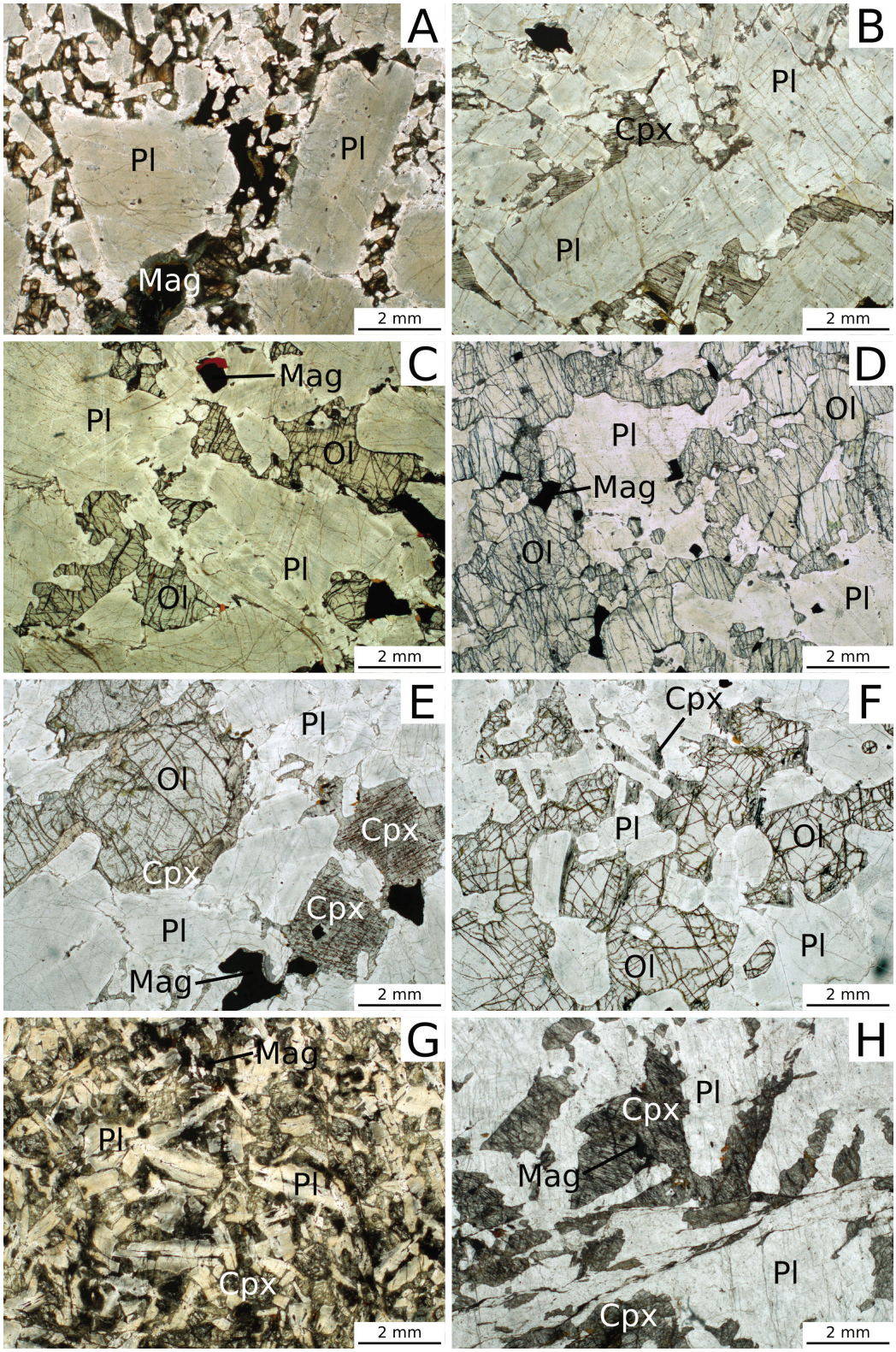
A
Pl
Pl
Mag
2 mm
B
Pl
Cpx
Pl
2 mm
C
Mag
Pl
Ol
Pl
Ol
2 mm
D
Ol
Pl
Mag
Ol
Pl
2 mm
E
Pl
Ol
Cpx
Cpx
Cpx
Pl
Mag
2 mm
F
Cpx
Pl
Ol
Pl
Ol
2 mm
G
Mag
Pl
Pl
Cpx
2 mm
H
Pl
Cpx
Mag
Pl
Cpx
2 mm

Figure 2.4 Micrographs of representative thin sections showing the lithologic units of the Bell Rock Range intrusion: **A**—microporphyritic gabbronorite (MPG) from the parallel-running ridges with large euhedral cumulus plagioclase in a fine- to medium-grained matrix comprising plagioclase, ortho- and clinopyroxene and magnetite (sample no. 191 872); **B**—anorthosite (ANO) with textural similarity to the MPG: large euhedral to subhedral plagioclase phenocrysts within a medium-grained matrix of plagioclase and clinopyroxene (sample no. 191 867); **C**—troctolitic member of the olivine gabbronorite and troctolite (OGT) with cumulus plagioclase, magnetite and ilmenite and intercumulus olivine (sample no. 191 856); **D**—olivine gabbronorite adcumulate (OGA) with cumulus plagioclase and olivine as well as minor intercumulus magnetite and ilmenite (sample no. 191 865); **E**—olivine gabbronoritic member of the OGT with cumulus plagioclase and relatively high amounts of intercumlus clinopyroxene, olivine as well as magnetite and ilmenite (sample no. 191 863); **F**—OGA with plagioclase and olivine as cumulus phases and minor intercumulus clinopyroxene (sample no. 191 860); **G**—microgabbronorite (MCG) with small- to medium-sized cumulus plagioclase laths in a fine-grained matrix of clinopyroxene, magnetite and amphibole (sample no. 191 854); **H**—coarse-grained gabbronorite (CGG) with cumulus plagioclase and intercumlus clinopyroxene and magnetite (sample no. 191 832). All samples are from the centre traverse; abbreviations used in the micrographs are Pl—plagioclase, Ol—olivine, Cpx—clinopyroxene, Opx—orthopyroxene, Bt—biotite, Mag—magnetite, Ilm—ilmenite and Amp—amphibole.

As a general rule, plagioclase is a cumulus phase in rocks of the main body of the Bell Rock Range intrusion. In contrast, clinopyroxene is always an intercumulus phase while olivine occurs in both cumulus and intercumlus assemblages (figure 2.4). Many differences in the lithologies thus merely reflect variations in the relative amount of interstitial space and therefore plagioclase, ortho- and clinopyroxene as well as olivine abundance. In particular, differences between OGT and OGA are often transitional: towards the top of the intrusive body, olivine and Fe-Ti-oxides occur more often as a cumulus phase together with plagioclase. Reaction textures such as symplectites occur in all major lithologic units of the main intrusion except CGG.

A distinct textural difference is apparent between the MPG and most units of the main body, except to the ANO, which are similar with respect to the bimodal grain size distribution (figure 2.4). Daniels (1974, p. 137) described the rocks of the parallel-running ridges as 'uralitized gabbroic masses' that intruded into the Tollu Group. It is unclear as to whether they are part of the Bell Rock Range intrusion (see discussion in section 2.6.2).

Microgabbro dykes were reported in most previous studies (e.g. Ballhaus and Glikson 1995; Glikson et al. 1996; Howard et al. 2009c). However, it is unclear whether the lithologies that were sampled for this study are the exact same ones that were sampled during previous studies, because the classification of different suites of dykes has been treated inconsistently across previous studies.

2.4.1 Microgabbronorite (MCG)

The late-intrusive dykes are assigned to the lithologic unit MCG (figure 2.4). Textural and mineralogical findings largely confirm previous studies (e.g. Ballhaus and Glikson 1995; Glikson et al. 1996) in that they consist of mostly fine-grained gabbronorites with an

ophitic to subophitic texture. Plagioclase laths of up to 2 mm length represent the main cumulus phase with clino- and orthopyroxene, biotite, magnetite and ilmenite in the interstitial spaces. Grain sizes of interstitial minerals are <250 µm. Fe-Ti-oxides are particularly abundant while olivine is commonly absent. The MCG are mineralogically similar to CGG (cf. section 2.4.5) but are texturally very different. One sample of MCG (sample ID 191 854) is slightly coarser-grained than the other samples and contains olivine.

2.4.2 Anorthosite (ANO)

The ANO occurs towards the top of the main intrusive body along the south-eastern and centre traverses, just below the top section of CGG. The ANO exhibits a bimondal grain-size distribution with coarse- and fine-grained cumulus plagioclase laths and intercumlus clinopyroxene. Magnetite occurs as lamellae in clinopyroxene and as intercumulus phase in rims around clinopyroxene and in interstitial spaces. Glikson et al. (1996) report minor intercumulus olivine and orthopyroxene oikocrysts; however, the Cross, Iddings, Pirsson, Washington (CIPW) norms indicate that there is less than 1 vol% olivine in the ANO rocks. Orthopyroxene exhibits magnetite exsolution within coronas. Biotite and amphibole are common accessory phases, found in assemblages with magnetite and/or rims around the latter. Sulphides are only an accessory phase and occur within small cracks and together with interstitial magnetite. Where present, sulphides are commonly chalcopyrite ($CuFeS_2$) with minor bornite (Cu_5FeS_4); Ni-sulphides are absent.

2.4.3 Olivine gabbronorite and troctolite (OGT)

The troctolites are grouped together with the olivine gabbronorites into the OGT because changes between the two rock types are gradual rather than creating a sharp contrast. The key criteria in this context is the normative pyroxene content: some members of this lithologic group contain normative total pyroxene of <5 vol% (hence, they are troctolites) while most contain anywhere between 0 and 30 vol% clinopyroxene as well as between 2 and 15 vol% orthopyroxene. The unit is very variable in terms of its remaining major normative mineral phase. Plagioclase contents vary between 34 82vol%, olivine between 5 35vol%; yet, aside from these modal variations all members of this lithologic unit are texturally similar (figure 2.4; see in particular micrographs **C** and **E**).

Layers of this lithologic unit up to several hundred metres thick occur throughout the intrusive body. They contain laths of cumulus plagioclase, with some cumulus but predominantly intercumulus olivine as well as intercumulus clino- and orthopyroxene; the latter commonly occurs in rims around olivine. Magnetite lamellae are common in both pyroxenes and is also a frequent intercumulus phase. It commonly contains ilmenite lamellae; small amounts of accessory sulphides are also present together with the other interstitial phases. The sulphide phases are similar to the ones found in ANO, i.e. they are commonly chalcopyrite ($CuFeS_2$) with minor bornite (Cu_5FeS_4). They occur within small cracks and also together with interstitial magnetite. Accessory biotite is associated with the intercumulus phases, predominantly with magnetite, and is interpreted to be postmagmatic by Ballhaus and Glikson (1995) and Glikson et al. (1996). Similar to the

ANO unit (section 2.4.2), biotite and amphibole are common accessory phases commonly associated with magnetite and often in rims around the latter.

Members of the OGT that are low in pyroxene (troctolites s.s., see above) exhibit strong variations in the remaining major mineral phase abundancies as well as variations in texture. They consist of medium to coarse grained cumulus plagioclase and (mostly) intercumlus olivine and variable amounts of intercumulus magnetite. At higher stratigraphic levels magnetite occurs as part of the cumulus assemblage (e.g. sample 191 864; magnetite seams were also reported by Ballhaus and Glikson 1995; Glikson et al. 1996). Common accessory phases are biotite together with amphibole.

Poikilitic textures are common and can generally be grouped into two types, i.e. (1) cumulus plagioclase in large olivine oikocrysts (this type of intercumulus olivine commonly has clinopyroxene coronas and occasional intercumlus magnetite; e.g. sample 191 842), and (2) cumulus plagioclase and olivine in clinopyroxene oikocrysts (coronas of clinopyroxene are rare on cumulus olivine grains; e.g. sample 191 855) The OGT samples contain thin coronas of orthopyroxenes that form outwards oriented prisms or 'columns' around olivine grains (e.g. sample 191 843). Such assemblages are also frequently associated with magnetite exsolution. Symplectites involving olivine, ortho- and clinopyroxene or magnetite are common in the OGT. These are believed to be the products of subsolidus rections as will be discussed in section 2.6.1.

2.4.4 Olivine gabbronorite adcumulate (OGA)

Although chemically similar to OGT (see discussion of whole-rock chemical compositions in chapter 3), this lithological unit marks a distinct change in igneous differentiation because olivine is a commonc umulus phase together with plagioclase. The unit is relatively rich in olivine compared to other units. Olivine often exhibits thin coronas of orthopyroxene (e.g. sample 191 865). Although poikilitic textures are preserved they are less frequent than in OGT. The OGA contain little interstitial spaces, thus, they contain mostly <5 vol% intercumulus clinopyroxene oikocrysts that engulf olivine grains and can contain exsolved magnetite. The crystallisation of plagioclase and olivine means that some observed oikocrysts are plagioclase with olivine chadacrysts and vice versa, since both phases crystallised together. Similar to the previous units (ANO and OGT), Fe-Cu-rich sulphides occur as accessory phases, that are frequently associated with magnetite.

Since most reaction textures are related to the intercumulus liquid they are rarer in the OGA compared to the OGT. Nevertheless, orthopyroxene occurs in thin coronas around cumulus olivine and is also associated with magnetite, which can exhibit biotite and amphibole rims. Coronas formed during reactions such as olivine with orthopyroxene and magnetite coronas often have symplectitic textures within the corona. These coronas are often associated with partial replacement of olivine.

2.4.5 Coarse-grained gabbronorite (CGG)

These coarse-grained poikilitic (subophitic?) gabbros are exposed at the base of the intrusive body and also towards the top in some areas. The unit comprises large cumulus

plagioclase grains and intercumulus clinopyroxene with minor additional intercumulus plagioclase. Clinopyroxene contains lamellae of magnetite although interstitial magnetite is also present and often surrounded by biotite and/or amphibole; orthopyroxene is present but rare. Daniels (1974) reported a poikilitic unit at the base of Bell Rock Range, which might be the CGG. Even though the samples of this unit are virtually olivine-free, all samples of this lithologic unit are olivine-normative (<10 wt%). Biotite and amphibole are common accessory phases, commonly found as rims around magnetite. Other opaque phases are accessory Cu-rich sulphides as in the units ANO, OGT and OGA.

2.4.6 Microporphyritic gabbronorite (MPG)

Unlike the main body of the Bell Rock Range intrusion, the MPG within the parallel-running ridges are not internally layered. The rocks of this unit are quartz normative and contain the largest amount of normative alkali-feldspar found in the Bell Rock Range intrusion (c. 7–8 vol%). The MPG have a porphyritic texture and contain plagioclase phenocrysts in a fine-grained matrix consisting of plagioclase and clinopyroxene as well as interstitial magnetite and ilmenite; dark-green amphibole with interstitial graphically intergrown quartz and K-feldspar is also present. The relative amount of phenocrystic plagioclase decreases from bottom to top within the unit, whereas the amount of interstitial space increases.

2.5 Chemical composition of mineral phases

The mineral chemistry was determined for samples from the centre traverse (see section 2.3 for details on the method). Figure 2.5 shows the compositional range in chemostratigraphic logs. Anorthite contents in plagioclase within the main body are variable with An_{51-79} although the sample averages remain relatively stable across the whole thickness of the intrusion. There are slight peaks in An at the centre of the intrusive body with An-values dropping towards the top and bottom. Olivine compositions are overall highly variable in the main body (Fo_{49-68}) with a slight increase from the bottom towards the top half of the intrusion. Two sharp upward compositional changes towards the lowest An and Fo contents in plagioclase and olivine, respectively, coincide and occur at a depth of c. 2500 m (figure 2.5). The top section of the main body of the Bell Rock Range intrusion contains the largest continuous layer of olivine-rich OGA. The remaining variations in An and Fo contents are cryptic. Clinopyroxenes are typical Mg-rich (diopside with minor augite and pigeonite) with strong endmember variations of Wo_{9-55}, En_{37-63} and Fs_{2-29}. Accessory minerals are chromite with some Al-spinel (probably hercynite).

Table 2.2 and figure 2.6 show the compositions of the major mineral phases in each lithologic unit. The strongest variations in mineral compositions occur between the lithologies of the main body (ANO, CGG, OGA and OGT) and the MPG from the parallel-running ridges and the late-stage MCG, respectively. The mineral chemistry of the MPG from the parallel-running ridges differs distinctly from the main body of the intrusion: they have by far the most Fe-rich olivines (Fo_{15}) and pyroxenes (clinopyroxenes—Wo_{6-44},

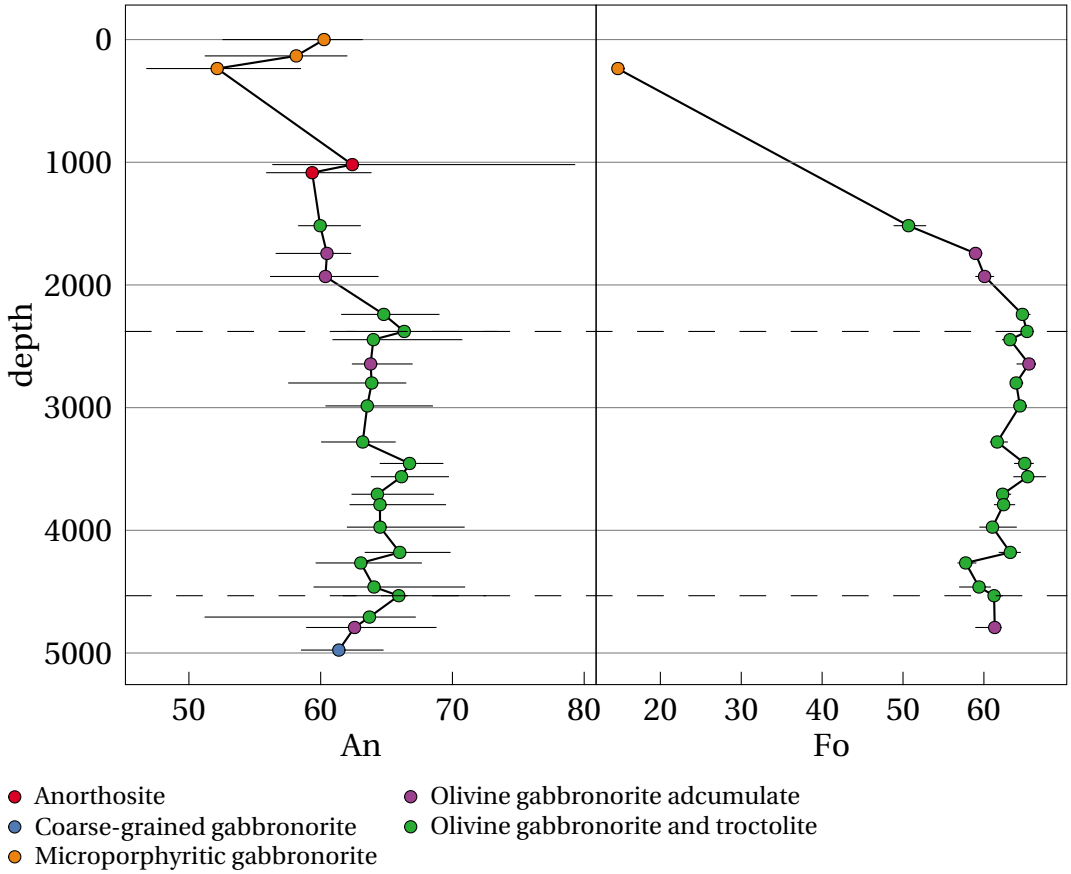

Figure 2.5 Chemostratigraphic log of olivine and plagioclase compositions. The length of the error bars represents the total range of values. The intrusive body can be subdivided into three zones (indicated by the dashed lines), with a slight anti-correlation at the bottom, a cryptic pattern at the centre and a significant drop of the forsterite content towards the top of the main body.

En_{32-42}, Fs_{16-56}; orthopyroxenes—En_{36-39}, Fs_{58-61}) as well as variable but relatively Ca-poor plagioclase compositions (An_{47-63}). From the MCG, only one sample (sample no. 191 854) contains olivine (Fo_{59-73}). Plagioclase and clinopyroxene in this sample are both Ca-rich with An_{67-72} as well as Wo_{31-41}, En_{49-55} and Fs_{10-13}, respectively. The plagioclase compositions in the doleritic samples are less primitive with An_{47-62}; some of the clinopyroxenes are extremely Ca-poor (pigeonite), similar to some samples from the main body (see above).

Table 2.2 Summary statistics of the relative compositions of the mineral endmembers An, Fo, Di and En in the Bell Rock Range intrusion. The table contains the extrema (min. and max.), average values (median and mean) as well as the 1st and 3rd quartiles (Q_1 and Q_3). The names and abbreviations of the lithologies are anorthosite (ANO), coarse-grained gabbronorite (CGG), microgabbronorite (MCG), microporphyritic gabbronorite (MPG), olivine gabbronorite adcumulate (OGA) and olivine gabbronorite and troctolite (OGT).

Lithology	Min.	Q_1	Median	Mean	Q_3	Max.
Anorthite						
Anorthosite	55.90	57.90	59.58	60.57	60.47	79.28
Coarse-grained gabbronorite	58.54	60.22	61.03	61.38	62.64	64.73
Microgabbronorite	47.37	50.72	56.60	57.05	60.45	71.92
Microporphyritic gabbronorite	46.81	53.23	58.94	57.15	61.06	63.16
Olivine gabbronorite adcumulate	56.20	60.51	62.11	61.99	63.36	68.75
Olivine gabbronorite and troctolite	51.23	62.68	63.97	64.24	65.82	73.39
Forsterite						
Microgabbronorite	59.10	63.00	64.20	66.38	72.70	72.90
Microporphyritic gabbronorite	14.70	14.72	14.75	14.75	14.78	14.80
Olivine gabbronorite adcumulate	58.20	59.90	61.15	61.68	62.05	66.30
Olivine gabbronorite and troctolite	48.90	60.90	62.60	61.88	64.50	67.60
Enstatite (clinopyroxene)						
Anorthosite	37.06	37.06	37.06	37.06	37.06	37.06
Microgabbronorite	48.73	51.37	52.29	52.66	54.96	55.22
Microporphyritic gabbronorite	31.87	34.76	36.68	37.57	40.86	42.17
Olivine gabbronorite adcumulate	42.50	43.02	43.94	45.08	45.24	60.97
Olivine gabbronorite and troctolite	39.16	43.00	43.86	44.79	45.04	62.56
Enstatite (orthopyroxene)						
Microgabbronorite	54.47	54.59	55.05	55.60	56.40	58.54
Microporphyritic gabbronorite	36.21	36.80	37.66	37.44	37.68	38.82
Olivine gabbronorite adcumulate	67.56	68.56	70.06	69.68	70.48	71.73
Olivine gabbronorite and troctolite	60.92	69.38	71.21	71.34	73.18	99.62

2.6 Discussion

2.6.1 Constraints on the petrogenesis

The mineral chemistry (section 2.5) shows that cumulus and intercumulus phases in the different lithologies from the Bell Rock Range area may have crystallised from magmas of varying degrees of fractionation. If individual samples are in fact representative of relatively thick igneous layers within the intrusive body (section 2.2.1), this would indicate a significant degree of mobility of intercumulus liquid within the pile of cumulate minerals. It is therefore likely that the large-scale layering within the Bell Rock Range intrusion has

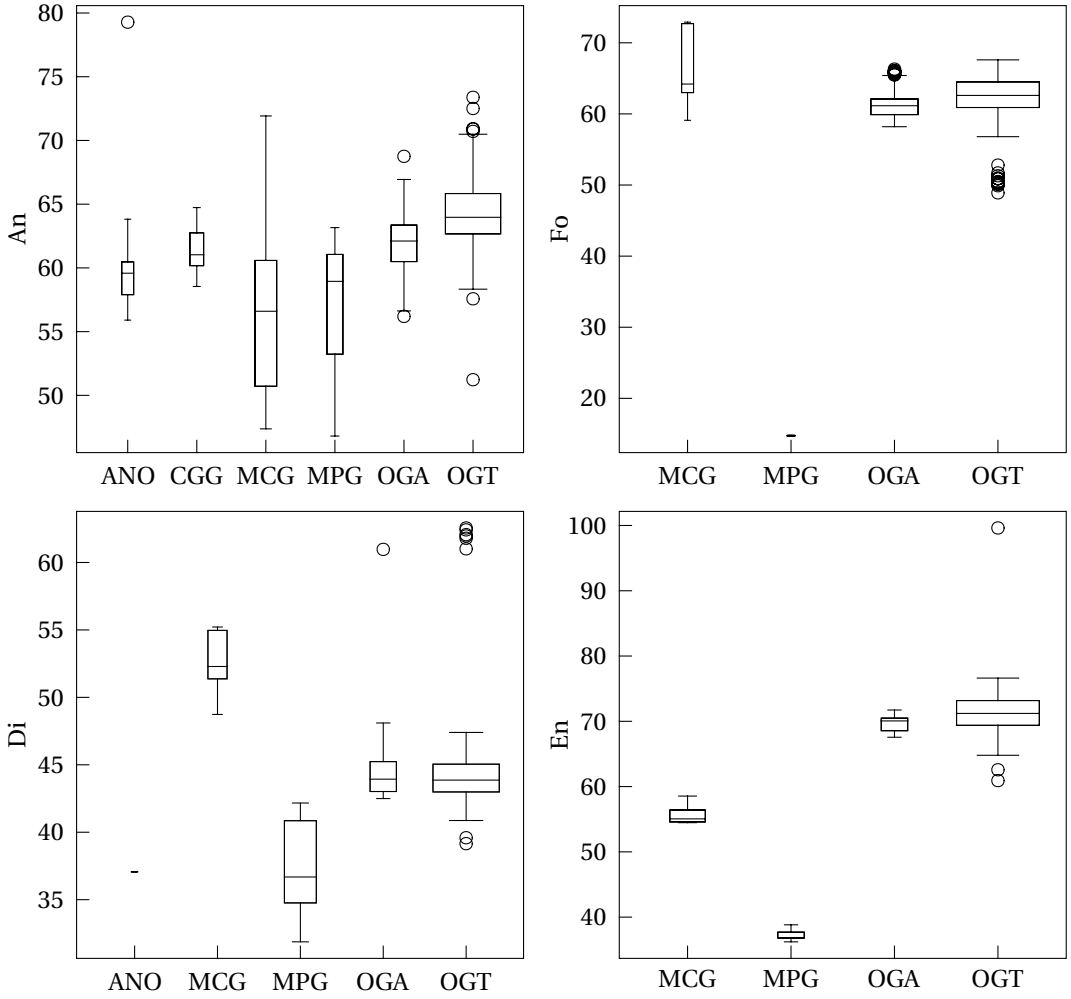

Figure 2.6 Boxplots of mineral compositions at Bell Rock Range. Outliers are defined as being located 1.5 times the interquartile range above the upper or below the lower quartile, respectively. The widths of the boxes are proportional to the square roots of the numbers of observations in the groups.

at least in part been formed by dynamic processes, i.e. involving internal transport of melt and/or crystals (e.g. Namur et al. 2015) and that the cumulus phases in those cases were not formed in equilibrium with the surrounding liquid. For instance, Sanfilippo et al. (2013) recently proposed that primitive plagioclase-rich troctolites from the Godzilla Megamullion were the result of an anorthositic cumulate from a mid-ocean ridge basalt (MORB)-type melt with new melt that crystallised oikocrystic olivine, clinopyroxene and a second generation of plagioclase. Applied to the Bell Rock Range intrusion, this would mean that each sample of the olivine gabbronorites and troctolites could have formed from multiple chemically different melt batches that formed the cumulus and intercumulus phases, respectively.

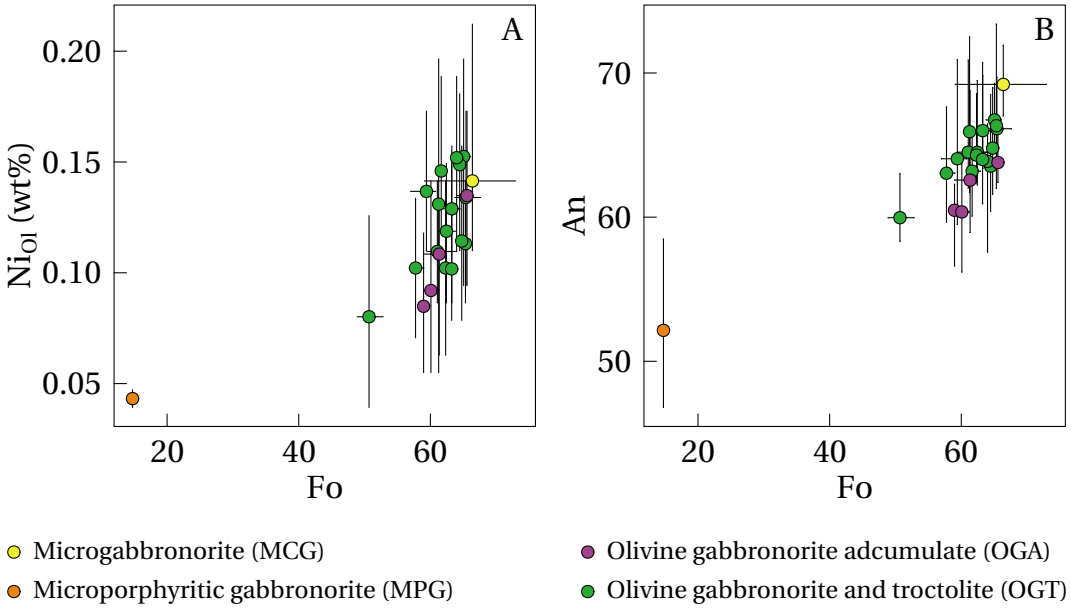

Figure 2.7 Ni and An versus Fo contents in the Bell Rock Range intrusion: **A**—Ni versus Fo contents of olivines from the Bell Rock Range intrusion; **B**—An versus Fo contents in olivine-bearing lithologies from the Bell Rock Range intrusion (error bars in both diagrams represent the total range of values). The microporphyritic gabbronorite (MPG) from the parallel-running ridges are strongly fractionated with the lowest Ni and An at low Fo contents. The most primitive sample is a late-stage member of the MCG (sample no. 191 854).

Plagioclase is the main cumulus phase within the main body of the Bell Rock Range intrusion and one of the major phases in the parallel-running ridges as well as the late-stage dykes. For plagioclase to crystallise out of a mafic melt before clinopyroxene and olivine the melt would have to contain very large relative amounts of Ca and in particular Al and be at a pressure of no more than 1.5 GPa to support the stability of anorthite, as can be seen from Di-An-Fo phase relationships (Presnall et al. 1978). On the other hand, if plagioclase crystallised later it must have been separated by a dynamic layer-forming process that involved movement of minerals and/or melt (Namur et al. 2015). For instance, dynamic processes that are known to form anorthositic layers are, according to Namur et al. (2015), crystal flotation (Namur et al. 2011) or vertical migration of liquid within the crystal mush, as e.g. suggested for the Stillwater Complex (Boudreau 1999). These could be viable models for the petrogenesis of the lithologic units of the ANO and the OGT, since plagioclase is the only apparent cumulus phase in these lithologies.

Olivines are another major phase and can account for much of a bulk rock's Ni budget, thus, the Fo versus Ni subcomposition carries information on magma sourcing in the mantle as well as early saturation of a magma with S. Several trends are visible in this subcomposition for olivines from the Bell Rock Range area (figure 2.7). The contents of Fo and Ni in olivine correlate positively, which is the result of normal fractionation where Ni substitutes for Mg in the crystal lattice. One of the main difference between the OGA

and the OGT is that olivine is intercumulus in the latter (section 2.4). Figure 2.7 further shows that there is a slight tendency for cumulus olivine in the OGA to contain less Ni at Fo contents that are similar to the OGT. The only exception to this is sample 191 856 from the OGT, which contains strongly fractionated olivines in its intercumulus liquid that have strikingly low concentrations of Ni. Ni is a highly chalcophile element and a sulphide phase, if present prior to olivine crystallisation, should cause a noticeable Ni-depletion in the magma and consequently in olivines, too. However, since the olivines are generally not strongly depleted in Ni and the differences between cumulus and intercumulus olivines are only subtle, the two different trends are not explained by the presence of a sulphide phase. Instead, the pressure and temperature dependency of Ni partitioning between olivine and a silicate melt readily explains the observed trends. In an experimental study on MORB compositions, Matzen et al. (2012) found that the solid-liquid partition coefficient for Ni in olivine $D_{\mathrm{Ni}}^{\mathrm{s/l}}$ increases with decreasing pressure and temperature. Thus, the cumulus olivine in the OGA may have crystallised earlier and at greater depth (e.g. in a staging chamber), causing Ni to partition stronger into the liquid phase. Later (intercumulus) olivine in the OGT crystallised at shallower levels, causing slightly higher Ni contents.

The Ni contents of olivine have also been used by Sobolev et al. (2005) to constrain the mantle source during partial melting in mantle plume settings. These authors thought that the high Ni contents in combination with high $D_{\mathrm{Ni}}^{\mathrm{s/l}}$ suggest that olivine is absent during partial melting. However, the study of Matzen et al. (2012) shows that melting of peridotite at high temperatures causes strong Ni partitioning into the melt. Subsequent crystallisation at lower pressures and temperatures is then able to produce Fo-rich olivine with Ni contents above the original mantle compositions. This model is accepted here, because it is more consistent with constraints on the mantle source from the whole-rock chemistry (chapter 3).

Finally, the MPG from the parallel-running ridges are the most fractionated rocks. The significant compositional difference in their major mineral phases and the apparent lack of any rocks that would link them with the lithologies of the main body may indicate that they are genetically unrelated.

The comparision of the compositions of An and Fo contents in plagioclase and olivine, respectively, shows that both mineral compositions correlate positively with each other (figure 2.7), which is in general agreement with normal magmatic fractionation and underlines the trends along depth in the chemostratigraphic logs (figure 2.5). Samples from the main body of the intrusion (OGA and OGT) are located between the MCG and the MPG within the compositional space. Both lithologies form a linear fractionation array, however, olivine in the OGA is commonly richer in Fo at similar An contents, compared to the OGT. Considering that olivine in the OGA is a cumulus phase, this confirms that the OGA crystallised before the OGT (see discussion on Ni in olivine above), with plagioclase and olivine on the liquidus. After continued fractionation, olivine crystallisation may have ceased, leaving plagioclase as the only cumulus phase. The intercumulus olivine in the OGT crystallised later and consequently is stronger fractionated than cumulus olivine in the OGA.

Subsolidus reactions

A very common feature of the lithologies of the ANO, OGA and OGT are coronas and symplectites caused by subsolidus reactions. Such coronas are common in olivine gabbronoritic and troctolitic intrusions and were for instance also reported from the Niquelândia layered igneous complex in Brazil (Candia et al. 1989), and interpreted as evidence for subsolidus re-equilibration. Candia et al. (1989) report reactions of the type

$$\mathrm{Ol} + \mathrm{Pl} \rightarrow \mathrm{Opx} + (\mathrm{Cpx} + \mathrm{Spl})_{\mathrm{sympl.}} \tag{2.1}$$

where symplectites of spinel in clinopyroxene formed under anhydrous conditions. Candia et al. (1989) concluded that the textures were produced during postmagmatic cooling because in addition to the anhydrous nature of the reaction, no plastic deformation was observed; they hence concluded that these features excluded a metamorphic origin. These authors also noted that secondary orthopyroxene frequently occurs in radially arranged prisms. This texture is very common around cumulus olivine grains and sometimes magnetite within samples from the Bell Rock Range intrusion. In the Musgrave Province similar reaction textures were described by Goode and Moore (1975) and Goode (2002) who reported evidence for high-pressure subsolidus equilibration for the South Australian Ewarara, Kalka and Gosse Pile intrusions. Goode and Moore (1975) suggested the reaction

$$\mathrm{Ol} + \mathrm{Pl}_{\text{high-Ca}} \rightarrow \mathrm{Opx} + \mathrm{Cpx} + \mathrm{Spl} + \mathrm{Pl}_{\text{high-Na}} \tag{2.2}$$

for the formation of these coronas. They also reported reactions involving garnet (a finding that was not observed at the Bell Rock Range) as well as high Al contents in pyroxene. These findings were later confirmed, at least for intrusions in South Australia, by Glikson et al. (1996) and in parts by Maier et al. (2014).

Holness et al. (2007a, 2011) reported a series of reactive rock textures, some of which occur in the rocks from the Bell Rock Range intrusion. The reported replacement symplectites, that occur in particular within the OGT, are based on a redox reaction where olivine and Fe-Ti oxides are in contact and form orthopyroxene-magnetite symplectites by replacing the olivine (figure 2.8). Barton and Gaans (1988) and Holness et al. (2011) point out that the reaction behind this type of texture is not conclusively clarified, yet. Goode (1974) explained this texture by late-stage oxidation of olivine through the reaction

$$\mathrm{Ol} + \mathrm{O}_2 \rightarrow (\mathrm{En} + \mathrm{Mag})_{\mathrm{sympl.}}, \tag{2.3}$$

Ashworth and Chambers (2000) by exsolution processes and Barton et al. (1991) by a chemical reaction of early olivine with a late-stage fluid or melt. In any case, Ashworth and Chambers (2000) note that symplectites must always form in a subsolidus process, because the diffusion coefficients would be too high otherwise, leading to a much less ordered distribution of the reaction products. Holness et al. (2011) themselves favour an explanation whereby the reaction is triggered by an increase of the oxygen fugacity fO_2 in the interstitial liquid during fractionation, expecially in the more primitive parts of the Skaergaard intrusion.

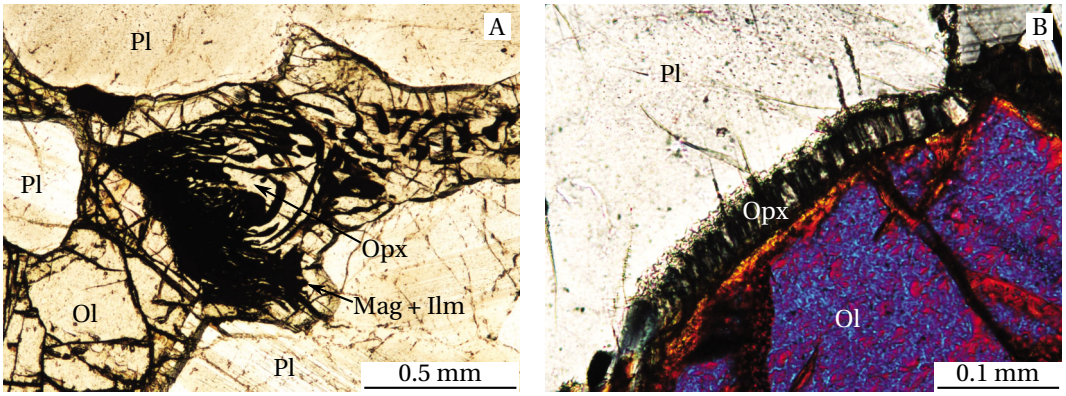

Figure 2.8 Micrographs of reactive rock textures in samples from the olivine gabbronorite and troctolite (OGT) of the Bell Rock Range intrusion. **A**—(sample no. 191 850). **B**—(sample no. 191 843).

2.6.2 Constraints on the emplacement of the Bell Rock Range intrusion

Scaling of the intrusive body

The possibility of the troctolitic and olivine gabbronoritic intrusions to be disconnected members of an originally continuous intrusive body has been discussed by several previous studies (e.g. Nesbitt and Talbot 1966; Daniels 1974; Ballhaus and Glikson 1995; Glikson et al. 1996; Evins et al. 2010b,c; Aitken et al. 2013, see also section 2.2.1). Maier et al. (2014, 2015) promoted this idea by assigning the name 'Mantamaru intrusion' to this extensive body, but there remains some ambiguity as to which of the c. 20 currently recognised intrusive bodies of the Giles Event were originally parts of the Mantamaru intrusion. Most previous authors agreed on the intrusions of the Bell Rock and Blackstone Ranges and potentially the Cavenagh Range (e.g. Nesbitt and Talbot 1966; Daniels 1974; Ballhaus and Glikson 1995; Glikson et al. 1996); recent studies extended this idea to include the combined Jameson and Finlayson Range intrusion (Evins et al. 2010b,c; Aitken et al. 2013; Maier et al. 2014, 2015).

Daniels (1974) attempted a stratigraphic correlation between the Bell Rock Range and the Blackstone Range and concluded that they are probably the lateral continuation of one another. The correlation attempt by Glikson et al. (1996) based on two marker horizons would offset the Bell Rock Range towards a higher stratigraphic level by c. 1000 m, but for the most part both intrusions would still vertically overlap. These interpretations are generally shared by Maier et al. (2014, 2015) and these authors further pointed out a magnetite layer towards top of the Blackstone Range intrusion and speculated that this could be the lateral equivalent of the lowermost magnetite layer at the base of the combined Jameson-Finlayson Range. Keeping in mind the available thickness estimates of c. 3.5–4 km for the Bell Rock and Blackstone Ranges and c. 10 km for the combined Jameson-Finlayson Range, the above considerations would mean that a thickness of 10 km of the Mantamaru intrusion (an estimate by Maier et al. 2014, 2015) might be rather

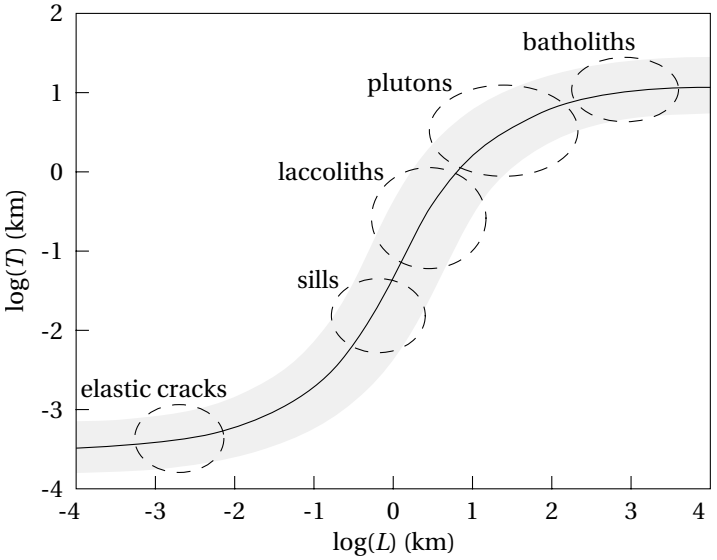

Figure 2.9 Relationships between thickness T and length L of different types of intrusive bodies, adopted from Cruden and McCaffrey (2002) and McCaffrey and Cruden (2002). The Mantamaru intrusion falls well within the typical scaling of plutons.

conservative and the true thickness may as well have been approximately 15 km. In this scenario, the Bell Rock Range intrusion would represent roughly the bottom third of the Mantamaru intrusion. It is worth noting in this context that a value of 15 km have been suggested as a natural upper boundary for the thickness of large intrusive bodies with horizontal extends that exceed 100 km (Cruden and McCaffrey 2006).

The relevance of the scaling of the Mantamaru intrusion is that it has implications for the emplacement depth and mechanism. The ratio between thickness and length of the Mantamaru intrusion is typical for that of plutons (figure 2.9; see also Cruden and McCaffrey 2002; McCaffrey and Cruden 2002). Cruden and McCaffrey (2006) pointed out that the transition from laccoliths to plutons is marked by a change in the slope a of the scaling relationship between thickness and length. For plutons, a commonly is <1, indicating that lateral growth begins to dominate over vertical growth. Cruden and McCaffrey (2006) further suggested that this transition is controlled by the emplacement depth. While at very shallow levels vertical growth can easily be accommodated by roof uplift, at depth this can most likely only happen by floor subsidence, which requires mass transfer on a crustal scale and tectonic movement. Estimates of this depth threshold vary from 3 km (Corry 1988; Cruden 1998) to 5–10 km (Cruden and McCaffrey 2002). It is unclear, however, whether this relationship implies that the converse argument is also true: that the pluton-like scaling of the Mantamaru intrusion implies deeper emplacement. Indeed, the emplacement mechanism in layered intrusions is often described as similar to laccoliths rather than plutons, i.e. it happens through vertical stacking of multiple sheets of magma by successive underplating accompanied by roof uplift (Cruden 1998). This type of emplacement process is therefore seen as a phenomenon that occurs at shallow depths of <3 km (Corry 1988; Cruden 1998; Annen et al. 2006).

Table 2.3 Compilation of lithostatic pressure estimates P and emplacement depths d for layered intrusions of the Giles Event. The values for pressure were taken from the respective referenced publication (except where no pressure estimate was provided) and the corresponding depths were calculated assuming an average density of felsic continental crust $\rho = 2.7\,g/cm^3$ as well as a gravitational acceleration $g = 9.81\,m/s^2$, and rounded to the nearest whole number.

Intrusion	P (GPa)	d (km)	Reference
Gosse Pile	1.0–1.4	38–52	Moore 1971b
Ewarara	1.0–1.2	38–45	Goode and Moore 1975
Murray Range	0.7–0.8	26–30	Glikson et al. 1996
Wingellina Hills	0.62–0.65	23–25	Ballhaus and Berry 1991
Blackstone Range	0.4	15	Glikson et al. 1995
Jameson & Finlayson Ranges	—	<15	Evins et al. 2010b,c
Mt Davies	—	<9	Nesbitt 1966
Wingellina Hills, The Wart	0.1	4	Maier et al. 2014

Emplacement depth

Table 2.3 shows a compilation of previous estimates of the lithostatic pressure during crystallisation and corresponding emplacement depth for the layered intrusions formed during the Giles Event (see also section 2.2). Some of the highest pressure estimates suggest that the Ewarara, Kalka and Gosse Pile intrusions in South Australia were emplaced into the lower crust at depths of 38 km or deeper (Moore 1971b; Goode and Moore 1975). However, Evins et al. (2010b,c) pointed out that many high-pressure rock textures have also been linked to the much later Petermann Orogeny (c. 570–530 Ma; e.g. Clarke and Powell 1995; Camacho 1997; Scrimgeour and Close 1999). Evins et al. (2010b,c) further identified the Petermann-aged Wingellina Fault as a boundary that appears to separate intrusions that exhibit high-pressure textures (north of the fault) from those that do not (south of it). Glikson et al. (1996) and Goode (2002) thought this boundary ran along the similar-aged Hinckley Fault instead. Thus, it appears that pressure estimates of 0.62–0.65 GPa (Ballhaus and Berry 1991) or below seem to be more realistic and in better agreement with crustal thinning caused by rifting during the Giles Event. In fact, Goode (1977a) estimated that the deformation in the Kalka intrusion that was caused by the Hinckley Fault occurred at conditions above 800–1000 °C and 0.8–1.0 GPa. Comparing this with the compilation of pressure and depth data in table 2.3 it does not seem unreasonable to conclude that these conditions might represent a threshold above which one must regard estimates of pressure that are thought to reflect initial *crystallisation* with caution.

Depth constraints from the Jameson-Finlayson Range and the Blackstone Range intrusions are sensible approximations for the Bell Rock Range intrusion, due to the generally accepted genetic link between the three intrusions (section 2.6.2). Howard et al. (2011b, 2015) suggested xenoliths of the greenschist-facies Mummawarrawarra Basalt (lower Bentley Supergroup; see also section 2.2) that occur at the base of the Jameson-Finlayson Range intrusion as evidence for shallow emplacement, though these authors did

not provide a numeric depth estimate. Considering that the pressure during greenschist-facies metamorphism can be up to 1 GPa (Bucher and Grapes 2011) the metamorphic grade of these xenoliths is not suitable to constrain the emplacement depth any further than the estimates discussed above.

The location of the xenoliths at the base of the Jameson-Finlayson Range intrusion can also be used to constrain the emplacement depth, although this depends on the thickness of the stratigraphic unit from which the xenoliths originate. Howard et al. (2011a) estimated the maximum thickness of the Mummawarrawarra Basalt (Geological Survey of Western Australia (GSWA) map symbol 'P_-KRm-bbg') at the MacDougall Bluff locality with c. 1100 m, and the thickness of those members of the Mummawarrawarra Basalt that outcrop along the margins of the layered Giles intrusions (GSWA map symbol 'P_-KRm-xmb-mo') with c. 300 m. This means that the preserved outcrop may suggest a total maximum thickness of c. 1400 m for the overlying rocks above the layered G1 intrusions at the time of emplacement, although the fact that outcrop is sparse and mostly around the Blackstone Range (Smithies et al. 2009b; Evins et al. 2010a; Evins et al. 2011) introduces some uncertainty to this estimate. The thickness considerations support shallow emplacement as suggested by Aitken et al. (2013) and Howard et al. (2015). However, the same authors disagree with the model of (Cruden 1998, see also discussion in section 2.6.2) by interpreting the lack of a contact aureole (i.e. a high-temperature metamorphic overprint in the Mummawarrawarra Basalt) as an indicator for intra-chamber filling rather than underplating. While the size of a contact aureole also depends on the temperature of the wall rocks which turn depends on the emplacement depth (Bucher and Grapes 2011), high ambient temperatures during emplacement (to inhibit the formation of a contact aureole) would require a much greater depth than the suggested 1.4 km.

In summary, indirect constraints on emplacement depth are largely ambiguous. While they may support shallow to subvolcanic emplacement their explanation does not require it either, which makes a final assessment difficult. The pressure estimate of Glikson et al. (1995) for the Blackstone Range of 0.4 GPa, corresponding to a depth of c. 15 km (see also table 2.3), might therefore still be the best estimate of the maximum emplacement depth to date, because it was directly determined through phase equilibria. The validity of the depth constraints for the Bell Rock Range intrusion can only be rejected if one assumes that the segments of the Mantamaru intrusion are not roughly lateral continuations from one another, but were originally physically connected in a more complex way. However, no previous study suggested such a setting (cf. Nesbitt and Talbot 1966; Daniels 1974; Ballhaus and Glikson 1995; Glikson et al. 1996; Evins et al. 2010b,c; Aitken et al. 2013; Maier et al. 2014, 2015).

Number, timing and levels of magma injections

Cawthorn (2012) showed that the question whether mafic magmas form a complex of individual sills or a single layered intrusion depends largely on the timing of the individual magma pulses. If the injections occur in rapid sequence it can greatly extend the overall cooling time of the intrusive body, which facilitates the development of a large magma

chamber. However, once the thickness of a melt column exceeds c. 10 m a convection cell will be established which greatly increases the cooling rate, making it more difficult to establish a large-scale magma chamber (Michaut and Jaupart 2011). Cawthorn (2012) therefore suggested that the rate of melt generation must be well above average to form a magma chamber that is capable of producing a large layered intrusion. In the case of the Mantamaru intrusion and its segment, such as the Bell Rock Range, the driver for this exceptionally high rate of melt generation was the Giles Event.

It is highly unlikely for magma chambers of large layered intrusions to have formed from single magma pulses, which are rarely over 200 m thick (Cawthorn 2012). As Michaut and Jaupart (2011) pointed out, the thickness of most individual sills varies between 10^{-3} and 10^{2} m, but seem to be one to several m on average. These scalings make it virtually impossible that the Bell Rock Range intrusion, let alone the Mantamaru intrusion as its parent body, crystallised from a single magma batch.

Another question is at which level within the intrusion these repeated magma injections occur. Cawthorn (2012) estimated that in a partially molten system with 50 % crystallinity and a temperature difference between the magma within the intrusion and fresh magma batches of no greater than c. 50–100 °C fresh magma can penetrate into the magma body of the intrusion and get trapped inside. If on the other side these conditions are not met subsequent injections may not be able to disturb the integrity of previous injections, resulting in a succession of individual sill-like intrusions (Cawthorn 2012). The model of Cawthorn (2012) would result in inflation of the intrusive body from the inside, an emplacement mechanism that has previously been suggested for the Mantamaru intrusion (Aitken et al. 2013; Howard et al. 2015, see also the discussion of the emplacement depth in section 2.6.2).

But other mechanisms are also possible, such as over- or underplating (e.g. Cruden 1998; Annen et al. 2006; Annen 2011). Overplating requires pathways for the fresh magma through the intrusive body. While mafic dykes were commonly observed at the base of the Bell Rock Range intrusion and could in principle represent such pathways, it is uncertain whether they are cogenetic or younger than the intrusion. Underplating on the other side would mean that younger magma batches, that are potentially more fractionated, get attached at the bottom; a finding that is not indicated, with the strongest fractionated mineral phases being located at the top of the intrusion (figure 2.5). The sharp drop in An and Fo contents of plagioclase and olivine, respectively, from c. 2500 m towards the top of the main body of the Bell Rock Range intrusion (figure 2.5) suggests that the magmas from which these minerals crystallised were the most fractionated. Assuming normal fractionation, then this would be strong evidence for overplating, at least in this upper part of the intrusion. Since this process would require pathways through the intrusive body, this could also explain why dykes are more common towards the base since the magma had to pass this area (see the area in the centre of the Bell Rock Range as displayed by Howard et al. 2009b). Given that sufficiently large portions of the intrusive body remained a semi-solidified state, such as the one described by Cawthorn (2012, and outlined above), vertical migration of melt would have been permitted. This could have provided additional pathways for later magma pulses. On the other hand, such melt

migration through interstitial spaces would almost certainly have been accompanied by extensive mixing between the intercumulus and fresh melts. It is debatable whether such a scenario would result in such a sharp change in the mineral compositions towards the top followed by a clear fractionation trend (as observed; see above as well as figure 2.5), and no strong signs of magma mixing.

However, migration of melt likely occurred within the bottom 2500 m of the Bell Rock Range intrusion, as evidenced by the disequilibrium between cumulus and intercumulus minerals (section 2.6.1). This section exhibits a slight downward trend towards stronger fractionated plagioclase and olivine compositions (figure 2.5) that could be explained by successive magma pulsed being attached to the intrusive body via underplating. As the discussion of Ni in olivines revealed (section 2.6.1), these may have crystallised earlier and at greater depth. Consequently, the lower section might have been emplaced after the top section.

Given that a distinct petrographical or chemical cyclicity is absent in the Bell Rock Range intrusion it is difficult to specify the exact number and thickness of the magma injections. The distinct change in plagioclase and olivine compositions (see above) may represent a marker that divides the intrusive body into two originally separate subchambers.

Parallel-running ridges

The MPG are petrographically markedly distinct from the other lithologies in the Bell Rock Range intrusion (section 2.4). The discussion of their petrogenesis underlines this by pointing out their highly fractionated parental magma, which stands in contrast to the remaining lithologies (section 2.6.1). A direct genetic link between the ridges and the main body of the Bell Rock Range intrusion is therefore questionable and the ridges need to be correlated with other lithologies in the Musgrave Province. Howard et al. (2009c, p. 4) reported several small intrusive bodies south of the Blackstone Range that exhibit a textural '[...] framework of coarse-grained crystals (mainly euhedral plagioclase) enclosing a mineralogically identical (except for the presence of accessory quartz in granophyric intergrowths) and locally granophyric-textured, fine-grained assemblage forming interstitial pockets filled with anhedral orthopyroxene, lesser magnetite, and fibrous aggregates of blue-green amphibole after clinopyroxene.' The MPG of the separate parallel-running ridges (section 2.2.1) seem to be texturally similar a (see petrographic description in section 2.4.6) and they are also located towards the south-east of the Bell Rock Range. This last point is important because the Bell Rock and Blackstone Ranges have both been interpreted to represent a fragment of a larger intrusion (e.g. Nesbitt and Talbot 1966; Daniels 1974; Ballhaus and Glikson 1995; Glikson et al. 1996; Evins et al. 2010b,c; Aitken et al. 2013; Maier et al. 2014, 2015). If this is the case, then a correlation between the reported lithologies from near the Blackstone Range and the MPG from the Bell Rock Range is fully justified. Howard et al. (2009c) grouped the above mentioned intrusive bodies from near the Blackstone Range together with the Alcurra Dolerite, a stratigraphic suite that is widespread in the Musgrave Province and hosts the Nebo-Babel Ni-Cu-platinum-group element (PGE) deposit (Baker and Waugh 2005; Seat et al. 2007;

Seat 2008; Seat et al. 2009; Godel et al. 2011; Seat et al. 2011). If the parallel-running ridges are gabbroic members of the Alcurra Dolerite, they could be a prospective lithologic unit in the Bell Rock Range area. It would also confirm that the ridges do not have a direct genetic link to the main body of the intrusion and may be up to c. 10 Ma younger (Howard et al. 2009c).

Late-intrusive dykes

Although the dykes are rather heterogeneous (see section 2.4.1 as well as previous studies by Glikson et al. 1996; Howard et al. 2009c), they are grouped together for the purpose of this study into a single unit, this being the MCG. The parental magma of most of the dykes was highly fractionated as indicated by the occurrence of minor K-feldspar and Ti-Fe-oxides, although the K-feldspar could also be due to a crustal component that the magma has assimilated.

The MCG must be younger than the main body of the Bell Rock Range intrusion since they cross-cut the latter, but it is unclear by how much because their precise age is unknown. They could be members of a later stage of the Giles Event, such as G2 or the Alcurra Dolerite or, if the age difference between them and the main intrusion is negligible, they could simply represent a late-stage phase of the emplacement of the Bell Rock Range intrusion or pathways for late magma pulses. In this latter case, they could closely resemble liquid compositions of the parental magma of the Bell Rock Range intrusion. Some of the dykes exhibit chilled margins that indicate a time gap between the emplacement of the main body and the dykes, because the main intrusion had to be significantly cooler. Consequently, these dykes are unlikely to have crystallised from the same magma than the main body of the Bell Rock Range intrusion.

Sample 191 854 from the lithologic unit of the MCG crystallised from a more primitive melt than the remaining samples of the MCG, as indicated by its high An and Fo contents in plagioclase and olivine, respectively. Its coarser-grained texture further distinguishes it from doleritic samples of the MCG and may suggest that this sample represents a late phase of the emplacement of the main body of the intrusion. Ballhaus and Glikson (1995) and Glikson et al. (1996) reported microgabbroic units in the Bell Rock Range intrusion and interpreted them as chilled equivalents of the coarser-grained lithologies that could be potential feeder dykes. Sample 191 854 may represent such a chilled equivalent that crystallised from a fresh (and primitive) batch of the same parental magma.

2.6.3 Orthomagmatic sulphide mineralisation

The Ni budget of a mafic or ultramafic rock is commonly controlled by olivine due to the high partition coefficients for Ni in olivine. Consequently, any sulphides that segregate after early Ni-rich olivine crystallisation will be Cu-rich. This relationship changes if an early sulphide phase is present, in which case Ni will be scavenged by the sulphides and subsequent fractionation of the silicate magma produces Ni-poor olivine. Makkonen et al. (2008) used this relationship to discriminate between mineralised and barren intrusions in Finland. Ni-undepleted olivines at lower Fo contents were interpreted by these authors as

indicative for barren intrusions, where fractionation occured at deeper stratigraphic levels than the present location within the crust. Such intrusions are generally not prospective for orthomagmatic Ni-Cu sulphide deposits. Instead, most mineralised deposits are located deeper in the stratigraphy of the respective igneous province and, consequently, have higher Fo contents as well as a wider range in Ni contents in olivine. Makkonen et al. (2008) interpreted this latter feature as an indicator for ore formation close to the current location, rather than at depth. On comparing these findings to the olivine compositions from the Bell Rock Range intrusion (figure 2.7) one may conclude that the Bell Rock Range intrusion is barren and probably not prospective for Ni-sulphides, due to its medium- to high-Ni olivines at relatively low Fo contents. The olivine compositions in the main body of the intrusion suggest that the olivines crystallised from a moderately fractionated magma that may not have lost much Ni to an early sulphide phase. The significance of the wide range in Ni (figure 2.7) is more difficult to assess: sample averages are commonly in the range of c. 0.05–0.15 wt% Ni, so rather than indicating any in-situ sulphide formation (see above), the range in values could simply be due to data precision caused by measurements taken on a wt%- instead of a ppm-scale (section 2.3).

Barnes (1986) pointed out, that care must be taken when comparing cumulus mineral compositions due to what he termed the 'trapped liquid shift': cumulus olivine can equilibrate with interstitial liquid, which can then shift Fo contents towards lower values in the cumulus minerals. However, the very narrow range of Fo contents between the OGT, with intercumulus olivine, and the OGA with cumulus olivine could indicate that this effect did not play a major role in the Bell Rock Range intrusion.

The most commonly accepted model for the formation and seggregation of sulphides in a mafic melt is the assimilation of crustal material, which causes a decrease in temperature and the felsification of the magma, all of which lower the solubility of S in the melt. The most important factor in the formation of many known major sulphide ore deposits, however, is assumed to be the addition of external (crustal) S through the contaminant to cause the oversaturation of the magma with S and subsequent segregation of sulphides (e.g. Keays and Lightfoot 2010; Lightfoot et al. 2012; Ripley and Li 2013). Without external S only systems with large volumes of magma undergoing extensive fractionation at low pressures are thought to be capable of forming (minor) mineralisation (Mavrogenes and O'Neill 1999; Ripley and Li 2013). Without doubt, the Bell Rock Range intrusion formed from a large volume of magma, considering its size and the evidence for it being a segment of the much larger Mantamaru intrusion (Maier et al. 2014, 2015). The lithostatic pressure during crystallisation of the Bell Rock Range intrusion may have been moderate to low with <0.5 GPa (see discussion in section 2.6.2). Finally, the sulphide mineralisation in the rock samples from the Bell Rock Range intrusion consists without exception of accessory Cu-rich sulphides, such as chalcopyrite and bornite, that are located in interstitial spaces. Hence, the mineralisation in the Bell Rock Range intrusion is best explained by low-pressure fractionation of a voluminous mafic magma in a staging chamber and may have little to do with a major crustal contamination event.

Many magmatic Ni-Cu-PGE deposits are located in conduits while the emplacement chambers of large layered intrusive bodies are commonly barren (Maier et al. 2001). The

reason for this is because only in conduits can structural controls concentrate the sulphide droplets to form economic ore deposits. While from the above it is still conceivable that minor Cu-rich sulphide mineralisation exists in the area, it is likely that this did not happen within the main body of the intrusion, where sulphides have not yet been reported to be more than an interstitial accessory phase. It is also not clear from the petrography and mineral chemistry alone whether the lack of significant mineralisation implies a lack of crustal contaminantion altogether. The discussion of the whole-rock geochemical data in chapter 3 will elucidate more on magma sourcing and crustal contamination.

2.7 Summary and conclusions

This chapter discussed the petrogenesis, emplacement and sulphide prospectivity of the Bell Rock Range intrusion from a petrographic and mineral-chemical point of view. The rock samples from the intrusion were grouped into several lithologic units, which are anorthosite (ANO), olivine gabbronorite adcumulate (OGA), olivine gabbronorite and troctolite (OGT) and coarse-grained gabbronorite (CGG) from the main body of the intrusion. Furthermore, the microporphyritic gabbronorite (MPG) and the microgabbronorite (MCG) have been defined as additional lithologic units from the parallel-running ridges and late-stage dykes, respectively. Based on the investigation of the above lithologic units, the following conclusions are made based on the results:

Petrogenesis Overall, the mineral chemical compositions are highly variable with An_{56-73} and Fo_{49-73}, respectively. This means that plagioclase and olivine are relatively sodic and, Fe-rich, respectivley; thus, they crystallised from a fractionated magma. This is supported by increasing amounts of cumulus magnetite towards the top of the Bell Rock Range intrusion. Layering is present on a large scale and formed by dynamic processes involving migration of melt and/or crystals. The resulting cumulus phases within the samples did not necessarily crystallise in equilibrium with the intercumulus liquid. Such dynamic processes separated plagioclase from other phases and formed plagioclase-rich lithologic units such as the ANO and OGT. Further evidence for this comes from the cumulus olivine in the OGA, which has slightly lower Ni concentrations than intercumulus olivine in the OGT. This subtle difference is not explained by sulphide segregation but by olivine crystallisation in OGA at higher pressure and temperature, likely earlier and at greater depth than the olivine in the OGT.

Otherwise however, compositional patterns are commonly cryptic across the intrusive body. The most distinct exception to this is a change in olivine and plagioclase compositions, that occurs at c. 2.5 km depth and indicates increasing fractionation towards the top of the main body of the intrusion. The MPG from the separate ridges are significantly stronger fractionated than any of the lithologies from the main body (ANO, OGA, OGT and CGG), which may indicate that they are not the product of a continuous fractionation series in the same parental magma.

Emplacement Based on the compositional differences (see above) but also based on textural comparisions it is likely that the lithologic units of the MPG and possibly the

CGG may not have originally been part of the Bell Rock Range intrusion. The MPG from the parallel-running ridges are proposed to be members of the stratigraphic unit of the Alcurra Dolerite, thus, they could be c. 10 Ma younger than the main intrusion.

The Bell Rock Range intrusion did not form from a single batch of magma. Instead, multiple pulses of magma in rapid succession created a magma chamber that allowed for the large-scale movement of melt and crystals. The heat flow during the Giles Event supported an exceptionally large rate of magma generation to establish magma chambers of the required scale, without individual sills to form before a continuous chamber is established. In the absence of a clear cyclicity that would allow for the recognition of the individual magma batches, the Bell Rock Range can be vertically subdivided into at least two parts, based on the sharp mineral compositional change (see above): (1) the bottom part of the Bell Rock Range intrusion (below c. 2.5 km) that may have formed by either intra- or underplating; (2) the top part (above c. 2.5 km) that may have formed at a relatively shallow depth of only several kilometres via overplating. This could also be the oldest part of the intrusion, since its cumulus mineral assemblage may have crystallised earlier and at greater depth. Some of the dykes within the bottom part may have provided pathways for later magma pulses but overall the MCG are a heterogeneous group. Their relationship with the Bell Rock Range intrusion is still ambiguous and requires further studies.

The scaling of the combined Mantamaru intrusion suggests a maximum thickness of c. 15 km and emplacement at no more than 5–10 km depth, but possibly as shallow as 3 km. Some indirect and less specific constraints on the emplacement depth, that were obtained from a stratigraphically higher member of the Mantamaru intrusion (the Jameson-Finlayson Range), may also support shallow (subvolcanic?) emplacement. On the other hand, a direct estimation of the maximum pressure during crystallisation, that was obtained from the stratigraphically lower Blackstone Range intrusion (Glikson et al. 1995) yielded 0.4 GPa which corresponds to emplacement at a mid-crustal depth of c. 15 km. Thick magnetitite layers such as the ones in the Jameson-Finlayson Range are absent in the Blackstone and Bell Rock Ranges, which is why the latter two are suggested to represent the bottom section of the Mantamaru intrusion. This, together with the total thickness of the intrusion, may also explain the variation in the estimates of the emplacement depth obtained from the different members of the Mantamaru intrusion.

Prospectivity Ni contents in olivine are generally high at moderate to low Fo contents. This suggests that no early S-saturation and sulphide segregation event occured at depth and affected the composition of the parental magma. Instead, the sulphides in the rocks are exclusively intercumulus Cu-rich phases that crystallised from a magma that had undergone extensive fractionation at moderate to low ambient pressures. The degree to which crustal contamination may have contributed to this is unknown, but it may not be required to explain the presence of the observed sulphides. Being a large layered intrusion rather than a magma conduit, the main body of the Bell Rock Range intrusion may not have met the structural prerequisites for concentrating sulphide droplets and hosting economic ore deposits. On the other side, the parallel-running ridges south-east of the

main body could be gabbroic members of the Alcurra Dolerite (see above), which is the host to much of the orthomagmatic sulphide mineralisation in the Musgrave Province.

Chapter 3

The Bell Rock Range intrusion II: isotope and trace element geochemistry

3.1 Introduction

The Giles Event in central Australia was accompanied by extensive mantle melting which lead to the emplacement of c. 20 intrusive bodies that together form of one of the largest known, yet underexplored, mafic-ultramafic igneous complexes. The Bell Rock Range is a large troctolitic and olivine gabbronoritic layered intrusion that formed during this event and may represent a segment of what might originally have been one of the largest known layered intrusive bodies, called the Mantamaru intrusion (e.g. Nesbitt and Talbot 1966; Daniels 1974; Ballhaus and Glikson 1995; Glikson et al. 1996; Evins et al. 2010b,c; Aitken et al. 2013; Maier et al. 2014, 2015).

Geochemists often face difficulties when attempting to discriminate between melt generation in mantle plumes, the subcontinental lithospheric mantle and/or additional assimilation of continental crust (e.g. Lassiter and DePaolo 1997; Campbell 2007). The reason for this is because most trace element signatures are not indicative of one single petrogenetic process and many magma source reservoirs are not homogeneous (Hofmann 2014; White 2015b). Consequently, the mantle source and potential crustal components within the parental melts of the Giles intrusions are not fully understood, as is evident from conflicting conclusions in previous studies (e.g. Glikson et al. 1996; Maier et al. 2014). This chapter uses multiple trace element techniques as well as Sr and Nd isotopes to identify the mantle source and detect crustal contamination.

Furthermore, the discovery of the Voisey's Bay Ni-Cu-Co deposit (e.g. Amelin et al. 1999; Li and Naldrett 1999) showed that troctolitic intrusions can host significant orthomagmatic sulphide ore deposits. For this reason, the Bell Rock Range intrusion an interesting exploration target for this deposit type. This chapter also evaluates the prospectivity of the Bell Rock Range for orthomagmatic Ni-Cu-PGE sulphide ore deposits.

3.2 Geological setting

The Bell Rock Range olivine gabbronoritic and troctolitic layered intrusion is located in the Mesoproterozoic Musgrave Province of central Australia, a terrain that extends c. 800 km east-west and 350 km north-south, between the North, South and West Australian Cratons (figure 3.1). The Musgrave Province is bounded to the north, east, south and west by the Neoproterozoic and Palaeozoic Amadeus, Eromanga, Officer and Canning basins, respectively. The Musgrave Province is divided by the Woodroffe Thrust into the northern amphibolite-facies Mulga Park Domain and the southern granulite-facies Fregon Domain (Camacho and Fanning 1995). This is a major south dipping and east-west trending structure and was active during the c. 570–530 Ma Petermann Orogeny (Camacho and Fanning 1995; Camacho 1997; Scrimgeour and Close 1999; Gregory et al. 2009; Raimondo et al. 2010). A detailed overview of the basement lithologies and geological history prior to the Giles Event can be found in section 1.2.1.

The Giles Event was magmatic event that comprised multiple stages and lasted from c. 1090 to 1040 Ma (Smithies et al. 2009a; Evins et al. 2010b,c; Aitken et al. 2013). It caused extensive intrusion and extrusion of mafic and felsic magmas in the failed Ngaanyatjarra Rift, and the Warakurna Supersuite is defined to include all igneous rocks that formed during this event. Evins et al. (2010b,c) reported the succession of the (at least) eight stages of the Giles Event. The extensive mafic-ultramafic layered intrusions and gabbroic plutons that formed during this event (Nesbitt and Kleeman 1964; Nesbitt and Talbot 1966; Daniels 1974; Ballhaus and Berry 1991; Ballhaus 1993; Ballhaus and Glikson 1995; Glikson et al. 1996; Maier et al. 2014) were in the past referred to as the 'Giles Complex' (section 1.1).

The age brackets for the emplacement of the intrusions are defined by the deposition of the Bentley Supergroup. The lower members of this volcaniclastic sequence define phase one of the Giles Event (Evins et al. 2010b,c). Three major suites of extensive mafic-ultramafic rocks were identified by Evins et al. (2010b,c) that constitute the main intrusive bodies and are referred to by these authors as G1, G2 and the Alcurra Dolerite, respectively. Some members of the Alcurra Dolerite were previously also referred to as the G3 suite by Evins et al. (2010b,c) but Howard et al. (2015) pointed out the larger age bracket for the Alcurra Dolerite and geochemically similar rocks that cross-cut the upper Bentley Supergroup. This makes the nature of the relationship between the Alcurra Dolerite and the Giles Suite ambiguous.

Phase two of the Giles Event, following the deposition of the lower Bentley Supergroup, involved the emplacement of the mafic-ultramafic G1 layered intrusions (Daniels 1974; Ballhaus and Glikson 1995; Glikson et al. 1996; Evins et al. 2010b,c). These are a group of c. 20 intrusions that are dispersed over an area that extends c. 550 km into east-west direction. The intrusions are dominated by olivine gabbronoritic-troctolitic, (leuco-)gabbronoritic or pyroxenitic-peridotitic lithologies, respectively. Ballhaus and Glikson (1995) and Glikson et al. (1996) broadly categorised the layered intrusions into either troctolitic, gabbroic or ultramafic cumulates; more recently, Maier et al. (2014) referred to the intrusions more generally as one of either mafic, mixed mafic-ultramafic

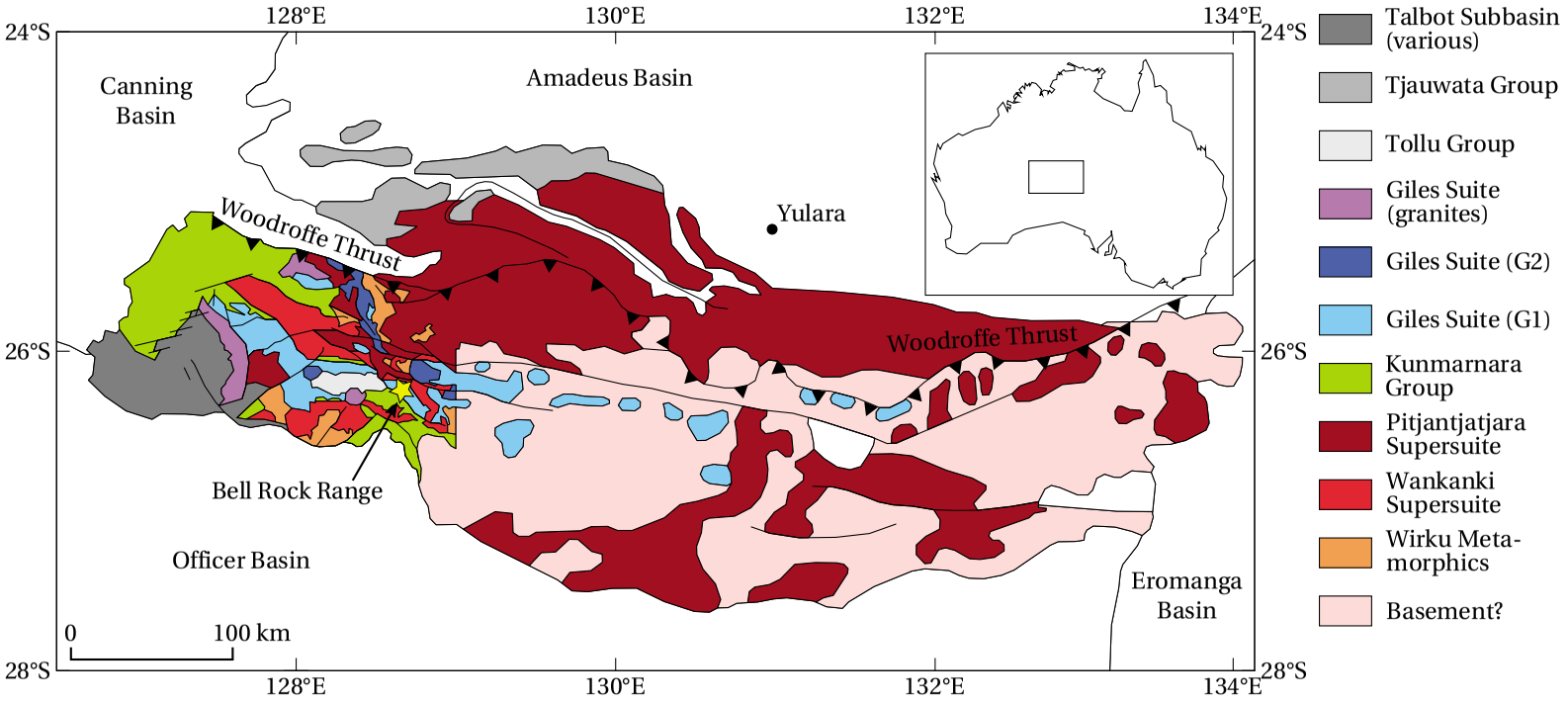

Figure 3.1 Geological map of the Musgrave Province, showing the location of the Bell Rock Range intrusion (modified after Howard et al. 2011a, 2015). The mafic-ultramafic layered and massive intrusions of the Giles Event are concentrated in the western parts of the Musgrave Province. The Bell Rock Range intrusion is located within a north-west to south-east trending chain of potentially genetically linked intrusive bodies (e.g. Daniels 1974; Glikson et al. 1996; Evins et al. 2010c; Maier et al. 2014). The inset map shows the location of the Musgrave Province in central Australia.

or ultramafic.

Wherever exposed, wall-rock contacts are mostly between the G1 intrusions and the greenschist-facies Kunmarnara Group (Howard et al. 2011b, 2015). An intrusive contact with a felsic granulite at Latitude Hill was reported by Ballhaus and Glikson (1995) and Glikson et al. (1996).

The depth of emplacement of the Giles intrusions is not well constrained, because they appear to have intruded at different crustal levels. As a result, estimates range from 1–1.2 GPa for the Ewarara, Kalka and Gosse Pile intrusions in South Australia (corresponding to lower crust at a depth of c. 38–45 km; Goode and Moore 1975) to rather low estimates of 0.1 GPa (corresponding to shallow emplacement at c. <4 km depth; Maier et al. 2014). Low- to mid-crustal levels were suggested by Ballhaus and Berry (1991) based on an estimation for the Wingellina Hills intrusion in Western Australia (0.62–0.65 GPa corresponding to c. 24 km) and Evins et al. (2010b,c) who suggested a depth of c. 15 km. This latter estimate was mainly based on field relationships around the Blackstone Range and combined Jameson and Finlayson Ranges intrusion in Western Australia. Despite all differences, there is general agreement on a shallowing trend from east to west (e.g. Daniels 1967; Nesbitt et al. 1970; Glikson et al. 1996; Maier et al. 2014). This finding is based to high-pressure crystallisation textures that occur mainly in eastern intrusions (Moore 1971b; Goode and Moore 1975; Ballhaus and Berry 1991) and field relationships around some of the western intrusions, that suggest shallow emplacement (Evins et al. 2010b,c).

Few geochronological data have been published for the Giles intrusions. A leucocratic dyke that was interpreted to be comagmatic with the Bell Rock Range intrusion yielded an age of 1078 ± 3 Ma (Sun et al. 1996). This sampling site was later interpreted to be a localised sill in the Kunmarnara Group and the age may represent a minimum age for the Giles Event (Howard et al. 2011a, 2015). More recently, Kirkland et al. (2011) obtained an age of 1076 ± 7 Ma for the Finlayson Range intrusion, which is a member of the G1 suite. Hence, an age bracket of c. 1078–1076 Ma has been proposed for phase two of the Giles Event (Howard et al. 2011a, 2015).

3.2.1 The Bell Rock Range intrusion

The Bell Rock Range intrusion (figure 3.2) is one of the largest single intrusions in the Musgrave Province. It trends northwest-southeast and has an exposed length of c. 35 km and a width of c. 6 km, respectively (Daniels 1974; Ballhaus and Glikson 1995; Glikson et al. 1996; Maier et al. 2014). Several ridges run parallel directly southwest of the intrusive body but they are disjoint and separated by an up to c. 1 km wide plain without any outcrop, although the bedrock geology of the main intrusion and the ridges has been interpreted to be connected (Geological Survey of Western Australia 2011). For this reason, the ridges are discussed together with the intrusive body, although, some legacy studies, such as Daniels (e.g. 1974), Ballhaus and Glikson (1995) and Glikson et al. (1996), did not. The intrusion is crosscut by microgabbroic dykes and sills, predominantly along the base at the northwestern margin. Maier et al. (2014) also report microgabbro sills around the top, a finding that was not observed during this study.

The contacts to the country rocks are not exposed around the margins of the Bell Rock

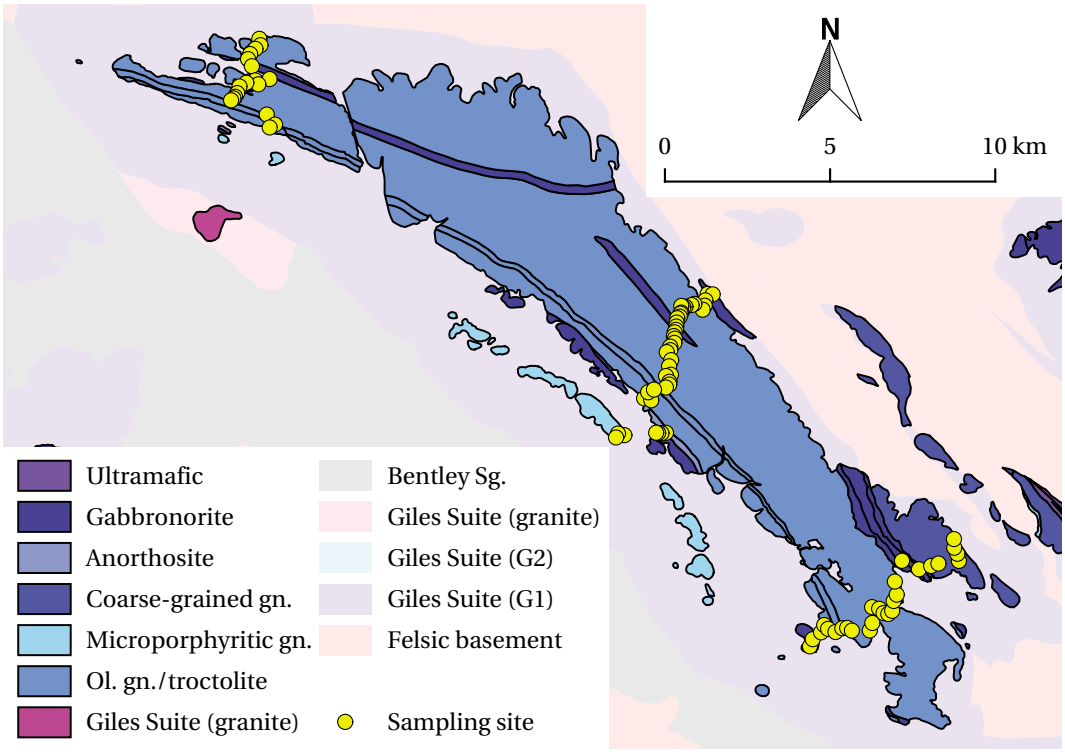

Figure 3.2 Geological map of the Bell Rock Range intrusion, indicating the locations of the sampling sites along the three sampling traverses in the northwest, centre and southeast of the intrusive body. Bold coloured areas show the surface outcrop with lithologies simplified from Howard et al. (2009b); light shaded areas show the interpreted bedrock geology (simplified from Howard et al. 2009b). The felsic basement includes the Wirku Metamorphics and the Wankanki and Pitjantjatjara Supersuites. Abbreviations are gn.—gabbronorite, Ol.—olivine, Sg.—supergroup.

Range. However, the neighbouring and potentially genetically linked Blackstone Range intrusion is overlain by members of the Bentley Supergroup. This led Maier et al. (2014) to suggest the same could be the case at the Bell Rock Range with the top contact being either eroded or fault-bound.

The Bell Rock Range intrusion is one of the most fractionated members of the G1 intrusions of the Giles Event. The thickness of the main body of the intrusion (i.e. without the separate ridges; see above) is c. 4.4 km (see method of thickness/depth estimation in appendix A.1). The main body consists of magnetite-bearing olivine gabbronorites and troctolites with minor anorthosites. The units of the intrusive body are mostly laterally continuous and can be up to several hundreds of m thick, however, there is occasional modal layering on a scale of several cm to m, although the cyclicity of layers on a large scale is poorly developed (figure 3.3). Magnetite is a common minor phase and is part of the cumulus assemblage towards the top of the intrusive main body.

Many past authors suggested that the Bell Rock Range intrusion was originally part of a much larger intrusive body; a finding that has been justified with the striking petrographic

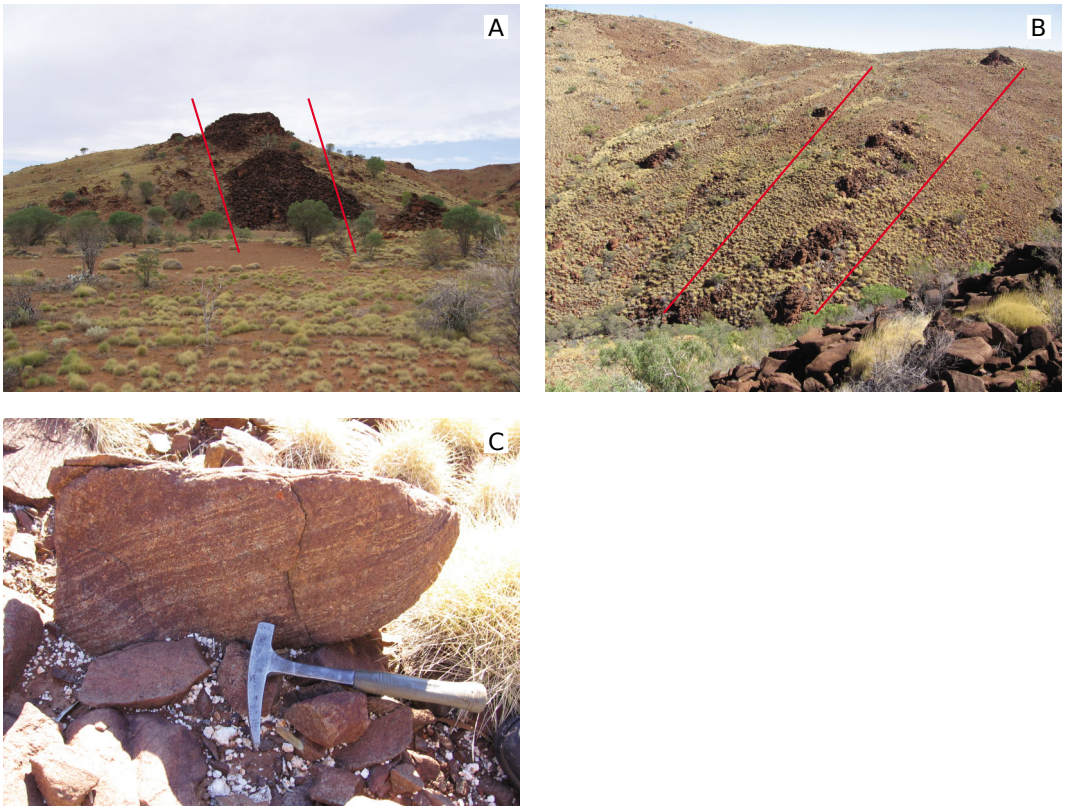

Figure 3.3 Photographs of igneous layering on different scales in the Bell Rock Range intrusion. Most lithologic units are massive on a typical outcrop scale: **A**—several tens of metres thick layer at the south-eastern sampling traverse (view from 480 484 m E, 7 094 346 m N towards south-east; red lines indicate direction of layering); **B**—several tens of metres thick layer at the centre sampling traverse (view from 471 756 m E, 7 099 804 m N towards north-west; red lines indicate direction of layering); **C**—cm-scale layering defined by modal variations between olivine and plagioclase at an outcrop at the centre sampling traverse (471 582 m E, 7 099 466 m N).

similarities between the Bell Rock and the Blackstone Ranges (Daniels 1974; Ballhaus and Glikson 1995; Glikson et al. 1996). In later studies the gabbronoritic-troctolitic Jameson and Finlayson Ranges as well as the gabbroic Michael Hills intrusion were suggested to be potential members of this intrusive body that could have been over 170 km long, 25 km wide and 10 km thick (Evins et al. 2010b,c). The proposed Mantamaru intrusion (named recently by Maier et al. 2014, 2015) could have comprised the Bell Rock, Blackstone, Jameson and Finlayson Ranges as well as potentially the Cavenagh Range. The individual members of this intrusion were suggested to have been displaced during the Petermann Orogeny.

Traverse	n	$\bar{\mathbf{a}}$	$d_{\max}$ (m)
South-east	27	241/09	5487
Centre	42	226/06	5410
North-west	18	017/04	2743

Table 3.1 Metadata for the three sampling traverses across the Bell Rock Range intrusion. Samples were collected during the 2010 field season. Data include the total number of samples per traverse n, averages for the attitude $\bar{\mathbf{a}}$ of the poles to the planes of igneous layering and a calculated estimate of the maximum thickness d_{max} (equals the depth estimate of the lowermost sample) in metres. The method of estimation is outlined in appendix A.1.

3.3 Sampling and analytical procedures

Rock samples were collected between March and April 2010 along three traverses across the troctolitic Bell Rock Range intrusion that ran approximately orthogonal to igneous layering (table 3.1 and figure 3.2). A total of 87 samples were collcected that can be broadly subdivided into three groups: (1) A total of 77 samples from the main body of the intrusion, (2) seven micrograbbros and (3) three samples collected from the separate, parallel-running ridges (see description of the Bell Rock Range in section 3.2.1).

3.3.1 Analytical procedures

Weathered material was removed from samples using a rock saw; grinding marks from the saw blade were subsequently ground off using a diamond grinding disk and the samples were washed with distilled water. Samples that underwent preparation at Monash University were crushed to a size of c. 1–2 cm in two stages: (1) using a hydraulic press with ceramic plates followed by (2) a ceramic jaw crusher. An agate mill was used to mill the rock samples to a grain size of <40 µm. Samples that were processed by Acme Analytical Laboratories in Vancouver, Canada, were crushed using Acme's in-house preparation facilities and ground to pass a size 200 mesh (74 µm). All rock pulps were dried at 105 °C prior to the major and trace element analyses described below. The results of the major and trace element as well as the isotope analyses are in appendix B.

Major, trace and precious metal analyses were carried out by Acme Analytical Laboratories. Major and trace element concentrations were determined on pulps that had been fused to glass disks in a mixture of $LiBO_2$ (lithium metaborate) and $Li_2B_4O_7$ (lithium tetraborate) and then digested in HNO_3. Borate fusion was followed by inductively coupled plasma optical emission spectrometry (ICP-OES) for major elements, and inductively coupled plasma mass spectrometry (ICP-MS) for trace elements, respectively. The base metals Ni and Cu were determined by 4-acid digestion followed by ICP-OES and ICP-MS analyses, respectively. Precious metal concentrations (Au, Pt and Pd) were determined by lead-collection fire assay and ICP-MS. Total C and S were determined by combustion analysis using a LECO furnace.

Isotope analyses were carried out at the School of Earth Sciences at the University

of Melbourne (the results of the isotope analyses are in appendix B). $^{87}Rb/^{86}Sr$ ratios were calculated from the concentrations of Rb and Sr from the trace element analyses (see above), except for sample 191 872, where Rb and Sr were determined by isotope dilution due to the elevated Rb/Sr ratio. The external precision (2σ) for $^{87}Rb/^{86}Sr$ is ±0.5 % for sample 191 872, otherwise it is assumed to be ±5 %. The $^{87}Sr/^{86}Sr$ ratio was normalised to $^{88}Sr/^{86}Sr = 8.375\,21$ and reported relative to the standard SRM987 ($^{87}Sr/^{86}Sr = 0.710\,23$). The internal precision (2σ) for $^{87}Sr/^{86}Sr$ is ±0.000 02, the external precision (2σ) is ±0.000 04.

The concentrations of Sm and Nd were determined by isotope dilution and used to calculate $^{147}Sm/^{144}Nd$ ratios. The external precision for $^{147}Sm/^{144}Nd$ (2σ) is ±0.2 %. The $^{143}Nd/^{144}Nd$ ratio was normalised to $^{146}Nd/^{145}Nd = 2.071\,942\,5$ (equivalent to $^{146}Nd/^{144}Nd = 0.7219$) and reported relative to the standard La Jolla ($^{143}Nd/^{144}Nd = 0.511\,860$). The internal precision (2σ) is ±0.000 014, the external precision (2σ) is ±0.000 020.

The $^{87}Sr/^{86}Sr$ ratio of bulk earth is assumed to be 0.7045 (Faure and Mensing 2005); the present-day values for the chondritic uniform reservoir (CHUR) for $^{147}Sm/^{144}Nd$ and $^{143}Nd/^{144}Nd$ were taken as 0.1967 (Wasserburg et al. 1981; DePaolo 1988) and 0.512 638 (DePaolo 1988), respectively. T_{DM} is the depleted mantle model age, assuming linear Nd isotope evolution within the depleted mantle from 4.56 Ga to present-day. The decay constants used were $\lambda = 1.42 \times 10^{-11}$ y^{-1} for ^{87}Rb and $\lambda = 6.54 \times 10^{-12}$ y^{-1} for ^{147}Sm.

3.3.2 Data processing

The whole-rock analyses (section 3.3.1) reported all Fe as Fe(III) (Fe_2O_3), thus, more realistic FeO and Fe_2O_3 contents were estmated following the recommendation of Le Maitre (1976), which is based on a linear regression analysis (see description of the procedure in appendix A.2). The CIPW (Cross, Iddings, Pirsson, Washington) normative mineralogy and average mineral densities were used to calculate modal rock compositions that in turn were used to classify rock samples and characterise the lithologies; details of the methods of norm calculations and classification are given in appendices A.3 and A.4, respectively. Any atomic weights used in calculations were taken from Wieser et al. (2013); the trace element values used to normalise samples against the primitive mantle (PM) are from McDonough and Sun (1995). The Eu-anomaly was calculated as the geometric mean between the relative amounts of the adjacent rare earth element (REE) Sm and Gd, respectively (Taylor and McLennan 1985).

3.4 Normative mineralogy and rock classification

Chapter 2 established a subdivision of all rock samples into lithologies based on their petrography (see the descriptions in section 2.4 in particular). The lithologies are the anorthosite (ANO), olivine gabbronorite and troctolite (OGT), olivine gabbronorite adcumulate (OGA) and coarse-grained gabbronorite (CGG) within the main body of the intrusion, the microporphyritic gabbronorite (MPG) from the parallel-running ridges as well as late-intrusives dykes consisting of microgabbronorite (MCG). This section ex-

tends this by comparing the lithologies with widely known rock classification schemas (Streckeisen 1976; Le Maitre 2002).

Most of the samples of the Bell Rock Range intrusion are SiO_2-undersaturated. Consequently, only two out of four samples of the ANO are quartz-normative (although in all four cases normative quartz or, respectively, normative olivine are <1 wt%) as are the MPG and one sample of the MCG (sample no. 191 831). The major mineral phases in the rocks from the Bell Rock Range intrusion are plagioclase, olivine and pyroxene, all of which are highly variable (modal and chemical) across the entire intrusive body and parallel-running ridges (see also the petrography and mineral chemistry in sections 2.4 and 2.5, respectively). The modal compositions calculated from the normative mineralogy reflect these findings: plagioclase varies from 34 to 90 vol%, olivine from 0 to 35 vol%, clinopyroxene (diopside) from 0 to 35 vol% and orthopyroxene (hypersthene) from 0 to 21 vol%. The relative amounts of total normative oxides (magnetite and ilmenite) vary between 1 and 14 vol%. The stratigraphic relationships between the different lithologies including their relative modal proportions are shown in figure 3.4. The bulk of the intrusive body consists of OGT and OGA. The latter occur in layers of up to several hundreds of metres thick and are characterised by significant increases in the relative abundance of modal olivine and occasionally a lesser increase in ortho- and clinopyroxene. Olivine is largely absent towards the top of the intrusion at the south-western and centre traverses, where layers of ANO are dominant. The CGG occurs at the top and bottom of the intrusive main body. They are most abundant at the base of the south-western traverse, where they are separated from the overlying units by faults and shear zones as evidenced by significant mylonitisation (Howard et al. 2009b). The north-western traverse essentially represents the middle section of the other two traverses as basal CGG and ANO are absent. The MCG occur mainly along the bottom half of the centre traverse where they cross-cut igneous layering. The stratigraphic relationships of the different lithologic units across the three sampling traverses (figure 3.4) indicate that, in a broad sense, these units are laterally continuous; however, a more detailed correlation would required a much higher sampling density.

The rocks from the Bell Rock Range intrusion classify mainly as leucocratic olivine-gabbronorites and minor gabbronorites (figure 3.5). Only a few samples classify as true troctolites or anorthosites, because most rocks generally contain total normative ortho- and clinopyroxene of >5 vol%. Three particular groups of samples stand out, these being leucocratic samples (corresponding to the lithologies of the ANO, MPG and OGT), gabbronoritic samples with total normative pyroxene >25 vol% (corresponding to the CGG and MCG) and the OGA with normative olivine contents of >20 vol%.

3.5 Whole-rock geochemistry

The following section describes the geochemical variations across the entire intrusion first, before focussing on the individual lithologic units. Significant variations are present in Cr_2O_3 (0.003–0.289 wt%) and TiO_2 concentrations (0.10–7.62 wt%); similarly, K_2O (0.03–0.73 wt%), MgO (1.20–16.84 wt%), Na_2O (0.24–3.78 wt%) and P_2O_5 (0.01–0.30 wt%) exhibit

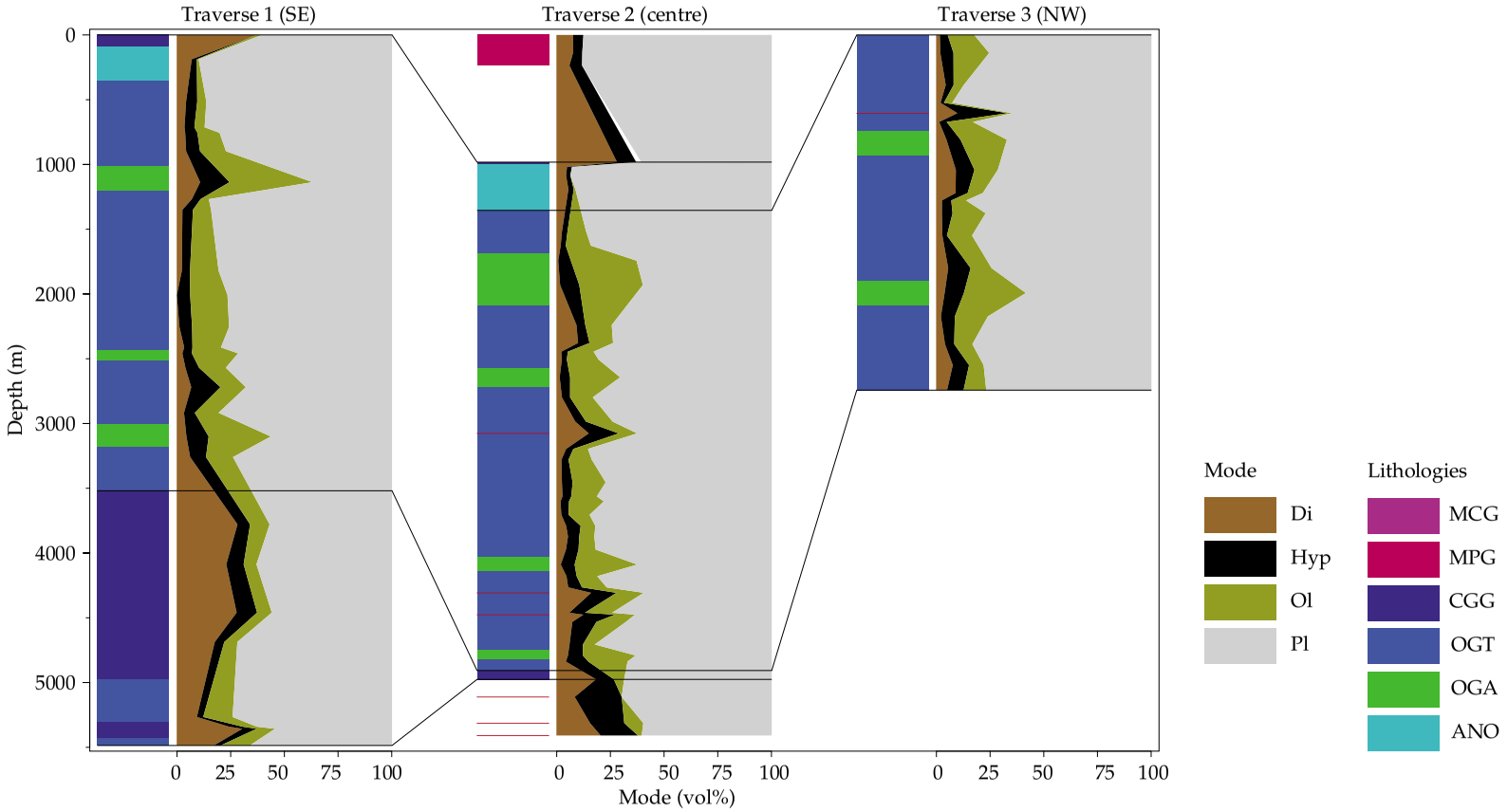

Figure 3.4 Stratigraphic columns of the sampling traverses across the Bell Rock Range intrusion and normative modal compositions of the respective lithologic units; an approximate cross-correlation between the traverses is suggested. The main sections of all three traverses consist of olivine gabbronorite and troctolite (OGT), olivine gabbronorite adcumulate (OGA) and minor anorthosite (ANO), with OGA showing the highest relative amounts of olivine. The top and bottom of the south-eastern traverse, and to a lesser degree the centre traverse, are dominated by coarse-grained gabbronorite (CGG). Microporphyritic gabbronorite (MPG), which make up the parallel-running ridges are only present at the centre traverse, as are most microgabbronorite (MCG) dykes (see section 2.4 for descriptions of all lithologies). Mineral abbreviations are Di—diopside (clinopyroxene), Hyp—hypersthene (orthopyroxene), Ol—olivine, Pl—plagioclase.

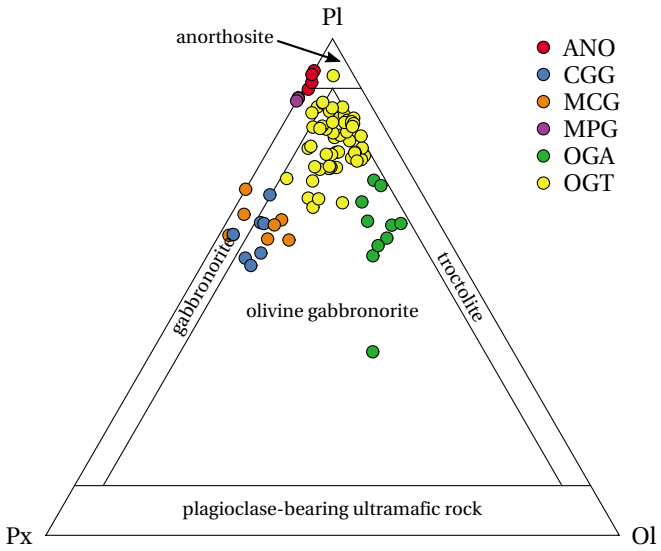

Figure 3.5 Mafic classification for rock samples from the Bell Rock Range intrusion after Streckeisen (1976) and Le Maitre (2002). The classification used the normative modal contents of plagioclase (Pl), olivine (Ol) and pyroxene (Px). The lithologies anorthosite (ANO), coarse-grained gabbronorite (CGG), microgabbronorite (MCG), microporphyritic gabbronorite (MPG), olivine gabbronorite adcumulate (OGA), olivine gabbronorite and troctolite (OGT) form three main sample populations: (1) leucocratic rocks with high plagioclase contents (ANO, MPG, OGT), (2) gabbronoritic samples with pyroxene >25 vol% (CGG, MCG) and (3) olivine-gabbronoritic adcumulates with olivine >20 vol% (OGA). True troctolites with total normative pyroxene contents of <5 vol% are rare.

strong variations over approximately one order of magnitude. The more abundant major element oxides Al_2O_3, CaO, total Fe_2O_3, MnO and SiO_2 show only moderate variablity. Figure 3.6 shows the major element concentrations against the Mg# as an indicator for fractionation. There is a general increase in Cr_2O_3 with increasing Mg#, however, the oxides K_2O, Na_2O and TiO_2 all decrease with increasing Mg#. The remaining major element oxides do not define distinct trends in figure 3.6.

Most of the samples from the Bell Rock Range intrusion have very low concentrations of strongly incompatible trace elements; for example, Th concentrations vary from 0.2 to 3.4 ppm and U from 0.1 to 0.5 ppm. Other trace elements of interest are Y (0.7–39.4 ppm), Nb (0.1–9.2 ppm) and Zr (3.7–181.25 ppm), but many incompatible element concentrations are below the limit of detection (LOD), as a result of the low amounts of trapped interstitial liquid in many lithologies. An important group of chemical elements to discuss are the REE (figure 3.7). In these rocks, the light rare earth element (LREE) budget of the rock samples is mainly controlled by plagioclase, while pyroxene and olivine have the stongest control over the heavy rare earth element (HREE) budget (see description of the major mineral phases in section 2.4). In accordance with common practice, the REE concentrations are normalised against their concentration in the PM (using the normalisation values from McDonough and Sun 1995). Variations in the normalised

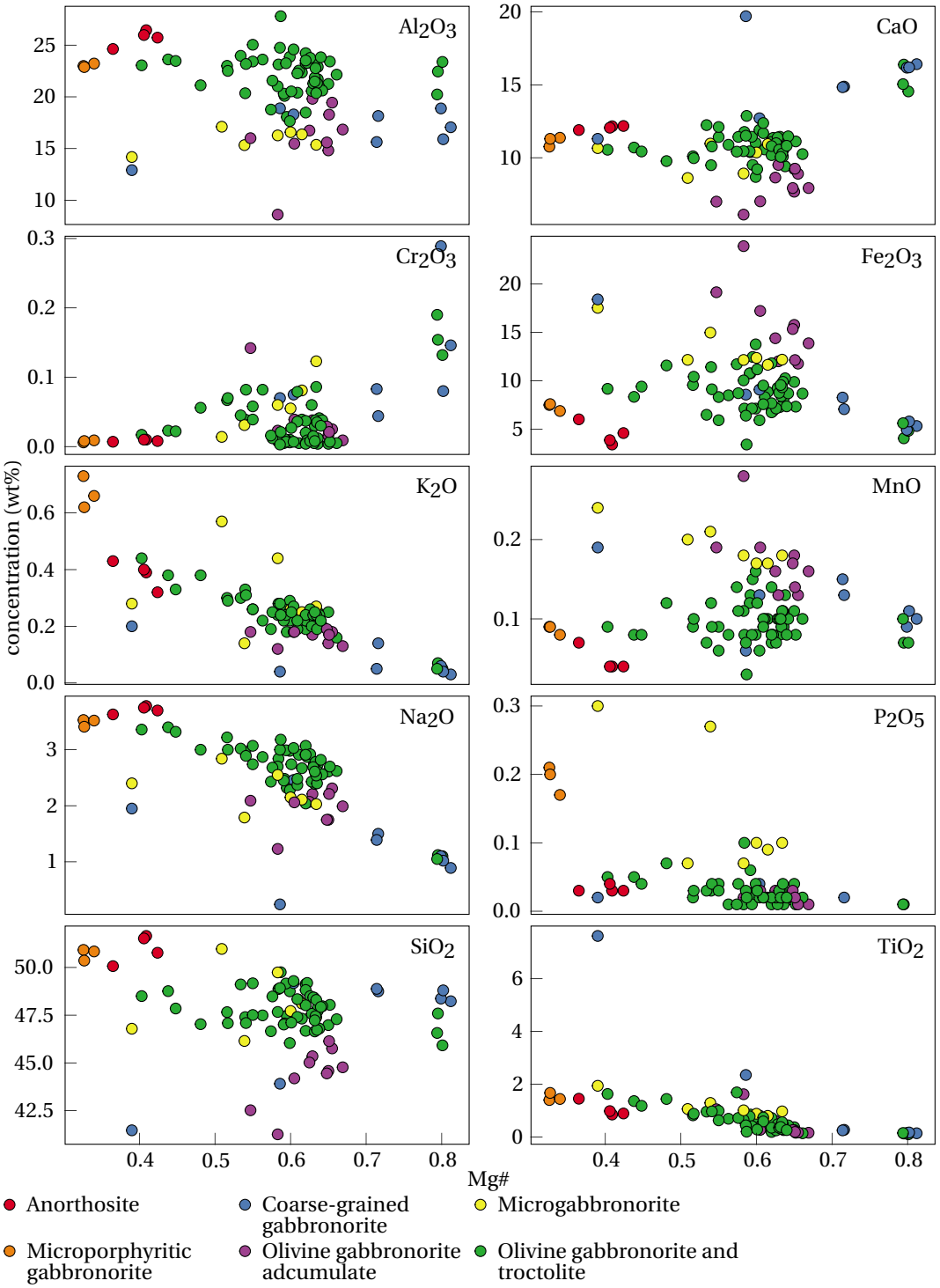

Figure 3.6 Concentrations of the major element oxides compared to the Mg# as a monitor of fractionation (see detailed description of the variations within the lithologies in the text).

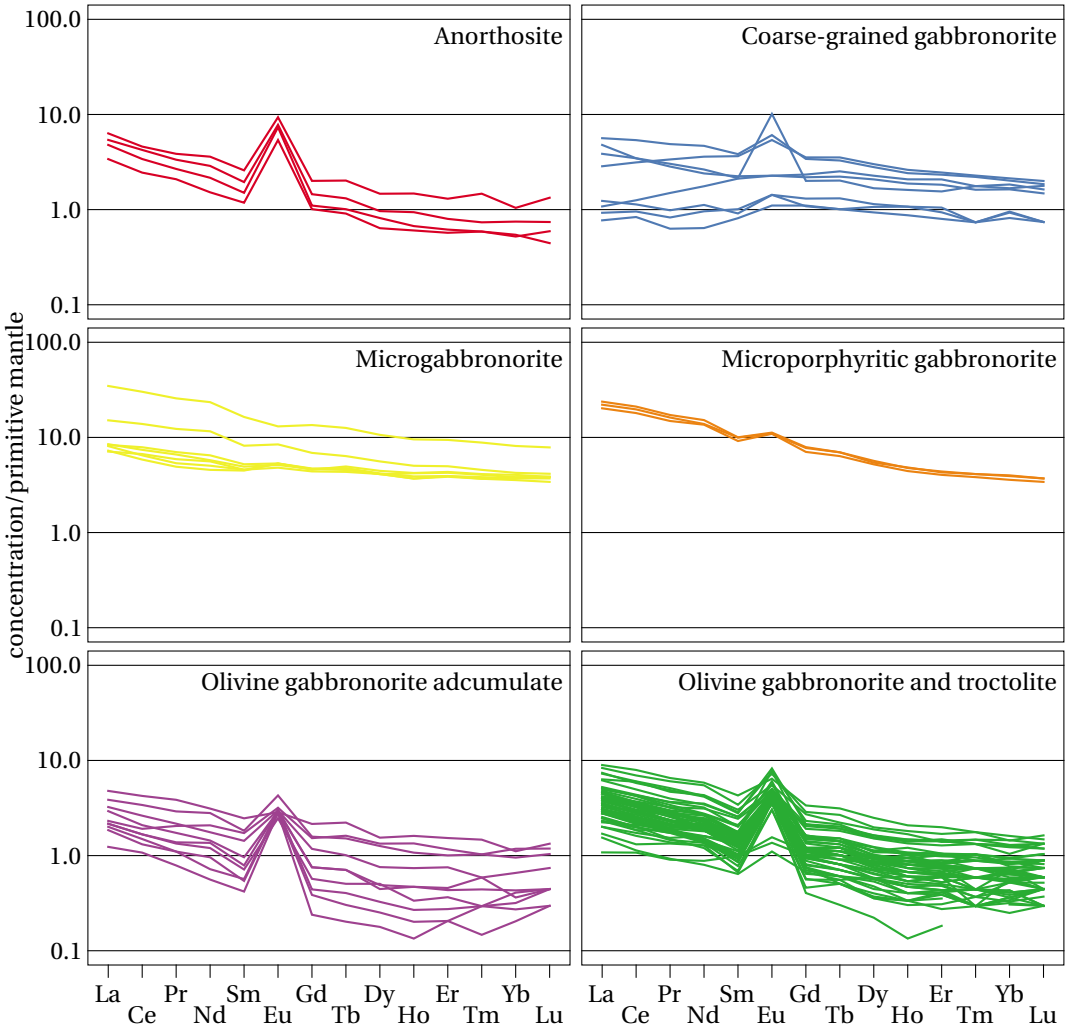

Figure 3.7 REE patterns for all lithologies, normalised against the primitive mantle (normalisation values from McDonough and Sun 1995, see detailed description of the variations within the lithologies in the text).

LREE expressed as $(La/Sm)_{PM}$ vary from 0.5–3.7 whereas those of the HREE expressed as $(Gd/Yb)_{PM}$ vary from 1.1–2.6.

Chalcophile element concentrations and ratios vary significantly within the intrusion with Cu ranging from 1.15 to 197.2 ppm and Ni ranging from 19.0 to 564.0 ppm. The platinum-group element (PGE) range from below the LOD up to 132.8 ppb for Pd (LOD = 0.5 ppb) and 16.3 ppb for Pt (LOD = 0.1 ppb), respectively. Overall Pd/Pt ratios exhibit strong variations over two orders of magnitude (0.4–40.2). Similarly, Cu/Pd ratios vary significantly between 0.6×10^3 and 1.6×10^5, however, variations within individual lithologic units are commonly weaker.

Initial isotopic ratios were calculated for an age of 1078 Ma (age taken from Sun et al.

1996, see also section 3.2). Initial $^{87}Sr/^{86}Sr$ ratios vary from 0.703 75 and 0.708 66 and initial ϵ_{Nd} from −4.0 to +4.8. Furthermore, there is a positive correlation between the abundance of intercumulus clinopyroxene and the values for initial $^{87}Sr/^{86}Sr$ and ϵ_{Nd}.

3.5.1 Layered intrusive main body

Anorthosite (ANO)

The MgO contents of the samples from the ANO are the lowest amongst all samples from the Bell Rock Range. However, due to abundant plagioclase they have high concentrations of SiO_2, Al_2O_3, CaO and Na_2O, but they are low in Fe_2O_3, MnO and Cr_2O_3. They form an approximately linear trend with the troctolites and olivine gabbros (figure 3.6), which may indicate a petrogenetic relationship between the lithologic units. The ANO are low in Nb (0.7–2.7 ppm), have a moderate range in Y (2.5–5.4 ppm) and a narrow range in Zr (13.8–22.6 ppm). The LREE and HREE show only moderate overall variation with $(La/Sm)_{PM}$ and $(Gd/Yb)_{PM}$ ratios between 2.4 and 3.2 and 1.9 and 2.1, respectively (figure 3.7). Likewise, there are only moderate variations in chalcophile element concentrations for Cu (20.7–106.5 ppm), Ni (21.0–48.0 ppm), Pd (1.4–2.3 ppb) and Pt (0.2–2.5 ppb) but a wider range in the Pd/Pt and Cu/Pd ratios with 0.6–9.0 and 1.2×10^4–7.6×10^4, respectively. Sample 191 867 yields initial $^{87}Sr/^{86}Sr$ ratio of 0.704 19 and initial ϵ_{Nd} value of +0.4.

Olivine gabbronorite and troctolite (OGT)

Most major element oxides in the OGT exhibit a roughly linear trend with the Mg#, with a more or less pronounced cluster at moderate to high Mg# values figure 3.6. Samples of this lithologic unit that are olivine gabbronoritic and samples that are troctolitic generally follow the same trend. The OGT have relatively low concentrations of Nb (0.1–3.5 ppm) and Y (0.8–8.9 ppm); Zr varies moderately (3.8–49.9 ppm). The LREE and to a lesser degree the HREE exhibit moderate variability with $(La/Sm)_{PM}$ ratios of 1.1–3.6 and $(Gd/Yb)_{PM}$ ratios of 1.4–2.6 (figure 3.7). The samples of the OGT are variable with respect to Cu (9.74–122.4 ppm), Ni (75.0–450.0 ppm), Pd (0.5–33.4 ppb) and Pt (0.1–5.6 ppb), however, Pd/Pt ratios are only moderatly variable (0.4–14.5). On the other hand, the Cu/Pd ratios vary significantly with 1.8×10^3–1.0×10^5. Isotopic compositions of nine samples of the OGT were determined and resulted in initial $^{87}Sr/^{86}Sr$ values of 0.703 84–0.705 61 and initial ϵ_{Nd} values within a close range of –1.1 to +1.2.

Olivine gabbronorite adcumulate (OGA)

The OGA are very similar to the OGT (see above), with the main difference being the significantly higher MgO concentrations caused by the higher relative amounts of olivine and lower amounts of interstitial liquid in the OGA (figure 3.6). The OGA contain relatively low concentrations of Nb (0.2–2.6 ppm) as well as Y (0.7–6.9 ppm); Zr concentrations vary moderately with 3.7–52.7 ppm. The LREE and to a lesser degree HREE exhibit moderate variability with $(La/Sm)_{PM}$ ratios of 1.3–3.7 and $(Gd/Yb)_{PM}$ ratios of 1.2–2.1 (figure 3.7).

Moderate variation in Cu (7.40–76.1 ppm) and the PGE (Pd = 0.6–2.2 ppb and Pt = 0.1–2.6 ppb). The Ni concentrations are generally higher than in other lithologies but vary only moderately with 364.0–564.0 ppm; the variations in the Pd/Pt ratios (0.6–12.0) and Cu/Pd ratios (1.2×10^4–5.9×10^4) are moderate, too. Five samples yield initial $^{87}Sr/^{86}Sr$ ratios of 0.703 75–0.704 41 and initial ϵ_{Nd} values of +0.6 to +1.4.

Coarse-grained gabbronorite (CGG)

The rocks of the CGG occur at the top and bottom of the intrusive body and have intermediate concentrations of MgO (5.96 wt%), low concentrations of SiO_2, Al_2O_3, Na_2O, K_2O and Cr_2O_3 (the latter below LOD) and high concentrations in Fe_2O_3, TiO_2 (very high) and MnO (figure 3.6). The CGG exhibit a great range in Nb (0.1–8.5 ppm) and a moderate range in Y (3.7–10.7 ppm) and Zr (4.3–42.7 ppm). The REE generally stay within a narrow range (with $(La/Sm)_{PM}$ ratios of 0.5–2.2 and $(Gd/Yb)_{PM}$ ratios of 1.1–1.7; figure 3.7). The CGG exhibit moderate variations in Cu (1.15–80.4 ppm), Ni (51.5–261.0 ppm) as well as Pt (1.3–12.3 ppb); however, Pd varies strongly with values between 1.2 and 132.8 ppb. The Pd/Pt and Cu/Pd ratios exhibit moderate variability with 0.9–40.2 and 6.1×10^2–1.1×10^4, respectively. Five samples yield initial $^{87}Sr/^{86}Sr$ ratios of 0.703 92–0.705 54 and initial ϵ_{Nd} values of –0.9 to +1.3.

3.5.2 Parallel-running ridges

Microporphyritic gabbronorite (MPG)

The parallel-running ridges are composed of MPG, which are low in MgO (1.78–1.85 wt%) and relatively high in MnO, TiO_2 and Fe_2O_3, caused by higher Fe-Ti-oxide contents. The MPG also show evidence for advanced magmatic fractionation through the significantly elevated K_2O and P_2O_5 concentration. This distinguishes them from the lithologic units of the main intrusive body (figure 3.6). The MPG yield the highest Nb concentrations (7.7–9.2 ppm) as well as relatively high Y (18.5–21.0 ppm) and Zr (107.3–116.6 ppm). The REE ratios $(La/Sm)_{PM}$ and $(Gd/Yb)_{PM}$ stay within very narrow ranges with 2.2–2.4 and 1.9–2.0, respectively (figure 3.7). The chalcophile elements show only little variations within the MPG as shown by the contents of Cu (117.2–120.9 ppm), Ni (19.0–23.0 ppm), Pd (1.8–4.5 ppb) and Pt (1.5–2.5 ppb). Further, moderately varying Pd/Pt ratios (0.7–2.7) and a very small range in the Cu/Pd ratios (2.7×10^4–6.7×10^4) characterise this lithology. With all these variations it is important to keep in mind, however, that only three samples of the MPG were collected. Two samples yield initial $^{87}Sr/^{86}Sr$ ratios of 0.704 14 and differing initial ϵ_{Nd} values with +0.4 and +4.8, respectively.

3.5.3 Late-intrusive dykes and sills

Microgabbronorite (MCG)

The dykes within the intrusion are grouped together to form the lithologic unit of the MCG. Overall, the samples of the MCG exhibit a range in MgO contents comparable to

the lithologic units of the main intrusive body but slightly lower Al_2O_3 concentrations. A more distinct difference between the MCG and the lithologies of the main intrusive body is defined by Fe_2O_3 and MnO, which are found in oxide phases and are more abundant in the MCG (figure 3.6). The unit exhibits a high range in Nb (1.9–7.7 ppm) as well as a wide range in Y (16.1–39.4 ppm) and Zr (30.9–181.3 ppm). The LREE and HREE exhibit moderate variability with $(La/Sm)_{PM}$ ratios of 1.5–2.1 and $(Gd/Yb)_{PM}$ ratios of 1.1–1.7, respectively (figure 3.7) as do the chalcophile trace elements Cu (95.0–197.2 ppm), Ni (75.0–294.0 ppm), Pd (0.6–18.7 ppb) and Pt (0.5–16.3 ppb). The Pd/Pt ratios stay within a moderate range (c. 1.1–1.7), however, the Cu/Pd ratios vary strongly (8.4×10^3–1.6×10^5). Six samples yield initial $^{87}Sr/^{86}Sr$ratios between 0.704 65 and 0.708 66 as well as initial ϵ_{Nd} values between –4.0 and +0.4.

3.6 Discussion

3.6.1 Identification of parental magma components

Unravelling mantle source characteristics and parental magma components

Ideally, one can identify rocks that represent true liquid compositions of the parental magma during the study of layered intrusions and several previous studies attempted this. For instance, Godel et al. (2011) investigated associated dykes from the Nebo-Babel deposit to identify the composition of the parental magma that produced the host intrusion of the deposit. They concluded that the dykes were the result of a mixture between partial melts from metasomatised subcontinental lithospheric mantle (SCLM) and the asthenospheric mantle (possibly mantle plume related) with only minor crustal material. Their results are therefore in partial conflict with Arndt (2013) who showed that the SCLM is too cold and thus unable to produce the high-flux melts that are needed to form orthomagmatic ore deposits such as Nebo-Babel. Arndt (2013) pointed out, that these deposits require a hotter source such as the asthenospheric mantle and significant crustal contamination and that the SCLM is generally not involved. Maier et al. (2014, 2015) added that the S contents (c. 1000 ppm), Pt/Pd ratios (≈1) and ϵ_{Nd} values (–2) of the dykes in the study of Godel et al. (2011) are not in agreement with SCLM.

During this study of the Bell Rock Range intrusion, no such direct candidate for the original parental magma was identified, thus, other methods were used to elucidate the magma source characteristics. However, chapter 4 discusses the gabbroic G2 suite and their potential to represent liquid compositions of the parental magmas of the G1 suite, a hypothesis that was briefly mentioned by Maier et al. (2014, 2015).

The Nb-Zr-Y chemistry of basaltic magmas has proven useful to distinguish between different magma sources in the mantle (e.g. Fitton et al. 1997; Fitton 2007). Fitton et al. (1997) showed that when plotting Zr/Y and Nb/Y ratios basalts from Iceland with >5 wt% MgO and normal mid-ocean ridge basalt (N-MORB) samples from other spreading centres are easily distinguishable, because samples from Iceland form a tight linear array (figure 3.8). Fitton et al. (1997) further defined the parameter

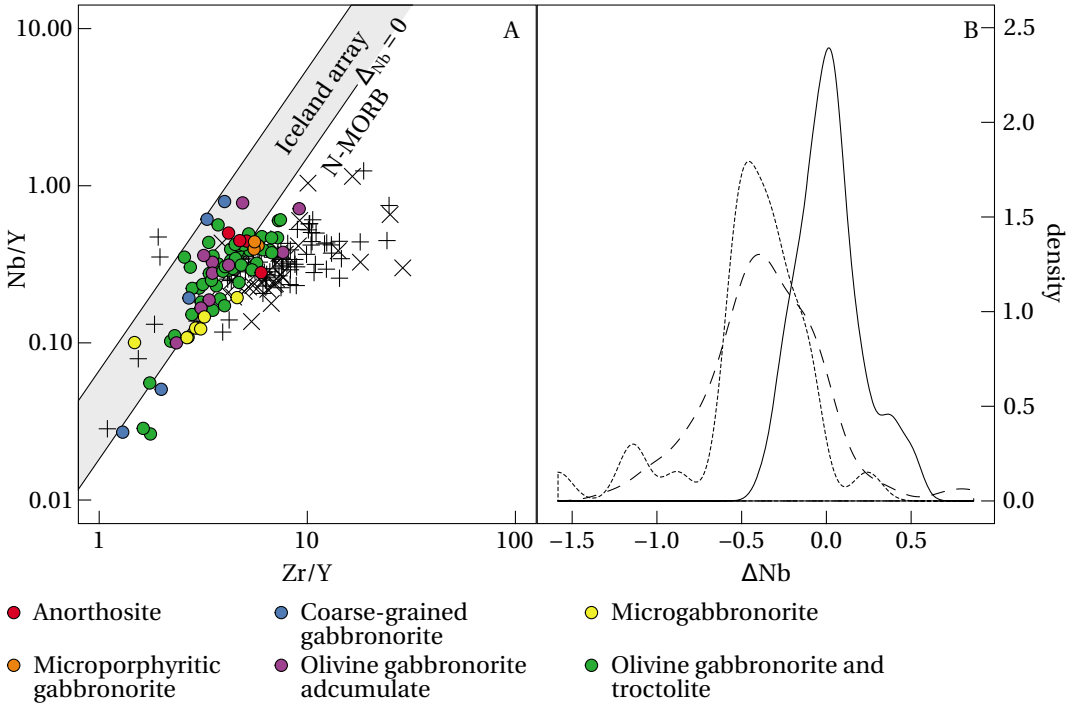

Figure 3.8 Zr-Nb-Y chemistry and Δ_{Nb} of the Bell Rock Range intrusion. The Nb/Y versus Zr/Y diagram after Fitton et al. (1997) indicates the membership of the Bell Rock Range magmas in either the Iceland or the normal mid-ocean ridge basalt (N-MORB) array. A Δ_{Nb} value of 0 (equation (3.1)) represents the boundary between the two linear arrays (see explanation in the text). The probability density curves estimated from Δ_{Nb} values show that the distribution of Δ_{Nb} sits right on the boundary.

$$\Delta_{Nb} = 1.74 + \log\left(\frac{w_{Nb}}{w_Y}\right) - 1.92\log\left(\frac{w_{Zr}}{w_Y}\right) \tag{3.1}$$

such that samples that plot along the boundary between the Iceland array and N-MORB have $\Delta_{Nb} = 0$, members of the Iceland array have $\Delta_{Nb} > 0$ and N-MORB-type rocks have $\Delta_{Nb} < 0$. The reason for this is, that primitive mantle is depleted in Nb (relative to other incompatible high field strength element (HFSE)) compared to the depleted mantle (DM). Partial melting and fractionation processes do not affect Δ_{Nb} (Fitton et al. 1997; Fitton 2007). This includes the fractional crystallization of olivine and plagioclase (Fitton 2007) which is important because these are the major cumulus phases in the Bell Rock Range intrusion. Since the HFSE are highly incompatible elements and accumulate mostly in the interstitial liquid (cf. partition coefficients in McKenzie and O'Nions 1991; Rollinson 1993; McKenzie and O'Nions 1995) it follows that the Δ_{Nb} parameter remains largely unaffected by cumulate effects.

The Iceland array (Fitton et al. 1997) broadly comprises ocean island basalt (OIB)-type melts. As Fitton et al. (1997) and Fitton (2007) point out, this includes melts that were generated in mantle plume settings and thus sampled primitive lower mantle but

also melts that sampled mantle that was enriched through previously subducted crust. Continental rift systems that have not progressed into the stage of seafloor spreading commonly produce alkali basalts with signatures similar to the Iceland array (Fitton 2007). Current tectonic models for the Giles Event generally involve some form of asthenospheric upwelling following the prior disruption of the lithosphere—subject of the ongoing debate is merely the *driver* behind these processes, such as a mantle plume or lithospheric delamination (cf. Pirajno and Hoatson 2012; Smithies et al. 2015, see also the discussion of the tectonic setting in section 6.2). Establishing a hypothesis as to which mantle reservoir(s) the parental magmas of the Bell Rock Range intrusion may have sampled is therefore not straightforward, because (1) the plate tectonic terms lithosphere and asthenosphere do not strictly correlate with the geochemical reservoirs of the depleted and enriched/primitive mantle (Anderson 1995, 1996), and (2) at least the upper mantle is not compositionally homogeneous (Hofmann 2014; White 2015b).

The rock samples from the Bell Rock Range cluster strongly over the discrimination line between the two mantle sources with Δ_{Nb} values of ≈0 (figure 3.8). Since N-MORB-type magma sources as well as typical contaminants from the continental crust (such as the Pitjantjatjara and Wankanki Supersuites in the Musgrave Province) have $\Delta_{Nb} < 0$ (Fitton 2007) it is impossible for any mixture between N-MORB-type melts and crustal material to result in OIB-like rocks with $\Delta_{Nb} > 0$ (i.e. plot in the Iceland array of Fitton et al. 1997). OIB magmas on the other hand, that have assimilated crustal material, can yield negative Δ_{Nb} values (Fitton et al. 1997; Fitton 2007). The overlap of the Bell Rock Range magmas with the Iceland array may therefore be a characteristic of the magma source, suggesting a significant melt component from the deeper lying primitive mantle. The existing continental crust during the Giles Event was extremely HFSE enriched from extensive crustal reworking during previous orogenic events (Kirkland et al. 2012a, 2013). Such a process would also have amplified the negative Nb anomaly of any felsic crustal rocks and consequently small amounts of contamination would already have been sufficient to decrease Δ_{Nb} towards N-MORB-type/crustal values. Fitton (2007) reported data from the Basin and Range Province in the United States that may be an analogue for the Nb-Zr-Y signatures of the Bell Rock Range, in that it is an example for a continental rift system where Δ_{Nb} values of c. 0 dominate. This is especially the case during the early stages of rifting and Fitton et al. (1991), Kempton et al. (1991) and Fitton (2007) argued that this is due to sourcing from SCLM that was enriched by fluids from a previously subducted slab.

The last (undisputed) subduction zone that predates the Giles Event existed during the 1345–1293 Ma Mount West Orogeny, while the Musgrave Orogeny was at least in most parts more likely characterised by crustal thinning, according to recent studies (cf. Giles et al. 2004; Betts and Giles 2006; Aitken and Betts 2008; Smithies et al. 2011; Howard et al. 2015, see also the geological history of the Musgrave Province in section 1.2.1). This means that HFSE enrichment of the mafic magmas during the early Giles Event can only have been due to dehydration of subducted crust if the slab from the Mount West Orogeny remained at the base of the crust. Indeed, Maier et al. (2014) did not rule out the involvement of old subducted crust for the formation of the Alcurra Dolerite.

Since this stratigraphic unit is younger than the G1 and G2 members of the Giles Suite (1075–1068 Ma for the Alcurra Suite versus 1078–1076 Ma and 1078–1074 Ma for the G1 and G2 stages, respectively Evins et al. 2010b,c; Howard et al. 2011a) the magma that later produced the G1 and G2 magmas may have been derived from a similar source. On the other side, no clear evidence for remnant subducted crust has been reported for the Musgrave Province during the Giles Event, which makes the above scenario rather speculative. Ultimately, this could underline that the OIB-type signatures were masked by the assimilation of strongly HFSE enriched crust Kirkland et al. (2012a, 2013).

Whether the SCLM is a realistic source for the magmas, like Fitton et al. (1991), Kempton et al. (1991) and Fitton (2007) suggested for the Basin and Range Province, is debatable. Maier et al. (2014, 2015) rejected this for the Nebo-Babel deposit (i.e. the Alcurra Dolerite, see above) but it is also c. 10 Ma younger than the troctolitic Giles intrusions, such as the Bell Rock Range. The change between a lithospheric and an asthenospheric mantle source in the western Basin and Range Province occurred within less than 10–15 Ma (e.g. Fitton et al. 1991; Gazel et al. 2012; Putirka and Platt 2012). This shows that the involvement of SCLM cannot be ruled out for the Bell Rock Range based on constraints from the Alcurra Dolerite.

It is reasonable to assume that an intrusive body the size of the Bell Rock Range would have experienced crustal contamination to some degree, however, during the field work for this study, no exposed contacts to country rocks were found around the Bell Rock Range and very few have been described in the literature for other intrusive bodies in the area (e.g. at the eastern margin of the Latitude Hill intrusion and the base of the Jameson-Finlayson Range, Glikson et al. 1996; Howard et al. 2011b). In addition, the contacts around the Bell Rock Range as far as suggested by the interpreted bedrock geology (Howard et al. 2009b) are fault bound. However, the predominantly felsic lithologies of the Pitjantjatjara and Wankanki Supersuites as well as the Wirku Metamorphics are widely exposed and are an appropriate choice for the most likely contaminants at the time of the Giles Event. Some minor potential contaminants are e.g. cogenetic felsic dykes that are the result of minor bimodal magmatic activity during the early stages of the Giles Event (Sun et al. 1996) and xenoliths of the lower Bentley Supergroup that were reported from the Jameson-Finlayson Ranges (Howard et al. 2011b; Maier et al. 2014, 2015).

Many of the Bell Rock Range rocks have contents of highly incompatible element such as Th that are below the LOD, however, this was not caused by the absence of crustal contamination but by generally low amounts of interstitial liquid (especially the samples from the OGA). This makes the use of several indicators for crustal contamination difficult, such as normalised $(Nb/Th)_N$ and $(Th/Yb)_N$ ratios (used for instance by Ihlenfeld and Keays 2011). Nevertheless, the available data (figure 3.9) suggest that the parental magma of the Bell Rock Range intrusion experienced crustal contamination. For example, Lightfoot and Hawkesworth (1988) and Ihlenfeld and Keays (2011) showed that $(Nb/Th)_{PM}$ ratios of <1 and $(Th/Yb)_{PM}$ ratios of >1 in magmas that originated from the mantle are commonly seen as evidence for crustal contamination. Both criteria are met by the sampled Bell Rock Range rocks, which also show a clear tendency towards low $(Nb/La)_{PM}$ and high $(La/Sm)_{PM}$ ratios (figure 3.9), thus, exhibiting a crustal signature with

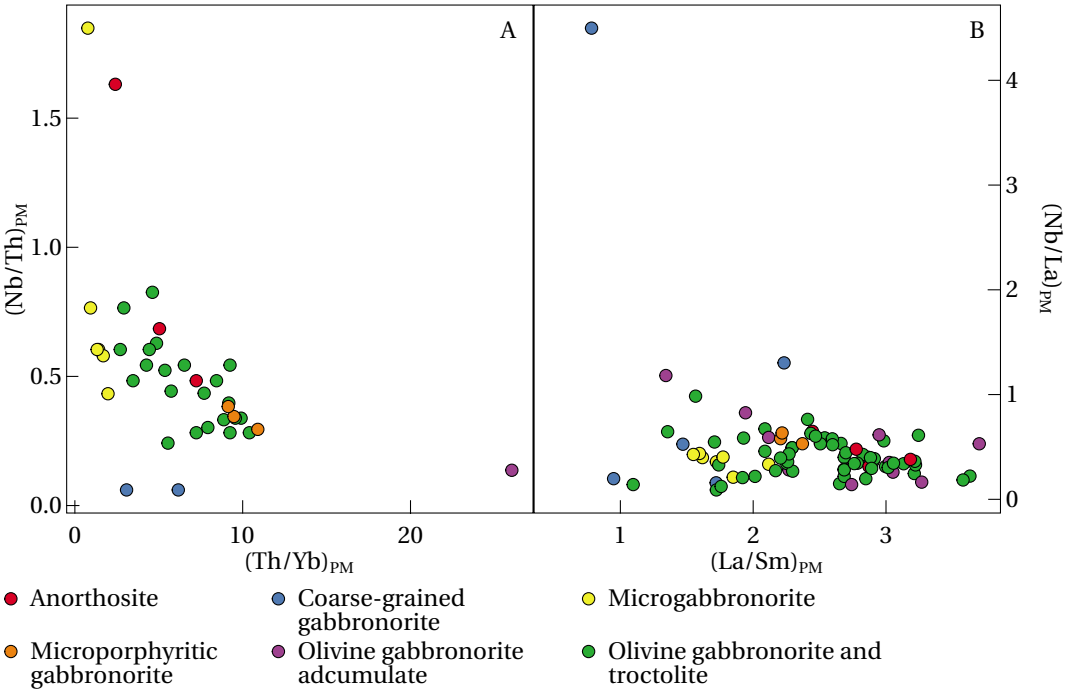

Figure 3.9 Trace element evidence for crustal contamination in rocks from the Bell Rock Range intrusion. Nb/Th ratios of <1 and Th/Yb ratios of >1 indicate crustal contamination in most lithologies Lightfoot and Hawkesworth (1988) and Ihlenfeld and Keays (2011). Exceptions are two samples from the microgabbronorite (MCG) and the ANO, respectively. Low Nb/La and high La/Sm ratios support the evidence for contamination in the magmas. All ratios were normalised against primitive mantle (PM) using the normalisation values of McDonough and Sun (1995).

a negative Nb-anomaly and LREE enrichment. The trends on both diagrams in figure 3.9 are not entirely consistent because they identify different lithologies as the most primitive. Furthermore, the data in figure 3.9 show some scatter, i.e. the contamination trends are not as tight as in some of the above mentioned studies (e.g. Ihlenfeld and Keays 2011). On the other hand, *individual* lithologic units form coherent clusters and such derivations from ideal trends can be explained by poor homogenisation of the contaminant with the mafic magma. Intuitively, it would be expected that the longer a magma remains within the crust, the greater the likelyhood that crustal material will be assimilated and the higher should be the degree of homogenisation. While there is clear evidence for contamination in the Bell Rock Range magma, the lack of homogenisation supports rapid emplacement.

Melting depth and source characteristics

The depth of melting can be used to further constrain the nature of the magma source. For instance, mid-ocean ridge basalt (MORB) melts at spreading centres are commonly produced at depths of c. 10–70 km while melting depths of within-plate alkali basalts, that are common in continental rift settings, can be much greater (up to 100 km), and

both types of mafic melts also have different source characteristics (Walter 2014). The depth of melting for the layered intrusions of the G1 suite is not very well constrained as most studies only provide rough brackets. Smithies et al. (2010, 2011) suggested that the difference in depth between emplacement of the granitic Pitjantjatjara Supersuite and melt generation during the Musgrave Orogeny was c. 7 km; a value that can therefore be assumed to represent the minimum crustal thickness at the onset of the Giles Event, that followed the Musgrave Orogeny. Seat et al. (2011) found evidence for residual spinel rather than garnet during partial melting of the mantle source of the Nebo-Babel deposit; thus, these authors placed the upper bracket for mantle melting at c. <70 km. These findings were confirmed by Godel et al. (2011), who assumed partial melting of metasomatised SCLM (i.e. hydrous lherzolite) and further narrowed the maximum depth for the parental magma of the Nebo-Babel deposit to c. 60 km. The Nebo-Babel deposit is, however, a member of the Alcurra Dolerite and not the G1 or G2 suites, and estimates for the latter two do not have to yield the same results.

The modal characteristics of the residual mantle during partial melting are unfortunately relatively unspecific when it comes to depth. For example, spinel lherzolite is stable at pressures of c. 1–2.5 GPa (Walter 2014, and references therein), which is roughly equivalent to depths of 30–75 km (Farmer 2014). Nevertheless is it instructive to elucidate the source characteristics for the rocks of the Bell Rock Range intrusion to obtain an estimate for a member of the G1 suite. Figure 3.10 shows the changes in HREE and LREE during batch melting of primitive and depleted mantle sources with either spinel peridotite or garnet peridotite in the residue. The two steep trends with strong variations in the LREE and relatively stable HREE compositions display partial mantle melting with a spinel-bearing residue; the two diagonal trends model partial melting of the same two mantle sources with a garnet-bearing residue. On comparison with the actual data from the Bell Rock Range rocks it is apparent, that melting under garnet-stability would cause a strong depletion in HREE in the resulting compositions, a feature for which there is little evidence. The absence of garnet would place the melting of the mantle within above mentioned brackets of 30–75 km. These estimates are in good agreement with Wang et al. (2002), who investigated into the melting depths below the Basin and Range Province during the late Cenozoic. These authors found that $(Tb/Yb)_N$ ratios and $Fe_{8.0}$ (total FeO at 8 wt% MgO; Klein and Langmuir 1987) are elevated in the east and in agreement with mantle melting in equilibrium with residual garnet, indicating a depth of 100–140 km. In the western Basin and Range Province on the other hand, the above geochemical signatures suggested shallower melting in the absence of garnet and at 50–75 km. These results compare well with the maximum depth of melting as suggested above for the Musgrave Province during the Giles Event.

With respect to a lithospheric versus an asthenospheric mantle source these numbers are not reliable, because in extensional settings the boundary between the lithosphere and the asthenosphere has been shown to be as low as 55 km (Big Pine Volcanic Field, western Basin and Range Province Gazel et al. 2012). The model in figure 3.10 is also difficult to evaluate with respect to potential mantle reservoirs, because only the lithologic unit of the CGG would require the DM as a source. All other lithologies are in agreement

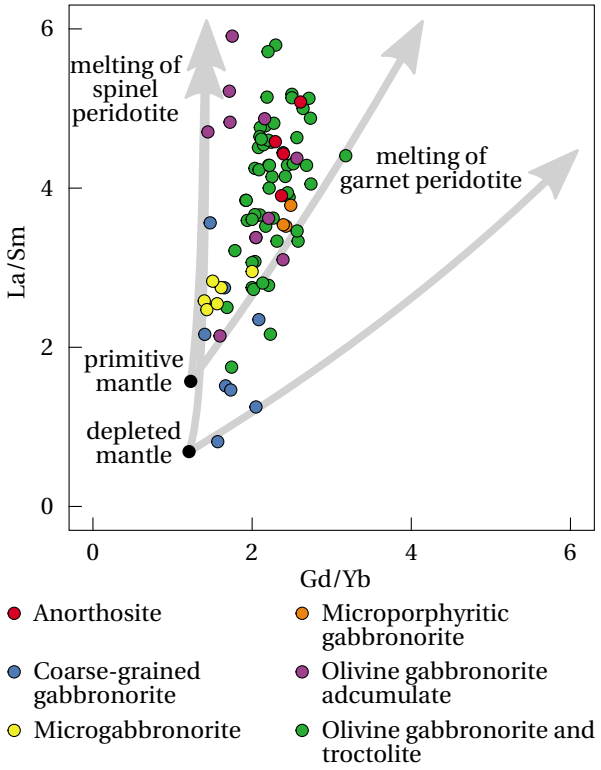

Figure 3.10 REE partial melting model for the Bell Rock Range rocks. The grey arrows indicate the changes of the REE compositions resulting from simple batch melting with a spinel peridotite and garnet peridotite residue, respectively, and varying melt fractions. The modal contents are normative compositions (see section 3.4) converted to vol%; the starting compositions for the model (primitive and depleted mantle) and the partition coefficients are from McKenzie and O'Nions (1991).

with either of the two mantle reservoirs.

The approach of Pearce (2008, figure 3.11) was motivated by the aim to better cope with the compositional complexities of the sources for basaltic magmas by using proxies for crustal input (Th-Nb) and melting depth (Ti-Nb). The Th-Nb proxy shows evidence for crustal contamination within the rocks from the Bell Rock Range intrusion, caused by elevated Th and low Nb contents relative to typical MORB- or OIB-type rocks that did not have contact with crustal rocks. The number of samples in figure 3.11 (Th-Nb proxy) is limited because many rocks samples from the Bell Rock Range intrusion yield Th concentrations that are below the LOD. However, it is apparent that there is some scatter from the MORB-OIB array (lithologies of the MCG and the ANO) towards elevated Th contents. Such a pattern is consistent with several examples presented by Pearce (2008), that show mafic igneous rocks that ascended through continental lithosphere, which in turn would be expected in a continental rift such as the Ngaanyatjarra Rift. The samples from the different Bell Rock Range lithologies generally cluster together. In particular the lithologies of the CGG and MCG exhibit a stronger relative depletion in Nb at comparable Th contents when compared to the lithologies of the main body of the intrusion. This may indicate that they were sourced from a different mantle reservoir, such as from the shallower lying DM, while the degree of crustal contamination is roughly the same. Consequently, this would suggest that these lithologies are not strictly part of the Bell Rock Range intrusions (as already indicated for the CGG and the MPG in chapter 2).

The Ti-Nb melting depth proxy (figure 3.11) indicates elevated Ti contents correspond-

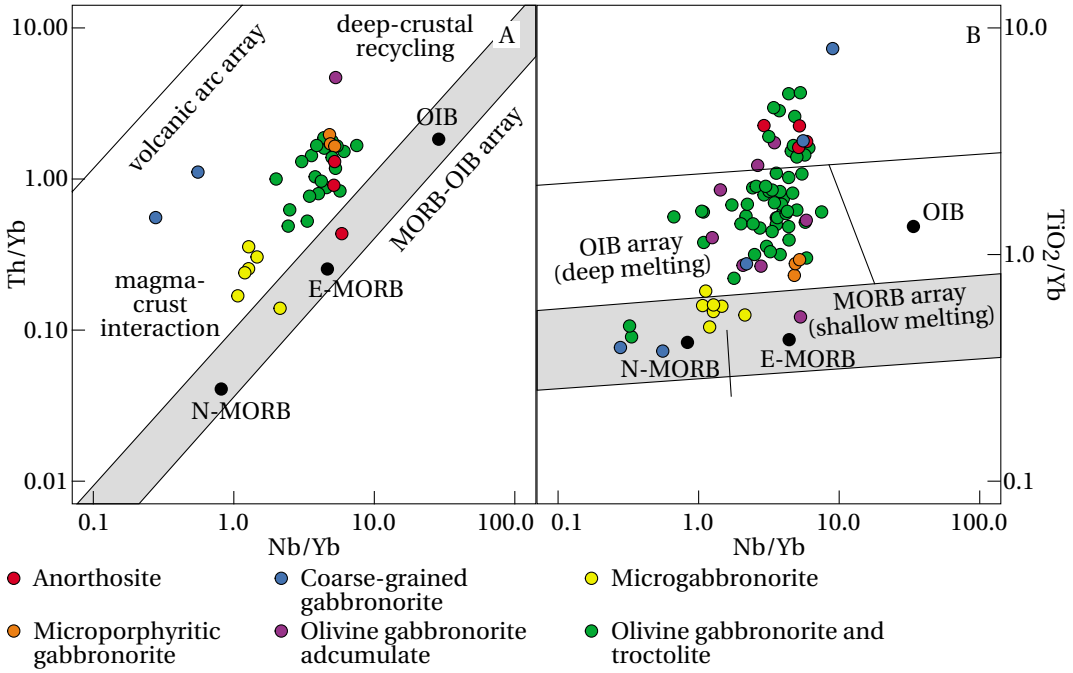

Figure 3.11 Trace element proxies for crustal input and melting depth after Pearce (2008). The Th-Nb proxy uses Th/Yb and Nb/Yb ratios to detect crustal input. The grey-shaded area is the MORB-OIB array, which is characterised by the absence of crustal input; outside of this array and at relatively lower Nb and higher Th concentrations are melts that were contaminated with lithospheric material. The plot showing the Th-Nb proxy contains only a subset of the samples compared to the plot showing the Ti-Nb proxy, due to many samples with Th contents below the LOD. The Ti-Nb proxy uses Ti/Yb and Nb/Yb ratios to estimate the depth where partial mantle melting occurred. The grey-shaded area represents shallow melting which generates MORB-type melt; at higher relative Ti concentrations are OIB-type melts that were produced at greater depths within the stability field for residual garnet.

ing to deeper melting. Pearce (2008) associated this with partial mantle melting within the stability field of garnet. But since there is strong evidence against a garnet-bearing residue (see the REE model in figure 3.10) it is suggested here that the elevated Ti contents are probably due to increased amounts of cumulus Fe-Ti-oxides, in particular within the upper parts of the intrusive body. This also explains, why the ANO and the OGT, which occur towards the top and contain some of the highest amounts of Fe-Ti-oxides (see petrographic descriptions in sections 2.4.2 and 2.4.3), also show some of the most extreme TiO_2/Yb ratios. Nevertheless, does the Ti-Nb proxy in figure 3.11 show a similar distribution of melting depths for the lithologies as was already suggested by the different negative Nb-anomalies (see the discussion of the Th-Nb proxy above). It is particularly worth noting that the MCG and half of the CGG samples overlap with shallow MORB-type melts.

Table 3.2 Average Sr-Nd-isotopic signatures of present-day mantle reservoirs. Data were compiled after Ernst and Buchan (2003) with references for the original data given in the table footnotes.

Reservoir	$^{87}Sr/^{86}Sr$	$^{143}Nd/^{144}Nd$	ϵ_{Nd}
EM 1	0.705 30 [ab]	0.512 36 [a]	−5.5 [a]
		0.512 33 [b]	−6 [b]
EM 2	0.707 80 [a]	0.512 58 [a]	−1 [a]
HIMU	0.702 85 [a]	0.512 85 [a]	+4 [a]
DMM	0.702 20 [a]	0.513 30 [a]	+13 [a]
FOZO	0.703 50 [c]	0.512 90 [c]	+5 [c]

[a] Hart 1988; Hart et al. 1992
[b] Eisele et al. 2002
[c] Hauri et al. 1994

Constraints from Sr-Nd-isotopes

The Sr-Nd isotopic compositions of mafic igneous rocks carry information about potential crustal contamination and mantle reservoirs. One common caveat is that mantle reservoirs are generally defined on the basis of modern basaltic rocks (see the references in table 3.2). In addition, the existence of some mantle reservoirs during the Mesoproterozoic might not be guaranteed, thus, care must be taken during the interpretation (Maas, personal communication, 2014). On the other hand does the time around 1.1 Ga ago mark the transition towards modern-style plate tectonics (Arndt and Davaille 2013), thus, unquestionable was the Mesoproterozoic Earth already chemically differentiated into the continental and oceanic crust and the mantle, and different mantle reservoirs such as the depleted and primitive mantle must have existed. However, these two reservoirs are probably not enough, as White (2015a) pointed out: a simple two-layer mantle model with a depleted upper and a primitive lower mantle does not explain the observed ϵ_{Nd} and $^{87}Sr/^{86}Sr$ signatures, because they cannot be produced by mixing of these two components. Instead, there are probably at least five main mantle reservoirs named depleted mid-ocean ridge basalt mantle (DMM), high-μ mantle (HIMU), enriched mantle 1 (EM 1), enriched mantle 2 (EM 2) and prevalent mantle (PREMA) (White 1985; Zindler and Hart 1986; White 2015a). Other mantle endmembers such as focal zone (FOZO) (Hart et al. 1992), primitive helium mantle (PHEM) (Farley et al. 1992) and common component (C) (Hanan and Graham 1996) are probably related to prevalent mantle (PREMA) according to White (2015a). Table 3.2 shows a list of the present-day Sr-Nd-isotopic characteristics of the different mantle reservoirs. The depleted mid-ocean ridge basalt mantle (DMM) reservoir is generally the result of the differentiation of the Earth into mantle and crust. The reservoir is compositionally clearly distinct from other reservoirs (e.g. strongly depleted in incompatible elements, hence the name) and is located in the upper mantle where MORB magmas are produced (Hart 1988; White 2015b). The origin of the enriched reservoirs enriched mantle 1 (EM 1), enriched mantle 2 (EM 2) and high-μ mantle (HIMU) is somewhat more enigmatic (White 2010, 2015b). Even though EM 1 and EM 2 are isotopically distinct, they cannot be distinguished reliably using trace element alone (Willbold and Stracke 2006). Willbold and Stracke (2006) therefore suggested that EM 1 and EM 2 were

produced by subduction and recycling of lower and upper continental crust, respectively. But while there is no consensus on the details, it is generally accepted that subduction processes may have been involved in the formation of EM 1 (Hart 1988) as well as EM 2, and both seem to be stored in the deep mantle (Hart 1988; Porter and White 2009; White 2015b). The HIMU mantle reservoir was likely formed by subduction and recycling of oceanic crust that underwent metasomatic alteration (Hart 1988; Willbold and Stracke 2006; White 2010, and references therein). While there is generally no mixing between EM 1, EM 2 and/or HIMU, all three reservoirs can contain small amounts of the PREMA reservoir. Further, all four reservoirs occur in mantle plumes (White 2015b).

The comparison of initial $^{87}Sr/^{86}Sr$ ratios and initial ϵ_{Nd} values from the Bell Rock Range intrusion with common mantle reservoirs (figure 3.12) shows that a DM source is not necessary to explain the observed signatures. Instead, the signatures can be explained

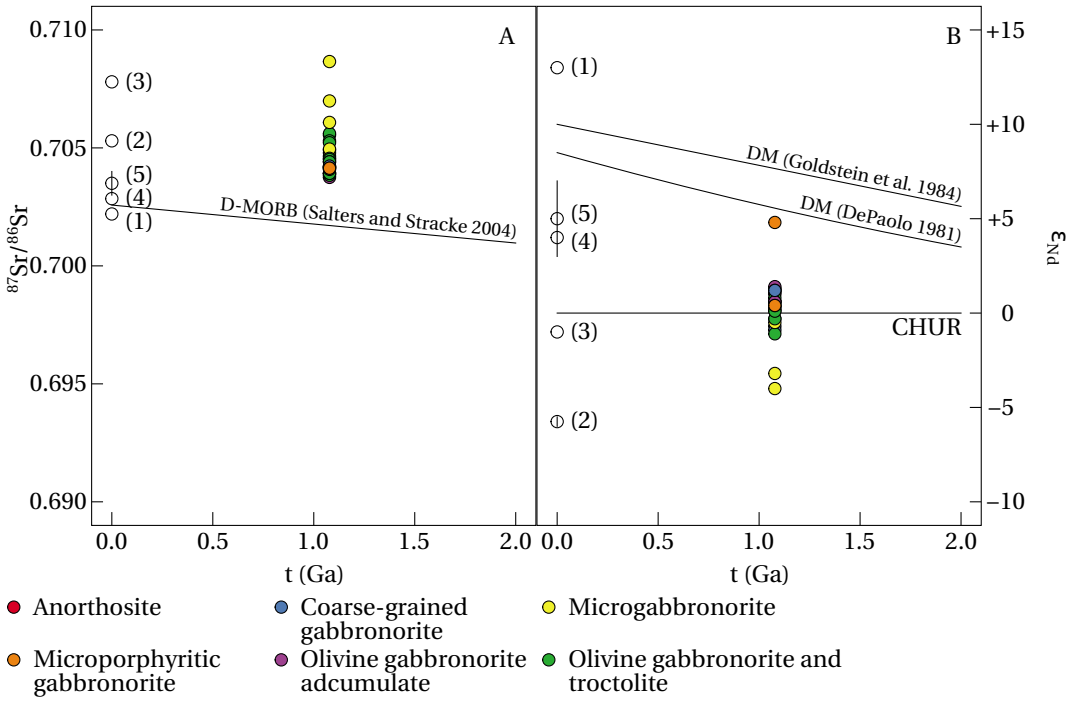

Figure 3.12 Sr and Nd isotopic mantle evolution diagrams. The present-day reservoirs in both diagrams are: (1)—depleted mid-ocean ridge basalt mantle (DMM), (2)—enriched mantle 1 (EM 1), (3)—enriched mantle 2 (EM 2), (4)—high-μ mantle (HIMU), (5)—focal zone (FOZO); the data and references for from table 3.2. **A**—Depleted mid-ocean ridge basalt (D-MORB) mantle evolution curve modelled with initial $^{87}Sr/^{86}Sr$ from Papanastassiou and Wasserburg (1968, basaltic achondrite best initial (BABI) = 0.698 98 at 4.5 Ga) and average present-day $^{87}Sr/^{86}Sr$ of 0.7026 from Salters and Stracke (2004). **B**—Mantle evolution curves for ϵ_{Nd} after DePaolo (1981) and Goldstein et al. (1984).

in several ways, including crustal contamination, an enriched mantle source or both. The trace elements suggest contamination with crustal material (see above). The components that together formed the parental magma of the Bell Rock Range intrusion have poorly

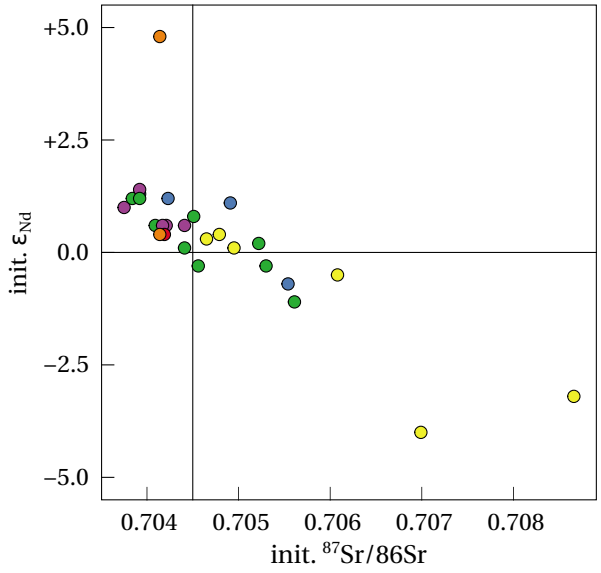

Figure 3.13 Sr-Nd isotopic signatures of the rocks from the Bell Rock Range intrusion. Initial (init.) ϵ_{Nd} and initial $^{87}Sr/^{86}Sr$ are calculated for an age of 1078 Ma (Sun et al. 1996).

homogenised, i.e. it is expected that some samples exhibit contamination signatures more than others. Contamination signatures are never low enough, however, to require a DM source, which makes this the least likely reservoir. The initial ϵ_{Nd} values for the Bell Rock Range intrusion roughly cluster over the CHUR ($\epsilon_{Nd} = 0$) with initial ϵ_{Nd} values of −1.1 to +1.4 (excluding the lithologies of the dykes (MCG) and the potentially unrelated MPG; see also figures 3.12 and 3.13). However, recent studies suggested that the bulk earth (i.e. the PM reservoir) is nonchondritic and that instead the PM has ϵ_{Nd} values in the range of +3.6 to +7 and $^{87}Sr/^{86}Sr$ ratios of <0.705 (e.g. Caro and Bourdon 2010; Campbell and O'Neill 2012; White 2013, 2015a). These are all values that were previously attributed to the DM (White 2015a), which in turn makes the enriched mantle (EM) the most likely mantle reservoir from which the parental melts of the Bell Rock Range intrusion were derived.

The only sample that yields an overall primitive initial ϵ_{Nd} value is a sample from the parallel-running ridges with +4.8. The same sample has also on of the lowest initial $^{87}Sr/^{86}Sr$ ratios. However, the high initial ϵ_{Nd} value is not confirmed by the other sample of the MPG that was analysed. The MCG on the other hand, exhibit the most crustal isotopic trends.

3.6.2 Sulphide prospectivity

During the solidification of the intrusive body, Ni entered early-formed olivine and to a lesser extent pyroxene (section 2.6.3), whereas Cu accumulated in the residual melt, eventually forming Ni-poor sulphides. The sulphides are only an interstitial accessory phase in

the Bell Rock Range intrusion and where present they are commonly chalcopyrite ($CuFeS_2$) with minor bornite (Cu_5FeS_4; see also the petrographic descriptions in section 2.4). Their generally elevated Cu/Ni ratios suggest crystallisation from the late-stage intercumulus liquid. This is the product of normal magmatic fractionation and not an accepted mechanism to form economic orthomagmatic Ni-Cu-PGE sulphide deposits (Mavrogenes and O'Neill 1999). If any sulphur depletion event happend, this was likely only a minor event that occurred at depth. The concentrations of Cu and Pd are relatively constant throughout the troctolites and anorthosites within the main intrusive body. A slight increase is observed towards the base and the top of the intrusion, where gabbroic units have higher concentrations in Cu and Pd, possibly due to larger amounts of interstitial liquid. The Cu/Pd ratios are for the most part in the range of c. 5×10^2–5×10^4 and variations are mostly cryptic. Only a slight increase is observed in the CGG towards the base of the main intrusive body as well as the MPG from the parallel-running ridges. Concentrations of Pt show greater variations, especially within troctolites and anorthosites; the Pt/Pd ratios yield cryptic variations that do not correlate with the lithologies.

3.7 Conclusions

The modal rock compositions, that are needed to perform rock classifications, can be calculated from the normative mineralogy. The variations in the modal mineral proportions in the samples from the Bell Rock Range intrusions are consistent with the grouping into the lithologies that was previously established (chapter 2). The following conclusions are made based on the data that was collected from the Bell Rock Range intrusion and above discussions on the matters of constraints on tectonic setting and melting depth with implications on melt sources and crustal contamination, as well as petrogenesis and emplacement of the intrusive body:

Magma sourcing The HFSE and Sr-Nd-isotopic signatures of the Bell Rock Range do not support a DM source for the main body of the intrusion. Instead, the Nb-Y-Zr signatures make an OIB-type source the most likely. While this is common for continental rifts, this does not necessarily indicate an active plume-driven rift but can also be caused by melting of metasomatised SCLM (Fitton et al. 1997; Fitton 2007). The Sr and Nd isotopes support these findings with compositions that are close to the EM reservoir, which has been shown to occur in mantle plumes (not exclusively) but also contains a reworked subducted slab component (White 2015b). The parental magmas of the Bell Rock Range intrusion were sourced from spinel-lherzolite mantle at a maximum depth of 75 km, because there is no evidence for a garnet-bearing residue during partial mantle melting. Even though garnet was not stable during melting, within an extensional tectonic setting this would still have occurred sufficiently deep for either a lithospheric or an asthenospheric mantle source (Gazel et al. 2012). Some samples from the MCG, the CGG and the MPG have MORB-type trace element and/or isotope characteristics, respectively. If this is caused by partial melting of a (shallower?) DM source, this would strongly suggest that these lithologies were not formed together with the main body of the intrusion (lithologies of the ANO, OGA and OGT).

Crustal contamination Crustal contamination signatures are present but often not very strong in the samples from the Bell Rock Range intrusion. Besides having MORB-type characteristics, some of the samples of the MCG, the CGG and the MPG do also exhibit the strongest crustal signatures. Some of the felsic country rocks in the area were previously reported to be extremely enriched in incompatible trace elements, caused by extensive crustal reworking (Kirkland et al. 2012a, 2013). Consequently, small amounts of contamination with crustal material were able to cause the observed signatures and the variations in the distinctiveness of these signatures are due to bad magma homogenisation.

Sulphide prospectivity The whole-rock geochemistry confirms previous conclusions on the sulphide prospectivity. No major early sulphide segregation event occurred, thus, olivine is the primary control for the Ni budget of the rocks. This renders the investigated areas of the Bell Rock Range intrusion unprospective for economic Ni-rich sulphide ore deposits. Following partial melting of the mantle, the igneous system underwent extensive fractionation, which lead to the crystallisation of late-stage Cu-rich sulphides within the interstitial liquid. For such a system to produce an economic sulphide ore deposit, the assimilation of crustal S would be essential; however, there is little evidence for this to have happened. Another impediment to ore formation is that the high-flux melts were most likely derived from an unsuitable mantle reservoir (SCLM; see above). This may later have changed when the Alcurra Dolerite formed, which means that the MPG from the parallel-running ridges may be the most prospective lithology, because the might be members of the Alcurra Dolerite.

Overall, the western Basin and Range Province (United States) may be an appropriate analogue to the Ngaanyatjarra Rift. The REE chemistry suggests partial mantle melting occurred at a depth above the stability of garnet and mafic igneous rocks from the Basin and Range Province were likely derived from a lithospheric mantle source that was previously enriched by a subducted slab and yield Δ_{Nb} values around 0, similar to the Bell Rock Range. The depth of melting and the type of mantle source did not remain constant over the geological history of the Basin and Range Province, thus, while many lithologies from the Bell Rock Range intrusion may have been sourced from metasomatised SCLM, the same may not be true for the Alcurra Dolerite, which might have been derived from an asthenospheric source.

Chapter 4

Latitude Hill and Wingellina Hills layered intrusions and massive gabbros

4.1 Introduction

The Mesoproterozoic Giles Event in central Australia was a major event that caused extensive melting in the Earth's mantle. One of the largest known mafic-ultramafic igneous complexes, comprising c. 20 layered intrusive bodies, formed during the event. The Latitude Hill and the Wingellina Hills are two layered intrusions of the Giles Event and are part of a group of intrusive bodies that are dominated by gabbroic and ultramafic cumulates. Many of these intrusions are associated with massive gabbroic intrusions that show strong signs of felsic crustal contamination. Moreover, the Latitude Hill intrusion may represent a segment of the Michael Hills intrusion (e.g. Ballhaus and Glikson 1995; Glikson et al. 1996; Maier et al. 2014, 2015).

Most previous studies noted the strongly contaminated gabbros (e.g. Daniels 1974; Glikson et al. 1996; Evins et al. 2010b,c; Maier et al. 2014, 2015). This chapter uses trace elements as well as Sr and Nd isotopes to first assess the crustal contamination signatures in the Latitude Hill and the Wingellina Hills layered intrusions and then revisit the boundary between the layered G1 and the massive G2 gabbros using a multivariate statistical approach. The multivariate techniques were carried out in compliance with compositional data analysis.

Compositional data are a type of data that has some inconvenient properties, such as that correlations between two variables can be spurious (Pearson 1896; Chayes 1960). A rich body of work has been published in recent decades that contains tools to handle compositional data in an appropriate way (e.g. Aitchison 1982, 1984, 1986; Egozcue et al. 2003; Pawlowsky-Glahn 2003; Mateu-Figueras et al. 2011). These methods are essentially based on log-ratio transformations of the original data, that remove the closure from the data and ensure that multivariate techniques can be applied.

4.2 Geological setting

The Latitude Hill and Wingellina Hills intrusions are two gabbroic-ultramafic layered intrusive bodies, located in the Mesoproterozoic Musgrave Province, central Australia (figure 4.1). The Musgrave Province is located between the North, South and West Australian cratons and extends c. 800 km east-west and 350 km north-south; it is bounded to the north, east, south and west by the Neoproterozoic/Palaeozoic Amadeus, Eromanga, Officer and Canning basins, respectively. The south dipping Woodroffe Thrust is a major east-west trending structure that divides the Musgrave Province into the northern amphibolite-facies Mulga Park Domain and the southern granulite-facies Fregon Domain, and was active during the c. 570–530 Ma Petermann Orogeny (Camacho and Fanning 1995; Camacho 1997; Scrimgeour and Close 1999; Gregory et al. 2009; Raimondo et al. 2010). Most of the western Musgrave Province (which hosts the Latitude Hill and Wingellina Hills intrusions) is located in the Fregon Domain, which can be further divided into several subdomains, i.e. the Walpa Pulka, Tjuni Purlka and Mamutjarra Zones as well as the Wanarn and Mitika Areas (Howard et al. 2011b, 2015). The subdivision into theses zones was established based on the spatial and temporal distribution of the stratigraphic units (in particular the Wankanki and Pitjantjatjara Supersuites, which predate the Giles Event) as well as differing styles and degrees of deformation (Smithies et al. 2009a, 2010; Aitken et al. 2013). Section 1.2.1 provides a detailed review of the basement lithologies and geological history prior to the Giles Event.

4.2.1 Latitude Hill intrusion

The Latitude Hill intrusion (figure 4.2; Ballhaus and Glikson 1995; Glikson et al. 1996) has been interpreted to represent a section of the Michael Hills intrusion and is distinct from most other layered intrusions of the Giles Event in that igneous layering strikes north-south. The intrusion has a total thickness of up to c. 8 km and is made up of two segments, which may have been displaced by a broadly WNW-ESE striking fault (Howard et al. 2009b). Igneous layering is subvertical and dips at c. 80° towards the southwest. The major lithologies are gabbronorites, pyroxenites and rare peridotites, which are interlayered on a scale of several tens of metres or more and only rarely on a smaller scale of several metres or centimetres. The gabbronorites can contain cumulus olivine, clinopyroxene and poikilitic orthopyroxene as well as plagioclase, whereas the pyroxenites are websterites with cumulus ortho- and clinopyroxene and accessory olivine. Orthopyroxene is often very coarse-grained, in particular in pyroxenitic cumulates, and the relative amounts of plagioclase are highly variable. Peridotites within the Latitude Hill intrusion contain cumulus olivine, clino- and orthopyroxene and chromite. They can be feldspathic and contain interstitial Na-rich plagioclase. The central section of the intrusion contains gabbronorites and anorthosites that are more fractionated and Fe-Ti-oxide bearing. Fine grained dolerites with a subophitic texture have been interpreted as intraplutonic chill zones by Ballhaus (1993). Ballhaus and Glikson (1995) and Glikson et al. (1996) reported one of the rarely exposed contacts between Giles intrusions and gneissic wall rocks at the eastern margin of Latitude Hill.

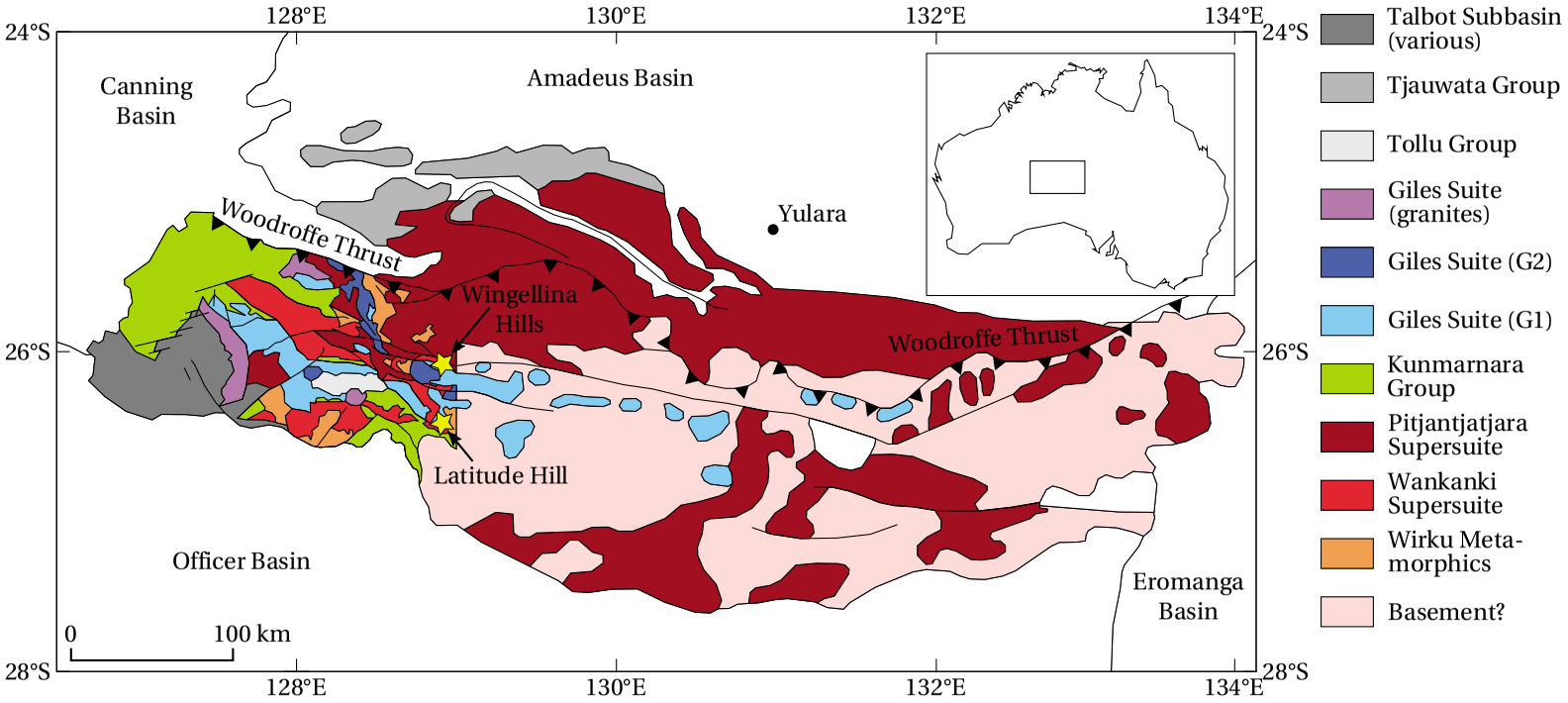

Figure 4.1 Geological map of the Musgrave Province, showing the location of the Latitude Hill and the Wingellina Hills intrusions (modified after Howard et al. 2011a, 2015). The mafic-ultramafic layered and massive intrusions of the Giles Event are concentrated in the western parts of the Musgrave Province. The inset map shows the location of the Musgrave Province in central Australia.

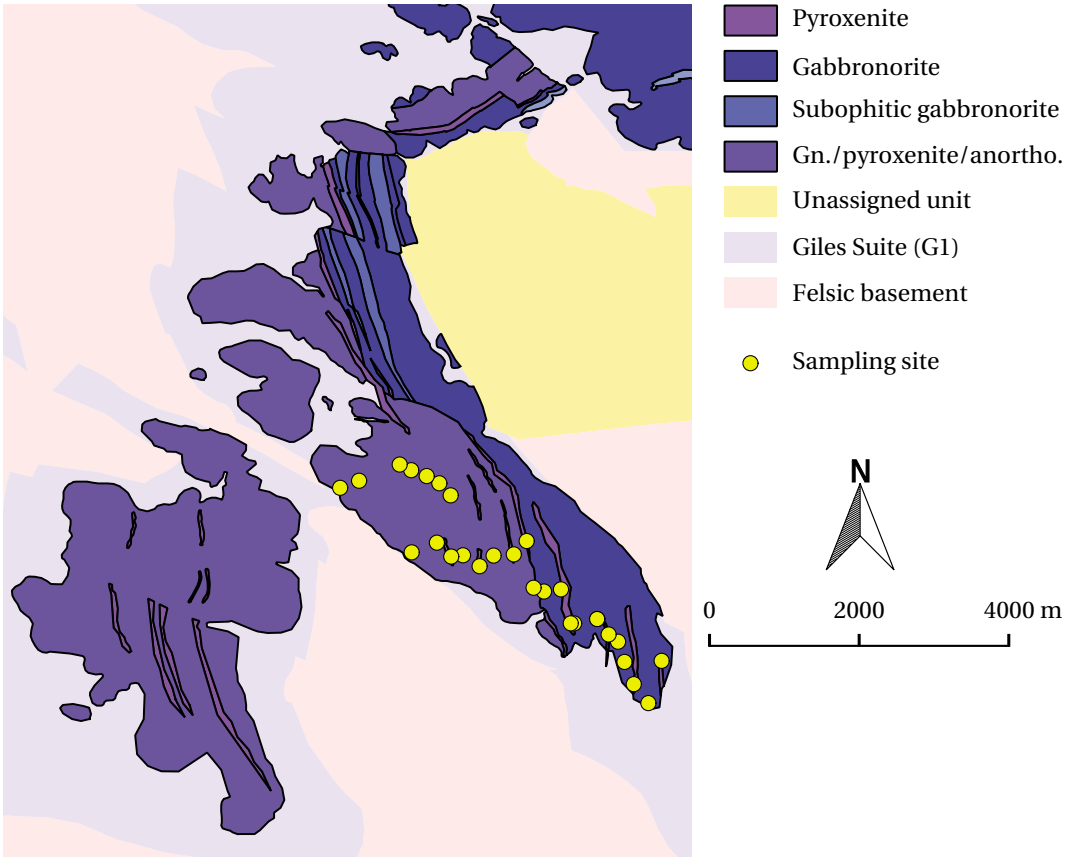

Figure 4.2 Geological map of the Latitude Hill intrusion, indicating the locations of the sampling sites along the sampling traverse. Bold coloured areas show the surface outcrop with lithologies simplified from Howard et al. (2009b); light shaded areas show the interpreted bedrock geology (simplified from Howard et al. 2009b). The felsic basement includes the Wirku Metamorphics and the Wankanki and Pitjantjatjara Supersuites; the unassigned unit is also felsic. Abbreviations are gn.—gabbronorite, anortho.—anorthosite.

4.2.2 Wingellina Hills intrusion

The Wingellina Hills intrusion (figure 4.3; Ballhaus and Glikson 1989, 1995; Glikson et al. 1996) is one of the smaller intrusive bodies in the area and outcrops over an area of c. 12 × 2 km. Igneous layering within the intrusion strikes at c. 110–120° and dips at 60–70° towards south-west; the southern margin of the intrusive body is thought to represent the top. This results in a true thickness of c. 1.6 km, with individual lithological units being up to c. 200 m thick. The Wingellina Hills intrusion is thought to record multiple pulses of a single olivine-saturated magma; the main lithologies (olivine gabbronorites and gabbronorites) are interlayered with pyroxenites and peridotites (Ballhaus and Glikson 1989). Ballhaus and Glikson (1989) reported the occurance of minor sulphides in the Wingellina Hills intrusion, although the only economic ore deposit that has been discovered in the area to date is the Wingellina Ni-Co limonite deposit that is located directly south of the

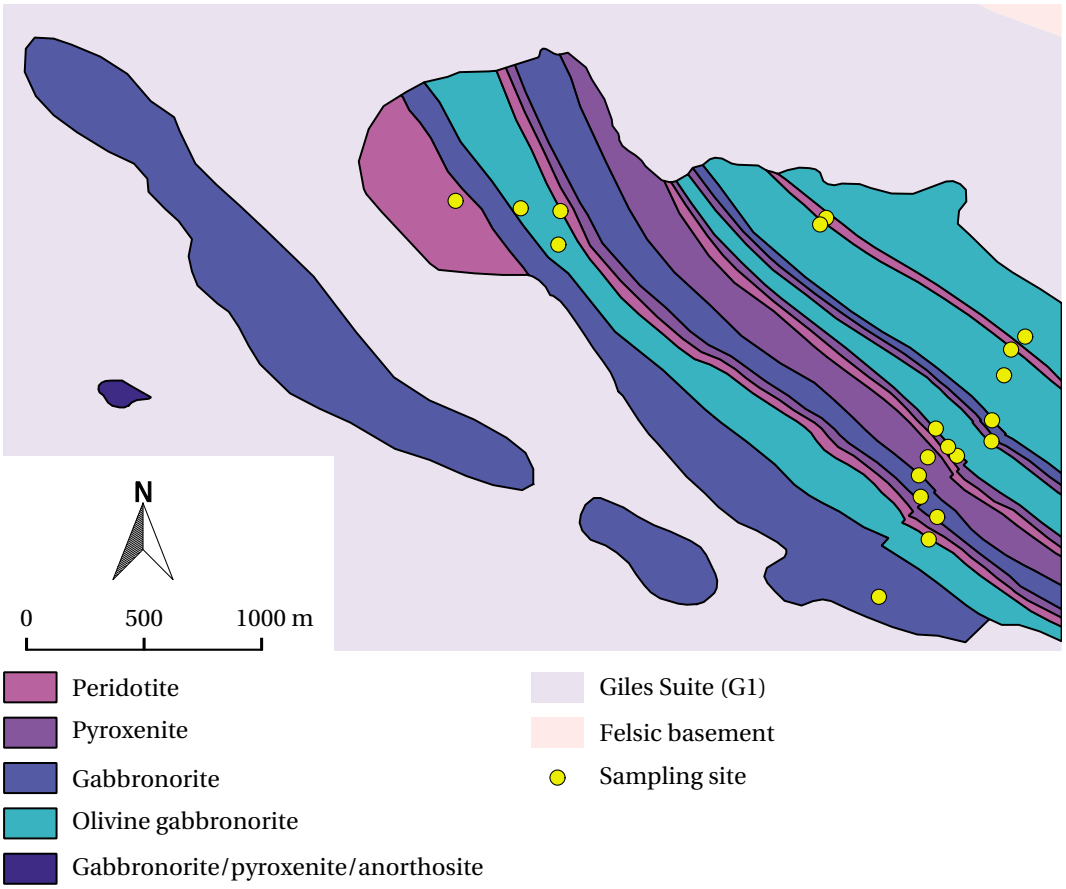

Figure 4.3 Geological map of the Wingellina Hills intrusion, indicating the locations of the sampling sites along the main sampling traverse in the centre of the intrusion as well as the partial traverse in the northwest. Bold coloured areas show the surface outcrop with lithologies simplified from Howard et al. (2009b); light shaded areas show the interpreted bedrock geology (simplified from Howard et al. 2009b). The felsic basement includes the Wirku Metamorphics and the Wankanki and Pitjantjatjara Supersuites.

intrusion (Goode 2002; see also `http://www.metalsx.com.au/nickel/`).

4.2.3 Massive gabbroic intrusions (G2)

Several of the layered intrusions in the Musgrave Province are located alongside massive gabbroic intrusive bodies. The most notable occurences of these massive gabbros are at the north-western part of the Hinckley Range, the western and south-western parts of the Murray Range as well as along the northern margin of the Michael Hills locality. Daniels (1974) thought these to be contaminated members of the Hinckley Range intrusion; Ballhaus (1993), Ballhaus and Glikson (1995) and Glikson et al. (1996) described the same rocks as mafic granulites that were locally intruded by granites, aplites and pegmatites. They locally exhibit a recrystallisation texture that was thought to be the result of a

metamorphic overprint (Clarke 1992). Evins et al. (2010b,c) suggested these gabbros represent a second phase of magmatic-intrusive activity following the emplacement of the layered intrusions. These authors termed the massive gabbroic intrusions the 'G2' member of the Giles Suite. They are currently only known from the western Musgrave Province, where they outcrop in a northwest- to southeast-trending band that follows the boundary between the Walpa Pulka and the Tjuni Purlka zones (figure 4.1). This zone was termed the Murray Range Shear Zone by Evins et al. (2010c) and it is thought to represent a reactivation of the Tjuni Purlka zone (at c. 1220, 1075 and 550 Ma; Howard et al. 2011b, 2015). The G2 suite consists of unlayered fine to medium grained gabbros and gabbronorites with an ophitic to subophitic texture and occasional interstitial magnetite. They exhibit localised evidence for the assimilation of felsic material, such as spectacular mixing and mingling textures with granitic melts (figure 4.4; Glikson et al. 1996; Evins et al. 2010b,c). These felsic magmas were assimilated to various degrees; as granitic blebs or

Figure 4.4 Photograph of mixing and mingling textures in massive G2 gabbros at the western Hinckley Range (472 836 m E 7 118 998 m N; the handle of the hammer is c. 30 cm in length).

xenoliths, mingled with the mafic magma or fully mixed with it, forming hybrid magmas. At least in places, multiple phases of felsic melts were detected and interpreted to be comagmatic. The contaminants are typically A-type granites that are thought to be similar to the Pitjantjatjara Supersuite granites but are more enriched in the rare earth element

Intrusion	n	$\bar{\mathbf{a}}$	$d_{\max}$ (m)
Latitude Hill	28	076/29	3106
Wingellina Hills	21	025/17	1494

Table 4.1 Metadata for the two sampling traverses across the Latitude Hill and Wingellina Hills intrusions, collected during the 2011 field season. Data include the total number of samples per traverse n, averages for the attitude $\bar{\mathbf{a}}$ of the poles to the planes of igneous layering and a calculated estimate of the maximum thickness d_{max} (equals the depth estimate of the lowermost sample) in metres. The method of estimation is outlined in appendix A.1.

(REE) and the high field strength element (HFSE) than the Pitjantjatjara granites (Evins et al. 2010b,c).

The age of the G2 suite has been constrained through the associated felsic rocks (see for instance the list of ages in Evins et al. 2010c), yielding a currently accepted age range of 1078–1074 Ma (Howard et al. 2015), largely overlapping with the age of the G1 suite. Howard et al. (2015) further reported areas where the massive G2 gabbros cross-cut the igneous layering in the central and eastern parts of the Hinckley Range intrusion, thus, it appears that the G2 suite is younger than the G1 suite. The field relationships, however, seem to be ambiguous because previous studies interpreted the same contact between the layered sequence and the contaminated gabbros to be sheared, thus, obscuring the true intrusive contact (Ballhaus and Glikson 1995, figure 11). Indeed, according to some authors the contaminated gabbros may have been produced by the later infiltration of granitic material into the originally intact layered sequence of the Hinckley Range intrusion, an event that could have happened around c. 1050 1070Ma (Clarke 1992; Glikson et al. 1996).

4.3 Sampling, analytical procedures and data processing

During the field season from April to May 2011 the gabbroic Latitude Hill and the ultramafic Wingellina Hills intrusions were sampled along a single traverse across each intrusion that were approximately orthogonal to igneous layering (table 4.1; figures 4.2 and 4.3). The Latitude Hill intrusion comprises two lobes (figure 4.2) of which only the eastern lobe was sampled. Three out of the total 49 samples that were collected are micrograbbroic dykes, all of which originate from Latitude Hill. The stratigraphic depth for individual samples was estimated from surface coordinates according to the procedure described in appendix A.1.

4.3.1 Analytical procedures

Weathering was removed from all samples using a rock saw and grinding marks from the saw blade were subsequently removed with a diamond grinding disk. The samples were then washed with distilled water and sent to Acme Analytical Laboratories in Vancouver,

Canada, for further preparation and analysis of the major, trace and precious metals. The rock samples were crushed and ground at Acme Analytical Laboratories to pass a size 200 mesh (74 µm) and the rock pulps were dried at 105 °C prior to the analyses. The results of the major and trace element as well as the isotope analyses are in appendix B.

Major and trace element concentrations were determined on pulps that had been fused to glass disks in a mixture of $LiBO_2$ (lithium metaborate) and $Li_2B_4O_7$ (lithium tetraborate) and then digested in HNO_3. Inductively coupled plasma optical emission spectrometry (ICP-OES) was used to determine the major element concentrations and inductively coupled plasma mass spectrometry (ICP-MS) for the trace elements. The Ni and Cu concentrations were determined by 4-acid digestion followed by ICP-OES and ICP-MS, respectively; precious metal concentrations (Au, Pt and Pd) were determined by lead-collection fire assay and ICP-MS. Total C and S were determined by combustion analysis using a LECO furnace. The analytical results reported all Fe as Fe(III) (Fe_2O_3), thus, more realistic relative FeO and Fe_2O_3 contents were estmated using the method of Le Maitre (1976), which is based on a linear regression analysis (see description of the procedure in appendix A.2).

Isotope analyses were carried out on two samples (sample 205 283 from Wingellina Hills and sample 205 298 from Latitude Hill) at the School of Earth Sciences at the University of Melbourne. The $^{87}Rb/^{86}Sr$ ratio for sample 205 298 was calculated from the concentrations of Rb and Sr from the trace element analyses and determined by isotope dilution for sample 205 283 due to the elevated Rb/Sr ratio. The external precision (2σ) of the $^{87}Rb/^{86}Sr$ ratio is ±0.5 % for sample 205 283 and ±5 % for sample 205 298. The $^{87}Sr/^{86}Sr$ ratios were normalised to $^{88}Sr/^{86}Sr = 8.375\,21$ and reported relative to the standard SRM987 ($^{87}Sr/^{86}Sr = 0.710\,23$). The internal precision (2σ) for the $^{87}Sr/^{86}Sr$ ratio is ±0.000 02, the external precision (2σ) is ±0.000 04.

Sm and Nd concentrations were determined by isotope dilution and used to calculate the $^{147}Sm/^{144}Nd$ ratios; the external precision for $^{147}Sm/^{144}Nd$ (2σ) is ±0.2 %. The $^{143}Nd/^{144}Nd$ ratios were normalised to $^{146}Nd/^{145}Nd = 2.071\,942\,5$ (equivalent to $^{146}Nd/^{144}Nd = 0.7219$) and reported relative to the LaJolla standard ($^{143}Nd/^{144}Nd = 0.511\,860$). The internal precision (2σ) is ±0.000 014, the external precision (2σ) is ±0.000 020.

The $^{87}Sr/^{86}Sr$ ratio of bulk earth is assumed to be 0.7045 (Faure and Mensing 2005); the present-day values for $^{147}Sm/^{144}Nd$ and $^{143}Nd/^{144}Nd$ of the chondritic uniform reservoir (CHUR) were taken as 0.1967 (Wasserburg et al. 1981; DePaolo 1988) and 0.512 638 (DePaolo 1988), respectively. T_{DM} is the depleted mantle model age, assuming linear Nd isotope evolution within the depleted mantle from 4.56 Ga to present-day. The decay constants were $\lambda = 1.42 \times 10^{-11}\ y^{-1}$ for ^{87}Rb and $\lambda = 6.54 \times 10^{-12}\ y^{-1}$ for ^{147}Sm.

Petrographic descriptions (section 4.5) were carried out on the same polished thin-sections that were used to determine the mineral chemistry via electron beam microprobe analysis (EMPA). Analyses were carried out at the School of Earth Sciences of the University of Melbourne, Australia, using a Cameca SX 50 microprobe and wavelength-dispersive spectroscopy (WDS). The analyses were done in several batches operating under beam currents of 35.1–35.77 kV and an accelerating current of 14.92 kV. The take off angle was 40°, the tilt and azimuth angles were 0°.

The CIPW (Cross, Iddings, Pirsson, Washington) normative mineralogy and average mineral densities were used to calculate modal rock compositions which were used to classify rock samples; details of the methods of norm calculations and classification are given in appendices A.3 and A.4, respectively. Any atomic weights used in calculations were taken from Wieser et al. (2013); the trace element values used to normalise the samples to primitive mantle are from McDonough and Sun (1995). The Eu-anomaly was calculated as the geometric mean between the relative amounts of the adjacent REEs Sm and Gd (Taylor and McLennan 1985).

4.4 Compilation of external geochemical datasets

Section 4.8.2 revisits the boundary between the G1 and the G2 members of the Giles Suite and uses additional data from the *WACHEM* database of the Geological Survey of Western Australia (GSWA), accessed through the *GeoChem Extract* web portal (`http://geochem.dmp.wa.gov.au/geochem/`) and then classified into G1 and G2 samples. The basis for the classification are the coordinates of the sampling sites, the surface geology on a scale of 1:100 000 (100k) and the interpreted bedrock geology on a scale of 1:500 000 (500k) (Geological Survey of Western Australia 2011). The surface geology was generally assumed to be the most accurate, since it is directly based on field observations. However, the 500k mapsheets do not currently cover the entire western Musgrave Province, which made it necessary to supplement the data with the interpreted bedrock geology. The classification was then carried out in the following way:

1. Samples that were collected within the boundaries of the west Musgrave Province and whose stratigraphic unit codes on both, the 100k or 500k geology, match and begin with either 'P_-WKg1' (for G1) or 'P_-WKg2' (for G2) were accepted as is.

2. The samples were then filtered according to their lithologies, such that only mafic-intrusive lithologies were kept in the dataset (these being 'olivine gabbro', 'gabbro', 'metagabbro', 'olivine gabbronorite', 'gabbronorite', 'dunite (intrusive)', 'troctolite', 'magnetitite', 'olivine norite', 'olivine pyroxenite', 'pyroxene peridotite', 'lherzolite', 'orthopyroxenite', 'olivine orthopyroxenite', 'anorthosite', 'norite' and 'meta-anorthosite'); samples with any other lithologies were removed (these being 'granitic rock', 'granophyre', 'dolerite', 'basaltic andesite', 'basalt', 'pegmatite', 'dacite', 'andesite', 'metadolerite', 'metagranitic rock', 'metasedimentary rock', 'monzogranite', 'rhyolite', 'metafelsic rock', 'Ironstone', 'Gossan', 'Alluvium', 'Ferruginous saprolite', 'quartz diorite' and 'meta-monzogranite').

3. Most intrusive bodies are surrounded by a regolith zone that contains abundant boulders of unweathered rocks. They cannot be considered strictly in-situ, however, their positioning is accurate enough to allow for the classification into G1 or G2. Rock samples that are either G1 or G2 members on the 500k geology but were sampled within the regolith according to the 100k geology were therefore accepted, because the regolith outcrop in the area generally reflects the bedrock geology underneath (the

Table 4.2 Rejected samples from the WACHEM dataset, showing map codes for 100k and 500k spatial datasets, the lithology as specified in the WACHEM dataset and a comment specifying the reason for rejection.

Sample no.	100k map code	500k map code	Lithology	Comment
180 829	P_-WKg1-ogj	P_-WKg2-o	Gabbro	[a]
185 598	P_-KRm-xmb-mo	P_-WKg1-xo-a	Gabbro	[b]
187 128	P_-PJ-mg	P_-WKg1-xo-a	Gabbro	[b]
189 316	P_-WKg1-ogj	P_-WKg2-o	Olivine gabbronorite	[a]
189 317	P_-WKg1-ogj	P_-WKg2-o	Olivine gabbronorite	[a]
189 318	P_-WKg1-ogj	P_-WKg2-o	Olivine gabbronorite	[a]
189 321	P_-WKg2-xog-g	P_-WKg1-xo-a	Gabbronorite	[a]
189 381	P_-WKg1-om	P_-WKg2-o	Gabbronorite	[a]
189 382	P_-WKg1-om	P_-WKg2-o	Gabbronorite	[a]
189 383	P_-WKg1-om	P_-WKg2-o	Gabbronorite	[a]

[a] Conflicting information regarding G1 and G2 on 100k and 500k mapsheets
[b] Member of Giles Suite on interpreted 500k but was sampled on different stratigraphic unit on 100k

regolith types were either one of colluvium ('_Cf-l' or '_Cf-m'), eolian dunefield ('_Ed'), eolian veneer over alluvium and/or colluvium ('_Et'), residual or relict ferruginous materials ('_R-f'), groundwater calcrete ('_Rr-kg') or sheetwash fan ('_Wf')).

4. Finally, four samples were selected upon individual inspection:

   - sample 183 456 (located outside the current extent of the 100k mapsheets but traceably sampled from a small G1 intrusion),
   - samples 174 524 and 180 479 (sampled from small mafic intrusive bodies on the 100k mapsheets that were too small to be included in the 500k bedrock geology, so the samples are members of the granitic Pitjantjatjara Supersuite in the 500k dataset) and
   - sample 183 500 (sampled from a small mafic intrusive body on the 100k mapsheets that was too small to be included in the 500k bedrock geology so the sample is a member of the Wirku Metamorphics in the 500k dataset).

Ten remaining samples were rejected (table 4.2) due to unresolvable conflicts in their suite membership. They either contained conflicting information regarding their membership in either the G1 or the G2 suites in their 100k and 500k map codes or their 100k map codes (based on field observations) are the Pitjantjatjara Supersuite or the Bentley Supergroup and the lithologies are mafic-intrusive. In the latter case it is assumed that the sample could represent a rare mafic-intrusive member of these respective stratigraphic unit.

The dataset contained two types of duplicate analyses: reassays of the same sample using the same analytical technique and also alternative analyses, where for a particular

sample the same chemical element(s) were determined using different techniques. This second case occurred in particular when major and trace elements were assayed in one batch, followed by a second assay of trace elements (e.g. including the REE) at a later stage. While the former type of duplicate was resolved simply by calculating the arithmetic mean of the data, the latter was resolved by careful inspection of the involved analytical techniques and subsequent prioritisation. Only the data from the highest prioritised method was kept, which were either X-ray fluorescence (XRF) or ICP-OES for major elements and ICP-MS for trace elements. Batches where only Sm and Nd were determined (commonly via isotope dilution) were deleted, barring the calculation of present-day $^{147}Sm/^{144}Nd$ ratios, to preserve the coherence of the remaining REE data.

4.4.1 Processing of compositional data and missing values

The log-ratio transformations of the compositional data as well as the treatment of missing values were handled as implemented by the *compositions* add-on package (Boogaart and Tolosana-Delgado 2006, 2008, 2013) for the *R* statistical software environment (R Core Team 2015). Following the classifications of missing data in Little and Rubin (2002), Martín-Fernández et al. (2003), Martín-Fernández and Thió-Henestrosa (2006) and Martín-Fernández et al. (2011), the two reasons for missing values in this study are (1) that some chemical element was assayed for but its concentration was below the limit of detection (LOD). This type is often called *rounded zero* and denoted as below detection limit (BDL). (2) Some chemical element was not assayed for in the first place, which is commonly called 'essential zero' and denoted as missing completely at random (MCAR). BDL values were replaced by a drop-in value of 2/3 of the detection limit. This strategy is based on the assumption that the tail of the distribution of the data between the detection limit l_d and 0 (zero) is approximately triangular in shape (Boogaart and Tolosana-Delgado 2013); hence, replacing BDL values with $2/3 l_d$ makes it equally likely that the true value is within the interval of $]0, 2/3 l_d[$ than that it is within the interval of $]2/3 l_d, l_d[$. MCAR values were automatically replaced by the software package with Not a Number (NaN).

4.5 Petrography

4.5.1 Pyroxenite (PYR)

The lithologic unit of the pyroxenite (PYR) is more common at Latitude Hill but does occur within both intrusions (figure 4.5). It is a commonly medium- to coarse-grained adcumulate of ortho- and clinopyroxenes (websterite), with interstitial liquid being absent or occurring in very small amounts only. Some samples from this unit yield more normative plagioclase than can be observed in thin sections, which is probably due to assignment of too much CaO to plagioclase during the calculation of the normative mineralogy. There is no apparent difference between the PYR in the Latitude Hill and in the Wingellina Hills intrusions.

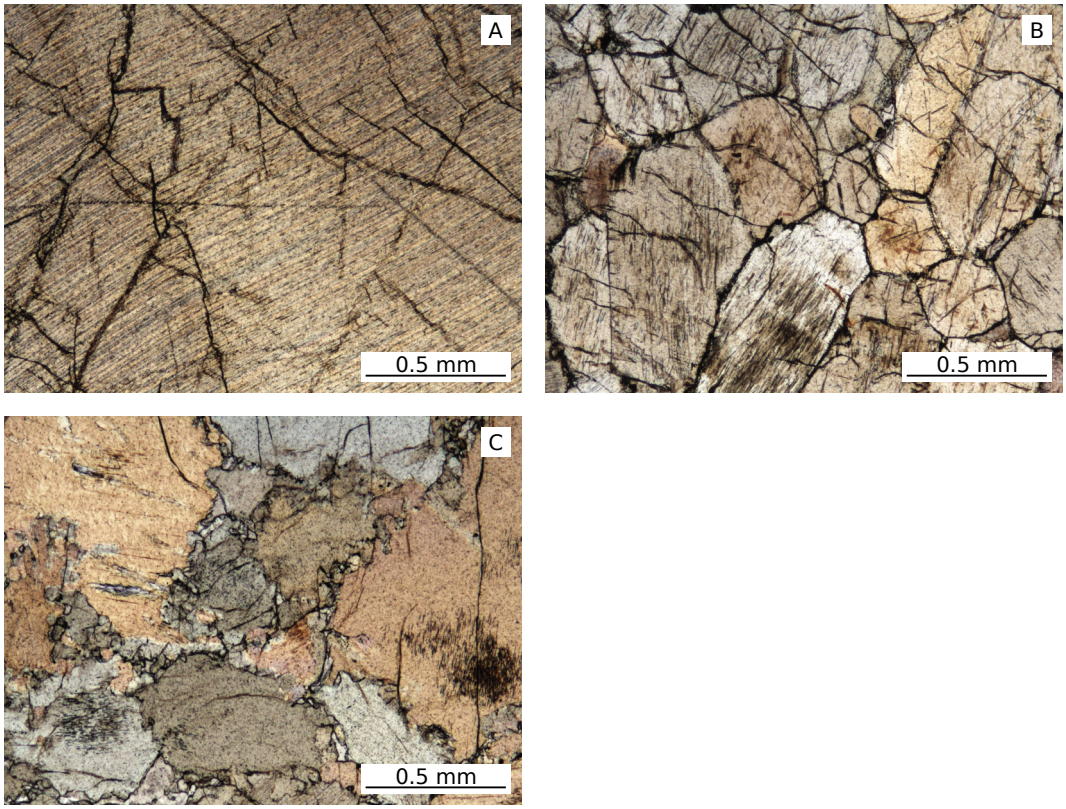

Figure 4.5 Micrographs of massive pyroxenite (PYR) (websterite) from the Latitude Hill (A—sample 205302, B—sample 205287) and Wingellina Hills intrusions (C—sample 205274).

4.5.2 Melagabbronorite (MLG)

The melagabbronorite (MLG) is one of the most abundant lithologic units in the Latitude Hill and Wingellina Hills intrusions. The rocks are texturally similar to the PYR (section 4.5.1), however, they contain more intercumulus plagioclase (figure 4.6). For this reason, they are described as mela-gabbronorites but there appears to be a spectrum of compositions between the PYR and the MLG. The MLG contain abundant cumulus pyroxene and intercumulus plagioclase, which occurs either between the cumulus pyroxene grains or in distinct melt pockets (e.g. in sample 205 305 from Latitude Hill; figure 4.6).

4.5.3 Variably-textured gabbronorite (VTG)

The majority of samples from the Latitude Hill and Wingellina Hills intrusions are variably-textured gabbronorite (VTG) that commonly contain cumulus plagioclase and pyroxene (figure 4.7). The textural variability in this lithology comes mainly from pyroxene which crystallised after plagioclase in several samples and is part of the intercumulus liquid. Differences between Latitude Hill and Wingellina Hills are, that especially the variably-

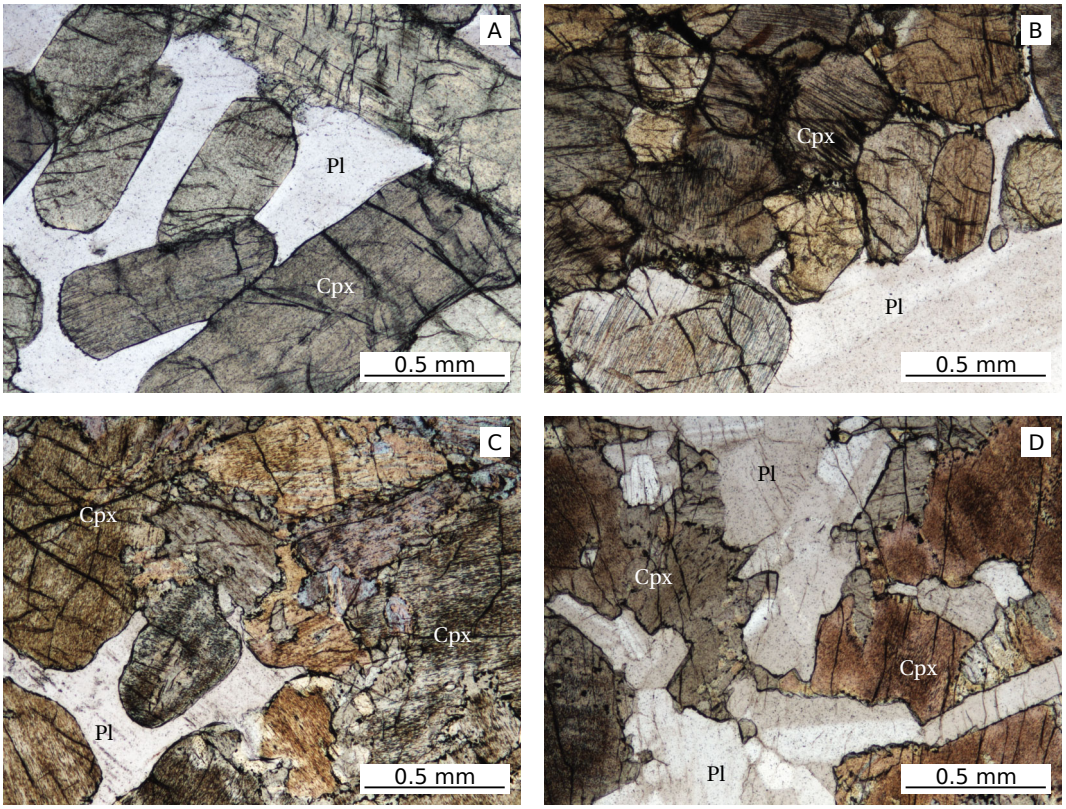

Figure 4.6 Micrographs of melagabbronorite (MLG) from the Latitude Hill (A—sample 205292, B—sample 205305) and Wingellina Hills intrusions (C—sample 205280, D—sample 205283).

textured gabbronorite (VTG) at Wingellina Hills are richer in normative olivine compared to the Latitude Hill intrusion.

4.5.4 Micrograbbronorite (MCG)

No microgabbronorites were sampled at Wingellina Hills, thus, all microgabbronorites are from the Latitude Hill intrusion. They are relatively variable in terms of texture.

4.5.5 Missing lithologic units

Several rock types were observed in former studies but could not be verified in this study (Ballhaus 1993; Ballhaus and Glikson 1995; Glikson et al. 1996). These are peridotitic and dunitic units that contain abundant modal cumulus olivine and minor chromite as well as anorthosites (the latter occur only in the central part of the Latitude Hill intrusion). No samples of these rock types were collected due to the high weathering rate and often lenticular outcrop, thus, the sampling traverses did not intersected fresh material of the respective layers. Due to the absence of geographic coordinates in the description of the lithologies of the above previous studies, the original field sites could not be revisited.

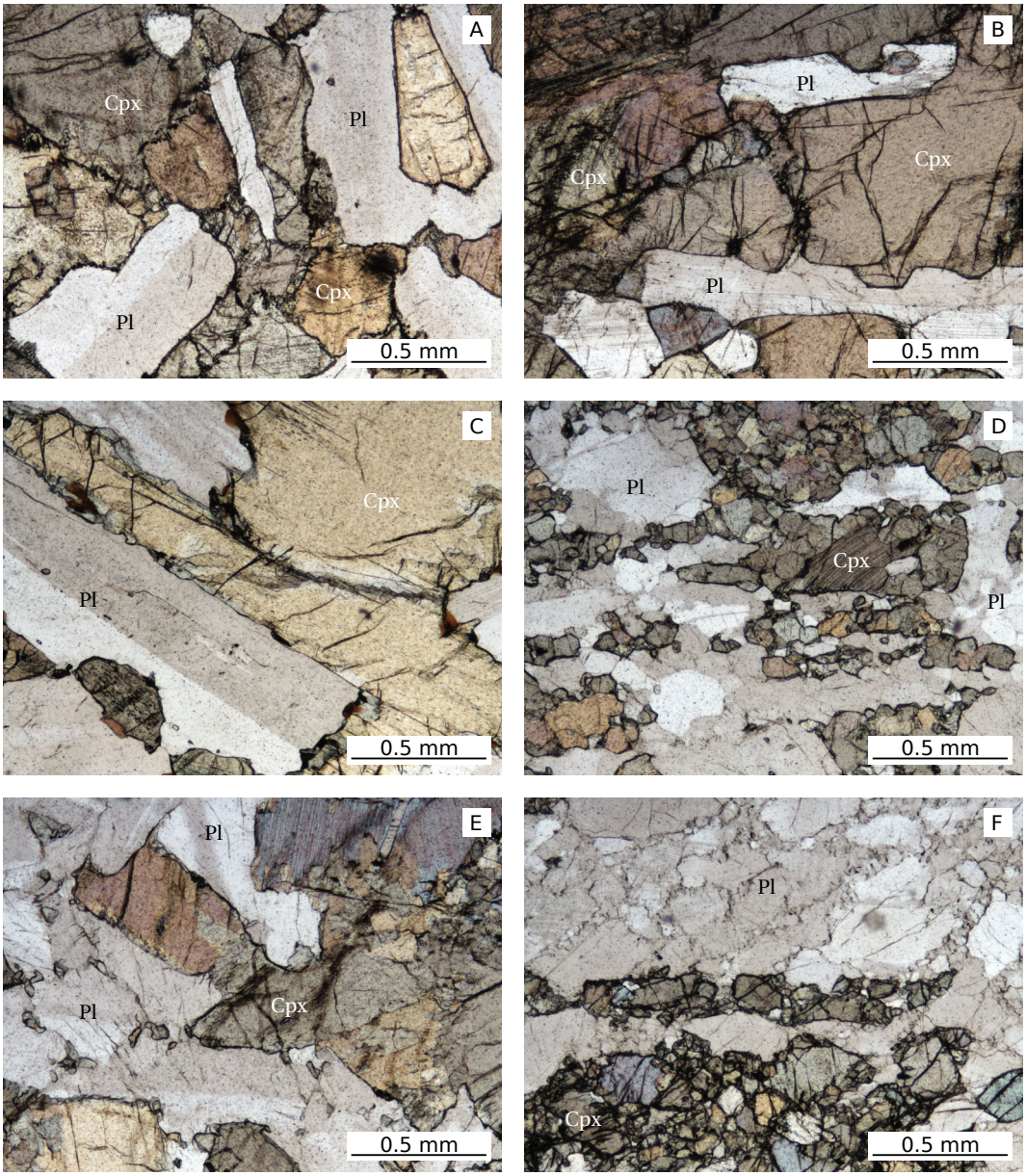

Figure 4.7 Micrographs of variably-textured gabbronorite (VTG) from the Latitude Hill (A—sample 205301, B—205293) and Wingellina Hills intrusions (C—sample 205284, D—sample 205281, E—sample 205278, F—sample 205268).

4.6 Rock classification and internal stratigraphies of the intrusions

This rock classification is based on modal compositions that were calculated from the normative mineralogy (details are given in section 4.3.1). Only a small number of samples from all four lithologies (microgabbronorite (MCG), MLG, PYR and VTG) across the Latitude Hill and Wingellina Hills intrusions are quartz normative and these samples generally contain less than 3 wt% normative quartz. The lithologies of the Wingellina Hills intrusion contain more normative olivine compared to the same lithologies of the Latitude Hill intrusion. Normative magnetite contents are under 6 wt% in all samples from both intrusive bodies, but normative Fe-Ti-oxide contents are generally slightly higher in the Latitude Hill intrusion. Both, the normative olivine and magnetite contents, support the common interpretation that, despite their similarities, the Wingellina Hills intrusion is the more primitive intrusion overall (e.g. Ballhaus 1993; Ballhaus and Glikson 1995; Glikson et al. 1996; Maier et al. 2014, 2015). Normative pyrite (i.e. sulphides) is rare (slightly more common at Latitude Hill than at Wingellina Hills) and occurs only in lithologies with more intercumulus liquid, such as MCG and VTG, where it is commonly <1 wt%. This is in good agreement with petrographic observations, that sulphides occur only as an accessory interstitial phase.

The rock classification (Streckeisen 1976; Le Maitre 2002) in figure 4.8 shows that the lithologic units of the MCG, MLG and PYR form tight clusters, whereas the samples from the VTG exhibit some scatter. The distribution of the clusters is in good agreement with the petrography (section 4.5) and normative mineralogy (see above) in that the most primitive cumulates are the PYR with very low plagioclase contents. It is worth noting that the PYR classify as gabbronorites. This is probably caused by the norm calculations that assign too much CaO to plagioclase, thereby overestimating the latter. This problem has already been mentioned in the petrographic description of the PYR in section 4.5.1. The remaining lithologies of the MLG, VTG and MCG are more evolved due to their higher contents in intercumulus liquid and lower contents in cumulus pyroxenes. Most olivine gabbronorites are from the more primitive Wingellina Hills intrusion and are members of the VTG. Other than that, the differences between the Latitude Hill and the Wingellina Hills intrusions are minor, which supports merging the lithologies from both intrusions, as undertaken here.

The stratigraphic relationships between the lithologic units in both intrusions are shown in figure 4.9. For the most part, the lithologic compositions of the Latitude Hill intrusion alternates between the VTG and the more mafic MLG, and both units can be several hundreds of metres thick. The bottom part of the Latitude Hill intrusion as well as a section at a depth of c. 1000–1500 m contain the ultramafic cumulates of the PYR. Other than the bimodal alternation between the VTG and the MLG, these two occurences of PYR are the only true evidence for cyclicity that could indicate two major batches of magma. Dykes of the MCG were only observed at several levels throughout the Latitude Hill intrusion. The Wingellina Hills intrusion is generally similar, in that the bottom comprises PYR, followed by an alternating sequence of MLG and VTG. While the Wingellina Hills

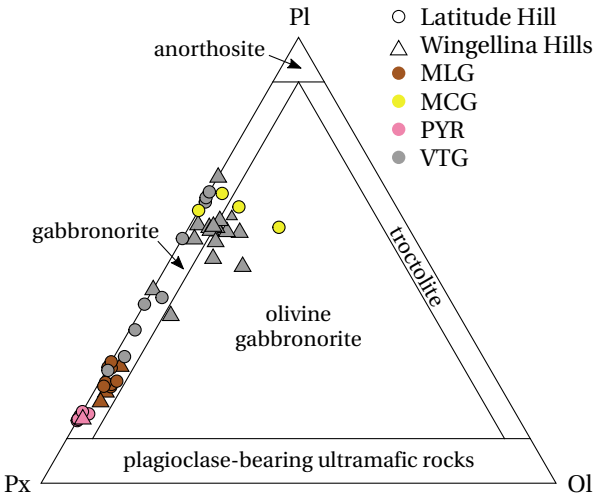

Figure 4.8 Mafic classification for rock samples from the Latitude Hill and Wingellina Hills intrusions after Streckeisen (1976) and Le Maitre (2002). The classification used the normative modal contents of plagioclase (Pl), olivine (Ol) and pyroxene (Px). The lithologies melagabbronorite (MLG), microgabbronorite (MCG), pyroxenite (PYR) and variably-textured gabbronorite (VTG) form two main sample populations: (1) a high-plagioclase group (c. 50 vol% plagioclase or more) consisting of most VTG and the MCG and (2) a low-plagioclase group that comprises some VTG as well as the MLG and the PYR. The calculation of the normative mineralogy overestimates the amount of plagioclase which causes the PYR to classify as gabbronorites; there is no significant difference between samples from the Latitude Hill and the Wingellina Hills intrusions.

intrusion is less thick than the Latitude Hill intrusion, the layers are generally of similar thickness, i.e. up to several hundreds of metres. No dykes were observed in the Wingellina Hills intrusion.

4.7 Whole-rock geochemistry

The Latitude Hill and Wingellina Hills intrusions are very similar in terms of their major element chemistry relative to the Mg# figure 4.10. Similar to the rock classification, the PYR and the MLG form relatively tight clusters or trends together. The MCG and the VTG, on the other hand, are very variable in both, Mg# values as well as many of the major element concentrations, with the exception of Cr_2O_3, P_2O_5, TiO_2 and K_2O. The VTG exhibit highly variable Mg# values as they are generally a heterogeneous group (see petrographic descriptions in section 4.5). They also yield the highest overall Mg# values, followed by the MLG and the PYR. Thus, despite being the most primitive cumulate the PYR may have crystallised from a less primitive magma than the MLG and the VTG, respectively (assuming that there is no other strong control on the total Fe and Mg contents except pyroxene). The MCG are the most evolved melts and yield the lowest Mg# values.

Figure 4.11 displays the patterns of the REE normalised against primitive mantle compositions given by McDonough and Sun (1995) for all four lithologies across both

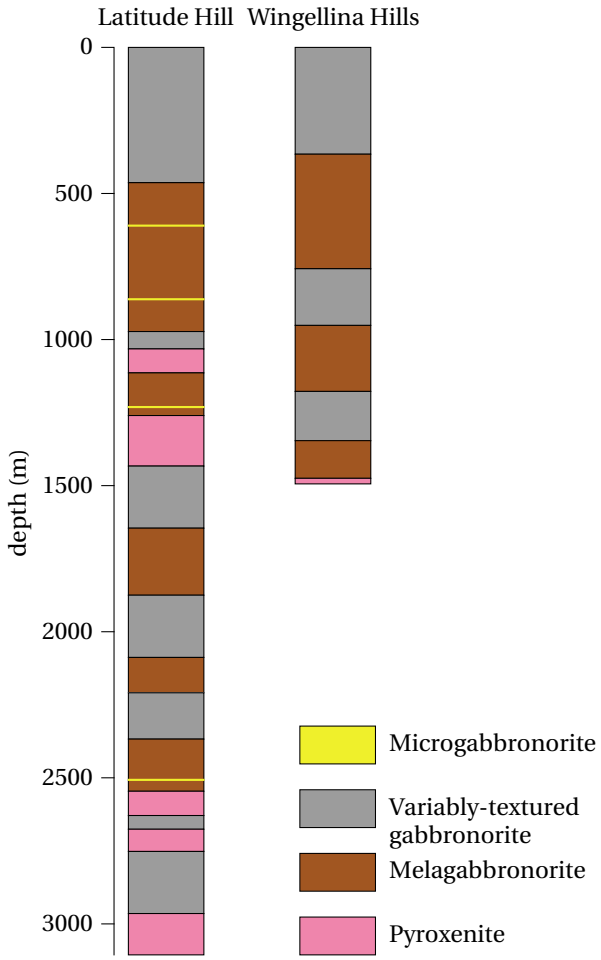

Figure 4.9 Stratigraphic columns of the Latitude Hill and Wingellina Hills intrusions. The base of both intrusions comprises PYR; dykes (MCG) were only sampled at Latitude Hill. The Latitude Hill intrusion consists of two large cycles that start with PYR at the base and continue with an alternating sequence of MLG and VTG. The Wingellina Hills intrusion contains only one such cycle.

intrusive bodies. None of the lithologies in the two intrusions have strongly fractionated LREE or heavy rare earth element (HREE) trends. For instance, all but one of the MCG and only few VTG samples from the Wingellina Hills intrusion are slightly depleted in the HREE, however, in none of these cases is the relative depletion in the HREE strong enough to suggest a garnet-bearing mantle residue during partial melting. All other rock samples from both intrusions exhibit a LREE depletion that is distinct but never over more than one order of magnitude. The MLG and PYR samples have relatively similar and homogeneous REE compositions, are slightly depleted in the LREE and do not have significant Eu anomalies. These characteristics support the findings from the petrography that the two lithologic units are generally very similar (section 4.5.2). The VTG samples (especially from the Wingellina Hills intrusion) exhibit the strongest LREE variations; several samples from the Latitude Hill intrusion have a distinct positive Eu anomaly.

The slight HREE depletion and most elevated REE patterns overall (up to c. 10–100 times over primitive mantle) of all but one of the MCG samples is very common for dyke suites in the Musgrave Province (Howard et al. 2007a), however, the REE patterns alone are

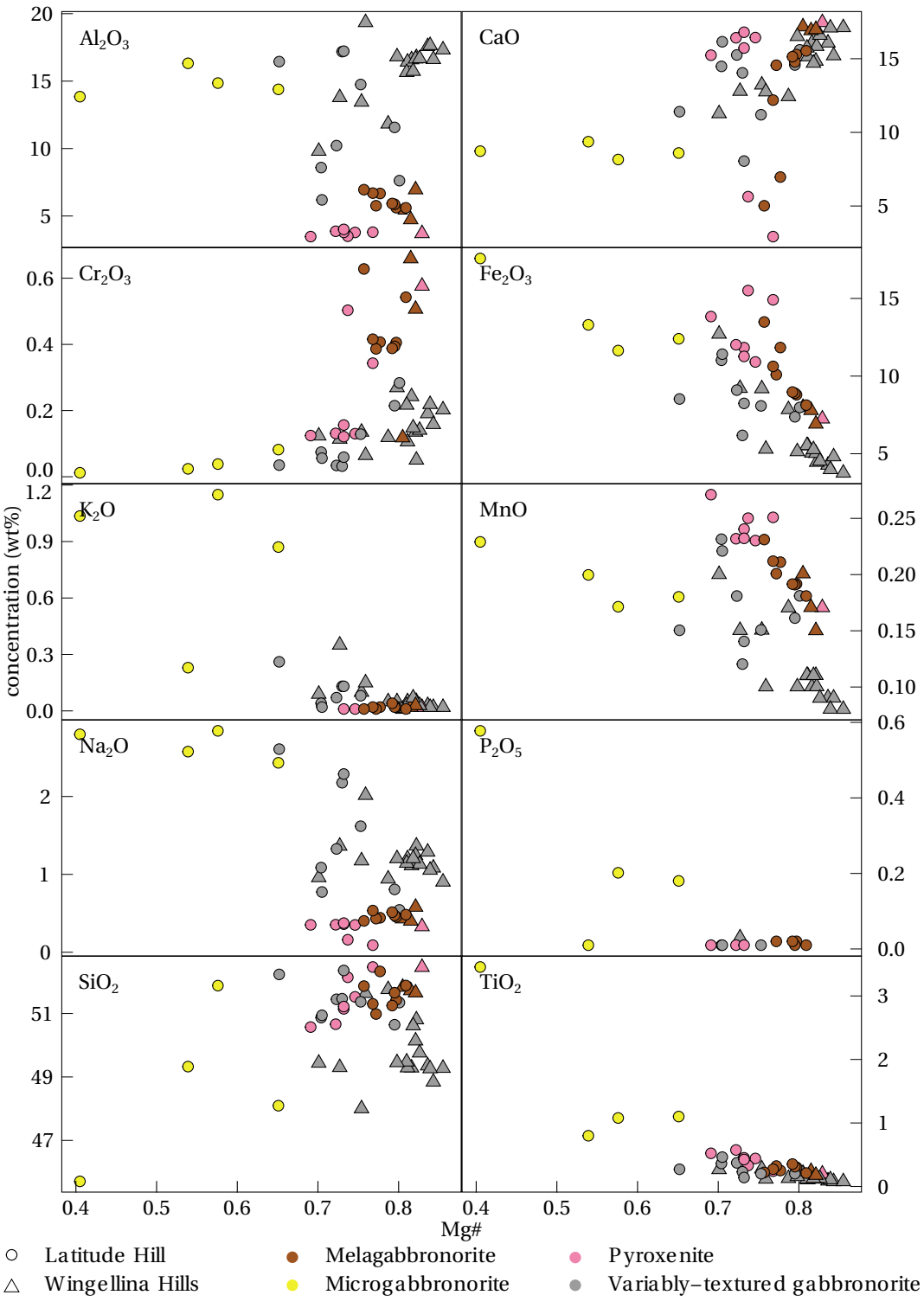

Figure 4.10 Concentrations of the major element oxides compared to the Mg# as a monitor of fractionation (see detailed description of the variations within the lithologies in the text).

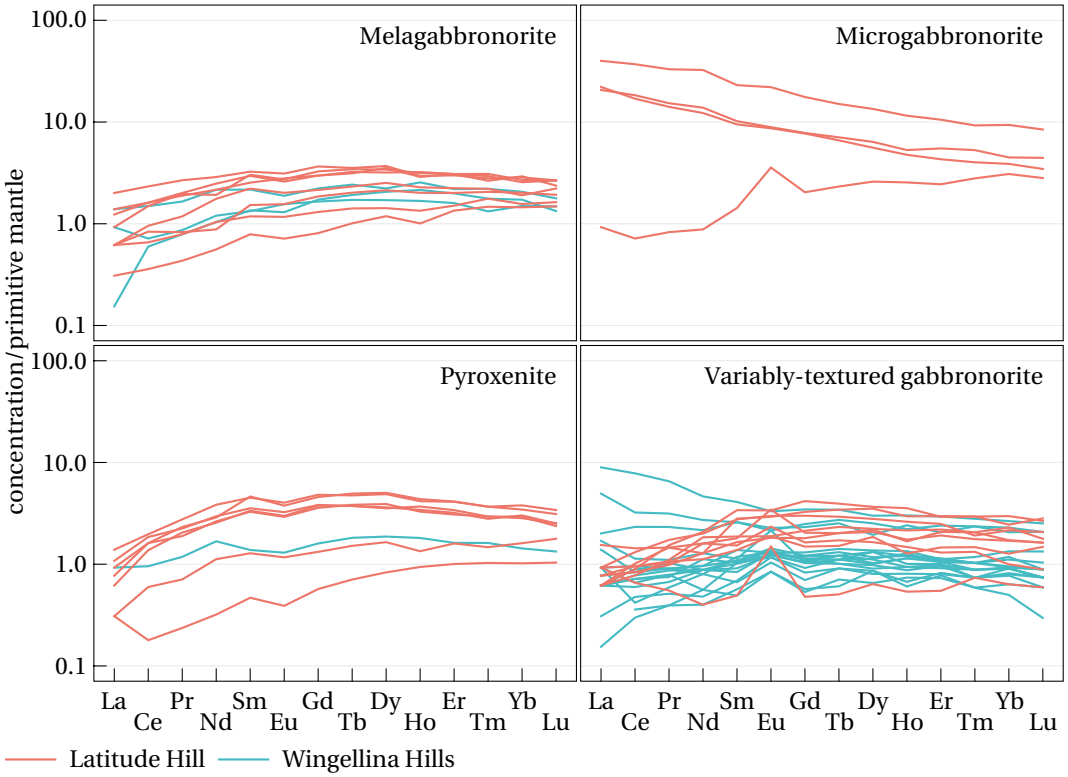

Figure 4.11 REE patterns for all lithologies, normalised against the primitive mantle (normalisation values from McDonough and Sun 1995, see detailed description of the variations within the lithologies in the text). Any differences between the Latitude Hill and Wingellina Hills intrusions are minor and restricted to few samples of the variably-textured gabbronorite (VTG) from Wingellina Hills with light rare earth element (LREE) enrichment.

not specific enough to unambiguously correlate the dykes from the Latitude Hill area with the dykes sampled by Howard et al. (2007a). The most likely dyke suites would probably be the Pitjantjatjara Supersuite and/or the Alcurra Dolerite, although Howard et al. (2007a, fig. 1) did not report the occurrence of any of these in the area around the Latitude Hill intrusion.

Only two samples (sample no. 205 283 from the Wingellina Hills intrusion and 205 298 from the Latitude Hill intrusion; both from the VTG) were analysed for their Sr and Nd isotopes. A summary of the data including, for comparison, the data from the Bell Rock Range intrusion (chapter 3) and all combined massive gabbroic intrusions of the G2 suite are presented in table 4.3. The Latitude Hill and Wingellina Hills intrusions have initial ϵ_{Nd} values (calculated for t = 1078 Ma; Sun et al. 1996) that are roughly comparable to those of the main body of the Bell Rock Range intrusion; the Latitude Hill sample yielded a slightly more crustal initial ϵ_{Nd} signature than the Wingellina Hills sample. The G2 gabbros on the other hand, have much stronger crustal signatures than any of the G1 intrusions. This is in agreement with the assimilation of crustal material in the G2 suite that, in places, leads

Table 4.3 Summary of the Sm- and Nd-isotope data for the Latitude Hill and Wingellina Hills intrusions, showing the initial ϵ_{Nd} ratios of both intrusive bodies including their median values in parentheses. For comparison, the table also contains a summary of the data for the Bell Rock Range intrusion (excluding microgabbronorite (MCG) as well as microporphyritic gabbronorite (MPG) samples; see chapter 3) as well as all combined massive gabbroic intrusions of the G2 suite. All initial isotope ratios were calculated for t = 1078 Ma (Sun et al. 1996).

Intrusion	Suite	initial ϵ_{Nd} (median)
Latitude Hill	G1	−1.8 (—)
Wingellina Hills	G1	+0.5 (—)
Bell Rock Range	G1	−1.1 to +1.4 (+0.6)
various	G2	−2.7 to −1.8 (−2.5)

to very obvious mixing and mingling textures (figure 4.4).

Maier et al. (2014, 2015) reported some of the lowest initial ϵ_{Nd} values for the G2 gabbros as well as the mafic G1 intrusions of the Cavenagh and Morgan Ranges (−1 to −4). Similarly low (i.e. crustal) initial ϵ_{Nd} values were reported for the ultramafic Kalka (−5.2 to −2.1), Ewarara (−3.2 to −0.8) and Gosse Pile intrusions (−3.8 to −1.1) in South Australia (Wade 2006). This suggests that despite the very small number of samples in this study, there appears to be a general trend towards more pronounced crustal initial ϵ_{Nd} in the G2 gabbros as well as those G1 intrusions that contain a higher proportion of melagabbronoritic, pyroxenitic and ultramafic cumulates.

4.8 Discussion

4.8.1 Magma sourcing and crustal contamination in the Latitude Hill and Wingellina Hills intrusions

Crustal contamination

Most of the layered intrusive bodies of the G1 suite exhibit crustal contamination and in the case of the massive G2 intrusions probably additional assimilation of comagmatic granitic magmas from the Warakurna Supersuite (Maier et al. 2014, 2015). It has also been pointed out by Kirkland et al. (2012a, 2013) and Maier et al. (2014, 2015), that in particular the granitic rocks of the Pitjantjatjara Supersuite (Musgrave Orogeny; section 1.2.1) are extremely rich in HFSE, so that very small amounts of contamination are sufficient to produce strong crustal signatures. For instance, Maier et al. (2014, 2015) reported ϵ_{Nd} values of −6 for the Cavenagh intrusion. These authors argued, that if the contaminant had not had extreme HFSE enrichment such negative ϵ_{Nd} values would have requried the assimilation of unrealistically large amounts of crustal material.

Highly incompatible elements such as Th are commonly used as proxies for crustal contamination; however, due to cumulate effects the concentrations of these elements can be extremely low in mafic-ultramafic cumulates with little interstitial liquid. Hence,

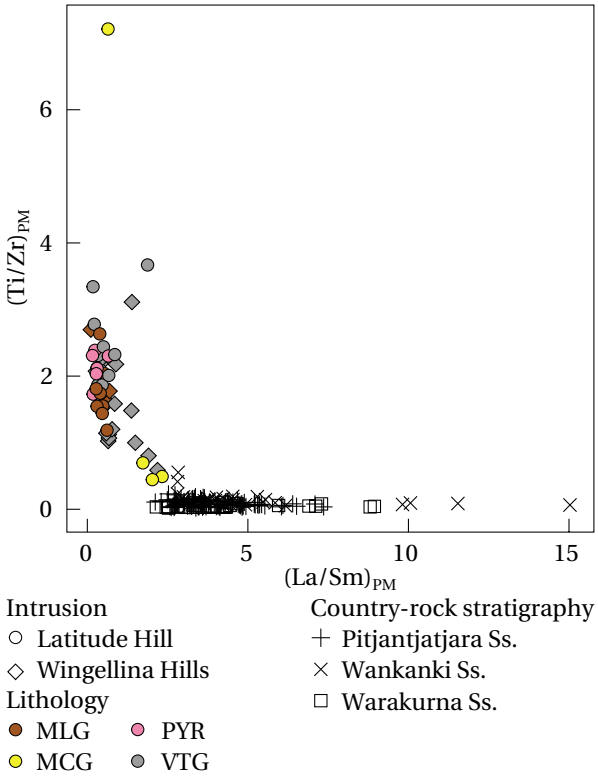

Figure 4.12 Primitive mantle normalised Ti-Zr-REE chemistry of the Latitude Hill and Wingellina Hills intrusions compared to crustal granites of the Wankanki, Pitjantjatjara and Warakurna Supersuites (Ss.). The generally primitive layered G1 intrusions exhibit low $(La/Sm)_{PM}$ and high $(Ti/Zr)_{PM}$ ratios, whereas the major crustal lithologies in Musgrave Province show the reverse signatures.

primitive mantle-normalised Ti/Zr and La/Sm ratios are used here to circumvent such problems (figure 4.12). Particular consideration is given to the granitic rocks of the Pitjantjatjara, Wankanki and Warakurna Supersuites as potential contaminants. The modal contents of Fe-Ti-oxides are relatively lower in the Latitude Hill and Wingellina Hills intrusions than for instance in the Bell Rock Range intrusion, so the $(Ti/Zr)_{PM}$ ratios should not be artificially elevated. Only one sample of the MCG, with an extreme $(Ti/Zr)_{PM}$ ratio, might be biased. Apart from this sample, most other rocks from the two G1 intrusions cluster around mid to high $(Ti/Zr)_{PM}$ and low $(La/Sm)_{PM}$ ratios. In contrast, the crustal rocks cluster at very low $(Ti/Zr)_{PM}$ ratios and mostly medium-high $(La/Sm)_{PM}$ ratios. This is caused by their negative Ti-anomalies and relative LREE enrichment. The samples from the layered intrusions and the samples from the felsic country rocks form relatively tight clusters each; only few rock samples of the VTG appear to represent mixtures between both clusters. If widespread mixing between the two would have occurred, a hyperbolic mixing array from the most primitive to the most evolved rocks should be visible. While both clusters could be connected with a calculated mixing line, the absence of a significant number of samples that would plot on such a line indicates that assimilation of crustal material and subsequent mixing between the mafic and felsic melts may have happened only to a limited extend.

Magma sourcing

The Nb-Zr-Y chemistry of basaltic magmas can be used to distinguish between different magma reservoirs in the mantle (e.g. Fitton et al. 1997; Fitton 2007). Ocean island basalt (OIB) and normal mid-ocean ridge basalt (N-MORB) rocks each form a distinct linear array in a Nb/Y versus Zr/Y space (figure 4.13). Fitton et al. (1997) devised the parameter

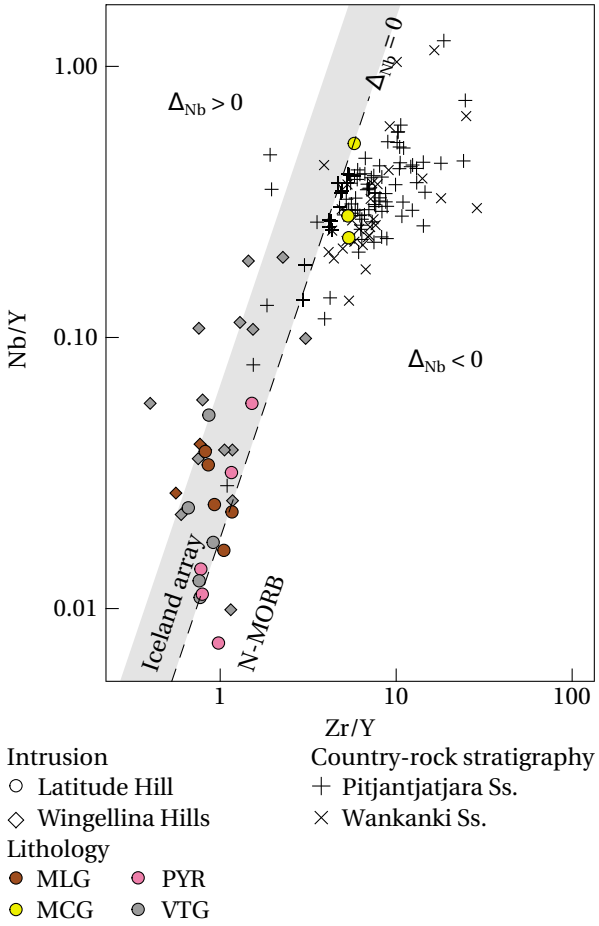

Figure 4.13 Zr-Nb-Y chemistry and Δ_{Nb} of the Latitude Hill and Wingellina Hills intrusions. The Nb/Y versus Zr/Y diagram after Fitton et al. (1997) indicates the membership of the magmas in either the Iceland or the normal mid-ocean ridge basalt (N-MORB) array. A Δ_{Nb} value of 0 (equation (3.1)) represents the boundary between the two linear arrays (see explanation in the text).

$$\Delta\text{Nb} = 1.74 + \log\left(\frac{w_{\text{Nb}}}{w_{\text{Y}}}\right) - 1.92\log\left(\frac{w_{\text{Zr}}}{w_{\text{Y}}}\right) \tag{4.1}$$

to separate the two types of mafic rocks and termed the two arrays Iceland array for OIB-type rocks that may have been produced by mantle plume magmas and the N-MORB array for mafic rocks that are not plume-related; a value of $\Delta\text{Nb} > 0$ is characteristic for the Iceland array and $\Delta\text{Nb} < 0$ for the N-MORB array, because membership in one array or the other depends on the Nb-anomaly as well as the observation that both average continental crust and N-MORB exhibit $\Delta\text{Nb} < 0$, caused by their distinct deficiency in Nb. This has an important consequence: it makes it impossible for magmas that were produced by the depleted upper mantle (i.e. N-MORB array) to obtain OIB-like signatures

Table 4.4 Arithmetic mean, minimum and maximum ΔNb values for all lithologies of the Latitude Hill and Wingellina Hills intrusions. For the Wingellina Hills intrusion no ΔNb values for the pyroxenite (PYR) could be calculated and no microgabbronorite (MCG) was samples.

Lithology	Intrusion	min	mean	max
Mela-gabbronorite	Latitude Hill	–0.09	0.19	0.48
	Wingellina Hills	0.57	0.61	0.65
Microgabbronorite	Latitude Hill	–0.29	–0.17	–0.01
Pyroxenite	Latitude Hill	–0.37	0.00	0.15
Variably-textured gabbronorite	Latitude Hill	0.00	0.23	0.58
	Wingellina Hills	–0.38	0.43	1.26

by contamination with crustal material (Fitton et al. 1997). Variable degrees of low pressure fractionation and/or partial melting or alteration do not affect ΔNb, thus, membership in the Iceland array is a characteristic of the magma source (Fitton et al. 1997; Fitton 2007).

The ΔNb values of the samples from the Latitude Hill and Wingellina Hills intrusions (figure 4.13) are highly variable (see also table 4.4 for a summary of ΔNb values). Although there are differences in the Zr-Nb-Y chemistry between the different lithologies there are none between the Latitude Hill and Wingellina Hills intrusions. The MCG is the only lithologic unit that consistently yields ΔNb values <0 that could be the result of crustal contamination. They are in good agreement with the ΔNb values of the A-type granitic country rocks from the Pitjantjatjara, Wankanki and Warakurna Supersuites. The remaining lithologic units of the Latitude Hill and Wingellina Hills intrusions yield largely ΔNb values >0, suggesting a primitive (possibly plume-related) magma source and minor amounts of crustal contamination. However, some of the data of the VTG and PYR samples are highly variable and need special consideration. The relationship between Nb/Y and Zr/Y ratios in mafic magmas is assumed to be stable against variable degrees of partial melting and alteration (Fitton et al. 1997). However, while fractionation of olivine and plagioclase will not affect either ratios, the crystallisation of clinopyroxene could do so due to an increased compatibility of Y (Fitton 2007). This could account for those samples of the PYR and VTG that have the lowest Nb/Y and Zr/Y ratios. On the other hand, this fails to explain why the likewise pyroxene-rich MLG do not yield similarly low ratios. Although Nb is moderately compatible in magnetite, modal contents of this phase are relatively low in the lithologies of the Latitude Hill and Wingellina Hills intrusions. This should generally limit the influence of a cumulate effect caused by magnetite, however, the samples of the VTG with the highest Nb/Y ratios could be affected by it.

Comparison of the Latitude Hill and Wingellina Hills G1 intrusions with the G2 intrusions

Figure 4.14 shows that the massive G2 gabbros are relatively enriched in the LREE and to a lesser extent in the HREE, and have variably positive and negative Eu anomalies compared to the mafic-ultramafic layered G1 intrusions of the Latitude Hill and Wingellina Hills

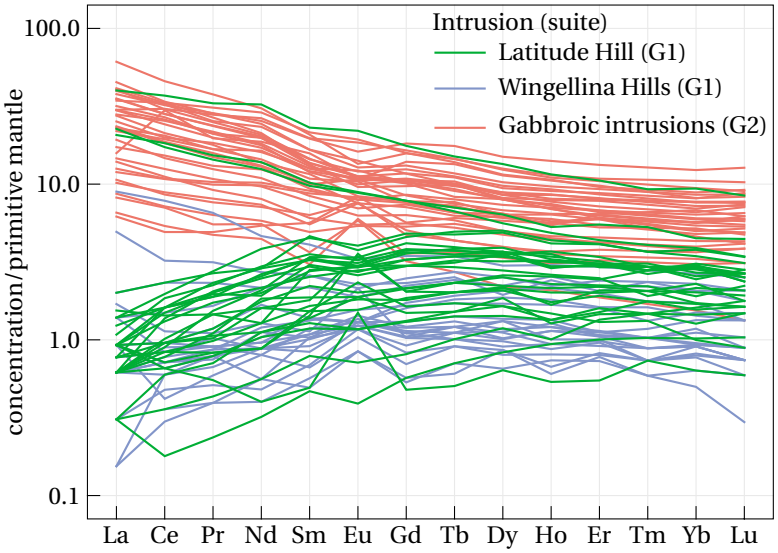

Figure 4.14 REE patterns for the Latitude Hill and Wingellina Hills intrusions as well as the gabbroic G2 intrusions. All data are normalised against the primitive mantle (normalisation values from McDonough and Sun 1995, see detailed description of the variations within the lithologies in the text).

areas. This is probably caused by variations in the abundance of cumulus plagioclase and pyroxene. G1 samples with similar REE patterns to the G2 samples are restricted to the LREE-enriched MCG as well as one sample of the VTG (figure 4.11). The observed patterns can be readily explained if one accepts that the rock samples of the MCG are closest to actual liquid compositions, closely followed by the gabbros of the G2 suite. The reason for this assumption with respect to the G2 gabbros is that they did not form any visible igneous layering, be it dynamic or nondynamic (Namur et al. 2015). The remaining lithologies of the Latitude Hill and Wingellina Hills intrusions follow probably in the order of VTG, MLG and PYR, all of which exhibit textural evidence for mineral accumulation processes (section 4.5). The REE patterns of the G2 gabbros, the MCG and some VTG are probably simply the result of larger amounts of intercumulus liquid, consisting mainly of plagioclase and clinopyroxene. Most of the VTG as well as all of the MLG contain a higher proportion of cumulus clino- and particularly orthopyroxene. Finally, the REE patterns of the websteritic samples of the PYR are heavily controlled by the presence of cumulus orthopyroxene, hence, their distinct LREE depletion. The isotope data indicate that the G2 gabbros are less radiogenic than the Latitude Hill and Wingellina Hills intrusions (table 4.3), supporting the idea of the former containing a higher proportion of crustal material. Finally, the spatial proximity of some of the layered G1 intrusions that contain ultramafic cumulates, such as the Latitude Hill and Wingellina Hills intrusions, to the massive G2 gabbros suggests that the apparent boundary between the G1 and G2 suites may be an artefact of some petrological process and may not require a separate phase of magmatic activity as an explanation (e.g. Evins et al. 2010b,c).

4.8.2 The boundary between the G1 and G2 suites revisited

This section revisits the boundary between the G1 and the G2 members of the Giles Suite, making use of additional data from the *WACHEM* database of the GSWA (see description

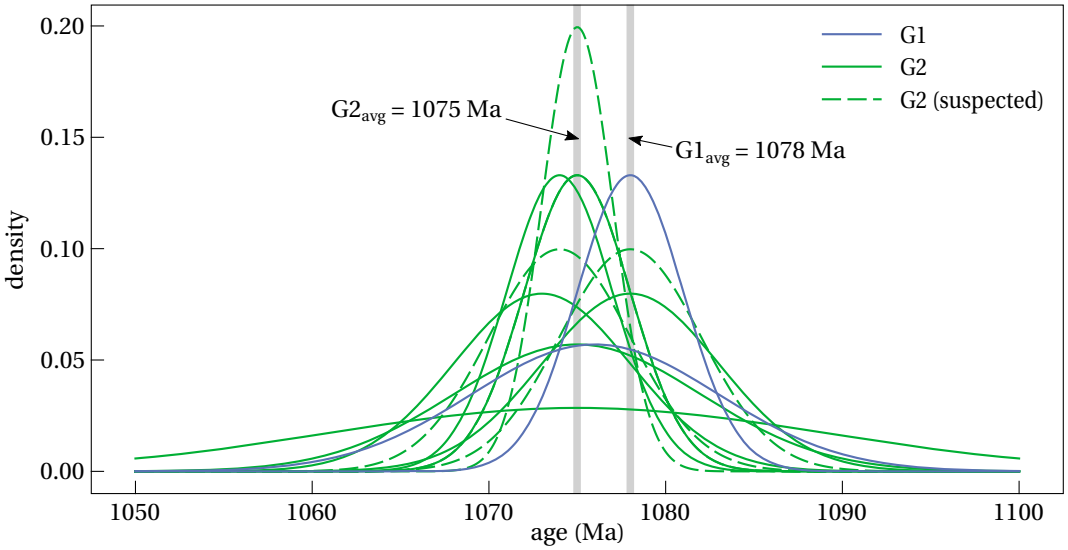

Figure 4.15 Kernel density estimation for geochronological data for the G1 and G2 suites. The suggested ages of c. 1078 Ma for the G1 suite and c. 1075 Ma for the G2 suite are indicated. Although the means are slightly different, there is significant overlap between the standard deviations of the geochronological results for the two suites. References for the data are given in table 4.5, including the suspected members of the G2 suite.

of sample selection and classification process in section 4.4). The distinction between the G1 and G2 suites was initially made by Evins et al. (2010b,c) (section 4.2.3); neither Daniels (1974) nor Ballhaus and Glikson (1995) and Glikson et al. (1996) saw the necessity to distinguish a separate phase of magmatic intrusive activity. Daniels (1974) only broadly subdivided the mafic intrusive rocks into the Jameson Range, Blackstone Range, Hinckley Range, Mount West and Michael Hills gabbros (here, the intrusion name simply labels the type locality for the respective lithology; the actual outcrop of a lithology can comprise several intrusive bodies: for instance, the Latitude Hill intrusion is part of the Michael Hills gabbro and the Wingellina Hills intrusion is a member of the Hinckley Range gabbro). While Daniels (1974) pointed out the assimilation of felsic rocks at Hinckley Range, he did not separate those rocks into their own magmatic suite or lithologic unit.

Ballhaus and Glikson (1995) and Glikson et al. (1996) followed a different approach and distinguished various lithologies derived from essentially three separate parental magmas (primitive, gabbroic, and troctolitic). They used these to group the various intrusions into three main groups. Glikson et al. (1996) also commented on the contaminated G2 suite at the western Hinckley Range, describing the rocks as mafic granulites with granitic veins caused by 'back intrusion' (Glikson et al. 1996, p. 13), i.e. essentially the assimilation of felsic wall rocks or cogenetic felsic magmas.

Apart from the petrographic differences between the G1 and G2 suite rocks that were already pointed out by previous authors Evins et al. (2010b,c) used geochronological data to discriminate between the G1 and G2 suites (table 4.5 and figure 4.15). The currently available data are very sparse and while the mean ages for the G1 and G2 suites are

Table 4.5 Compilation of geochronological data for the G1 and G2 suites after Glikson et al. (1996) and Evins et al. (2010b,c). Evins et al. (2010b,c) calculated an average of 1075 ± 1 Ma for the G2 suite from this data. Note that Evins et al. (2010b,c) also interpret the 1078 ± 3 Ma age of Sun et al. (1996) from the Bell Rock Range intrusion to represent G2 rather than G1. The variation is given as two standard deviations 2σ, the original references for the data are a—Kirkland et al. 2011, b—Bodorkos and Wingate 2008, c—Kirkland et al. 2008a, d—Kirkland et al. 2008b, e—Sun et al. 1996, f—Glikson et al. 1996, g—Camacho 1997, h—Evins et al. 2010b, i—Close et al. 2003b and k—Kirkland et al. 2012b.

Sample ID	E	N	$t \pm 2\sigma$ (Ma)	Description	Ref.
ages of G1 suite					
194762	390576	7135230	1076 ± 7	leucogabbro	a
ages of G2 suite					
174589	451114	7133869	1074 ± 3	granite dyke	b
174761	473626	7116039	1075 ± 7	granite dyke	c
185509	471391	7120896	1075 ± 3	leucogranite	d
ages of G1 or G2					
91989313B	477439	7091516	1078 ± 3	leucogranite	e
ages of suspected G2					
91988053	473292	7117866	1073 ± 5	recrystallized gabbronorite	f
91988005	458131	7104425	1078 ± 5	rhyolite	f
M2a	517278	7116021	1075 ± 14	granite	g
ages of rocks located elsewhere that could be G2					
190256	421981	7186055	1074 ± 4	rhyolite	h
BR97CJE153	540600	7274480	1075 ± 2	Puntitjata Rhyolite	i
BR98DFC429	551843	7261231	1075 ± 3	Rowley Granophyre	i
183847	439840	7079281	1078 ± 4	syenite	k

slightly different, the uncertainty in the data do not appear to permit an unambiguous distinction between two discrete events. In fact, the newer of the two reported ages for the G1 intrusions (Kirkland et al. 2011) introduces a larger error than the previously accepted age (Sun et al. 1996) and moves the suggested age of the G1 suite even closer towards the G2 suite. This suggests that the distinction between the G1 and G2 suites may need to be investigated further. This is particularly true because 5–10 Ma may well be the duration of an entire intrusion emplacement process, especially when this happens via multiple injections rather than a single batch (Menand 2008). A Neoarchaean granitic pluton in Western Australia was emplaced over 10–20 Ma through overplating (Zibra et al. 2014); thus, even if the standard deviations are ignored, the differences in the mean values for the G1 and G2 suites may not be indicative for separate phases of intrusive activities. This might also explain the conflicting field relationships between G1 and G2 intrusions that were reported (cf. Clarke 1992; Evins et al. 2010c).

The unambiguous definition of two subsequent events requires some discontinuity

between them, either geochronological or compositional (if the compositional differences are of a nature that implies petrogenetic differences). In the absence of geochronological data of higher resolution the boundary between G1 and G2 is still essentially unconstrained and the field record is ambiguous with respect to relative timing (c.f. Glikson et al. 1996; Howard et al. 2011a, see also details on the boundary in section 4.8.2). A classification based on textural features, such as layered and massive, not necessarily a good choice because igneous layering is largely by physical parameters during the emplacement. In a recent review, Namur et al. (2015, and references therein) described various ways for the formation of igneous layering. They distinguished between dynamic layer formation, caused by the movement of melt, crystals or both, and nondynamic layer formation, caused by a change in the crystallisation conditions (e.g. pressure or oxygen fugacity). The influence of the bulk chemical composition of the mantle reservoir as well as subsequent assimilation and fractional crystallisation (AFC) processes is limited. An important question to address is therefore whether the explanation of the apparent compositional differences between the G1 and the G2 suites requires indeed a separate phase of magmatic activity or whether those differences may simply be a function of the larger amount of interstitial liquid that the massive gabbros clearly contain, considering they are not (ad)cumulate rocks.

4.8.3 A multivariate approach to a new petrogenetic model

The available data are evaluated using a two-way approach: a hierarchical cluster analysis (HCA; see appendix A.7.1) on the variation between all pairs of variables is used to find the most 'expressive' variables (elements/oxides), i.e. those variables that exhibit the strongest variations with respect to the classification into the G1 and the G2 suites and thus may convey the most information on the petrogenetic processes that underlie the differences between the two suites. Following the hierarchical cluster analysis (HCA), a principal component analysis (PCA; see appendix A.6.1) is used to find 'natural' clustering patterns within those variables. These patterns can then be compared with the existing classification to determine which petrogenetic processes are needed to explain the G1 and G2 suites.

Extracting the subcompositions via hierarchical cluster analysis (HCA)

The degree of variation between all variable pairs (or their 'expressiveness', see above) is measured using a distance matrix. Following the recommendation of Chayes (1975) and Aitchison (1986), a variation matrix **T** was used instead of a matrix of correlations or covariances. In a D-dimensional compositional space (i.e. a geochemical dataset that contains a total of D elements and/or oxides; see appendix A.5 for further details on compositional data analysis) the variation matrix will have D^2 elements. Each of the D^2 elements of **T** contains the variation of the log-ratio of two components x_i and x_j, hence, the matrix elements are defined as

$$\tau_{ij} = \mathrm{var}\left(\ln \frac{x_i}{x_j}\right). \tag{4.2}$$

A small value in the matrix indicates a 'good proportionality' (Boogaart and Tolosana-Delgado 2013, p. 76) between the two components in question. In order to compute the variation matrix only those analytes were considered that have full data coverage, i.e. valid data is available for each of the 82 samples. The order of the elements of the matrix was established via Q-mode HCA (using complete-linkage clustering; see appendix A.7.1); figure 4.16 visualises the variation matrix with a heatmap including the dedrograms that show the results of the HCA. The values in the variation matrix are a valid measure for distance (or 'differentness') in a compositional sense. This allows for the computation of the euclidean distance between data clusters, which would otherwise not be guaranteed to give meaningful results when applied to compositional data.

For futher analysis the number of variables was restricted to the ones with the largest variation, due to the expectation that these would be the ones that are most expressive with respect to the problem at hand (see above). Based on the heatmap (figure 4.16; white frame) the variables Cr_2O_3, Ni, MgO, CaO and Sc were chosen as well as Nd, Pr, Pb, Cu, Zn, Ba, Zr and Ce, since these variables form a cluster on the heatmap with higher variation. The important thing to note here is that these two groups of variables are also two groups of compatible and incompatible elements during magmatic processes in mafic-ultramafic melts, respectively (see the compilation of partition coefficients in Rollinson 1993, tab. 4.1).

Data clustering via principal component analysis (PCA)

After the dimensionality was reduced to 13 with the HCA, a principal component analysis (PCA) was performed on the new sample space. The purpose of this step is to investigate if any clustering that results from the PCA would agree with the currently established discrimination between the G1 and G2 suites or if there is general disagreement. Figure 4.17 shows that the first principal component does account for almost all variation that separates the samples from the Latitude Hill and Wingellina Hills intrusions from the samples from the G2 gabbros and the MCG. The discrimination between the two groups is entirely based on the incompatible elements on the one hand, accounting for the G2 gabbros and the MCG, and compatible elements on the other hand, accounting for the Latitude Hill and Wingellina Hills intrusions. It therefore appears, that the difference between mafic-ultramafic G1 intrusions and G2 intrusions depends largely on the higher incompatible element content of the latter. These results are fully consistent with the interpretation that incompatible elements are concentrated in the liquid phase during fractional crystallisation, thus, the degree of their variations in rock samples will be proportional to the amount of interstitial liquid; an actual petrogenetic process, such as different degrees of crustal contamination, is not required to explain the observations in figure 4.17. The second principal component, which accounts for a much smaller amount of variation in the log-ratios, is mainly controlled by the highly incompatible elements Cu and Pb and no discrimination between the G1 and G2 samples is possible on the basis of this principle component. What is apparent, however, is that the variation along the second principal component is generally larger for the G1 samples from the Latitude Hill and Wingellina Hills intrusions. Incompatible elements accumulate in the interstitial

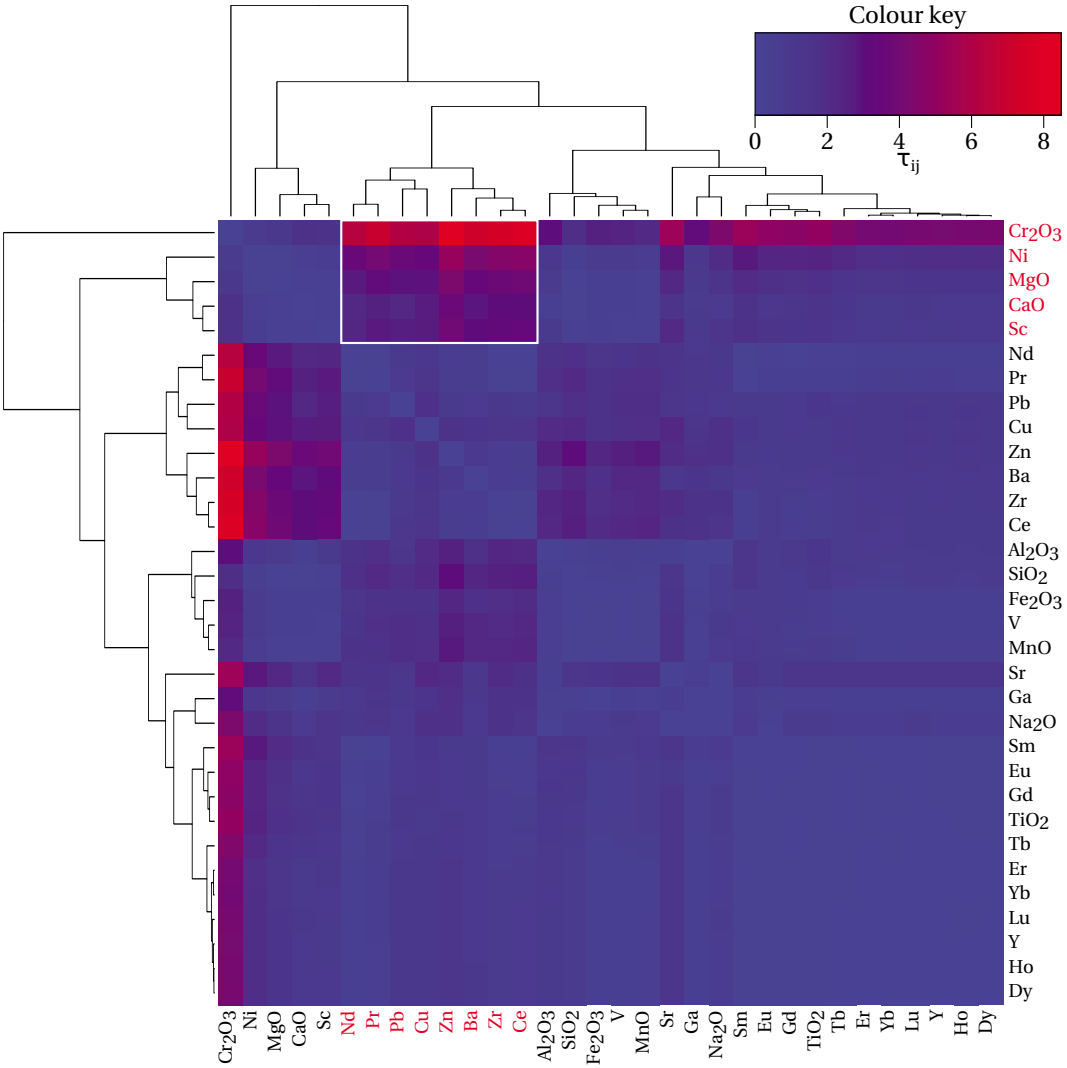

Figure 4.16 Heatmap of the variation matrix. The dendrograms are the result of a Q-mode hierarchical cluster analysis (HCA) using the euclidean distance as measure for the distance between clusters. Clustering was done using complete-linkage clustering (see appendix A.7.1). The colour key shows the mapping of the variation of the log-ratios (0–8.483 73) onto the colour space with red representing the highest variation and blue the lowest.

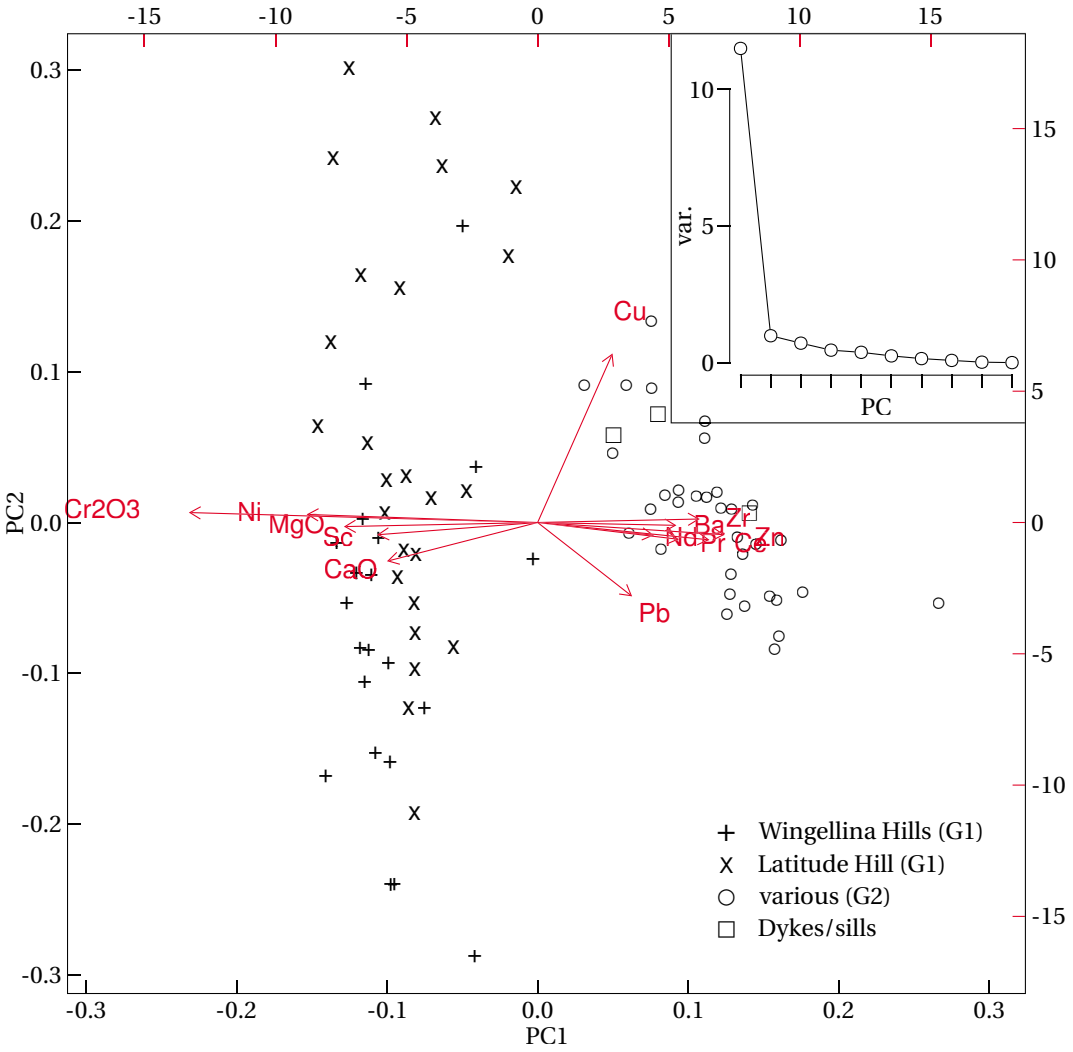

Figure 4.17 Biplot of principal components (PCs) for all selected 13 oxides and elements (Ba, CaO, Ce, Cr_2O_3, Cu, MgO, Nd, Ni, Pb, Pr, Sc, Zn and Zr). The inset plot shows the strong control of the first principal component (PC).

liquid, which occurs in G1 rocks in variable abundance. On the other hand, the rocks from the MCG and the G2 suite are closer to liquid compositions, thus, more consistent with respect to the amount of late-stage liquids.

Figure 4.18 shows the result of a subsequent PCA in which the two groups of compatible and incompatible elements were analysed separately. The motivation behind this approach is to investigate whether within each group (i.e. elements that are concentrated in early-crystallising phases and elements that are concentrated in late-stage phases) it is in fact impossible to distinguish between the G1 and the G2 suites. When comparing the two results, this assumption holds true; variations in compatible or incompatible elements alone are not indicative for the membership of a sample in either the layered

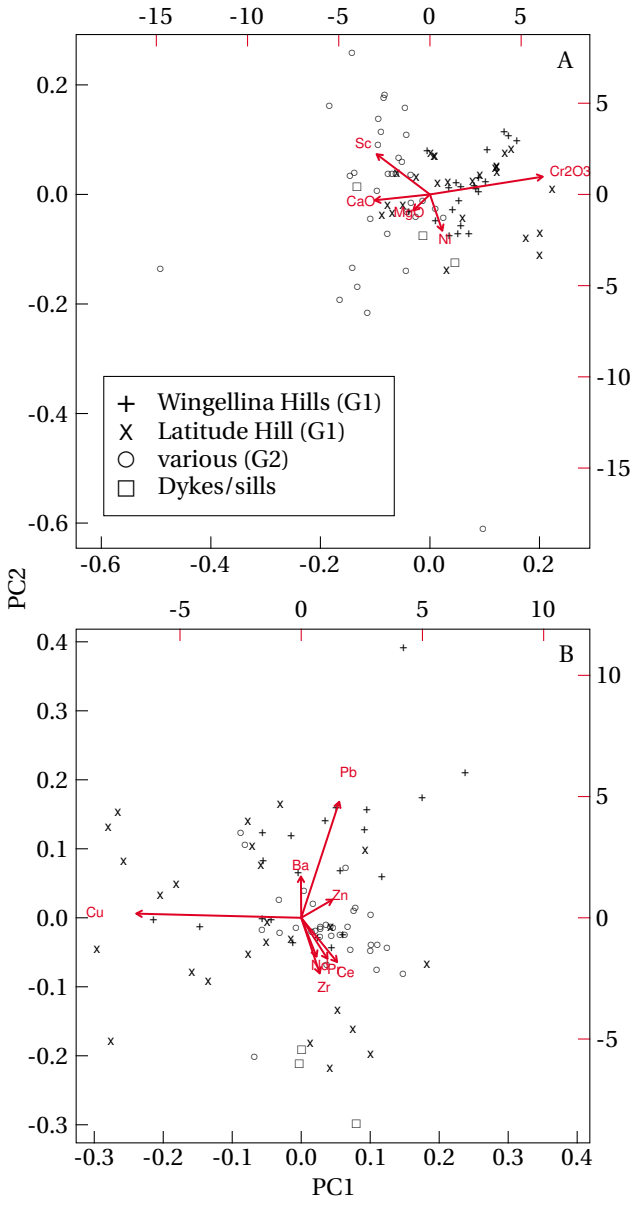

Figure 4.18 Biplots of principal components (PCs): **A**—compatible oxides and elements (CaO, Cr_2O_3, MgO, Ni and Sc); **B**—incompatible elements (Ba, Ce, Cu, Nd, Pb, Pr, Zn and Zr). The biplots show the low separation for each individual class.

G1 intrusions or the G2 gabbros together with the MCG. Thus, the massive G2 gabbros together with the MCG do most likely closely resemble liquid compositions, while the mafic-ultramafic G1 cumulates on the other hand do not. Instead, they lost some of their original content of interstitial liquid in which most of the incompatible elements from the crustal contamination were concentrated. This simple cumulate effect may be sufficient to explain the lower content in incompatible elements and no neccessity is seen for the invocation of petrogenetic processes such as varying degrees of fractionation or assimilation of crust (Mojoie et al. 2005).

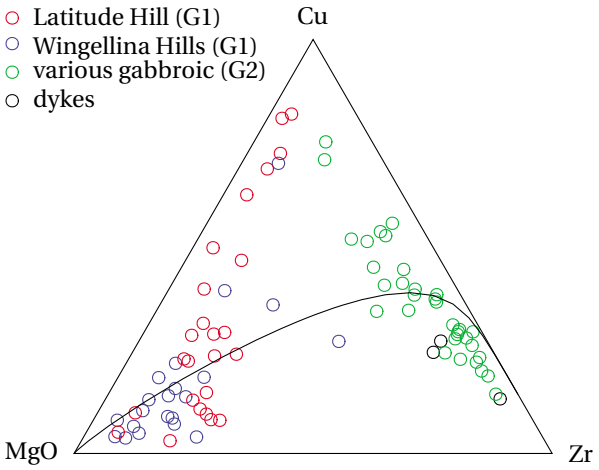

Figure 4.19 Ternary plot of the centered log-ratios of the subcomposition Cu-Zr-MgO with a curved line displaying the first principal component (see figure 4.17) projected into the ternary subcomposition.

4.8.4 Chalcophile element controls

The results of this study indicate that the subcomposition Cu-Zr-MgO (figure 4.19) is an appropriate subcomposition to further investigate the mobility of Cu, because this subcomposition displays Cu concentrations against proxies for compatible and incompatible element variations using MgO and Zr, respectively. The Latitude Hill and Wingellina Hills intrusions on one hand and the G2 gabbros and dykes on the other hand form separate groups that were affected differently by removal of incompatible elements through cumulate formation in the G1 intrusions. Both groups yield a range of Cu concentrations but in no case does Cu exhibit any signs that it would be controlled by this process of fractionation as well as subsequent accumulation and liquid removal. This is because Cu does not form a one-dimensional relationship with MgO and Zr which proxy the petrogenetic processes in this projection. This finding is in agreement with the Cu-sulphides being highly mobile and having formed relatively late.

4.8.5 Thou Shalt Not Ignore Occam's Razor

The results of this multivariate approach indicate that these data do not support or at least require a significant change in the magmatic system to have occurred between the emplacement of the G1 and G2 suites. While the G2 gabbros might carry stronger contamination signatures these signatures are probably just an expression of fractionation followed by cumulate effects. As a consequence, the G2 gabbros simply retained more incompatible elements due to their higher content in interstitial liquid, because they are not layered cumulates and clearly should be closer to liquid compositions than the mafic-ultramafic rocks of the G1 suite. Consequently, there is no reason to assume that the G2 gabbros assimilated significantly more crustal material than the mafic-ultramafic layered G1 intrusions.

A second aspect that requires discussion is why some members of the Giles Suite are layered and others are not. The way layering forms has been investigated in a recent study by Namur et al. (2015) who distinguish between dynamic and nondynamic formation of

layers. While processes involving currents, convection or any migration of liquids can efficiently separate mineral phases and establish layers they can only remain stable if the system is not too dynamic so as to disturb and destroy the separation into layers. This is also true if external conditions change and enforce crystallisation of different phases, like it is the case for nondynamic layering. Cawthorn (2012) demonstrated in his recent study that the thickness as well as the frequency of repeated magma injections might be the most important controls for a body of magma to either form a layered intrusion or individual sills. In case of a high frequency of magma injections that exceed a certain thickness solidification of individual sills is inhibited which supports the formation of a layered intrusive body.

Howard et al. (2009c) already recognised problems with the interpretation of whole-rock chemical data from the Giles intrusions, that are caused by cumulate effects. A bimodal grain size distribution in rocks of the Alcurra Dolerite (termed 'dual texture' by Howard et al. 2009c, p. 4) was seen as evidence for the migration of melts through mush columns of cumulate crystals (a similar texture was observed in this study in rocks from the parallel-running ridges near the Bell Rock Range intrusion; see section 2.6.2). These processes then cause whole-rock compositions that do not represent the compositions of the original magma. In summary, the formation of the unlayered G2 gabbros probably established a highly dynamic environment that inhibited layer formation; it is not necessary to invoke a second phase of magmatic activity to explain the textural, geochemical and geochronological characteristics, because they are sufficiently explained by cumulate effects. It is therefore concluded, that the suggestion of a separate G2 phase within the Giles Event seems to be an over-complication that is not required.

4.9 Conclusions

The Latitude Hill and Wingellina Hills intrusions are relatively similar as they belong to the same broadly defined group of layered intrusions of the Giles Event, these being the gabbroic-ultramafic G1 intrusions. The Wingellina Hills has a higher proportion of ultramafic/pyroxenitic cumulates compared to the Latitude Hill intrusion; other than that the lithologies are very similar. Both intrusive bodies exhibit moderate but clearly visible signs of crustal contamination (in particular most of the MCG) based on trace elements and isotopic signatures. However, the signatures are less strong than in the massive G2 gabbros, that are associated with some of the gabbroic-ultramafic layered intrusions. These chemical characteristics define a contrast between the gabbroic-ultramafic and the troctolitic G1 intrusions, such as the Bell Rock Range. Any Cu-rich sulphides in the Latitude Hill and Wingellina Hills intrusions are a late-stage accessory phase and formed from interstitial liquid.

A general distinction between members of the Giles Suite has previously essentially been made based on their petrography, i.e. layered versus massive rocks, which were subsequently termed G1 and G2 (Evins et al. 2010b,c). They were interpreted to represent two separate phases of magmatic activity during the Giles Event. However, the evidence based on geochronological data for these two phases is very sparse, and the field

relationships are ambiguous and do not allow to reliably establish the relative timing. A multivariate approach was used to revisit this previously defined boundary between the two phases. The dimensionality reduction using hierarchical cluster analysis was able to find a subgroup of geochemical indicators that express the relevant variations between the G1 and the G2 members of the Giles Suite. Subsequent principal component analysis found 'natural' groupings within these indicators. The comparison of these groups with the classification into G1 and G2 showed, that this classification essentially distinguishes between layered rocks that do not represent liquid compositions and massive rocks that do. Therefore, the differences between the G1 and G2 suites can be attributed to cumulate effects; a separate phase of magmatic activity is not required to explain these findings.

It is thus proposed here, that a distinction between the various intrusive bodies, if required, should be made differently. Previous research suggested that significant petrogenetic changes may have occurred between the production of the parental magma of the troctolitic layered intrusions and of the gabbroic-ultramafic intrusions (e.g. Ballhaus and Glikson 1995; Glikson et al. 1996). The massive gabbroic intrusion (G2) could then be grouped together with the gabbroic-ultramafic layered intrusions instead.

Chapter 5

Generation of exploration vectors with discriminant analysis

5.1 Introduction

Ni-Cu-PGE sulphide ore deposits are often small and elusive exploration targets, however, these deposits are parts of much larger magmatic systems and the mafic/ultramafic sills that host the deposits are also much larger than the deposits themselves. If the host rocks to the Ni-Cu-PGE sulphide deposits carry a geochemical signature that reflects the presence of the sulphides, then the lithogeochemistry of the host rocks present a much larger exploration target than the ore deposits themselves. Surprisingly, there have been very few academic studies directed at developing geochemical tools that can be used to discriminate between mafic/ultramafic sills that host mineralisation and similar intrusions in the same camp or district that host few or no Ni-Cu-PGE sulphides. Some rare exceptions to this are the studies by Burnham et al. (1996, 1998) who developed geochemical discriminants for mineralised versus barren comagmatic mafic/ultramafic sills formed from komatiitic basaltic magmas in the Cape Smith Fold Belt, northern Quebec, Canada and those by Layton-Mathews et al. (2010) who conducted similar studies on ultramafic sills formed by komatiitic magmas in the Thompson Nickel Belt, also in Canada. Lesher et al. (1999, 2001) reported on geochemical discrimination of barren and mineralised komatiites associated with magmatic Ni-Cu-PGE sulphide deposits in Australia. Makkonen et al. (2008) developed geochemical tools to discriminate between barren and mineralised intrusions in the Kotalahti Nickel Belt of Finland.

Choosing small subsets of variables for bivariate scatter plots is common in geochemistry and is essentially a reduction of the dimensionality of the dataset (see also appendix A.6). The choice of the variables is often made in an exploratory way, where a number of combinations of elements are tried and the interpretation is done using the ones that yield the most visually distinct correlations or clusters. Common choices are ratios involving major element oxides (MgO, Mg# or TiO_2), lithophile trace elements (Nb, Th, Zr, Y or REE) or chalcophile and siderophile trace elements (Cu, Ni or PGE).

Seemingly uninteresting combinations of variables often remain unreported, even though the absence of a clear trend can be important, too. For instance, it may suggest the absence of a particular process or that a magmatic system did not have the time to homogenise as a consequence of rapid emplacement. This study is an attempt to reduce the dimensionality in a systematic way that is based on the measured importance of the variables. A multivariate approach is used where the geological problem is translated into a statistical one that can be approached using multivariate techniques to reduce the number of dimensions to the ones that are relevant to the problem. A linear model is used in this study because they generally have a better interpretability compared to nonlinear models. Discriminant analysis for classification and for studying the importance of input variables has been more popular in the analysis of soil chemistry (e.g. Peh et al. 2007; Braun et al. 2013; Roshani et al. 2013; Lin et al. 2014; Laceby et al. 2015). Attempts on using discriminant analysis in igneous geochemistry are seemingly rare: one example is Burnham et al. (1996) on Ni deposits that are hosted by komatiites and basaltic komatiites.

This study also uses methods of compositional data analysis methods to these types of problems: in particular when using multivariate methods that might seem more 'opaque' to the analyst it is important to ensure that no relationships are spurious (Chayes 1960; Buccianti and Grunsky 2014). There is a rich body of work on methods based on log-ratio transformations that has been developed to assist in the analysis of compositional data without the fear of chasing after spurious relationships (e.g. Aitchison 1986; Pawlowsky-Glahn and Egozcue 2001; Egozcue et al. 2003; Filzmoser and Hron 2009).

5.2 Geological setting

The Mesoproterozoic Musgrave Province (see figure 5.1) is located between the North, South and West Australian Cratons. It extends c. 800 km east-west and 350 km north-south and is bounded on all sides by Neoproterozoic and Palaeozoic sedimentary basins. The Giles Event is a multi-phase magmatic event that occurred between c. 1085 and 1040 Ma and caused the emplacement and eruption of mafic to felsic magmas throughout the Musgrave Province (Smithies et al. 2009a; Evins et al. 2010b,c; Aitken et al. 2013, ; see also section 1.2.2). The magmatic activity led to the formation of large mafic-ultramafic layered intrusions and as well as gabbroic plutons. The tectonic processes accompanying the Giles Event are thought to have formed the failed intracontinental Ngaanyatjarra Rift (Evins et al. 2010b,c; Aitken et al. 2013)

5.2.1 Warakurna Supersuite

The Warakurna Supersuite was defined to comprise all igneous rocks formed during the Giles Event including all rocks that are part of the the Warakurna large igneous province (LIP) (Howard et al. 2011a). Three members of this supersuite are of particular interest for this study because they are assumed to be the most prospective for orthomagmatic sulphide ore deposits. These three stratigraphic units are described below.

Giles Suite (layered G1 intrusions) The mafic-ultramafic layered intrusions of the Giles

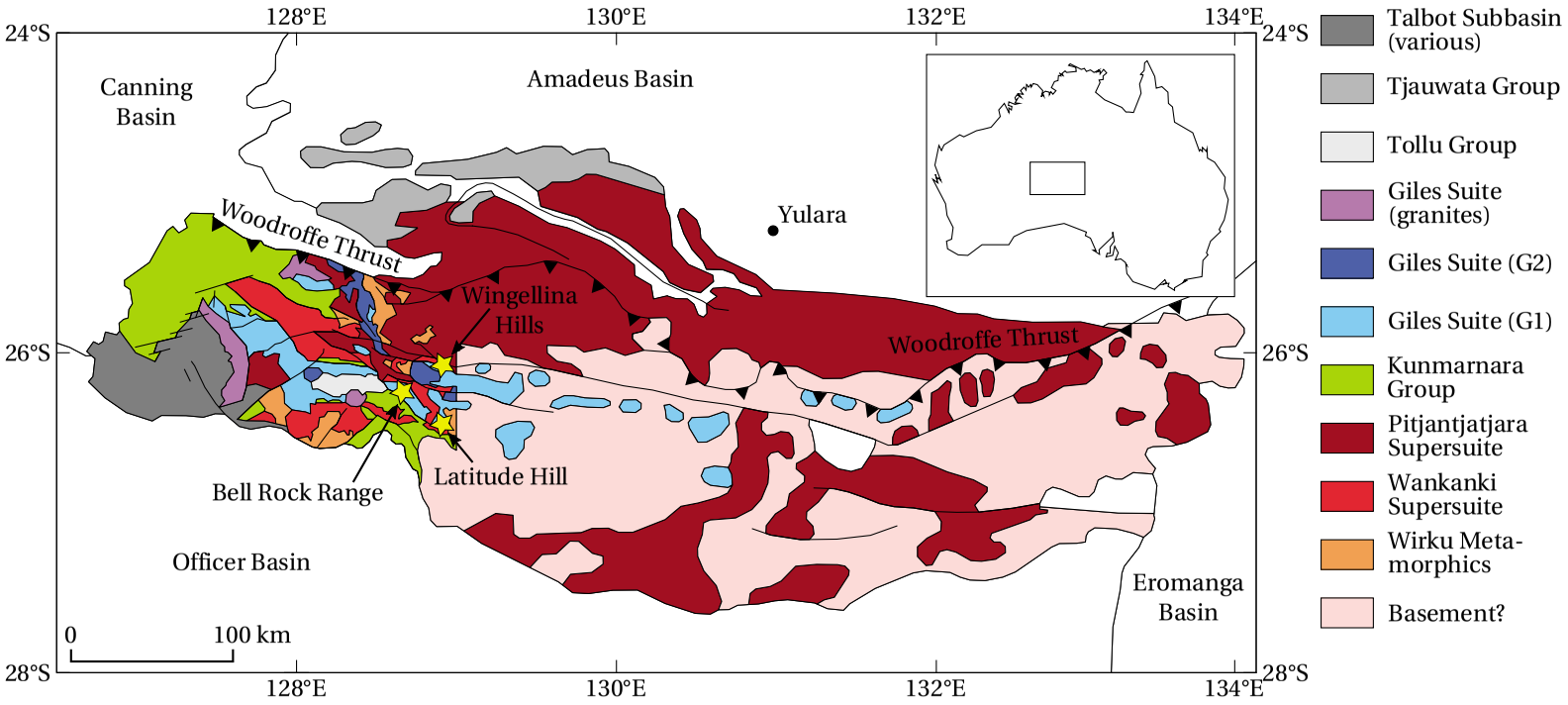

Figure 5.1 Geological map of the Musgrave Province, showing the locations of the Bell Rock Range, Latitude Hill and Wingellina Hills intrusions (modified after Howard et al. 2011a, 2015, the apparent higher degree of known detail in the west is an artefact that results from the progress of recent field mapping campaigns and does not necessarily reflect the true geology). The mafic-ultramafic layered and massive intrusions of the Giles Event are concentrated in the western part of the Musgrave Province. The inset map shows the location of the Musgrave Province within central Australia.

Event are often referred to as the G1 members of the Giles Suite (Evins et al. 2010b,c) and include large intrusive bodies that are dominated by troctolitic and olivine gabbronoritic lithologies, such as the Bell Rock Range (chapters 2 and 3), the Blackstone Range and combined Jameson-Finlayson Range intrusions. Other layered intrusions, that are dominated by gabbroic and ultramafic cumulates, are the Latitude Hill and Wingellina Hills intrusions (chapter 4) but also the Hinckley and Murray Ranges as well as Ewarara, Kalka and Gosse Pile.

Giles Suite (massive G2 intrusions) The massive gabbroic intrusions of the Giles Suite were thought to have formed after the G1 intrusion (Evins et al. 2010b,c, see also discussion in chapter 4). They occur mostly in close proximity to those G1 intrusions that contain gabbroic-ultramafic sequences, such as the Hinckley and Murray Ranges. Many of the members of this unit exhibit strong signs of assimilation of granitic magmas.

Alcurra Dolerite (previously G3) The unit of the Alcurra Dolerite was previously referred to as the G3 member of the Giles Suite. However, many gabbroic intrusions appear to be related to compositionally similar dolerite dykes (Howard et al. 2009c). Therefore, not all members of the stratigraphic units of the Alcurra Dolerite are also dolerites in a lithological sense; for instance, the host intrusion of the Nebo-Babel sulphide ore deposit is a member of this suite.

5.2.2 Orthomagmatic sulphide mineralisation in the Musgrave Province

Very little data has been published on mineralised localities and prospects in the Musgrave Province, although some minor discoveries have been made in recent years. Examples for such discoveries are platinum-group element (PGE) reefs that were reported from Wingellina Hills, V and PGE mineralisation in magnetite seams at the Jameson Range (Maier et al. 2014), a dyke cross-cutting the Jameson Range intrusion containing altered Cu mineralisation (Geological Survey of Western Australia (GSWA) sample no. 194 354; Howard et al. 2009c) as well as Cu-Ni-PGE-Au mineralisation at the Halleys prospect (Redstone Resources Limited 2014). The latter two occurrences are probably related to Alcurra Dolerite (Howard et al. 2009c). Some more recent discoveries are the Succoth, Yappsu and Esagila Cu-Ni-PGE prospects, all within c. 20 km of the Nebo-Babel deposit, as well as the Handpump Au prospect (Cassini Resources Limited 2014). The big exception to this so far is the Nebo-Babel Ni-Cu-PGE deposit, which has been studied in more detail (Baker and Waugh 2005; Seat et al. 2007; Seat 2008; Seat et al. 2009; Godel et al. 2011; Seat et al. 2011).

The Nebo-Babel Ni-Cu-PGE sulphide deposit

The Nebo-Babel Ni-Cu-PGE deposit is the most significant discovery within the stratigraphic section of the Alcurra Dolerite to date (Baker and Waugh 2005; Seat et al. 2007; Seat 2008; Seat et al. 2009; Godel et al. 2011; Seat et al. 2011, see also section 1.3.1). The host intrusion of the deposit is tube-shaped with a length of c. 5 km and a cross section of c. 1×0.5 km. It trends approximately in east-western direction. The Jameson fault

separates the intrusion into the eastern Nebo and the western Babel segments. It was emplaced into late-Musgravian (c. 1150 Ma; Seat et al. 2011) amphibolite-facies felsic orthogneisses and the ambient pressure during crystallisation was estimated to be at least 0.3 GPa, corresponding to a depth of c. 10–12 km (Seat et al. 2011). The main lithologies of the Nebo-Babel host intrusion are barren and mineralised gabbronorites and leucogabbronorites. The $^{207}Pb/^{206}Pb$ crystallisation age of the Nebo-Babel host intrusion is 1068 ± 4 Ma (Seat et al. 2011), obtained from a barren gabbronorite.

The emplacement model proposed by Seat et al. (2007, 2011) is of particular relevance for this study. This is because it forms the basis on which the samples (or their parental magmas, respectively) are classified as either sulphide undersaturated, leading to generally barren lithologies, or oversaturated, producing the lithologies containing the mineralisation (table 5.1). Following the discussions in Seat et al. (2007, 2011), the four stages of the emplacement process of the Nebo-Babel deposit can be summarised as follows: initial magma injections during stage I formed the chilled margins and marginal microgabbros, followed by the emplacement of variably-textured leucogabbronorites. The magmas of stage I carry some mineralisation and are therefore interpreted to have been oversaturated with a sulphide phase. Stage II followed with the contemporaneous emplacement of the mineralised gabbronorites and melagabbronorites. All magmas during this stage were sulphide oversaturated as evidenced by the presence of mineralisation. A thin layer of troctolite was found in the variably-texture leucogabbronorite that contains minor mineralisation and was most likely also formed during this stage. The marginal brecciation and the massive sulphides could have formed either during this or the following stage III of the emplacement process. The volumetric bulk of the inflation of the intrusive body occurred during stage III with the emplacement of the barren as well as the oxide-apatite gabbronorite. The magmas are interpreted to have been undersaturated with sulphides (Seat et al. 2007, 2011); as a result, no economic mineralisation is contained in these lithologic units. Finally, stage IV is characterised by the cross-cutting of several doleritic and, respectively, monzogranitic dyke suites as well as faulting and displacement of the Nebo and Babel segments by the Jameson fault.

Godel et al. (2011) studied five suites of dolerite dykes (labelled NB-1 to NB-5) from the immediate vicinity of the Nebo-Babel deposit in order to reveal the composition of the parental magma of the Nebo-Babel deposit. The relative timing between the intrusion of the dykes and the emplacement of the deposit was established on the basis of field relationships: while the low-Ti suites NB-1, NB-2 and NB-3 predate the emplacement of the Nebo-Babel host intrusion, the high-Ti NB-4 suite postdates it. All four suites are, however, considered genetically linked with the host intrusion and the parental magma is suggested to have been some mixture between low and high-Ti melts (Godel et al. 2011). Unpublished geochronological data from Godel (2008) and Godel et al. (2011) suggest that the alkali basaltic NB-5 suite might be as young as c. 1030 Ma, thus, suggesting that this suite is unrelated to Nebo-Babel. Only very minor sulphide mineralisation (<1 vol%) is reported to occur in the dolerite dykes (Godel et al. 2011). That being said, Godel et al. (2011) found chalcophile element concentrations in the low-Ti dykes to be similar to the mineralised units of the Nebo-Babel deposit, indicating that the magmas forming these

dykes were at least close to sulphide saturation if not already oversaturated.

5.3 A case for discriminant analysis in prospectivity assessment

Apart from a fertile magma which controls the formation of sulphide droplets there are commonly complex dynamic and structural controls involved that enable the accumulation of the sulphide phase in a constricted space, such that the resulting zone of mineralisation reaches economic ore grades/tenors and minimises the amount of rock to process. Such magmatic ore deposits are geochemical anomalies, where one or more commodities may enriched by several orders of magnitude above the crustal average (cf. compilation of ore grades in Chinese gold deposits by Zhou et al. 2000 and average concentrations in continental crust in Rudnick and Gao 2014). As a direct consequence of this, there must always be barren rocks associated with a deposit that are volumetrically much larger than the deposit itself and depleted in the respective metal.

The R-factor (Campbell and Naldrett 1979) is a widely known concept that aims to quantify the mass ratio R between a silicate and a sulphide phase. Assuming thermodynamic equilibrium between the two phases, then D_i is the silicate-sulphide partition coefficient of element i and C_i^0 and C_i^s are its concentrations in the silicate liquid (prior to sulphide segregation) and in the sulphide phase, respectively. Hence,

$$R = \frac{\left(C_i^s - C_i^0\right) D_i}{C_i^0 D_i - C_i^s}. \tag{5.1}$$

The R-factor is commonly assumed to be in the order of magnitude of 10^3 but values in the order of magnitude of 10^5 have been reported (values depend on the system and type of mineralisation; e.g. Lambert et al. 1999, 2000; Lightfoot et al. 2012; Holwell and Keays 2014). Taking average densities of silicate and sulphide melts, it can be seen that the volumetric ratios between the resulting silicate lithologies and the sulphide mineralisation will be within the same orders of magnitude.

This is the starting point for this application of linear discriminant analysis (LDA; Fisher 1936) to the assessment of the prospectivity. The goal is to find discriminator variables that classify barren and mineralised lithologies based on the lithophile elements, i.e. elements that are controlled by silicate phases. A sulphide depletion event can be due to S-saturation in the near surface region, leading to prospective magmas, or it can occur at depth, caused by high-flux partial melting (Keays 1995) or partial melting under high oxygen fugacities (Mungall et al. 2006). This approach removes any issues with the unknown location of chalcophile element depletion by performing the fit of the linear discriminator based on known examples of mineralised and barren rocks. The relative importance of the variables for this fit can then be measured and the most important elements can be used as exploration vectors. In this study, linear discriminant analysis (LDA) is therefore used as a technique for dimensionality reduction to find optimal subcompositions to investigate the problem:

$$y = \beta_1 x_1 + \beta_2 x_2 + \cdots + \beta_i x_i \tag{5.2}$$

where y represents the output or classification score. All x_i with small absolute values for β_i do not contribute significantly to the class separation.

Important characteristics of lithologies associated with Ni-Cu-PGE deposits are fertile magmas (i.e. that are not depleted in chalcophile elements), S-bearing country rocks and depletion of chalcophile elements together with crustal contamination (e.g. increased incompatible elements; Naldrett 2004; Lightfoot and Keays 2005; Zhang et al. 2008; Keays and Lightfoot 2010; Jowitt and Ernst 2013). The Ni-Cu-PGE deposit chosen as proxy to compare the Giles Suite against is Nebo-Babel because it is the only major discovery of orthomagmatic mineralisation in the area so far and is therefore an example of what might be (at least one of) the predominant deposit type in the area.

5.4 Setup of the statistical procedure

This study makes extensive use of previously published data. Data for the Nebo-Babel deposit come from Seat (2008) and Seat et al. (2009, 2011). The data for the dolerite dykes were published by Godel et al. (2011). Data for the various intrusions of the Giles Suite (previously termed 'G1' and 'G2') as well as the Alcurra Dolerite come from the *WACHEM* database of the GSWA, accessed through the *GeoChem Extract* web portal (`http://geochem.dmp.wa.gov.au/geochem/`). In addition, all data generated in this study (chapters 2–4) were used as well. As part of the general data cleaning and sanitising process, missing values were treated appropriately. Since the amount of data that contain missing values was relatively small, a simple replacement strategy was chosen, where values are simply replaced with 2/3 of the limit of detection (LOD). A problem with the data as published by Seat (2008), Seat et al. (2009), Godel et al. (2011) and Seat et al. (2011) was that no detection limits were reported by these authors. The detection limit was therefore estimated to be the lowest measured value that is reported from a variable that contains values below the LOD. This strategy is based on the assumption that such missing values are less likely to be extreme outliers. Instead, and because the dataset contains multiple samples per lithologic unit, it is assumed that if values below the LOD occur in a variable there will be some other value from anorther sample of the same lithology, where the value was at least close to the detection limit, thereby minimising the estimation error.

5.4.1 Definition of outcome classes

Statistical classification requires a dependent or target variable containing the classification outcome for each observation (i.e. rock sample in this case). The motivation behind this study is an assessment of the prospectivity of the mafic intrusions of the Giles Suite for orthomagmatic sulphide ore deposits. For a lithogeochemical study an obvious choice for the outcome classes is therefore the sulphide saturation status (i.e. *sulphide oversaturated* and *sulphide undersaturated*) of the magmas that were parental to the rock samples, because this gives a direct indicator as to whether the magma met the prerequisites for significant sulphide segregation from a geochemical point of view and may have carried mineralisation.

The idea is that each observation belongs to one particular lithologic unit which in turn is the result of crystallisation from a particular parental magma which was either oversaturated with a sulphide phase during emplacement into higher crustal levels, or not. It is important to note that S-saturation processes in the mantle are excluded by this method. This is also irrespective of whether the different parental magmas of the different lithologies share a common source or not or whether they are mixtures of different sources or not. Instead the grouping represents an abstraction: it simply reflects the sum of all processes that caused a particular parental magma to reach sulphide saturation, segregate sulphides and thus experience significant loss of chalcophile elements to the sulphide phase, regardless of what exactly those processes were.

The models for the emplacement of the host intrusion (Seat et al. 2007, 2011) as well as ore genesis (Seat et al. 2009) of the Nebo-Babel deposit form the basis for the classification outcome for Nebo-Babel. Further, the dolerite and chilled margin samples from Godel et al. (2011) were included in this study with the exception of all samples from the NB-5 dyke suite, because their age does not match that of the deposit (section 5.2.2). The deposit was produced by at least three distinct magma injections which are assumed to share a similar source (Seat et al. 2007, 2011, ; see also section 5.2.2). What mainly distinguishes the magma batches is that they were affected by varying degrees of early (i.e. pre-emplacement) depletion in chalcophile elements and wall-rock assimilation, possibly in some (nearby?) staging chamber (Seat et al. 2009). In addition to that, the resulting lithologies of subsequent magma batches became progressingly more evolved (Seat et al. 2007, 2011). All these processes were able to change the chemical composition of the magma batches and are thus suitable candidates to base the classification of the lithologies into the two outcome groups on. The groups are defined as follows (and summarised in table 5.1):

Sulphide oversaturated group This group comprises all lithologies that carry the bulk of the mineralisation of the deposit. They were formed during stages I and II of the emplacement of the Nebo-Babel host intrusion. The group also comprises the marginal breccia and obviously the associated massive sulphides. Furthermore, the dolerite dykes of the NB-4 suite belong to this group because they were interpreted by Godel et al. (2011) to postdate the emplacement of the Nebo-Babel host intrusion and have equilibrated with significant amounts of a sulphide phase which in turn led to significant depletion in chalcophile elements.

Sulphide undersaturated group Accordingly, this group comprises the lithologies of stage III, including the dolerite dyke suites NB-1, NB-2 and NB-3 because they predate the formation of the Nebo-Babel deposit and show evidence for only very minor equilibration with a sulphide phase, most likely at depth and not related to the Nebo-Babel deposit (Godel et al. 2011). Most mafic rocks contain at least trace amounts of sulphides and these rocks are no exception to this, although they are considered barren from an economic viewpoint. The very small amounts of sulphides (commonly <1 vol%; table 5.1) that are present indicate that the whole system was probably close to sulphide saturation for the entire time as Seat et al. (2009) pointed out. Those trace amounts of sulphides were

Table 5.1 Outcome class membership of lithologies of the Nebo-Babel host intrusion, based on whether they are considered oversaturated and undersaturated in sulphides. Modal sulphide contents following Seat et al. (2007, table 2). Note that for a lithology to be oversaturated does not require the respective lithologic unit to be significantly mineralised throughout, because the distribution of sulphide minerals is controlled by magma flow dynamics (Seat et al. 2009).

Deposit	Saturation status	Lithology	Modal sulphides (vol%)
Nebo-Babel	oversaturated	chilled margin	<1
		dolerite (NB-4)	—[a]
		fine-grained mineralised gabbronorite	5–30
		marginal breccia	60–85
		marginal microgabbronorite	1–10
		massive sulphide	—[b]
		melagabbronorite	1–15
		mineralised gabbronorite	5–25
		troctolite	<2
		variably-textured leucogabbronorite	1–20
	undersaturated	barren gabbronorite	<1
		dolerite (NB-1)	—[c]
		dolerite (NB-2)	1
		dolerite (NB-3)	—[a]
		oxide-apatite gabbronorite	<1
		xenolithic oxide-apatite gabbronorite	<1

[a] no information given but assumed to be ≈0
[b] no information given but assumed to be ≈100
[c] 'trace amounts' (Godel et al. 2011)

Table 5.2 Chemical compositions of base- and precious-metal phases that constitute the mineralisation at the Nebo-Babel deposit based on descriptions of the mineralisation in Seat et al. (2007). The table does not contain precious metal phases that occur only in trace amounts. Chemical formulas and common substituting elements are compiled from Anthony et al. (n.d.) and the mineralogical database (`http://www.mindat.org/`).

Phase	Empirical formula	Substitutions/impurities
Base-metal phases		
Altaite	PbTe	Ag, Au, Bi, Cu, Fe
Bornite	Cu_5FeS_4	Ag, Bi, Ge, In, Pb
Chalcopyrite	$CuFeS_2$	Ag, Au, In, Tl
Galena	PbS	Ag, Bi, Cu, Fe, chSb
Melonite	$NiTe_2$	Pd, Pt, Ag, Bi
Pentlandite	$(Fe,Ni)_9S_8$	Au, Co, Cu
Pyrite	FeS_2	Ag, As, Au, Co, Cu, Ni, Tl, V, Zn
Pyrrhotite	$Fe_{1-x}S$[a]	Co, Cu, Ni
Sphalerite	(Zn,Fe)S	Ag, Cd, Ga, Ge, Hg, In, Mn, Pb, Sb, Sn, Tl
Precious-metal phases		
Merenskyite	$(Pd,Pt)(Te,Bi)_2$	Sb
Michenerite	PdBiTe	Ag, Ni, Pt, Sb
Moncheite	$(Pt,Pd)(Te,Bi)_2$	

[a] x between 0 and 0.17

considered to be cumulus by Seat et al. (2009). However, Seat et al. (2009) also pointed out, that the barren gabbronorites have the highest mantle-normalised Cu/Pd ratios. The fact that they are cumulus is explained by in-situ crystallisation from a fractionated magma that has experienced some sulphide segregation before emplacement (Seat et al. 2009; Godel et al. 2011).

5.4.2 Analyte preselection

In order to investigate the prospectivity based on the silicate-controlled lithogeochemistry it is important to exclude all chalcophile elements, not just the ones that would be potential exploration targets (Ni, Cu and the PGE). The sulphide mineralogy of the Nebo-Babel deposit was described in detail by Seat et al. (2007) and is used to constrain the chalcophile elements. The mineralisation at Nebo-Babel comprises the major sulphide phases pyrrhotite, pentlandite, chalcopyrite and pyrite and the phases bornite, sphalerite and galena in trace amounts (mostly nonrecognisable under optical microscope). The tellurides moncheite, melonite, merenskyite, michenerite and altaite are also present and carry the PGE. Table 5.2 contains chemical formulas and common substituting elements for all phases that make up the mineralisation. From this table it is apparent that a large array of base metals (Bi, Cd, Co, Cu, Fe, Ga, Hg, In, Mn, Ni, Pb, Sn, Tl, V and Zn), precious

metals (Ag, Au, PGEs (Ir, Os, Pd, Pt, Rh and Ru), semi-metals (As, Ge, Sb and Te) as well as nonmetals (S) are partially or fully controlled by the presence or absence of a sulphide phase. Unless one has good reasons to assume that the precise modal composition of the mineralisation is known in great detail and with absolute certainty, this confirms the intuition based on Goldschmidt (1937) that essentially the entire array of chalcophile and most siderophile elements must be assumed to be controlled by the abundance of sulphide mineralisation.

Redundant data are removed prior to the application of multivariate classification techniques because it can reduce the risk of overfitting the data. Geochemical data contain many chemical elements that can behave in a very similar way during petrogenetic processes, such as the incompatible elements Th, La and Zr during crustal contamination (Keays and Lightfoot 2007, 2010; Ihlenfeld and Keays 2011). Which elements to remove in a particular case depends on several factors, such as pressure, temperature or the overall composition of the system. Here, the choice was made to exclude most of the rare earth element (REE) and keep only a small selection of light, middle and heavy REEs (La, Ce, Sm, Gd and Yb). This is because the REE have very similar chemical properties as their most common oxidation state is +3 (barring Ce and Eu) and differences in chemical behaviour are mainly controlled by the gradual change in their ionic radii (Shannon 1976; Rollinson 1993). As a consequence REE with a small difference in atomic number Z differ only slightly in their chemical behaviour, which makes it often sufficient to examine them in groups of light rare earth element (LREE) and heavy rare earth element (HREE).

5.4.3 Data transformation and standardisation

The Euclidean distance is a common metric for statistical techniques to measure how different observations are, and LDA is no exception to this. To ensure correct results, log-ratio transformations were applied to the compositional data. This approach has been known as the *principle of working in coordinates* (Pawlowsky-Glahn 2003; Mateu-Figueras et al. 2011): the compositional data are transformed, then the statistical technique is applied and where necessary the results transformed back into compositions (see details on compositional data analysis in appendix A.5). This approach uses the isometric log-ratio (ilr) transformation defined by Egozcue et al. (2003) as a function $\mathrm{ilr} : \mathscr{S}^D \rightarrow \mathbb{R}^{D-1}$ that represents an isometric projection of the composition into an orthogonal coordinate system. Since it is an isometric projection (hence the name) the transformation happens at the expense of reducing the number of dimensions by 1 to $D-1$ in such a way, that the resulting dimensions do not represent a single variable each but are orthonormal. This means that for the purpose of model interpretation the results need to be transformed back into centered log-ratio (clr) or original compositions through the inverse operaton ilr^{-1}. The advantage of this method is, however, that the isometric projection that results from the ilr transformation has the same metric in all $D-1$ dimensions, which is essential for LDA to work. All data transformations are used as implemented by the R package *compositions* in version 1.40-1 (`https://cran.r-project.org/package=compositions`) which is described by Boogaart and Tolosana-Delgado (2008, 2013). The last step is data standardisation, which means centering and scaling of the data to remove any influence

of the different scale of the input data, e.g. measurements taken in wt%, ppm and ppb. Centering is done by perturbation of each observation by the inverse $\hat{g}^{-1}$ of its centre (i.e. mean) $\hat{g}$:

$$X* = X \ominus \bar{x} \tag{5.3}$$

The centered dataset is then scaled to unit variance by powering each variable with $1/sqrt(totvar[X])$ (Pawlowsky-Glahn et al. 2015):

$$Z = \frac{1}{\sqrt{\mathrm{var}_{\mathrm{total}}(X)}} \odot X* \tag{5.4}$$

After data preprocessing is complete the LDA can be performed. LDA requires that the prior probabilities be specified, i.e. the probability of each outcome class to occur. This information is often difficult to determine. In this case, the best information would be the volumetric proportions of the lithologies of the Nebo-Babel intrusion. This information could be extracted from a 3D model of the intrusion (e.g. as displayed in Seat et al. 2007; Seat 2008). Unfortunately, these data are proprietary and cannot be accessed through published material. The proportions of the samples in the dataset are not a good approximation because they are heavily biased by the sampling bias, because sampling from drill core is commonly not based on the volumetric proportions of the lithologies. The prior probability was therefore set to 0.5 for both classes, which means it is assumed to be neutral for lack of a better value and so as to not introduce a bias.

5.5 Results and validation of the model and its assumptions

The results of the fit of the linear discriminator between the two groups (over- and undersaturated) are visualised in figures 5.2–5.4. The plots show that LDA overall results in a satisfactory class separation, i.e. the overlaps between the two histograms that represent the two outcome classes in each figure are minimal and the model is able to separate the two outcome classes by using the input variables. The chalcophile/siderophile set of variables yields the largest overlap and also the largest deviation from normality. Some of the irregularity of the plots could be due to the small size of the dataset (<190 rock samples).

The next step is to test the performance of the model. Table 5.3 shows the confusion matrix that results from 10-fold cross-validation. It confirms that all three variable sets are generally able to classify the data. However, the classification using the chalcophile/siderophile set has the highest error rate, thus, performs the worst. Using this set of variables may produce misleading results. The other two sets perform better, which supports the strategy of focussing on the lithophile elements. A visualisation of the data contained in the confusion matrices in table 5.3 is shown in figure 5.5. The receiver operating characteristic (ROC) curves confirm the information of the confusion matrix, that the performance of the lithophile and the full variable sets perform similarly well. The chalcophile/siderophile variable set on the other hand performs slightly worse. While the classification outcome is not perfect (i.e. the curves do not go through the top-left corner)

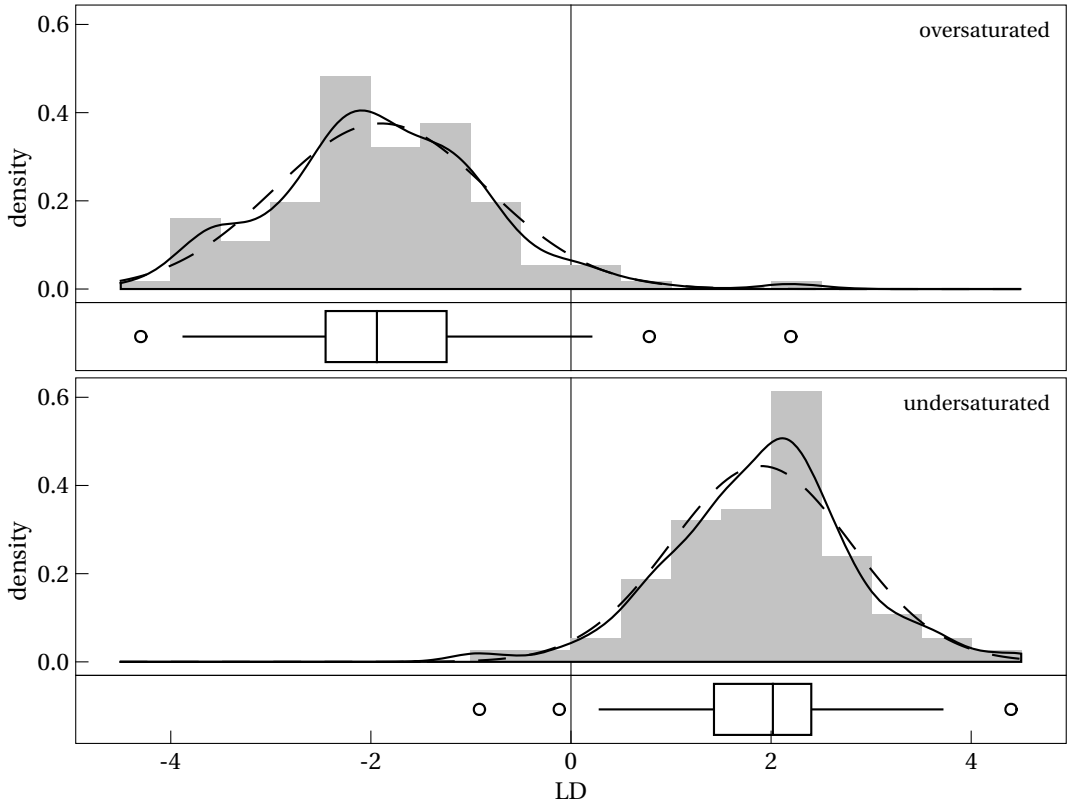

Figure 5.2 Visualisation of fit of the linear discriminator for all variables. The variable *LD* represents the discriminant score of the observations (i.e. rock samples) centered around 0, the descision boundary between the two groups. The histogram (frequency) and the solid line (density estimate/curve) are based on the actual results, the dashed line represents a normal distribution with the same mean and standard deviation. The boxplot shows the same data, outliers are defined as 1.5 times the inter-quartile range (IQR).

	oversaturated	**undersaturated**
lithophile variables (error rate = 0.15)		
oversaturated	94	13
undersaturated	15	61
chalcophile/siderophile variables (error rate = 0.20)		
oversaturated	91	17
undersaturated	21	58
all variables (error rate = 0.16)		
oversaturated	97	14
undersaturated	15	61

Table 5.3 Confusion matrices for linear classifier on data from the Nebo-Babel deposit. Columns show the true class memberships, rows the predicted class memberships. Error rates are the proportions of all false classifications to the total number of observations for each subset of variables.

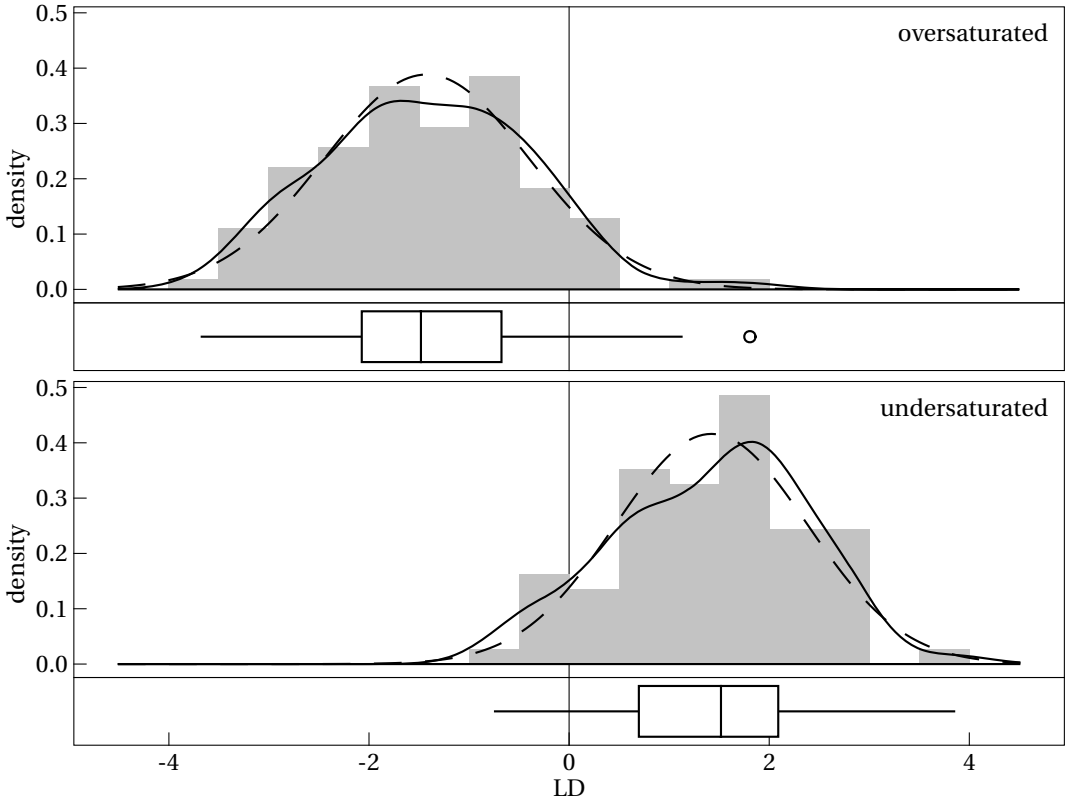

Figure 5.3 Visualisation of fit of the linear discriminator for lithophile variables. The variable *LD* represents the discriminant score of the observations (i.e. rock samples) centered around 0, the descision boundary between the two groups. The histogram (frequency) and the solid line (density estimate/curve) are based on the actual results, the dashed line represents a normal distribution with the same mean and standard deviation. The boxplot shows the same data, outliers are defined as 1.5 times the inter-quartile range (IQR).

all classifiers clearly perform better than random classification, as shown by the diagonal line.

5.6 Discussion

5.6.1 Model performance

First, it is instructive to verify that the assumptions of the statistical technique were met. This is particularly true for LDA which makes a strong assumption of data normality. The kernel density curves in figures 5.2–5.4 (solid line) match an ideal normal distribution (dashed line) well, so that the normality of the data can be assumed. Further, geochemical relationships can be nonlinear and therefore a linear model is not necessarily the right choice. However, given that the assumptions are met and the classification performance of the linear model is satisfactory (section 5.5) it is a legitimate approximation that particu-

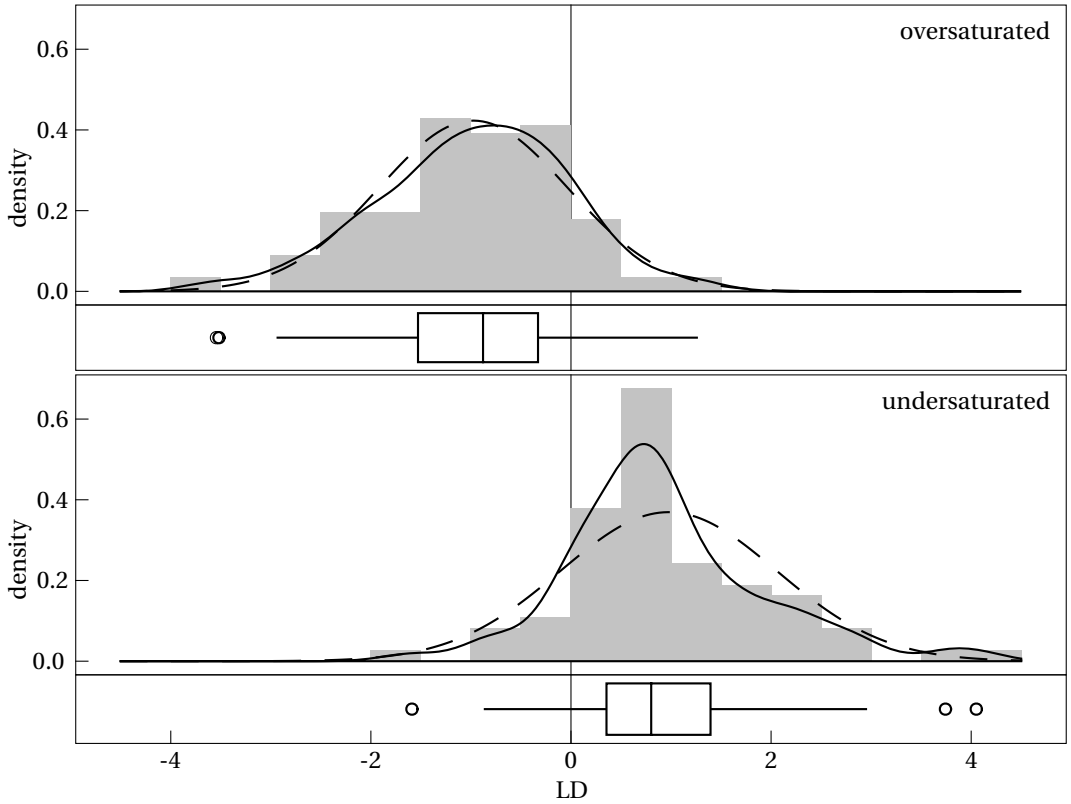

Figure 5.4 Visualisation of fit of the linear discriminator for chalcophile/siderophile variables. The variable *LD* represents the discriminant score of the observations (i.e. rock samples) centered around 0, the descision boundary between the two groups. The histogram (frequency) and the solid line (density estimate/curve) are based on the actual results, the dashed line represents a normal distribution with the same mean and standard deviation. The boxplot shows the same data, outliers are defined as 1.5 times the inter-quartile range (IQR).

larly allows the interpretation of the underlying relationship better than nonlinear models; the question of a nonlinear ('black-box') classifier versus a linear one is essentially the question of a more accurate predictor versus a model with better interpretability (Kuhn and Johnson 2013). Once the assumptions of the LDA are met, more data will commonly not improve the classification. An important aspect to discuss is therefore the data *quality*. One of the causes for lacking data quality are missing data, that were treated appropriately (section 5.4).

A potentially more important reason for nonsatisfactory class separation is that geochemical datasets do not contain all information that is needed to fully understand why a particular set of rocks turns out to be mineralised or barren. In fact, the question whether a magma loses its chalcophile elements to a sulphide phase or not is not only one of magma chemistry and the various processes modifying it; instead, structural controls and magma dynamics exert great control over the efficiency of sulphide and metal concentration, once a separate sulphide phase is present (e.g. Maier et al. 2001; Lightfoot and

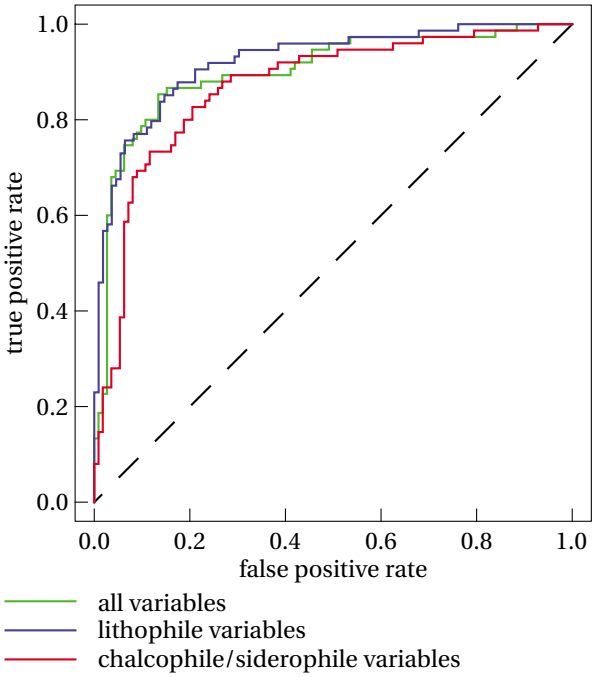

Figure 5.5 Receiver operating characteristic (ROC) curves for linear classifiers on data from the Nebo-Babel deposit showing true vs false positive rate ('positive' being oversaturated). The coloured curves show the performances of the three different variable sets. The dash diagonal line represent classification at random/by chance.

Evans-Lamswood 2015; Saumur et al. 2015). Several studies investigated the key-criteria for the formation of magmatic sulphide mineralisation across different ore deposits worldwide (e.g. Naldrett 1999; Maier et al. 2001). These studies indicate that the formation of economic ore deposits requires (1) a mafic or ultramafic magma, (2) the saturation of that magma with S and subsequent separation of a sulphide phase, and (3) some structural control (commonly a channel or conduit) that serves twofold purpose: first, it provides an efficient mechanism for the equilibration of as much silicate melt with the sulphide phase as possible. This concentrates chalcophile metals in the sulphide phase. Second, it concentrates the sulphides within a compact space in order to facilitate economic ore grades. Some of the biggest known sulphide ore deposits, such as Noril'sk (Russia), Jinchuan (China), Uitkomst (South Africa) and Voisey's Bay (Canada), formed this way. Any process involved in the first two points should under most circumstances be measureable through variations in the *lithophile* element contents. The broader chemical affinity of a magma within the ultramafic to felsic spectrum is obviously easily detectable in the geochemistry and needs no further explanation. However, different degrees of partial mantle melting or varying oxygen fugacities during magma generation can greatly influence the fertility of the resulting magmas (e.g. Keays 1995; Mungall et al. 2006; Jugo 2009). The structural controls on the other hand are essentially opaque from a geochemical point of view. This is because they simply cause a separation of the lithophile from the chalcophile and siderophile elements without affecting relative differences within each group of elements. In their models for intrusion emplacement and formation of the mineralisation Seat et al. (2007, 2009) discuss the influence of magma chemistry versus magma dynamics on the ore formation. Seat et al. (2009) argue that differences in the distribution of sulphide

mineralisation throughout the lithologies were largely controlled by the dynamics of magma flow rather than chemistry. With that, they broadly follow the general ideas of Lightfoot and Keays (2005), who use the example of Noril'sk and the Siberian trap flood basalts to illustrate that wall-rock assimilation and sulphide segregation do not necessarily happen in-situ but in a staging chamber with subsequent transport into the emplacement chamber.

Nevertheless, changes in chemistry between magma batches occur, mainly caused by magma mixing and contamination in the staging chamber Lightfoot and Keays (2005). In agreement with that, what mainly distinguishes the magma batches that formed the Nebo-Babel deposit is, that they were affected by varying degrees of early (i.e. pre-emplacement) depletion in chalcophile elements, as well as varying degrees of wall-rock assimilation (Seat et al. 2009). Furthermore, subsequent batches, and thus the resulting lithologies, became progressingly more evolved (Seat et al. 2007, 2011). In summary this means that the changes in lithophile elements that are modelled by the LDA with the grouping variable above encapsulates all chemistry-modifying processes in the emplacement and staging chambers. These, however, are potentially only supporting processes as some main reasons for some lithologies being mineralised are not detectable with this technique.

5.6.2 Reduction of the dimensionality through variable selection

LDA coefficients β do not express which variable is most related to a particular response, i.e. over- or undersaturated. The reason for this is, that they are not coefficients from a regression through a particular response. Their absolute values do, however, indicate how much a variable contributes to the separation *between* the different classes. Figures 5.6–5.8 show the absolute values of the linear discriminant coefficients in the order from highest (variable is very important for the class separation) to lowest(variable contributes only little to the class separation) for all three sets of variables. They can be as low as $\approx$0.05 for U and Li, indicating that the elements with the lowest coefficients do indeed barely contribute to the discrimination. In all three plots is an approximately exponential relationship in the decrease of importance. There is also no clear threshold or cut-off between 'important' and 'unimportant' variables. The full set of variables exhibits a very constant exponential relationship between the linear discrimination coefficients. There are distinct changes, however, within the lithophile set of variables, where a distinct descrease in β values appears from Cr_2O_3 towards the least important variables (Ba, U, Li, Sr, Cs and Eu). All of these elements are highly incompatible and some are strongly controlled by feldspars such as Ba and Eu. They may be recording the degree of fractionation of the magma. From the lithophile set of variables it can further be seen that amongst the best predictors of class membership are ternary major element system CaO-Al_2O_3-SiO_2 as well as the REE (La-Sm-Yb). It is interesting that, while these elements could indicate both feldspar and/or pyroxene control, the trace elements Sc (pyroxene-controlled) and Eu (plagioclase-controlled) are apparently of little importance. It is also interesting that MgO, which would be the most obvious choice to explain geochemical trends with magmatic fractionation, is only of minimal relevance for the discrimination modelling. Whether this has petrogenetic reasons, or whether MgO data are simply too noisy due to varying

degrees of cumulate effects is difficult to assess.

5.7 Conclusions

LDA can be used to discriminate between mafic-ultramafic intrusions that are known to host orthomagmatic sulphide mineralisation and similar intrusions in the same area that are barren. For such tasks, LDA is an effective tool for the reduction of the data dimensionality and the measurement of the variable importance, which can then form the basis for further data interpretation. The above definition of outcome variables and preselection of analytes (grouping into chalcophile, siderophile and lithophile) can be used to control which processes to model. The outcome variable, which is based on the emplacement model, controls what is being distinguished: if the distribution of the mineralisation would be entirely controlled by magma dynamics the results of the LDA may have little to do with the mineralisation. The decision whether to include or exclude the chalcophile and/or siderophile elements can for instance be based on the question whether there are different generations or types of sulphides that should be discriminated or whether the discrimination should be entirely based on the petrogenesis of the silicate magma. Depending on the situation, both options can be viable. Appropriate methods for the analysis of compositional data are an important part of multivariate data analyses because they can offer protection against erroneous conclusions caused by spurious relationships between variables.

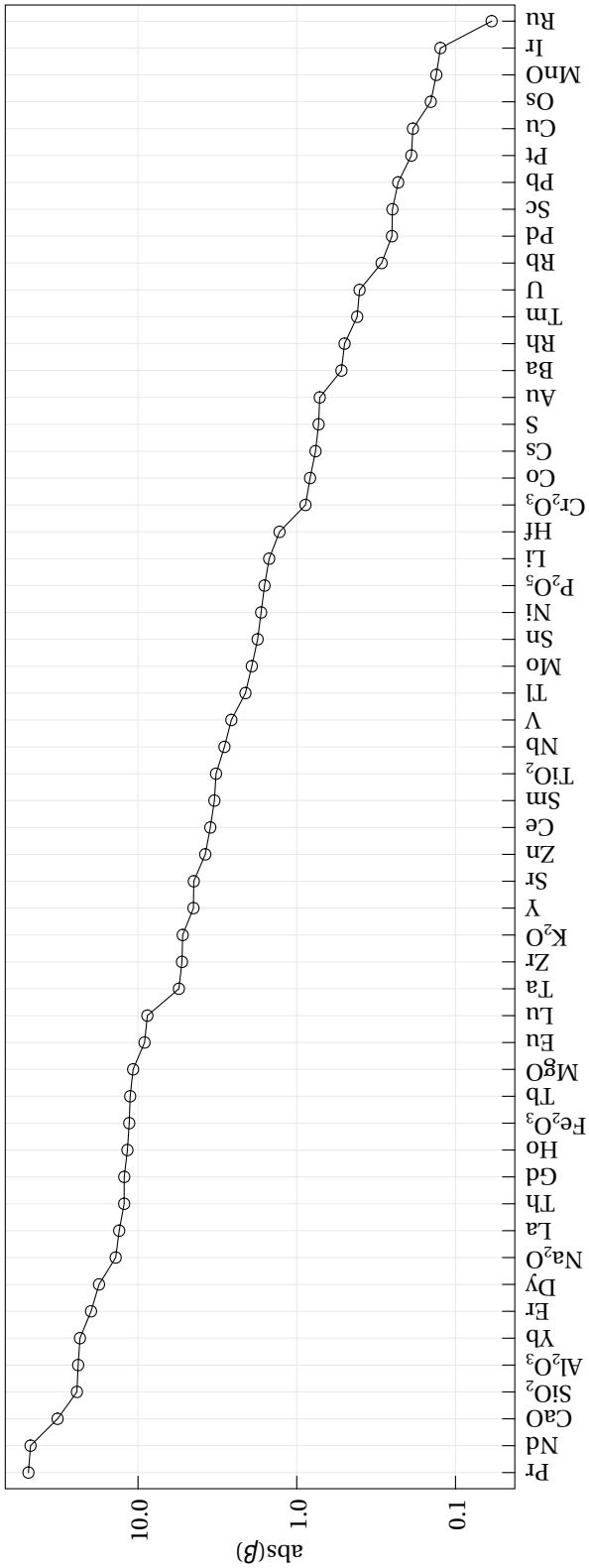

Figure 5.6 Parallel coordinate plot with ordered absolute values of LDA coefficients β for all variables in the Nebo-Babel dataset.

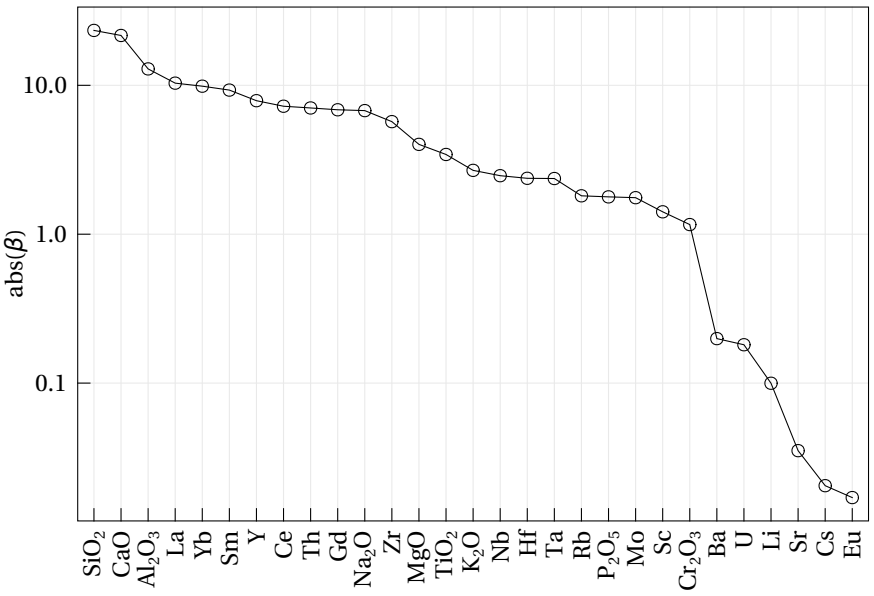

Figure 5.7 Parallel coordinate plot with ordered absolute values of LDA coefficients β for all lithophile variables in the Nebo-Babel dataset.

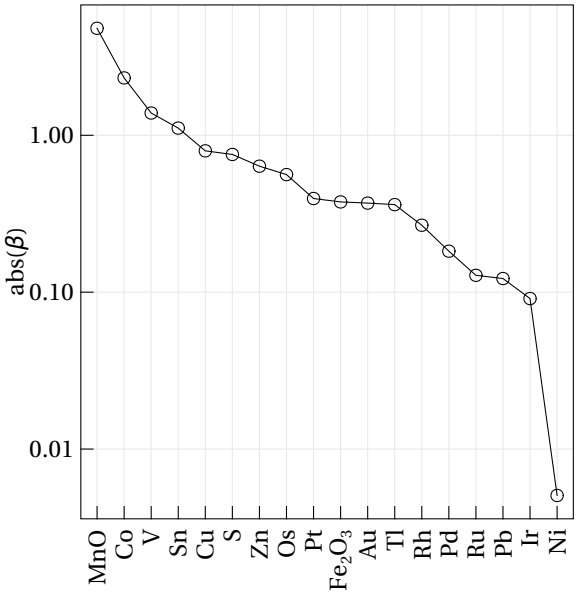

Figure 5.8 Parallel coordinate plot with ordered absolute values of LDA coefficients β for all chalco- and siderophile variables in the Nebo-Babel dataset.

Chapter 6

Concluding remarks

This thesis discusses various aspects of the petrogenesis of the Giles Suite and the prospectivity of its member intrusions for orthomagmatic sulphide ore deposits (section 1.4). The Giles Suite is a member of the Warakurna Supersuite that outcrops throughout the Musgrave Province in central Australia (Howard et al. 2011a). This study also examines the applicability of several supervised and unsupervised methods for data clustering and classification to the above problems.

Much of this study on the petrogenesis of the individual Bell Rock Range, Latitude Hill and Wingellina Hills intrusions was done using traditional methods of petrology and lithogeochemistry. In contrast, the relationship between the previously defined G1 and G2 members of the Giles Suite (Evins et al. 2010b,c) as well as the evaluation of the sulphide prospectivity of the Giles Suite was investigated using modern multivariate methods applied to compositional data.

6.1 The petrogenesis of the Giles Suite

The Giles Suite comprises all mafic and ultramafic rocks that formed at c. 1078–1076 Ma, at an early stage of the c. 1090–1040 Ma Giles Event (Evins et al. 2010b,c; Smithies et al. 2015). The Giles Suite is itself a member of the much larger Warakurna Supersuite, which Howard et al. (2006) defined to comprise all additional mafic and felsic igneous rocks from the Bentley Supergroup (Daniels 1969), the Alcurra Dolerite (Edgoose et al. 2004) and the Warakurna large igneous province (LIP; Wingate et al. 2004; Morris et al. 2005; Pirajno 2007), i.e. it contains all magmatic rocks that are somehow genetically linked to the Giles Event. The intrusions that make up the Giles Suite have previoulsy been grouped into layered ('G1', troctolitic and mafic-ultramafic) and massive ('G2').

6.1.1 The Bell Rock Range intrusion

Chapters 2 and 3 study the Bell Rock Range as an example of a troctolitic-olivine gabbronoritic layered intrusions of the Giles Event. Igneous layering is present in the main body of the intrusion and on a very large scale of up to several hundreds of metres thickness

per layer. The mineral compositions are variable and show that two generations of olivine exist, cumulus and intercumulus, that crystallised under different pressures, most likely at different depths. Strongly increasing fractionation from the centre of the intrusive body towards its top caused distinct drops in Fo and An contents of olivine and plagioclase, respectively, and the crystallisation of cumulus Fe-Ti-oxides, although no magnetitite seams were observed.

The parental magmas were produced in the upper mantle by partial melting of spinel-lherzolite, at a depth of no more than 75 km. The resulting magma shows the characteristics of an ocean island basalt (OIB) melt derived from the enriched mantle (EM) reservoir. While such magmas may be plume-related they can also be generated in the subcontinental lithospheric mantle (SCLM) that has previously been metasomatised, e.g. from a subducted slab. Only moderate subsequent crustal contamination occurred. The felsic country rocks were highly enriched in incompatible elements during the Musgrave Orogeny (Smithies et al. 2011), thus, only small amounts of contamination were sufficient to cause the observed signatures.

The Bell Rock Range intrusion was most likely rapidly emplaced through the injection of multiple magma batches. Even though the intrusion is lacking evidence for magma homogenisation, the main body can be broken down into at least two large vertical sections. The basal segment exhibits mostly cryptic variations with depth and may have formed via intra- or underplating. On the other hand, the top segment exhibits a strong upwards fractionation trend which indicates that the magma injections became increasingly fractionated.

The Bell Rock Range intrusion is a segment from the basal part of the Mantamaru intrusion, which was overall no more than 15 km thick. Emplacement of the Mantamaru intrusion occurred most likely at mid-crustal levels between 3 10km depth. The estimates vary greatly due to the unconstrained cross-correlation of the different segments of the Mantamaru intrusion (e.g. the Bell Rock, Blackstone, Jameson-Finlayson Ranges and Cavenagh Ranges; Ballhaus and Glikson 1995; Glikson et al. 1996; Evins et al. 2010b,c; Aitken et al. 2013; Maier et al. 2014, 2015) as well as the different possibilities in the emplacement mechanics.

Three of the sampled lithologies may not originally have been part of the Bell Rock Range intrusion; these being the microporphyritic gabbronorite (MPG) from the parallel-running ridges, the microgabbronorite (MCG) from the late-stage dykes and the coarse-grained gabbronorite (CGG) from the base of the southeastern end of the Bell Rock Range. The rocks from the parallel-running ridges are more fractionated than the magma from the main body and are also stronger contaminated by crustal material. They are probably members of the Alcurra Dolerite and may be cross-correlated with several small intrusive bodies south of the Blackstone Range (Howard et al. 2009c).

6.1.2 The Latitude Hill and Wingellina Hills intrusions

Chapter 4 characterises the Latitude Hill and Wingellina Hills intrusions. These intrusions were chosen as examples for the mafic-ultramafic layered intrusions of the Giles Event. Both intrusions are relatively similar in terms of their lithologies, however, Wingellina

Hills has a higher proportion of ultramafic rocks and pyroxenites. Unlike the Bell Rock Range intrusion, olivine is rare in both intrusions and plagioclase is mostly intercumulus. The Δ_{Nb} values are highly variable and range from primitive to crustal, which could be caused by strong cumulate effects and obscures the identification of the magma source. Nevertheless, trace element evidence suggests that crustal contamination was stronger than in the rocks from the Bell Rock Range, a finding that is also supported by the Sr-Nd-isotopic signatures, which are in-between the more primitive Bell Rock Range intrusion and the G2 members of Giles Suite, the latter of which exhibit stronger crustal signatures. However, no evidence is present for a fundamentally different mantle source compared to the EM source of the Bell Rock Range intrusion, thus, the differences may trace back to a higher degree of crustal contamination as well as crystallisation at a different (deeper?) level in the crust. The CGG from the base of the southeastern part of the Bell Rock Range intrusion exhibit a similarly strong crustal signature and may be related to a gabbronoritic-ultramafic layered intrusion, such as the Latitude Hill or The Wart, both of which are located closeby.

6.1.3 Relationship between layered and massive intrusions of the Giles Suite

Chapter 4 studies the relationship between the mafic-ultramafic layered intrusions and the massive gabbroic intrusions of the Giles Suite. The distinction between these two members of the Giles Suite has previously been made based on rock textures (layered versus massive; e.g. Daniels 1974; Ballhaus and Glikson 1995; Glikson et al. 1996). The layered intrusions were later interpreted to predate the massive intrusions and they were accordingly labelled 'G1' and 'G2', respectively (Evins et al. 2010b,c). However, geochronological data (table 4.5) and field relationships to support the suggested succession are ambiguous (cf. Clarke 1992; Evins et al. 2010c). It is suggested here that this distinction is an overcomplication that is not required to explain the apparent differences between the two groups of intrusions. Instead, the differences between the G1 and the G2 members of the Giles Suite can be attributed to cumulate effects, where the G1 layered intrusions, many of which are adcumulates, lost much of their intercumulus liquid during layer formation. This probably happened through dynamic layer formation processes, i.e. involving migration of melt and/or crystals. The gabbroic G2 intrusions on the other hand, did not form any igneous layering, thus, their composition closely resembles that of the original parental magma. This is evidenced by the well preserved mixing and mingling textures, that are original magmatic textures. The reason for the stronger crustal signatures in the G2 gabbros is that they retained more intercumulus liquid, which is where most incompatible elements concentrate. Whether magmatic systems form igneous layering or not does mostly depend on physical and mechanical parameters during the emplacement, such as heat flow, pressure changes, frequency of magma injections, magma viscosity and convective currents (e.g. Cawthorn 2012; Namur et al. 2015). Changes in such parameters may have been caused by geological structures, which seems likely because the massive G2 gabbros intruded along the boundary between the Tjuni Purlka and Walpa Pulka Zones (Evins et al. 2010b,c; Maier et al. 2014, 2015).

Howard et al. (2009c) already recognised the problems that cumulate effects can cause

during research on the rocks from the Warakurna Supersuite. For instance, a bimodal grain size distribution in rocks of the Alcurra Dolerite (termed 'dual texture' by Howard et al. 2009c, p. 4) was seen as evidence for the migration of melts through mush columns of cumulate crystals (suggesting dynamic layer formation as pointed out above; Namur et al. 2015). A similar texture was observed in this study in rocks from the parallel-running ridges near the Bell Rock Range intrusion (section 2.6.2).

A new grouping of the mafic-ultramafic intrusions of the early stages of the Giles Event is proposed, where the massive gabbroic intrusions are not considered to represent a later phase of magmatic activity but are instead considered contemporaneous and comagmatic with the gabbronoritic-ultramafic layered intrusions that they are commonly associated with. The textural difference merely reflects physical changes during the emplacement, causing only some intrusive bodies to develop igneous layering.

Previous research concluded that the troctolitic layered intrusions and the gabbroic-ultramafic layered intrusions did not form from the same parental magma through continued fractionation (Ballhaus and Glikson 1995; Glikson et al. 1996). The troctolitic-olivine gabbronoritic layered intrusions (such as the Bell Rock Range) and the gabbronoritic-ultramafic layered intrusions (such as the Latitude Hill and Wingellina Hills) are therefore the result of two separate petrogenetic processes derived from different parental magma compositions. However, it is not clear whether this necessarily implies a difference in timing, too. The relationship of the dykes with these newly defined groups of intrusive bodies is ambiguous, but they could be related to the massive gabbros and therefore to the gabbroic-ultramafic layered intrusions.

Another still unclear relationship is between some of the felsic intrusive members of the Giles Suite and the mafic-ultramafic layered and massive intrusions. Many of the felsic intrusions were most likely emplaced contemporaneously with the massive mafic-ultramafic intrusions, as is evidenced by mixing and mingling textures in some of the gabbroic intrusions (e.g. Clarke 1992; Glikson et al. 1996; Evins et al. 2010b,c; Maier et al. 2014, 2015, see also chapter 4). Despite these findings, a direct petrogenetic relationship between mafic and felsic magmas was never established. Instead, it has been suggested that most felsic magmas were likely formed by crustal melting rather than by differentiation from the mafic-ultramafic magmas (Glikson et al. 1996). However, recent advances in petrogenetic modelling of the Bushveld Complex concluded that in principle a more direct relationship is certainly within the realms of possibility. While there remains some debate as to which lithologies are part of the highly fractionated section of the Bushveld Complex, it appears to be generally accepted that some quartz and K-feldspar bearing intermediate or felsic rocks are cogenetic with the mafic units (cf. VanTongeren et al. 2010; Cawthorn 2013). It is currently unknown to what extend these models can be applied to the Giles Suite.

6.2 The enigmatic tectonic setting during the Giles Event

The tectonic setting of the Musgrave Province during the Giles Event is still debated (cf. Pirajno and Hoatson 2012; Smithies et al. 2015). Some of the earlier models include rifting

(Mathur and Shaw 1982) or mantle melting caused by a plume or decompression melting of SCLM through lithospheric thinning (Zhao and McCulloch 1993). The proposed genetic link between the Giles Suite in the Musgrave Province and the then newly discovered Warakurna large igneous province (LIP) (Wingate et al. 2004; Morris et al. 2005; Pirajno 2007) fuelled the discussion around a possible mantle plume under the Musgrave Province. Evins et al. (2010b,c) on the other side revived the idea of rifting. The four possibilities that these authors discuss as potential causes for the rift are the delamination of the lithosphere, thermal blanketing, a mantle plume and active tectonic environments such as subduction zones and transform faults.

Evins et al. (2010b,c) considered a mantle plume only for the massive gabbroic magmas ('G2') that are contemporaneous with the Warakurna LIP and for the layered intrusions ('G1'). The remainder of the (bimodal) magmas of the Giles Event, however, was interpreted to have formed by decompression melting due to continued rifting by these authors. In their more recent work, Smithies et al. (2015) reject the mantle plume hypothesis. The main reason for this is that the duration of the Warakurna LIP (c. 1078–1070 Ma, Wingate et al. 2004; Morris et al. 2005) was much shorter than the rather long-lived Giles Event (assumed minimum age brackets of 1090–1040 Ma, Howard et al. 2015; Smithies et al. 2015) and that LIPs do generally not exceed a lifespan of c. 50 Ma (Bryan and Ernst 2008). Instead, the geological record was interpreted to suggests a complex tectonic setting during the Giles Event that caused widespread bimodal plutonic and volcanic activity and deposition of the volcaniclastic Bentley Supergroup (Evins et al. 2010b,c). This led Smithies et al. (2013, p. 5) to point out that '[...] the Warakurna Large Igneous Province should be regarded simply as a component of the Giles Event rather that [sic] the expression of it [...]' and that the entire event may have lasted (continuously?) for >200 Ma. This would in turn mean that the c. 1220–1150 Ma Musgrave Orogeny would be an episode of the Giles Event. Smithies et al. (2013, 2015) found asthenospheric upwelling or lithospheric delamination to be the most likely driver for mantle melting and that the whole process was driven by some form of plate dynamics rather than mantle dynamics.

Pirajno and Hoatson (2012) argued that even though LIPs might not commonly exceed a lifespan of c. 50 Ma mantle plumes easily can; thus, they eliminate the need for an additional driver behind the advanced stages of the Giles Event (Evins et al. 2010b,c). Since parts of the Warakurna LIP are much more widespread (c. 1.5×10^6 km^2; Wingate et al. 2004; Morris et al. 2005) than just the Musgrave Province (c. 1.4×10^5 km^2; Pirajno and Hoatson 2012) it seems that if one accepts a genetic relationship between the two then intuitively a driver for mantle melting is needed that not only greatly exceeds the scale of localised plate tectonics in the Musgrave Province but also causes significant magmatic activity deep within the West Australian Craton (figure 6.1), such as the mineralised Gifford Creek Ferrocarbonatite Complex (GFC) at the western end of the Warakurna LIP (Pirajno et al. 2014). Carbonatites were previously linked with LIPs (Ernst and Bell 2010; Ernst and Jowitt 2013). The origin of the mineralisation that is associated with such alkaline rocks as well as the alkaline rocks themselves are often attributed to low-degree partial melts of metasomatised SCLM (e.g. as found in the East African Rift; Bailey 1987) and some carbonatites in particular could also be linked with mantle plumes (Bell 2001). Smithies

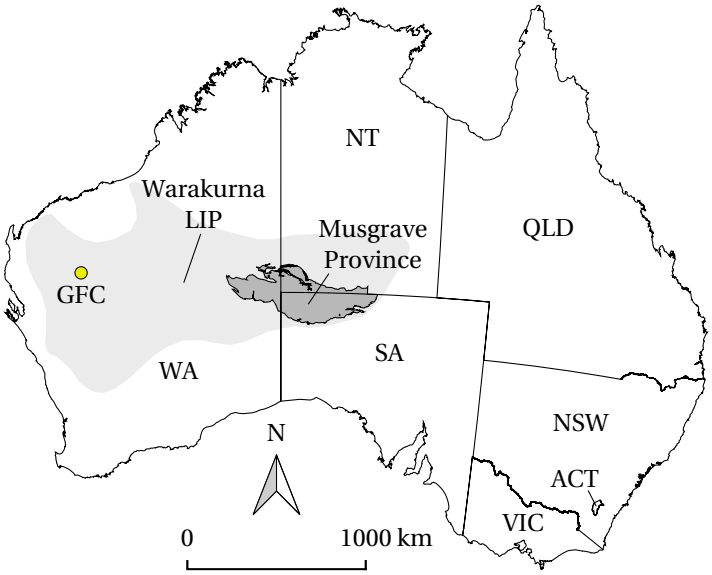

Figure 6.1 Map of Australia showing the relative locations and spatial extends of the Musgrave Province and the Warakurna large igneous province (LIP) with respect to the West Australian Craton and the Capricorn Orogen (modified after Wingate et al. 2004; Howard et al. 2011a; Pirajno and Hoatson 2012). The yellow point indicates the position of the Gifford Creek Ferrocarbonatite Complex (GFC; Pirajno et al. 2014).

et al. (2015) point out that during the Giles Event the Musgrave Province was partially aligned with the east-west trending Capricorn Orogen in Western Australia; however, these authors do not identify an actual process that could have facilitated the lateral extension of the magmatic activity, far beyond the Musgrave Province. Pirajno and Hoatson (2012) on the other side genetically link the spatially dispersed members of the Warakurna LIP, such as the sill complexes in the Bangemall Supergroup (Morris et al. 2005), by lateral flow of mantle plume material, similar to the models proposed by Ebinger and Sleep (1998) and Forte et al. (2010) for the East African Rift. This links well with carbonatites in general which in LIPs occur largely away from the plume head with lateral flow of plume material being facilitated by structural zones of weakness in the crust (Bell and Rukhlov 2004). Such zones of structural weakness have also been identified by Howard et al. (2011a) and Pirajno and Hoatson (2012).

The current debate is essentially one of *active* versus *passive* rifting (Sengör and Burke 1978; Turcotte and Emerman 1983), i.e. one of mantle dynamics causing magmatism and rifting as a secondary process versus crustal dynamics causing rifting and magmatism as a secondary process (figure 6.2). A common way to distinguish between the two is the relative timing between the onsets of crustal thinning and magmatism (Schmeling 2010). The oldest direct ages of the Giles Event were obtained from the layered mafic-ultramafic intrusions (c. 1078–1076 Ma, Sun et al. 1996; Kirkland et al. 2011); however, field evidence suggests that the basal sequence of the Ngaanyatjarra Rift are the coarse-grained clastic sediments of the MacDougall Formation (Kunmarnara Group, lower Bentley Supergroup; Howard et al. 2011a,b, 2015), which is in agreement with typical early syn-rift deposits in alluvial fans and lacustrine settings (e.g. Cavazza 1989; Doutsos and Piper 1990; Köykkä 2011). If the MacDougall Formation represents an early syn-rift deposit and no magmatic activity occurred prior to c. 1078 Ma then this could be strong evidence for the onset of rifting having been driven by plate dynamics. Whether rifting in the Musgrave Province

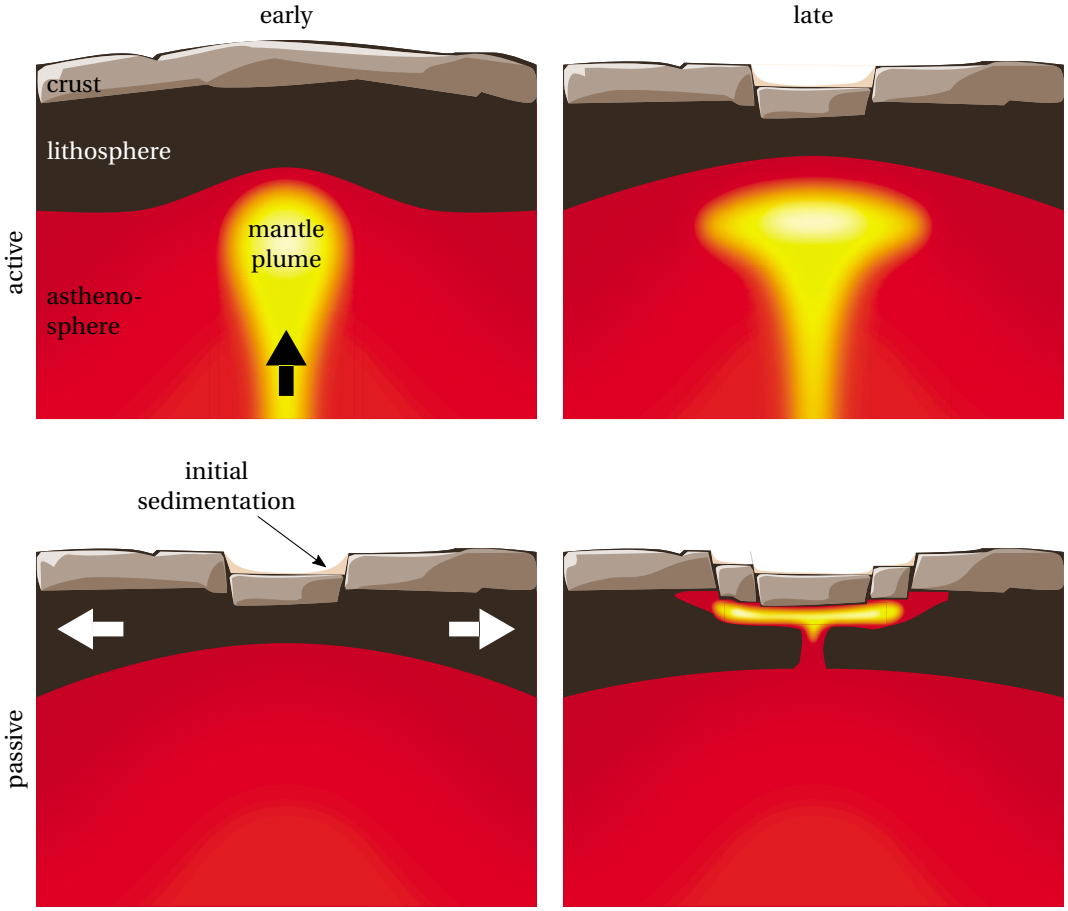

Figure 6.2 Early and late stages of active and passive rifting (inspired by Turcotte and Emerman 1983; Merle 2011). Much of the final resulting evidence that is accessible from the Earth's surface is the same for both types of rifting. Obvious differences are due to the relative timing of rifting and magmatism.

was accompanied by topographic upwelling as another means to distinguish between active and passive rifting (Schmeling 2010) is currently unknown.

Merle (2011) presented an interesting perspective on the classification of continental rifts that differs from the traditional approach which distinguishes active and passive types. Instead his classification is based on the finding that four tectonic regimes (subduction zones, mantle plumes, transform faults and mountain chains) are responsible for the formation of all continental rifts. Accordingly, rifts should be dinstinguished on the basis of the tectonic regime that they are associated with. The terms 'active' and 'passive' merely describe processes that occur within these four rifting types, either individually or together. Merle (2011) also points out some important consequences of this classification. For instance, while upwelling of the asthenosphere is a characteristic feature of plume-related (active) rifts it can also occur in (passive) rifts that are related to other tectonic settings such as subduction- or mountain-chain-related. Consequently, many features of rifting and associated magmatism may not be diagnostic for a particular dynamic process, active or passive, and almost certainly not for a tectonic regime. As convincing as the evidence for the Ngaanyatjarra Rift as a tectonic expression of the Giles Event is in general, it seems premature to rule out categorically any involvement of mantle dynamics (or a mantle plume, respectively) over the entire suggested duration of the Giles Event including the Warakurna LIP.

The concept of Merle (2011) is appealing because it allows to unify the two seemingly conflicting models. Shorter-lived episode of mantle dynamics may have caused temporary peak magmatism around the time of emplacement of the layered and massive intrusions in the Musgrave Province as well as other members of the Warakurna LIP throughout central and western Australia. This provided the necessary heat over the spatial extend that was required during the Giles Event, that was otherwise largely controlled by localised plate dynamics. The migration of the melting anomaly (Smithies et al. 2015) does also not rule out a mantle plume because the latter are not always stationary (Griffiths and Richards 1989; White 2015b).

6.3 The prospectivity of the Giles Suite for orthomagmatic sulphide deposits

Wherever observed, sulphides are Cu-rich and occur exclusively as a late-stage intercumulus phase; the most common sulphide minerals are chalcopyrite and bornite. The sulphides crystallised late and after considerable magmatic fractionation. On the other hand, Ni is mostly contained in olivine and to a lesser extend in pyroxene, thus, no significant sulphide segregation occurred at depth because the sulphide phase would have scavenged Ni before olivine crystallisation begins. Consequently, the rocks from the Bell Rock Range, Latitude Hill and Wingellina Hills intrusions are lacking Ni-sulphides. Even though the assimilation of crustal S through contamination is not required to explain the observations the lithologies in all three intrusions show evidence for moderate crustal contamination.

The parental magma of the Bell Rock Range intrusion was derived from the EM

reservoir. While this may have been plume related or at least within the asthenosphere melting did not occur in great depth as indicated by the absence of residual garnet. This makes it possible that partial melting occurred still within the metasomatised SCLM. If this was the case, it would make it unlikely that the magma could produce a significant ore depost, because orthomagmatic sulphide deposits are commonly formed by melts from the deeper and hotter mantle (Arndt 2013). Further, there are no indications that the Bell Rock Range intrusion met the structural prerequisites for the formation of economic ore deposits. This is important because most Ni-Cu-platinum-group element (PGE) deposits are located in conduit settings (Maier et al. 2001). The Bell Rock Range intrusion is most likely only prospective for smaller PGE-rich deposits, but it is unprospective for large orthomagmatic Ni-Cu ore deposits.

Southwest of the main body of the Bell Rock Range run several ridges parallel to the strike of the intrusion. They consist of the lithology of the MPG and are likely members of the stratigraphic unit of the Alcurra Dolerite. The Alcurra Dolerite is an interesting exploration target because most of the currently known sulphide mineralisation in the Musgrave Province, including the Nebo-Babel Ni-Cu-PGE deposit, is hosted by members of this stratigraphic unit. The rocks of the MPG show trace element and isotope evidence for higher degrees of crustal contamination than for instance the main intrusion. It is uncertain whether they assimilated any crustal sulphur, however, with respect to these general conditions the parallel-running ridges may be the most prospective lithology in the area around the Bell Rock Range.

6.4 On the relevance of multivariate methods of compositional data analysis for igneous petrology, geochemistry and economic geology

Chapters 4 and 5 illustrate ways to apply multivariate classification and clustering methods to petrological and geochemical problems. Principal component analysis (PCA) is nowadays one of the more commonly used multivariate techniques used in petrology and geochemistry (e.g. Gorelikova et al. 2006; Grunsky 2010; Levitan et al. 2015; Scealy et al. 2015). Through the use of this method the 'natural' clustering within rocks from the previously labelled G1 and G2 suites was found and traced back to effects of crystal accumulation within the magma chamber.

Linear discriminant analysis (LDA) can be used for classification, but also provides an efficient way to select variables based on their importance for the outcome class separation. This is particularly interesting because LDA uses a very simple linear model that remains interpretable. However, the linearity of LDA can be a double-edged sword: if the dataset is rather small and potentially noisy, then LDA can provide a reasonable fit that generalises well. On the other hand, if the dataset is very rich and is to be used solely for classification purposes, then LDA might not provide the desired accuracy and nonlinear classifiers are to be preferred. In the case of the dataset from the Nebo-Babel Ni-Cu-PGE deposit (Seat et al. 2007; Seat 2008; Seat et al. 2009; Godel et al. 2011; Seat et al.

2011) the application of LDA was able to extract geochemical exploration vectors.

Hierarchical cluster analysis (HCA) is rarely used in geochemisty but is an efficient method for data clustering that is able to measure distances on compositional data. The main advantage of this method is that it is not required to specify the number of clusters, unlike other popular clustering methods such as k-means. In this study, a visual representation of the data clustering was obtained via a dendrogram, which was used to discover a cluster that represents a group of chemical elements that are most descriptive with respect to a 'real-world' petrogenetic process. This technique may have interesting applications in geochemistry, where data analysis is often carried out in an exploratory manner.

6.5 Suggestions for further research

There are many ways for future research projects to tie in with the results of this study and continue into different domains of the geological sciences as well as the modern field of data science applied to geochemistry.

One of the most important aspects in the research on the Giles Event is certainly the timing. The early phases of magmatic activity during which the layered and massive mafic-ultramafic intrusions formed are still poorly constrained. Only two direct ages have been published so far from the layered intrusions (Sun et al. 1996; Kirkland et al. 2011) and both ages only constrain the troctolitic-oivine gabbronoritic intrusions. The ages of intrusions with a significant ultramafic component such as the Wingellina Hills or Latitude Hill are only very crudely defined by field relationships. But in the light of the revised relationships between the different suites of intrusive bodies (chapter 4) it would be valuable to elucidate the relative timing. A difficulty could be the very low contents in Zr of the rocks and consequently the low prospect in obtaining enough suitable minerals (zircon or baddeleyite) for a geochronological study. Furthermore, the time differences between the emplacement of different suites could be well within the error of current analytical techniques.

Considering the difficulties with whole-rock geochemistry on cumulate rocks, it could prove fruitful to focus on mineral chemistry in future studies. Research of this kind would essentially build upon the work of Ballhaus and Berry (1991), Ballhaus (1993), Ballhaus and Glikson (1995), Glikson et al. (1996) and Wade (2006) but should focus on trace element and isotope analyses of mineral separates.

Although this is a petrological and geochemical study and not one of plate tectonics, the hypotheses in section 6.2 could provide some stating points for future research in the direction of the geodynamic setting surrounding the Musgrave Orogeny and the Giles Event. The results could then be applied to the rifting classification of Merle (2011). Of particular interest could also be the geological setting during the time period between the Musgrave Orogeny and the Giles Event because of the suspected connection between the two (e.g. Smithies et al. 2010, 2013; Howard et al. 2015; Smithies et al. 2015).

The use of predictive statistical modelling techiques (often called 'machine learning') have become widespread in many areas of science and engineering. Many such tech-

niques suffer from loss of performance if data are missing. Unfortunately, missing data are very common in geochemical dataset, be it because certain concentrations were below the limit of detection (LOD) or because some chemical elements were not assayed for. One useful application of predictive modelling is the imputation of such missing values. A future study could apply a variety of techniques to this problem on the same dataset and evaluate their respective performances. Unlike this study, which uses classification and clustering techniques, this would be a study using regression techniques in a wider sense. While such a study links with the present one from a methodological point of view, the efficient assessment of predictive modelling techniques for the purpose of imputation of missing data should be carried out on a large and rich dataset. Only then can missing values be artificially inserted and the predicted value be compared with the measured one. A datasets from an underexplored terrain such as the Musgrave Province might not be suitable for this purpose.

References

Aborigines Protection Board (1957). *Report of the Aborigines Protection Board for the year ended 30th June, 1957*. Adelaide. 12 pp.

Aitchison, J. (1982). The statistical analysis of compositional data. In: Journal of the Royal Statistical Society. Series B (Methodological) 44.2, pp. 139–177.

— (1984). The statistical analysis of geochemical compositions. In: Mathematical Geology 16.6, pp. 531–564. DOI: 10.1007/BF01029316.

— (1986). *The statistical analysis of compositional data*. Monographs on statistics and applied probability 25. London: Chapman & Hall. 416 pp.

Aitken, A. R. A. and Betts, P. G. (2008). High-resolution aeromagnetic data over central Australia assist Grenville-era (1300–1100 Ma) Rodinia reconstructions. In: Geophysical Research Letters 35.1, p. L01306. DOI: 10.1029/2007GL031563.

Aitken, A. R. A., Smithies, R. H., Dentith, M. C., Joly, A., Evans, S. and Howard, H. M. (2013). Magmatism-dominated intracontinental rifting in the Mesoproterozoic: the Ngaanyatjarra Rift, central Australia. In: Gondwana Research 24.3–4, pp. 886–901. DOI: 10.1016/j.gr.2012.10.003.

Amelin, Y., Li, C. and Naldrett, A. J. (1999). Geochronology of the Voisey's Bay intrusion, Labrador, Canada, by precise U-Pb dating of coexisting baddeleyite, zircon, and apatite. In: Lithos 47.1–2, pp. 33–51. DOI: 10.1016/S0024-4937(99)00006-7.

Anderson, D. L. (1995). Lithosphere, asthenosphere, and perisphere. In: Reviews of Geophysics 33.1, pp. 125–149. DOI: 10.1029/94RG02785.

— (1996). Enriched asthenosphere and depleted plumes. In: International Geology Review 38.1, pp. 1–21. DOI: 10.1080/00206819709465320.

Annen, C. (2011). Implications of incremental emplacement of magma bodies for magma differentiation, thermal aureole dimensions and plutonism-volcanism relationships. In: Tectonophysics 500.1–4, pp. 3–10. DOI: 10.1016/j.tecto.2009.04.010.

Annen, C., Blundy, J. D. and Sparks, R. S. J. (2006). The sources of granitic melt in Deep Hot Zones. In: Transactions of the Royal Society of Edinburgh. Earth Sciences 97.4, pp. 297–309. DOI: 10.1017/S0263593300001462.

Anthony, J. W., Bideaux, R. A., Bladh, K. W. and Nichols, M. C., eds. (n.d.). *Handbook of mineralogy*. Chantilly, VA: Mineralogical Society of America. URL: http://www.handbookofmineralogy.com/ (visited on 21/09/2015).

Arndt, N. (2013). The lithospheric mantle plays no active role in the formation of orthomagmatic ore deposits. In: Economic Geology 108.8, pp. 1953–1970. DOI: 10.2113/econgeo.108.8.1953.

Arndt, N. and Davaille, A. (2013). Episodic Earth evolution. In: Tectonophysics 609, pp. 661–674. DOI: 10.1016/j.tecto.2013.07.002.

Ashworth, J. R. and Chambers, A. D. (2000). Symplectic reaction in olivine and the controls of intergrowth spacing in symplectites. In: Journal of Petrology 41.2, pp. 285–304. DOI: 10.1093/petrology/41.2.285.

Bailey, D. K. (1987). Mantle metasomatism—perspective and prospect. In: Alkaline igneous rocks. Ed. by Fitton, J. G. and Upton, B. G. J. Special Publication 30. London: Geological Society, pp. 1–13. DOI: 10.1144/GSL.SP.1987.030.01.02.

Baker, P. M. and Waugh, R. S. (2005). The role of surface geochemistry in the discovery of the Babel and Nebo magmatic nickel-copper-PGE deposits. In: Geochemistry: Exploration, Environment, Analysis 5.3, pp. 195–200. DOI: 10.1144/1467-7873/03-032.

Ball, N. M. and Brunner, R. J. (2010). Data mining and machine learning in astronomy. In: International Journal of Modern Physics. D 19.7, pp. 1049–1106. DOI: 10.1142/S0218271810017160.

Ballhaus, C. G. (1993). *Petrology of the layered mafic/ultramafic Giles Complex, western Musgrave Block, Western Australia. Igneous stratigraphy, mineralogy and petrogenesis of the Jameson Range, Murray Range, Blackstone Range, Hinckley Range, Bell Rock Range, south Mt. West and Latitude Hill intrusions*. Record 1992/73. Canberra: Australian Geological Survey Organisation. 75 pp.

Ballhaus, C. G. and Glikson, A. Y. (1989). Magma mixing and intraplutonic quenching in the Wingellina Hills intrusion, Giles Complex, central Australia. In: Journal of Petrology 30.6, pp. 1443–1469. DOI: 10.1093/petrology/30.6.1443.

— (1995). The petrology of layered mafic-ultramafic intrusions of the Giles Complex, western Musgrave Block, Western Australia. In: AGSO Journal of Australian Geology and Geophysics 16.1–2, pp. 69–89.

Ballhaus, C. and Berry, R. F. (1991). Crystallization pressure and cooling history of the Giles layered igneous complex, central Australia. In: Journal of Petrology 32.1, pp. 1–28. DOI: 10.1093/petrology/32.1.1.

Barber, D. (2012). *Bayesian reasoning and machine learning*. Cambridge: Cambridge University Press. 720 pp.

Barnes, S. J. (1986). The effect of trapped liquid crystallization on cumulus mineral compositions in layered intrusions. In: Contributions to Mineralogy and Petrology 93.4, pp. 524–531. DOI: 10.1007/BF00371722.

Barton, M. and Gaans, C. van (1988). Formation of orthopyroxene-Fe-Ti oxide symplectites in Precambrian intrusives, Rogaland, southwestern Norway. In: American Mineralogist 73.1–2, pp. 1046–1059.

Barton, M., Sheets, J. M., Lee, W. E. and Gaans, C. van (1991). Occurrence of low-Ca clinopyroxene and the role of deformation in the formation of pyroxene-Fe-Ti oxide

symplectites. In: Contributions to Mineralogy and Petrology 108.1–2, pp. 181–195. DOI: 10.1007/BF00307337.

Basedow, H. (1905). Geological report on the country traversed by the South Australian government north-west prospecting expedition, 1903. In: Transactions of the Royal Society of South Australia 29, pp. 57–102.

Bell, K. (2001). Carbonatites: relationships to mantle-plume activity. In: Mantle plumes: their identification through time. Ed. by Ernst, R. E. and Buchan, K. L. Special Paper 352. Boulder, CO: Geological Society of America, pp. 267–290. DOI: 10.1130/0-8137-2352-3.267.

Bell, K. and Rukhlov, A. S. (2004). Carbonatites from the Kola Alkaline Province: origin, evolution and source characteristics. In: Phoscorites and carbonatites from mantle to mine. The key example of the Kola alkaline province. Ed. by Wall, F. and Zaitsev, A. N. Mineralogical Society Series 10. London: Mineralogical Society, pp. 433–468. DOI: 10.1180/MSS.10.13.

Betts, P. G. and Giles, D. (2006). The 1800–1100 Ma tectonic evolution of Australia. In: Precambrian Research 144.1–2, pp. 92–125. DOI: 10.1016/j.precamres.2005.11.006.

Bodorkos, S. and Wingate, M. T. D. (2008). *174 589: quartz syenite dyke, Amy Giles Hill. (Warakurna Supersuite, Musgrave Complex)*. Geochronology dataset 715. Perth: Geological Survey of Western Australia. 4 pp.

Boogaart, K. G. van den, Tolosana, R. and Bren, M. (2014). *compositions: compositional data analysis*. version 1.40-1. URL: https://cran.r-project.org/package=compositions (visited on 16/07/2015).

Boogaart, K. G. van den and Tolosana-Delgado, R. (2006). Compositional data analysis with 'R' and the package 'compositions'. In: Compositional data analysis in the geosciences: from theory to practice. Ed. by Buccianti, A., Mateu-Figueras, A. and Pawlowsky-Glahn, V. Special Publication 264. London: Geological Society, pp. 119–127. DOI: 10.1144/GSL.SP.2006.264.01.09.

— (2008). 'compositions': a unified R package to analyze compositional data. In: Computers & Geosciences 34.4, pp. 320–338. DOI: 10.1016/j.cageo.2006.11.017.

— (2013). *Analyzing compositional data with R*. Berlin, Heidelberg: Springer. 258 pp. DOI: 10.1007/978-3-642-36809-7.

Boudreau, A. (1999). Fluid fluxing of cumulates: the J-M reef and associated rocks of the Stillwater Complex, Montana. In: Journal of Petrology 40.5, pp. 755–772. DOI: 10.1093/petroj/40.5.755.

Braun, M., Hubay, K., Magyari, E., Veres, D., Papp, I. and Bálint, M. (2013). Using linear discriminant analysis (LDA) of bulk lake sediment geochemical data to reconstruct lateglacial climate changes in the South Carpathian Mountains. In: Quarternary International 293, pp. 114–122. DOI: 10.1016/j.quaint.2012.03.025.

Bryan, S. E. and Ernst, R. E. (2008). Revised definition of large igneous provinces (LIPs). In: Earth-Science Reviews 86.1–4, pp. 175–202. DOI: 10.1016/j.earscirev.2007.08.008.

Buccianti, A. and Grunsky, E. (2014). Compositional data analysis in geochemistry: are we sure to see what really occurs during natural processes? In: Journal of Geochemical Exploration 141, pp. 1–5. DOI: 10.1016/j.gexplo.2014.03.022.

Bucher, K. and Grapes, R. (2011). *Petrogenesis of metamorphic rocks*. 8th ed. Berlin, Heidelberg: Springer. 428 pp. DOI: 10.1007/978-3-540-74169-5.

Burnham, O. M., Keays, R. R. and Lesher, C. M. (1996). *Application of PGE geochemistry to exploration for komatiite-hosted Ni sulphide deposits in Canada*. Annual report to CAMIRO. Sudbury, ON: Laurentian University. 32 pp.

Burnham, O. M., Keays, R. R., Lesher, C. M. and Hulbert, L. (1998). *Application of PGE geochemistry to exploration for Ni sulphide deposits in Canada*. Final report for CAMIRO project 94E04. Sudbury, ON: Laurentian University. 108 pp.

Camacho, A. (1997). An isotopic study of deep-crustal orogenic processes: Musgrave Block, central Australia. PhD thesis. Canberra: Australian National University.

Camacho, A. and Fanning, C. M. (1995). Some isotopic constraints on the evolution of the granulite and upper amphibolite facies terranes in the eastern Musgrave Block, central Australia. In: Precambrian Research 71.1–4, pp. 155–181. DOI: 10.1016/0301-9268(94)00060-5.

Campbell, I. H. (2007). Testing the plume theory. In: Chemical Geology 241.3–4, pp. 153–176. DOI: 10.1016/j.chemgeo.2007.01.024.

Campbell, I. H. and Naldrett, A. J. (1979). The influence of slicate:sulfide ratios on the geochemistry of magmatic sulfides. In: Economic Geology 74.6, pp. 1503–1506. DOI: 10.2113/gsecongeo.74.6.1503.

Campbell, I. H. and O'Neill, H. S. C. (2012). Evindence against a chondritic Earth. In: Nature 483.7391, pp. 553–558. DOI: 10.1038/nature10901.

Candia, M. A. F., Mazzuchelli, M. and Siena, F. (1989). Sub-solidus reactions and corona structures in the Niquelândia layered complex (central Goiás, Brazil). In: Mineralogy and Petrology 40.1, pp. 17–37. DOI: 10.1007/BF01162467.

Caro, G. and Bourdon, B. (2010). Non-chondritic Sm/Nd ratio in the terrestrial planets: consequences for the geochemical evolution of the mantle-crust system. In: Geochimica et Cosmochimica Acta 74.11, pp. 3333–3349. DOI: 10.1016/j.gca.2010.02.025.

Cassini Resources Limited (2014). *Annual report*. Perth.

Cavazza, W. (1989). Sedimentation pattern of a rift-filling unit, Tesuque Formation (Miocene), Espanola Basin, Rio Grande Rift, New Mexico. In: Journal of Sedimentary Research 59.2, pp. 287–296.

Cawthorn, R. G. (2012). Multiple sills or a layered intrusion? Time to decide. In: South African Journal of Geology 115.3, pp. 283–290. DOI: 10.2113/gssajg.115.3.283.

— (2013). The Residual or Roof Zone of the Bushveld Complex, South Africa. In: Journal of Petrology 54.9, pp. 1875–1900. DOI: 10.1093/petrology/egt034.

Chayes, F. (1960). On correlation between variables of constant sum. In: Journal of Geophysical Research 65.12, pp. 4185–4193. DOI: 10.1029/JZ065i012p04185.

— (1975). A priori and experimental approximation of simple ratio correlations. In: Concepts in Geostatistics. Ed. by McCammon, R. B. Springer Study Edition. Berlin, Heidelberg: Springer, pp. 106–137. DOI: 10.1007/978-3-642-85976-2_5.

Cherkassky, V. and Mulier, P. (2007). *Learning from data. Concepts, theory, and methods*. 2nd ed. Hoboken, NJ: John Wiley & Sons. 538 pp. DOI: 10.1002/9780470140529.

Clarke, G. L. (1992). *Field relationships and tectonic history of the Hinckley Gabbro felsic to mafic granulites and granitoids, West Hinckley Range and Champ de Mars areas, Tomkinson Ranges, Musgrave Block, WA*. Record 1992/33. Canberra: Bureau of Mineral Resources, Geology and Geophysics. 48 pp.

Clarke, G. L. and Powell, R. (1995). Decompressional coronas and symplectites in granulites of the Musgrave Complex, central Australia. In: Journal of Metamorphic Geology 9.4, pp. 441–450. DOI: 10.1111/j.1525-1314.1991.tb00538.x.

Clarke, G. L., Sun, S.-S. and White, R. W. (1995). Grenville age belts and associated older terranes in Australia and Antarctica. In: AGSO Journal of Australian Geology and Geophysics 16.1–2, pp. 25–39.

Close, D. F., Edgoose, C. J. and Scrimgeour, I. R. (2003a). *Hull and Bloods Range, Northern Territory. Sheets 4748, 4848*. 1:100 000 Geological Map Series Explanatory Notes. Darwin: Northern Territory Geological Survey. 46 pp.

Close, D. F., Scrimgeour, I. R. and Edgoose, C. J. (2003b). *Compilation of geochronological data from the northwestern Musgrave Block, Northern Territory*. Technical note 2003-005. Darwin: Northern Territory Geological Survey. 39 pp.

Corry, C. E. (1988). *Laccoliths; mechanics of emplacement and growth*. Special Paper 220. Boulder, CO: Geological Society of America. 114 pp. DOI: 10.1130/SPE220.

Cruden, A. R. (1998). On the emplacement of tabular granites. In: Journal of the Geological Society 155.5, pp. 853–862. DOI: 10.1144/gsjgs.155.5.0853.

Cruden, A. and McCaffrey, K. (2002). Different scaling laws for sills, laccoliths and plutons: mechanical thresholds on roof lifting and floor depression. In: First international workshop on the physical geology of subvolcanic systems. Laccoliths, sills, and dykes. (Freiberg, Germany), pp. 15–17.

— (2006). Dimensional scaling relationships of tabular igneous intrusions and their implications for a size, depth and compositionally dependent spectrum of emplacement processes in the crust. In: Eos Transactions American Geophysical Union. Fall Meeting Supplement. (San Francisco). Vol. 87. 52. Washington, D.C.: American Geophysical Union, V12B–06.

Daniels, J. L. (1967). Subdivision of the Giles Complex, central Australia. In: Annual report for the year 1966. Perth: Geological Survey of Western Australia, pp. 58–62.

— (1969). *Explanatory notes on the Bentley 1:250 000 geological sheet, W.A*. Record 1969/13. Perth: Geological Survey of Western Australia. 21 pp.

— (1974). *The geology of the Blackstone region, Western Australia*. Bulletin 123. Perth: Geological Survey of Western Australia. 255 pp.

Daniels, J. L., Horwitz, R. C., Kriewaldt, M. J. B., Doepel, J. J. G. and Farbridge, R. A. (1971). *Cooper, WA sheet SG 52-10*. 1:250 000 Geological Series map. Perth: Geological Survey of Western Australia.

DePaolo, D. J. (1981). Neodymium isotopes in the Colorado Front Range and crust-mantle evolution in the Proterozoic. In: Nature 291.5812, pp. 193–196. DOI: 10.1038/291193a0.

DePaolo, D. J. (1988). *Neodymium isotope geochemistry. An introduction*. Minerals and Rocks 20. Berlin, Heidelberg: Springer. 187 pp. DOI: 10.1007/978-3-642-48916-7.

Doutsos, T. and Piper, D. J. W. (1990). Listric faulting, sedimentation, and morphological evolution of the Quaternary eastern Corinth rift, Greece: first stages of continental rifting. In: Geological Society of America Bulletin 102.6, pp. 812–829. DOI: 10.1130/0016-7606(1990)102<0812:LFSAME>2.3.CO;2.

Ebinger, C. J. and Sleep, N. H. (1998). Cenozoic magmatism throughout east Africa resulting from impact of a single plume. In: Nature 395.6704, pp. 788–791. DOI: 10.1038/27417.

Edgoose, C. J., Camacho, A., Wakelin-King, G. A. and Simons, B. A. (1993). *Kulgera, sheet SG 53-5*. 1:250 000 Geological Series explanatory notes. Darwin: Northern Territory Geological Survey. 46 pp.

Edgoose, C. J., Scrimgeour, I. R. and Close, D. F. (2004). *Geology of the Musgrave Block, Northern Territory*. Report 15. Darwin: Northern Territory Geological Survey. 44 pp.

Egorova, V. and Latypov, R. (2012). Processes operating during the initial stage of magma chamber evolution: insights from the marginal reversal of the Imandra layered intrusion, Russia. In: Journal of Petrology 53.1, pp. 3–26. DOI: 10.1093/petrology/egr054.

Egozcue, J. J., Pawlowsky-Glahn, V., Mateu-Figueras, G. and Barceló-Vidal, C. (2003). Isometric logratio transformations for compositional data analysis. In: Mathematical Geology 35.3, pp. 279–300. DOI: 10.1023/A:1023818214614.

Eisele, J., Sharma, M., Galer, S. J. G., Blichert-Toft, J., Devey, C. W. and Hofmann, A. W. (2002). The role of sediment recycling in EM-1 inferred from Os, Pb, Hf, Nd, Sr isotope and trace element systematics of the Pitcairn hotspot. In: Earth and Planetary Science Letters 196.3–4, pp. 197–212. DOI: 10.1016/S0012-821X(01)00601-X.

Ernst, R. E. and Bell, K. (2010). Large igneous provinces (LIPs) and carbonatites. In: Mineralogy and Petrology 98.1–4, pp. 55–76. DOI: 10.1007/s00710-009-0074-1.

Ernst, R. E. and Buchan, K. L. (2003). Recognizing mantle plumes in the geological record. In: Annual Reviews of Earth and Planetary Sciences 31.1, pp. 469–523. DOI: 10.1146/annurev.earth.31.100901.145500.

Ernst, R. E. and Jowitt, S. M. (2013). Large igneous provinces (LIPs) and Metallogeny. In: Tectonics, metallogeny, and discovery: the North American Cordillera and similar accretionary settings. Ed. by Colpron, M., Bissig, T., Rusk, B. G. and Thompson, J. F. H. Special Publication 17. Littleton, CO: Society of Economic Geologists. Chap. 2, pp. 17–51.

Everitt, B. S., Landau, S., Leese, M. and Stahl, D. (2011). *Cluster analysis*. 5th ed. Chichester, West Sussex: John Wiley & Sons. 330 pp. DOI: 10.1002/9780470977811.

Everitt, B. and Hothorn, T. (2011). *An introduction to applied multivariate analysis with R*. New York: Springer. 273 pp. DOI: 10.1007/978-1-4419-9650-3.

Evins, P. M., Howard, H. M., Smithies, R. H. and Maier, W. D. (2010a). *Finlayson, WA sheet 4446*. 1:100 000 Geological Series map. Perth: Geological Survey of Western Australia.

Evins, P. M., Kirkland, C. L., Wingate, M. T. D., Smithies, R. H., Howard, H. M. and Bodorkos, S. (2012). *Provenance of the 1340–1270 Ma Ramarama Basin in the west Musgrave*

Province, central Australia. Report 116. Perth: Geological Survey of Western Australia. 39 pp.

Evins, P. M., Smithies, R. H., Howard, H. M., Kirkland, C. L., Wingate, M. T. D. and Bodorkos, S. (2010b). Devil in the detail; the 1150–1000 Ma magmatic and structural evolution of the Ngaanyatjarra Rift, west Musgrave Province, central Australia. In: Precambrian Research 183.3, pp. 572–588. DOI: 10.1016/j.precamres.2010.02.011.

— (2010c). *Redefining the Giles Event within the setting of the 1120–1020 Ma Ngaanyatjarra Rift, west Musgrave Province, central Australia*. Record 2010/6. Perth: Geological Survey of Western Australia. 36 pp.

Evins, P., Smithies, R. H., Howard, H. M., Werner, M. and Maier, W. D. (2011). *Cooper, WA sheet 4445*. 1:100 000 Geological Series map. Perth: Geological Survey of Western Australia.

Farley, K. A., Natland, J. H. and Craig, H. (1992). Binary mixing of enriched and undegassed (primitive?) mantle components (He, Sr, Nd, Pb) in Samoan lavas. In: Earth and Planetary Science Letters 111.1, pp. 183–199. DOI: 10.1016/0012-821X(92)90178-X.

Farmer, G. L. (2014). Continental basaltic rocks. In: The crust. Ed. by Holland, H. D., Turekian, K. K. and Rudnick, R. L. 2nd ed. Treatise on geochemistry 4. Oxford: Elsevier. Chap. 4.3, pp. 75–110. DOI: 10.1016/B978-0-08-095975-7.00303-X.

Faure, G. and Mensing, T. M. (2005). *Isotopes. Principles and applications*. 3rd ed. Hoboken, New Jersey: John Wiley & Sons. 897 pp.

Filzmoser, P. and Hron, K. (2009). Correlation analysis for compositional data. In: Mathematical Geosciences 41.8, pp. 905–919. DOI: 10.1007/s11004-008-9196-y.

Fisher, R. A. (1936). The use of multiple measurements in taxonomic problems. In: Annals of Eugenics 7.2, pp. 179–188. DOI: 10.1111/j.1469-1809.1936.tb02137.x.

Fitton, J. G. (2007). The OIB paradox. In: Plates, plumes and planetary processes. Ed. by Foulger, G. R. and Jurdy, D. M. Special Paper 430. Boulder, CO: Geological Society of America, pp. 387–412. DOI: 10.1130/2007.2430(20).

Fitton, J. G., James, D. and Leeman, W. P. (1991). Basic magmatism associated with Late Cenozoic extension in the western United States: compositional variations in space and time. In: Journal of Geophysical Research 96.B8, pp. 13693–13711. DOI: 10.1029/91JB00372.

Fitton, J. G., Saunders, A. D., Norry, M. J., Hardarson, B. S. and Taylor, R. N. (1997). Thermal and chemical structure of the Iceland plume. In: Earth and Planetary Science Letters 153.3–4, pp. 197–208. DOI: 10.1016/S0012-821X(97)00170-2.

Forte, A. M., Quéré, S., Moucha, R., Simmons, N. A., Grand, S. P., Mitrovica, J. X. and Rowley, D. B. (2010). Joint seismic-geodynamic-mineral physical modelling of African geodynamics: a reconciliation of deep-mantle convection with surface geophysical constraints. In: Earth and Planetary Science Letters 295.3–4, pp. 329–341. DOI: 10.1016/j.epsl.2010.03.017.

Gabriel, K. R. (1971). The biplot graphic display of matrices with application to principal component analysis. In: Biometrika 58.3, pp. 453–467. DOI: 10.1093/biomet/58.3.453.

Gazel, E., Plank, T., Forsyth, D. W., Bendersky, C., Lee, C.-T. A. and Hauri, E. H. (2012). Lithosphere versus asthenosphere mantle sources at the Big Pine Volcanic Field, California. In: Geochemistry, Geophysics, Geosystems 13.6, Q0AK06. DOI: 10.1029/2012GC004060.

Geological Survey of Western Australia (2011). *West Musgrave, 2011 update*. Geological Information Series. URL: http://dmpbookshop.eruditetechnologies.com.au/product/west-musgrave-2011-update.do (visited on 25/02/2015).

Giles, D., Betts, P. G. and Lister, G. S. (2004). 1.8–1.5-Ga links between the North and South Australian Cratons and the Early–Middle Proterozoic configuration of Australia. In: Tectonophysics 380.1–2, pp. 27–41. DOI: 10.1016/j.tecto.2003.11.010.

Giles, E. (1889). *Australia twice traversed: the romance of exploration, being a narrative compiled from the journals of five exploring expeditions into and through central South Australia, and Western Australia, from 1872 to 1876*. London: Sampson Low, Marston, Searle & Rivington. 320 pp.

Glikson, A. Y., Ballhaus, C. G., Clarke, G. L., Sheraton, J. W., Stewart, A. J. and Sun, S.-S. (1995). Geological framework and crustal evolution of the Giles mafic-ultramafic complex and environs, western Musgrave Block, central Australia. In: AGSO Journal of Australian Geology and Geophysics 16.1–2, pp. 41–67.

Glikson, A. Y., Stewart, A. J., Ballhaus, C. G., Clarke, G. L., Feeken, E. H. J., Leven, J. H., Sheraton, J. W. and Sun, S.-S. (1996). *Geology of the western Musgrave Block, central Australia, with particular reference to the mafic-ultramafic Giles Complex*. Bulletin 239. Canberra: Australian Geological Survey Organisation. 206 pp.

Godel, B. (2008). *Fingerprinting prospective magma suites at the Nebo-Babel Ni-Cu-PGE prospect (west Musgrave block)*. unpublished report. Perth: Centre for Exploration Targeting, University of Western Australia. 205 pp.

Godel, B., Seat, Z., Maier, W. D. and Barnes, S.-J. (2011). The Nebo-Babel Ni-Cu-PGE sulfide deposit (west Musgrave Block, Australia): pt. 2. constraints on parental magma and processes, with implications for mineral exploration. In: Economic Geology 106.4, pp. 557–584. DOI: 10.2113/econgeo.106.4.557.

Goldschmidt, V. M. (1937). The principles of distribution of chemical elements in minerals and rocks. The seventh Hugo Müller Lecture, delivered before the Chemical Society on March 17th, 1937. In: Journal of the Chemical Society, pp. 655–673. DOI: 10.1039/JR9370000655.

Goldstein, S. L., O'Nions, R. K. and Hamilton, P. J. (1984). A Sm-Nd isotopic study of atmospheric dusts and particulates from major river systems. In: Earth and Planetary Science Letters 70.2, pp. 221–236. DOI: 10.1016/0012-821X(84)90007-4.

Goode, A. (2002). *The Western Musgrave Block—Australia*. District overview. Melbourne: Data Metallogenica. 42 pp.

Goode, A. D. T. (1974). Oxidation of natural olivines. In: Nature 248.5448, pp. 500–501. DOI: 10.1038/248500a0.

— (1975). A transgressive picrite suite from the western Musgrave block, central Australia. In: Journal of the Geological Society of Australia 22.2, pp. 187–194. DOI: 10.1080/00167617508728887.

— (1977a). High temperature, high strain rate deformation in the lower crustal Kalka Intrusion, central Australia. In: Contributions to Mineralogy and Petrology 66.2, pp. 137–148. DOI: 10.1007/BF00372152.
— (1977b). Intercumulus igneous layering in the Kalka layered intrusion, central Australia. In: Geological Magazine 114.3, pp. 215–218. DOI: 10.1017/S0016756800044794.
Goode, A. D. T. and Moore, A. C. (1975). High pressure crystallization of the Ewarara, Kalka and Gosse Pile intrusions, Giles Complex, central Australia. In: Contributions to Mineralogy and Petrology 51.2, pp. 77–97. DOI: 10.1007/BF00403750.
Gorczyk, W., Smithies, H., Korhonen, F., Howard, H. and Quentin De Gromard, R. (2014). Ultra-hot Mesoproterozoic evolution of intracontinental central Australia. In: Geoscience Frontiers in press. DOI: 10.1016/j.gsf.2014.03.001.
Gorelikova, N., Tolosana-Delgado, R., Pawlowsky-Glahn, V., Khanchuk, A. and Gonevchuk, V. (2006). Discriminating geodynamical regimes of tin ore formation using trace element composition of cassiterite: the Sikhote'Alin case (Far Eastern Russia). In: Compositional data analysis in the geosciences: from theory to practice. Ed. by Buccianti, A., Mateu-Figueras, A. and Pawlowsky-Glahn, V. 264. London: Geological Society, pp. 43–57. DOI: 10.1144/GSL.SP.2006.264.01.04.
Gosse, W. C. (1874). *W. C. Gosse's explorations, 1873. Report and diary of Mr. W. C. Gosse's central and western exploring expedition, 1873.* Parliamentary paper 48. Adelaide: Parliament of South Australia. 23 pp. URL: http://gutenberg.net.au/ebooks13/1306451h.html (visited on 04/12/2014). Digital edition published in 2013 by the Project Gutenberg Australia.
Gray, C. M. (1971). Strontium isotope studies on granulites. PhD thesis. Canberra: Australian National University. 242 pp.
— (1978). Geochronology of granulite-facies gneisses in the western Musgrave Block, central Australia. In: Journal of the Geological Society of Australia 25.7–8, pp. 403–414. DOI: 10.1080/00167617808729050.
Gray, C. M. and Compston, W. (1978). A rubidium-strontium chronology of the metamorphism and prehistory of central Australian granulites. In: Geochimica et Cosmochimica Acta 42.11, pp. 1735–1747. DOI: 10.1016/0016-7037(78)90259-4.
Gregory, C. J., Buick, I. S., Hermann, J. and Rubatto, D. (2009). Mineral-scale trace element and U-Th-Pb age constraints on metamorphism and melting during the Petermann Orogeny (central Australia). In: Journal of Petrology 50.2, pp. 251–287. DOI: 10.1093/petrology/egn077.
Griffiths, R. W. and Richards, M. A. (1989). The adjustment of mantle plumes to changes in plate motion. In: Geophysical Research Letters 16.5, pp. 437–440. DOI: 10.1029/GL016i005p00437.
Grunsky, E. C. (2010). The interpretation of geochemical survey data. In: Geochemistry: Exploration, Environment, Analysis 10.1, pp. 27–74. DOI: 10.1144/1467-7873/09-210.
Hanan, B. B. and Graham, D. W. (1996). Lead and helium isotope evidence from oceanic basalts for a common deep source of mantle plumes. In: Science 272.5264, pp. 991–995. DOI: 10.1126/science.272.5264.991.

Härdle, W. K. and Simar, L. (2015). *Applied multivariate statistical analysis*. 4th ed. Berlin, Heidelberg: Springer. 580 pp. DOI: 10.1007/978-3-662-45171-7.

Hart, S. R. (1988). Heterogeneous mantle domains: signatures, genesis and mixing chronologies. In: Earth and Planetary Science Letters 90.3, pp. 273–296. DOI: 10.1016/0012-821X(88)90131-8.

Hart, S. R., Hauri, E. H., Oschmann, L. A. and Whitehead, J. A. (1992). Mantle plumes and entrainment: isotopic evidence. In: Science 256.5056, pp. 517–520. DOI: 10.1126/science.256.5056.517.

Hastie, T., Tibshirani, R. and Friedman, J. (2009). *The elements of statistical learning. Data mining, inference, and prediction*. 2nd ed. New York, NY: Springer. 745 pp. DOI: 10.1007/978-0-387-84858-7.

Hauri, E. H., Whitehead, J. A. and Hart, S. R. (1994). Fluid dynamic and geochemical aspects of entrainment in mantle plumes. In: Journal of Geophysical Research. Solid Earth 99.B12, pp. 24275–24300. DOI: 10.1029/94JB01257.

Hofmann, A. W. (2014). Sampling mantle heterogeneity through oceanic basalts: isotopes and trace elements. In: The mantle and core. Ed. by Holland, H. D., Turekian, K. K. and Carlson, R. W. 2nd ed. Treatise on geochemistry 3. Oxford: Elsevier. Chap. 3.3, pp. 67–101. DOI: 10.1016/B978-0-08-095975-7.00203-5.

Holness, M. B., Nielsen, T. F. D. and Tegner, C. (2007a). Textural maturity of cumulates: a record of chamber filling, liquidus assemblage, cooling rate and large-scale convection in mafic layered intrusions. In: Journal of Petrology 48.1, pp. 141–157. DOI: 10.1093/petrology/egl057.

Holness, M. B., Stripp, G., Humphreys, M. C. S., Veksler, I. V., Nielsen, T. F. D. and Tegner, C. (2011). Silicate liquid immiscibility within the crystal mush: late-stage magmatic microstructures in the Skaergaard intrusion, East Greenland. In: Journal of Petrology 52.1, pp. 175–222. DOI: 10.1093/petrology/egq077.

Holness, M. B., Tegner, C., Nielsen, T. F. D., Stripp, G. and Morse, S. A. (2007b). A textural record of solidification and cooling in the Skaergaard intrusion, East Greenland. In: Journal of Petrology 48.12, pp. 2359–2377. DOI: 10.1093/petrology/egm064.

Holwell, D. A. and Keays, R. R. (2014). The formation of low-volume, high-tenor magmatic PGE-Au sulfide mineralization in closed systems: evidence from precious and base metal geochemistry of the Platinova Reef, Skaergaard Intrusion, East Greenland. In: Economic Geology 109.2, pp. 387–406. DOI: 10.2113/econgeo.109.2.387.

Hotelling, H. (1933). Analysis of a complex of statistical variables into principal components. In: Journal of Educational Psychology 24.6, pp. 417–441. DOI: 10.1037/h0071325.

Howard, H. M., Smithies, R. H., Evins, P. M., Pirajno, F. and Skwarnecki, M. S. (2009a). *Bates, WA sheet 4646, 2nd edition*. 1:100 000 Geological Series map. Perth: Geological Survey of Western Australia.

— (2009b). *Bell Rock, WA sheet 4645, 2nd edition*. 1:100 000 Geological Series map. Perth: Geological Survey of Western Australia.

Howard, H. M., Smithies, R. H., Evins, P., Kirkland, C. L., Werner, M., Wingate, M. T. D. and Pirajno, F. (2011a). *Explanatory notes for the west Musgrave Province*. Perth: Geological Survey of Western Australia. 349 pp.

Howard, H. M., Smithies, R. H., Kirkland, C. L., Evins, P. M. and Wingate, M. T. D. (2009c). *Age and geochemistry of the Alcurra Suite and implications for orthomagmatic mineralization during the Giles Event*. Record 2009/16. Perth: Geological Survey of Western Australia. 16 pp.

Howard, H. M., Smithies, R. H., Kirkland, C. L., Kelsey, D. E., Aitken, A., Wingate, M. T. D., Quentin de Gromard, R., Spaggiari, C. V. and Maier, W. D. (2015). The burning heart—The Proterozoic geology and geological evolution of the west Musgrave Region, central Australia. In: Gondwana Research 27.1, pp. 64–94. DOI: 10.1016/j.gr.2014.09.001.

Howard, H. M., Smithies, R. H. and Pirajno, F. (2007a). Geochemical and Nd isotopic signatures of mafic dykes in the western Musgrave Complex. In: Annual Review 2005–06. Perth: Geological Survey of Western Australia, pp. 64–71.

Howard, H. M., Smithies, R. H., Pirajno, F. and Skwarnecki, M. S. (2006). *Bates, WA sheet 4646*. 1:100 000 Geological Series map. Perth: Geological Survey of Western Australia.

— (2007b). *Bell Rock, WA sheet 4645*. 1:100 000 Geological Series map. Perth: Geological Survey of Western Australia.

Howard, H. M., Werner, M., Smithies, R. H., Evins, P., Kirkland, C. L., Kelsey, D. E., Hand, M., Collins, A. S., Pirajno, F., Wingate, M. T. D., Maier, W. D. and Raimondo, T. (2011b). *The geology of the west Musgrave Province and the Bentley Supergroup—a field guide*. Record 2011/4. Perth: Geological Survey of Western Australia. 116 pp.

Huber, W., Carey, V. J., Gentleman, R., Anders, S., Carlson, M., Carvalho, B. S., Bravo, H. C., Davis, S., Gatto, L., Girke, T., Gottardo, R., Hahne, F., Hansen, K. D., Irizarry, R. A., Lawrence, M., Love, M. I., MacDonald, J., Obenchain, V., Oleś, A. K., Pagès, H., Reyes, A., Shannon, P., Smyth, G. K., Tenenbaum, D., Waldron, L. and Morgan, M. (2015). Orchestrating high-throughput genomic analysis with Bioconductor. In: Nature Methods 12.2, pp. 115–121. DOI: 10.1038/nmeth.3252.

Humphreys, M. C. S. (2011). Silicate liquid immiscibility within the crystal mush: evidence from Ti in plagioclase from the Skaergaard intrusion. In: Journal of Petrology 52.1, pp. 147–174. DOI: 10.1093/petrology/egq076.

Ihlenfeld, C. and Keays, R. R. (2011). Crustal contamination and PGE mineralization in the Platreef, Bushveld Complex, South Africa: evidence for multiple contamination events and transport of magmatic sulfides. In: Mineralium Deposita 46.7, pp. 813–832. DOI: 10.1007/s00126-011-0340-0.

Jain, A. K., Murty, M. N. and Flynn, P. J. (1999). Data clustering: a review. In: ACM Computing Surveys 31.3, pp. 264–323. DOI: 10.1145/331499.331504.

Jowitt, S. M. and Ernst, R. E. (2013). Geochemical assessment of the metallogenic potential of Proterozoic LIPs of Canada. In: Lithos 174, pp. 291–307. DOI: 10.1016/j.lithos.2012.03.026.

Jugo, P. J. (2009). Sulfur content at sulfide saturation in oxidized magmas. In: Geology 37.5, pp. 415–418. DOI: 10.1130/G25527A.1.

Keays, R. R. (1995). The role of komatiitic and picritic magmatism and S-saturation in the formation of ore deposits. In: Lithos 34.1–3, pp. 1–18. DOI: 10.1016/0024-4937(95)90003-9.

Keays, R. R. and Lightfoot, P. C. (2007). Siderophile and chalcophile metal variations in Tertiary picrites and basalts from West Greenland with implications for the sulphide saturation history of continental flood basalt magmas. In: Mineralium Deposita 42.4, pp. 319–336. DOI: 10.1007/s00126-006-0112-4.

— (2010). Crustal sulfur is required to form magmatic Ni-Cu sulfide deposits: evidence from chalcophile element signatures of Siberian and Deccan Trap basalts. In: Mineralium Deposita 45.3, pp. 241–257. DOI: 10.1007/s00126-009-0271-1.

Kempton, P. D., Fitton, J. G., Hawkesworth, C. J. and Ormerod, D. S. (1991). Isotopic and trace element constraints on the composition and evolution of the lithosphere beneath the southwestern United States. In: Journal of Geophysical Research 96.B8, pp. 13713–13735. DOI: 10.1029/91JB00373.

Kirkland, C. L., Smithies, R. H., Woodhouse, A. J., Howard, H. M., Wingate, M. T. D., Belousova, E. A., Cliff, J. B., Murphy, R. C. and Spaggiari, C. V. (2013). Constraints and deception in the isotopic record; the crustal evolution of the west Musgrave Province, central Australia. In: Gondwana Research 23.2, pp. 759–781. DOI: 10.1016/j.gr.2012.06.001.

Kirkland, C. L., Smithies, R. H., Woodhouse, A., Howard, H. M., Wingate, M. T. D., Belousova, E. A., Cliff, J. B., Murphy, R. C. and Spaggiari, C. V. (2012a). *A multi-isotopic approach to the crustal evolution of the west Musgrave Province, central Australia*. Report 115. Perth: Geological Survey of Western Australia. 47 pp.

Kirkland, C. L., Wingate, M. T. D. and Bodorkos, S. (2008a). *174 761: porphyritic granite dyke, Charnockite Flats. (Warakurna Supersuite, Musgrave Complex)*. Geochronology dataset 721. Perth: Geological Survey of Western Australia. 4 pp.

— (2008b). *185 509: leucogranite, Mount Aloysius. (Warakurna Supersuite, Musgrave Complex)*. Geochronology dataset 725. Perth: Geological Survey of Western Australia. 4 pp.

Kirkland, C. L., Wingate, M. T. D., Howard, H. M., Smithies, R. H. and Pirajno, F. (2012b). *183 847: syenite, Skirmish Hill. (Kunmarnara Group, Bentley Supergroup, Musgrave Province)*. Geochronology Record 1059. Perth: Geological Survey of Western Australia. 5 pp.

Kirkland, C. L., Wingate, M. T. D. and Smithies, R. H. (2011). *194 762: leucogabbro, Mount Finlayson. (Warakurna Supersuite, Musgrave Province)*. Geochronology Record 966. Perth: Geological Survey of Western Australia. 4 pp.

Klein, E. M. and Langmuir, C. H. (1987). Global correlations of ocean ridge basalt chemistry with axial depth and crustal thickness. In: Journal of Geophysical Research. Solid Earth 92.B8, pp. 8089–8115. DOI: 10.1029/JB092iB08p08089.

Kononenko, I. (2001). Machine learning for medical diagnosis: history, state of the art and perspective. In: Artificial Intelligence in Medicine 23.1, pp. 89–109. DOI: 10.1016/S0933-3657(01)00077-X.

Köykkä, J. (2011). Precambrian alluvial fan and braidplain sedimentation patterns: example from the Mesoproterozoic Rjukan Rift Basin, southern Norway. In: Sedimentary Geology 234.1–4, pp. 89–108. DOI: 10.1016/j.sedgeo.2010.12.004.

Kuhn, M. and Johnson, K., eds. (2013). *Applied predictive modeling*. New York, NY: Springer. 600 pp. DOI: 10.1007/978-1-4614-6849-3.

Laceby, J. P., McMahon, J., Evrard, O. and Olley, J. (2015). A comparison of geological and statistical approaches to element selection for sediment fingerprinting. In: Journal of Soils and Sediments 15.10, pp. 2117–2131. DOI: 10.1007/s11368-015-1111-9.

Lambert, D. D., Foster, J. G., Frick, L. R., Li, C. and Naldrett, A. J. (1999). Re-Os isotope systematics of the Voisey's Bay Ni-Cu-Co magmatic ore system, Labrador, Canada. In: Lithos 47.1–2, pp. 69–88. DOI: 16/S0024-4937(99)00008-0.

Lambert, D. D., Frick, L. R., Foster, J. G., Li, C. and Naldrett, A. J. (2000). Re-Os isotope systematics of the Voisey's Bay Ni-Cu-Co magmatic sulfide system, Labrador, Canada: II. Implications for parental magma chemistry, ore genesis, and metal redistribution. In: Economic Geology 95.4, pp. 867–888. DOI: 10.2113/gsecongeo.95.4.867.

Lance, G. N. and Williams, W. T. (1967). A general theory of classificatory sorting strategies. 1. Hierarchical systems. In: The Computer Journal 9.4, pp. 373–380. DOI: 10.1093/comjnl/9.4.373.

Lassiter, J. C. and DePaolo, D. J. (1997). Plume/lithosphere interaction in the generation of continental and oceanic flood basalts: chemical and isotopic constraints. In: Large igneous provinces. Continental, oceanic, and planetary flood volcanism. Ed. by Mahoney, J. J. and Coffin, M. F. Geophysical Monograph 100. Washington, D.C.: American Geophysical Union, pp. 335–355. DOI: 10.1029/GM100p0335.

Layton-Mathews, D., Lesher, C. M., Burnham, O. M., Hulbert, L., Peck, D. C., Golightly, J. P. and Keays, R. R. (2010). Exploration for komatiite-associated Ni-Cu-(PGE) mineralization in the Thompson Nickel Belt, Manitoba. In: The Challenge of Finding New Mineral Resources: Global Metallogeny, Innovative Exploration, and New Discoveries. Ed. by Goldfarb, R. J., Marsh, E. E. and Monecke, T. Special Publication 15. Littleton, CO: Society of Economic Geologists. Chap. 27, pp. 513–538.

Le Maitre, R. W. (1976). Some problems of the projection of chemical data into mineralogical classifications. In: Contributions to Mineralogy and Petrology 56.2, pp. 181–189. DOI: 10.1007/BF00399603.

— ed. (2002). *Igneous rocks. A classification and glossary of terms*. Recommendations of the International Union of Geological Sciences, Subcommission on the Systematics of Igneous Rocks. 2nd ed. Cambridge: Cambridge University Press. 236 pp. DOI: 10.1017/CBO9780511535581.

Lesher, C. M., Burnham, O. M., Keays, R. R., Barnes, S. J. and Hulbert, L. (1999). Geochemical discrimination of barren and mineralized komatiites in dynamic ore-forming magmatic systems. In: Dynamic Processes in Magmatic Ore Deposits and their Application to Mineral Exploration. Ed. by Keays, R. R., Lesher, C. M., Lightfoot, P. C. and Farrow, C. E. G. Vol. 13. Short Course Notes. St. John's: Geological Association of Canada, pp. 451–477.

Lesher, C. M., Burnham, O. M., Keays, R. R., Barnes, S. J. and Hulbert, L. (2001). Trace-element geochemistry and petrogenesis of barren and ore-associated komatiites. In: Canadian Mineralogist 39.2, pp. 673–696. DOI: 10.2113/gscanmin.39.2.673.

Levitan, D. M., Zipper, C. E., Donovan, P., Schreiber, M. E., Seal II, R. R., Engle, M. A., Chermak, J. A., Bodnar, R. J., Johnson, D. K. and Aylor Jr., J. G. (2015). Statistical analysis of soil geochemical data to identify pathfinders associated with mineral deposits: an example from the Coles Hill uranium deposit, Virginia, USA. In: Journal of Geochemical Exploration 154, pp. 238–251. DOI: 10.1016/j.gexplo.2014.12.012.

Li, C., Lightfoot, P. C., Amelin, Y. and Naldrett, A. J. (2000). Contrasting petrological and geochemical relationships in the Voisey's Bay and Mushuau intrusions, Labrador, Canada: implications for ore genesis. In: Economic Geology 95.4, pp. 771–799. DOI: 10.2113/gsecongeo.95.4.771.

Li, C. and Naldrett, A. J. (1999). Geology and petrology of the Voisey's Bay intrusion: reaction of olivine with sulfide and silicate liquids. In: Lithos 47.1–2, pp. 1–31. DOI: 10.1016/S0024-4937(99)00005-5.

Lightfoot, P. C. and Evans-Lamswood, D. (2015). Structural controls on the primary distribution of mafic–ultramafic intrusions containing Ni-Cu-Co-(PGE) sulfide mineralization in the roots of large igneous provinces. In: Ore Geology Reviews 64, pp. 354–386. DOI: 10.1016/j.oregeorev.2014.07.010.

Lightfoot, P. C. and Hawkesworth, C. (1988). Origin of Deccan Trap lavas: evidence from combined trace element and Sr-, Nd- and Pb-isotope studies. In: Earth and Planetary Science Letters 91.1–2, pp. 89–104. DOI: 10.1016/0012-821X(88)90153-7.

Lightfoot, P. C. and Keays, R. R. (2005). Siderophile and chalcophile metal variations in flood basalts from the Siberian Trap, Noril'sk region: implications for the origin of the Ni-Cu-PGE sulfide ores. In: Economic Geology 100.3, pp. 439–462. DOI: 10.2113/gsecongeo.100.3.439.

Lightfoot, P. C., Keays, R. R., Evans-Lamswood, D. and Wheeler, R. (2012). S saturation history of Nain Plutonic Suite mafic intrusions: origin of the Voisey's Bay Ni-Cu-Co sulfide deposit, Labrador, Canada. In: Mineralium Deposita 47.1–2, pp. 23–50. DOI: 10.1007/s00126-011-0347-6.

Lin, X., Wang, X., Zhang, B. and Yao, W. (2014). Multivariate analysis of regolith sediment geochemical data from the Jinwozi gold field, north-western China. In: Journal of Geochemical Exploration 137, pp. 48–54. DOI: 10.1016/j.gexplo.2013.11.006.

Little, R. J. A. and Rubin, D. B. (2002). *Statistical analysis with missing data*. 2nd ed. Hoboken, New Jersey: John Wiley & Sons. 408 pp. DOI: 10.1002/9781119013563.

Maboko, M. A. H., Williams, I. S. and Compston, W. (1991). Zircon U-Pb chronometry of the pressure and temperature history of granulites in the Musgrave Ranges, central Australia. In: Journal of Geology 99.5, pp. 675–697. DOI: 10.2307/30068777.

Maier, W. D., Howard, H. M., Smithies, R. H., Yang, S. H., Barnes, S.-J., O'Brien, H., Huhma, H. and Gardoll, S. (2015). Magmatic ore deposits in mafic-ultramafic intrusions of the Giles Event, Western Australia. In: Ore Geology Reviews 71, pp. 405–436. DOI: 10.1016/j.oregeorev.2015.06.010.

Maier, W. D., Howard, H. M., Smithies, R. H., Yang, S., Barnes, S.-J., O'Brien, H., Huhma, H. and Gardoll, S. (2014). *Mafic-ultramafic intrusions of the Giles Event, Western Australia: petrogenesis and prospectivity for magmatic ore deposits*. Report 134. Perth: Geological Survey of Western Australia. 82 pp.

Maier, W. D., Li, C. and De Waal, S. A. (2001). Why are there no major Ni-Cu sulfide deposits in large layered mafic-ultramafic intrusions? In: Canadian Mineralogist 39.2, pp. 547–556. DOI: 10.2113/gscanmin.39.2.547.

Major, R. B. and Conor, C. H. H. (1993). Musgrave Block. In: The Precambrian. Ed. by Drexel, J. F., Preiss, W. V. and Parker, A. J. The Geology of South Australia 1. Adelaide: Mines and Energy South Australia, pp. 156–167.

Makkonen, H. V., Mäkinen, J. and Kontoniemi, O. (2008). Geochemical discrimination between barren and mineralized intrusions in the Svecofennian (1.9 Ga) Kotalahti Nickel Belt, Finland. In: Ore Geology Reviews 33.1, pp. 101–114. DOI: 10.1016/j.oregeorev.2006.05.011.

Marsh, B. (2004). A magmatic mush column rosetta stone: the McMurdo Dry Valleys of Antarctica. In: Eos, Transactions American Geophysical Union 85.47, pp. 497–508. DOI: 10.1029/2004EO470001.

Marsh, B. D. (2006). Dynamics of magmatic systems. In: Elements 2.5, pp. 287–292. DOI: 10.2113/gselements.2.5.287.

Martín-Fernández, J. A., Barceló-Vidal, C. and Pawlowsky-Glahn, V. (2003). Dealing with zeros and missing values in compositional data sets using nonparametric imputation. In: Mathematical Geology 35.3, pp. 253–278. DOI: 10.1023/A:1023866030544.

Martín-Fernández, J. A., Palarea-Albaladejo, J. and Olea, R. A. (2011). Dealing with zeros. In: Compositional data analysis. Theory and applications. Ed. by Pawlowsky-Glahn, V. and Buccianti, A. Chichester, West Sussex: John Wiley & Sons, pp. 43–58. DOI: 10.1002/9781119976462.ch4.

Martín-Fernández, J. A. and Thió-Henestrosa, S. (2006). Rounded zeros: some practical aspects for compositional data. In: Compositional data analysis in the geosciences: from theory to practice. Ed. by Buccianti, A., Mateu-Figueras, A. and Pawlowsky-Glahn, V. Special Publication 264. London: Geological Society, pp. 191–201. DOI: 10.1144/GSL.SP.2006.264.01.14.

Mateu-Figueras, G., Pawlowsky-Glahn, V. and Egozcue, J. J. (2011). The principle of working on coordinates. In: Compositional data analysis. Theory and applications. Ed. by Pawlowsky-Glahn, V. and Buccianti, A. Chichester, West Sussex: John Wiley & Sons, pp. 31–42. DOI: 10.1002/9781119976462.ch3.

Mathur, S. P. and Shaw, R. D. (1982). Australian orogenic belts: evidence for evolving plate tectonics? In: Earth Evolution Sciences 4, pp. 281–308.

Matzen, A. K., Baker, M. B., Beckett, J. R. and Stolper, E. M. (2012). The temperature and pressure dependence of nickel partitioning between olivine and silicate melt. In: Journal of Petrology 54.12, pp. 2521–2545. DOI: 10.1093/petrology/egt055.

Mavrogenes, J. A. and O'Neill, H. S. C. (1999). The relative effects of pressure, temperature and oxygen fugacity on the solubility of sulfide in mafic magmas. In: Geochimica et Cosmochimica Acta 63.7–8, pp. 1173–1180. DOI: 10.1016/S0016-7037(98)00289-0.

McCaffrey, K. and Cruden, A. (2002). Dimensional data and growth models for intrusions. In: First international workshop on the physical geology of subvolcanic systems. Laccoliths, sills, and dykes. (Freiberg, Germany), pp. 37–39.

McDonough, W. F. and Sun, S.-s. (1995). The composition of the Earth. In: Chemical Geology 120.3–4, pp. 223–253. DOI: 10.1016/0009-2541(94)00140-4.

McKenzie, D. and O'Nions, R. K. (1991). Partial melt distributions from inversion of rare earth element concentrations. In: Journal of Petrology 32.5, pp. 1021–1091. DOI: 10.1093/petrology/32.5.1021.

— (1995). The source regions of ocean island basalts. In: Journal of Petrology 36.1, pp. 133–159. DOI: 10.1093/petrology/36.1.133.

Medlin, C. C. (2014). The volcanology, petrogenesis, and economic potential of the Mesoproterozoic shallow-water, intra-caldera, lava-like rheomorphic Kathleen Ignimbrite, west Musgrave Province, central Australia. PhD thesis. Melbourne: Monash University. 272 pp.

Menand, T. (2008). The mechanics and dynamics of sills in layered elastic rocks and their implications for the growth of laccoliths and other igneous complexes. In: Earth and Planetary Science Letters 167.1–2, pp. 93–99. DOI: 10.1016/j.epsl.2007.11.043.

Merle, O. (2011). A simple continental rift classification. In: Tectonophysics 513.1–4, pp. 88–95. DOI: 10.1016/j.tecto.2011.10.004.

Michaut, C. and Jaupart, C. (2011). Two models for the formation of magma reservoirs by small increments. In: Tectonophysics 500.1–4, pp. 34–49. DOI: 10.1016/j.tecto.2009.08.019.

Mojoie, P., Bussy, F., Lapierre, H. and Pfeifer, H.-R. (2005). Modeling of in-situ crystallization processes in the Permian mafic layered intrusion of Mont Collon (Dent Blanche nappe, western Alps). In: Lithos 83.3–4, pp. 317–346. DOI: 10.1016/j.lithos.2005.03.008.

Moore, A. C. (1971a). Some aspects of the geology of the Gosse Pile ultramafic intrusion, central Australia. In: Journal of the Geological Society of Australia 18.1, pp. 69–80. DOI: 10.1080/00167617108728744.

— (1971b). The mineralogy of the Gosse Pile ultramafic intrusion, central Australia. II. Pyroxenes. In: Journal of the Geological Society of Australia 18.3, pp. 243–258. DOI: 10.1080/00167617108728764.

— (1973). Studies of igneous and tectonic textures and layering in the rocks of the Gosse Pile intrusion, central Australia. In: Journal of Petrology 14.1, pp. 49–79. DOI: 10.1093/petrology/14.1.49.

Morris, P. A., Pirajno, F. and Wingate, M. T. D. (2005). *Mesoproterozoic sill complexes in the Bangemall Supergroup, Western Australia: geology, geochemistry, and mineralization potential*. Report 99. Perth: Geological Survey of Western Australia. 75 pp.

Mungall, J. E., Hanley, J. J., Arndt, N. T. and Debecdelievre, A. (2006). Evidence from meimechites and other low-degree mantle melts for redox controls on mantle-crust fractionation of platinum-group elements. In: Proceedings of the National Academy of Sciences 103.34, pp. 12695–12700. DOI: 10.1073/pnas.0600878103.

Murtagh, F. and Contreras, P. (2011). Methods of hierarchical clustering. In: ArXiv e-prints. arXiv: 1105.0121 [cs.IR].

Naldrett, A. J. (1999). World-class Ni-Cu-PGE deposits: key factors in their genesis. In: Mineralium Deposita 34.3, pp. 227–240. DOI: 10.1007/s001260050200.

— (2004). *Magmatic sulfide deposits. Geology, geochemistry and exploration.* Berlin, Heidelberg: Springer. 727 pp. DOI: 10.1007/978-3-662-08444-1.

Naldrett, A. J., Asif, M., Krstic, S. and Li, C. (2000a). The composition of mineralization at the Voisey's Bay Ni-Cu sulfide deposit, with special reference to platinum-group elements. In: Economic Geology 95.4, pp. 845–865. DOI: 10.2113/gsecongeo.95.4.845.

Naldrett, A. J., Singh, J., Krstic, S. and Li, C. (2000b). The mineralogy of the Voisey's Bay Ni-Cu-Co deposit, Northern Labrador, Canada: influence of oxidation state on textures and mineral compositions. In: Economic Geology 95.4, pp. 889–900. DOI: 10.2113/gsecongeo.95.4.889.

Namur, O., Abily, B., Boudreau, A. E., Blanchette, F., Bush, J. W. M., Ceuleneer, G., Charlier, B., Donaldson, C. H., Duchesne, J.-C., Higgins, M. D., Morata, D., Nielsen, T. F. D., O'Driscoll, B., Pang, K. N., Peacock, T., Spandler, C. J., Toramaru, A. and Veksler, I. V. (2015). Igneous layering in basaltic magma chambers. In: Layered intrusions. Ed. by Charlier, B., Namur, O., Latypov, R. and Tegner, C. Dordrecht: Springer, pp. 75–152. DOI: 10.1007/978-94-017-9652-1_2.

Namur, O., Charlier, B., Pirard, C., Hermann, J., Liégeois, J.-P. and Vander Auwera, J. (2011). Anorthosite formation by plagioclase flotation in ferrobasalt and implications for the lunar crust. In: Geochimica et Cosmochimica Acta 75.17, pp. 4998–5018. DOI: 10.1016/j.gca.2011.06.013.

Nesbitt, R. W. (1966). The Giles igneous province, central Australia. An example of an eroded volcanic zone. In: Bulletin Volcanologique 29.1, pp. 271–281. DOI: 10.1007/BF02597157.

Nesbitt, R. W., Goode, A. D. T., Moore, A. C. and Hopwood, T. P. (1970). The Giles Complex, central Australia: a stratified sequence of mafic and ultramafic intrusions. In: Geological Society of South Africa Special Publication 1, pp. 547–564.

Nesbitt, R. W. and Kleeman, A. W. (1964). Layered intrusions of the Giles Complex, central Australia. In: Nature 203.4943, pp. 391–393. DOI: 10.1038/203391a0.

Nesbitt, R. W. and Talbot, J. L. (1966). The layered basic and ultrabasic intensives of the Giles Complex, central Australia. In: Contributions to Mineralogy and Petrology 13.1, pp. 1–11. DOI: 10.1007/BF00518123.

Papanastassiou, D. J. and Wasserburg, G. J. (1968). Initial strontium isotopic abundances and the resolution of small time differences in the formation of planetary objects. In: Earth and Planetary Science Letters 5, pp. 361–376. DOI: 10.1016/S0012-821X(68)80066-4.

Pawlowsky-Glahn, V. (2003). Statistical modeling on coordinates. In: CoDaWork'03. Proceedings of the 1st compositional data analysis workshop. University of Girona. Girona, Spain. URL: http://ima.udg.edu/activitats/codawork03/ (visited on 30/10/2015).

Pawlowsky-Glahn, V. and Egozcue, J. J. (2001). Geometric approach to statistical analysis on the simplex. In: Stochastic Environmental Research and Risk Assessment 15.5, pp. 384–398. DOI: 10.1007/s004770100077.

Pawlowsky-Glahn, V., Egozcue, J. J. and Tolosana-Delgado, R. (2015). *Modeling and analysis of compositional data.* Chichester, West Sussex: John Wiley & Sons. 247 pp. DOI: 10.1002/9781119003144.

Pearce, J. A. (2008). Geochemical fingerprinting of oceanic basalts with applications to ophiolite classification and the search for Archean oceanic crust. In: Lithos 100.1–4, pp. 14–48. DOI: 10.1016/j.lithos.2007.06.016.

Pearson, K. (1896). Mathematical contributions to the theory of evolution.—On a form of spurious correlation which may arise when indices are used in the measurement of organs. In: Proceedings of the Royal Society of London 60.359–367, pp. 489–498. DOI: 10.1098/rspl.1896.0076.

— (1901). On lines and planes of closest fit to systems of points in space. In: Philosophical Magazine. Series 6 2.11, pp. 559–572. DOI: 10.1080/14786440109462720.

Peh, Z., Šajn, R., Halamić, J. and Galović, L. (2007). Multiple discriminant analysis of the Drava River alluvial plain sediments. In: Environmental Geology 55.7, pp. 1519–1535. DOI: 10.1007/s00254-007-1102-2.

Pirajno, F. (2007). Mantle plumes, associated intraplate tectono-magmatic processes and ore systems. In: Episodes 30.1, pp. 6–19.

Pirajno, F., González-Álvarez, I., Chen, W., Kyser, K. T., Simonetti, A., Leduc, E. and leGras, M. (2014). The Gifford Creek Ferrocarbonatite Complex, Gascoyne Province, Western Australia: associated fenitic alteration and a putative link with the 1075 Ma Warakurna LIP. In: Lithos 202–203, pp. 100–119. DOI: 10.1016/j.lithos.2014.05.012.

Pirajno, F. and Hoatson, D. M. (2012). A review of Australia's large igneous provinces and associated mineral systems: implications for mantle dynamics through geological time. In: Ore Geology Reviews 48, pp. 2–54. DOI: 10.1016/j.oregeorev.2012.04.007.

Porter, K. A. and White, W. M. (2009). Deep mantle subduction flux. In: Geochemistry, Geophysics, Geosystems 10.12, Q12016. DOI: 10.1029/2009GC002656.

Presnall, D. C., Dixon, S. A., Dixon, J. R., O'Donnell, T. H., Brenner, N. L., Schrock, R. L. and Dycus, D. W. (1978). Liquidus phase relations on the join diopside-forsterite-anorthite from 1 atm to 20 kbar: their bearing on the generation and crystallization of basaltic magma. In: Contributions to Mineralogy and Petrology 66.2, pp. 203–220. DOI: 10.1007/BF00372159.

Pruseth, K. L. (2009a). Calculation of the CIPW norm: new formulas. In: Journal of Earth System Science 118.1, pp. 101–113. DOI: 10.1007/s12040-009-0010-0.

— (2009b). MATNORM: calculating NORM using composition matrices. In: Computers & Geosciences 35.9, pp. 1785–1788. DOI: 10.1016/j.cageo.2008.09.014.

Putirka, K. and Platt, B. (2012). Basin and Range volcanism as a passive response to extensional tectonics. In: Geosphere 8.6, pp. 1274–1285. DOI: 10.1130/GES00803.1.

Quentin De Gromard, R., Wingate, M. T. D., Howard, H. M. and Smithies, R. H. (2016). *Geology and U-Pb geochronology of the Warlawurru Supersuite and MacDougall Formation in the Mitika and Wanarn areas, west Musgrave Province.* Record 2016/4. Perth: Geological Survey of Western Australia. 29 pp.

R Core Team (2015). *R: a language and environment for statistical computing*. R Foundation for Statistical Computing. Vienna, Austria. URL: http://www.r-project.org (visited on 30/10/2015).

Raimondo, T., Collins, A. S., Hand, M., Walker-Hallam, A., Smithies, R. H., Evins, P. M. and Howard, H. M. (2010). The anatomy of a deep intracontinental orogen. In: Tectonics 29.4, TC4024. DOI: 10.1029/2009TC002504.

Ramakrishnan, R., Dral, P. O., Rupp, M. and Lilienfeld, O. A. von (2015). Big data meets quantum chemistry approximations: the Δ-machine learning approach. In: Journal of Chemical Theory and Computation 11.5, pp. 2087–2096. DOI: 10.1021/acs.jctc.5b00099.

Redstone Resources Limited (2014). *Annual report*. Perth.

Ripley, E. M. and Li, C. (2013). Sulfide saturation in mafic magmas: is external sulfur required for magmatic Ni-Cu-(PGE) ore genesis? In: Economic Geology 108.1, pp. 45–58. DOI: 10.2113/econgeo.108.1.45.

Rollinson, H. R. (1993). *Using geochemical data. Evaluation, presentation, interpretation*. Harlow: Longman Scientific & Technical. 352 pp.

Roshani, P., Mokhtari, A. R. and Tabatabaei, S. H. (2013). Objective based geochemical anomaly detection—application of discriminant function analysis in anomaly delineation in the Kuh Panj porphyry Cu mineralization (Iran). In: Journal of Geochemical Exploration 130, pp. 65–73. DOI: 10.1016/j.gexplo.2013.03.005.

Rudin, C., Waltz, D., Anderson, R. N., Boulanger, A., Salleb-Aouissi, A., Chow, M., Dutta, H., Gross, P. N., Huang, B., Ierome, S., Isaac, D. F., Kressner, A., Passonneau, R. J., Radeva, A. and Wu, L. (2012). Machine learning for the New York City power grid. In: IEEE Transactions on Pattern Analysis and Machine Intelligence 34.2, pp. 328–345. DOI: 10.1109/TPAMI.2011.108.

Rudnick, R. L. and Gao, S. (2014). Composition of the continental crust. In: The crust. Ed. by Holland, H. D., Turekian, K. K. and Carlson, R. W. 2nd ed. Treatise on geochemistry 4. Oxford: Elsevier. Chap. 4.1, pp. 1–51. DOI: 10.1016/B978-0-08-095975-7.00301-6.

Ryan, B. (2000). The Nain-Churchill boundary and the Nain Plutonic Suite: a regional perspective on the geologic setting of the Voisey's Bay Ni-Cu-Co deposit. In: Economic Geology 95.4, pp. 703–724. DOI: 10.2113/gsecongeo.95.4.703.

Salters, V. J. M. and Stracke, A. (2004). Composition of the depleted mantle. In: Geochemistry, Geophysics, Geosystems 5.5, Q05B07. DOI: 10.1029/2003GC000597.

Sanfilippo, A., Dick, H. J. B. and Ohara, Y. (2013). Melt-rock reaction in the mantle: mantle troctolites from the Parece Vela ancient back-arc spreading center. In: Journal of Petrology 54.5, pp. 861–885. DOI: 10.1093/petrology/egs089.

Saumur, B. M., Cruden, A. R., Evans-Lamswood, D. and Lightfoot, P. C. (2015). Wall-rock structural controls on the genesis of the Voisey's Bay intrusion and its Ni-Cu-Co magmatic sulfide mineralization (Labrador, Canada). In: Economic Geology 110.3, pp. 691–711. DOI: 10.2113/econgeo.110.3.691.

Scealy, J. L., De Cariat, P., Grunsky, E. C., Tsagris, M. T. and Welsh, A. H. (2015). Robust principal component analysis for power transformed compositional data. In: Journal

of the American Statistical Association 110.509, pp. 136–148. DOI: 10.1080/01621459.2014.990563.

Schmeling, H. (2010). Dynamic models of continental rifting with melt generation. In: Tectonophysics 480.1–4, pp. 33–47. DOI: 10.1016/j.tecto.2009.09.005.

Schmidt, P. W., Williams, G. E., Camacho, A. and Lee, J. K. W. (2006). Assembly of Proterozoic Australia: implications of a revised pole for the ~1070 Ma Alcurra Dyke Swarm, central Australia. In: Geophysical Journal International 167.2, pp. 626–634. DOI: 10.1111/j.1365-246X.2006.03192.x.

Scoates, J. S. and Mitchell, J. N. (2000). The evolution of troctolitic and high Al basaltic magmas in Proterozoic anorthosite plutonic suites and implications for the Voisey's Bay massive Ni-Cu sulfide deposit. In: Economic Geology 95.4, pp. 677–701. DOI: 10.2113/gsecongeo.95.4.677.

Scrimgeour, I. R. and Close, D. F. (1999). Regional high-pressure metamorphism during intracratonic deformation: the Petermann Orogeny, central Australia. In: Journal of Metamorphic Geology 17.5, pp. 557–572. DOI: 10.1046/j.1525-1314.1999.00217.x.

Scrimgeour, I. R., Close, D. F. and Edgoose, C. J. (1999). *Petermann Ranges, sheet SG 52-7, 2nd edition*. 1:250 000 Geological Series explanatory notes. Darwin: Northern Territory Geological Survey. 59 pp.

Seat, Z. (2008). Geology, petrology, mineral and whole-rock chemistry, stable and radiogenic isotope systematics and Ni-Cu-PGE mineralisation of the Nebo-Babel intrusion, west Musgrave, Western Australia. PhD thesis. Perth: University of Western Australia. 220 pp.

Seat, Z., Beresford, S. W., Grguric, B. A., Gee, M. A. M. and Grassineau, N. V. (2009). Reevaluation of the role of external sulfur addition in the genesis of Ni-Cu-PGE deposits: evidence from the Nebo-Babel Ni-Cu-PGE deposit, west Musgrave, Western Australia. In: Economic Geology 104.4, pp. 521–538. DOI: 10.2113/gsecongeo.104.4.521.

Seat, Z., Beresford, S. W., Grguric, B. A., Waugh, R. S., Hronsky, J. M. A., Gee, M. A. M., Groves, D. I. and Mathison, C. I. (2007). Architecture and emplacement of the Nebo-Babel gabbronorite-hosted magmatic Ni-Cu-PGE sulphide deposit, west Musgrave, Western Australia. In: Mineralium Deposita 42.6, pp. 551–581. DOI: 10.1007/s00126-007-0123-9.

Seat, Z., Gee, M. A. M., Grguric, B. A., Beresford, S. W. and Grassineau, N. V. (2011). The Nebo-Babel Ni-Cu-PGE sulfide deposit (west Musgrave, Australia): pt. 1. U/Pb zircon ages, whole-rock and mineral chemistry, and O-Sr-Nd isotope compositions of the intrusion, with constraints on petrogenesis. In: Economic Geology 106.4, pp. 527–556. DOI: 10.2113/econgeo.106.4.527.

Sengör, A. M. C. and Burke, K. (1978). Relative timing of rifting and volcanism on Earth and its tectonic implications. In: Geophysical Research Letters 5.6, pp. 419–421. DOI: 10.1029/GL005i006p00419.

Shannon, R. D. (1976). Revised effective ionic radii and systematic studies of interatomic distances in halides and chalcogenides. In: Acta Crystallographica. Section A 32.5, pp. 751–767. DOI: 10.1107/S0567739476001551.

Smithies, R. H., Howard, H. M., Evins, P. M., Kirkland, C. L., Bodorkos, S. and Wingate, M. T. D. (2009a). *The west Musgrave Complex—new geological insights from recent mapping, geochronology, and geochemical studies*. Record 2008/19. Perth: Geological Survey of Western Australia. 20 pp.

Smithies, R. H., Howard, H. M., Evins, P. M., Kirkland, C. L., Kelsey, D. E., Hand, M., Wingate, M. T. D., Collins, A. S. and Belousova, E. (2011). High-temperature granite magmatism, crust-mantle interaction and the Mesoproterozoic intracontinental evolution of the Musgrave Province, central Australia. In: Journal of Petrology 52.5, pp. 931–958. DOI: 10.1093/petrology/egr010.

Smithies, R. H., Howard, H. M., Evins, P. M., Kirkland, C. L., Kelsey, D. E., Hand, M., Wingate, M. T. D., Collins, A. S., Belousova, E. A. and Allchurch, S. (2010). *Geochemistry, geochronology and petrogenesis of Mesoproterozoic felsic rocks in the west Musgrave Province, central Australia, and implications for the Mesoproterozoic tectonic evolution of the region*. Report 106. Perth: Geological Survey of Western Australia. 73 pp.

Smithies, R. H., Howard, H. M., Kirkland, C. L., Werner, M., Medlin, C. C., Wingate, M. T. D. and Cliff, J. B. (2013). *Geochemical evolution of rhyolites of the Talbot Sub-basin and associated felsic units of the Warakurna Supersuite*. Report 118. Perth: Geological Survey of Western Australia. 74 pp.

Smithies, R. H., Howard, H. M., Maier, W. D. and Evins, P. M. (2009b). *Blackstone, WA sheet 4545*. 1:100 000 Geological Series map. Perth: Geological Survey of Western Australia.

Smithies, R. H., Kirkland, C. L., Korhonen, F. J., Aitken, A. R. A., Howard, H. M., Maier, W. D., Wingate, M. T. D., Quentin de Gromard, R. and Gessner, K. (2015). The Mesoproterozoic thermal evolution of the Musgrave Province in central Australia—plume vs. the geological record. In: Gondwana Research 27.4, pp. 1419–1429. DOI: 10.1016/j.gr.2013.12.014.

Sobolev, A. V., Hofmann, A. W., Sobolev, S. V. and Nikogosian, I. K. (2005). An olivine-free mantle source of Hawaiian shield basalts. In: Nature 434.7033, pp. 590–597. DOI: 10.1038/nature03411.

Sprigg, R. C. and Wilson, R. B. (1959). The Musgrave Mountain Belt in South Australia. In: Geologische Rundschau 47.2, pp. 531–542. DOI: 10.1007/BF01800672.

Streckeisen, A. (1976). To each plutonic rock its proper name. In: Earth-Science Reviews 12, pp. 1–33. DOI: 10.1016/0012-8252(76)90052-0.

Streich, V. (1893). Geology. In: Transactions of the Royal Society of South Australia 16, pp. 74–115. Geological observations made on the Elder Exploring Expedition (1891–1892), including supplementary material by A. W. Stelzer and R. Tate.

Sun, S.-S., Sheraton, J. W., Glikson, A. Y. and Stewart, A. J. (1996). A major magmatic event during 1050–1080 Ma in central Australia, and an emplacement age for the Giles Complex. In: AGSO Research Newsletter 24, pp. 13–15.

Talbot, H. W. B., Clarke, E. d. C. and Farquharson, R. A. (1917). *A geological reconnaissance of the country between Laverton and the South Australian border (near south latitude 26°), including part of the Mount Margaret goldfield*. Bulletin 75. Perth: Geological Survey of Western Australia. 207 pp.

Taylor, S. R. and McLennan, S. M. (1985). *The continental crust: its composition and evolution. An examination of the geochemical record preserved in sedimentary rocks*. Oxford: Blackwell Scientific Publishing. 312 pp.

Turcotte, D. L. and Emerman, S. H. (1983). Mechanisms of active and passive rifting. In: Tectonophysics 94.1–4, pp. 39–50. DOI: 10.1016/0040-1951(83)90008-2.

VanTongeren, J. A., Mathez, E. A. and Kelemen, P. B. (2010). A felsic end to Bushveld differentiation. In: Journal of Petrology 51.9, pp. 1891–1912. DOI: 10.1093/petrology/egq042.

Venables, W. N. and Ripley, B. D. (2002). *Modern applied statistics with S*. 4th ed. New York, NY: Springer. 498 pp. DOI: 10.1007/978-0-387-21706-2.

Verma, S. P., Torres-Alvarado, I. S. and Sotelo-Rodríguez, Z. T. (2002). SINCLAS: standard igneous norm and volcanic rock classification system. In: Computers & Geosciences 28.5, pp. 711–715. DOI: 10.1016/S0098-3004(01)00087-5.

Verma, S. P., Torres-Alvarado, I. S. and Velasco-Tapia, F. (2003). A revised CIPW norm. In: Schweizerische Mineralogische und Petrographische Mitteilungen 83.2, pp. 197–216. DOI: 10.5169/seals-63145.

Wade, B. P. (2006). Unravelling the tectonic framework of the Musgrave Province, central Australia. PhD thesis. Adelaide: University of Adelaide. 219 pp.

Wade, B. P., Barovich, K. M., Hand, M., Scrimgeour, I. R. and Close, D. F. (2006). Evidence for early Mesoproterozoic arc magmatism in the Musgrave Block, central Australia: implications for Proterozoic crustal growth and tectonic reconstructions of Australia. In: Journal of Geology 114.1, pp. 43–63. DOI: 10.1086/498099.

Wade, B. P., Kelsey, D. E., Hand, M. and Barovich, K. M. (2008). The Musgrave Province: stitching north, west and south Australia. In: Precambrian Research 166.1–4, pp. 370–386. DOI: 10.1016/j.precamres.2007.05.007.

Walter, M. J. (2014). Melt extraction and compositional variability in mantle lithosphere. In: The mantle and core. Ed. by Holland, H. D., Turekian, K. K. and Carlson, R. W. 2nd ed. Treatise on geochemistry 3. Oxford: Elsevier. Chap. 3.10, pp. 393–419. DOI: 10.1016/B978-0-08-095975-7.00208-4.

Wang, K., Plank, T., Walker, J. D. and Smith, E. I. (2002). A mantle melting profile across the Basin and Range, SW USA. In: Journal of Geophysical Research. Solid Earth 107.B1, pages. DOI: 10.1029/2001JB000209.

Wasserburg, G. J., Jacobsen, S. B., DePaolo, D. J., McCulloch, M. T. and Wen, T. (1981). Precise determination of Sm/Nd ratios, Sm and Nd isotopic abundances in standard solutions. In: Geochimica et Cosmochimica Acta 45.12, pp. 2311–2323. DOI: 10.1016/0016-7037(81)90085-5.

White, R. W., Clarke, G. L. and Nelson, D. R. (1999). SHRIMP U-Pb zircon dating of Grenville-age events in the western part of the Musgrave Block, central Australia. In: Journal of Metamorphic Geology 17.5, pp. 465–481. DOI: 10.1046/j.1525-1314.1999.00211.x.

White, W. M. (1985). Sources of oceanic basalts: radiogenic isotopic evidence. In: Geology 13.2, pp. 115–118. DOI: 10.1130/0091-7613(1985)13<115:SOOBRI>2.0.CO;2.

— (2010). Oceanic island basalts and mantle plumes: the geochemical perspective. In: Annual Review of Earth and Planetary Sciences 38, pp. 133–160. DOI: 10.1146/annurev-earth-040809-152450.
— (2013). *Geochemistry*. Chichester, West Sussex: Wiley-Blackwell. 660 pp.
— (2015a). Isotopes, DUPAL, LLSVPs, and Anekantavada. In: Chemical Geology 419, pp. 10–28. DOI: 10.1016/j.chemgeo.2015.09.026.
— (2015b). Probing the Earth's deep interior through geochemistry. In: Geochemical Perspectives 4.2, pp. 95–251. DOI: 10.7185/geochempersp.4.2.
Whitney, D. L. and Evans, B. W. (2010). Abbreviations for names of rock-forming minerals. In: American Mineralogist 95.1, pp. 185–187. DOI: 10.2138/am.2010.3371.
Wieser, M. E., Holden, N., Coplen, T. B., Böhlke, J. K., Berglund, M., Brand, W. A., De Bièvre, P., Gröning, M., Loss, R. D., Meija, J., Hirata, T., Prohaska, T., Schoenberg, R., O'Connor, G., Walczyk, T., Yoneda, S. and Zhu, X.-K. (2013). Atomic weights of the elements 2011 (IUPAC technical report). In: Pure and Applied Chemistry 85.5, pp. 1047–1078. DOI: 10.1351/PAC-REP-13-03-02.
Willbold, M. and Stracke, A. (2006). Trace element composition of mantle end-members: implications for recycling of oceanic and upper and lower continental crust. In: Geochemistry, Geophysics, Geosystems 7.4, Q04004. DOI: 10.1029/2005GC001005.
Wingate, M. T. D., Pirajno, F. and Morris, P. A. (2004). Warakurna large igneous province: a new Mesoproterozoic large igneous province in west-central Australia. In: Geology 32.2, pp. 105–108. DOI: 10.1130/G20171.1.
Xu, R. and Wunsch, D. C. (2008). *Clustering*. Hoboken, New Jersey and Piscataway, New Jersey: John Wiley & Sons and IEEE Press. 358 pp. DOI: 10.1002/9780470382776.
Zhang, M., O'Reilly, S. Y., Wang, K.-L., Hronsky, J. and Griffin, W. L. (2008). Flood basalts and metallogeny: the lithospheric mantle connection. In: Earth-Science Reviews 86.1–4, pp. 145–174. DOI: 10.1016/j.earscirev.2007.08.007.
Zhao, J.-x. and McCulloch, M. T. (1993). Melting of a subduction-modified continental lithospheric, mantle: evidence from Late Proterozoic mafic dike swarms, in central Australia. In: Geology 21.5, pp. 463–466. DOI: 10.1130/0091-7613(1993)021<0463:MOASMC>2.3.CO;2.
Zhou, J., Flood, P. G. and Li, W. (2000). Gold grade and tonnage models of the gold deposits, China. In: Resource Geology 50.1, pp. 53–64. DOI: 10.1111/j.1751-3928.2000.tb00055.x.
Zhu, M. (2001). Feature extraction and dimension reduction with applications to classification and the analysis of co-occurrence data. PhD thesis. Stanford: Stanford University. 137 pp.
Zibra, I., Smithies, R. H., Wingate, M. T. D. and Kirkland, C. L. (2014). Incremental pluton emplacement during inclined transpression. In: Tectonophysics 623, pp. 100–122. DOI: 10.1016/j.tecto.2014.03.020.
Zindler, A. and Hart, S. (1986). Chemical geodynamics. In: Annual Review of Earth and Planetary Sciences 14, pp. 493–571. DOI: 10.1146/annurev.ea.14.050186.002425.

Appendix A

Methodology

A.1 Depth estimation for stratigraphic and chemostratigraphic logs from surface coordinates

Especially for layered intrusions it is common to plot chemical elements against the depth. Since the samples that were collected for this study are surface samples the depth D needs to be estimated from the coordinates of the sampling sites and averages of the attitude of igneous layering along the respective sampling traverse (see tables 2.1 and 4.1 for the traverse metadata). The procedure for this estimation is documented here because there are surprisingly large differences in previous thickness estimates for the intrusions: Nesbitt and Talbot (1966) for instance gave a thickness of c. 6000 m for the Bell Rock Range intrusion, which might simply be the exposed width of the intrusion. The value was later revised downward to c. 3800 m (Ballhaus and Glikson 1995; Glikson et al. 1996; Goode 2002; Maier et al. 2014), probably based on a dip of the igneous layering at 70° towards southwest (Ballhaus and Glikson 1995). The calculations in this study were done using a simple geometric point-plane-distance approach. They are assumed to give realistic results under the assumptions that (1) igneous layering defined an approximately horizontal plane at the time of formation, (2) the attitude of igneous layering does not change significantly along a sampling traverse and (3) the effects of the relationship between the topography and the readings of the elevation above sea level of the sampling sites on the relative depth positions of the sites is negligible. The first assumption can generally be regarded as true, since nonhorizontal planar structures like igneous cross-bedding were only observed on a cm-scale (e.g. Daniels 1974) and should therefore not cause any bias on repeated measurements of igneous layering that were taken over a large area. The second assumption can be made based on the stereographic projections of igneous layering (figure A.1), that show 95 % confidence intervals within reasonable radii around the average attitude of the poles. The third assumption was accepted because igneous layering within the intrusions is generally significantly steeper than topography and therefore topographic effects should not be significant. The values for the attitude of igneous layering are taken from Howard et al. (2009b). For each sampling traverse those

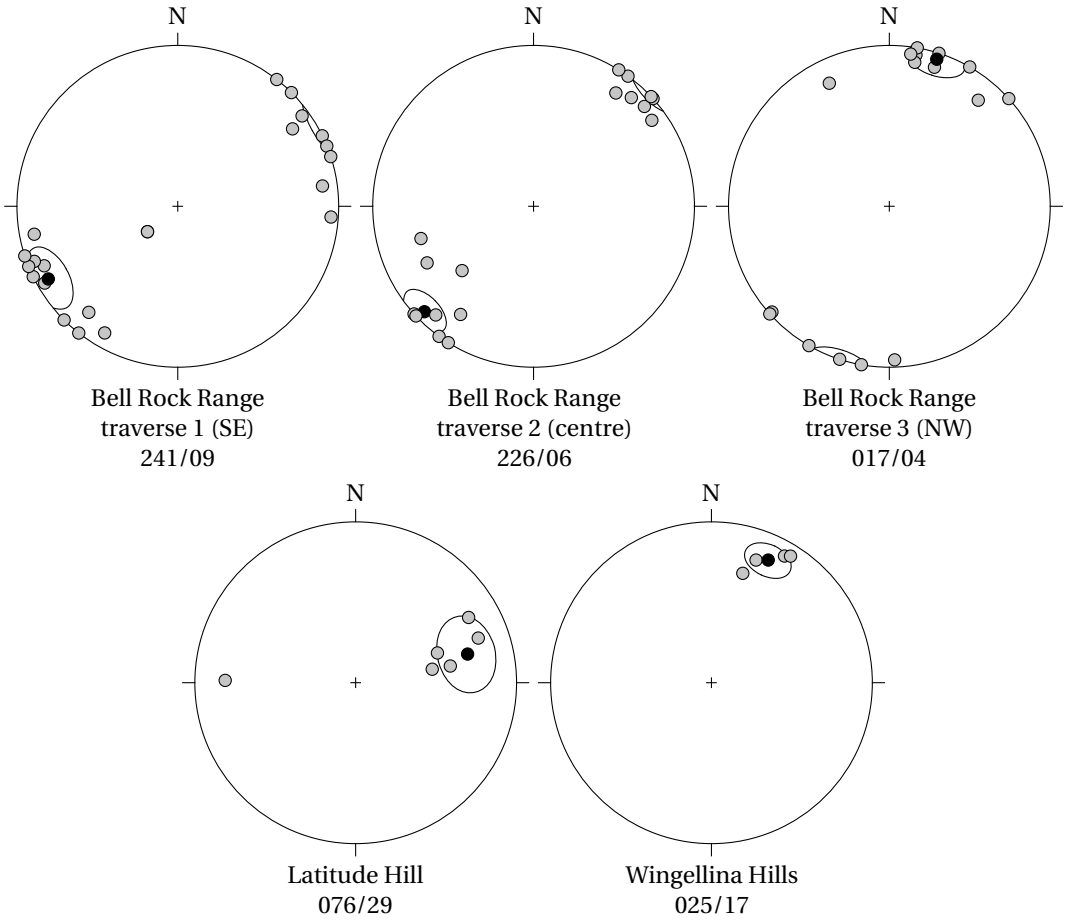

Figure A.1 Stereographic projection of the poles of igneous layering planes as measured along sampling traverses (data from Geological Survey of Western Australia *West Musgrave, 2011 update*, Howard et al. 2009b). Circles around average attitude show the 95 % confidence interval.

values were taken that were closest to that traverse.

The locations of the sampling sites were determined in the universal transverse mercator (UTM) coordinate system which displays easting and northing in m. Together with height above sea level z this results in a three dimensional position vector (x, y, z) for each site $\mathbf{s}$ in a cartesian coordinate system. Measurements of attitude of planar and linear features on the other side are commonly expressed in spherical coordinates: the pole of an igneous layering plane is a unit vector $\hat{\mathbf{p}}$ that is defined by the coordinates (r, θ, ϕ), i.e. its radial length r, its azimuth θ and its inclination ϕ. The first step is therefore the conversion of $\hat{\mathbf{p}}$ to cartesian coordinates. The length r of a pole is meaningless in a geological context, thus $r = 1$ (unit vector) and

$$\hat{\mathbf{p}} = \begin{bmatrix} a \\ b \\ c \end{bmatrix} = \begin{bmatrix} \sin\theta\cos\phi \\ \cos\theta\cos\phi \\ \sin\phi \end{bmatrix} \tag{A.1}$$

with positive a as east component, positive b as north component and positive c as downwards component of the pole. Next, an arbitrary sampling site $\mathbf{s_0}$ with coordinates (x_0, y_0, z_0) is choosen as a reference point, thus,

$$ax_0 + by_0 + cz_0 + d = 0 \tag{A.2}$$

is the plane of igneous layering through $\mathbf{s_0}$ with pole $\hat{\mathbf{p}}$ in cartesian coordinates. After rearranging equation (A.2),

$$d = -ax_0 - by_0 - cz_0, \tag{A.3}$$

and the signed relative distance D_{rel} between $\mathbf{s_0}$ and any other sampling site $\mathbf{s}$ with coordinates (x, y, z) is then

$$D_{rel} = \frac{ax + by + cz + d}{\sqrt{a^2 + b^2 + c^2}}. \tag{A.4}$$

Finally, one end of the sampling traverse is defined as the top of the intrusive body where $D_{top} = 0$ and the remaining distances D are calculated, taking into account the sign of D_{top}:

$$D = \begin{cases} D_{rel} + D_{top} & \text{if } D_{top} < 0, \\ -\left(D_{rel} - D_{top}\right) & \text{if } D_{top} \geq 0 \end{cases} \tag{A.5}$$

Self-evidently, the maximum depth D_{max} (i.e. the bottom-most sampling site) is also the estimated total thickness of the intrusive body. The values are given in the text in tables 2.1 and 4.1.

A.2 Estimation of relative Fe(II)- and Fe(III)-oxide amounts

The chemical analyses in this study (see method descriptions in sections 2.3, 3.3 and 4.3) report only Fe(III)-oxide (Fe_2O_3), while Fe(II)-oxide (FeO) needs to be estimated if needed. Instead of using a fixed ratio between FeO and Fe_2O_3 the procedure used here follows Le Maitre (1976) who recommended the regression

$$r_{ox} = .88 - .0016 w_{SiO_2} - .027\left(w_{Na_2O} + w_{K_2O}\right) \tag{A.6}$$

to calculate the oxidation ratio r_{ox} for plutonic rocks with mass fractions w given in wt%. From the definition of the oxidation ratio r_{ox} as

$$r_{ox} = \frac{w_{FeO}}{w_{FeO} + w_{Fe_2O_3}} \tag{A.7}$$

it follows that

$$w_{Fe_2O_3} = \frac{w_{FeO}}{r_{ox}} - w_{FeO}. \tag{A.8}$$

Total Fe as given in the analytical results is defined as

$$w^{total}_{Fe_2O_3} = 1.1113 w_{FeO} + w_{Fe_2O_3}, \tag{A.9}$$

thus, by substituting equation (A.8) into equation (A.9) one obtains

$$w^{total}_{Fe_2O_3} = 1.1113\, w_{FeO} + \frac{w_{FeO}}{r_{ox}} - w_{FeO} \tag{A.10}$$

and w_{FeO} can be calculated with

$$w_{FeO} = \frac{w^{total}_{Fe_2O_3}}{.1113 + (r_{ox})^{-1}}. \tag{A.11}$$

Once w_{FeO} is known, $w_{Fe_2O_3}$ results from equation (A.9):

$$w_{Fe_2O_3} = w^{total}_{Fe_2O_3} - 1.1113\, w_{FeO} \tag{A.12}$$

A.3 Calculation of normative modal compositions

Calculations of the CIPW (Cross, Iddings, Pirsson, Washington) norm were carried-out following the method of Pruseth (2009a,b), which itself is based on Verma et al. (2002, 2003). As inputs this method uses the major element oxides Al_2O_3, CaO, Cr_2O_3, FeO, Fe_2O_3, K_2O, MgO, MnO, Na_2O, P_2O_5, SiO_2 and TiO_2, as well as the trace elements Ba, Ni, Sr and Zr, converted to the oxides BaO, NiO, SrO and ZrO_2, respectively; all inputs are given in wt%. The procedure in appendix A.2 was used to estimate the true relative amounts of FeO and Fe_2O_3 from total Fe reported as Fe_2O_3. Further, S was included wherever analysed and the results were above the limit of detection. The analyses were then reclosed to 100 wt% (appendix A.5). The normative calculations return the endmembers diopside and hypersthene, which were assumed to represent general clino- and orthopyroxene, respectively, in order to comply with common rock classification schemas of Streckeisen (1976) and Le Maitre (2002) that were used in this study (appendix A.4).

A.4 Rock classification

The rock samples were classified using the standard rock classification scheme from Streckeisen (1976) and Le Maitre (2002). Since these schemes were originally based on modal proportions (vol%) the normative mineralogy (appendix A.3) was converted from wt%, using the average mineral densities listed in table A.1. For the purpose of rock classification, the pyroxenes hypersthene and diopside were assumed to be equivalent to the more generic terms ortho- and clinopyroxene, respectively. Furthermore, the normative amounts of orthoclase (Or), albite (Ab) and anorthite (An) were converted to alkali-feldspar (Afs) and plagioclase (Pl), respectively (Le Maitre 1976). Following these data transformations the classification was performed by plotting the data into the widely known ternary diagrams for mafic and ultramafic rocks (Streckeisen 1976; Le Maitre 2002).

Mineral	ρ (g/cm^3)
Albite	2.62
Anorthite	2.74
Apatite	3.19
Chromite	4.80
Diopside	3.40
Hypersthene	3.55
Ilmenite	4.72
Magnetite	5.15
Nepheline	2.60
Olivine	3.32
Orthoclase	2.56
Pyrite	5.01
Quartz	2.63
Zircon	4.65

Table A.1 Average densities ρ of minerals used for the conversion of mineral amounts from wt% to vol%. The data was taken from Mineralogy Database; Mineralogy Database (`http://webmineral.com/determin/metallic_minerals_by_density.shtml`; `http://webmineral.com/determin/non-metallic_minerals_by_density.shtml`).

A.5 Treatment and analysis of compositional data

Lithogeochemical data report the elemental and isotopic contents of rocks and minerals, and are typical examples for what is called 'compositional data'. These data have certain inconvenient properties, such as the spurious nature of correlations between variables, that are known for a long time from the field of biostatistics (Pearson 1896). It was not until much later that the relevance of this work for the geosciences was realised (Chayes 1960) and appropriate methods to analyse such data were developed (Aitchison 1982, 1984, 1986).

The fundamental problem with the direct application of most statistical methods to compositional data is that those methods assume a real vector space $\mathbb{R}^D$ as the underlying sample space. However, this assumption is not appropriate for compositional data because they contain only *relative* information—the numeric value alone is meaningless. For instance, 20 wt% Al_2O_3 is a meaningful quantity while 20 Al_2O_3 is not, thus, the data get their meaning only from the relationship between the different components expressed as ratios (Aitchison 1982, 1984, 1986). Appropriate treatment of compositional data is therefore fundamental to this study, because the multivariate techniques used for dimensionality reduction and clustering (appendices A.6 and A.7) measure distances and variances using Euclidean metrics in real space. All of the following descriptions of the data preprocessing steps carried-out in this study are compiled from the comprehensive reviews of Aitchison (1986), Boogaart and Tolosana-Delgado (2013) and Pawlowsky-Glahn et al. (2015).

For better understanding, it is instructive to formalise the above concept of compositional data. A composition is a vector

$$\mathbf{x} = [x_1, x_2, \ldots, x_D], \tag{A.13}$$

of D strictly positive real components $x_i \in \mathbb{R}_+$ for all $i = 1,2,\ldots,D$, that sum up to a constant κ. In geochemical datasets κ typically takes on values like 100, 10^6 or 10^9, corresponding to measurements taken in the units %, ppm or ppb, respectively. The operation of assigning a constant sum κ to a composition is called 'closure' operation $\mathscr{C}(\cdot)$ and is defined as

$$\mathscr{C}(\mathbf{x}) = \left[\frac{\kappa x_1}{\sum_{i=1}^{D} x_i}, \frac{\kappa x_2}{\sum_{i=1}^{D} x_i}, \ldots, \frac{\kappa x_D}{\sum_{i=1}^{D} x_i} \right], \kappa > 0. \tag{A.14}$$

For any dataset one must be able to define a sample space, i.e. a set that contains all possible values, and geochemical data are no exception to this. Often the real space is used because it is most convenient to use the well-known Euclidean geometry, however, this is not an appropriate choice for compositions for several reasons as Pawlowsky-Glahn et al. (2015) outlined. For instance, if confidence intervals are computed based on Euclidean geometry they could fall outside the sample space because the methods are oblivious to the closure condition. Likewise, the Euclidean distance is an inappropriate metric for the measurement of compositional distances because compositions carry only relative information (see above). Aitchison (1982, 1984, 1986) was the first to realise that the appropriate sample space for compositional data is a simplex

$$\mathscr{S}^D = \left\{ \mathbf{x} = [x_1, x_2, \ldots, x_D] \,\middle|\, x_i > 0, i = 1,2,\ldots,D; \sum_{i=1}^{D} x_i = \kappa \right\}. \tag{A.15}$$

The simplex has the properties of a true vector space, thus, Aitchison (1982, 1984, 1986) defined the appropriate vector operations of perturbation and powering for it.

The particular properties of compositional data as outlined above impose the following requirements on any statistical method that is used to analyse such data (Aitchison 1986; Pawlowsky-Glahn et al. 2015):

Scale invariance This means that compositions can be multiplied by any constant positive scalar $\lambda \in \mathbb{R}_+$ without loss of information or, in other words, two compositions $\mathbf{x}$ and $\mathbf{y}$ are *compositionally equivalent* if $f(\lambda\mathbf{x}) = f(\mathbf{y})$. Any method (or function f) applied to the data must yield identical results regardless of the scale of the data, or equivalently, independent of the value of κ (equation (A.14)). A trivial example of a rescaling operation that should never change any results of any method is the conversion from % to ppm in which case $\lambda = 10^4$.

Permutation invariance Compositional vectors do not possess a natural order. Any statistical method must therefore be oblivious to the order of the components of a composition.

Subcompositional coherence A subcomposition $\mathbf{x_S}$ of $\mathbf{x}$ is obtained by forming a vector from any subset of the components $1,2,\ldots,D$ of $\mathbf{x}$ and reclosing by applying $\mathscr{C}(\mathbf{x_S})$. This is an important concept because virtually every geochemical dataset does in fact represent only a subcomposition of the original rock. The reason for this is, that almost never is every single chemical element assayed for. Subcompositional coherence means that ratios between two components of a subcomposition must be equal to the ratio between the same two components of the original composition.

Most statistical methods if directly applied to compositional data will not meet above requirements and can therefore lead to unexpected results and/or erroneous interpretations. The solution proposed by Aitchison (1986) is to apply log-ratio transformations that map each component x_i of the data onto a different value $y_i = f(x_i)$, where f is some function that removes the closure. This has become known as the *principle of working in coordinates* (Pawlowsky-Glahn 2003; Mateu-Figueras et al. 2011).

The log-ratio transformation used in this study are the centered log-ratio (clr) (Aitchison 1986) and the isometric log-ratio (ilr) (Egozcue et al. 2003) transformation. The clr expresses a composition in clr coefficients which results in a vector that is symmetric in its components, that then sum up to 0. The ilr transformation was used for operations that require orthonormal coordinates. It is an isometric mapping $\mathscr{S}^D \rightarrow \mathbb{R}^{D-1}$, thus, the new compositional vector contains $D-1$ ilr coordinates of $\mathbf{x}$. For the sake of completeness it shall be mentioned that Aitchison (1986) also introduced the additive log-ratio (alr) transformation. This transformation is not used in this study because it does not preserve distances between components which are essential for the application of techniques such as linear discriminant analysis (LDA) or principal component analysis (PCA).

A.6 Dimensionality reduction

Whole-rock datasets in igneous geochemistry typically report c. 10 major elements and often 15 or more trace elements. The interpretation of these data, however, rarely involves (or requires) all available variables. Instead, geochemists commonly interpret only selected subcompositions (appendix A.5), e.g. in scatterplots or the rare earth element (REE) in parallel-coordinate plots (so-called 'Spider plots'). There is a wealth of multivariate statistical techniques available that facilitate the reduction of the dimensionality of a dataset, i.e. the selection of the most appropriate/descriptive subcomposition for a particular problem. This section describes the techniques used for this purpose in this study, these being hierarchical cluster analysis (HCA), PCA and LDA.

A.6.1 Principal component analysis

Principal component analysis (PCA; Pearson 1901; Hotelling 1933) is one of the most common techniques for dimensionality reduction. It is an unsupervised multivariate procedure that uses a set of potentially correlated variables $x^T = (x_1, x_2, \ldots, x_D)$, and applies an orthogonal transformation, such that a new set of fully uncorrelated variables $y^T = \left(y_1, y_2, \ldots, y_D\right)$, termed the 'principle components', is obtained. Each of these new variables is a linear combination of all original variables; for instance, the first principle component is obtained with

$$y_1 = a_{11}x_1 + a_{12}x_2 + \cdots + a_{1D}x_D. \tag{A.16}$$

The coefficients a_1^T are chosen such that the variance of this first principle component is the largest possible. PCA in compositional data analysis is described by Boogaart and Tolosana-Delgado (2013) and is carried out by way of a singular value decomposition

(SVD) of the dataset represented as a clr-transformed matrix (appendix A.5). The SVD is the product of the matrixes **U** (orthogonal matrix of left singular values or scores), **D** (diagonal matrix of singular values) and **V** (orthogonal matrix of right singular values or principal components), thus,

$$\mathrm{clr}(X^*) = UDV^T. \tag{A.17}$$

The scaling of the original variables relative to each other affects the results of the PCA. It is therefore important to centre and scale the original set of variables, prior to the analysis. The clr transformation (appendix A.5) takes care of centering the data around the compositional mean.

PCA always results in a number of principle components that is equal or less than the number of original variables. As pointed out above, the first principle component accounts for as much variation in the dataset as possible, with subsequent principle components being orthogonal to the previous ones. Consequently, these subsequent principle components account for a decreasing amount of variation. The actual process of dimensionality reduction is done by selecting a subset of principle components, such that a predefined amount of variation is explained by them. Common values for this threshold are often in the range of 70–90 % of the variation (Everitt and Hothorn 2011). The common tool to explore the results of PCA is the biplot (Gabriel 1971). Biplots can convey information on both, the variables (i.e. their variances and covariances) as well as the samples (i.e. the distances between them). The variance of a variable is displayed as the length of its vector, the covariance between two variables is proportional to the angle between their two vectors; the points on a biplot represent the samples.

A.6.2 Linear discriminant analysis

LDA (e.g. Venables and Ripley 2002; Cherkassky and Mulier 2007; Hastie et al. 2009; Barber 2012; Kuhn and Johnson 2013; Härdle and Simar 2015) is a well-established supervised statistical learning technique that can be used for two different purposes: for classification as well as for dimensionality reduction/variable selection. The aim here is not to classify, i.e. to predict class membership after training the model, but rather to use the accepted (i.e. assumed to be correct) class memberships to reveal the relative importance of the variables. LDA is a convenient technique for this because it results in simple (linear) easy to interpret models. An examples for LDA used for dimensionality reduction rather than classification is Zhu (2001)

Used in this study is the approach after Fisher (1936), which is based on the idea of maximising the *between-class* variance, defined as

$$B = \frac{(GM - 1\bar{x})^T (GM - 1\bar{x})}{g - 1}, \tag{A.18}$$

while at the same time minimising the *within-class* variance, defined as

$$W = \frac{(X - GM)^T (X - GM)}{n - g}. \tag{A.19}$$

In the case of two outcome classes (sulphide oversaturated and sulphide undersaturated; chapter 5) the LDA results in $g-1$, i.e. one set of eigenvalues. The absolute values of the linear discriminant coefficients $abs(\beta)$ are the measure for the importance of the variables. Prior to the analysis the variables are sphered, such that the within-class correlation matrix is the identity matrix. This step removes any influence of the different scales of the variables on the absolute values of the discrimination coefficients $abs(\beta)$. The implementation of the method as used in this study is described in detail in Venables and Ripley (2002) and implemented by the same authors in the R package *MASS* (`https://cran.r-project.org/package=MASS`). The following description follows the implementation and notation of Venables and Ripley (2002):

A.7 Data clustering

Data clustering techniques solve problems of unsupervised classification, where the task is commonly to group some elements such that all elements that are members of one particular group (i.e. cluster) are more 'similar' to each other than to other elements that are not members of that group. There are various ways to cluster data and define measures of similarity. General overviews over different methods can be found in Jain et al. (1999), Xu and Wunsch (2008) and Everitt et al. (2011).

A.7.1 Hierarchical clustering

This study makes use of agglomerative hierarchical clustering (e.g. Jain et al. 1999; Xu and Wunsch 2008; Everitt et al. 2011; Murtagh and Contreras 2011). The particular convenience of hierarchical over partitional clustering methods (e.g. k-means) lies in the fact that the 'natural' number of clusters (i.e. which have some 'real-world' representation within the context of the problem) does not need to be known a priori. The algorithm generally follows a procedure (figure A.2) where each element represents its own cluster at the beginning. The algorithm then enters a loop in which the distance matrix D is computed for all clusters. The two most proximate or similar clusters are then irreversibly joined. The loop is repeated until only a single cluster remains. The algorithm then creates a tree-like data structure made up of nested data partitions.

'Similarity' is measured by computing the pair-wise distance between clusters, which is also called the *linkage*. Used in this study is the complete-linkage method, which means that the distance is defined with a *farthest neighbour* approach: the distance D between two clusters X and Y is the maximum distance out of the distances between all element pairs (x, y), where $x \in X$ and $y \in Y$, or more formally

$$D(X,Y) = \max_{x \in X, y \in Y} d(x,y). \tag{A.20}$$

The complete-linkage method tends to detect compact clusters with small diameters. As a downside, the clusters can sometimes violate the closeness condition, i.e. at the end of the procedure an element of a cluster can in some cases end up being closer to members of another cluster than to its own (Xu and Wunsch 2008; Hastie et al. 2009; Everitt et al.

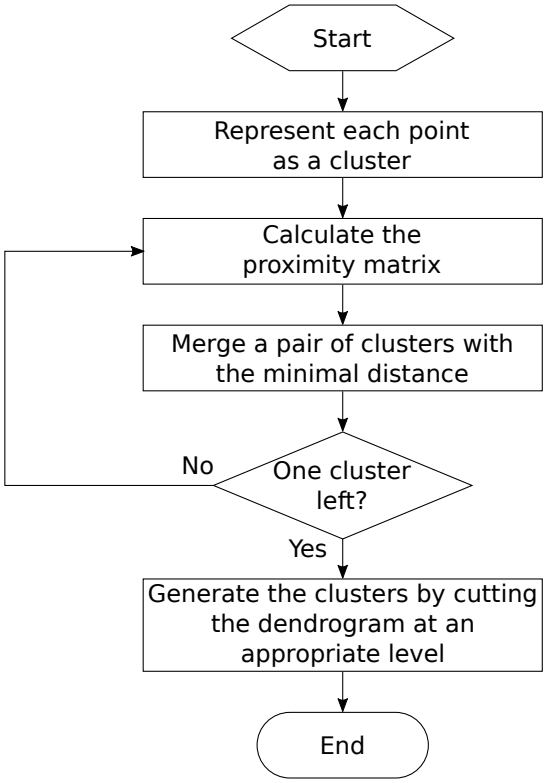

Figure A.2 Flowchart of the hierarchical clustering algorithm (figure adopted from Xu and Wunsch 2008). Each element represents its own cluster at the beginning of the procedure. The algorithm then enters a loop in which the distance matrix D is computed for all clusters. The two most similar clusters are then identified and joined and the loop repeated until only one cluster is left. The algorithm finishes by creating the hierarchical data structure, as visualised in a dendrogram.

2011). The calculation of the distance is then carried-out using the recurrence relation of Lance and Williams (1967, also called Lance-Williams dissimilarity update formula). For instance, assuming three clusters C_i, C_j and C_l, and with $C_{(ij)}$ being a new cluster formed by joining C_i and C_j, the function

$$D(C_l, C_{(ij)}) = \alpha_i D(C_l, C_i) + \alpha_j D(C_l, C_j) + \beta D(C_i, C_j) + \gamma \left| D(C_l, C_i) - D(C_l, C_j) \right| \quad \text{(A.21)}$$

computes the distance D between C_l and $C_{(ij)}$. The coefficients α_i, α_j, β and γ are the agglomeration weights. Their actual values depend on the choice of linkage method (equation (A.20)) and they determine which clusters will be the most proximate and thus be joined. For the complete-linkage method the values for the agglomeration weights in equation (A.21) are $\alpha_i, \alpha_j, \gamma = 1/2$ and $\beta = 0$, respectively. The choice of linkage method must be made individually for each use case and there is no generally optimal method (Xu and Wunsch 2008; Everitt et al. 2011).

Dendrograms are the canonical way to visualise the tree-like hierarchical data structure consisting of the nested clusters or data partitionings as well as the distances between

them. Figure A.3 shows an example of such a dendrogram, where data partitioning 1 is the starting point of the algorithm (see also figure A.2) with each element representing its own cluster. Out of all four elements, c and d are the most similar according to the

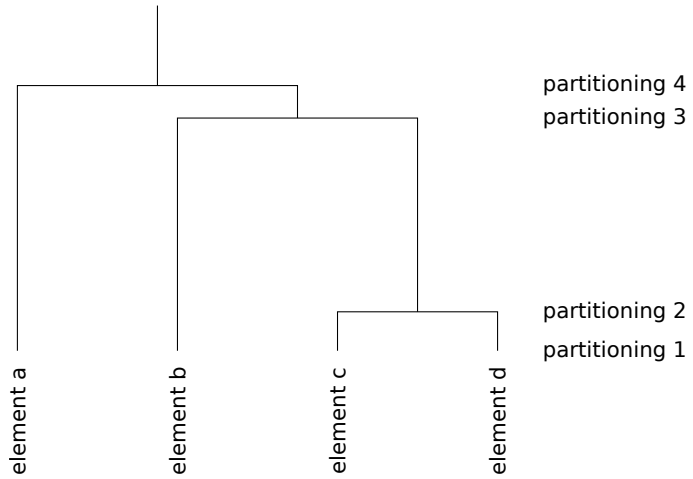

Figure A.3 Example dendrogram for hierarchical clustering (modified from Everitt et al. 2011). Clusters are represented by the nodes of the tree. Internal nodes are drawn as horizontal lines, connecting the members of that cluster, the terminal nodes or leaves are the end points of the tree that represent the individual elements a, b, c and d. The single cluster at the top (the end point of the algorithm, see figure A.2) is the root of the tree. The lengths of the vertical lines (stems) are proportional to the distances between the clusters.

chosen distance metric which leads to partitioning 2. The next join (between (c,d) and b; partitioning 3) is made at a far greater distance as the greater length of the vertical line (stem) shows. The last join is between (b,c,d) and a (partitioning 4). Both clusters (b,c,d) and a are much more similar, however, than (c,d) and b. Finally, the tree structure of the dendrogram needs to be cut at a suitable level, that results in a 'natural' clustering.

Appendix B

Data

The data tables only include the data for those samples that were collected for this study. In addition to the original data, this study is based on data from other published sources. Data for other mafic-ultramafic intrusions of the Giles Event that are located within Western Australia are from the *WACHEM* database of the Geological Survey of Western Australia (GSWA), accessed through the *GeoChem Extract* web portal (`http://geochem.dmp.wa.gov.au/geochem/`). Data for the Nebo-Babel Ni-Cu-PGE sulphide deposit are from Seat (2008), Seat et al. (2009), Godel et al. (2011) and Seat et al. (2011). Appropriate references for all external data are given in the text of the respective chapters.

Table B.1 List of samples including sampling metadata and the estimated stratigraphic depth d. See sections 2.3, 3.3 and 4.3 for a description of the sampling, preparation and analytical procedures, as well as appendix A.1 for the method of depth estimation.

Sample no.	Intrusion	Traverse	UTM zone	m E	m N	d
191 801	Bell Rock Range	south-east	52J	476133	7090736	0
191 802	Bell Rock Range	south-east	52J	476217	7090978	188
191 803	Bell Rock Range	south-east	52J	476467	7091208	515
191 804	Bell Rock Range	south-east	52J	476560	7091454	713
191 805	Bell Rock Range	south-east	52J	476681	7091326	756
191 806	Bell Rock Range	south-east	52J	476904	7091220	898
191 807	Bell Rock Range	south-east	52J	477111	7091347	1137
191 808	Bell Rock Range	south-east	52J	477257	7091357	1268
191 809	Bell Rock Range	south-east	52J	477401	7091267	1350
191 810	Bell Rock Range	south-east	52J	477943	7091274	1821
191 811	Bell Rock Range	south-east	52J	478020	7091526	2008
191 812	Bell Rock Range	south-east	52J	478011	7092057	2255
191 813	Bell Rock Range	south-east	52J	478224	7092003	2413
191 814	Bell Rock Range	south-east	52J	478358	7091858	2459
191 815	Bell Rock Range	south-east	52J	478502	7091829	2570
191 816	Bell Rock Range	south-east	52J	478618	7091933	2720
191 817	Bell Rock Range	south-east	52J	478663	7092265	2918
191 818	Bell Rock Range	south-east	52J	478756	7092479	3101
191 819	Bell Rock Range	south-east	52J	478698	7092917	3260
191 820	Bell Rock Range	south-east	52J	478914	7093614	3780
191 821	Bell Rock Range	south-east	52J	479427	7093330	4088
191 822	Bell Rock Range	south-east	52J	479796	7093443	4461
191 823	Bell Rock Range	south-east	52J	480015	7093523	4688
191 824	Bell Rock Range	south-east	52J	480635	7093614	5267
191 825	Bell Rock Range	south-east	52J	480590	7093852	5342
191 826	Bell Rock Range	south-east	52J	480495	7094056	5358
191 827	Bell Rock Range	south-east	52J	480484	7094346	5487
191 829	Bell Rock Range	centre	52J	473013	7102565	5314
191 830	Bell Rock Range	centre	52J	473164	7102548	5410
191 831	Bell Rock Range	centre	52J	472944	7102345	5112
191 832	Bell Rock Range	centre	52J	472925	7102167	4976
191 834	Bell Rock Range	centre	52J	472862	7102034	4839
191 836	Bell Rock Range	centre	52J	472609	7102228	4792
191 837	Bell Rock Range	centre	52J	472528	7102189	4707
191 838	Bell Rock Range	centre	52J	472341	7102131	4533
191 839	Bell Rock Range	centre	52J	472277	7102117	4477
191 840	Bell Rock Range	centre	52J	472215	7102159	4462

Continued on next page

Table B.1 *Continued from previous page*

Sample no.	Intrusion	Traverse	UTM zone	m E	m N	*d*
191 841	Bell Rock Range	centre	52J	472216	7101935	4308
191 842	Bell Rock Range	centre	52J	472192	7101899	4266
191 843	Bell Rock Range	centre	52J	472168	7101799	4180
191 844	Bell Rock Range	centre	52J	472093	7101747	4090
191 845	Bell Rock Range	centre	52J	472073	7101599	3974
191 846	Bell Rock Range	centre	52J	472061	7101466	3873
191 847	Bell Rock Range	centre	52J	472052	7101356	3791
191 848	Bell Rock Range	centre	52J	472015	7101272	3706
191 849	Bell Rock Range	centre	52J	471991	7101146	3602
191 850	Bell Rock Range	centre	52J	472021	7101059	3563
191 851	Bell Rock Range	centre	52J	472006	7100918	3455
191 852	Bell Rock Range	centre	52J	471882	7100793	3280
191 853	Bell Rock Range	centre	52J	471883	7100672	3197
191 854	Bell Rock Range	centre	52J	471778	7100606	3077
191 855	Bell Rock Range	centre	52J	471911	7100337	2986
191 856	Bell Rock Range	centre	52J	471096	7099054	1517
191 857	Bell Rock Range	centre	52J	471312	7098990	1627
191 858	Bell Rock Range	centre	52J	471216	7099258	1743
191 859	Bell Rock Range	centre	52J	471848	7100132	2799
191 860	Bell Rock Range	centre	52J	471905	7099848	2644
191 861	Bell Rock Range	centre	52J	471756	7099804	2507
191 862	Bell Rock Range	centre	52J	471858	7099610	2446
191 863	Bell Rock Range	centre	52J	471854	7099518	2379
191 864	Bell Rock Range	centre	52J	471754	7099420	2240
191 865	Bell Rock Range	centre	52J	471393	7099347	1931
191 866	Bell Rock Range	centre	52J	471758	7097899	1192
191 867	Bell Rock Range	centre	52J	471623	7097883	1085
191 868	Bell Rock Range	centre	52J	471523	7097891	1019
191 869	Bell Rock Range	centre	52J	471462	7097901	982
191 870	Bell Rock Range	centre	52J	470501	7097816	236
191 871	Bell Rock Range	centre	52J	470306	7097869	133
191 872	Bell Rock Range	centre	52J	470248	7097737	0
191 873	Bell Rock Range	north-west	52J	459406	7111092	2743
191 874	Bell Rock Range	north-west	52J	459441	7110879	2550
191 875	Bell Rock Range	north-west	52J	459289	7110756	2388
191 876	Bell Rock Range	north-west	52J	459129	7110580	2174
191 877	Bell Rock Range	north-west	52J	459065	7110410	1993
191 878	Bell Rock Range	north-west	52J	459182	7110173	1801
191 879	Bell Rock Range	north-west	52J	459721	7109744	1549

Continued on next page

Table B.1 *Continued from previous page*

Sample no.	Intrusion	Traverse	UTM zone	m E	m N	*d*
191 880	Bell Rock Range	north-west	52J	459286	7109697	1377
191 881	Bell Rock Range	north-west	52J	459379	7109565	1278
191 882	Bell Rock Range	north-west	52J	459016	7109616	1221
191 883	Bell Rock Range	north-west	52J	458809	7109491	1042
191 884	Bell Rock Range	north-west	52J	458741	7109268	809
191 885	Bell Rock Range	north-west	52J	458676	7109144	672
191 886	Bell Rock Range	north-west	52J	458628	7109088	604
191 887	Bell Rock Range	north-west	52J	458556	7109026	524
191 888	Bell Rock Range	north-west	52J	459638	7108551	387
191 889	Bell Rock Range	north-west	52J	459889	7108215	139
191 890	Bell Rock Range	north-west	52J	459728	7108118	0
195 161	Wingellina Hills		52J	499471	7115039	426
205 265	Wingellina Hills		52J	497423	7116527	888
205 266	Wingellina Hills		52J	497700	7116492	970
205 267	Wingellina Hills		52J	497860	7116321	886
205 268	Wingellina Hills		52J	499223	7114663	0
205 269	Wingellina Hills		52J	499435	7114933	320
205 270	Wingellina Hills		52J	499401	7115134	480
205 271	Wingellina Hills		52J	499393	7115235	564
205 272	Wingellina Hills		52J	499431	7115320	653
205 273	Wingellina Hills		52J	499555	7115327	710
205 274	Wingellina Hills		52J	500046	7116003	1494
205 275	Wingellina Hills		52J	499845	7115888	1313
205 276	Wingellina Hills		52J	499785	7115827	1236
205 277	Wingellina Hills		52J	499755	7115706	1119
205 278	Wingellina Hills		52J	499704	7115494	915
205 279	Wingellina Hills		52J	499702	7115395	828
205 280	Wingellina Hills		52J	499517	7115369	731
205 281	Wingellina Hills		52J	499465	7115455	784
205 282	Wingellina Hills		52J	498999	7116447	1456
205 283	Wingellina Hills		52J	498973	7116416	1418
205 284	Wingellina Hills		52J	497869	7116479	1027
205 285	Latitude Hill		52J	495891	7085799	3106
205 286	Latitude Hill		52J	495714	7085172	2823
205 287	Latitude Hill		52J	495519	7085453	2717
205 288	Latitude Hill		52J	495395	7085783	2681
205 289	Latitude Hill		52J	495308	7086083	2671
205 290	Latitude Hill		52J	495182	7086190	2587
205 291	Latitude Hill		52J	495031	7086420	2507

Continued on next page

Table B.1 *Continued from previous page*

Sample no.	Intrusion	Traverse	UTM zone	m E	m N	*d*
205 292	Latitude Hill		52J	495029	7086419	2505
205 293	Latitude Hill		52J	494721	7086354	2230
205 294	Latitude Hill		52J	494676	7086355	2192
205 295	Latitude Hill		52J	494545	7086859	2188
205 296	Latitude Hill		52J	494318	7086827	1988
205 297	Latitude Hill		52J	494179	7086883	1882
205 298	Latitude Hill		52J	491592	7088364	0
205 299	Latitude Hill		52J	494086	7087576	1950
205 300	Latitude Hill		52J	493914	7087378	1762
205 301	Latitude Hill		52J	493644	7087360	1529
205 302	Latitude Hill		52J	493457	7087202	1337
205 303	Latitude Hill		52J	493235	7087364	1183
205 304	Latitude Hill		52J	493078	7087345	1045
205 305	Latitude Hill		52J	492886	7087551	926
205 306	Latitude Hill		52J	492549	7087407	610
205 307	Latitude Hill		52J	491845	7088469	237
205 308	Latitude Hill		52J	493070	7088253	1231
205 309	Latitude Hill		52J	492918	7088432	1140
205 310	Latitude Hill		52J	492749	7088539	1019
205 311	Latitude Hill		52J	492542	7088626	862
205 312	Latitude Hill		52J	492388	7088710	749

Table B.2 Whole-rock major element concentrations for all samples. All data are listed in wt%; LOD is the limit of detection (see description of analytical method in sections 3.3.1 and 4.3.1).

Element	Lab/method	LOD	191801	191802	191803	191804	191805	191806	191807	191808	191809
Al_2O_3	Acme/4A	0.01	18.51	24.54	22.96	23.51	21.17	20.36	8.72	23.82	23.76
C	Acme/2A	0.01		0.02	0.03	0.03	0.04	0.04	0.01	0.02	0.03
CaO	Acme/4A	0.01	19.32	11.86	10.51	10.65	9.79	9.49	6.18	12.16	10.96
Cr_2O_3	Acme/4A	0.002	0.069	0.007	0.017	0.023	0.056	0.039	0.023	0.045	0.010
Fe_2O_3	Acme/4A	0.04	8.41	6.01	9.14	8.31	11.61	11.44	24.23	6.46	7.11
K_2O	Acme/4A	0.01	0.04	0.43	0.44	0.38	0.38	0.33	0.12	0.30	0.29
LOI	Acme/2A	-5.1	1.7	0.3	0.2	0.3	-0.4	-0.3	-1.7	0.5	0.3
MgO	Acme/4A	0.01	6.00	1.74	3.12	3.26	5.43	6.77	17.06	3.74	5.37
MnO	Acme/4A	0.01	0.06	0.07	0.09	0.08	0.12	0.12	0.28	0.07	0.08
Na_2O	Acme/4A	0.01	0.24	3.62	3.35	3.38	3.01	2.96	1.25	3.00	2.97
P_2O_5	Acme/4A	0.01	0.02	0.03	0.05	0.05	0.07	0.03	0.02	0.03	0.03
S	Acme/2A	0.01									
SiO_2	Acme/4A	0.01	43.04	49.89	48.31	48.53	47.11	47.42	41.81	48.80	48.53
TiO_2	Acme/4A	0.01	2.30	1.44	1.62	1.35	1.45	1.09	1.64	0.95	0.44

Continued on next page

Table B.2 *Continued from previous page*

Element	Lab/method	LOD	191810	191811	191812	191813	191814	191815	191816	191817	191818
Al_2O_3	Acme/4A	0.01	22.92	21.23	20.84	22.26	19.81	21.74	18.05	22.50	14.87
C	Acme/2A	0.01	0.03	0.02	0.05	0.06	0.05	0.03	0.02	0.02	0.06
CaO	Acme/4A	0.01	10.66	9.21	9.36	10.65	9.51	10.59	9.51	10.55	7.69
Cr_2O_3	Acme/4A	0.002	0.004	0.004	0.041	0.039	0.038	0.012	0.009	0.005	0.016
Fe_2O_3	Acme/4A	0.04	8.15	9.88	10.21	8.82	12.02	8.84	12.46	8.31	15.83
K_2O	Acme/4A	0.01	0.25	0.25	0.24	0.24	0.17	0.20	0.18	0.24	0.14
LOI	Acme/2A	-5.1	-0.3	-0.2	0.3	0.2	-0.3	-0.3	-0.2	0.0	-0.7
MgO	Acme/4A	0.01	7.18	9.28	9.07	7.12	10.27	7.80	9.24	6.59	14.82
MnO	Acme/4A	0.01	0.09	0.11	0.13	0.10	0.13	0.10	0.15	0.10	0.18
Na_2O	Acme/4A	0.01	2.74	2.61	2.55	2.66	2.21	2.61	2.32	2.90	1.76
P_2O_5	Acme/4A	0.01	0.03	0.04	0.02	0.02	0.02	0.01	0.02	0.02	0.02
S	Acme/2A	0.01				0.01					
SiO_2	Acme/4A	0.01	47.77	46.94	46.54	47.13	45.35	47.94	47.45	48.22	44.72
TiO_2	Acme/4A	0.01	0.29	0.37	0.44	0.55	0.47	0.26	0.57	0.39	0.26

Continued on next page

Table B.2 *Continued from previous page*

Element	Lab/method	LOD	191819	191820	191821	191822	191823	191824	191825	191826	191827
Al_2O_3	Acme/4A	0.01	20.05	16.93	18.03	15.42	22.28	22.97	18.65	15.72	20.01
C	Acme/2A	0.01	0.06	0.02	0.06	0.04	0.02	0.03	0.04	0.04	0.06
CaO	Acme/4A	0.01	10.36	16.30	14.78	14.64	16.27	14.29	15.99	16.02	14.89
Cr_2O_3	Acme/4A	0.002	0.011	0.145	0.044	0.082	0.153	0.130	0.286	0.079	0.188
Fe_2O_3	Acme/4A	0.04	10.75	5.30	7.03	8.17	4.04	4.75	4.88	5.75	5.57
K_2O	Acme/4A	0.01	0.26	0.03	0.14	0.05	0.07	0.05	0.06	0.04	0.05
LOI	Acme/2A	-5.1	0.0	0.5	0.5	1.1	0.6	1.6	1.0	0.9	0.9
MgO	Acme/4A	0.01	7.87	11.56	8.97	10.31	7.89	9.69	9.82	11.73	10.85
MnO	Acme/4A	0.01	0.13	0.10	0.13	0.15	0.07	0.07	0.09	0.11	0.10
Na_2O	Acme/4A	0.01	2.47	0.88	1.49	1.37	1.11	1.08	1.09	1.01	1.04
P_2O_5	Acme/4A	0.01	0.06		0.02		0.01	0.01			0.01
S	Acme/2A	0.01			0.02	0.02	0.01	0.01			0.01
SiO_2	Acme/4A	0.01	46.97	47.88	48.43	48.23	47.24	45.11	47.79	48.26	46.07
TiO_2	Acme/4A	0.01	0.85	0.14	0.27	0.25	0.13	0.10	0.15	0.17	0.15

Continued on next page

Table B.2 *Continued from previous page*

Element	Lab/method	LOD	191829	191830	191831	191832	191834	191836	191837	191838	191839
Al_2O_3	Acme/4A	0.01	15.22	14.19	17.03	18.15	17.70	16.81	23.06	18.52	16.53
C	Acme/2A	0.01	0.01	0.05	0.08	0.07	0.03	0.04	0.02	0.05	0.08
CaO	Acme/4A	0.01	10.89	10.67	8.57	12.60	8.71	8.67	11.74	10.20	10.33
Cr_2O_3	Acme/4A	0.002	0.031	0.002	0.014	0.075	0.006	0.008	0.007	0.020	0.055
Fe_2O_3	Acme/4A	0.04	14.87	17.56	12.11	9.02	13.81	14.46	7.12	11.84	12.33
K_2O	Acme/4A	0.01	0.14	0.28	0.57	0.19	0.22	0.20	0.28	0.19	0.26
LOI	Acme/2A	-5.1	0.4	-0.4	0.2	0.7	-0.6	-0.7	0.1	-0.8	0.0
MgO	Acme/4A	0.01	8.77	5.67	6.35	6.96	10.43	12.17	5.05	9.74	9.34
MnO	Acme/4A	0.01	0.21	0.24	0.20	0.13	0.16	0.16	0.08	0.14	0.17
Na_2O	Acme/4A	0.01	1.78	2.40	2.83	2.44	2.29	2.08	2.83	2.04	2.14
P_2O_5	Acme/4A	0.01	0.27	0.31	0.07	0.05	0.04	0.03	0.10	0.02	0.10
S	Acme/2A	0.01	0.02	0.02	0.05	0.01	0.01	0.01	0.01		0.07
SiO_2	Acme/4A	0.01	45.81	46.82	50.74	48.76	46.18	45.20	48.73	46.77	47.58
TiO_2	Acme/4A	0.01	1.28	1.94	1.06	0.80	0.75	0.61	0.71	0.72	0.88

Continued on next page

Table B.2 *Continued from previous page*

Element	Lab/method	LOD	191840	191841	191842	191843	191844	191845	191846	191847	191848
Al_2O_3	Acme/4A	0.01	20.32	15.33	20.86	22.97	16.89	23.12	23.13	23.11	24.24
C	Acme/2A	0.01	0.05	0.08	0.03	0.03	0.05	0.03	0.04	0.07	0.03
CaO	Acme/4A	0.01	10.45	10.67	10.37	11.36	7.94	11.19	11.38	11.27	11.08
Cr_2O_3	Acme/4A	0.002	0.005	0.123	0.008	0.005	0.009	0.005	0.007	0.009	0.004
Fe_2O_3	Acme/4A	0.04	10.79	12.16	9.98	7.25	13.92	7.05	7.11	6.85	6.75
K_2O	Acme/4A	0.01	0.22	0.27	0.24	0.20	0.13	0.23	0.24	0.22	0.22
LOI	Acme/2A	-5.1	-0.3	-0.1	0.5	0.5	-0.6	0.3	0.3	0.6	-0.2
MgO	Acme/4A	0.01	7.86	10.66	7.03	6.26	14.17	5.81	5.25	5.68	5.55
MnO	Acme/4A	0.01	0.12	0.18	0.11	0.08	0.16	0.08	0.08	0.08	0.07
Na_2O	Acme/4A	0.01	2.45	2.03	2.68	2.73	2.00	2.90	2.97	2.85	3.07
P_2O_5	Acme/4A	0.01	0.02	0.10	0.01	0.02	0.01	0.01	0.01	0.02	0.02
S	Acme/2A	0.01		0.08							
SiO_2	Acme/4A	0.01	47.04	47.29	47.32	48.08	44.89	48.88	48.91	48.80	48.83
TiO_2	Acme/4A	0.01	0.78	0.97	0.65	0.34	0.16	0.22	0.41	0.32	0.19

Continued on next page

Table B.2 *Continued from previous page*

Element	Lab/method	LOD	191849	191850	191851	191852	191853	191854	191855	191856	191857
Al_2O_3	Acme/4A	0.01	22.07	23.33	21.79	23.30	24.48	16.36	20.50	23.47	23.02
C	Acme/2A	0.01	0.03	0.04	0.04	0.06	0.03	0.08	0.03		0.02
CaO	Acme/4A	0.01	10.21	11.08	10.42	10.75	11.85	10.93	11.35	10.43	10.11
Cr_2O_3	Acme/4A	0.002	0.005	0.007	0.030	0.081	0.007	0.081	0.060	0.022	0.067
Fe_2O_3	Acme/4A	0.04	8.66	7.31	9.50	8.40	5.91	11.65	9.25	9.41	9.58
K_2O	Acme/4A	0.01	0.17	0.18	0.22	0.22	0.27	0.25	0.20	0.33	0.30
LOI	Acme/2A	-5.1	0.2	0.2	0.1	1.1	0.3	-0.2	0.1	-0.2	-0.3
MgO	Acme/4A	0.01	8.54	6.90	8.24	5.46	4.56	9.41	7.88	3.86	5.17
MnO	Acme/4A	0.01	0.10	0.08	0.10	0.08	0.06	0.17	0.10	0.08	0.09
Na_2O	Acme/4A	0.01	2.61	2.69	2.38	2.83	3.02	2.11	2.42	3.32	3.22
P_2O_5	Acme/4A	0.01	0.02	0.01	0.03	0.01	0.02	0.09	0.01	0.04	0.02
S	Acme/2A	0.01						0.04			
SiO_2	Acme/4A	0.01	47.11	47.85	46.48	46.86	49.06	48.07	47.41	47.85	47.71
TiO_2	Acme/4A	0.01	0.14	0.16	0.44	0.68	0.30	0.80	0.48	1.18	0.82

Continued on next page

Table B.2 *Continued from previous page*

Element	Lab/method	LOD	191858	191859	191860	191861	191862	191863	191864	191865	191866
Al_2O_3	Acme/4A	0.01	16.10	23.60	19.48	22.72	23.45	20.38	20.61	15.55	25.38
C	Acme/2A	0.01	0.02	0.02	0.04	0.05	0.03	0.02	0.04	0.03	0.02
CaO	Acme/4A	0.01	7.04	10.92	8.92	10.55	10.77	11.69	11.47	7.04	12.02
Cr_2O_3	Acme/4A	0.002	0.143	0.008	0.025	0.038	0.037	0.079	0.038	0.039	0.008
Fe_2O_3	Acme/4A	0.04	19.28	7.10	11.81	8.40	7.67	9.51	8.71	17.31	4.55
K_2O	Acme/4A	0.01	0.18	0.26	0.18	0.24	0.24	0.19	0.20	0.18	0.32
LOI	Acme/2A	-5.1	-1.0	0.5	-0.5	0.0	0.1	-0.2	-0.2	-0.8	1.1
MgO	Acme/4A	0.01	11.76	6.01	11.32	7.31	6.31	7.47	7.87	13.41	1.69
MnO	Acme/4A	0.01	0.19	0.07	0.13	0.09	0.08	0.10	0.10	0.19	0.04
Na_2O	Acme/4A	0.01	2.10	2.90	2.31	2.77	2.90	2.37	2.56	2.07	3.65
P_2O_5	Acme/4A	0.01		0.02	0.01	0.02	0.02	0.02	0.02	0.03	0.03
S	Acme/2A	0.01									
SiO_2	Acme/4A	0.01	42.80	48.16	45.86	47.34	47.87	47.36	47.96	44.41	50.08
TiO_2	Acme/4A	0.01	1.06	0.25	0.17	0.30	0.35	0.74	0.44	0.27	0.88

Continued on next page

Table B.2 *Continued from previous page*

Element	Lab/method	LOD	191867	191868	191869	191870	191871	191872	191873	191874	191875
Al_2O_3	Acme/4A	0.01	26.15	25.64	12.91	22.84	23.06	22.80	21.34	21.57	23.40
C	Acme/2A	0.01									0.02
CaO	Acme/4A	0.01	12.02	11.90	11.30	10.69	11.29	11.26	10.57	11.43	11.40
Cr_2O_3	Acme/4A	0.002	0.010	0.010		0.006	0.009	0.008	0.015	0.012	0.058
Fe_2O_3	Acme/4A	0.04	3.39	3.83	18.41	7.46	6.84	7.57	8.79	8.73	8.32
K_2O	Acme/4A	0.01	0.39	0.39	0.20	0.73	0.66	0.62	0.24	0.25	0.26
LOI	Acme/2A	-5.1	1.0	1.2	-0.4	0.5	0.5	0.2	-0.4	-0.2	-0.1
MgO	Acme/4A	0.01	1.19	1.32	5.94	1.82	1.78	1.85	7.54	5.98	5.14
MnO	Acme/4A	0.01	0.04	0.04	0.19	0.09	0.08	0.09	0.10	0.11	0.09
Na_2O	Acme/4A	0.01	3.74	3.70	1.95	3.51	3.50	3.40	2.70	2.68	2.74
P_2O_5	Acme/4A	0.01	0.03	0.04	0.03	0.21	0.17	0.20	0.03	0.04	0.04
S	Acme/2A	0.01									0.02
SiO_2	Acme/4A	0.01	51.07	50.84	41.47	50.58	50.49	50.18	48.52	48.49	47.44
TiO_2	Acme/4A	0.01	0.84	0.97	7.62	1.39	1.43	1.66	0.35	0.72	0.99

Continued on next page

Table B.2 *Continued from previous page*

Element	Lab/method	LOD	191876	191877	191878	191879	191880	191881	191882	191883	191884
Al_2O_3	Acme/4A	0.01	21.30	15.64	20.33	23.18	21.56	24.73	22.07	18.81	18.34
C	Acme/2A	0.01	0.02	0.01	0.01	0.02	0.04	0.03	0.02	0.01	0.05
CaO	Acme/4A	0.01	10.07	7.95	10.27	10.77	10.09	11.50	12.27	10.44	9.28
Cr_2O_3	Acme/4A	0.002	0.035	0.029	0.086	0.082	0.009	0.003	0.036	0.016	0.021
Fe_2O_3	Acme/4A	0.04	9.89	15.40	9.33	9.13	9.59	6.41	7.52	11.74	12.19
K_2O	Acme/4A	0.01	0.19	0.19	0.24	0.31	0.25	0.28	0.22	0.19	0.17
LOI	Acme/2A	-5.1	-0.1	-0.7	-0.1	-0.2	0.8	-0.1	0.7	-0.5	-0.6
MgO	Acme/4A	0.01	8.69	14.31	8.14	5.44	8.30	4.58	5.92	7.98	11.45
MnO	Acme/4A	0.01	0.11	0.17	0.11	0.09	0.10	0.07	0.09	0.14	0.14
Na_2O	Acme/4A	0.01	2.40	1.76	2.54	2.89	2.63	3.00	2.46	2.43	2.22
P_2O_5	Acme/4A	0.01	0.04	0.03	0.02	0.04	0.03	0.03	0.02	0.01	0.02
S	Acme/2A	0.01									
SiO_2	Acme/4A	0.01	46.66	44.61	48.24	47.08	47.35	48.88	47.90	46.76	46.28
TiO_2	Acme/4A	0.01	0.47	0.26	0.56	0.97	0.38	0.44	0.58	1.69	0.19

Continued on next page

Table B.2 *Continued from previous page*

Element	Lab/method	LOD	191885	191886	191887	191888	191889	191890	195161	205265	205266
Al_2O_3	Acme/4A	0.01	23.82	16.21	27.72	25.00	20.62	22.49	17.46	16.54	13.75
C	Acme/2A	0.01	0.01	0.11	0.02	0.03	0.02	0.04	0.02	0.02	0.04
CaO	Acme/4A	0.01	10.83	8.89	12.83	12.09	9.25	9.96	15.97	16.01	12.76
Cr_2O_3	Acme/4A	0.002	0.030	0.060	0.021	0.039	0.027	0.070	0.190	0.242	0.114
Fe_2O_3	Acme/4A	0.04	7.37	12.11	3.42	5.93	11.24	10.42	4.25	5.04	9.19
K_2O	Acme/4A	0.01	0.23	0.44	0.24	0.26	0.25	0.29	0.03	0.04	0.35
LOI	Acme/2A	-5.1	-0.2	0.1	0.2	0.0	-0.7	-0.1	0.5	0.2	0.1
MgO	Acme/4A	0.01	6.61	8.56	2.45	3.65	8.56	5.62	10.91	11.28	12.38
MnO	Acme/4A	0.01	0.08	0.19	0.03	0.06	0.12	0.10	0.09	0.10	0.15
Na_2O	Acme/4A	0.01	2.82	2.54	3.17	3.07	2.75	3.00	1.28	1.11	1.36
P_2O_5	Acme/4A	0.01	0.02	0.07	0.02	0.03	0.03	0.03			0.03
S	Acme/2A	0.01		0.05							
SiO_2	Acme/4A	0.01	47.92	49.55	49.60	49.10	47.32	47.03	48.99	49.08	49.11
TiO_2	Acme/4A	0.01	0.26	1.01	0.20	0.63	0.28	0.88	0.09	0.13	0.41

Continued on next page

Table B.2 *Continued from previous page*

Element	Lab/method	LOD	205267	205268	205269	205270	205271	205272	205273	205274	205275
Al_2O_3	Acme/4A	0.01	13.39	19.29	16.55	16.68	11.80	16.38	16.58	3.70	17.25
C	Acme/2A	0.01	0.04		0.03	0.02	0.02	0.04	0.02	0.01	0.02
CaO	Acme/4A	0.01	13.16	12.72	15.15	15.77	12.40	15.10	14.78	17.39	17.04
Cr_2O_3	Acme/4A	0.002	0.135	0.065	0.158	0.051	0.119	0.106	0.135	0.574	0.202
Fe_2O_3	Acme/4A	0.04	9.15	5.29	4.80	4.44	7.83	5.51	5.01	7.22	3.75
K_2O	Acme/4A	0.01	0.10	0.15	0.02	0.05	0.05	0.05	0.05	0.02	0.02
LOI	Acme/2A	-5.1	0.2	0.2	0.2	0.3	0.1	0.1	0.3	0.1	0.3
MgO	Acme/4A	0.01	14.16	8.42	12.98	10.35	14.61	11.96	11.57	17.70	11.12
MnO	Acme/4A	0.01	0.15	0.10	0.09	0.10	0.17	0.11	0.11	0.17	0.08
Na_2O	Acme/4A	0.01	1.17	2.01	1.08	1.36	0.94	1.20	1.24	0.33	0.90
P_2O_5	Acme/4A	0.01									
S	Acme/2A	0.01						0.01			
SiO_2	Acme/4A	0.01	47.73	51.43	48.61	50.53	51.56	49.12	49.88	52.20	49.01
TiO_2	Acme/4A	0.01	0.28	0.12	0.08	0.12	0.13	0.11	0.12	0.20	0.08

Continued on next page

Table B.2 *Continued from previous page*

Element	Lab/method	LOD	205276	205277	205278	205279	205280	205281	205282	205283	205284
Al_2O_3	Acme/4A	0.01	17.55	5.37	16.64	15.58	4.72	15.68	6.95	16.76	9.81
C	Acme/2A	0.01	0.02	0.01	0.01		0.02	0.02	0.02	0.02	0.02
CaO	Acme/4A	0.01	17.00	17.11	16.56	15.66	16.83	14.65	16.96	16.46	11.27
Cr_2O_3	Acme/4A	0.002	0.218	0.118	0.141	0.216	0.656	0.148	0.506	0.269	0.124
Fe_2O_3	Acme/4A	0.04	3.97	7.96	4.53	5.51	7.76	5.26	6.91	5.13	12.70
K_2O	Acme/4A	0.01	0.02	0.01	0.03	0.03	0.02	0.07	0.03	0.05	0.09
LOI	Acme/2A	-5.1	0.4	0.1	0.1	0.3	0.2	0.2	-0.1	0.2	-0.2
MgO	Acme/4A	0.01	10.41	16.54	10.83	11.87	17.20	11.91	15.95	10.20	15.05
MnO	Acme/4A	0.01	0.08	0.20	0.09	0.11	0.17	0.11	0.15	0.10	0.20
Na_2O	Acme/4A	0.01	1.05	0.43	1.13	1.14	0.40	1.20	0.58	1.20	0.96
P_2O_5	Acme/4A	0.01									
S	Acme/2A	0.01									0.01
SiO_2	Acme/4A	0.01	48.95	51.60	49.61	49.20	51.43	50.39	51.52	49.25	49.36
TiO_2	Acme/4A	0.01	0.11	0.21	0.13	0.12	0.24	0.13	0.18	0.16	0.27

Continued on next page

Table B.2 *Continued from previous page*

Element	Lab/method	LOD	205285	205286	205287	205288	205289	205290	205291	205292	205293
Al_2O_3	Acme/4A	0.01	3.78	10.17	3.50	3.78	17.14	3.79	14.73	6.64	7.58
C	Acme/2A	0.01	0.02	0.06	0.03	0.02	0.02	0.03	0.16	0.04	0.04
CaO	Acme/4A	0.01	16.42	15.18	5.63	15.70	14.00	2.91	8.07	6.93	15.51
Cr_2O_3	Acme/4A	0.002	0.130	0.034	0.503	0.156	0.032	0.342	0.039	0.405	0.282
Fe_2O_3	Acme/4A	0.04	10.90	9.05	15.50	11.81	6.16	14.86	11.64	11.78	7.93
K_2O	Acme/4A	0.01	0.01	0.07		0.01	0.13		1.14	0.02	0.02
LOI	Acme/2A	-5.1	-0.3	0.2	-0.5	-0.2	0.1	-0.2	0.5	0.0	0.2
MgO	Acme/4A	0.01	16.17	11.94	21.96	16.26	8.41	24.89	7.94	20.77	16.08
MnO	Acme/4A	0.01	0.23	0.18	0.25	0.24	0.12	0.25	0.18	0.21	0.18
Na_2O	Acme/4A	0.01	0.35	1.32	0.16	0.36	2.17	0.09	2.81	0.44	0.54
P_2O_5	Acme/4A	0.01							0.20		
S	Acme/2A	0.01							0.08		
SiO_2	Acme/4A	0.01	51.47	51.19	52.11	51.05	51.31	52.28	51.39	52.07	51.04
TiO_2	Acme/4A	0.01	0.44	0.37	0.33	0.45	0.23	0.24	1.06	0.25	0.25

Continued on next page

Table B.2 *Continued from previous page*

Element	Lab/method	LOD	205294	205295	205296	205297	205298	205299	205300	205301	205302
Al_2O_3	Acme/4A	0.01	5.57	5.74	11.48	5.84	16.40	5.88	5.58	8.54	3.46
C	Acme/2A	0.01	0.06	0.17	0.06	0.05	0.03	0.13	0.05	0.02	0.05
CaO	Acme/4A	0.01	15.15	14.50	14.46	14.70	11.37	15.02	15.46	14.39	15.18
Cr_2O_3	Acme/4A	0.002	0.402	0.385	0.213	0.392	0.035	0.385	0.540	0.074	0.124
Fe_2O_3	Acme/4A	0.04	8.72	10.05	7.32	8.85	8.50	8.90	8.09	10.95	13.78
K_2O	Acme/4A	0.01	0.02	0.01	0.03	0.02	0.26	0.04	0.01	0.04	
LOI	Acme/2A	-5.1	0.5	0.0	0.5	0.1	0.1	0.4	0.1	0.3	0.0
MgO	Acme/4A	0.01	17.32	17.16	14.30	17.31	8.04	17.07	17.32	13.15	15.54
MnO	Acme/4A	0.01	0.19	0.20	0.16	0.19	0.15	0.19	0.18	0.23	0.27
Na_2O	Acme/4A	0.01	0.45	0.43	0.80	0.47	2.60	0.51	0.48	1.08	0.35
P_2O_5	Acme/4A	0.01	0.02	0.02		0.01		0.02	0.01	0.01	0.01
S	Acme/2A	0.01									
SiO_2	Acme/4A	0.01	50.97	50.77	50.24	51.38	52.07	50.84	51.62	50.55	50.37
TiO_2	Acme/4A	0.01	0.30	0.32	0.20	0.31	0.27	0.35	0.21	0.36	0.52

Continued on next page

Table B.2 *Continued from previous page*

Element	Lab/method	LOD	205303	205304	205305	205306	205307	205308	205309	205310	205311
Al_2O_3	Acme/4A	0.01	6.64	3.84	6.92	16.35	17.16	14.38	3.97	6.17	13.91
C	Acme/2A	0.01	0.11	0.16	0.02	0.07	0.04	0.07	0.14	0.03	0.05
CaO	Acme/4A	0.01	12.08	16.29	4.99	9.38	8.02	8.59	16.64	16.08	8.76
Cr_2O_3	Acme/4A	0.002	0.412	0.130	0.625	0.024	0.059	0.082	0.120	0.056	0.012
Fe_2O_3	Acme/4A	0.04	10.53	11.92	13.42	13.32	8.21	12.39	11.16	11.36	17.65
K_2O	Acme/4A	0.01	0.02		0.01	0.23	0.13	0.87		0.02	1.04
LOI	Acme/2A	-5.1	0.5	0.4	0.0	-0.4	0.1	-0.3	0.6	0.1	-0.8
MgO	Acme/4A	0.01	17.57	15.60	21.09	7.86	11.33	11.66	15.40	13.69	6.06
MnO	Acme/4A	0.01	0.21	0.23	0.23	0.20	0.14	0.18	0.23	0.22	0.23
Na_2O	Acme/4A	0.01	0.53	0.35	0.40	2.58	2.28	2.43	0.37	0.77	2.81
P_2O_5	Acme/4A	0.01		0.01		0.01		0.18	0.01	0.01	0.58
S	Acme/2A	0.01				0.02		0.06			0.07
SiO_2	Acme/4A	0.01	50.84	50.25	51.61	49.40	52.16	48.05	50.73	50.71	45.90
TiO_2	Acme/4A	0.01	0.27	0.57	0.22	0.80	0.14	1.10	0.42	0.46	3.47

Continued on next page

Table B.2 *Continued from previous page*

Element	Lab/method	LOD	205312
Al_2O_3	Acme/4A	0.01	14.68
C	Acme/2A	0.01	0.05
CaO	Acme/4A	0.01	11.14
Cr_2O_3	Acme/4A	0.002	0.128
Fe_2O_3	Acme/4A	0.04	8.04
K_2O	Acme/4A	0.01	0.08
LOI	Acme/2A	-5.1	0.2
MgO	Acme/4A	0.01	12.35
MnO	Acme/4A	0.01	0.15
Na_2O	Acme/4A	0.01	1.61
P_2O_5	Acme/4A	0.01	0.01
S	Acme/2A	0.01	0.01
SiO_2	Acme/4A	0.01	51.11
TiO_2	Acme/4A	0.01	0.20

Table B.3 Whole-rock trace element concentrations for all samples. All data are listed in ppm; LOD is the limit of detection (see description of analytical method in sections 3.3.1 and 4.3.1).

Element	Lab/method	LOD	191801	191802	191803	191804	191805	191806	191807	191808	191809
Ag	Acme/1EX	0.1									
Ag	Acme/1F-MS	0.002	0.003	0.046	0.030	0.024	0.026	0.026	0.015	0.024	0.019
As	Acme/1EX	1									
As	Acme/1F-MS	0.1			0.2		0.1	0.2	0.2		0.1
Au	Acme/3B-MS	0.001		0.007			0.001				
B	Acme/1F-MS	1									
Ba	Acme/4B	1	16	139	125	124	112	112	36	90	91
Be	Acme/1EX	1									
Be	Acme/1F-MS	0.1					0.1			0.1	
Bi	Acme/1EX	0.1									
Bi	Acme/1F-MS	0.02									
Cd	Acme/1EX	0.1									
Cd	Acme/1F-MS	0.01		0.01	0.02	0.02	0.03	0.01	0.03	0.01	0.01
Ce	Acme/4B	0.1	5.8	7.7	9.7	10.1	11.7	5.5	3.2	6.1	5.7
Co	Acme/1EX	0.2									
Co	Acme/1F-MS	0.1	1.6	6.5	22.6	23.9	40.8	49.5	116.0	15.5	35.8
Cs	Acme/4B	0.1									
Cu	Acme/1EX	0.1									
Cu	Acme/1F-MS	0.01	1.15	106.47	65.82	48.50	57.25	52.55	26.80	59.86	49.25
Dy	Acme/4B	0.05	1.13	0.99	1.10	1.05	1.34	0.67	0.90	0.82	0.53
Er	Acme/4B	0.03	0.68	0.57	0.63	0.62	0.74	0.44	0.51	0.44	0.27
Eu	Acme/4B	0.02	1.56	1.44	1.27	1.16	1.12	1.21	0.49	0.86	0.76
Ga	Acme/4B	0.5	27.9	27.6	27.0	26.5	24.7	23.6	10.4	25.0	23.5

Continued on next page

Table B.3 *Continued from previous page*

Element	Lab/method	LOD	191801	191802	191803	191804	191805	191806	191807	191808	191809
Gd	Acme/4B	0.05	1.09	1.09	1.16	1.26	1.57	0.81	0.83	0.87	0.66
Ge	Acme/1F-MS	0.1					0.1		0.2		
Hf	Acme/4B	0.1	0.7	0.8	0.9	1.0	1.2	0.5	0.5	0.5	0.3
Hg	Acme/1F-MS	0.005			0.008	0.008					0.007
Ho	Acme/4B	0.02	0.24	0.22	0.22	0.21	0.27	0.14	0.20	0.15	0.10
In	Acme/1F-MS	0.02									
La	Acme/4B	0.1	3.1	4.1	4.8	4.7	5.4	2.9	1.5	3.0	2.9
Li	Acme/1EX	0.1									
Li	Acme/1F-MS	0.1		1.9	1.4	2.6	2.8	2.2	3.0	1.8	1.5
Lu	Acme/4B	0.01	0.12	0.09	0.09	0.09	0.11	0.06	0.08	0.07	0.04
Mo	Acme/1EX	0.1									
Mo	Acme/1F-MS	0.01	0.01	0.09	0.11	0.11	0.13	0.05	0.09	0.06	0.03
Nb	Acme/4B	0.1	4.1	2.7	2.6	2.8	3.5	1.7	1.8	1.5	1.0
Nd	Acme/4B	0.3	3.3	4.5	5.2	5.3	6.9	2.9	2.6	3.4	2.8
Ni	Acme/7TD	10	144	22	83	81	144	169	511	95	160
Pb	Acme/1EX	0.1									
Pb	Acme/1F-MS	0.01	0.72	1.03	0.46	1.05	0.53	0.49	0.51	0.59	0.40
Pd	Acme/3B-MS	0.0005	0.0012	0.0014	0.0013		0.0014	0.0005	0.0006	0.0011	
Pr	Acme/4B	0.02	0.77	0.98	1.24	1.30	1.54	0.72	0.52	0.76	0.70
Pt	Acme/3B-MS	0.0001	0.0014	0.0025	0.0019	0.0014	0.0006	0.0007	0.0003	0.0025	0.0008
Rb	Acme/4B	0.1	0.5	3.4	5.0	4.6	6.3	1.8	1.0	2.2	2.3
Re	Acme/1F-MS	0.001		0.001							
Sb	Acme/1EX	0.1									

Continued on next page

Table B.3 *Continued from previous page*

Element	Lab/method	LOD	191801	191802	191803	191804	191805	191806	191807	191808	191809
Sb	Acme/1F-MS	0.02									
Sc	Acme/4B	1	14	11	8	7	8	9	21	11	5
Se	Acme/1F-MS	0.1									
Se	GeoLabs/IMH-100	0.0035									
Sm	Acme/4B	0.05	0.87	1.05	1.13	1.16	1.39	0.70	0.70	0.82	0.58
Sn	Acme/4B	1									
Sr	Acme/4B	0.5	864.8	446.4	402.2	420.2	379.0	366.1	161.4	416.6	408.7
Ta	Acme/4B	0.1	0.3	0.2	0.2	0.2	0.2	0.1	0.1		
Tb	Acme/4B	0.01	0.20	0.20	0.20	0.21	0.27	0.14	0.16	0.14	0.10
Te	Acme/1F-MS	0.02									
Te	GeoLabs/IMH-100	0.001									
Th	Acme/4B	0.2		0.2	0.5	0.7	1.1				
Tl	Acme/1F-MS	0.02									
Tm	Acme/4B	0.01	0.12	0.10	0.10	0.09	0.12	0.07	0.07	0.07	0.04
U	Acme/4B	0.1				0.1	0.1				
V	Acme/4B	8	664	240	398	374	391	243	272	209	47
W	Acme/4B	0.5									
Y	Acme/4B	0.1	6.7	5.4	5.7	5.9	7.4	3.9	5.0	4.2	2.9
Yb	Acme/4B	0.05	0.74	0.46	0.57	0.46	0.64	0.36	0.52	0.42	0.25
Zn	Acme/1EX	1									
Zn	Acme/1F-MS	0.1	0.7	9.5	18.4	13.7	30.8	31.1	95.0	10.9	24.8
Zr	Acme/4B	0.1	22.1	22.6	32.0	35.7	49.9	13.1	15.9	14.8	13.1

Continued on next page

Table B.3 *Continued from previous page*

Element	Lab/method code	LOD	191810	191811	191812	191813	191814	191815	191816	191817	191818
Ag	Acme/1EX	0.1									
Ag	Acme/1F-MS	0.002	0.014	0.019	0.039	0.034	0.026	0.017	0.022	0.019	0.013
As	Acme/1EX	1									
As	Acme/1F-MS	0.1	0.1	0.2	0.1		0.1				
Au	Acme/3B-MS	0.001		0.001				0.001			
B	Acme/1F-MS	1									
Ba	Acme/4B	1	79	73	90	76	61	58	58	76	47
Be	Acme/1EX	1									
Be	Acme/1F-MS	0.1				0.1	0.1	0.1			
Bi	Acme/1EX	0.1									
Bi	Acme/1F-MS	0.02									
Cd	Acme/1EX	0.1									
Cd	Acme/1F-MS	0.01	0.01	0.02	0.07	0.03	0.02	0.02		0.01	0.02
Ce	Acme/4B	0.1	5.8	5.9	4.3	5.6	3.5	3.4	3.7	4.7	4.4
Co	Acme/1EX	0.2									
Co	Acme/1F-MS	0.1	45.0	59.0	52.8	41.1	68.3	45.2	49.4	43.4	96.1
Cs	Acme/4B	0.1									
Cu	Acme/1EX	0.1									
Cu	Acme/1F-MS	0.01	28.37	37.20	33.35	66.45	50.85	29.04	40.49	32.43	20.56
Dy	Acme/4B	0.05	0.55	0.51	0.39	0.57	0.33	0.39	0.64	0.44	0.51
Er	Acme/4B	0.03	0.23	0.26	0.23	0.35	0.19	0.21	0.37	0.26	0.33
Eu	Acme/4B	0.02	0.66	0.60	0.54	0.64	0.45	0.57	0.54	0.67	0.46
Ga	Acme/4B	0.5	20.8	19.6	20.3	21.6	18.8	20.6	18.6	22.1	13.9

Continued on next page

Table B.3 *Continued from previous page*

Element	Lab/method code	LOD	191810	191811	191812	191813	191814	191815	191816	191817	191818
Gd	Acme/4B	0.05	0.56	0.60	0.52	0.64	0.41	0.48	0.66	0.52	0.64
Ge	Acme/1F-MS	0.1									0.1
Hf	Acme/4B	0.1	0.4	0.4	0.2	0.3	0.2	0.2	0.3	0.3	0.3
Hg	Acme/1F-MS	0.005			0.006	0.005				0.007	0.006
Ho	Acme/4B	0.02	0.09	0.09	0.09	0.13	0.07	0.08	0.14	0.08	0.11
In	Acme/1F-MS	0.02									
La	Acme/4B	0.1	2.7	2.9	2.2	2.7	1.9	1.7	1.8	2.3	2.1
Li	Acme/1EX	0.1									
Li	Acme/1F-MS	0.1	2.1	1.9	3.1	2.9	2.4	1.8	1.7	2.2	2.8
Lu	Acme/4B	0.01	0.04	0.04	0.03	0.05	0.03	0.04	0.06	0.03	0.05
Mo	Acme/1EX	0.1									
Mo	Acme/1F-MS	0.01	0.05	0.06	0.05	0.06	0.03	0.05	0.05	0.04	0.04
Nb	Acme/4B	0.1	1.1	1.8	0.7	1.1	0.5	0.3	0.4	1.0	0.6
Nd	Acme/4B	0.3	3.0	2.9	2.3	2.9	1.8	1.7	2.4	2.3	2.2
Ni	Acme/7TD	10	343	450	383	299	440	247	236	176	564
Pb	Acme/1EX	0.1									
Pb	Acme/1F-MS	0.01	0.34	0.34	5.12	1.95	0.29	0.43	0.27	0.50	0.48
Pd	Acme/3B-MS	0.0005	0.0006	0.0008		0.0025	0.0022	0.0010	0.0006		0.0006
Pr	Acme/4B	0.02	0.70	0.75	0.54	0.69	0.44	0.44	0.50	0.58	0.55
Pt	Acme/3B-MS	0.0001	0.0008	0.0010	0.0003	0.0016	0.0026	0.0014	0.0004	0.0008	0.0010
Rb	Acme/4B	0.1	2.4	2.8	2.5	2.3	1.0	0.9	1.1	1.6	0.7
Re	Acme/1F-MS	0.001									
Sb	Acme/1EX	0.1									

Continued on next page

Table B.3 *Continued from previous page*

Element	Lab/method code	LOD	191810	191811	191812	191813	191814	191815	191816	191817	191818
Sb	Acme/1F-MS	0.02									
Sc	Acme/4B	1	4	4	5	7	6	7	13	5	9
Se	Acme/1F-MS	0.1									
Se	GeoLabs/IMH-100	0.0035									
Sm	Acme/4B	0.05	0.59	0.56	0.46	0.63	0.39	0.39	0.56	0.51	0.58
Sn	Acme/4B	1									
Sr	Acme/4B	0.5	398.4	348.9	344.5	359.7	307.3	340.4	299.5	370.1	244.0
Ta	Acme/4B	0.1		0.1							
Tb	Acme/4B	0.01	0.09	0.10	0.08	0.11	0.07	0.07	0.12	0.08	0.10
Te	Acme/1F-MS	0.02									
Te	GeoLabs/IMH-100	0.001									
Th	Acme/4B	0.2	0.4	0.4		0.3				0.2	
Tl	Acme/1F-MS	0.02									
Tm	Acme/4B	0.01	0.04	0.04	0.04	0.05	0.03	0.03	0.06	0.02	0.04
U	Acme/4B	0.1									
V	Acme/4B	8	40	32	81	108	114	57	178	57	53
W	Acme/4B	0.5									
Y	Acme/4B	0.1	2.6	3.0	2.2	3.6	1.8	2.3	3.9	2.4	3.2
Yb	Acme/4B	0.05	0.25	0.24	0.24	0.29	0.19	0.23	0.37	0.25	0.29
Zn	Acme/1EX	1									
Zn	Acme/1F-MS	0.1	33.1	43.7	23.3	25.7	43.4	34.7	25.1	34.2	70.2
Zr	Acme/4B	0.1	11.7	21.8	8.2	14.5	6.3	6.2	8.6	11.2	10.8

Continued on next page

Table B.3 *Continued from previous page*

Element	Lab/method code	LOD	191819	191820	191821	191822	191823	191824	191825	191826	191827
Ag	Acme/1EX	0.1									
Ag	Acme/1F-MS	0.002	0.026	0.010	0.018	0.028	0.009	0.010	0.013	0.011	0.009
As	Acme/1EX	1									
As	Acme/1F-MS	0.1	0.1	0.2			0.2			0.2	
Au	Acme/3B-MS	0.001		0.002		0.002			0.002		
B	Acme/1F-MS	1									
Ba	Acme/4B	1	81	12	48	13	21	17	20	13	23
Be	Acme/1EX	1									
Be	Acme/1F-MS	0.1									
Bi	Acme/1EX	0.1									
Bi	Acme/1F-MS	0.02									
Cd	Acme/1EX	0.1									
Cd	Acme/1F-MS	0.01	0.02	0.02	0.01	0.01		0.02			0.02
Ce	Acme/4B	0.1	10.0	1.4	5.8	2.1	2.2	1.9	1.9	1.6	1.8
Co	Acme/1EX	0.2									
Co	Acme/1F-MS	0.1	46.0	25.9	13.6	23.2	16.5	33.3	18.2	23.3	25.1
Cs	Acme/4B	0.1									
Cu	Acme/1EX	0.1									
Cu	Acme/1F-MS	0.01	68.66	18.07	54.73	66.79	13.82	18.48	23.92	18.00	23.67
Dy	Acme/4B	0.05	1.27	0.63	1.40	1.53	0.64	0.40	0.72	0.77	0.56
Er	Acme/4B	0.03	0.61	0.35	0.80	0.91	0.39	0.22	0.41	0.46	0.33
Eu	Acme/4B	0.02	0.85	0.17	0.35	0.35	0.24	0.17	0.22	0.22	0.21
Ga	Acme/4B	0.5	21.4	9.3	14.0	13.1	12.8	11.6	11.7	11.0	10.0

Continued on next page

Table B.3 *Continued from previous page*

Element	Lab/method code	LOD	191819	191820	191821	191822	191823	191824	191825	191826	191827
Gd	Acme/4B	0.05	1.48	0.60	1.19	1.27	0.60	0.37	0.59	0.71	0.54
Ge	Acme/1F-MS	0.1									
Hf	Acme/4B	0.1	0.9	0.2	0.5	0.4	0.2	0.2	0.1	0.1	0.2
Hg	Acme/1F-MS	0.005				0.006	0.011	0.008			0.006
Ho	Acme/4B	0.02	0.25	0.13	0.28	0.31	0.13	0.07	0.16	0.16	0.12
In	Acme/1F-MS	0.02									
La	Acme/4B	0.1	4.1	0.5	2.5	0.7	1.1	1.0	0.8	0.6	0.7
Li	Acme/1EX	0.1									
Li	Acme/1F-MS	0.1	2.6	3.0	2.0	1.2	1.0	2.4	0.4	0.6	1.1
Lu	Acme/4B	0.01	0.09	0.05	0.10	0.11	0.04	0.02	0.05	0.05	0.03
Mo	Acme/1EX	0.1									
Mo	Acme/1F-MS	0.01	0.06	0.01	0.04	0.01	0.02	0.04	0.01	0.01	0.02
Nb	Acme/4B	0.1	2.8	0.1	0.4		0.1	0.2			0.1
Nd	Acme/4B	0.3	5.4	0.8	3.0	2.2	1.6	1.0	1.4	1.2	1.1
Ni	Acme/7TD	10	264	261	153	222	199	322	238	229	294
Pb	Acme/1EX	0.1									
Pb	Acme/1F-MS	0.01	0.56	1.29	1.53	0.99	0.69	0.47	0.60	0.65	1.81
Pd	Acme/3B-MS	0.0005	0.0011	0.0017	0.0053	0.0129	0.0011	0.0016	0.0059	0.0039	0.0011
Pr	Acme/4B	0.02	1.19	0.16	0.72	0.38	0.34	0.24	0.25	0.21	0.23
Pt	Acme/3B-MS	0.0001	0.0016	0.0017	0.0053	0.0123	0.0021	0.0017	0.0052	0.0025	0.0013
Rb	Acme/4B	0.1	1.8	0.9	3.8		1.1	1.0	0.4	0.4	0.6
Re	Acme/1F-MS	0.001						0.002			
Sb	Acme/1EX	0.1									

Continued on next page

Table B.3 *Continued from previous page*

Element	Lab/method code	LOD	191819	191820	191821	191822	191823	191824	191825	191826	191827
Sb	Acme/1F-MS	0.02									
Sc	Acme/4B	1	11	36	34	40	23	14	34	41	24
Se	Acme/1F-MS	0.1									
Se	GeoLabs/IMH-100	0.0035		0.0252		0.1684					0.0264
Sm	Acme/4B	0.05	1.23	0.33	0.91	0.86	0.40	0.26	0.37	0.41	0.40
Sn	Acme/4B	1									
Sr	Acme/4B	0.5	335.9	101.0	141.9	102.3	141.9	141.9	110.8	106.8	124.1
Ta	Acme/4B	0.1	0.2								
Tb	Acme/4B	0.01	0.22	0.10	0.22	0.25	0.09	0.06	0.10	0.13	0.10
Te	Acme/1F-MS	0.02					0.04	0.03			
Te	GeoLabs/IMH-100	0.001		0.002		0.016					0.006
Th	Acme/4B	0.2		0.2	0.8			0.2			
Tl	Acme/1F-MS	0.02									
Tm	Acme/4B	0.01	0.10	0.05	0.11	0.12	0.05	0.03	0.05	0.05	0.03
U	Acme/4B	0.1									
V	Acme/4B	8	151	109	148	171	74	46	104	123	84
W	Acme/4B	0.5									
Y	Acme/4B	0.1	7.1	3.7	7.9	9.3	3.8	2.4	4.1	4.5	3.5
Yb	Acme/4B	0.05	0.64	0.36	0.72	0.81	0.30	0.19	0.42	0.41	0.31
Zn	Acme/1EX	1									
Zn	Acme/1F-MS	0.1	35.9	6.9	6.2	8.9	5.8	11.6	3.6	6.1	3.9
Zr	Acme/4B	0.1	30.4	4.8	15.7	5.2	6.7	5.0	4.3	5.5	5.7

Continued on next page

Table B.3 *Continued from previous page*

Element	Lab/method code	LOD	191829	191830	191831	191832	191834	191836	191837	191838	191839
Ag	Acme/1EX	0.1	0.1	0.1				0.1			
Ag	Acme/1F-MS	0.002				0.033	0.025				
As	Acme/1EX	1	3	2				1		3	2
As	Acme/1F-MS	0.1				0.2					
Au	Acme/3B-MS	0.001	0.003	0.001		0.002				0.001	0.002
B	Acme/1F-MS	1					2				
Ba	Acme/4B	1	217	306	207	71	73	64	98	58	99
Be	Acme/1EX	1									
Be	Acme/1F-MS	0.1				0.1	0.1				
Bi	Acme/1EX	0.1									
Bi	Acme/1F-MS	0.02				0.14	0.03				
Cd	Acme/1EX	0.1	0.3	0.1	0.1						0.2
Cd	Acme/1F-MS	0.01				0.01	0.04				
Ce	Acme/4B	0.1	23.2	50.6	9.8	9.0	8.3	5.7	13.3	6.2	12.4
Co	Acme/1EX	0.2	75.3	65.1	57.9			95.5	39.3	72.4	69.0
Co	Acme/1F-MS	0.1				15.3	69.2				
Cs	Acme/4B	0.1									
Cu	Acme/1EX	0.1	171.9	197.2	95.0			76.1	57.1	54.0	121.3
Cu	Acme/1F-MS	0.01				68.02	64.29				
Dy	Acme/4B	0.05	3.77	7.17	3.00	1.89	1.02	0.85	1.68	1.10	2.78
Er	Acme/4B	0.03	2.18	4.13	1.90	1.02	0.56	0.44	0.87	0.65	1.72
Eu	Acme/4B	0.02	1.30	2.01	0.82	0.94	0.77	0.66	0.99	0.68	0.79
Ga	Acme/4B	0.5	16.7	21.9	17.0	19.6	18.7	17.1	22.7	19.1	16.0

Continued on next page

Table B.3 *Continued from previous page*

Element	Lab/method code	LOD	191829	191830	191831	191832	191834	191836	191837	191838	191839
Gd	Acme/4B	0.05	3.74	7.34	2.49	1.86	1.04	0.86	1.83	1.11	2.53
Ge	Acme/1F-MS	0.1					0.2				
Hf	Acme/4B	0.1	1.0	4.7	1.4	0.9	0.6	0.5	0.8	0.7	1.4
Hg	Acme/1F-MS	0.005									
Ho	Acme/4B	0.02	0.75	1.42	0.63	0.36	0.20	0.16	0.31	0.21	0.55
In	Acme/1F-MS	0.02									
La	Acme/4B	0.1	9.8	22.5	4.7	3.7	4.0	2.5	5.8	2.7	5.5
Li	Acme/1EX	0.1	1.8	4.9	3.5			6.3	3.5	3.1	1.6
Li	Acme/1F-MS	0.1				1.2	2.9				
Lu	Acme/4B	0.01	0.28	0.53	0.26	0.13	0.08	0.07	0.10	0.09	0.23
Mo	Acme/1EX	0.1	0.2	0.8	0.1					0.1	0.2
Mo	Acme/1F-MS	0.01				0.09	0.05				
Nb	Acme/4B	0.1	2.1	7.7	1.9	2.0	3.1	1.5	2.7	1.5	2.0
Nd	Acme/4B	0.3	14.5	29.4	5.7	5.9	4.3	3.5	7.3	3.9	7.2
Ni	Acme/7TD	10	261	75	136	127	317	364	145	304	255
Pb	Acme/1EX	0.1	3.4	7.0	2.9			1.7	1.7	1.0	2.2
Pb	Acme/1F-MS	0.01				0.83	0.56				
Pd	Acme/3B-MS	0.0005	0.0187	0.0139	0.0006	0.1328	0.0031	0.0013	0.0035	0.0022	0.0121
Pr	Acme/4B	0.02	3.12	6.54	1.25	1.24	1.01	0.74	1.66	0.82	1.68
Pt	Acme/3B-MS	0.0001	0.0163	0.0095	0.0005	0.0033	0.0047	0.0020	0.0022	0.0022	0.0100
Rb	Acme/4B	0.1	0.8	1.5	7.4	2.1	1.3	1.3	2.5	1.4	4.0
Re	Acme/1F-MS	0.001					0.001				
Sb	Acme/1EX	0.1									

Continued on next page

Table B.3 *Continued from previous page*

Element	Lab/method code	LOD	191829	191830	191831	191832	191834	191836	191837	191838	191839
Sb	Acme/1F-MS	0.02									
Sc	Acme/4B	1	34	41	24	28	10	11	10	14	32
Se	Acme/1F-MS	0.1									
Se	GeoLabs/IMH-100	0.0035				0.0558					
Sm	Acme/4B	0.05	3.32	6.66	1.82	1.56	1.04	0.74	1.74	0.99	2.00
Sn	Acme/4B	1									
Sr	Acme/4B	0.5	279.6	278.9	263.7	297.0	296.9	264.9	380.1	298.1	181.2
Ta	Acme/4B	0.1	0.1	0.4		0.2	0.2	0.1	0.1	0.1	0.1
Tb	Acme/4B	0.01	0.63	1.25	0.49	0.33	0.18	0.15	0.31	0.19	0.45
Te	Acme/1F-MS	0.02									
Te	GeoLabs/IMH-100	0.001				0.013					
Th	Acme/4B	0.2		0.5	0.3	0.3					0.4
Tl	Acme/1F-MS	0.02									
Tm	Acme/4B	0.01	0.31	0.60	0.28	0.15	0.09	0.07	0.12	0.09	0.25
U	Acme/4B	0.1		0.2							
V	Acme/4B	8	302	406	214	217	111	69	135	148	212
W	Acme/4B	0.5									
Y	Acme/4B	0.1	20.9	39.4	17.6	10.1	5.5	4.6	8.9	6.0	16.3
Yb	Acme/4B	0.05	1.87	3.59	1.78	0.89	0.54	0.42	0.71	0.55	1.57
Zn	Acme/1EX	1	109	145	89			93	48	72	81
Zn	Acme/1F-MS	0.1				10.0	29.2				
Zr	Acme/4B	0.1	30.9	181.3	46.5	27.3	20.5	16.1	24.4	20.8	50.1

Continued on next page

Table B.3 *Continued from previous page*

Element	Lab/method code	LOD	191840	191841	191842	191843	191844	191845	191846	191847	191848
Ag	Acme/1EX	0.1		0.2			0.2				
Ag	Acme/1F-MS	0.002									0.014
As	Acme/1EX	1	2	2	2	1	3		1	2	
As	Acme/1F-MS	0.1									
Au	Acme/3B-MS	0.001		0.006							
B	Acme/1F-MS	1									
Ba	Acme/4B	1	62	100	74	56	38	70	70	67	64
Be	Acme/1EX	1									
Be	Acme/1F-MS	0.1									0.2
Bi	Acme/1EX	0.1									
Bi	Acme/1F-MS	0.02									
Cd	Acme/1EX	0.1		0.1						0.2	
Cd	Acme/1F-MS	0.01									0.02
Ce	Acme/4B	0.1	5.4	13.2	4.7	4.2	2.8	4.9	4.7	4.9	3.9
Co	Acme/1EX	0.2	64.2	68.2	61.8	48.8	104.9	50.6	47.6	47.4	
Co	Acme/1F-MS	0.1									35.2
Cs	Acme/4B	0.1									
Cu	Acme/1EX	0.1	49.3	129.2	58.7	30.2	19.0	23.5	34.9	31.0	
Cu	Acme/1F-MS	0.01									13.14
Dy	Acme/4B	0.05	0.83	2.82	0.64	0.57	0.34	0.57	0.66	0.59	0.32
Er	Acme/4B	0.03	0.46	1.72	0.35	0.28	0.16	0.29	0.32	0.34	0.18
Eu	Acme/4B	0.02	0.67	0.82	0.73	0.53	0.38	0.65	0.65	0.62	0.58
Ga	Acme/4B	0.5	20.5	14.4	21.4	21.4	15.6	22.9	22.7	22.1	23.4

Continued on next page

Table B.3 *Continued from previous page*

Element	Lab/method code	LOD	191840	191841	191842	191843	191844	191845	191846	191847	191848
Gd	Acme/4B	0.05	0.86	2.56	0.64	0.59	0.31	0.60	0.61	0.64	0.38
Ge	Acme/1F-MS	0.1									
Hf	Acme/4B	0.1	0.4	1.7	0.4	0.4	0.3	0.4	0.3	0.5	0.2
Hg	Acme/1F-MS	0.005									
Ho	Acme/4B	0.02	0.16	0.58	0.12	0.11	0.05	0.10	0.11	0.12	0.05
In	Acme/1F-MS	0.02									
La	Acme/4B	0.1	2.6	5.4	2.3	1.8	1.4	2.5	2.2	2.2	2.0
Li	Acme/1EX	0.1	2.6	2.3	4.0	5.9	4.1	2.2	3.1	3.2	
Li	Acme/1F-MS	0.1									1.5
Lu	Acme/4B	0.01	0.06	0.25	0.05	0.04	0.03	0.04	0.04	0.04	0.02
Mo	Acme/1EX	0.1	0.1	0.2							
Mo	Acme/1F-MS	0.01									0.03
Nb	Acme/4B	0.1	1.3	2.4	0.8	0.5	0.5	0.5	0.6	0.8	0.5
Nd	Acme/4B	0.3	3.1	8.1	2.3	2.3	1.5	2.3	2.6	2.6	1.8
Ni	Acme/7TD	10	252	294	198	189	496	174	142	161	164
Pb	Acme/1EX	0.1	1.2	3.5	1.2	0.9	0.7	1.1	1.5	1.0	
Pb	Acme/1F-MS	0.01									0.57
Pd	Acme/3B-MS	0.0005	0.0014	0.0098	0.0334	0.0007		0.0006	0.0007		
Pr	Acme/4B	0.02	0.69	1.78	0.58	0.52	0.34	0.60	0.58	0.60	0.47
Pt	Acme/3B-MS	0.0001	0.0031	0.0078	0.0023	0.0006	0.0006	0.0008	0.0014	0.0007	0.0003
Rb	Acme/4B	0.1	1.6	4.2	1.5	1.7	1.1	1.9	1.8	2.0	2.0
Re	Acme/1F-MS	0.001									
Sb	Acme/1EX	0.1								0.1	

Continued on next page

Table B.3 *Continued from previous page*

Element	Lab/method code	LOD	191840	191841	191842	191843	191844	191845	191846	191847	191848
Sb	Acme/1F-MS	0.02									
Sc	Acme/4B	1	12	35	9	7	5	6	8	7	4
Se	Acme/1F-MS	0.1									
Se	GeoLabs/IMH-100	0.0035			0.0514				0.0270		
Sm	Acme/4B	0.05	0.71	2.12	0.64	0.52	0.29	0.55	0.60	0.61	0.39
Sn	Acme/4B	1									
Sr	Acme/4B	0.5	334.4	175.0	343.5	361.6	271.6	383.6	387.2	370.1	385.2
Ta	Acme/4B	0.1		0.1							
Tb	Acme/4B	0.01	0.15	0.47	0.11	0.10	0.05	0.10	0.11	0.10	0.06
Te	Acme/1F-MS	0.02									0.03
Te	GeoLabs/IMH-100	0.001			0.002				0.002		
Th	Acme/4B	0.2		0.5					0.3	0.2	0.2
Tl	Acme/1F-MS	0.02									
Tm	Acme/4B	0.01	0.07	0.26	0.05	0.04	0.02	0.04	0.04	0.05	0.02
U	Acme/4B	0.1									
V	Acme/4B	8	197	233	105	67	24	41	88	67	29
W	Acme/4B	0.5									
Y	Acme/4B	0.1	4.7	16.4	3.4	2.9	1.6	3.1	3.3	3.3	1.6
Yb	Acme/4B	0.05	0.41	1.64	0.33	0.23	0.18	0.28	0.30	0.32	0.14
Zn	Acme/1EX	1	67	77	66	47	84	48	44	42	
Zn	Acme/1F-MS	0.1									22.4
Zr	Acme/4B	0.1	15.9	52.5	10.7	11.6	6.7	10.9	10.2	15.5	7.7

Continued on next page

Table B.3 *Continued from previous page*

Element	Lab/method code	LOD	191849	191850	191851	191852	191853	191854	191855	191856	191857
Ag	Acme/1EX	0.1			0.1			0.1			0.2
Ag	Acme/1F-MS	0.002	0.016	0.019		0.029	0.026				
As	Acme/1EX	1			2			2	1	2	2
As	Acme/1F-MS	0.1									
Au	Acme/3B-MS	0.001						0.008			
B	Acme/1F-MS	1									
Ba	Acme/4B	1	52	51	70	74	79	90	56	97	80
Be	Acme/1EX	1									
Be	Acme/1F-MS	0.1		0.2			0.1				
Bi	Acme/1EX	0.1									
Bi	Acme/1F-MS	0.02				0.02					
Cd	Acme/1EX	0.1						0.2			
Cd	Acme/1F-MS	0.01		0.02		0.02					
Ce	Acme/4B	0.1	3.1	2.7	5.9	3.6	4.0	11.2	3.3	6.6	4.2
Co	Acme/1EX	0.2			62.3			65.5	62.3	49.4	59.7
Co	Acme/1F-MS	0.1	53.5	42.3		34.2	24.6				
Cs	Acme/4B	0.1									
Cu	Acme/1EX	0.1			35.7			126.4	19.7	34.7	24.0
Cu	Acme/1F-MS	0.01	13.20	13.84		49.41	27.20				
Dy	Acme/4B	0.05	0.24	0.27	0.56	0.30	0.38	2.78	0.63	0.64	0.38
Er	Acme/4B	0.03	0.14	0.12	0.32	0.17	0.19	1.69	0.30	0.32	0.19
Eu	Acme/4B	0.02	0.47	0.47	0.58	0.60	0.59	0.74	0.54	0.93	0.71
Ga	Acme/4B	0.5	19.4	20.3	20.3	22.7	23.7	15.5	20.1	26.8	24.1

Continued on next page

Table B.3 *Continued from previous page*

Element	Lab/method code	LOD	191849	191850	191851	191852	191853	191854	191855	191856	191857
Gd	Acme/4B	0.05	0.31	0.25	0.62	0.35	0.44	2.39	0.64	0.73	0.41
Ge	Acme/1F-MS	0.1	0.1								
Hf	Acme/4B	0.1	0.3	0.1	0.4	0.3	0.3	1.2	0.3	0.6	0.3
Hg	Acme/1F-MS	0.005									
Ho	Acme/4B	0.02	0.05	0.05	0.12	0.06	0.07	0.55	0.11	0.12	0.07
In	Acme/1F-MS	0.02									
La	Acme/4B	0.1	1.5	1.3	2.6	1.8	1.8	4.6	1.5	3.1	1.9
Li	Acme/1EX	0.1			2.7			2.4	3.0	1.9	2.9
Li	Acme/1F-MS	0.1	2.0	1.8		1.9	2.2				
Lu	Acme/4B	0.01	0.03	0.02	0.04	0.02	0.03	0.26	0.04	0.05	0.03
Mo	Acme/1EX	0.1						0.2		0.1	0.1
Mo	Acme/1F-MS	0.01	0.05	0.01		0.02	0.02				
Nb	Acme/4B	0.1	0.9	0.4	1.4	0.6	0.4	2.0	0.5	1.4	0.7
Nd	Acme/4B	0.3	1.7	1.6	3.0	1.8	1.9	7.0	2.0	3.3	1.7
Ni	Acme/7TD	10	298	225	337	242	167	237	281	114	148
Pb	Acme/1EX	0.1			1.5			3.2	1.5	1.4	1.4
Pb	Acme/1F-MS	0.01	0.35	0.65		0.97	0.75				
Pd	Acme/3B-MS	0.0005			0.0008	0.0035	0.0006	0.0150	0.0010	0.0013	0.0010
Pr	Acme/4B	0.02	0.37	0.35	0.72	0.45	0.47	1.50	0.44	0.81	0.48
Pt	Acme/3B-MS	0.0001	0.0001	0.0003	0.0014	0.0044	0.0003	0.0090	0.0018	0.0009	0.0003
Rb	Acme/4B	0.1	1.3	1.1	2.7	1.6	1.7	4.1	1.2	3.3	2.2
Re	Acme/1F-MS	0.001				0.001					
Sb	Acme/1EX	0.1									

Continued on next page

Table B.3 *Continued from previous page*

Element	Lab/method code	LOD	191849	191850	191851	191852	191853	191854	191855	191856	191857
Sb	Acme/1F-MS	0.02									
Sc	Acme/4B	1	4	4	5	4	6	35	13	5	4
Se	Acme/1F-MS	0.1									
Se	GeoLabs/IMH-100	0.0035			0.0290						
Sm	Acme/4B	0.05	0.32	0.27	0.65	0.35	0.42	1.86	0.54	0.72	0.41
Sn	Acme/4B	1									
Sr	Acme/4B	0.5	347.5	356.4	331.6	379.0	404.2	163.3	343.4	404.2	395.3
Ta	Acme/4B	0.1						0.2			
Tb	Acme/4B	0.01	0.06	0.05	0.10	0.06	0.07	0.43	0.11	0.12	0.06
Te	Acme/1F-MS	0.02		0.04		0.03					
Te	GeoLabs/IMH-100	0.001			0.009						
Th	Acme/4B	0.2			0.5			0.4		0.5	0.3
Tl	Acme/1F-MS	0.02									
Tm	Acme/4B	0.01	0.03	0.02	0.05	0.02	0.03	0.25	0.05	0.05	0.02
U	Acme/4B	0.1									
V	Acme/4B	8	34	24	80	198	65	210	165	396	339
W	Acme/4B	0.5									
Y	Acme/4B	0.1	1.4	1.4	3.1	1.6	2.1	16.1	3.3	3.4	1.8
Yb	Acme/4B	0.05	0.15	0.11	0.28	0.16	0.18	1.67	0.29	0.29	0.16
Zn	Acme/1EX	1			62			77	58	64	62
Zn	Acme/1F-MS	0.1	21.3	23.6		11.7	10.0				
Zr	Acme/4B	0.1	10.4	5.5	16.2	10.8	8.0	46.8	9.2	19.6	11.9

Continued on next page

Table B.3 *Continued from previous page*

Element	Lab/method code	LOD	191858	191859	191860	191861	191862	191863	191864	191865	191866
Ag	Acme/1EX	0.1	0.1							0.1	
Ag	Acme/1F-MS	0.002						0.014			
As	Acme/1EX	1	3	2	2	2	2			2	
As	Acme/1F-MS	0.1									
Au	Acme/3B-MS	0.001		0.003	0.002	0.002			0.002	0.001	
B	Acme/1F-MS	1									
Ba	Acme/4B	1	64	73	55	67	69	60	57	54	99
Be	Acme/1EX	1									
Be	Acme/1F-MS	0.1						0.1			
Bi	Acme/1EX	0.1									
Bi	Acme/1F-MS	0.02									
Cd	Acme/1EX	0.1									
Cd	Acme/1F-MS	0.01									
Ce	Acme/4B	0.1	1.8	5.0	2.5	4.3	3.8	3.5	3.1	2.2	4.1
Co	Acme/1EX	0.2	116.0	50.5	85.2	58.7	51.8		60.5	109.2	22.7
Co	Acme/1F-MS	0.1						35.6			
Cs	Acme/4B	0.1									
Cu	Acme/1EX	0.1	7.4	26.5	13.3	22.2	21.4		15.3	15.3	20.7
Cu	Acme/1F-MS	0.01						19.03			
Dy	Acme/4B	0.05	0.12	0.47	0.17	0.39	0.36	0.76	0.61	0.22	0.43
Er	Acme/4B	0.03	0.09	0.22	0.09	0.19	0.18	0.43	0.34	0.12	0.25
Eu	Acme/4B	0.02	0.43	0.57	0.45	0.61	0.56	0.55	0.55	0.47	0.83
Ga	Acme/4B	0.5	18.0	22.3	18.5	21.2	21.8	21.4	20.2	16.1	27.7

Continued on next page

Table B.3 *Continued from previous page*

Element	Lab/method code	LOD	191858	191859	191860	191861	191862	191863	191864	191865	191866
Gd	Acme/4B	0.05	0.13	0.51	0.21	0.43	0.40	0.83	0.64	0.24	0.55
Ge	Acme/1F-MS	0.1						0.1			
Hf	Acme/4B	0.1	0.2	0.3	0.1	0.2	0.3	0.4	0.3		0.4
Hg	Acme/1F-MS	0.005									
Ho	Acme/4B	0.02	0.02	0.08	0.03	0.06	0.06	0.16	0.13	0.04	0.09
In	Acme/1F-MS	0.02									
La	Acme/4B	0.1	0.8	2.4	1.3	2.0	1.9	1.5	1.6	1.2	2.2
Li	Acme/1EX	0.1	3.5	3.1	3.4	2.8	2.7		3.2	4.0	3.1
Li	Acme/1F-MS	0.1						2.3			
Lu	Acme/4B	0.01	0.02	0.03	0.02	0.03	0.03	0.06	0.05	0.03	0.03
Mo	Acme/1EX	0.1									
Mo	Acme/1F-MS	0.01						0.04			
Nb	Acme/4B	0.1	0.5	0.7	0.7	0.7	0.7	1.0	0.2	0.2	0.7
Nd	Acme/4B	0.3	0.7	2.4	1.2	1.8	1.8	2.3	2.0	0.9	1.9
Ni	Acme/7TD	10	366	232	408	243	202	199	199	399	48
Pb	Acme/1EX	0.1	0.7	1.4	0.9	1.1	1.8		1.3	2.5	1.2
Pb	Acme/1F-MS	0.01						0.33			
Pd	Acme/3B-MS	0.0005	0.0006		0.0006	0.0007				0.0012	0.0018
Pr	Acme/4B	0.02	0.20	0.60	0.28	0.49	0.46	0.49	0.47	0.28	0.53
Pt	Acme/3B-MS	0.0001	0.0001	0.0008	0.0001	0.0005	0.0002			0.0001	0.0002
Rb	Acme/4B	0.1	0.9	2.5	0.9	1.9	1.7	1.1	1.4	1.5	1.9
Re	Acme/1F-MS	0.001									
Sb	Acme/1EX	0.1									

Continued on next page

Table B.3 *Continued from previous page*

Element	Lab/method code	LOD	191858	191859	191860	191861	191862	191863	191864	191865	191866
Sb	Acme/1F-MS	0.02									
Sc	Acme/4B	1	6	4	4	4	4	18	15	6	8
Se	Acme/1F-MS	0.1									
Se	GeoLabs/IMH-100	0.0035			0.0054						
Sm	Acme/4B	0.05	0.17	0.56	0.22	0.45	0.37	0.67	0.57	0.23	0.48
Sn	Acme/4B	1									
Sr	Acme/4B	0.5	267.3	393.1	332.3	375.7	381.7	334.1	351.1	272.4	455.1
Ta	Acme/4B	0.1									
Tb	Acme/4B	0.01	0.02	0.08	0.03	0.07	0.06	0.14	0.12	0.04	0.09
Te	Acme/1F-MS	0.02									
Te	GeoLabs/IMH-100	0.001			0.001						
Th	Acme/4B	0.2		0.3		0.3					
Tl	Acme/1F-MS	0.02									
Tm	Acme/4B	0.01	0.01	0.03	0.02	0.03	0.03	0.07	0.05	0.02	0.04
U	Acme/4B	0.1									
V	Acme/4B	8	549	37	36	59	84	300	155	99	327
W	Acme/4B	0.5									
Y	Acme/4B	0.1	0.7	2.4	0.9	1.8	1.8	4.3	3.6	1.2	2.5
Yb	Acme/4B	0.05	0.09	0.23	0.12	0.18	0.16	0.37	0.30	0.14	0.24
Zn	Acme/1EX	1	104	46	71	52	49		51	88	32
Zn	Acme/1F-MS	0.1						17.4			
Zr	Acme/4B	0.1	6.4	13.0	4.4	9.0	9.5	12.9	6.3	3.7	15.0

Continued on next page

Table B.3 *Continued from previous page*

Element	Lab/method code	LOD	191867	191868	191869	191870	191871	191872	191873	191874	191875
Ag	Acme/1EX	0.1									
Ag	Acme/1F-MS	0.002			0.009		0.039		0.023	0.028	0.039
As	Acme/1EX	1	2			2		2			
As	Acme/1F-MS	0.1							0.4	0.2	0.2
Au	Acme/3B-MS	0.001	0.001	0.003		0.004	0.006	0.012	0.004		
B	Acme/1F-MS	1									
Ba	Acme/4B	1	123	112	75	204	184	178	71	66	81
Be	Acme/1EX	1				1					
Be	Acme/1F-MS	0.1					0.2		0.2		0.3
Bi	Acme/1EX	0.1									
Bi	Acme/1F-MS	0.02									
Cd	Acme/1EX	0.1									
Cd	Acme/1F-MS	0.01					0.01		0.01	0.01	0.02
Ce	Acme/4B	0.1	5.7	7.1	5.3	35.3	30.2	33.0	5.5	7.2	7.1
Co	Acme/1EX	0.2	17.0	18.6		25.9		26.8			
Co	Acme/1F-MS	0.1			21.5		7.4		42.9	29.3	31.8
Cs	Acme/4B	0.1				0.2	0.1	0.2			
Cu	Acme/1EX	0.1	26.7	35.3		117.2		120.9			
Cu	Acme/1F-MS	0.01			32.44		112.99		26.95	49.77	93.00
Dy	Acme/4B	0.05	0.55	0.65	2.03	3.66	3.51	3.82	0.69	1.03	0.73
Er	Acme/4B	0.03	0.27	0.35	1.08	1.88	1.77	1.92	0.37	0.62	0.46
Eu	Acme/4B	0.02	1.13	1.20	0.83	1.73	1.68	1.69	0.64	0.77	0.76
Ga	Acme/4B	0.5	28.3	28.0	21.3	27.5	27.6	26.8	21.0	21.5	25.5

Continued on next page

Table B.3 *Continued from previous page*

Element	Lab/method code	LOD	191867	191868	191869	191870	191871	191872	191873	191874	191875
Gd	Acme/4B	0.05	0.60	0.79	1.93	4.30	3.83	4.21	0.77	1.16	0.88
Ge	Acme/1F-MS	0.1			0.1					0.1	
Hf	Acme/4B	0.1	0.4	0.5	1.6	3.3	2.7	3.4	0.7	0.9	0.7
Hg	Acme/1F-MS	0.005									
Ho	Acme/4B	0.02	0.10	0.14	0.39	0.72	0.66	0.71	0.13	0.22	0.16
In	Acme/1F-MS	0.02									
La	Acme/4B	0.1	3.1	3.5	1.9	15.4	13.1	14.3	2.5	3.2	3.4
Li	Acme/1EX	0.1	4.0	4.1		7.6		5.5			
Li	Acme/1F-MS	0.1			1.6		5.0		1.9	1.3	2.2
Lu	Acme/4B	0.01	0.04	0.05	0.14	0.25	0.23	0.25	0.05	0.08	0.06
Mo	Acme/1EX	0.1		0.1		0.6		0.6			
Mo	Acme/1F-MS	0.01			0.10		0.31		0.07	0.09	0.07
Nb	Acme/4B	0.1	1.2	1.7	8.5	8.3	7.7	9.2	1.1	1.9	2.1
Nd	Acme/4B	0.3	2.7	3.6	4.5	19.0	17.0	17.3	2.4	4.4	3.5
Ni	Acme/7TD	10	21	22	52	23	19	20	243	145	198
Pb	Acme/1EX	0.1	1.3	2.2		5.1		4.5			
Pb	Acme/1F-MS	0.01			0.21		1.54		0.43	0.49	0.59
Pd	Acme/3B-MS	0.0005	0.0023	0.0018	0.0078	0.0018	0.0018	0.0045		0.0008	0.0101
Pr	Acme/4B	0.02	0.68	0.85	0.86	4.37	3.78	4.11	0.69	0.93	0.87
Pt	Acme/3B-MS	0.0001	0.0004	0.0003	0.0013	0.0025	0.0015	0.0017	0.0004	0.0017	0.0019
Rb	Acme/4B	0.1	2.5	3.1	1.6	20.4	16.0	16.0	2.7	3.1	2.6
Re	Acme/1F-MS	0.001									0.001
Sb	Acme/1EX	0.1									

Continued on next page

Table B.3 *Continued from previous page*

Element	Lab/method code	LOD	191867	191868	191869	191870	191871	191872	191873	191874	191875
Sb	Acme/1F-MS	0.02									0.41
Sc	Acme/4B	1	6	7	50	10	13	13	9	13	7
Se	Acme/1F-MS	0.1									
Se	GeoLabs/IMH-100	0.0035			0.0059			0.0972			
Sm	Acme/4B	0.05	0.61	0.79	1.48	4.07	3.72	4.04	0.69	1.04	0.85
Sn	Acme/4B	1				1	1	1			
Sr	Acme/4B	0.5	481.7	470.4	237.4	430.9	431.8	428.1	355.1	355.5	373.1
Ta	Acme/4B	0.1		0.2	0.6	0.6	0.5	0.6	0.1	0.1	0.2
Tb	Acme/4B	0.01	0.10	0.13	0.35	0.69	0.63	0.69	0.13	0.19	0.15
Te	Acme/1F-MS	0.02									
Te	GeoLabs/IMH-100	0.001						0.001			
Th	Acme/4B	0.2	0.3	0.3	0.5	3.4	2.7	2.9		0.3	0.3
Tl	Acme/1F-MS	0.02									
Tm	Acme/4B	0.01	0.04	0.05	0.16	0.28	0.26	0.28	0.07	0.09	0.06
U	Acme/4B	0.1				0.5	0.4	0.4			
V	Acme/4B	8	167	182	1189	204	208	207	72	149	164
W	Acme/4B	0.5									
Y	Acme/4B	0.1	2.7	3.8	10.7	21.0	18.5	20.9	3.7	5.7	4.2
Yb	Acme/4B	0.05	0.23	0.33	0.94	1.73	1.58	1.76	0.34	0.57	0.36
Zn	Acme/1EX	1	25	31		67		66			
Zn	Acme/1F-MS	0.1			25.4		19.4		31.6	24.6	24.6
Zr	Acme/4B	0.1	13.8	18.0	42.7	116.5	107.3	116.6	16.2	24.4	21.7

Continued on next page

Table B.3 *Continued from previous page*

Element	Lab/method code	LOD	191876	191877	191878	191879	191880	191881	191882	191883	191884
Ag	Acme/1EX	0.1									
Ag	Acme/1F-MS	0.002	0.024	0.017	0.022	0.046	0.021	0.025	0.034	0.048	0.011
As	Acme/1EX	1									
As	Acme/1F-MS	0.1		0.4			0.2			0.4	0.3
Au	Acme/3B-MS	0.001			0.001						0.003
B	Acme/1F-MS	1									
Ba	Acme/4B	1	70	51	72	93	76	85	65	66	53
Be	Acme/1EX	1									
Be	Acme/1F-MS	0.1	0.2			0.1	0.2		0.2		0.1
Bi	Acme/1EX	0.1									
Bi	Acme/1F-MS	0.02									
Cd	Acme/1EX	0.1									
Cd	Acme/1F-MS	0.01			0.02	0.02					
Ce	Acme/4B	0.1	7.1	7.1	5.1	7.3	5.5	6.1	4.1	2.9	2.8
Co	Acme/1EX	0.2									
Co	Acme/1F-MS	0.1	50.3	85.4	38.7	35.8	49.2	26.6	27.2	40.5	73.2
Cs	Acme/4B	0.1		0.2							
Cu	Acme/1EX	0.1									
Cu	Acme/1F-MS	0.01	42.24	18.82	40.85	101.81	37.75	51.97	68.74	122.35	13.34
Dy	Acme/4B	0.05	0.56	1.04	0.76	0.68	0.48	0.50	0.62	0.66	0.30
Er	Acme/4B	0.03	0.33	0.67	0.46	0.36	0.28	0.27	0.36	0.39	0.20
Eu	Acme/4B	0.02	0.61	0.44	0.70	0.74	0.62	0.69	0.65	0.67	0.46
Ga	Acme/4B	0.5	21.8	14.8	20.5	25.0	20.7	23.2	22.0	20.4	17.8

Continued on next page

Table B.3 *Continued from previous page*

Element	Lab/method code	LOD	191876	191877	191878	191879	191880	191881	191882	191883	191884
Gd	Acme/4B	0.05	0.65	1.17	0.89	0.87	0.54	0.55	0.76	0.64	0.41
Ge	Acme/1F-MS	0.1					0.1		0.1	0.2	
Hf	Acme/4B	0.1	0.4	1.3	0.3	0.6	0.5	0.6	0.3	0.4	0.1
Hg	Acme/1F-MS	0.005						0.007		0.005	
Ho	Acme/4B	0.02	0.13	0.24	0.18	0.14	0.10	0.10	0.15	0.13	0.07
In	Acme/1F-MS	0.02									
La	Acme/4B	0.1	3.3	3.1	2.5	3.4	2.6	3.0	1.9	1.3	1.4
Li	Acme/1EX	0.1									
Li	Acme/1F-MS	0.1	1.8	2.3	1.4	2.1	1.9	1.2	1.7	1.3	1.7
Lu	Acme/4B	0.01	0.06	0.09	0.07	0.06	0.04	0.04	0.05	0.06	0.03
Mo	Acme/1EX	0.1									
Mo	Acme/1F-MS	0.01	0.04	0.22	0.04	0.06	0.04	0.04	0.02	0.02	0.02
Nb	Acme/4B	0.1	1.3	2.6	1.0	1.8	1.1	0.9	0.4	1.3	0.2
Nd	Acme/4B	0.3	3.4	3.9	2.7	4.0	2.5	3.3	2.7	2.0	1.7
Ni	Acme/7TD	10	363	539	307	251	382	198	213	293	489
Pb	Acme/1EX	0.1									
Pb	Acme/1F-MS	0.01	0.51	0.38	0.40	0.59	0.42	0.44	0.49	0.24	0.17
Pd	Acme/3B-MS	0.0005	0.0016	0.0009	0.0014		0.0015	0.0011	0.0064	0.0028	0.0009
Pr	Acme/4B	0.02	0.81	0.98	0.66	0.92	0.65	0.71	0.52	0.39	0.35
Pt	Acme/3B-MS	0.0001	0.0028	0.0007	0.0007		0.0024	0.0026	0.0056	0.0055	0.0004
Rb	Acme/4B	0.1	2.0	6.9	2.0	3.6	2.3	2.6	1.2	0.6	0.8
Re	Acme/1F-MS	0.001		0.002		0.002	0.003	0.003	0.001		0.002
Sb	Acme/1EX	0.1									

Continued on next page

Table B.3 *Continued from previous page*

Element	Lab/method code	LOD	191876	191877	191878	191879	191880	191881	191882	191883	191884
Sb	Acme/1F-MS	0.02									
Sc	Acme/4B	1	5	8	11	5	5	4	13	16	8
Se	Acme/1F-MS	0.1			0.1	0.2				0.1	
Se	GeoLabs/IMH-100	0.0035									
Sm	Acme/4B	0.05	0.71	1.00	0.71	0.82	0.57	0.65	0.62	0.52	0.32
Sn	Acme/4B	1									
Sr	Acme/4B	0.5	349.9	264.2	320.4	386.4	372.7	419.4	376.9	319.3	319.1
Ta	Acme/4B	0.1		0.1		0.1				0.1	
Tb	Acme/4B	0.01	0.12	0.22	0.14	0.14	0.09	0.10	0.13	0.12	0.07
Te	Acme/1F-MS	0.02					0.05				
Te	GeoLabs/IMH-100	0.001									
Th	Acme/4B	0.2	0.3	2.3	0.2	0.5		0.2			
Tl	Acme/1F-MS	0.02									
Tm	Acme/4B	0.01	0.05	0.10	0.06	0.07	0.04	0.05	0.06	0.06	0.04
U	Acme/4B	0.1		0.2							
V	Acme/4B	8	79	59	112	189	55	83	157	275	52
W	Acme/4B	0.5									
Y	Acme/4B	0.1	3.1	6.9	4.5	3.9	2.8	2.8	3.6	3.7	2.0
Yb	Acme/4B	0.05	0.31	0.49	0.41	0.36	0.25	0.26	0.38	0.38	0.16
Zn	Acme/1EX	1									
Zn	Acme/1F-MS	0.1	26.6	58.7	25.3	17.3	24.2	19.3	17.0	27.8	47.2
Zr	Acme/4B	0.1	15.3	52.7	12.6	20.9	12.8	16.0	8.3	9.5	4.7

Continued on next page

Table B.3 *Continued from previous page*

Element	Lab/method code	LOD	191885	191886	191887	191888	191889	191890	195161	205265	205266
Ag	Acme/1EX	0.1									
Ag	Acme/1F-MS	0.002	0.013	0.025	0.010	0.017	0.012	0.016	0.012	0.013	0.018
As	Acme/1EX	1									
As	Acme/1F-MS	0.1	0.3			0.4	0.2		0.1		0.2
Au	Acme/3B-MS	0.001								0.000	0.001
B	Acme/1F-MS	1									
Ba	Acme/4B	1	74	171	77	78	86	105	14	13	88
Be	Acme/1EX	1									
Be	Acme/1F-MS	0.1	0.1	0.2			0.1				0.2
Bi	Acme/1EX	0.1									
Bi	Acme/1F-MS	0.02								0.03	
Cd	Acme/1EX	0.1									
Cd	Acme/1F-MS	0.01		0.02					0.03	0.01	0.01
Ce	Acme/4B	0.1	4.3	10.9	3.4	4.5	3.8	5.4	0.7	1.4	13.1
Co	Acme/1EX	0.2									
Co	Acme/1F-MS	0.1	42.5	26.6	15.7	19.3	64.3	46.3	2.2	5.3	15.4
Cs	Acme/4B	0.1		0.1							
Cu	Acme/1EX	0.1									
Cu	Acme/1F-MS	0.01	15.51	95.40	9.74	33.05	22.49	24.40	3.07	7.60	32.85
Dy	Acme/4B	0.05	0.25	2.77	0.15	0.47	0.24	0.43	0.54	0.75	2.02
Er	Acme/4B	0.03	0.16	1.86	0.08	0.26	0.17	0.26	0.35	0.43	1.29
Eu	Acme/4B	0.02	0.57	0.82	0.56	0.59	0.63	0.73	0.16	0.19	0.51
Ga	Acme/4B	0.5	22.8	17.6	25.8	26.0	21.1	23.4	9.6	8.8	11.2

Continued on next page

Table B.3 *Continued from previous page*

Element	Lab/method code	LOD	191885	191886	191887	191888	191889	191890	195161	205265	205266
Gd	Acme/4B	0.05	0.31	2.54	0.22	0.51	0.41	0.54	0.38	0.65	1.88
Ge	Acme/1F-MS	0.1	0.2			0.1		0.2			
Hf	Acme/4B	0.1	0.2	1.6		0.2	0.2	0.4	0.1		1.0
Hg	Acme/1F-MS	0.005									
Ho	Acme/4B	0.02	0.05	0.63	0.02	0.09	0.05	0.08	0.12	0.14	0.45
In	Acme/1F-MS	0.02		0.02							
La	Acme/4B	0.1	2.0	5.3	1.6	2.1	2.0	2.6	0.6	0.9	5.8
Li	Acme/1EX	0.1									
Li	Acme/1F-MS	0.1	1.6	3.2	1.5	1.0	1.1	1.4	0.1	0.3	0.3
Lu	Acme/4B	0.01	0.02	0.26		0.02	0.03	0.03	0.05	0.05	0.17
Mo	Acme/1EX	0.1									
Mo	Acme/1F-MS	0.01	0.04	0.09	0.02	0.04	0.02	0.04	0.52	0.11	0.21
Nb	Acme/4B	0.1	0.5	2.2	0.3	0.6	0.7	0.9	0.2	0.1	1.2
Nd	Acme/4B	0.3	1.8	6.3	1.5	2.3	1.8	3.0	1.0	1.1	5.8
Ni	Acme/7TD	10	245	237	75	112	230	174	269	285	313
Pb	Acme/1EX	0.1									
Pb	Acme/1F-MS	0.01	0.32	0.45	0.37	0.29	0.16	0.19	5.87	1.57	2.46
Pd	Acme/3B-MS	0.0005		0.0024		0.0063	0.0009	0.0009			
Pr	Acme/4B	0.02	0.48	1.36	0.38	0.55	0.45	0.58	0.15	0.26	1.66
Pt	Acme/3B-MS	0.0001	0.0002	0.0019		0.0024		0.0002			0.0040
Rb	Acme/4B	0.1	1.7	6.4	1.1	1.8	1.5	2.2	0.3	0.6	5.9
Re	Acme/1F-MS	0.001	0.001	0.002			0.002	0.001			
Sb	Acme/1EX	0.1									

Continued on next page

Table B.3 *Continued from previous page*

Element	Lab/method code	LOD	191885	191886	191887	191888	191889	191890	195161	205265	205266
Sb	Acme/1F-MS	0.02							0.02		
Sc	Acme/4B	1	3	25	1	6	4	4	31	31	35
Se	Acme/1F-MS	0.1		0.2							
Se	GeoLabs/IMH-100	0.0035									
Sm	Acme/4B	0.05	0.35	1.86	0.28	0.49	0.41	0.59	0.27	0.41	1.66
Sn	Acme/4B	1									
Sr	Acme/4B	0.5	399.8	241.7	464.8	418.9	349.8	405.1	126.1	107.1	108.0
Ta	Acme/4B	0.1		0.2				0.1			
Tb	Acme/4B	0.01	0.05	0.47	0.03	0.08	0.05	0.08	0.09	0.12	0.34
Te	Acme/1F-MS	0.02									
Te	GeoLabs/IMH-100	0.001									
Th	Acme/4B	0.2		0.6				0.2			0.9
Tl	Acme/1F-MS	0.02									
Tm	Acme/4B	0.01	0.02	0.28		0.03	0.02	0.03	0.05	0.06	0.19
U	Acme/4B	0.1									
V	Acme/4B	8	50	215	32	150	65	324	99	120	182
W	Acme/4B	0.5									
Y	Acme/4B	0.1	1.6	17.2	0.8	2.6	1.5	2.3	3.5	4.0	12.1
Yb	Acme/4B	0.05	0.14	1.69	0.10	0.19	0.15	0.17	0.36	0.40	1.17
Zn	Acme/1EX	1									
Zn	Acme/1F-MS	0.1	24.5	11.5	9.1	11.9	49.0	27.4	16.3	3.1	4.9
Zr	Acme/4B	0.1	6.6	51.5	3.8	9.5	10.8	14.1	1.4	4.7	37.0

Continued on next page

Table B.3 *Continued from previous page*

Element	Lab/method code	LOD	205267	205268	205269	205270	205271	205272	205273	205274	205275
Ag	Acme/1EX	0.1									
Ag	Acme/1F-MS	0.002	0.017	0.009	0.004	0.011	0.003	0.008	0.006	0.004	0.006
As	Acme/1EX	1									
As	Acme/1F-MS	0.1	0.1	0.2							0.3
Au	Acme/3B-MS	0.001	0.001	0.001		0.000				0.000	0.000
B	Acme/1F-MS	1									
Ba	Acme/4B	1	50	93	7	24	18	20	19	87	7
Be	Acme/1EX	1									
Be	Acme/1F-MS	0.1									
Bi	Acme/1EX	0.1									
Bi	Acme/1F-MS	0.02									
Cd	Acme/1EX	0.1									
Cd	Acme/1F-MS	0.01		0.01		0.01	0.01			0.02	0.01
Ce	Acme/4B	0.1	5.4	1.9	0.5	1.3	1.5	1.2	1.1	1.6	0.6
Co	Acme/1EX	0.2									
Co	Acme/1F-MS	0.1	14.4	1.9	5.8	1.4	2.5	8.8	2.1	2.8	4.7
Cs	Acme/4B	0.1									
Cu	Acme/1EX	0.1									
Cu	Acme/1F-MS	0.01	38.28	1.41	1.80	5.26	2.59	1.56	2.74	10.58	6.44
Dy	Acme/4B	0.05	1.31	0.61	0.44	0.69	0.92	0.66	0.89	1.26	0.58
Er	Acme/4B	0.03	0.90	0.40	0.32	0.46	0.49	0.42	0.44	0.71	0.34
Eu	Acme/4B	0.02	0.35	0.33	0.13	0.19	0.20	0.20	0.18	0.20	0.13
Ga	Acme/4B	0.5	12.1	13.4	8.5	10.4	8.4	9.4	9.8	4.7	7.9

Continued on next page

Table B.3 *Continued from previous page*

Element	Lab/method code	LOD	205267	205268	205269	205270	205271	205272	205273	205274	205275
Gd	Acme/4B	0.05	1.26	0.56	0.29	0.57	0.71	0.60	0.50	0.87	0.31
Ge	Acme/1F-MS	0.1									
Hf	Acme/4B	0.1	0.3	0.2		0.1	0.1			0.4	
Hg	Acme/1F-MS	0.005									
Ho	Acme/4B	0.02	0.36	0.14	0.11	0.17	0.20	0.13	0.15	0.27	0.09
In	Acme/1F-MS	0.02									
La	Acme/4B	0.1	3.2	1.1	0.1	0.4	0.4	0.4	0.6	0.6	
Li	Acme/1EX	0.1									
Li	Acme/1F-MS	0.1	0.3	1.0	0.2	0.5	0.1	0.1	0.2		
Lu	Acme/4B	0.01	0.14	0.05	0.02	0.06	0.09	0.05	0.05	0.09	0.04
Mo	Acme/1EX	0.1									
Mo	Acme/1F-MS	0.01	0.13	0.29	0.12	0.23	0.13	0.24	0.12	0.28	0.13
Nb	Acme/4B	0.1	1.6		0.1	0.1	0.2		0.4		0.3
Nd	Acme/4B	0.3	3.4	1.6	0.5	1.1	1.2	1.1	0.7	2.1	0.7
Ni	Acme/7TD	10	366	202	383	227	289	347	278	426	282
Pb	Acme/1EX	0.1									
Pb	Acme/1F-MS	0.01	1.44	2.26	0.66	1.10	0.61	1.31	0.73	0.71	0.72
Pd	Acme/3B-MS	0.0005	0.0100								
Pr	Acme/4B	0.02	0.80	0.28	0.10	0.22	0.23	0.20	0.20	0.30	0.10
Pt	Acme/3B-MS	0.0001	0.0050								
Rb	Acme/4B	0.1	1.2	0.4		0.3	0.7	0.3	0.3	0.6	0.3
Re	Acme/1F-MS	0.001									0.002
Sb	Acme/1EX	0.1									

Continued on next page

Table B.3 *Continued from previous page*

Element	Lab/method code	LOD	205267	205268	205269	205270	205271	205272	205273	205274	205275
Sb	Acme/1F-MS	0.02									
Sc	Acme/4B	1	33	23	29	35	43	30	32	61	31
Se	Acme/1F-MS	0.1						0.1		0.1	
Se	GeoLabs/IMH-100	0.0035									
Sm	Acme/4B	0.05	1.05	0.46	0.23	0.44	0.56	0.34	0.42	0.56	0.20
Sn	Acme/4B	1									
Sr	Acme/4B	0.5	115.7	227.6	108.7	138.4	87.9	113.3	115.1	16.6	100.8
Ta	Acme/4B	0.1									
Tb	Acme/4B	0.01	0.25	0.10	0.07	0.12	0.14	0.10	0.11	0.18	0.06
Te	Acme/1F-MS	0.02				0.02					
Te	GeoLabs/IMH-100	0.001									
Th	Acme/4B	0.2									
Tl	Acme/1F-MS	0.02									
Tm	Acme/4B	0.01	0.16	0.06	0.04	0.06	0.08	0.05	0.05	0.11	0.04
U	Acme/4B	0.1	0.2								
V	Acme/4B	8	185	96	89	115	134	96	104	191	103
W	Acme/4B	0.5									
Y	Acme/4B	0.1	8.1	4.3	2.8	4.5	5.2	3.9	3.7	6.8	2.8
Yb	Acme/4B	0.05	0.91	0.40	0.22	0.41	0.59	0.35	0.40	0.63	0.28
Zn	Acme/1EX	1									
Zn	Acme/1F-MS	0.1	3.0	6.3	1.9	2.8	2.7	3.3	2.1	2.2	1.9
Zr	Acme/4B	0.1	18.4	6.1	2.1	2.7	4.3	2.7	2.8	9.3	4.3

Continued on next page

Table B.3 *Continued from previous page*

Element	Lab/method code	LOD	205276	205277	205278	205279	205280	205281	205282	205283	205284
Ag	Acme/1EX	0.1									
Ag	Acme/1F-MS	0.002	0.004	0.003	0.008	0.006	0.003	0.005	0.004	0.011	0.055
As	Acme/1EX	1									
As	Acme/1F-MS	0.1				0.2					
Au	Acme/3B-MS	0.001	0.000						0.000	0.001	0.002
B	Acme/1F-MS	1									
Ba	Acme/4B	1	10	9	15	13	28	19	52	18	35
Be	Acme/1EX	1									
Be	Acme/1F-MS	0.1									
Bi	Acme/1EX	0.1									
Bi	Acme/1F-MS	0.02									
Cd	Acme/1EX	0.1									
Cd	Acme/1F-MS	0.01		0.02	0.01			0.01			0.01
Ce	Acme/4B	0.1	0.8	1.0	1.4	1.0	2.5	1.2	1.2	1.6	3.9
Co	Acme/1EX	0.2									
Co	Acme/1F-MS	0.1	5.8	3.1	2.9	3.7	6.1	1.7	3.2	3.3	19.4
Cs	Acme/4B	0.1									
Cu	Acme/1EX	0.1									
Cu	Acme/1F-MS	0.01	7.94	6.48	9.55	4.12	6.16	3.42	15.59	25.03	144.70
Dy	Acme/4B	0.05	0.58	1.39	0.76	0.68	1.50	0.89	1.15	0.79	1.70
Er	Acme/4B	0.03	0.36	0.87	0.46	0.49	0.96	0.50	0.70	0.47	1.05
Eu	Acme/4B	0.02	0.18	0.20	0.20	0.19	0.29	0.21	0.24	0.22	0.33
Ga	Acme/4B	0.5	8.9	5.5	10.1	9.5	6.6	11.4	7.4	11.6	10.3

Continued on next page

Table B.3 *Continued from previous page*

Element	Lab/method code	LOD	205276	205277	205278	205279	205280	205281	205282	205283	205284
Gd	Acme/4B	0.05	0.45	0.94	0.62	0.56	1.21	0.60	0.90	0.66	1.35
Ge	Acme/1F-MS	0.1									
Hf	Acme/4B	0.1	0.2	0.2	0.3	0.2	0.5	0.2	0.3	0.1	0.6
Hg	Acme/1F-MS	0.005									
Ho	Acme/4B	0.02	0.10	0.32	0.19	0.17	0.38	0.18	0.25	0.18	0.33
In	Acme/1F-MS	0.02									
La	Acme/4B	0.1	0.2	0.1	0.5	0.4	0.9	0.4	0.6	0.6	1.3
Li	Acme/1EX	0.1									
Li	Acme/1F-MS	0.1	0.1		0.2	0.3	0.1	0.1		0.4	
Lu	Acme/4B	0.01	0.04	0.09	0.06	0.06	0.12	0.06	0.10	0.07	0.14
Mo	Acme/1EX	0.1									
Mo	Acme/1F-MS	0.01	0.20	0.09	0.18	0.12	0.29	0.10	0.24	0.12	0.22
Nb	Acme/4B	0.1	0.2	0.2	0.9	0.5	0.4	0.2		0.2	0.1
Nd	Acme/4B	0.3	0.6	1.3	1.0	1.1	2.7	1.4	1.5	1.2	2.7
Ni	Acme/7TD	10	281	320	256	339	484	268	380	240	451
Pb	Acme/1EX	0.1									
Pb	Acme/1F-MS	0.01	0.44	0.24	0.45	0.66	0.55	0.26	0.84	0.39	0.86
Pd	Acme/3B-MS	0.0005									0.0150
Pr	Acme/4B	0.02	0.13	0.20	0.23	0.17	0.42	0.19	0.22	0.23	0.59
Pt	Acme/3B-MS	0.0001								0.0020	0.0070
Rb	Acme/4B	0.1	0.2	0.3	0.3	0.2	0.9	0.5	0.5	0.6	0.8
Re	Acme/1F-MS	0.001							0.001		
Sb	Acme/1EX	0.1									

Continued on next page

Table B.3 *Continued from previous page*

Element	Lab/method code	LOD	205276	205277	205278	205279	205280	205281	205282	205283	205284
Sb	Acme/1F-MS	0.02									
Sc	Acme/4B	1	33	78	35	35	60	35	58	35	38
Se	Acme/1F-MS	0.1		0.1							0.2
Se	GeoLabs/IMH-100	0.0035									
Sm	Acme/4B	0.05	0.28	0.55	0.48	0.37	0.88	0.42	0.54	0.44	1.05
Sn	Acme/4B	1									
Sr	Acme/4B	0.5	103.9	22.5	107.7	105.2	21.7	144.9	43.6	120.4	88.7
Ta	Acme/4B	0.1									
Tb	Acme/4B	0.01	0.09	0.19	0.11	0.11	0.24	0.12	0.17	0.13	0.27
Te	Acme/1F-MS	0.02								0.04	0.03
Te	GeoLabs/IMH-100	0.001									
Th	Acme/4B	0.2									
Tl	Acme/1F-MS	0.02									
Tm	Acme/4B	0.01	0.05	0.12	0.07	0.07	0.15	0.07	0.09	0.07	0.16
U	Acme/4B	0.1					0.1				
V	Acme/4B	8	108	221	130	127	219	127	242	152	195
W	Acme/4B	0.5									
Y	Acme/4B	0.1	3.4	7.5	4.7	4.4	9.9	5.2	7.7	5.2	10.1
Yb	Acme/4B	0.05	0.34	0.76	0.41	0.42	0.91	0.52	0.66	0.49	1.01
Zn	Acme/1EX	1									
Zn	Acme/1F-MS	0.1	1.0	2.0	0.7	2.1	2.4	0.8	2.6	0.5	4.0
Zr	Acme/4B	0.1	2.7	4.2	6.8	5.7	7.6	6.1	5.4	5.5	11.6

Continued on next page

Table B.3 *Continued from previous page*

Element	Lab/method code	LOD	205285	205286	205287	205288	205289	205290	205291	205292	205293
Ag	Acme/1EX	0.1									
Ag	Acme/1F-MS	0.002	0.002	0.009	0.045	0.005	0.007	0.004	0.031	0.013	0.007
As	Acme/1EX	1									
As	Acme/1F-MS	0.1									
Au	Acme/3B-MS	0.001		0.003	0.002					0.001	
B	Acme/1F-MS	1									
Ba	Acme/4B	1	14	24	12	17	40	15	428	24	20
Be	Acme/1EX	1									
Be	Acme/1F-MS	0.1							0.1		
Bi	Acme/1EX	0.1									
Bi	Acme/1F-MS	0.02									
Cd	Acme/1EX	0.1									
Cd	Acme/1F-MS	0.01	0.01				0.01		0.01	0.01	
Ce	Acme/4B	0.1	2.3	2.2	1.0	3.1	1.6	0.3	29.0	1.1	1.3
Co	Acme/1EX	0.2									
Co	Acme/1F-MS	0.1	4.4	4.1	6.8	4.7	3.1	4.8	19.6	5.7	4.2
Cs	Acme/4B	0.1							0.2		
Cu	Acme/1EX	0.1									
Cu	Acme/1F-MS	0.01	5.98	19.74	128.09	7.79	4.80	9.05	67.51	47.48	16.83
Dy	Acme/4B	0.05	2.44	1.88	1.11	2.39	1.11	0.56	3.78	0.96	1.50
Er	Acme/4B	0.03	1.40	1.09	0.70	1.49	0.57	0.44	1.91	0.66	0.96
Eu	Acme/4B	0.02	0.46	0.46	0.18	0.50	0.36	0.06	1.35	0.18	0.29
Ga	Acme/4B	0.5	7.8	12.0	7.3	7.1	15.5	6.4	19.6	7.9	7.3

Continued on next page

Table B.3 *Continued from previous page*

Element	Lab/method code	LOD	205285	205286	205287	205288	205289	205290	205291	205292	205293
Gd	Acme/4B	0.05	2.05	1.63	0.72	2.08	0.89	0.31	4.26	0.71	1.16
Ge	Acme/1F-MS	0.1									
Hf	Acme/4B	0.1	0.5	0.5	0.3	0.4	0.3	0.2	3.2	0.4	0.4
Hg	Acme/1F-MS	0.005									
Ho	Acme/4B	0.02	0.51	0.39	0.20	0.55	0.22	0.14	0.73	0.20	0.32
In	Acme/1F-MS	0.02									
La	Acme/4B	0.1	0.4	0.6	0.2	0.7	0.5	0.2	14.7	0.4	0.4
Li	Acme/1EX	0.1									
Li	Acme/1F-MS	0.1	0.2	0.3	0.1	0.1	0.5		0.4	0.2	0.1
Lu	Acme/4B	0.01	0.17	0.14	0.12	0.17	0.06	0.07	0.23	0.11	0.12
Mo	Acme/1EX	0.1									
Mo	Acme/1F-MS	0.01	0.09	0.17	0.09	0.19	0.07	0.12	0.82	0.11	0.22
Nb	Acme/4B	0.1	0.1		0.2	0.2	0.3	0.2	10.3	0.1	0.1
Nd	Acme/4B	0.3	3.2	2.5	1.4	3.7	2.0	0.4	15.6	1.3	2.3
Ni	Acme/7TD	10	437	290	911	467	186	871	193	819	493
Pb	Acme/1EX	0.1									
Pb	Acme/1F-MS	0.01	0.13	0.45	0.21	0.30	0.30	0.36	0.72	0.46	0.27
Pd	Acme/3B-MS	0.0005		0.0100				0.0120			
Pr	Acme/4B	0.02	0.52	0.44	0.18	0.57	0.26	0.06	3.65	0.20	0.28
Pt	Acme/3B-MS	0.0001			0.0070			0.0030		0.0070	
Rb	Acme/4B	0.1	0.2	0.3	0.2	0.5	0.6		25.0	0.2	0.2
Re	Acme/1F-MS	0.001									
Sb	Acme/1EX	0.1									

Continued on next page

Table B.3 *Continued from previous page*

Element	Lab/method code	LOD	205285	205286	205287	205288	205289	205290	205291	205292	205293
Sb	Acme/1F-MS	0.02									
Sc	Acme/4B	1	69	53	41	68	32	35	22	39	59
Se	Acme/1F-MS	0.1							0.1		0.1
Se	GeoLabs/IMH-100	0.0035									
Sm	Acme/4B	0.05	1.36	1.12	0.52	1.44	0.62	0.19	3.96	0.48	0.76
Sn	Acme/4B	1							1		
Sr	Acme/4B	0.5	14.8	132.0	5.2	15.0	243.4	2.7	337.9	31.6	38.2
Ta	Acme/4B	0.1							0.7		
Tb	Acme/4B	0.01	0.37	0.29	0.15	0.37	0.17	0.07	0.66	0.14	0.23
Te	Acme/1F-MS	0.02									
Te	GeoLabs/IMH-100	0.001									
Th	Acme/4B	0.2							1.3		
Tl	Acme/1F-MS	0.02									
Tm	Acme/4B	0.01	0.19	0.13	0.10	0.20	0.09	0.07	0.28	0.12	0.14
U	Acme/4B	0.1							0.2		
V	Acme/4B	8	370	315	236	368	172	189	174	208	265
W	Acme/4B	0.5							0.8		1.6
Y	Acme/4B	0.1	13.4	10.3	6.3	14.3	5.8	3.5	20.1	6.1	9.1
Yb	Acme/4B	0.05	1.33	0.95	0.71	1.25	0.44	0.45	1.72	0.69	1.01
Zn	Acme/1EX	1									
Zn	Acme/1F-MS	0.1	2.6	4.2	3.4	4.7	1.9	3.7	15.8	2.9	2.6
Zr	Acme/4B	0.1	13.1	8.3	7.3	11.1	5.0	5.3	114.4	6.4	7.0

Continued on next page

Table B.3 *Continued from previous page*

Element	Lab/method code	LOD	205294	205295	205296	205297	205298	205299	205300	205301	205302
Ag	Acme/1EX	0.1									
Ag	Acme/1F-MS	0.002	0.012	0.015	0.006	0.008	0.031	0.007	0.006	0.002	0.002
As	Acme/1EX	1									
As	Acme/1F-MS	0.1	0.7	0.3	1.6	0.3	0.5	0.8	0.4	0.4	0.2
Au	Acme/3B-MS	0.001		0.001	0.001	0.001	0.010	0.002	0.001	0.001	
B	Acme/1F-MS	1									
Ba	Acme/4B	1	68	29	37	107	98	59	7	15	5
Be	Acme/1EX	1									
Be	Acme/1F-MS	0.1									
Bi	Acme/1EX	0.1									
Bi	Acme/1F-MS	0.02	0.03					0.04			
Cd	Acme/1EX	0.1									
Cd	Acme/1F-MS	0.01	0.02	0.03		0.01		0.01			0.01
Ce	Acme/4B	0.1	2.7	2.5	1.4	2.7	2.4	3.9	1.4	1.7	2.7
Co	Acme/1EX	0.2									
Co	Acme/1F-MS	0.1	4.9	5.8	3.1	4.8	7.8	6.3	5.4	6.2	7.3
Cs	Acme/4B	0.1									
Cu	Acme/1EX	0.1									
Cu	Acme/1F-MS	0.01	26.99	58.54	15.17	21.12	86.18	23.06	24.63	1.57	6.66
Dy	Acme/4B	0.05	2.38	2.30	1.47	2.15	1.40	2.49	1.44	2.37	3.39
Er	Acme/4B	0.03	1.35	1.35	0.91	1.35	0.84	1.31	0.88	1.30	1.81
Eu	Acme/4B	0.02	0.43	0.42	0.28	0.40	0.53	0.48	0.24	0.45	0.58
Ga	Acme/4B	0.5	7.6	7.8	9.0	7.5	16.4	7.6	6.7	11.0	8.1

Continued on next page

Table B.3 *Continued from previous page*

Element	Lab/method code	LOD	205294	205295	205296	205297	205298	205299	205300	205301	205302
Gd	Acme/4B	0.05	1.62	1.78	0.98	1.62	1.11	1.99	1.01	1.78	2.49
Ge	Acme/1F-MS	0.1									
Hf	Acme/4B	0.1	0.4	0.5	0.3	0.6	0.4	0.8	0.3	0.5	0.7
Hg	Acme/1F-MS	0.005					0.007				
Ho	Acme/4B	0.02	0.43	0.47	0.25	0.48	0.26	0.44	0.30	0.44	0.65
In	Acme/1F-MS	0.02									
La	Acme/4B	0.1	0.8	0.6	0.5	0.9	1.0	1.3	0.4	0.4	0.5
Li	Acme/1EX	0.1									
Li	Acme/1F-MS	0.1		0.1	0.1	0.2	0.8	0.3	0.2	0.3	0.2
Lu	Acme/4B	0.01	0.16	0.18	0.11	0.18	0.11	0.18	0.13	0.19	0.23
Mo	Acme/1EX	0.1									
Mo	Acme/1F-MS	0.01	0.09	0.23	0.08	0.22	0.06	0.18	0.09	0.15	0.07
Nb	Acme/4B	0.1	0.4		0.2	0.3	0.1	0.3	0.3		
Nd	Acme/4B	0.3	2.7	2.4	1.6	3.1	2.0	3.6	1.1	1.6	3.6
Ni	Acme/7TD	10	525	497	394	540	173	517	446	302	359
Pb	Acme/1EX	0.1									
Pb	Acme/1F-MS	0.01	3.23	0.31	0.72	0.55	0.40	0.68	0.18	0.26	0.32
Pd	Acme/3B-MS	0.0005	0.0110			0.0200	0.0200	0.0200			
Pr	Acme/4B	0.02	0.48	0.50	0.25	0.51	0.37	0.68	0.21	0.37	0.59
Pt	Acme/3B-MS	0.0001	0.0050	0.0050		0.0100	0.0150	0.0080			
Rb	Acme/4B	0.1	0.9	0.3	0.4	0.6	0.9	0.9	0.3		
Re	Acme/1F-MS	0.001									
Sb	Acme/1EX	0.1									

Continued on next page

Table B.3 *Continued from previous page*

Element	Lab/method code	LOD	205294	205295	205296	205297	205298	205299	205300	205301	205302
Sb	Acme/1F-MS	0.02	0.04					0.18			
Sc	Acme/4B	1	60	57	48	58	30	59	55	61	77
Se	Acme/1F-MS	0.1									
Se	GeoLabs/IMH-100	0.0035									
Sm	Acme/4B	0.05	1.03	1.23	0.67	1.20	0.73	1.32	0.62	1.14	1.88
Sn	Acme/4B	1				1					
Sr	Acme/4B	0.5	25.4	20.1	67.1	29.0	265.8	31.5	18.7	84.9	10.8
Ta	Acme/4B	0.1									
Tb	Acme/4B	0.01	0.31	0.34	0.20	0.32	0.20	0.35	0.20	0.34	0.49
Te	Acme/1F-MS	0.02					0.02		0.03		
Te	GeoLabs/IMH-100	0.001									
Th	Acme/4B	0.2		0.3							
Tl	Acme/1F-MS	0.02									
Tm	Acme/4B	0.01	0.18	0.21	0.14	0.20	0.12	0.19	0.14	0.20	0.25
U	Acme/4B	0.1									
V	Acme/4B	8	263	290	209	259	173	263	235	370	484
W	Acme/4B	0.5									
Y	Acme/4B	0.1	11.8	13.1	8.5	12.4	7.9	13.2	7.9	12.9	17.6
Yb	Acme/4B	0.05	1.29	1.19	0.76	1.13	0.75	1.26	0.89	1.08	1.67
Zn	Acme/1EX	1									
Zn	Acme/1F-MS	0.1	3.8	4.6	1.7	2.7	4.8	8.1	2.6	6.5	6.8
Zr	Acme/4B	0.1	10.1	10.7	5.6	11.5	6.0	15.4	6.5	6.9	11.7

Continued on next page

Table B.3 *Continued from previous page*

Element	Lab/method code	LOD	205303	205304	205305	205306	205307	205308	205309	205310	205311
Ag	Acme/1EX	0.1									
Ag	Acme/1F-MS	0.002	0.009		0.017	0.046	0.004	0.021	0.003	0.028	0.021
As	Acme/1EX	1									
As	Acme/1F-MS	0.1	0.5		0.1	0.6	1.2	0.4	0.1		0.5
Au	Acme/3B-MS	0.001	0.001		0.002	0.002		0.001		0.002	0.002
B	Acme/1F-MS	1									
Ba	Acme/4B	1	10	3	18	111	48	326	3	19	503
Be	Acme/1EX	1									
Be	Acme/1F-MS	0.1						0.2			0.1
Bi	Acme/1EX	0.1									
Bi	Acme/1F-MS	0.02									
Cd	Acme/1EX	0.1									
Cd	Acme/1F-MS	0.01	0.02			0.04		0.02		0.01	0.01
Ce	Acme/4B	0.1	1.6	3.3	0.6	1.2	1.1	30.7	2.7	1.5	62.0
Co	Acme/1EX	0.2									
Co	Acme/1F-MS	0.1	7.1	9.0	6.8	20.3	4.6	38.2	7.7	5.8	32.4
Cs	Acme/4B	0.1									0.6
Cu	Acme/1EX	0.1									
Cu	Acme/1F-MS	0.01	29.38	5.81	69.28	145.16	2.01	68.70	10.63	113.69	56.97
Dy	Acme/4B	0.05	1.70	3.29	0.80	1.75	0.43	4.30	2.63	2.47	9.07
Er	Acme/4B	0.03	0.98	1.80	0.59	1.07	0.24	2.41	1.35	1.28	4.62
Eu	Acme/4B	0.02	0.31	0.62	0.11	0.55	0.23	1.37	0.45	0.52	3.39
Ga	Acme/4B	0.5	8.0	8.6	8.8	17.5	14.3	17.4	8.1	10.2	24.3

Continued on next page

Table B.3 *Continued from previous page*

Element	Lab/method code	LOD	205303	205304	205305	205306	205307	205308	205309	205310	205311
Gd	Acme/4B	0.05	1.17	2.62	0.44	1.11	0.26	4.25	1.95	2.27	9.58
Ge	Acme/1F-MS	0.1									
Hf	Acme/4B	0.1	0.3	0.8	0.1	0.3		2.8	0.6	0.6	6.6
Hg	Acme/1F-MS	0.005		0.006							
Ho	Acme/4B	0.02	0.34	0.62	0.15	0.38	0.08	0.79	0.49	0.53	1.72
In	Acme/1F-MS	0.02									
La	Acme/4B	0.1	0.4	0.9	0.2	0.6	0.6	13.4	0.6	0.4	25.9
Li	Acme/1EX	0.1									
Li	Acme/1F-MS	0.1	0.2	0.3	0.2	0.7	0.7	0.4	0.1	0.2	0.1
Lu	Acme/4B	0.01	0.15	0.21	0.10	0.19	0.04	0.30	0.16	0.18	0.57
Mo	Acme/1EX	0.1									
Mo	Acme/1F-MS	0.01	0.22	0.09	0.25	0.12	0.19	0.52	0.23	0.10	0.85
Nb	Acme/4B	0.1		0.2				5.6			13.7
Nd	Acme/4B	0.3	2.2	4.8	0.7	1.1	0.5	17.3	3.3	2.6	40.6
Ni	Acme/7TD	10	399	358	583	160	254	384	328	282	96
Pb	Acme/1EX	0.1									
Pb	Acme/1F-MS	0.01	1.83	0.37	0.30	0.62	0.24	1.25	0.28	0.08	0.90
Pd	Acme/3B-MS	0.0005								0.0130	
Pr	Acme/4B	0.02	0.30	0.70	0.11	0.21	0.14	3.89	0.48	0.39	8.39
Pt	Acme/3B-MS	0.0001			0.0107	0.0030				0.0090	
Rb	Acme/4B	0.1	0.3	0.1	0.3	1.1	0.6	16.0	0.2	0.3	22.6
Re	Acme/1F-MS	0.001									
Sb	Acme/1EX	0.1									

Continued on next page

Table B.3 *Continued from previous page*

Element	Lab/method code	LOD	205303	205304	205305	205306	205307	205308	205309	205310	205311
Sb	Acme/1F-MS	0.02	0.03	0.02		0.03					
Sc	Acme/4B	1	52	76	39	32	18	25	75	70	30
Se	Acme/1F-MS	0.1						0.1			0.2
Se	GeoLabs/IMH-100	0.0035									
Sm	Acme/4B	0.05	0.90	1.83	0.32	0.58	0.20	4.14	1.33	1.38	9.36
Sn	Acme/4B	1									1
Sr	Acme/4B	0.5	29.8	12.2	29.6	264.0	254.0	258.4	14.0	54.3	330.7
Ta	Acme/4B	0.1						0.4			0.9
Tb	Acme/4B	0.01	0.23	0.47	0.10	0.23	0.05	0.70	0.38	0.39	1.49
Te	Acme/1F-MS	0.02			0.04					0.04	
Te	GeoLabs/IMH-100	0.001									
Th	Acme/4B	0.2						0.6			2.5
Tl	Acme/1F-MS	0.02						0.02			
Tm	Acme/4B	0.01	0.15	0.25	0.10	0.19	0.05	0.36	0.20	0.20	0.63
U	Acme/4B	0.1						0.1			0.6
V	Acme/4B	8	263	467	222	317	110	197	432	471	368
W	Acme/4B	0.5									
Y	Acme/4B	0.1	8.7	17.7	4.5	10.8	2.3	24.0	13.4	13.4	48.8
Yb	Acme/4B	0.05	0.84	1.52	0.64	1.36	0.28	1.98	1.29	1.31	4.13
Zn	Acme/1EX	1									
Zn	Acme/1F-MS	0.1	4.7	5.7	3.5	8.4	3.3	8.3	4.6	4.2	31.6
Zr	Acme/4B	0.1	7.7	14.0	4.3	5.8	1.9	129.0	10.7	7.3	259.8

Continued on next page

Table B.3 *Continued from previous page*

Element	Lab/method code	LOD	205312
Ag	Acme/1EX	0.1	
Ag	Acme/1F-MS	0.002	0.051
As	Acme/1EX	1	
As	Acme/1F-MS	0.1	0.4
Au	Acme/3B-MS	0.001	0.012
B	Acme/1F-MS	1	
Ba	Acme/4B	1	38
Be	Acme/1EX	1	
Be	Acme/1F-MS	0.1	
Bi	Acme/1EX	0.1	
Bi	Acme/1F-MS	0.02	
Cd	Acme/1EX	0.1	
Cd	Acme/1F-MS	0.01	0.01
Ce	Acme/4B	0.1	1.6
Co	Acme/1EX	0.2	
Co	Acme/1F-MS	0.1	8.3
Cs	Acme/4B	0.1	
Cu	Acme/1EX	0.1	
Cu	Acme/1F-MS	0.01	190.19
Dy	Acme/4B	0.05	1.25
Er	Acme/4B	0.03	0.64
Eu	Acme/4B	0.02	0.29
Ga	Acme/4B	0.5	12.4

Continued on next page

Table B.3 *Continued from previous page*

Element	Lab/method code	LOD	205312
Gd	Acme/4B	0.05	0.81
Ge	Acme/1F-MS	0.1	
Hf	Acme/4B	0.1	0.3
Hg	Acme/1F-MS	0.005	
Ho	Acme/4B	0.02	0.19
In	Acme/1F-MS	0.02	
La	Acme/4B	0.1	0.6
Li	Acme/1EX	0.1	
Li	Acme/1F-MS	0.1	0.6
Lu	Acme/4B	0.01	0.10
Mo	Acme/1EX	0.1	
Mo	Acme/1F-MS	0.01	0.07
Nb	Acme/4B	0.1	0.1
Nd	Acme/4B	0.3	1.4
Ni	Acme/7TD	10	364
Pb	Acme/1EX	0.1	
Pb	Acme/1F-MS	0.01	0.96
Pd	Acme/3B-MS	0.0005	
Pr	Acme/4B	0.02	0.27
Pt	Acme/3B-MS	0.0001	0.0180
Rb	Acme/4B	0.1	0.8
Re	Acme/1F-MS	0.001	
Sb	Acme/1EX	0.1	

Continued on next page

Table B.3 *Continued from previous page*

Element	Lab/method code	LOD	205312
Sb	Acme/1F-MS	0.02	
Sc	Acme/4B	1	34
Se	Acme/1F-MS	0.1	0.2
Se	GeoLabs/IMH-100	0.0035	
Sm	Acme/4B	0.05	0.56
Sn	Acme/4B	1	
Sr	Acme/4B	0.5	172.3
Ta	Acme/4B	0.1	
Tb	Acme/4B	0.01	0.15
Te	Acme/1F-MS	0.02	0.10
Te	GeoLabs/IMH-100	0.001	
Th	Acme/4B	0.2	
Tl	Acme/1F-MS	0.02	
Tm	Acme/4B	0.01	0.10
U	Acme/4B	0.1	
V	Acme/4B	8	166
W	Acme/4B	0.5	
Y	Acme/4B	0.1	5.7
Yb	Acme/4B	0.05	0.56
Zn	Acme/1EX	1	
Zn	Acme/1F-MS	0.1	5.3
Zr	Acme/4B	0.1	5.2

Table B.4 Whole-rock Sr- and Nd-isotope compositions for selected samples. All trace element data are quoted in ppm (Rb and Sr data marked with an asterisk (*) were determined via isotope dilution at the University of Melbourne; all other trace element data were adopted from table B.3). Initial isotope ratios were calculated for t = 1078 Ma. Descriptions of the analytical methods are in sections 3.3.1 and 4.3.1.

Sample no.	Rb	Sr	$^{87}Rb/^{86}Sr$	$^{87}Sr/^{86}Sr$	$^{87}Sr/^{86}Sr(t)$	Sm	Nd	$^{147}Sm/^{144}Nd$	$^{143}Nd/^{144}Nd$	$\epsilon_{Nd}(t)$
191 820	0.9	101.0	0.0258	0.705308	0.70491	0.37	0.98	0.2283	0.512916	+1.1
191 821	3.8	141.9	0.0774	0.706733	0.70554	0.93	3.26	0.1731	0.512433	-0.7
191 822	—	102.3	—	0.705290	—	0.98	2.50	0.2372	0.512876	-0.9
191 823	1.1	141.9	0.0224	0.705952	0.70561	0.46	1.58	0.1779	0.512451	-1.1
191 824	1.0	141.9	0.0204	0.705617	0.70530	0.30	1.10	0.1669	0.512410	-0.3
191 827	0.6	124.1	0.0140	0.705434	0.70522	0.41	1.28	0.1957	0.512639	+0.2
191 829	0.8	279.6	0.0083	0.707123	0.70699	3.70	15.19	0.1470	0.512080	-4.0
191 830	1.5	278.9	0.0155	0.708904	0.70866	7.35	30.79	0.1442	0.512102	-3.2
191 831	7.44*	251.6*	0.0855	0.707402	0.70608	2.02	6.21	0.1961	0.512610	-0.5
191 832	2.1	297.0	0.0204	0.704232	0.70392	1.63	5.84	0.1681	0.512500	+1.3
191 836	1.3	264.9	0.0142	0.703969	0.70375	0.89	3.48	0.1537	0.512386	+1.0
191 839	4.0	181.2	0.0638	0.705779	0.70479	2.17	8.04	0.1631	0.512423	+0.4
191 840	1.6	334.4	0.0138	0.704048	0.70384	0.86	3.29	0.1579	0.512423	+1.2
191 841	4.2	175.0	0.0694	0.705718	0.70465	2.31	8.54	0.1632	0.512416	+0.3
191 844	1.1	271.6	0.0117	0.704101	0.70392	0.31	1.45	0.1307	0.512243	+1.4

Continued on next page

Table B.4 *Continued from previous page*

Sample no.	Rb	Sr	$^{87}Rb/^{86}Sr$	$^{87}Sr/^{86}Sr$	$^{87}Sr/^{86}Sr(t)$	Sm	Nd	$^{147}Sm/^{144}Nd$	$^{143}Nd/^{144}Nd$	$\epsilon_{Nd}(t)$
191 848	2.0	385.2	0.0150	0.704152	0.70392	0.41	2.00	0.1235	0.512182	+1.2
191 851	2.7	331.6	0.0235	0.704454	0.70409	0.70	3.11	0.1352	0.512232	+0.6
191 854	4.1	163.3	0.0726	0.706071	0.70495	2.03	7.34	0.1672	0.512432	+0.1
191 855	1.2	343.4	0.0101	0.704720	0.70456	0.55	2.03	0.1628	0.512384	-0.3
191 858	0.9	267.3	0.0097	0.704359	0.70421	0.16	0.85	0.1136	0.512082	+0.6
191 859	2.5	393.1	0.0184	0.704789	0.70451	0.60	2.79	0.1303	0.512209	+0.8
191 860	0.9	332.3	0.0078	0.704527	0.70441	0.23	1.19	0.1165	0.512099	+0.6
191 861	1.9	375.7	0.0146	0.704637	0.70441	0.47	2.26	0.1268	0.512148	+0.1
191 865	1.5	272.4	0.0159	0.704420	0.70417	0.24	1.12	0.1282	0.512185	+0.6
191 867	2.5	481.7	0.0150	0.704424	0.70419	0.59	2.68	0.1323	0.512202	+0.4
191 869	1.6	237.4	0.0189	0.704524	0.70423	1.44	4.32	0.2017	0.512733	+1.2
191 871	15.70*	416.1*	0.1092	0.705821	0.70414	4.19	18.13	0.1395	0.512477	+4.8
191 872	16.17*	411.5*	0.1140	0.705900	0.70414	4.37	18.76	0.1405	0.512263	+0.4
205 283	0.6	108.9*	0.0159	0.706566	0.70632	0.46	1.26	0.2177	0.512811	+0.5
205 298	0.9	265.8	0.0098	0.706252	0.70610	0.52	1.46	0.2151	0.512676	-1.8

Table B.5 Plagioclase major and minor element compositions (see description of analytical method in sections 2.3 and 4.3.1).

Sample no.	191830	191830	191830	191830	191830	191830	191830	191830	191830
Analysis no.	pl_1_1	pl_10_10	pl_11_11	pl_12_12	pl_13_13	pl_14_14	pl_15_15	pl_16_16	pl_17_17
Al_2O_3	28.13	28.25	27.88	27.97	28.07	28.10	27.94	27.98	27.87
CaO	10.41	10.43	10.46	10.41	10.77	10.54	10.69	10.71	10.64
Cr_2O_3		0.01				0.01	0.01	0.01	0.04
Fe_2O_3	0.07	0.10	0.05	0.03	0.04	0.08	0.10	0.18	0.05
K_2O	0.19	0.21	0.18	0.19	0.17	0.19	0.25	0.21	0.22
MgO									
MnO		0.02			0.02	0.01	0.01		0.01
Na_2O	5.55	5.59	5.61	5.66	5.54	5.78	5.56	5.45	5.56
Nb_2O_5		0.02	0.03				0.04		
NiO	0.02			0.02			0.01	0.03	0.02
SiO_2	54.51	54.87	53.90	54.50	53.78	54.27	53.83	53.70	53.63
TiO_2	0.04	0.02	0.03	0.02	0.01		0.04	0.02	0.03
V_2O_3	0.02	0.03	0.03	0.05		0.01	0.04	0.01	0.03
ZnO		0.03	0.02	0.01	0.02	0.01		0.02	
Ab	48.5	48.6	48.8	49.1	47.7	49.3	47.8	47.4	48.0
An	50.4	50.2	50.2	49.8	51.3	49.7	50.8	51.5	50.8
Or	1.1	1.2	1.0	1.1	1.0	1.1	1.4	1.2	1.3

Continued on next page

Table B.5 *Continued from previous page*

Sample no.	191830	191830	191830	191830	191830	191830	191830	191830	191830
Analysis no.	pl_18_18	pl_19_19	pl_2_2	pl_20_20	pl_3_3	pl_4_4	pl_5_5	pl_6_6	pl_7_7
Al_2O_3	28.16	27.72	28.21	28.29	28.36	28.19	28.17	27.97	28.14
CaO	10.67	10.83	10.41	10.65	10.68	10.68	10.56	10.45	10.41
Cr_2O_3		0.01	0.02		0.01			0.01	
Fe_2O_3	0.03	0.08	0.06	0.17	0.07	0.04	0.07	0.03	0.03
K_2O	0.13	0.46	0.20	0.18	0.19	0.24	0.17	0.22	0.15
MgO		0.02		0.01				0.00	0.01
MnO		0.01	0.01				0.02	0.01	0.02
Na_2O	5.64	5.42	5.62	5.67	5.60	5.58	5.61	5.53	5.62
Nb_2O_5		0.04	0.02	0.02		0.04		0.03	
NiO	0.03		0.01			0.02	0.03		0.01
SiO_2	54.40	53.41	54.55	54.78	54.75	54.68	54.09	54.03	54.66
TiO_2	0.02	0.03	0.03		0.04	0.01	0.03	0.04	0.04
V_2O_3			0.01				0.01	0.01	0.03
ZnO		0.02		0.01	0.03		0.04	0.02	0.02
Ab	48.6	46.3	48.9	48.6	48.2	47.9	48.5	48.3	49.0
An	50.7	51.2	50.0	50.4	50.8	50.7	50.5	50.4	50.1
Or	0.7	2.6	1.1	1.0	1.1	1.4	1.0	1.3	0.9

Continued on next page

Table B.5 *Continued from previous page*

Sample no.	191830	191830	191831	191831	191831	191831	191831	191831	191831
Analysis no.	pl_8_8	pl_9_9	pl_1_1	pl_10_10	pl_11_11	pl_12_12	pl_13_13	pl_14_14	pl_15_15
Al_2O_3	28.24	27.62	29.65	29.94	27.44	28.71	29.10	29.13	29.39
CaO	10.55	10.85	12.15	12.70	10.08	11.72	11.92	12.69	12.42
Cr_2O_3		0.02	0.02			0.01		0.01	
Fe_2O_3	0.13	0.17	0.26	0.07	0.17	0.43	0.13	0.29	0.22
K_2O	0.16	0.28	0.12	0.09	0.18	0.14	0.11	0.17	0.11
MgO		0.05	0.07					0.03	0.01
MnO	0.01	0.02			0.02	0.02	0.01		0.01
Na_2O	5.73	5.42	4.67	4.61	6.07	4.95	4.90	4.60	4.58
Nb_2O_5				0.02	0.02			0.01	0.06
NiO	0.04			0.01		0.03			
SiO_2	54.99	53.46	52.79	52.21	55.01	51.99	53.04	51.51	51.54
TiO_2	0.02	0.03	0.03	0.01		0.11	0.04	0.01	0.06
V_2O_3	0.03	0.05	0.01		0.04			0.02	
ZnO	0.01		0.01	0.07					0.02
Ab	49.1	46.7	40.7	39.4	51.6	43.0	42.4	39.2	39.7
An	50.0	51.7	58.6	60.0	47.4	56.2	57.0	59.8	59.6
Or	0.9	1.6	0.7	0.5	1.0	0.8	0.6	1.0	0.6

Continued on next page

Table B.5 *Continued from previous page*

Sample no.	191831	191831	191831	191831	191831	191831	191831	191831	191831
Analysis no.	pl_16_16	pl_17_17	pl_18_18	pl_19_19	pl_2_2	pl_20_20	pl_3_3	pl_4_4	pl_5_5
Al_2O_3	29.94	29.01	29.86	29.32	29.41	29.71	29.51	27.64	28.82
CaO	12.76	12.10	12.91	12.15	12.02	12.24	12.70	10.83	11.08
Cr_2O_3	0.01	0.01			0.02		0.01	0.00	
Fe_2O_3	0.16	0.24	0.20	0.04	0.50	0.49	0.13	0.41	0.18
K_2O	0.13	0.11	0.15	0.18	0.15	0.17	0.16	0.45	0.15
MgO				0.01	0.06	0.15	0.02	0.06	
MnO	0.04	0.01		0.04	0.03	0.04	0.03	0.02	0.01
Na_2O	4.50	4.68	4.34	4.73	4.77	4.69	4.43	5.26	5.33
Nb_2O_5			0.05	0.02	0.02		0.05	0.06	0.01
NiO		0.01					0.02		
SiO_2	52.14	51.31	51.35	51.99	52.77	53.09	50.98	53.35	53.80
TiO_2	0.02	0.03	0.04		0.05	0.07		0.03	0.03
V_2O_3	0.02			0.01			0.03	0.01	
ZnO	0.01	0.00	0.03			0.04		0.00	0.01
Ab	38.7	40.9	37.5	40.9	41.4	40.6	38.4	45.6	46.1
An	60.6	58.5	61.7	58.1	57.8	58.5	60.7	51.8	53.0
Or	0.7	0.6	0.8	1.0	0.9	1.0	0.9	2.6	0.9

Continued on next page

Table B.5 *Continued from previous page*

Sample no.	191831	191831	191831	191831	191832	191832	191832	191832	191832
Analysis no.	pl_6_6	pl_7_7	pl_8_8	pl_9_9	pl_1_1	pl_10_1	pl_11_1	pl_12_1	pl_13_1
Al_2O_3	28.46	29.39	29.93	29.55	29.72	29.42	29.47	28.94	29.82
CaO	10.95	12.27	12.40	12.31	13.02	12.76	12.71	12.42	13.23
Cr_2O_3			0.01					0.02	
Fe_2O_3	0.06	0.26	0.15	0.16	0.03	0.06	0.05	0.02	0.03
K_2O	1.08	0.11	0.12	0.16	0.11	0.10	0.09	0.10	0.09
MgO	0.01		0.01	0.01			0.04		
MnO	0.01		0.01	0.01	0.02	0.03	0.03	0.02	0.01
Na_2O	4.87	4.60	4.51	4.60	4.67	4.62	4.65	4.80	4.32
Nb_2O_5	0.02	0.06	0.01	0.01	0.02		0.03		
NiO			0.01		0.02		0.03	0.01	0.03
SiO_2	54.51	51.68	52.16	52.66	53.30	53.38	53.08	52.58	52.37
TiO_2		0.05	0.03	0.05		0.05	0.03		0.04
V_2O_3	0.03		0.02	0.01	0.03		0.02	0.01	0.01
ZnO	0.03	0.03	0.04		0.06		0.02		0.04
Ab	41.9	40.1	39.4	40.0	39.1	39.4	39.6	40.9	37.0
An	52.0	59.2	59.9	59.1	60.3	60.1	59.9	58.5	62.5
Or	6.1	0.6	0.7	0.9	0.6	0.5	0.5	0.6	0.5

Continued on next page

Table B.5 *Continued from previous page*

Sample no.	191832	191832	191832	191832	191832	191832	191832	191832	191832
Analysis no.	pl_14_1	pl_15_1	pl_16_1	pl_17_1	pl_18_1	pl_19_1	pl_2_1	pl_20_1	pl_3_1
Al_2O_3	29.15	28.74	29.89	29.94	29.36	29.46	30.19	29.90	29.00
CaO	12.69	13.79	13.41	13.48	13.04	12.88	13.71	13.28	12.49
Cr_2O_3	0.03					0.01		0.02	0.05
Fe_2O_3	0.03	0.52		0.28	0.01		0.01	0.18	0.21
K_2O	0.07	0.08	0.14	0.21	0.08	0.09	0.07	0.09	0.06
MgO		0.15	0.01	0.11	0.01		0.01		0.01
MnO	0.02			0.01		0.03	0.02		0.02
Na_2O	4.58	4.17	4.26	4.07	4.49	4.51	4.08	4.17	4.69
Nb_2O_5	0.04	0.02					0.01	0.06	
NiO	0.04	0.02	0.05	0.01		0.01	0.01		
SiO_2	52.79	50.76	52.29	51.30	52.16	52.37	51.38	52.23	52.80
TiO_2	0.03	0.05	0.01	0.10	0.02	0.03	0.04	0.09	0.06
V_2O_3				0.01					0.03
ZnO			0.04				0.05	0.01	0.03
Ab	39.3	35.2	36.2	34.9	38.2	38.6	34.9	36.1	40.3
An	60.3	64.4	63.0	63.9	61.3	60.9	64.7	63.4	59.3
Or	0.4	0.4	0.8	1.2	0.5	0.5	0.4	0.5	0.4

Continued on next page

Table B.5 *Continued from previous page*

Sample no.	191832	191832	191832	191832	191832	191832	191836	191836	191836
Analysis no.	pl_4_1	pl_5_1	pl_6_1	pl_7_1	pl_8_1	pl_9_1	pl_1_1	pl_10_1	pl_11_1
Al_2O_3	29.67	29.15	29.22	29.36	29.33	29.44	29.50	29.76	29.73
CaO	12.84	12.67	12.78	12.84	12.86	12.81	12.94	13.07	12.89
Cr_2O_3	0.01			0.02	0.03				
Fe_2O_3	0.01	0.01	0.03	0.09		0.07	0.17	0.22	0.18
K_2O	0.06	0.09	0.07	0.15	0.06	0.08	0.29	0.23	0.26
MgO			0.05			0.05	0.03	0.01	0.01
MnO	0.01	0.01	0.02		0.02			0.03	
Na_2O	4.72	4.56	4.44	4.39	4.40	4.50	4.08	4.00	4.29
Nb_2O_5							0.01	0.01	0.03
NiO		0.01	0.03		0.04	0.01			0.01
SiO_2	52.76	53.01	51.66	52.51	52.03	52.95	51.04	50.22	50.99
TiO_2	0.05	0.03	0.01	0.06	0.03	0.03	0.01	0.05	0.05
V_2O_3	0.01			0.02	0.02	0.05			0.04
ZnO			0.02				0.03		0.02
Ab	39.8	39.2	38.4	37.9	38.1	38.7	35.7	35.2	37.0
An	59.9	60.3	61.1	61.3	61.6	60.8	62.6	63.5	61.5
Or	0.3	0.5	0.4	0.8	0.3	0.5	1.7	1.3	1.5

Continued on next page

Table B.5 *Continued from previous page*

Sample no.	191836	191836	191836	191836	191836	191836	191836	191836	191836
Analysis no.	pl_12_1	pl_13_1	pl_14_1	pl_15_1	pl_16_1	pl_17_1	pl_18_1	pl_19_1	pl_2_1
Al_2O_3	29.75	29.72	29.43	30.54	30.38	30.06	29.62	29.86	30.12
CaO	12.66	12.81	12.60	13.33	13.26	13.30	12.78	12.55	13.21
Cr_2O_3		0.02							
Fe_2O_3	0.17	0.19	0.14	0.18	0.16	0.24	0.15	0.16	0.20
K_2O	0.24	0.21	0.35	0.21	0.31	0.24	0.26	0.35	0.21
MgO	0.03	0.01		0.01	0.01	0.02	0.03	0.02	0.02
MnO	0.01	0.01		0.03		0.01		0.05	
Na_2O	4.29	4.26	4.36	4.14	4.06	4.10	4.38	4.61	4.10
Nb_2O_5	0.03		0.01	0.04	0.01	0.02			
NiO			0.02				0.01	0.07	0.01
SiO_2	51.00	50.99	51.63	51.35	51.75	50.60	50.65	52.59	51.45
TiO_2	0.06	0.04	0.02	0.05	0.05	0.05	0.04	0.04	0.05
V_2O_3									
ZnO			0.04				0.07		0.02
Ab	37.5	37.2	37.8	35.5	35.0	35.3	37.7	39.1	35.5
An	61.1	61.7	60.3	63.3	63.2	63.3	60.8	58.9	63.2
Or	1.4	1.2	2.0	1.2	1.8	1.4	1.5	1.9	1.2

Continued on next page

Table B.5 *Continued from previous page*

Sample no.	191836	191836	191836	191836	191836	191836	191836	191836	191837
Analysis no.	pl_20_1	pl_3_1	pl_4_1	pl_5_1	pl_6_1	pl_7_1	pl_8_1	pl_9_1	pl_1_1
Al_2O_3	30.46	29.80	28.99	30.46	29.47	29.97	31.17	29.54	30.00
CaO	13.39	13.18	13.49	13.96	12.77	12.83	14.44	12.70	13.20
Cr_2O_3	0.01	0.01							0.01
Fe_2O_3	0.19	0.16	0.96	0.13	0.13	0.14	0.14	0.12	0.16
K_2O	0.25	0.29	1.28	0.21	0.22	0.33	0.14	0.27	0.27
MgO	0.02	0.02	0.16	0.01	0.04	0.02			0.01
MnO	0.01	0.02	0.01			0.02			0.03
Na_2O	4.20	4.03	3.35	3.93	4.22	4.18	3.53	4.49	4.11
Nb_2O_5	0.01	0.01	0.02		0.02	0.03	0.05	0.02	
NiO					0.01	0.01			0.02
SiO_2	50.96	50.34	49.79	50.25	50.62	51.78	49.57	51.70	51.27
TiO_2	0.04	0.02		0.04	0.05	0.07	0.03	0.01	0.03
V_2O_3		0.01	0.02		0.01			0.01	
ZnO	0.02		0.07				0.01		0.06
Ab	35.7	35.0	28.8	33.3	36.9	36.4	30.4	38.4	35.5
An	62.9	63.3	64.0	65.5	61.8	61.7	68.8	60.0	63.0
Or	1.4	1.6	7.2	1.2	1.2	1.9	0.8	1.5	1.5

Continued on next page

Table B.5 *Continued from previous page*

Sample no.	191837	191837	191837	191837	191837	191837	191837	191837	191837
Analysis no.	pl_10_10	pl_11_11	pl_12_12	pl_13_13	pl_14_14	pl_15_15	pl_16_16	pl_17_17	pl_18_18
Al_2O_3	30.03	30.36	30.22	30.37	29.84	30.23	30.54	30.66	30.73
CaO	13.44	13.62	13.43	13.12	13.14	13.50	13.75	14.27	13.94
Cr_2O_3					0.01	0.04			0.01
Fe_2O_3	0.14	0.22	0.12	0.19	0.20	0.15	0.22	0.20	0.18
K_2O	0.23	0.29	0.34	0.33	0.29	0.28	0.24	0.29	0.27
MgO		0.02	0.03	0.08	0.01	0.01	0.02	0.03	0.02
MnO	0.06	0.01	0.01	0.02	0.03	0.01	0.03		
Na_2O	3.96	3.74	3.94	4.08	4.20	3.84	3.92	3.66	3.83
Nb_2O_5	0.02					0.03	0.01		0.01
NiO	0.02						0.01		
SiO_2	50.60	50.79	51.16	51.98	50.96	50.67	50.69	49.80	50.97
TiO_2	0.03	0.02	0.04	0.08	0.05	0.05		0.03	
V_2O_3	0.03	0.01		0.02					
ZnO	0.01	0.03	0.05		0.04		0.02		
Ab	34.3	32.6	34.0	35.3	36.0	33.4	33.6	31.2	32.7
An	64.3	65.7	64.1	62.8	62.3	65.0	65.1	67.2	65.8
Or	1.3	1.7	2.0	1.9	1.7	1.6	1.4	1.6	1.5

Continued on next page

Table B.5 *Continued from previous page*

Sample no.	191837	191837	191837	191837	191837	191837	191837	191837	191837
Analysis no.	pl_19_19	pl_2_2	pl_20_20	pl_3_3	pl_4_4	pl_5_5	pl_6_6	pl_7_7	pl_8_8
Al_2O_3	29.92	30.26	30.15	30.14	30.00	28.13	30.35	30.29	29.55
CaO	13.20	13.43	13.31	13.67	13.18	10.72	13.16	13.70	12.97
Cr_2O_3		0.01	0.01	0.04			0.01	0.01	0.01
Fe_2O_3	0.21	0.17	0.21	0.22	0.14	0.13	0.20	0.11	0.15
K_2O	0.38	0.43	0.37	0.28	0.32	0.70	0.36	0.29	0.32
MgO	0.02	0.01	0.01	0.01	0.02	0.01		0.02	
MnO	0.02						0.01		
Na_2O	4.00	3.77	3.96	3.78	4.05	5.18	4.11	3.67	4.01
Nb_2O_5	0.02		0.01					0.01	
NiO			0.02	0.01	0.02			0.01	
SiO_2	50.84	50.37	51.26	50.61	51.50	54.33	51.87	50.04	51.01
TiO_2		0.04	0.06	0.03	0.04	0.04	0.04	0.02	0.02
V_2O_3	0.04	0.01	0.01						
ZnO	0.07	0.01		0.02		0.03			0.02
Ab	34.7	32.9	34.3	32.8	35.1	44.8	35.4	32.1	35.2
An	63.2	64.6	63.6	65.6	63.1	51.2	62.6	66.2	62.9
Or	2.2	2.5	2.1	1.6	1.8	4.0	2.1	1.7	1.9

Continued on next page

Table B.5 *Continued from previous page*

Sample no.	191837	191838	191838	191838	191838	191838	191838	191838	191838
Analysis no.	pl_9_9	pl_1_1	pl_10_1	pl_11_1	pl_12_1	pl_13_1	pl_14_1	pl_15_1	pl_16_1
Al_2O_3	30.83	29.79	29.08	30.97	30.16	30.03	30.13	30.08	30.45
CaO	13.85	13.76	13.21	15.30	14.26	13.99	14.02	14.16	14.37
Cr_2O_3					0.03	0.01	0.01	0.02	0.01
Fe_2O_3	0.18	0.18	0.79	0.19	0.21	0.11	0.25	0.31	0.21
K_2O	0.30	0.28	0.28	0.20	0.25	0.26	0.29	0.36	0.26
MgO	0.01	0.03	0.02	0.01	0.01		0.02	0.10	0.02
MnO	0.01				0.01		0.01		
Na_2O	3.78	3.77	4.02	3.07	3.55	3.76	3.81	3.55	3.39
Nb_2O_5	0.01	0.04		0.01			0.02		0.02
NiO	0.01		0.02				0.01		0.01
SiO_2	51.00	51.23	51.09	49.61	50.36	50.77	51.59	50.47	49.97
TiO_2	0.07	0.02	0.12	0.03	0.04	0.05	0.03	0.06	0.03
V_2O_3					0.01	0.01		0.01	
ZnO		0.03	0.03			0.03		0.01	
Ab	32.5	32.6	34.9	26.4	30.6	32.2	32.5	30.6	29.4
An	65.8	65.8	63.5	72.5	68.0	66.3	65.9	67.4	69.1
Or	1.7	1.6	1.6	1.1	1.4	1.4	1.6	2.0	1.5

Continued on next page

Table B.5 *Continued from previous page*

Sample no.	191838	191838	191838	191838	191838	191838	191838	191838	191838
Analysis no.	pl_17_1	pl_18_1	pl_19_1	pl_2_1	pl_20_1	pl_3_1	pl_4_1	pl_5_1	pl_6_1
Al_2O_3	29.67	29.12	29.86	29.69	29.66	29.64	30.22	29.84	29.45
CaO	13.42	12.84	13.85	13.57	13.51	13.46	14.16	13.71	13.55
Cr_2O_3		0.02		0.01				0.03	0.00
Fe_2O_3	0.19	0.21	0.23	0.37	0.26	0.15	0.18	0.18	0.19
K_2O	0.38	0.40	0.30	0.34	0.35	0.26	0.18	0.23	0.22
MgO	0.01	0.03	0.04	0.01	0.02	0.02	0.01	0.01	0.02
MnO	0.01	0.02	0.01	0.01	0.01	0.01	0.02	0.01	
Na_2O	4.02	4.14	3.72	3.84	3.85	4.03	3.46	3.74	3.86
Nb_2O_5		0.01			0.01	0.05	0.03	0.02	0.02
NiO					0.02			0.01	0.01
SiO_2	52.24	51.74	51.33	51.62	51.29	51.85	50.19	50.66	50.65
TiO_2	0.02	0.03	0.05	0.05	0.05	0.04	0.03	0.02	0.04
V_2O_3	0.01	0.03			0.01	0.02		0.01	0.00
ZnO	0.05	0.03	0.02		0.01	0.03		0.03	0.02
Ab	34.4	36.0	32.1	33.2	33.3	34.6	30.3	32.6	33.6
An	63.4	61.7	66.2	64.9	64.7	63.9	68.6	66.1	65.1
Or	2.1	2.3	1.7	1.9	2.0	1.5	1.1	1.3	1.3

Continued on next page

Table B.5 *Continued from previous page*

Sample no.	191838	191838	191838	191840	191840	191840	191840	191840	191840
Analysis no.	pl_7_1	pl_8_1	pl_9_1	pl_1_1	pl_10_10	pl_11_11	pl_12_12	pl_13_13	pl_14_14
Al_2O_3	29.87	30.15	29.34	30.03	30.04	30.28	30.19	30.28	28.83
CaO	13.65	14.13	13.17	12.99	12.76	13.34	13.32	13.22	12.33
Cr_2O_3		0.02			0.03	0.03	0.01	0.01	
Fe_2O_3	0.19	0.20	0.17	0.12	0.15	0.13	0.12	0.13	1.23
K_2O	0.24	0.26	0.28	0.16	0.16	0.11	0.09	0.07	0.43
MgO	0.03	0.02	0.02	0.02	0.02		0.02	0.17	0.24
MnO	0.02	0.02			0.04		0.01	0.01	0.01
Na_2O	3.90	3.66	4.03	4.18	4.35	4.14	4.11	4.08	4.36
Nb_2O_5	0.01	0.04				0.03		0.01	0.02
NiO						0.01	0.03		
SiO_2	51.26	50.95	52.10	51.08	51.74	50.63	50.52	50.68	50.33
TiO_2	0.04	0.03	0.06	0.05	0.03	0.03	0.08	0.04	0.37
V_2O_3	0.02	0.02		0.01	0.03				0.02
ZnO	0.03	0.03	0.05		0.04	0.03			
Ab	33.6	31.4	35.1	36.5	37.8	35.7	35.7	35.7	38.0
An	65.0	67.1	63.3	62.6	61.3	63.7	63.8	63.9	59.5
Or	1.4	1.4	1.6	0.9	0.9	0.6	0.5	0.4	2.5

Continued on next page

Table B.5 *Continued from previous page*

Sample no.	191840	191840	191840	191840	191840	191840	191840	191840	191840
Analysis no.	pl_15_15	pl_16_16	pl_17_17	pl_18_18	pl_19_19	pl_2_2	pl_20_20	pl_3_3	pl_4_4
Al_2O_3	29.89	30.54	30.17	31.07	30.21	29.85	29.69	30.29	31.02
CaO	13.05	13.71	12.93	14.25	13.14	12.81	13.15	13.37	14.10
Cr_2O_3	0.04	0.01		0.01		0.01	0.01		0.01
Fe_2O_3	0.05	0.13	0.05	0.40	0.06	0.12	0.20	0.25	0.09
K_2O	0.16	0.08	0.07	0.04	0.12	0.19	0.11	0.18	0.08
MgO		0.01	0.01	0.37		0.02		0.10	0.07
MnO	0.01		0.02		0.02	0.01			0.01
Na_2O	4.15	3.85	4.39	3.20	4.25	4.36	4.26	4.00	3.64
Nb_2O_5		0.01	0.05			0.04		0.04	0.01
NiO				0.01	0.02	0.02			0.01
SiO_2	50.90	50.18	51.51	48.70	50.71	51.02	50.50	50.61	49.56
TiO_2	0.04	0.03	0.04		0.05	0.07	0.04	0.07	0.02
V_2O_3							0.01	0.03	0.03
ZnO				0.02	0.04	0.07	0.07	0.01	
Ab	36.2	33.5	37.9	28.8	36.6	37.7	36.7	34.7	31.7
An	62.9	66.1	61.7	70.9	62.7	61.2	62.7	64.3	67.9
Or	0.9	0.4	0.4	0.3	0.7	1.1	0.6	1.0	0.4

Continued on next page

Table B.5 *Continued from previous page*

Sample no.	191840	191840	191840	191840	191840	191842	191842	191842	191842
Analysis no.	pl_5_5	pl_6_6	pl_7_7	pl_8_8	pl_9_9	pl_1_1	pl_10_1	pl_10_10	pl_11_1
Al_2O_3	30.83	30.31	30.13	30.21	31.39	29.94	29.45	30.85	29.42
CaO	13.74	13.27	13.42	12.98	14.49	12.91	12.98	13.68	12.85
Cr_2O_3	0.01		0.02	0.01	0.02			0.03	0.01
Fe_2O_3	0.18	0.17	0.06	0.20	0.13	0.28	0.17	0.18	0.35
K_2O	0.13	0.13	0.13	0.14	0.09	0.30	0.34	0.21	0.39
MgO	0.03	0.02	0.03	0.02	0.29	0.02	0.02	0.02	0.01
MnO		0.01		0.02	0.03	0.03	0.01	0.02	0.01
Na_2O	3.81	4.15	3.93	4.36	3.44	4.13	4.23	3.57	4.16
Nb_2O_5	0.03	0.02	0.01			0.04		0.02	0.05
NiO	0.01	0.04	0.01		0.01	0.01			0.02
SiO_2	50.23	51.20	49.51	51.79	49.11	51.27	50.86	50.47	50.41
TiO_2	0.05	0.05	0.04	0.17	0.02	0.04	0.03	0.02	0.05
V_2O_3	0.02		0.04		0.02	0.01		0.01	0.02
ZnO	0.02		0.01	0.05	0.05		0.01		0.03
Ab	33.1	35.9	34.4	37.5	29.8	36.0	36.4	31.7	36.1
An	66.2	63.4	64.9	61.7	69.6	62.3	61.7	67.1	61.6
Or	0.7	0.8	0.7	0.8	0.5	1.7	1.9	1.2	2.2

Continued on next page

Table B.5 *Continued from previous page*

Sample no.	191842	191842	191842	191842	191842	191842	191842	191842	191842
Analysis no.	pl_12_1	pl_13_1	pl_14_1	pl_15_1	pl_16_1	pl_17_1	pl_18_1	pl_19_1	pl_2_1
Al_2O_3	29.49	29.95	29.88	29.88	30.07	29.71	30.08	30.53	29.46
CaO	13.84	13.18	13.01	13.10	13.22	13.06	13.23	13.67	12.71
Cr_2O_3					0.04	0.01		0.01	
Fe_2O_3	1.25	0.21	0.17	0.19	0.19	0.20	0.22	0.20	0.19
K_2O	0.24	0.32	0.33	0.31	0.32	0.30	0.26	0.22	0.33
MgO	0.17	0.02	0.02	0.02	0.01		0.02	0.01	0.03
MnO			0.04					0.03	0.02
Na_2O	3.64	4.16	4.29	4.19	4.12	4.24	3.92	3.95	4.53
Nb_2O_5		0.02	0.03	0.02	0.04	0.02			
NiO		0.02						0.01	
SiO_2	48.92	51.43	51.82	51.29	50.96	50.88	51.52	51.48	51.86
TiO_2	0.15	0.04	0.03	0.03	0.04	0.05	0.05	0.02	0.05
V_2O_3	0.02	0.04	0.04	0.03		0.01			0.03
ZnO	0.02	0.01	0.04	0.06		0.02		0.05	
Ab	31.8	35.7	36.7	36.0	35.4	36.4	34.4	33.9	38.5
An	66.8	62.5	61.4	62.2	62.8	61.9	64.1	64.9	59.7
Or	1.4	1.8	1.9	1.8	1.8	1.7	1.5	1.2	1.8

Continued on next page

Table B.5 *Continued from previous page*

Sample no.	191842	191842	191842	191842	191842	191842	191842	191842	191842
Analysis no.	pl_2_2	pl_20_1	pl_3_1	pl_3_3	pl_4_1	pl_4_4	pl_5_1	pl_5_5	pl_6_1
Al_2O_3	29.93	29.98	29.81	30.46	29.40	30.79	29.85	30.04	29.47
CaO	12.89	12.87	13.29	13.43	12.85	13.66	13.44	12.75	12.98
Cr_2O_3		0.05		0.01	0.01	0.06		0.01	
Fe_2O_3	0.17	0.21	0.19	0.22	0.22	0.22	0.19	0.23	0.22
K_2O	0.21	0.30	0.28	0.29	0.32	0.23	0.27	0.32	0.24
MgO	0.01	0.02	0.01	0.02	0.03		0.03	0.02	0.01
MnO			0.02		0.01			0.01	
Na_2O	4.07	4.24	4.05	3.71	4.30	3.59	3.89	4.13	4.39
Nb_2O_5			0.04		0.01	0.04	0.03	0.02	
NiO		0.02		0.01	0.01	0.02			
SiO_2	51.69	52.30	50.56	50.82	51.15	50.83	49.99	51.86	50.88
TiO_2	0.04	0.06	0.05	0.05	0.04	0.02	0.02	0.03	0.01
V_2O_3				0.06	0.02		0.03	0.03	
ZnO					0.04	0.01		0.08	0.01
Ab	35.9	36.7	35.0	32.8	37.0	31.8	33.8	36.3	37.5
An	62.9	61.6	63.4	65.5	61.2	66.8	64.6	61.9	61.2
Or	1.2	1.7	1.6	1.7	1.8	1.4	1.6	1.9	1.4

Continued on next page

Table B.5 *Continued from previous page*

Sample no.	191842	191842	191842	191842	191842	191842	191843	191843	191843
Analysis no.	pl_7_1	pl_7_7	pl_8_1	pl_8_8	pl_9_1	pl_9_9	pl_1_1	pl_10_1	pl_11_1
Al_2O_3	29.89	30.91	29.08	29.92	30.00	30.21	29.95	30.30	30.06
CaO	13.03	13.90	12.57	12.73	13.21	13.06	13.82	14.20	13.64
Cr_2O_3					0.02				
Fe_2O_3	0.26	0.17	0.21	0.16	0.18	0.22	0.18	0.34	0.19
K_2O	0.34	0.22	0.34	0.36	0.32	0.28	0.18	0.27	0.19
MgO		0.01	0.02	0.01	0.02	0.03		0.03	0.02
MnO				0.02					
Na_2O	4.24	3.53	4.38	4.06	4.29	3.91	3.84	3.74	4.23
Nb_2O_5			0.03		0.03	0.02	0.04	0.06	0.01
NiO	0.01					0.03	0.05		
SiO_2	50.61	50.71	50.94	52.25	51.75	51.47	51.04	51.72	52.19
TiO_2	0.06		0.03	0.03	0.02	0.04	0.03	0.09	0.03
V_2O_3		0.05			0.04		0.02	0.02	
ZnO			0.02	0.01		0.02	0.03		
Ab	36.3	31.1	37.9	35.9	36.4	34.5	33.1	31.8	35.5
An	61.7	67.6	60.2	62.1	61.8	63.8	65.9	66.7	63.4
Or	1.9	1.3	1.9	2.1	1.8	1.6	1.0	1.5	1.1

Continued on next page

Table B.5 *Continued from previous page*

Sample no.	191843	191843	191843	191843	191843	191843	191843	191843	191843
Analysis no.	pl_12_1	pl_13_1	pl_14_1	pl_15_1	pl_16_1	pl_17_1	pl_18_1	pl_19_1	pl_2_1
Al_2O_3	29.99	30.23	30.33	29.94	29.80	29.92	29.96	30.42	30.70
CaO	14.18	14.03	14.17	13.70	13.96	13.87	13.90	14.13	14.35
Cr_2O_3	0.02		0.01		0.02	0.01		0.01	0.04
Fe_2O_3	0.24	0.21	0.12	1.72	0.52	0.22	0.36	0.32	0.17
K_2O	0.25	0.15	0.14	0.23	0.14	0.20	0.24	0.21	0.15
MgO	0.02	0.03			0.05	0.03	0.19	0.03	
MnO		0.01		0.02	0.01	0.01		0.03	0.01
Na_2O	3.82	4.02	3.88	3.98	3.80	3.72	3.88	3.73	3.80
Nb_2O_5		0.04			0.03		0.03	0.03	
NiO				0.02		0.01	0.01	0.01	
SiO_2	50.48	52.06	50.96	50.82	50.70	50.26	51.46	51.48	51.28
TiO_2	0.02	0.02	0.05	0.24	0.07	0.04	0.06	0.05	0.05
V_2O_3			0.04		0.01	0.02		0.03	
ZnO				0.03	0.06	0.02	0.05		
Ab	32.3	33.9	32.9	34.0	32.7	32.3	33.1	31.9	32.1
An	66.3	65.3	66.4	64.7	66.5	66.6	65.5	66.9	67.0
Or	1.4	0.8	0.8	1.3	0.8	1.1	1.3	1.2	0.9

Continued on next page

Table B.5 *Continued from previous page*

Sample no.	191843	191843	191843	191843	191843	191843	191843	191843	191845
Analysis no.	pl_20_1	pl_3_1	pl_4_1	pl_5_1	pl_6_1	pl_7_1	pl_8_1	pl_9_1	pl_1_1
Al_2O_3	30.37	30.50	30.31	30.21	30.90	29.62	30.53	29.68	29.73
CaO	14.28	14.03	14.11	13.83	14.71	13.32	14.12	13.59	12.98
Cr_2O_3	0.02	0.02						0.02	0.01
Fe_2O_3	0.24	0.18	0.27	0.25	0.26	0.21	0.21	0.35	0.21
K_2O	0.21	0.29	0.12	0.25	0.15	0.26	0.11	0.20	0.35
MgO	0.04	0.03	0.02	0.02	0.01	0.01	0.04	0.03	0.03
MnO				0.01	0.01				0.01
Na_2O	3.79	3.82	3.83	3.94	3.41	4.04	3.99	3.87	4.14
Nb_2O_5		0.02			0.03				0.04
NiO	0.04		0.01	0.02					0.02
SiO_2	51.13	52.14	50.95	52.07	50.36	51.65	51.27	50.74	51.48
TiO_2	0.05	0.03	0.06	0.06	0.05	0.07	0.09	0.09	0.03
V_2O_3			0.01			0.01	0.01	0.04	0.01
ZnO					0.03	0.04	0.08	0.02	0.01
Ab	32.1	32.5	32.7	33.6	29.3	34.9	33.6	33.6	35.8
An	66.7	65.9	66.6	65.1	69.8	63.6	65.7	65.3	62.2
Or	1.2	1.6	0.7	1.4	0.9	1.5	0.6	1.1	2.0

Continued on next page

Table B.5 *Continued from previous page*

Sample no.	191845	191845	191845	191845	191845	191845	191845	191845	191845
Analysis no.	pl_10_1	pl_10_10	pl_11_1	pl_12_1	pl_13_1	pl_14_1	pl_15_1	pl_16_1	pl_17_1
Al_2O_3	30.44	30.71	30.78	31.57	30.13	30.46	31.36	30.22	29.83
CaO	13.36	13.51	13.85	14.49	13.23	13.43	14.88	13.43	13.26
Cr_2O_3	0.01	0.01				0.01			
Fe_2O_3	0.22	0.35	0.30	0.28	0.18	0.24	0.23	0.23	0.27
K_2O	0.27	0.25	0.26	0.23	0.33	0.27	0.19	0.29	0.38
MgO	0.04	0.17	0.03	0.01		0.02	0.03	0.02	0.01
MnO	0.02	0.02	0.01		0.02	0.01	0.02		
Na_2O	4.05	3.78	3.84	3.64	4.08	4.15	3.32	3.82	3.95
Nb_2O_5				0.03	0.03	0.01	0.02		0.10
NiO	0.01					0.02	0.01		
SiO_2	52.01	52.06	51.22	50.97	51.74	52.15	49.57	50.92	50.44
TiO_2	0.05	0.02	0.02	0.02	0.03	0.03	0.03	0.02	0.10
V_2O_3		0.02	0.02	0.01					0.02
ZnO		0.04	0.01					0.01	0.03
Ab	34.9	33.1	33.0	30.9	35.2	35.3	28.4	33.4	34.3
An	63.6	65.5	65.6	67.8	63.0	63.1	70.5	64.9	63.6
Or	1.6	1.4	1.5	1.3	1.8	1.5	1.1	1.7	2.2

Continued on next page

Table B.5 *Continued from previous page*

Sample no.	191845	191845	191845	191845	191845	191845	191845	191845	191845
Analysis no.	pl_18_1	pl_19_1	pl_2_1	pl_2_2	pl_20_1	pl_3_1	pl_3_3	pl_4_1	pl_4_4
Al_2O_3	29.97	29.86	30.27	30.22	30.04	30.28	31.36	30.25	30.35
CaO	13.53	13.05	13.73	13.18	13.30	13.37	14.39	13.42	13.48
Cr_2O_3	0.01	0.02		0.04	0.01	0.04			0.01
Fe_2O_3	0.18	0.23	0.32	0.22	0.22	0.22	0.30	0.22	0.23
K_2O	0.33	0.28	0.25	0.31	0.31	0.30	0.21	0.31	0.31
MgO	0.02	0.03	0.05	0.02	0.02	0.02		0.04	0.03
MnO	0.02		0.02			0.01		0.03	0.03
Na_2O	3.93	4.10	3.87	3.85	4.04	4.13	3.13	4.03	3.66
Nb_2O_5	0.02	0.06		0.02			0.04	0.01	0.02
NiO			0.03		0.02	0.03	0.04		
SiO_2	50.11	51.35	50.35	51.55	51.51	51.92	49.64	51.79	50.89
TiO_2	0.03	0.03	0.05	0.02	0.04		0.01	0.02	0.02
V_2O_3		0.02	0.03		0.01			0.02	
ZnO		0.06	0.09	0.04	0.02	0.06			
Ab	33.8	35.7	33.3	34.0	34.8	35.3	27.9	34.6	32.3
An	64.3	62.8	65.3	64.2	63.4	63.1	70.9	63.7	65.9
Or	1.9	1.6	1.4	1.8	1.8	1.7	1.2	1.8	1.8

Continued on next page

Table B.5 *Continued from previous page*

Sample no.	191845	191845	191845	191845	191845	191845	191845	191845	191847
Analysis no.	pl_5_1	pl_5_5	pl_6_1	pl_7_1	pl_7_7	pl_8_1	pl_8_8	pl_9_1	pl_1_1
Al_2O_3	30.22	29.93	30.26	29.46	30.47	29.60	29.78	30.28	30.15
CaO	13.35	12.72	13.34	12.95	13.49	13.08	13.00	13.18	13.15
Cr_2O_3	0.02	0.01	0.02		0.01		0.01	0.01	0.01
Fe_2O_3	0.25	0.17	0.25	1.82	0.70	0.26	0.30	0.18	0.30
K_2O	0.25	0.28	0.29	0.29	0.24	0.34	0.21	0.28	0.19
MgO		0.05		0.07	0.61	0.06	0.04	0.07	0.01
MnO					0.01				0.01
Na_2O	3.96	4.10	4.04	4.19	3.19	4.18	4.13	4.15	4.13
Nb_2O_5		0.03				0.03		0.03	0.03
NiO	0.03			0.05	0.02			0.02	
SiO_2	51.04	51.59	51.38	50.59	49.57	51.36	51.71	52.20	51.25
TiO_2	0.04		0.03	0.07	0.01	0.02	0.04	0.02	0.06
V_2O_3		0.01	0.01	0.01		0.02			0.01
ZnO		0.03	0.05		0.06	0.09			0.01
Ab	34.4	36.2	34.8	36.3	29.5	36.0	36.1	35.7	35.9
An	64.1	62.2	63.6	62.0	69.0	62.1	62.7	62.7	63.1
Or	1.4	1.6	1.6	1.7	1.5	1.9	1.2	1.6	1.1

Continued on next page

Table B.5 *Continued from previous page*

Sample no.	191847	191847	191847	191847	191847	191847	191847	191847	191847
Analysis no.	pl_10_10	pl_11_11	pl_12_12	pl_13_13	pl_14_14	pl_15_15	pl_16_16	pl_17_17	pl_18_18
Al_2O_3	30.42	30.35	30.14	30.37	30.05	29.76	29.93	30.41	29.91
CaO	13.48	13.84	13.28	13.60	13.10	12.99	13.16	13.45	13.17
Cr_2O_3	0.02		0.02				0.01		
Fe_2O_3	0.65	0.21	0.18	0.22	0.23	0.19	0.21	0.22	0.19
K_2O	0.19	0.17	0.12	0.27	0.25	0.21	0.18	0.25	0.25
MgO	0.18	0.02	0.02	0.03	0.02	0.02	0.03	0.02	0.03
MnO			0.02				0.02	0.03	
Na_2O	3.98	3.99	4.35	3.99	4.16	4.22	4.04	3.98	3.99
Nb_2O_5			0.07	0.04		0.01			
NiO	0.02		0.01		0.03			0.01	
SiO_2	51.20	50.37	52.04	50.83	51.52	51.13	50.83	51.34	50.85
TiO_2	0.07	0.02	0.03		0.04	0.06	0.04	0.07	0.02
V_2O_3	0.02	0.01	0.02	0.03		0.01	0.03	0.01	0.02
ZnO			0.07				0.04		0.03
Ab	34.5	34.0	36.9	34.1	36.0	36.6	35.3	34.4	34.9
An	64.5	65.1	62.4	64.4	62.6	62.2	63.6	64.2	63.7
Or	1.0	0.9	0.7	1.5	1.4	1.2	1.0	1.4	1.4

Continued on next page

Table B.5 *Continued from previous page*

Sample no.	191847	191847	191847	191847	191847	191847	191847	191847	191847
Analysis no.	pl_19_19	pl_2_2	pl_20_20	pl_3_3	pl_4_4	pl_5_5	pl_6_6	pl_7_7	pl_8_8
Al_2O_3	30.30	30.46	30.31	30.36	30.13	30.57	30.85	30.78	30.93
CaO	13.49	13.55	13.18	13.40	13.05	13.55	14.14	13.42	14.15
Cr_2O_3	0.01	0.02	0.04		0.01			0.02	
Fe_2O_3	0.21	0.24	0.26	0.17	0.22	0.18	0.24	0.24	0.23
K_2O	0.18	0.23	0.23	0.19	0.26	0.17	0.12	0.15	0.17
MgO	0.03	0.01	0.02	0.02	0.06	0.02	0.01	0.05	0.03
MnO		0.01		0.02	0.02	0.02	0.02	0.02	0.01
Na_2O	3.95	3.91	4.15	4.03	4.12	3.88	3.61	4.01	3.56
Nb_2O_5			0.01	0.02	0.02			0.02	
NiO	0.01	0.01			0.02	0.02	0.02		
SiO_2	50.76	51.35	52.22	51.32	51.67	51.26	49.91	51.70	50.09
TiO_2	0.05	0.08	0.07	0.02	0.07	0.08	0.04	0.05	0.02
V_2O_3	0.01	0.01	0.01	0.01	0.02	0.03			0.04
ZnO			0.01		0.07		0.04	0.02	
Ab	34.3	33.9	35.8	34.9	35.8	33.8	31.4	34.8	31.0
An	64.7	64.8	62.9	64.1	62.7	65.2	67.9	64.4	68.0
Or	1.0	1.3	1.3	1.1	1.5	1.0	0.7	0.8	1.0

Continued on next page

Table B.5 *Continued from previous page*

Sample no.	191847	191848	191848	191848	191848	191848	191848	191848	191848
Analysis no.	pl_9_9	pl_1_1	pl_10_1	pl_11_1	pl_12_1	pl_13_1	pl_14_1	pl_15_1	pl_16_1
Al_2O_3	31.51	29.70	30.00	29.13	29.34	29.71	30.63	29.32	29.77
CaO	14.57	13.66	13.74	13.34	13.45	13.51	14.51	13.50	13.39
Cr_2O_3	0.01	0.01	0.03		0.01	0.06	0.02	0.01	
Fe_2O_3	0.22	0.21	0.22	0.19	0.29	0.27	0.25	0.21	0.25
K_2O	0.16	0.28	0.30	0.29	0.28	0.26	0.25	0.24	0.31
MgO	0.03			0.02	0.31	0.04	0.03	0.02	0.01
MnO	0.01		0.02	0.01	0.02		0.01	0.03	0.06
Na_2O	3.43	4.07	3.92	4.04	3.71	3.86	3.51	3.96	4.09
Nb_2O_5	0.06		0.02			0.01	0.03		0.02
NiO		0.01		0.01	0.02				0.03
SiO_2	50.08	51.59	52.41	50.72	50.85	51.43	50.65	51.13	52.11
TiO_2	0.02	0.02	0.05	0.03	0.05	0.09	0.04	0.04	0.03
V_2O_3	0.01	0.03	0.01				0.02		
ZnO	0.04			0.03	0.02	0.06	0.01		
Ab	29.7	34.5	33.5	34.8	32.7	33.6	30.1	34.2	35.0
An	69.5	64.0	64.9	63.6	65.6	64.9	68.6	64.4	63.3
Or	0.9	1.5	1.7	1.6	1.6	1.5	1.4	1.4	1.8

Continued on next page

Table B.5 *Continued from previous page*

Sample no.	191848	191848	191848	191848	191848	191848	191848	191848	191848
Analysis no.	pl_17_1	pl_18_1	pl_19_1	pl_2_1	pl_20_1	pl_3_1	pl_4_1	pl_5_1	pl_6_1
Al_2O_3	29.53	30.23	29.10	29.60	29.66	29.94	29.79	29.32	29.31
CaO	13.36	13.91	12.97	13.38	13.37	13.95	13.53	13.45	13.35
Cr_2O_3			0.02						0.01
Fe_2O_3	0.20	0.42	0.23	0.28	0.21	0.23	0.31	0.21	0.21
K_2O	0.27	0.24	0.31	0.28	0.29	0.27	0.32	0.31	0.34
MgO	0.03	0.01	0.01	0.02	0.01	0.01	0.03	0.01	0.02
MnO	0.01		0.01		0.01		0.01		0.02
Na_2O	4.00	3.72	4.12	3.97	4.09	3.87	4.05	4.02	4.19
Nb_2O_5	0.01		0.02	0.06		0.09			0.03
NiO								0.03	
SiO_2	51.91	51.02	51.61	51.83	51.90	51.16	52.04	51.65	51.77
TiO_2	0.04	0.03	0.04	0.04	0.03	0.02	0.03	0.03	0.09
V_2O_3	0.02		0.01	0.03	0.02			0.02	0.01
ZnO	0.02		0.01		0.02			0.05	0.03
Ab	34.6	32.2	35.9	34.4	35.0	32.9	34.5	34.5	35.6
An	63.9	66.5	62.4	64.0	63.3	65.6	63.7	63.8	62.6
Or	1.5	1.4	1.8	1.6	1.6	1.5	1.8	1.7	1.9

Continued on next page

Table B.5 *Continued from previous page*

Sample no.	191848	191848	191848	191850	191850	191850	191850	191850	191850
Analysis no.	pl_7_1	pl_8_1	pl_9_1	pl_1_1	pl_10_10	pl_11_11	pl_12_12	pl_13_13	pl_14_14
Al_2O_3	29.81	30.06	29.55	30.48	30.33	30.57	30.50	30.66	30.82
CaO	13.61	13.75	13.36	13.65	13.67	13.90	13.48	13.91	13.75
Cr_2O_3				0.01		0.02	0.01	0.02	0.03
Fe_2O_3	0.23	0.47	0.26	0.26	0.29	0.27	0.23	0.23	0.30
K_2O	0.22	0.28	0.32	0.23	0.26	0.22	0.23	0.22	0.25
MgO	0.03	0.03	0.02	0.02	0.04		0.04	0.03	0.01
MnO			0.04		0.02		0.01		
Na_2O	3.98	4.07	4.20	3.70	3.75	3.77	3.93	3.71	3.69
Nb_2O_5						0.02	0.04		0.04
NiO		0.01	0.01	0.01	0.01		0.01		
SiO_2	51.70	52.35	52.54	50.46	50.18	50.49	51.44	50.58	50.31
TiO_2	0.01	0.08	0.07	0.04	0.06	0.11	0.03	0.07	0.09
V_2O_3	0.01	0.01		0.02		0.01		0.01	0.02
ZnO	0.02		0.01	0.01		0.05	0.03		0.02
Ab	34.2	34.4	35.6	32.5	32.6	32.5	34.1	32.2	32.2
An	64.6	64.1	62.6	66.2	65.9	66.2	64.6	66.6	66.4
Or	1.2	1.5	1.8	1.3	1.5	1.3	1.3	1.2	1.4

Continued on next page

Table B.5 *Continued from previous page*

Sample no.	191850	191850	191850	191850	191850	191850	191850	191850	191850
Analysis no.	pl_15_15	pl_16_16	pl_17_17	pl_18_18	pl_19_19	pl_2_2	pl_20_20	pl_3_3	pl_4_4
Al_2O_3	31.07	30.60	30.81	30.24	29.71	30.75	30.95	31.07	31.04
CaO	14.25	13.61	13.85	13.24	13.26	14.08	14.46	14.26	13.89
Cr_2O_3		0.02	0.05	0.01	0.01	0.03			0.01
Fe_2O_3	0.21	0.35	0.26	0.20	0.85	0.25	0.26	0.22	0.21
K_2O	0.25	0.24	0.23	0.23	0.23	0.22	0.21	0.20	0.23
MgO	0.02	0.05	0.03			0.03	0.01	0.03	0.03
MnO	0.02	0.02	0.01	0.01		0.04		0.01	
Na_2O	3.69	3.85	3.68	3.99	3.81	3.52	3.34	3.40	3.76
Nb_2O_5			0.02					0.01	
NiO	0.01	0.02						0.01	
SiO_2	50.29	50.92	50.92	51.04	50.37	50.11	49.38	49.95	51.09
TiO_2	0.09	0.05	0.07	0.02	0.13	0.03	0.03	0.06	0.06
V_2O_3		0.04		0.02	0.02	0.04	0.01	0.01	0.01
ZnO			0.02					0.03	0.03
Ab	31.5	33.4	32.1	34.8	33.7	30.7	29.1	29.8	32.4
An	67.1	65.2	66.6	63.8	64.9	68.0	69.7	69.1	66.3
Or	1.4	1.4	1.3	1.3	1.3	1.3	1.2	1.1	1.3

Continued on next page

Table B.5 *Continued from previous page*

Sample no.	191850	191850	191850	191850	191850	191851	191851	191851	191851
Analysis no.	pl_5_5	pl_6_6	pl_7_7	pl_8_8	pl_9_9	pl_1_1	pl_10_10	pl_2_2	pl_3_3
Al_2O_3	30.57	30.10	30.30	29.82	30.27	30.96	31.04	31.51	30.59
CaO	13.61	13.43	13.28	13.42	13.43	13.85	13.97	14.22	13.28
Cr_2O_3	0.02	0.01			0.02		0.03	0.03	
Fe_2O_3	0.23	0.22	0.21	1.19	0.22	0.23	0.27	0.33	0.28
K_2O	0.23	0.24	0.25	0.22	0.25	0.22	0.25	0.21	0.20
MgO	0.02	0.02	0.02	0.03	0.03	0.03	0.02	0.03	0.18
MnO		0.02		0.03			0.02		0.03
Na_2O	3.74	3.84	3.89	3.73	3.83	3.61	3.65	3.39	3.77
Nb_2O_5	0.03	0.01	0.03	0.03		0.05	0.02	0.01	
NiO	0.02	0.03		0.02					
SiO_2	50.12	50.57	50.94	49.49	50.42	50.65	50.93	50.63	50.80
TiO_2	0.02	0.04	0.02	0.27	0.03	0.01	0.04	0.03	0.01
V_2O_3	0.01	0.02	0.03	0.01		0.03			0.01
ZnO		0.01	0.01	0.01	0.07	0.08		0.01	
Ab	32.8	33.6	34.2	33.1	33.6	31.6	31.7	29.8	33.5
An	65.9	65.0	64.4	65.7	65.0	67.1	66.9	69.0	65.3
Or	1.3	1.4	1.5	1.3	1.4	1.3	1.4	1.2	1.2

Continued on next page

Table B.5 *Continued from previous page*

Sample no.	191851	191851	191851	191851	191851	191851	191852	191852	191852
Analysis no.	pl_4_4	pl_5_5	pl_6_6	pl_7_7	pl_8_8	pl_9_9	pl_1_1	pl_10_1	pl_11_1
Al_2O_3	31.47	30.63	31.10	30.99	30.65	30.89	28.80	30.15	29.22
CaO	14.38	13.84	13.67	13.69	13.39	13.62	13.06	13.62	12.96
Cr_2O_3	0.05	0.01		0.01			0.02		0.04
Fe_2O_3	0.17	0.24	0.21	0.24	0.20	0.12	0.22	0.24	0.20
K_2O	0.21	0.30	0.27	0.21	0.35	0.16	0.20	0.13	0.18
MgO	0.02	0.02	0.01	0.03	0.02	0.01	0.04	0.01	0.02
MnO	0.03								0.01
Na_2O	3.38	3.51	3.82	3.69	3.84	3.74	3.98	4.16	4.32
Nb_2O_5						0.01	0.02	0.03	0.03
NiO	0.01		0.02			0.01	0.01	0.02	
SiO_2	50.66	50.35	51.48	50.01	51.18	50.68	50.46	51.56	52.02
TiO_2	0.02	0.03	0.03	0.03	0.05	0.02	0.04	0.19	0.04
V_2O_3	0.01	0.01			0.04		0.01	0.04	0.03
ZnO	0.01	0.06	0.02				0.01		
Ab	29.5	30.9	33.1	32.4	33.5	32.9	35.1	35.3	37.2
An	69.3	67.4	65.4	66.4	64.5	66.2	63.8	64.0	61.8
Or	1.2	1.8	1.5	1.2	2.0	0.9	1.1	0.7	1.0

Continued on next page

Table B.5 *Continued from previous page*

Sample no.	191852	191852	191852	191852	191852	191852	191852	191852	191852
Analysis no.	pl_12_1	pl_13_1	pl_14_1	pl_15_1	pl_16_1	pl_17_1	pl_18_1	pl_19_1	pl_2_1
Al_2O_3	29.83	29.88	29.55	30.03	29.03	29.56	29.73	29.74	29.64
CaO	13.35	13.60	13.14	13.74	12.83	13.21	13.34	13.38	13.15
Cr_2O_3		0.02	0.03				0.05	0.02	0.01
Fe_2O_3	0.21	0.36	0.14	0.30	0.05	0.12	0.25	0.07	0.16
K_2O	0.15	0.20	0.12	0.12	0.09	0.14	0.20	0.11	0.13
MgO	0.02	0.04	0.03	0.03	0.01	0.02	0.03		0.01
MnO		0.01			0.01	0.01		0.01	0.02
Na_2O	4.15	4.01	4.25	3.93	4.19	4.04	4.15	4.19	4.18
Nb_2O_5		0.01			0.01		0.02		0.01
NiO					0.01	0.03	0.02		0.01
SiO_2	50.93	51.38	51.48	51.27	50.99	51.75	51.35	51.19	52.16
TiO_2	0.04	0.41	0.04	0.14	0.05	0.03	0.03	0.03	0.03
V_2O_3				0.02			0.03		0.01
ZnO	0.03	0.04	0.04	0.15	0.03		0.03	0.04	
Ab	35.7	34.4	36.6	33.9	37.0	35.3	35.6	36.0	36.3
An	63.5	64.5	62.6	65.4	62.5	63.9	63.3	63.4	63.0
Or	0.8	1.1	0.7	0.7	0.5	0.8	1.1	0.6	0.8

Continued on next page

Table B.5 *Continued from previous page*

Sample no.	191852	191852	191852	191852	191852	191852	191852	191852	191854
Analysis no.	pl_20_1	pl_3_1	pl_4_1	pl_5_1	pl_6_1	pl_7_1	pl_8_1	pl_9_1	pl_1_1
Al_2O_3	30.15	29.65	29.53	29.47	29.77	29.79	29.40	29.61	30.28
CaO	13.80	13.00	13.34	13.14	13.53	13.25	12.73	13.20	13.59
Cr_2O_3		0.03					0.01		0.06
Fe_2O_3	0.14	0.09	0.20	1.63	0.25	0.09	0.18	0.16	0.25
K_2O	0.17	0.16	0.24	0.27	0.20	0.11	0.12	0.10	0.05
MgO			0.01	0.01	0.02	0.02	0.01		0.20
MnO	0.02		0.01	0.01			0.04	0.01	
Na_2O	3.88	4.35	4.24	4.09	4.06	4.33	4.60	4.28	3.62
Nb_2O_5	0.02			0.09		0.04	0.09		
NiO	0.01								
SiO_2	51.25	52.62	51.56	51.03	52.06	52.05	52.52	51.89	50.36
TiO_2	0.04	0.07	0.03	0.07	0.06	0.05	0.06		0.02
V_2O_3		0.01	0.02					0.01	
ZnO				0.02		0.05		0.02	0.06
Ab	33.4	37.4	36.1	35.4	34.8	36.9	39.3	36.8	32.4
An	65.7	61.7	62.6	63.0	64.1	62.4	60.1	62.7	67.3
Or	0.9	0.9	1.3	1.5	1.1	0.6	0.7	0.6	0.3

Continued on next page

Table B.5 *Continued from previous page*

Sample no.	191854	191854	191854	191854	191854	191854	191854	191854	191854
Analysis no.	pl_10_10	pl_2_2	pl_3_3	pl_4_4	pl_5_5	pl_6_6	pl_7_7	pl_8_8	pl_9_9
Al_2O_3	31.57	30.69	30.68	30.91	30.69	30.36	31.07	30.45	30.35
CaO	14.41	14.22	14.06	13.89	13.66	13.49	14.41	14.15	13.73
Cr_2O_3	0.01	0.05			0.02		0.01	0.01	
Fe_2O_3	0.06	0.52	0.43	0.26	0.16	0.42	0.28	0.48	0.42
K_2O	0.02	0.04	0.03	0.04	0.02	0.03	0.03	0.04	0.05
MgO	0.02	0.33	0.30	0.12	0.04	0.23	0.26	0.33	0.30
MnO		0.01			0.06	0.01	0.02		0.02
Na_2O	3.27	3.28	3.23	3.43	3.57	3.65	3.09	3.37	3.61
Nb_2O_5						0.07	0.05	0.03	
NiO	0.01	0.02	0.03	0.03		0.01			
SiO_2	49.32	48.41	48.00	49.24	48.63	49.50	48.44	48.76	49.47
TiO_2	0.02	0.02	0.03	0.03	0.04	0.02	0.03	0.04	0.02
V_2O_3	0.02			0.02	0.03			0.02	
ZnO	0.05	0.04	0.06	0.01	0.03	0.01	0.04		
Ab	29.0	29.4	29.3	30.8	32.1	32.8	27.9	30.1	32.1
An	70.8	70.4	70.5	69.0	67.8	67.0	71.9	69.7	67.6
Or	0.1	0.2	0.2	0.2	0.1	0.2	0.2	0.2	0.3

Continued on next page

Table B.5 *Continued from previous page*

Sample no.	191855	191855	191855	191855	191855	191855	191855	191855	191855
Analysis no.	pl_1_1	pl_10_10	pl_11_11	pl_12_12	pl_13_13	pl_14_14	pl_15_15	pl_16_16	pl_17_17
Al_2O_3	30.07	30.28	29.61	30.48	29.92	30.93	30.03	30.37	30.48
CaO	12.77	13.10	12.62	13.41	12.71	13.93	13.14	13.17	13.24
Cr_2O_3	0.01	0.02	0.01					0.02	
Fe_2O_3	0.23	0.30	0.17	0.28	1.25	0.17	0.28	0.20	0.22
K_2O	0.23	0.24	0.32	0.30	0.28	0.20	0.22	0.25	0.31
MgO	0.02	0.05	0.02	0.03	0.02	0.01	0.02	0.04	0.02
MnO	0.03			0.02		0.01			
Na_2O	4.17	4.14	4.36	3.97	4.16	3.45	4.07	4.31	4.14
Nb_2O_5	0.01	0.05	0.02	0.02	0.02	0.03	0.02	0.03	0.03
NiO	0.02	0.03	0.05		0.06	0.03		0.01	0.01
SiO_2	51.80	51.83	52.30	51.94	52.00	50.52	52.14	52.42	52.57
TiO_2	0.03	0.11	0.03	0.16	0.94		0.06	0.02	0.05
V_2O_3		0.01	0.02		0.01	0.01			
ZnO			0.06		0.03	0.02	0.03		
Ab	36.6	35.9	37.8	34.3	36.6	30.6	35.5	36.6	35.5
An	62.0	62.8	60.4	64.0	61.8	68.3	63.3	62.0	62.8
Or	1.3	1.3	1.8	1.7	1.6	1.2	1.3	1.4	1.7

Continued on next page

Table B.5 *Continued from previous page*

Sample no.	191855	191855	191855	191855	191855	191855	191855	191855	191855
Analysis no.	pl_18_18	pl_19_19	pl_2_2	pl_20_20	pl_3_3	pl_4_4	pl_5_5	pl_6_6	pl_7_7
Al_2O_3	30.12	30.47	30.41	30.16	30.00	30.64	30.21	31.04	30.48
CaO	13.01	13.87	13.15	13.22	12.87	13.34	13.09	13.88	13.11
Cr_2O_3				0.01	0.01	0.03	0.01	0.02	
Fe_2O_3	0.20	0.28	0.25	0.20	0.46	0.33	0.24	0.32	0.21
K_2O	0.24	0.25	0.21	0.30	0.19	0.19	0.25	0.26	0.27
MgO	0.05	0.03	0.04	0.03	0.03	0.05	0.02	0.03	0.03
MnO	0.01	0.03	0.02	0.02		0.01	0.01	0.01	0.01
Na_2O	4.26	3.75	4.14	4.04	4.23	4.10	4.19	3.65	4.27
Nb_2O_5	0.06				0.07	0.01	0.01	0.01	0.03
NiO	0.01		0.01		0.01		0.02		0.01
SiO_2	52.15	50.43	51.64	51.78	51.68	52.06	51.79	51.30	52.26
TiO_2	0.06	0.03	0.06	0.01	0.24	0.04	0.06	0.05	0.03
V_2O_3		0.01		0.01		0.02	0.01		0.01
ZnO	0.06		0.02			0.02	0.01	0.02	0.01
Ab	36.7	32.4	35.9	35.0	36.8	35.3	36.1	31.7	36.5
An	61.9	66.2	63.0	63.3	62.1	63.6	62.5	66.8	62.0
Or	1.3	1.4	1.2	1.7	1.1	1.1	1.4	1.5	1.5

Continued on next page

Table B.5 *Continued from previous page*

Sample no.	191855	191855	191856	191856	191856	191856	191856	191856	191856
Analysis no.	pl_8_8	pl_9_9	pl_1_1	pl_10_1	pl_11_1	pl_12_1	pl_13_1	pl_14_1	pl_15_1
Al_2O_3	30.58	31.05	29.23	28.66	28.72	28.80	28.81	28.87	28.70
CaO	13.46	14.13	12.90	12.31	12.26	12.47	12.40	12.67	12.53
Cr_2O_3	0.01		0.02		0.03	0.02			
Fe_2O_3	0.30	0.18	0.23	0.21	0.13	0.20	0.30	0.25	0.19
K_2O	0.26	0.17	0.32	0.42	0.29	0.31	0.42	0.36	0.35
MgO	0.03	0.03	0.02	0.01	0.03	0.04	0.04	0.03	
MnO	0.01			0.02		0.04			
Na_2O	4.05	3.49	4.19	4.51	4.61	4.50	4.48	4.24	4.37
Nb_2O_5	0.03	0.02			0.02	0.08	0.04	0.05	0.01
NiO	0.01				0.03	0.01			
SiO_2	51.92	49.99	52.76	52.88	52.79	52.67	53.29	52.05	52.22
TiO_2	0.12		0.04	0.06	0.05	0.04	0.12	0.05	0.01
V_2O_3		0.02		0.02	0.03			0.02	
ZnO	0.01	0.03	0.03	0.03	0.06	0.06	0.01	0.11	
Ab	34.7	30.6	36.3	38.9	39.8	38.8	38.6	36.9	37.9
An	63.8	68.5	61.8	58.7	58.5	59.5	59.0	61.0	60.1
Or	1.5	1.0	1.8	2.4	1.7	1.7	2.4	2.1	2.0

Continued on next page

Table B.5 *Continued from previous page*

Sample no.	191856	191856	191856	191856	191856	191856	191856	191856	191856
Analysis no.	pl_16_1	pl_17_1	pl_18_1	pl_19_1	pl_2_1	pl_20_1	pl_3_1	pl_4_1	pl_5_1
Al_2O_3	28.53	29.05	28.55	28.71	28.29	29.18	28.62	28.94	29.26
CaO	12.23	12.86	12.42	12.51	11.99	12.63	12.21	12.63	12.97
Cr_2O_3			0.02	0.01	0.01	0.02	0.02		0.01
Fe_2O_3	0.16	0.18	0.20	0.22	0.21	0.19	0.15	0.12	0.22
K_2O	0.34	0.43	0.38	0.41	0.32	0.40	0.42	0.34	0.41
MgO	0.02	0.02	0.02	0.01	0.02	0.03	0.01	0.01	0.02
MnO	0.01	0.03			0.01				
Na_2O	4.54	4.06	4.34	4.53	4.29	4.37	4.55	4.35	3.93
Nb_2O_5	0.02	0.01	0.01			0.03			0.02
NiO		0.03	0.03		0.01				
SiO_2	52.37	51.79	51.89	52.93	51.07	53.05	53.17	52.19	51.53
TiO_2	0.10	0.07	0.06	0.08	0.03	0.06	0.04	0.06	0.05
V_2O_3	0.02		0.02			0.04	0.02		0.04
ZnO	0.01						0.03		0.05
Ab	39.4	35.5	37.9	38.7	38.5	37.7	39.3	37.6	34.6
An	58.7	62.1	59.9	59.0	59.6	60.1	58.3	60.4	63.0
Or	1.9	2.5	2.1	2.3	1.9	2.3	2.4	1.9	2.4

Continued on next page

Table B.5 *Continued from previous page*

Sample no.	191856	191856	191856	191856	191858	191858	191858	191858	191858
Analysis no.	pl_6_1	pl_7_1	pl_8_1	pl_9_1	pl_1_1	pl_10_10	pl_2_2	pl_3_3	pl_4_4
Al_2O_3	29.24	28.76	28.72	28.75	30.44	30.53	30.17	30.46	30.26
CaO	12.83	12.48	12.33	12.44	12.65	12.90	12.44	12.93	12.61
Cr_2O_3	0.01				0.01				
Fe_2O_3	0.24	0.20	0.16	0.24	0.10	0.21	0.16	0.08	0.16
K_2O	0.31	0.37	0.40	0.35	0.32	0.34	0.31	0.28	0.30
MgO	0.01	0.01	0.01	0.02	0.04	0.02	0.02	0.01	0.01
MnO		0.01			0.05				0.03
Na_2O	4.24	4.42	4.54	4.41	4.28	4.10	4.43	4.20	4.30
Nb_2O_5	0.03				0.03				
NiO		0.02	0.02				0.01	0.02	
SiO_2	52.39	52.50	53.04	52.74	52.88	52.04	53.39	52.67	53.11
TiO_2	0.06	0.04	0.06	0.07	0.03	0.04	0.07	0.05	0.08
V_2O_3		0.01						0.04	0.02
ZnO	0.12	0.07			0.05		0.04		
Ab	36.8	38.2	39.1	38.3	37.3	35.8	38.5	36.4	37.5
An	61.5	59.6	58.7	59.7	60.9	62.2	59.8	62.0	60.8
Or	1.8	2.1	2.2	2.0	1.8	2.0	1.8	1.6	1.7

Continued on next page

Table B.5 *Continued from previous page*

Sample no.	191858	191858	191858	191858	191858	191859	191859	191859	191859
Analysis no.	pl_5_5	pl_6_6	pl_7_7	pl_8_8	pl_9_9	pl_10_10	pl_2_2	pl_3_3	pl_4_4
Al_2O_3	30.38	30.39	29.67	29.75	30.24	30.79	30.70	31.11	29.92
CaO	12.92	12.68	11.79	12.31	12.64	13.57	13.35	13.82	12.63
Cr_2O_3		0.01		0.03		0.03	0.01		
Fe_2O_3	0.18	0.20	0.05	0.15	0.13	0.22	0.25	0.23	0.19
K_2O	0.29	0.37	0.31	0.33	0.27	0.20	0.27	0.20	0.52
MgO	0.02	0.02		0.02		0.02	0.01	0.02	0.02
MnO			0.02	0.01		0.02			
Na_2O	4.13	4.29	4.79	4.50	4.38	3.65	3.79	3.73	4.06
Nb_2O_5	0.02		0.03	0.01	0.03	0.05		0.02	
NiO			0.01	0.02	0.02	0.02		0.04	
SiO_2	52.72	52.98	54.00	52.55	53.07	50.61	51.18	51.68	51.58
TiO_2	0.07	0.05	0.02	0.10	0.03	0.05	0.04	0.01	0.02
V_2O_3	0.01		0.01			0.01	0.02		
ZnO		0.01	0.03	0.05					
Ab	36.0	37.2	41.6	39.0	37.9	32.4	33.4	32.4	35.7
An	62.3	60.7	56.6	59.1	60.5	66.5	65.0	66.4	61.3
Or	1.7	2.1	1.8	1.9	1.6	1.2	1.6	1.2	3.0

Continued on next page

Table B.5 *Continued from previous page*

Sample no.	191859	191859	191859	191859	191859	191860	191860	191860	191860
Analysis no.	pl_5_5	pl_6_6	pl_7_7	pl_8_8	pl_9_9	pl_1_1	pl_10_10	pl_11_11	pl_12_12
Al_2O_3	30.67	30.14	29.26	30.43	30.57	30.30	30.14	30.14	30.27
CaO	13.54	12.86	11.93	13.42	13.44	13.29	13.36	13.21	13.66
Cr_2O_3				0.01		0.03	0.01	0.02	
Fe_2O_3	0.26	0.15	0.17	0.39	0.24	0.21	0.39	0.37	0.21
K_2O	0.27	0.28	0.51	0.27	0.31	0.31	0.33	0.33	0.34
MgO	0.04	0.02	0.03	0.04	0.03	0.03	0.05	0.05	0.01
MnO			0.02		0.02	0.02	0.02		0.02
Na_2O	3.79	4.19	4.53	3.71	3.76	4.06	3.87	4.09	3.90
Nb_2O_5	0.01		0.02	0.01	0.02				0.04
NiO		0.02		0.01					0.04
SiO_2	50.87	51.96	53.06	51.15	51.13	51.57	50.47	51.28	51.03
TiO_2	0.03	0.01	0.02	0.05	0.07	0.04	0.47	0.19	0.05
V_2O_3		0.02		0.02				0.02	
ZnO	0.03			0.02			0.02		
Ab	33.1	36.5	39.5	32.8	33.0	34.9	33.7	35.2	33.4
An	65.4	61.9	57.6	65.6	65.2	63.3	64.4	62.9	64.7
Or	1.5	1.6	2.9	1.6	1.8	1.8	1.9	1.9	1.9

Continued on next page

Table B.5 *Continued from previous page*

Sample no.	191860	191860	191860	191860	191860	191860	191860	191860	191860
Analysis no.	pl_13_13	pl_14_14	pl_15_15	pl_16_16	pl_17_17	pl_18_18	pl_19_19	pl_2_2	pl_20_20
Al_2O_3	29.65	30.19	30.10	30.07	30.07	30.17	30.08	30.66	30.40
CaO	13.15	13.41	13.42	13.26	13.38	13.58	13.53	13.71	13.24
Cr_2O_3	0.01			0.01	0.02				0.03
Fe_2O_3	0.42	0.22	0.26	0.19	0.30	0.22	0.20	0.30	0.24
K_2O	0.31	0.30	0.31	0.30	0.32	0.26	0.26	0.25	0.33
MgO	0.01	0.04	0.04	0.01	0.01	0.03	0.02	0.60	0.04
MnO	0.01	0.01			0.01	0.02			
Na_2O	3.92	4.09	4.01	4.01	3.89	3.82	4.08	3.58	4.13
Nb_2O_5	0.02			0.04	0.01	0.04			0.04
NiO			0.01						
SiO_2	50.26	51.38	50.86	51.45	50.66	50.76	50.79	50.77	52.52
TiO_2	0.09	0.04	0.05	0.02	0.10	0.02	0.07	0.05	0.05
V_2O_3					0.02		0.01		0.02
ZnO	0.03	0.03	0.01			0.01			0.02
Ab	34.4	34.9	34.5	34.8	33.8	33.2	34.8	31.6	35.4
An	63.8	63.4	63.8	63.5	64.3	65.3	63.8	66.9	62.7
Or	1.8	1.7	1.7	1.7	1.8	1.5	1.4	1.4	1.9

Continued on next page

Table B.5 *Continued from previous page*

Sample no.	191860	191860	191860	191860	191860	191860	191860	191862	191862
Analysis no.	pl_3_3	pl_4_4	pl_5_5	pl_6_6	pl_7_7	pl_8_8	pl_9_9	pl_1_1	pl_10_1
Al_2O_3	30.83	30.06	30.39	30.14	30.06	30.01	30.46	30.71	29.85
CaO	13.51	13.17	13.46	13.27	13.21	13.09	13.26	14.85	13.43
Cr_2O_3		0.02			0.01	0.02			0.01
Fe_2O_3	0.19	0.34	0.21	0.22	0.30	0.19	0.22	0.21	0.18
K_2O	0.29	0.28	0.28	0.32	0.29	0.33	0.33	0.19	0.29
MgO	0.03	0.04		0.02	0.02	0.02	0.03	0.03	0.02
MnO	0.02		0.01			0.01			0.02
Na_2O	4.01	4.20	3.96	4.01	4.06	3.97	4.19	3.27	4.11
Nb_2O_5		0.05	0.02					0.08	0.02
NiO	0.01	0.05						0.03	
SiO_2	52.14	51.99	51.31	51.58	51.22	51.21	52.56	49.70	51.44
TiO_2	0.05	0.16	0.11	0.04	0.16	0.06	0.09	0.03	0.05
V_2O_3		0.02		0.05				0.02	0.02
ZnO	0.03						0.02		0.03
Ab	34.4	36.0	34.2	34.7	35.1	34.8	35.7	28.2	35.1
An	64.0	62.4	64.2	63.5	63.2	63.4	62.4	70.7	63.3
Or	1.6	1.6	1.6	1.8	1.7	1.9	1.9	1.1	1.6

Continued on next page

Table B.5 *Continued from previous page*

Sample no.	191862	191862	191862	191862	191862	191862	191862	191862	191862
Analysis no.	pl_11_1	pl_12_1	pl_13_1	pl_14_1	pl_15_1	pl_16_1	pl_17_1	pl_18_1	pl_19_1
Al_2O_3	29.53	29.62	29.47	29.77	30.04	29.46	30.48	29.76	29.82
CaO	13.39	13.29	13.35	13.26	13.81	12.92	14.40	13.42	13.39
Cr_2O_3		0.01			0.02	0.02		0.02	
Fe_2O_3	0.18	0.22	0.21	0.14	0.20	0.21	0.17	0.24	0.20
K_2O	0.32	0.26	0.26	0.25	0.28	0.24	0.23	0.22	0.28
MgO	0.01	0.01	0.02	0.01	0.01	0.03	0.01	0.02	
MnO		0.02	0.01		0.03			0.02	0.03
Na_2O	3.98	3.97	4.08	3.99	4.05	4.42	3.69	4.04	4.11
Nb_2O_5	0.03	0.04	0.02	0.01	0.01		0.01		
NiO			0.02	0.03		0.02		0.02	
SiO_2	51.48	51.74	51.53	51.94	51.82	52.50	51.13	51.34	52.04
TiO_2	0.02	0.02	0.02	0.01	0.06	0.04	0.06	0.07	0.06
V_2O_3	0.02		0.03			0.01	0.02	0.01	0.01
ZnO	0.01		0.05	0.02		0.07			0.08
Ab	34.3	34.6	35.1	34.8	34.1	37.7	31.3	34.8	35.1
An	63.8	64.0	63.5	63.8	64.3	60.9	67.4	63.9	63.3
Or	1.8	1.5	1.5	1.4	1.6	1.4	1.3	1.3	1.6

Continued on next page

Table B.5 *Continued from previous page*

Sample no.	191862	191862	191862	191862	191862	191862	191862	191862	191862
Analysis no.	pl_2_1	pl_20_1	pl_3_1	pl_4_1	pl_5_1	pl_6_1	pl_7_1	pl_8_1	pl_9_1
Al_2O_3	29.53	30.11	29.77	29.45	29.54	29.47	29.56	29.55	29.23
CaO	13.35	13.36	13.27	13.24	13.42	13.39	13.16	13.30	13.14
Cr_2O_3			0.02		0.03	0.02		0.01	
Fe_2O_3	0.31	0.17	0.20	0.22	0.13	0.19	0.18	0.14	0.29
K_2O	0.27	0.31	0.33	0.29	0.23	0.29	0.27	0.27	0.27
MgO	0.01		0.01	0.02	0.03	0.01	0.02	0.02	0.01
MnO	0.01	0.01	0.02	0.01		0.01			
Na_2O	3.97	4.11	4.12	4.04	4.03	4.03	4.02	4.10	4.02
Nb_2O_5	0.01			0.02			0.04		0.03
NiO	0.02				0.02	0.01			0.04
SiO_2	51.13	52.79	52.14	51.76	51.37	51.13	51.77	51.48	51.18
TiO_2	0.10	0.03	0.03	0.05	0.02	0.04	0.05	0.05	0.04
V_2O_3	0.02	0.02	0.01	0.03			0.02		
ZnO	0.01						0.02	0.07	0.02
Ab	34.5	35.1	35.3	35.0	34.8	34.7	35.1	35.3	35.1
An	64.0	63.1	62.9	63.4	63.9	63.7	63.4	63.2	63.4
Or	1.5	1.7	1.8	1.6	1.3	1.6	1.5	1.5	1.5

Continued on next page

Table B.5 *Continued from previous page*

Sample no.	191863	191863	191863	191863	191863	191863	191863	191863	191863
Analysis no.	pl_1_1	pl_10_10	pl_2_2	pl_3_3	pl_4_4	pl_5_5	pl_6_6	pl_7_7	pl_8_8
Al_2O_3	30.44	30.93	29.57	31.60	30.97	29.84	29.88	29.92	30.79
CaO	13.67	13.88	12.73	14.99	14.09	12.63	12.75	12.84	13.82
Cr_2O_3	0.03			0.01	0.01	0.01		0.03	0.01
Fe_2O_3	0.18	0.20	0.25	0.16	0.23	0.15	0.21	0.18	0.23
K_2O	0.21	0.25	0.26	0.17	0.21	0.22	0.32	0.29	0.24
MgO	0.02		0.04	0.01	0.01	0.01	0.03	0.02	0.03
MnO						0.01			
Na_2O	3.51	3.43	4.02	2.89	3.31	4.13	3.96	4.02	3.56
Nb_2O_5		0.06		0.05				0.01	0.06
NiO	0.01			0.01	0.02			0.01	
SiO_2	48.46	50.09	49.70	48.59	49.42	50.87	50.46	51.23	50.46
TiO_2	0.01	0.04	0.05	0.01	0.02	0.04	0.05	0.03	0.04
V_2O_3			0.01				0.04		
ZnO	0.03	0.08	0.07		0.02			0.01	
Ab	31.3	30.5	35.8	25.6	29.5	36.7	35.3	35.6	31.3
An	67.4	68.1	62.7	73.4	69.3	62.0	62.8	62.8	67.3
Or	1.2	1.5	1.5	1.0	1.2	1.3	1.9	1.7	1.4

Continued on next page

Table B.5 *Continued from previous page*

Sample no.	191863	191864	191864	191864	191864	191864	191864	191864	191864
Analysis no.	pl_9_9	pl_1_1	pl_10_10	pl_11_11	pl_12_12	pl_13_13	pl_14_14	pl_15_15	pl_16_16
Al_2O_3	30.74	30.87	30.02	29.84	30.14	30.29	30.62	29.85	29.55
CaO	13.76	14.09	13.20	12.83	13.52	13.26	13.48	13.01	13.01
Cr_2O_3		0.01	0.02			0.02			
Fe_2O_3	0.26	0.19	0.21	0.17	0.18	0.21	0.18	0.25	0.34
K_2O	0.24	0.23	0.28	0.30	0.23	0.26	0.28	0.34	0.29
MgO	0.03	0.02	0.02	0.02	0.01	0.02	0.02	0.01	0.01
MnO		0.04	0.02		0.03			0.01	
Na_2O	3.46	3.47	3.89	4.22	3.97	3.84	4.01	4.01	3.99
Nb_2O_5		0.04	0.04			0.05			0.02
NiO		0.02			0.01	0.05		0.01	0.02
SiO_2	49.99	50.08	50.71	51.74	50.67	51.47	51.32	50.89	51.07
TiO_2	0.03	0.03	0.06	0.04	0.05	0.04	0.04	0.03	0.23
V_2O_3		0.02	0.02	0.02					0.02
ZnO			0.05	0.09					
Ab	30.8	30.4	34.2	36.7	34.2	33.9	34.4	35.1	35.1
An	67.7	68.3	64.2	61.6	64.5	64.6	64.0	62.9	63.3
Or	1.4	1.3	1.6	1.7	1.3	1.5	1.6	2.0	1.7

Continued on next page

Table B.5 *Continued from previous page*

Sample no.	191864	191864	191864	191864	191864	191864	191864	191864	191864
Analysis no.	pl_17_17	pl_18_18	pl_19_19	pl_2_2	pl_20_20	pl_3_3	pl_4_4	pl_5_5	pl_6_6
Al_2O_3	30.58	30.62	30.51	30.72	31.12	30.17	30.35	31.17	30.24
CaO	13.37	13.62	13.85	13.60	14.11	13.24	13.37	14.15	13.27
Cr_2O_3			0.02			0.01			0.01
Fe_2O_3	0.16	0.14	0.15	0.19	0.30	0.22	0.22	0.19	0.26
K_2O	0.27	0.21	0.25	0.27	0.28	0.24	0.25	0.18	0.30
MgO	0.02	0.02	0.02	0.02	0.02	0.04	0.01	0.01	0.04
MnO	0.01			0.01			0.04	0.02	0.01
Na_2O	4.00	3.90	3.66	3.77	3.60	3.96	3.78	3.40	3.76
Nb_2O_5	0.02			0.03	0.03	0.03	0.04		
NiO	0.01		0.01	0.01		0.03	0.03		
SiO_2	51.74	51.40	50.26	51.03	50.83	51.31	50.42	49.99	50.61
TiO_2	0.05	0.07	0.03	0.04	0.04	0.03	0.05	0.03	0.05
V_2O_3			0.01	0.01	0.06	0.01		0.02	
ZnO			0.08	0.01	0.01	0.01	0.04		
Ab	34.6	33.7	31.9	32.8	31.1	34.6	33.3	30.0	33.3
An	63.9	65.1	66.7	65.6	67.3	64.0	65.2	69.0	65.0
Or	1.5	1.2	1.4	1.5	1.6	1.4	1.4	1.0	1.7

Continued on next page

Table B.5 *Continued from previous page*

Sample no.	191864	191864	191864	191865	191865	191865	191865	191865	191865
Analysis no.	pl_7_7	pl_8_8	pl_9_9	pl_1_1	pl_10_1	pl_11_1	pl_12_1	pl_13_1	pl_14_1
Al_2O_3	30.44	29.72	29.88	28.64	28.76	28.91	29.41	29.57	28.48
CaO	13.65	12.75	12.90	12.49	12.54	12.40	12.87	13.00	11.89
Cr_2O_3	0.01	0.01				0.01		0.01	
Fe_2O_3	0.18	1.00	0.21	0.17	0.20	0.19	0.16	0.22	0.22
K_2O	0.20	0.26	0.31	0.38	0.33	0.31	0.34	0.33	0.40
MgO	0.02	0.02	0.02	0.01	0.05	0.02	0.02	0.02	0.01
MnO	0.01		0.04						0.03
Na_2O	3.75	4.17	4.05	4.39	4.39	4.54	4.36	4.24	4.86
Nb_2O_5	0.03		0.03		0.01	0.02	0.08		
NiO		0.01			0.01	0.01		0.02	0.01
SiO_2	50.31	50.88	51.28	51.50	51.80	52.41	53.01	52.30	53.99
TiO_2	0.02	0.19	0.06	0.06		0.06	0.05	0.08	0.06
V_2O_3			0.01		0.01			0.03	0.02
ZnO	0.02		0.03	0.03	0.06	0.02	0.04		
Ab	32.8	36.6	35.6	38.0	38.1	39.1	37.3	36.4	41.5
An	66.0	61.9	62.6	59.8	60.1	59.1	60.8	61.7	56.2
Or	1.2	1.5	1.8	2.2	1.9	1.8	1.9	1.8	2.3

Continued on next page

Table B.5 *Continued from previous page*

Sample no.	191865	191865	191865	191865	191865	191865	191865	191865	191865
Analysis no.	pl_15_1	pl_16_1	pl_17_1	pl_18_1	pl_19_1	pl_2_1	pl_20_1	pl_3_1	pl_4_1
Al_2O_3	29.37	29.69	29.23	29.23	28.79	28.41	28.81	29.12	30.10
CaO	12.99	12.94	12.57	12.79	12.24	12.27	12.59	12.79	13.73
Cr_2O_3	0.02			0.01	0.02	0.03	0.03	0.02	
Fe_2O_3	0.21	0.17	0.14	0.19	0.99	0.34	0.24	0.17	0.22
K_2O	0.35	0.28	0.34	0.30	0.87	0.27	0.21	0.34	0.30
MgO	0.01	0.02	0.02		0.82	0.01	0.02	0.03	0.02
MnO		0.01		0.02	0.01		0.02		
Na_2O	4.09	4.43	4.44	4.46	4.10	4.53	4.35	4.40	4.01
Nb_2O_5	0.02				0.02		0.02		
NiO			0.02		0.03	0.01	0.03		0.02
SiO_2	51.66	53.54	52.52	52.01	51.83	52.00	51.71	52.58	52.25
TiO_2	0.08	0.03	0.03	0.16	0.18	0.08	0.07	0.05	0.06
V_2O_3	0.02	0.01		0.04		0.01			
ZnO			0.01				0.02		0.08
Ab	35.6	37.6	38.3	38.1	35.8	39.4	38.0	37.6	34.0
An	62.4	60.8	59.8	60.3	59.1	59.0	60.8	60.4	64.4
Or	2.0	1.6	1.9	1.7	5.0	1.6	1.2	1.9	1.7

Continued on next page

Table B.5 *Continued from previous page*

Sample no.	191865	191865	191865	191865	191865	191867	191867	191867	191867
Analysis no.	pl_5_1	pl_6_1	pl_7_1	pl_8_1	pl_9_1	pl_1_1	pl_2_2	pl_3_3	pl_4_4
Al_2O_3	29.00	29.06	29.13	29.33	29.00	29.90	28.93	28.89	29.37
CaO	12.61	12.91	12.46	12.92	12.76	12.99	11.66	11.48	12.23
Cr_2O_3			0.01			0.03		0.02	
Fe_2O_3	0.11	0.23	0.21	0.17	0.13	0.18	0.26	0.12	0.11
K_2O	0.32	0.21	0.20	0.37	0.33	0.25	0.38	0.42	0.25
MgO	0.01			0.01	0.02	0.01		0.02	
MnO					0.01	0.01	0.02	0.01	0.02
Na_2O	4.34	4.38	4.67	4.27	4.37	3.90	4.57	4.73	4.42
Nb_2O_5						0.04	0.02	0.04	0.01
NiO	0.01	0.02		0.02					
SiO_2	51.89	51.65	52.54	52.04	52.87	50.93	52.67	53.05	51.41
TiO_2	0.07	0.05	0.08	0.09	0.05	0.04	0.02	0.01	
V_2O_3	0.03				0.01	0.02	0.02	0.01	0.03
ZnO	0.03	0.03	0.03		0.02		0.01		
Ab	37.7	37.6	40.0	36.6	37.6	34.7	40.6	41.7	38.9
An	60.5	61.2	58.9	61.3	60.5	63.8	57.2	55.9	59.6
Or	1.8	1.2	1.1	2.1	1.9	1.5	2.2	2.4	1.5

Continued on next page

Table B.5 *Continued from previous page*

Sample no.	191867	191867	191867	191867	191867	191868	191868	191868	191868
Analysis no.	pl_5_5	pl_6_6	pl_7_7	pl_8_8	pl_9_9	pl_10_10	pl_2_2	pl_3_3	pl_6_6
Al_2O_3	29.63	28.96	29.30	29.43	29.56	30.06	29.74	29.70	29.54
CaO	12.44	11.77	12.11	12.42	12.39	12.77	12.42	12.34	11.98
Cr_2O_3		0.03	0.02				0.01	0.02	0.01
Fe_2O_3	0.17	0.20	0.20	0.14	0.18	0.16	0.28	0.18	0.22
K_2O	0.24	0.33	0.28	0.29	0.29	0.32	0.42	0.28	0.40
MgO	0.01	0.01		0.01	0.02	0.01	0.02	0.01	0.01
MnO				0.02	0.01		0.01		
Na_2O	4.31	4.58	4.46	4.35	4.31	4.22	4.38	4.47	4.48
Nb_2O_5	0.03							0.01	0.01
NiO				0.02					
SiO_2	51.74	52.75	52.39	52.10	51.65	52.23	52.89	52.91	53.24
TiO_2	0.03	0.08	0.05	0.04	0.04	0.03	0.03	0.02	0.03
V_2O_3	0.05	0.01	0.03		0.01	0.02	0.01		0.01
ZnO	0.09		0.07	0.02	0.02	0.05		0.06	
Ab	38.0	40.5	39.4	38.1	38.0	36.7	38.0	38.9	39.4
An	60.6	57.5	59.0	60.2	60.3	61.4	59.6	59.5	58.3
Or	1.4	1.9	1.6	1.7	1.7	1.8	2.4	1.6	2.3

Continued on next page

Table B.5 *Continued from previous page*

Sample no.	191868	191868	191870	191870	191870	191870	191870	191870	191870
Analysis no.	pl_7_7	pl_9_9	pl_1_1	pl_10_10	pl_2_2	pl_4_4	pl_5_5	pl_7_7	pl_8_8
Al_2O_3	29.47	32.67	29.56	28.01	28.89	27.63	28.74	28.46	28.58
CaO	11.70	15.95	12.16	10.28	10.91	9.74	10.92	10.62	10.52
Cr_2O_3	0.01	0.01			0.02	0.01			0.03
Fe_2O_3	0.13	0.33	0.19	0.13	0.22	0.06	0.10	0.27	0.08
K_2O	0.34	0.08	0.21	0.24	0.23	0.22	0.22	0.25	0.16
MgO		0.01	0.01	0.01	0.04			0.02	
MnO			0.02	0.02	0.01	0.03			0.01
Na_2O	4.78	2.25	4.64	5.71	5.16	5.98	5.15	5.33	5.44
Nb_2O_5	0.04	0.03		0.06	0.01		0.01	0.02	
NiO	0.01	0.02	0.01	0.04	0.02				0.02
SiO_2	53.76	47.51	52.36	55.40	54.27	56.32	54.17	54.63	54.62
TiO_2	0.02	0.02	0.03	0.03	0.04	0.02	0.02	0.04	0.02
V_2O_3	0.05		0.02					0.02	0.01
ZnO	0.01	0.01	0.02		0.09				
Ab	41.7	20.2	40.4	49.5	45.5	51.9	45.4	46.9	47.9
An	56.4	79.3	58.5	49.2	53.2	46.8	53.3	51.6	51.2
Or	2.0	0.5	1.2	1.4	1.3	1.3	1.3	1.5	0.9

Continued on next page

Table B.5 *Continued from previous page*

Sample no.	191870	191871	191871	191871	191871	191871	191871	191871	191871
Analysis no.	pl_9_9	pl_1_1	pl_10_10	pl_2_2	pl_3_3	pl_4_4	pl_5_5	pl_6_6	pl_7_7
Al_2O_3	28.78	30.10	29.66	30.47	29.92	30.44	29.75	29.06	28.65
CaO	10.95	12.67	12.27	12.78	12.28	12.85	12.06	11.12	10.76
Cr_2O_3	0.02			0.04		0.02	0.04		
Fe_2O_3	0.29	0.19	0.22	0.15	0.39	0.13	0.62	0.26	0.16
K_2O	0.23	0.16	0.15	0.13	0.24	0.09	0.22	0.25	0.14
MgO	0.01	0.04	0.01		0.05	0.01	0.02	0.04	0.02
MnO	0.02		0.01	0.01	0.01		0.02		
Na_2O	5.12	4.26	4.50	4.42	4.57	4.30	4.67	5.20	5.57
Nb_2O_5			0.03	0.01			0.02	0.01	0.01
NiO		0.01	0.01	0.01	0.01				
SiO_2	54.19	52.55	52.68	52.28	52.85	52.01	53.06	54.28	55.32
TiO_2	0.04	0.04	0.07	0.04	0.09	0.08	0.08	0.06	0.06
V_2O_3	0.02	0.01					0.03		
ZnO	0.04	0.05							
Ab	45.2	37.5	39.5	38.2	39.7	37.5	40.7	45.2	48.0
An	53.4	61.6	59.6	61.1	58.9	62.0	58.1	53.4	51.2
Or	1.4	0.9	0.9	0.8	1.4	0.5	1.3	1.4	0.8

Continued on next page

Table B.5 *Continued from previous page*

Sample no.	191871	191872	191872	191872	191872	191872	191872	191872	191872
Analysis no.	pl_8_8	pl_1_1	pl_10_10	pl_2_2	pl_3_3	pl_4_4	pl_5_5	pl_6_6	pl_7_7
Al_2O_3	29.59	30.31	30.20	30.11	30.10	29.78	29.76	29.52	30.01
CaO	11.88	12.82	12.68	12.61	12.73	12.25	13.25	12.29	12.76
Cr_2O_3							0.04	0.01	
Fe_2O_3	0.05	0.20	0.25	0.58	0.30	0.31	0.92	0.42	0.58
K_2O	0.13	0.17	0.17	0.18	0.17	0.18	0.22	0.22	0.19
MgO		0.01	0.03	0.01	0.02	0.05	0.13	0.06	0.06
MnO			0.01	0.01		0.03	0.01		
Na_2O	4.78	4.17	4.30	4.33	4.37	4.47	4.13	4.45	4.27
Nb_2O_5				0.02		0.01		0.04	0.03
NiO	0.01		0.02	0.01		0.04			
SiO_2	53.59	51.80	52.51	52.15	51.93	52.52	51.83	52.67	52.03
TiO_2	0.06	0.11	0.05	0.09	0.08	0.06	0.11	0.10	0.11
V_2O_3		0.03	0.02	0.05		0.03	0.01	0.04	
ZnO			0.04			0.01	0.01	0.02	0.01
Ab	41.8	36.7	37.7	37.9	38.0	39.3	35.6	39.1	37.3
An	57.4	62.3	61.4	61.0	61.1	59.6	63.2	59.6	61.6
Or	0.8	1.0	1.0	1.0	1.0	1.1	1.2	1.3	1.1

Continued on next page

Table B.5 *Continued from previous page*

Sample no.	191872	191872
Analysis no.	pl_8_8	pl_9_9
Al_2O_3	29.87	28.49
CaO	12.41	10.98
Cr_2O_3		0.03
Fe_2O_3	0.26	0.20
K_2O	0.19	0.33
MgO	0.02	0.02
MnO		
Na_2O	4.41	5.25
Nb_2O_5	0.05	
NiO		0.02
SiO_2	52.84	53.61
TiO_2	0.08	0.06
V_2O_3	0.01	0.02
ZnO	0.04	0.02
Ab	38.7	45.5
An	60.2	52.6
Or	1.1	1.9

Table B.6 Clinopyroxene major and minor element compositions (see description of analytical method in sections 2.3 and 4.3.1).

Sample no.	191831	191838	191838	191838	191838	191838	191838	191838	191840
Analysis no.	px_12_12	px_1_1	px_2_1	px_3_1	px_4_1	px_5_1	px_7_1	px_9_1	px_21_21
Al_2O_3	3.32	2.63	2.77	2.84	2.53	2.79	2.90	2.67	2.73
CaO	2.66	22.21	20.11	21.49	20.10	21.94	22.17	21.59	20.52
Cr_2O_3	0.17	0.04	0.07	0.11	0.09	0.01	0.01		0.02
FeO	22.69	5.52	7.09	6.68	6.89	6.78	5.91	6.26	7.11
Fe_2O_3	2.74	2.63	3.08	2.36	2.97	2.29	2.79	2.75	2.36
K_2O	0.12	0.01	0.02		0.01				0.01
MgO	17.87	14.71	14.84	14.30	15.02	14.16	14.23	14.73	14.87
MnO	0.63	0.17	0.25	0.20	0.25	0.23	0.22	0.23	0.20
Na_2O	0.07	0.31	0.36	0.33	0.37	0.38	0.39	0.32	0.28
Nb_2O_5	0.02			0.03		0.08		0.01	
NiO		0.03	0.06	0.03	0.04				0.07
SiO_2	49.44	51.32	50.75	50.81	51.00	51.33	51.00	51.31	50.90
TiO_2	0.18	0.57	0.73	0.77	0.60	0.74	0.81	0.63	0.71
V_2O_3	0.06	0.04	0.07	0.05	0.05	0.07	0.08	0.08	0.07
ZnO	0.03	0.04			0.08			0.06	
En	55.0	43.6	44.6	42.7	45.1	42.0	42.5	43.6	44.2
Fs	39.2	9.2	12.0	11.2	11.6	11.3	9.9	10.4	11.9
Wo	5.9	47.3	43.4	46.1	43.3	46.8	47.6	46.0	43.9

Continued on next page

Table B.6 *Continued from previous page*

Sample no.	191840	191840	191840	191840	191840	191840	191840	191840	191842
Analysis no.	px_23_23	px_24_24	px_27_27	px_28_28	px_29_29	px_30_30	px_31_31	px_32_32	px_11_11
Al_2O_3	2.55	2.49	2.42	1.80	2.92	2.72	2.59	2.94	2.55
CaO	21.05	18.93	21.20	4.18	21.79	20.57	20.74	21.86	20.93
Cr_2O_3	0.03	0.01	0.03	0.03	0.06	0.03	0.02	0.06	0.02
FeO	6.97	7.14	6.76	17.87	5.97	7.68	7.23	6.60	8.03
Fe_2O_3	2.40	3.55	2.88	1.94	2.87	1.33	2.50	1.41	1.60
K_2O		0.01		0.02					
MgO	14.56	15.62	14.44	21.32	14.29	14.58	14.29	13.99	14.17
MnO	0.21	0.25	0.20	0.44	0.22	0.22	0.23	0.21	0.19
Na_2O	0.31	0.28	0.24	0.08	0.34	0.26	0.32	0.33	0.21
Nb_2O_5			0.02	0.01	0.02			0.01	
NiO	0.08	0.06	0.01	0.07	0.02	0.07	0.01	0.05	0.03
SiO_2	51.10	50.58	50.62	51.78	50.60	51.01	50.50	50.68	50.84
TiO_2	0.55	0.51	0.51	0.25	0.76	0.64	0.68	0.81	0.60
V_2O_3	0.09	0.01	0.05	0.04	0.06	0.05	0.02	0.10	0.04
ZnO		0.09	0.02	0.02		0.05			0.04
En	43.3	47.0	43.1	62.1	42.9	43.3	43.0	41.9	42.0
Fs	11.6	12.1	11.3	29.2	10.1	12.8	12.2	11.1	13.4
Wo	45.0	40.9	45.5	8.7	47.0	43.9	44.8	47.0	44.6

Continued on next page

Table B.6 *Continued from previous page*

Sample no.	191842	191842	191842	191842	191842	191842	191842	191842	191843
Analysis no.	px_12_12	px_13_13	px_14_14	px_15_15	px_16_16	px_17_17	px_19_19	px_20_20	px_3_1
Al_2O_3	2.42	2.74	2.69	2.26	2.57	2.34	2.68	2.71	2.81
CaO	18.81	21.78	21.78	22.07	21.35	21.53	17.03	21.20	22.29
Cr_2O_3	0.09	0.03	0.01	0.02		0.02	0.03	0.07	0.05
FeO	8.72	6.88	6.85	6.92	7.78	7.36	9.47	7.37	5.51
Fe_2O_3	1.70	2.37	2.88	2.48	1.99	1.77	2.84	2.22	2.78
K_2O		0.01	0.01	0.01	0.01		0.01	0.01	0.01
MgO	15.35	13.76	13.78	13.68	13.67	14.20	15.79	14.05	14.73
MnO	0.21	0.26	0.26	0.23	0.24	0.22	0.35	0.19	0.13
Na_2O	0.21	0.33	0.34	0.36	0.31	0.24	0.26	0.34	0.28
Nb_2O_5							0.01		0.05
NiO		0.03	0.02			0.07	0.05	0.05	
SiO_2	50.95	50.59	50.65	51.01	50.72	51.19	50.62	50.89	51.13
TiO_2	0.51	0.71	0.74	0.62	0.64	0.54	0.58	0.65	0.68
V_2O_3	0.05	0.04	0.06	0.04	0.03	0.05	0.01	0.01	0.05
ZnO	0.04	0.01	0.07	0.05	0.02	0.05	0.03	0.03	
En	45.5	41.3	41.4	40.9	41.0	42.0	47.4	42.0	43.5
Fs	14.5	11.6	11.5	11.6	13.1	12.2	15.9	12.4	9.1
Wo	40.0	47.1	47.0	47.5	46.0	45.8	36.7	45.6	47.3

Continued on next page

Table B.6 *Continued from previous page*

Sample no.	191843	191843	191843	191843	191845	191845	191845	191845	191847
Analysis no.	px_5_1	px_7_1	px_8_1	px_9_1	px_15_15	px_18_18	px_19_19	px_20_20	px_21_21
Al_2O_3	2.65	12.58	3.00	2.84	12.94	2.28	12.62	2.62	2.73
CaO	20.43	11.76	21.42	21.24	12.13	21.69	12.15	22.42	22.28
Cr_2O_3		0.02		0.01	0.01	0.01	0.01		0.04
FeO	7.30		5.69	6.52		7.18		5.80	5.35
Fe_2O_3	2.38	12.14	2.64	2.56	11.48	2.35	12.01	3.03	3.35
K_2O		1.80	0.02		1.21	0.01	1.70	0.01	
MgO	15.23	14.12	15.42	14.53	14.11	14.95	14.23	14.80	14.29
MnO	0.23	0.11	0.18	0.26	0.10	0.21	0.06	0.23	0.22
Na_2O	0.28	1.86	0.28	0.38	2.13	0.26	1.95	0.30	0.32
Nb_2O_5	0.06		0.04		0.01	0.06			0.01
NiO	0.01	0.08		0.04	0.06		0.02	0.03	0.04
SiO_2	51.47	42.01	51.43	50.98	42.62	52.32	42.80	51.86	50.59
TiO_2	0.63	2.55	0.70	0.81	2.99	0.46	2.47	0.66	0.73
V_2O_3	0.04	0.04	0.03	0.01	0.12	0.02	0.06	0.05	0.04
ZnO	0.03	0.03							0.02
En	44.8	62.6	45.3	43.4	61.8	43.2	62.0	43.3	42.9
Fs	12.0		9.4	10.9		11.7		9.5	9.0
Wo	43.2	37.4	45.3	45.6	38.2	45.1	38.0	47.2	48.1

Continued on next page

Table B.6 *Continued from previous page*

Sample no.	191847	191847	191847	191847	191847	191847	191847	191847	191847
Analysis no.	px_22_22	px_23_23	px_24_24	px_25_25	px_26_26	px_27_27	px_28_28	px_29_29	px_30_30
Al_2O_3	2.61	2.40	2.69	2.87	2.66	2.74	2.75	2.87	2.52
CaO	21.63	21.66	20.73	20.53	22.09	21.09	21.44	20.79	20.66
Cr_2O_3			0.11	0.04	0.06	0.04	0.01	0.13	0.01
FeO	6.19	5.58	6.69	6.33	5.15	6.37	5.02	6.04	6.23
Fe_2O_3	3.35	3.32	2.94	3.49	3.27	3.54	4.07	3.11	3.12
K_2O		0.01	0.02		0.01	0.01	0.01	0.01	0.01
MgO	14.54	15.05	14.55	15.07	14.79	14.36	14.12	14.88	15.27
MnO	0.25	0.14	0.23	0.25	0.18	0.23	0.23	0.20	0.18
Na_2O	0.30	0.28	0.36	0.31	0.32	0.35	0.37	0.35	0.30
Nb_2O_5	0.07	0.04		0.08	0.04	0.06		0.01	
NiO	0.05	0.03	0.03		0.06	0.01	0.04	0.03	
SiO_2	50.93	51.13	50.59	50.55	51.02	50.21	49.38	50.58	51.02
TiO_2	0.64	0.54	0.81	0.74	0.60	0.82	0.70	0.69	0.58
V_2O_3	0.04	0.01	0.03	0.02	0.06			0.08	0.04
ZnO	0.03	0.02	0.04		0.05	0.01		0.04	
En	43.3	44.6	43.8	45.1	44.1	43.4	43.6	44.8	45.4
Fs	10.3	9.3	11.3	10.6	8.6	10.8	8.7	10.2	10.4
Wo	46.3	46.1	44.9	44.2	47.3	45.8	47.7	45.0	44.2

Continued on next page

Table B.6 *Continued from previous page*

Sample no.	191848	191848	191848	191848	191848	191848	191848	191848	191848
Analysis no.	px_1_1	px_10_1	px_2_1	px_3_1	px_4_1	px_5_1	px_6_1	px_7_1	px_8_1
Al_2O_3	2.33	1.89	2.48	2.83	2.40	2.67	2.85	2.56	2.75
CaO	22.47	22.16	21.54	21.14	22.64	21.66	21.51	21.67	21.77
Cr_2O_3	0.01	0.03	0.02	0.01	0.01	0.02	0.03	0.01	0.03
FeO	5.50	6.49	6.04	8.45	6.36	7.04	7.18	6.46	7.20
Fe_2O_3	2.67	1.78	2.66	1.90	2.30	2.26	2.63	2.16	2.05
K_2O								0.01	0.03
MgO	14.88	14.91	15.20	13.77	14.14	14.17	13.94	14.76	13.83
MnO	0.20	0.23	0.19	0.24	0.23	0.16	0.26	0.23	0.25
Na_2O	0.30	0.28	0.28	0.37	0.33	0.30	0.36	0.28	0.35
Nb_2O_5				0.04	0.04	0.02		0.03	0.02
NiO	0.01	0.04		0.02	0.01		0.01	0.01	0.01
SiO_2	51.81	52.47	51.63	51.30	51.74	51.03	50.93	51.39	51.01
TiO_2	0.52	0.33	0.56	0.71	0.51	0.62	0.76	0.66	0.78
V_2O_3	0.05	0.07	0.05	0.07	0.06		0.08	0.05	0.04
ZnO	0.03		0.04		0.06	0.02	0.10		
En	43.6	43.2	44.6	40.9	41.6	42.1	41.7	43.5	41.3
Fs	9.0	10.6	9.9	14.1	10.5	11.7	12.0	10.7	12.0
Wo	47.3	46.2	45.5	45.1	47.9	46.2	46.3	45.9	46.7

Continued on next page

Table B.6 *Continued from previous page*

Sample no.	191850	191850	191850	191850	191850	191850	191851	191851	191851
Analysis no.	px_11_11	px_12_12	px_13_13	px_15_15	px_16_16	px_19_19	px_21_21	px_24_24	px_25_25
Al_2O_3	2.45	2.33	2.84	2.75	2.29	2.73	2.76	2.24	1.89
CaO	21.85	21.72	22.65	22.17	21.85	21.43	20.66	21.76	22.68
Cr_2O_3	0.01		0.04	0.03	0.03	0.02	0.05	0.05	0.08
FeO	5.36	5.79	3.65	5.12	3.89	5.70	6.90	5.52	4.22
Fe_2O_3	3.20	2.44	3.58	2.95	4.18	2.32	2.87	2.33	2.94
K_2O	0.01	0.01	0.01	0.01		0.01	0.02		0.01
MgO	15.03	15.43	15.00	14.66	15.41	15.03	14.54	15.31	15.46
MnO	0.19	0.21	0.17	0.16	0.23	0.17	0.25	0.21	0.21
Na_2O	0.30	0.26	0.34	0.31	0.28	0.28	0.29	0.30	0.24
Nb_2O_5	0.01		0.03	0.01					0.01
NiO			0.02	0.04	0.02	0.03			0.05
SiO_2	51.19	51.96	50.58	50.75	50.60	50.97	50.38	51.83	51.90
TiO_2	0.62	0.49	0.75	0.69	0.48	0.63	0.79	0.44	0.23
V_2O_3	0.07	0.05	0.06	0.10	0.04		0.07	0.07	
ZnO	0.03	0.04		0.03	0.05	0.07	0.02	0.05	
En	44.5	45.0	45.0	43.8	46.3	44.7	43.7	45.0	45.3
Fs	8.9	9.5	6.1	8.6	6.6	9.5	11.6	9.1	6.9
Wo	46.5	45.5	48.8	47.6	47.2	45.8	44.7	45.9	47.8

Continued on next page

Table B.6 *Continued from previous page*

Sample no.	191852	191852	191852	191852	191852	191852	191854	191854	191854
Analysis no.	px_1_1	px_10_10	px_2_2	px_3_3	px_6_6	px_8_8	px_11_11	px_13_13	px_14_14
Al_2O_3	2.58	13.21	13.14	2.26	2.53	1.89	5.32	3.86	4.19
CaO	21.31	12.00	11.89	21.72	21.91	21.64	16.02	16.05	15.55
Cr_2O_3	0.05	0.24	0.19	0.08	0.07	0.01	0.72	0.21	0.36
FeO	6.70			5.72	5.72	6.54	5.94	6.93	6.44
Fe_2O_3	2.02	12.30	11.43	2.55	2.81	1.95	4.96	4.62	3.38
K_2O		1.87	1.93			0.01	0.01	0.01	
MgO	15.02	13.50	14.19	15.25	14.82	15.39	16.28	16.30	17.75
MnO	0.20	0.07	0.09	0.15	0.18	0.22	0.23	0.28	0.24
Na_2O	0.28	1.64	1.61	0.26	0.22	0.25	0.49	0.53	0.26
Nb_2O_5					0.07	0.03			
NiO	0.06	0.11	0.08	0.01		0.01	0.02	0.03	0.06
SiO_2	51.67	41.99	42.07	51.58	50.82	52.46	48.13	49.30	49.43
TiO_2	0.65	2.52	2.64	0.54	0.61	0.37	0.54	0.46	0.48
V_2O_3	0.05	0.11	0.09	0.05	0.08	0.05	0.09	0.10	0.02
ZnO		0.04		0.06				0.03	0.07
En	44.0	61.0	62.4	44.8	43.9	44.5	52.3	51.4	54.5
Fs	11.0			9.4	9.5	10.6	10.7	12.3	11.1
Wo	44.9	39.0	37.6	45.8	46.6	44.9	37.0	36.4	34.3

Continued on next page

Table B.6 *Continued from previous page*

Sample no.	191854	191854	191854	191854	191854	191855	191855	191855	191855
Analysis no.	px_16_16	px_17_17	px_18_18	px_19_19	px_20_20	px_11_11	px_18_18	px_19_19	px_20_20
Al_2O_3	3.19	4.64	5.39	5.54	2.69	2.25	2.56	2.54	2.13
CaO	14.48	16.34	18.02	18.28	14.74	22.40	21.14	21.52	22.54
Cr_2O_3	0.24	0.42	0.63	0.76	0.08	0.07	0.05	0.10	0.01
FeO	7.82	6.80	5.69	5.95	7.99	4.14	5.75	6.11	5.87
Fe_2O_3	2.97	2.85	2.64	2.52	2.54	2.86	2.97	1.94	2.72
K_2O	0.01	0.01	0.01		0.01	0.01	0.01		0.02
MgO	18.24	16.98	15.89	15.66	18.46	15.38	15.44	15.49	13.83
MnO	0.24	0.24	0.17	0.18	0.28	0.21	0.22	0.17	0.20
Na_2O	0.29	0.32	0.37	0.36	0.28	0.24	0.35	0.25	0.25
Nb_2O_5	0.09		0.02	0.06	0.01				
NiO		0.04	0.03	0.03	0.04	0.07			0.06
SiO_2	50.22	49.64	49.00	49.03	51.13	51.22	51.57	51.91	50.66
TiO_2	0.41	0.52	0.52	0.57	0.35	0.48	0.68	0.67	0.38
V_2O_3	0.04	0.04	0.11	0.05	0.03	0.04	0.10	0.05	
ZnO			0.05	0.03	0.07		0.04	0.05	0.06
En	55.2	52.2	49.6	48.7	55.0	45.5	45.6	45.0	41.5
Fs	13.3	11.7	10.0	10.4	13.4	6.9	9.5	10.0	9.9
Wo	31.5	36.1	40.4	40.9	31.6	47.6	44.9	45.0	48.6

Continued on next page

Table B.6 *Continued from previous page*

Sample no.	191856	191856	191856	191856	191856	191858	191858	191858	191858
Analysis no.	px_10_10	px_3_3	px_4_4	px_5_5	px_6_6	px_21_21	px_22_22	px_23_23	px_24_24
Al_2O_3	1.79	1.87	1.48	2.01	2.04	1.98	2.22	2.35	2.30
CaO	21.69	21.58	16.74	20.45	17.98	22.14	22.10	21.81	21.43
Cr_2O_3			0.03	0.05	0.05	0.12	0.12	0.12	0.09
FeO	8.58	9.08	11.99	8.73	9.59	5.11	6.79	6.63	7.41
Fe_2O_3	2.55	2.10	2.16	2.50	2.63	2.55	2.09	2.73	1.82
K_2O	0.01		0.01	0.01	0.03	0.01			
MgO	13.37	13.26	15.71	13.74	15.31	15.58	14.66	14.57	14.98
MnO	0.25	0.26	0.29	0.21	0.22	0.20	0.18	0.22	0.24
Na_2O	0.25	0.24	0.15	0.25	0.30	0.23	0.26	0.30	0.24
Nb_2O_5								0.01	0.04
NiO	0.06	0.04	0.02			0.01		0.01	
SiO_2	51.22	51.26	51.84	50.41	51.15	51.97	51.95	51.42	52.14
TiO_2	0.54	0.51	0.57	0.61	0.54	0.44	0.68	0.74	0.64
V_2O_3	0.04	0.08	0.08	0.08	0.08	0.09	0.14	0.12	0.12
ZnO	0.02		0.02		0.03		0.11		0.07
En	39.6	39.2	45.6	41.2	45.6	45.3	42.7	42.9	43.4
Fs	14.2	15.0	19.5	14.7	16.0	8.4	11.1	11.0	12.0
Wo	46.2	45.8	34.9	44.1	38.4	46.3	46.2	46.2	44.6

Continued on next page

Table B.6 *Continued from previous page*

Sample no.	191858	191858	191858	191858	191859	191859	191859	191859	191859
Analysis no.	px_25_25	px_26_26	px_27_27	px_30_30	px_21_21	px_23_23	px_24_24	px_27_27	px_29_29
Al_2O_3	1.71	2.04	1.99	2.47	2.23	2.68	2.50	2.79	2.70
CaO	18.85	22.13	21.64	22.30	21.77	21.54	23.79	22.00	21.92
Cr_2O_3	0.07	0.10	0.08	0.11		0.06	0.05	0.02	0.02
FeO	8.23	6.66	6.76	6.37	4.71	4.54	1.27	4.17	5.01
Fe_2O_3	1.97	2.10	2.25	2.03	3.72	4.48	7.50	4.15	3.75
K_2O	0.01			0.02	0.01	0.01	0.01	0.01	0.01
MgO	16.84	14.83	14.99	14.69	15.27	14.42	13.41	14.55	14.33
MnO	0.20	0.22	0.23	0.19	0.26	0.20	0.17	0.19	0.22
Na_2O	0.21	0.24	0.23	0.30	0.24	0.38	0.35	0.34	0.32
Nb_2O_5					0.06		0.04	0.02	0.02
NiO	0.03	0.03		0.03	0.03	0.03	0.02	0.07	0.02
SiO_2	53.01	52.17	51.85	52.01	50.85	49.50	47.64	49.82	49.99
TiO_2	0.26	0.49	0.57	0.69	0.40	0.77	0.61	0.70	0.67
V_2O_3	0.06	0.07	0.06	0.13	0.08	0.08		0.06	
ZnO	0.02	0.01		0.04		0.02	0.04	0.05	
En	48.1	43.0	43.7	42.8	45.5	44.4	42.9	44.5	43.6
Fs	13.2	10.8	11.0	10.4	7.9	7.9	2.3	7.2	8.5
Wo	38.7	46.1	45.3	46.7	46.6	47.7	54.8	48.4	47.9

Continued on next page

Table B.6 *Continued from previous page*

Sample no.	191862	191862	191862	191862	191862	191862	191862	191862	191862
Analysis no.	px_1_1	px_10_10	px_11_11	px_2_2	px_3_3	px_4_4	px_5_5	px_6_6	px_7_7
Al_2O_3	2.86	2.95	2.70	2.17	2.53	2.91	2.82	2.71	2.72
CaO	21.13	21.32	22.27	22.44	21.28	22.33	21.45	21.90	19.11
Cr_2O_3	0.07	0.09	0.08	0.05	0.06	0.07	0.08	0.08	0.07
FeO	6.87	6.76	5.45	6.17	6.15	6.09	6.14	5.90	7.45
Fe_2O_3	2.43	2.08	3.18	3.01	2.64	2.84	3.05	2.40	3.27
K_2O		0.01							
MgO	14.69	14.98	14.58	14.62	15.54	14.42	14.97	14.93	16.14
MnO	0.18	0.24	0.19	0.21	0.24	0.21	0.20	0.25	0.25
Na_2O	0.38	0.35	0.33	0.26	0.28	0.34	0.32	0.34	0.28
Nb_2O_5	0.01		0.02	0.02				0.05	
NiO	0.05	0.05	0.03	0.07	0.07	0.02	0.03		
SiO_2	51.42	51.87	51.07	51.78	52.00	51.50	51.36	51.69	51.59
TiO_2	0.67	0.77	0.72	0.58	0.63	0.72	0.66	0.62	0.60
V_2O_3	0.09	0.07	0.06	0.05	0.03	0.05	0.07	0.02	0.03
ZnO	0.03	0.03	0.03		0.06	0.05		0.02	
En	43.5	43.9	43.3	42.7	45.3	42.5	44.2	43.9	47.4
Fs	11.4	11.1	9.1	10.1	10.1	10.1	10.2	9.7	12.3
Wo	45.0	45.0	47.6	47.2	44.6	47.4	45.6	46.3	40.3

Continued on next page

Table B.6 *Continued from previous page*

Sample no.	191862	191863	191863	191863	191863	191863	191863	191863	191863
Analysis no.	px_8_8	px_21_21	px_22_22	px_23_23	px_25_25	px_26_26	px_27_27	px_28_28	px_29_29
Al_2O_3	2.52	2.64	2.67	2.58	2.70	2.32	2.03	2.58	2.00
CaO	21.54	21.10	21.60	20.95	21.79	20.87	20.63	22.38	21.15
Cr_2O_3	0.04	0.09	0.11	0.10	0.10	0.10	0.08	0.07	0.05
FeO	6.31	3.86	5.53	5.73	5.36	6.39	6.04	5.65	4.23
Fe_2O_3	3.00	4.34	3.74	3.94	3.38	3.50	3.61	2.89	4.57
K_2O		0.03	0.02		0.01				0.01
MgO	14.85	15.36	14.46	14.63	14.26	14.55	14.99	14.23	14.09
MnO	0.24	0.17	0.24	0.24	0.21	0.23	0.25	0.21	0.24
Na_2O	0.30	0.36	0.25	0.30	0.27	0.26	0.21	0.27	0.29
Nb_2O_5					0.02		0.01	0.02	
NiO	0.04	0.01	0.05	0.03	0.04	0.04	0.03	0.02	
SiO_2	51.45	49.88	50.02	49.83	49.81	50.28	50.29	50.66	48.22
TiO_2	0.59	0.64	0.76	0.82	0.71	0.55	0.41	0.65	0.45
V_2O_3	0.04	0.11	0.06	0.05	0.11	0.08	0.03	0.09	0.05
ZnO		0.01	0.04			0.06	0.07		
En	43.8	47.0	43.7	44.5	43.3	43.9	45.1	42.5	44.5
Fs	10.5	6.6	9.4	9.8	9.1	10.8	10.2	9.5	7.5
Wo	45.7	46.4	46.9	45.8	47.6	45.3	44.7	48.0	48.0

Continued on next page

Table B.6 *Continued from previous page*

Sample no.	191863	191864	191864	191864	191864	191864	191864	191864	191865
Analysis no.	px_31_31	px_11_11	px_12_12	px_14_14	px_15_15	px_16_16	px_17_17	px_20_20	px_1_1
Al_2O_3	2.50	2.53	2.56	2.31	2.54	2.00	2.20	2.38	2.25
CaO	20.58	22.03	21.23	22.39	22.37	20.05	22.43	22.40	21.14
Cr_2O_3	0.03	0.15	0.12	0.10	0.09	0.10	0.09	0.07	0.07
FeO	5.48	5.27	4.57	5.14	4.62	6.97	5.58	4.09	6.08
Fe_2O_3	4.98	2.33	3.65	2.81	3.40	2.38	2.20	3.00	1.74
K_2O	0.02	0.01				0.01			0.02
MgO	14.01	14.96	15.45	14.68	14.59	15.63	14.53	15.24	15.37
MnO	0.24	0.19	0.18	0.19	0.24	0.23	0.20	0.18	0.24
Na_2O	0.35	0.29	0.29	0.25	0.31	0.28	0.31	0.27	0.24
Nb_2O_5	0.05		0.01		0.03		0.01		
NiO		0.02	0.02	0.04			0.03	0.01	
SiO_2	48.54	51.18	50.46	50.94	50.58	51.59	51.40	50.90	51.41
TiO_2	0.72	0.61	0.61	0.56	0.63	0.42	0.51	0.58	0.55
V_2O_3	0.09	0.04	0.03	0.03	0.03	0.01	0.07	0.07	0.11
ZnO			0.04		0.09		0.06		
En	44.0	44.3	46.4	43.6	43.9	46.0	43.0	45.3	45.2
Fs	9.6	8.8	7.7	8.6	7.8	11.5	9.3	6.8	10.0
Wo	46.4	46.9	45.9	47.8	48.4	42.5	47.7	47.9	44.7

Continued on next page

Table B.6 *Continued from previous page*

Sample no.	191865	191865	191865	191865	191865	191865	191865	191865	191867
Analysis no.	px_10_10	px_2_2	px_3_3	px_35_1	px_36_1	px_4_4	px_5_5	px_7_7	px_13_13
Al_2O_3	2.07	2.14	2.07	2.42	2.24	2.30	2.58	0.57	1.81
CaO	20.96	21.41	21.83	22.72	22.06	20.19	21.42	7.67	22.43
Cr_2O_3	0.14	0.15	0.18	0.18	0.10	0.12	0.15		0.07
FeO	6.33	6.16	5.88	5.61	5.07	6.92	6.10	14.39	8.76
Fe_2O_3	2.77	2.09	1.82	2.91	3.46	1.89	2.28	0.37	2.14
K_2O	0.01	0.01	0.01	0.02	0.01		0.01	0.02	0.02
MgO	14.74	14.89	14.88	14.40	14.84	15.66	14.38	21.22	12.39
MnO	0.25	0.18	0.20	0.23	0.22	0.20	0.24	0.28	0.25
Na_2O	0.29	0.26	0.23	0.26	0.25	0.24	0.30	0.12	0.28
Nb_2O_5			0.03		0.03	0.03			
NiO	0.02	0.04		0.04	0.02	0.03	0.02		0.03
SiO_2	50.68	51.10	51.14	51.25	50.68	51.33	50.38	52.64	50.87
TiO_2	0.61	0.57	0.53	0.70	0.64	0.72	0.70		0.46
V_2O_3	0.05	0.09	0.08	0.06	0.06	0.08	0.10		0.10
ZnO	0.09	0.04			0.01	0.01	0.01		0.02
En	44.2	44.1	43.9	42.5	44.2	46.0	43.3	61.0	37.1
Fs	10.6	10.2	9.7	9.3	8.5	11.4	10.3	23.2	14.7
Wo	45.2	45.6	46.3	48.2	47.3	42.6	46.4	15.8	48.2

Continued on next page

Table B.6 *Continued from previous page*

Sample no.	191870	191870	191870	191870	191870	191871	191871	191871	191871
Analysis no.	px_12_12	px_14_14	px_19_19	px_20_20	px_22_22	px_11_11	px_12_12	px_13_13	px_14_14
Al_2O_3	1.28	1.77	0.40	0.36	1.50	2.49	2.18	2.21	1.70
CaO	18.58	17.64	2.84	3.17	20.18	18.79	19.49	18.06	18.25
Cr_2O_3		0.02	0.03		0.01	0.04	0.06	0.07	
FeO	14.63	13.34	31.12	32.66	14.04	10.42	10.37	11.54	11.51
Fe_2O_3	2.62	2.86	2.00	1.85	1.94	2.43	1.97	2.24	2.66
K_2O	0.02	0.01		0.01	0.02		0.01		0.02
MgO	11.49	12.79	12.95	11.94	10.88	14.11	13.90	13.96	13.48
MnO	0.40	0.41	0.78	0.61	0.35	0.24	0.30	0.32	0.30
Na_2O	0.20	0.19	0.02	0.04	0.20	0.26	0.25	0.25	0.27
Nb_2O_5		0.03			0.03	0.03	0.12	0.03	0.03
NiO	0.01	0.02		0.01	0.03		0.03	0.02	
SiO_2	50.03	49.78	49.01	49.18	50.30	50.09	50.51	50.07	49.86
TiO_2	0.52	0.65	0.21	0.12	0.57	1.36	1.24	1.31	0.99
V_2O_3	0.03	0.10			0.04	0.19	0.06	0.10	0.11
ZnO		0.05	0.06	0.10	0.06	0.09		0.02	0.03
En	34.8	38.8	39.9	36.7	32.7	42.2	41.2	41.8	40.8
Fs	24.8	22.7	53.8	56.3	23.7	17.5	17.3	19.4	19.5
Wo	40.4	38.5	6.3	7.0	43.6	40.4	41.5	38.8	39.7

Continued on next page

Table B.6 *Continued from previous page*

Sample no.	191871	191871	191871	191871	191871	191871	191872	191872	191872
Analysis no.	px_15_15	px_16_16	px_17_17	px_18_18	px_19_19	px_20_20	px_11_11	px_12_12	px_13_13
Al_2O_3	1.82	1.33	1.35	1.25	1.30	1.35	1.79	1.09	1.15
CaO	18.72	17.62	17.14	16.41	16.68	17.23	18.63	16.35	16.69
Cr_2O_3	0.02			0.01	0.07		0.03		0.02
FeO	11.22	15.56	15.93	18.07	16.55	16.34	10.30	19.29	17.66
Fe_2O_3	3.02	2.00	2.64	1.74	2.13	2.17	3.40	1.27	2.24
K_2O					0.01	0.01			0.01
MgO	13.65	11.98	11.81	11.44	12.08	11.77	13.83	10.56	10.71
MnO	0.29	0.41	0.45	0.48	0.44	0.42	0.30	0.51	0.43
Na_2O	0.27	0.23	0.18	0.20	0.20	0.21	0.21	0.17	0.17
Nb_2O_5						0.05			0.04
NiO		0.02				0.02	0.03	0.01	
SiO_2	50.30	50.42	49.83	50.40	50.33	50.25	49.48	50.07	49.21
TiO_2	1.10	0.79	0.75	0.69	0.74	0.79	1.05	0.55	0.59
V_2O_3	0.12	0.04	0.04	0.04	0.07	0.04	0.03	0.03	0.03
ZnO	0.06		0.01	0.01		0.02			0.06
En	40.9	35.9	35.7	34.3	36.2	35.3	41.9	31.9	32.8
Fs	18.9	26.2	27.0	30.4	27.8	27.5	17.5	32.7	30.4
Wo	40.3	37.9	37.3	35.3	35.9	37.2	40.6	35.5	36.8

Continued on next page

Table B.6 *Continued from previous page*

Sample no.	191872	191872	191872	191872	191872	191872	191872
Analysis no.	px_14_14	px_15_15	px_16_16	px_17_17	px_18_18	px_19_19	px_20_20
Al_2O_3	1.39	1.94	2.31	1.47	1.50	1.03	1.24
CaO	16.91	19.28	18.95	17.22	18.12	16.58	16.76
Cr_2O_3		0.03	0.07	0.01		0.01	0.01
FeO	16.39	9.64	10.07	13.96	12.73	17.10	16.34
Fe_2O_3	2.41	2.85	2.58	1.69	2.64	3.47	2.51
K_2O					0.01		
MgO	11.35	13.96	13.83	13.38	12.85	10.47	11.76
MnO	0.48	0.25	0.23	0.36	0.40	0.47	0.47
Na_2O	0.17	0.25	0.24	0.18	0.24	0.19	0.18
Nb_2O_5						0.03	
NiO	0.02	0.01			0.05		
SiO_2	49.25	49.85	49.43	50.28	49.93	48.44	49.83
TiO_2	0.77	1.17	1.37	1.02	0.94	0.49	0.64
V_2O_3	0.03	0.10	0.13	0.03	0.08	0.03	0.04
ZnO					0.09	0.07	0.06
En	34.7	42.0	41.8	39.8	38.9	32.7	35.7
Fs	28.1	16.3	17.1	23.3	21.6	30.0	27.8
Wo	37.2	41.7	41.1	36.8	39.4	37.3	36.5

Table B.7 Orthopyroxene major and minor element compositions (see description of analytical method in sections 2.3 and 4.3.1).

Sample no.	191831	191831	191831	191831	191831	191831	191831	191831	191831
Analysis no.	px_11_11	px_13_13	px_14_14	px_15_15	px_16_16	px_17_17	px_18_18	px_19_19	px_20_20
Al_2O_3	2.46	1.96	3.00	1.09	1.70	1.24	0.75	1.10	1.13
CaO	1.43	1.59	1.92	0.36	0.92	0.64	0.31	0.47	1.89
Cr_2O_3	0.14	0.10	0.09	0.05	0.12	0.05		0.03	0.02
FeO	23.74	24.05	23.91	27.03	25.30	26.55	25.15	26.49	24.99
Fe_2O_3	2.92	2.41	2.17	2.22	2.97	1.85	1.29	3.61	1.70
K_2O		0.04		0.01		0.01	0.01		0.09
MgO	18.81	18.94	18.38	18.54	18.20	18.55	20.24	18.19	18.44
MnO	0.64	0.63	0.63	0.70	0.70	0.62	0.56	0.63	0.63
Na_2O	0.03	0.07	0.06	0.02	0.02	0.02	0.02		0.08
Nb_2O_5		0.01				0.08	0.02		
NiO		0.03	0.04		0.01	0.02	0.05	0.07	
SiO_2	50.03	50.90	50.20	51.28	49.96	51.08	52.09	50.34	51.41
TiO_2	0.10	0.09	0.13	0.09	0.05	0.05	0.05	0.08	0.12
V_2O_3	0.01	0.02	0.03		0.04			0.01	0.02
ZnO		0.03	0.05	0.05	0.07	0.02		0.04	0.03
En	56.7	56.4	55.4	54.6	55.1	54.7	58.5	54.5	54.5
Fs	40.2	40.2	40.4	44.6	42.9	43.9	40.8	44.5	41.5
Wo	3.1	3.4	4.2	0.8	2.0	1.4	0.6	1.0	4.0

Continued on next page

Table B.7 *Continued from previous page*

Sample no.	191838	191838	191838	191840	191840	191840	191842	191843	191843
Analysis no.	px_10_1	px_6_1	px_8_1	px_22_22	px_25_25	px_26_26	px_18_18	px_1_1	px_10_1
Al_2O_3	1.40	1.56	1.46	1.14	1.38	1.28	1.34	1.52	0.32
CaO	1.21	0.98	0.76	0.76	0.86	1.13	1.04	1.00	0.32
Cr_2O_3	0.01		0.02					0.01	
FeO	17.34	18.26	17.66	19.25	19.27	19.80	19.44	17.25	16.78
Fe_2O_3	2.82	1.85	2.68	2.04	1.50	1.87	0.92	2.59	2.34
K_2O			0.01	0.02		0.01		0.01	0.01
MgO	24.47	24.48	24.81	23.40	23.47	22.96	23.35	24.73	26.30
MnO	0.41	0.38	0.42	0.42	0.44	0.36	0.38	0.36	0.46
Na_2O	0.02	0.01	0.03	0.05	0.02	0.03	0.02	0.03	0.08
Nb_2O_5		0.02	0.01		0.03	0.04			
NiO	0.01	0.02	0.03	0.06	0.06	0.04	0.05	0.07	0.05
SiO_2	52.57	52.99	52.90	52.23	52.38	52.19	52.44	52.63	54.34
TiO_2	0.25	0.26	0.21	0.26	0.21	0.31	0.23	0.31	
V_2O_3		0.04	0.01	0.06	0.04			0.06	
ZnO	0.07	0.03			0.04				
En	69.8	69.1	70.3	67.3	67.2	65.8	66.7	70.4	73.2
Fs	27.8	28.9	28.1	31.1	31.0	31.8	31.2	27.5	26.2
Wo	2.5	2.0	1.6	1.6	1.8	2.3	2.1	2.1	0.6

Continued on next page

Table B.7 *Continued from previous page*

Sample no.	191843	191843	191843	191845	191845	191845	191845	191845	191848
Analysis no.	px_2_1	px_4_1	px_6_1	px_11_11	px_12_12	px_14_14	px_16_16	px_17_17	px_9_1
Al_2O_3	1.66	1.53	1.50	1.67	1.49	1.51	1.50	1.36	1.31
CaO	1.05	1.08	1.02	0.50	0.47	0.69	0.75	1.07	0.88
Cr_2O_3	0.01	0.02		0.01	0.01		0.02		0.01
FeO	17.04	17.40	15.88	18.84	19.05	15.74	15.91	17.01	18.14
Fe_2O_3	1.91	2.64	3.65	1.05	0.75	2.60	2.08	1.94	1.38
K_2O			0.01				0.01		
MgO	25.37	24.68	25.68	24.76	24.90	26.55	26.46	25.40	24.99
MnO	0.38	0.41	0.39	0.35	0.43	0.38	0.40	0.42	0.37
Na_2O		0.01	0.03		0.02	0.02	0.03	0.02	
Nb_2O_5				0.04	0.01				
NiO	0.07	0.04	0.06	0.08	0.02	0.03		0.04	0.05
SiO_2	53.38	52.69	53.06	53.51	53.95	53.78	53.82	53.50	53.58
TiO_2	0.30	0.38	0.20	0.06	0.08	0.16	0.33	0.28	0.18
V_2O_3		0.04	0.01			0.02	0.02	0.01	
ZnO	0.04	0.07	0.06	0.02			0.03		0.01
En	71.1	70.1	72.7	69.4	69.3	74.0	73.6	71.1	69.8
Fs	26.8	27.7	25.2	29.6	29.8	24.6	24.8	26.7	28.4
Wo	2.1	2.2	2.1	1.0	0.9	1.4	1.5	2.1	1.8

Continued on next page

Table B.7 *Continued from previous page*

Sample no.	191850	191850	191850	191851	191851	191851	191852	191852	191852
Analysis no.	px_14_14	px_18_18	px_20_20	px_22_22	px_23_23	px_26_26	px_4_4	px_5_5	px_9_9
Al_2O_3	1.23	1.16	1.40	1.28	1.32	0.42	1.24	1.35	1.45
CaO	0.72	0.83	0.87	0.62	0.64	0.14	0.74	1.27	0.77
Cr_2O_3	0.03	0.01		0.02		0.01	0.04	0.04	0.06
FeO	15.01	15.48	15.41	16.56	16.60		16.40	15.07	18.12
Fe_2O_3	3.53	2.64	2.74	2.05	1.98	32.73	2.74	3.76	2.08
K_2O	0.02					0.04	0.01	0.01	
MgO	26.15	26.14	26.45	25.93	26.15	27.13	25.58	25.55	24.83
MnO	0.37	0.42	0.35	0.39	0.41	0.32	0.41	0.33	0.38
Na_2O		0.06	0.01	0.03	0.03	0.03	0.04	0.06	
Nb_2O_5					0.02				0.08
NiO	0.05	0.01	0.04	0.05	0.05	0.17	0.04	0.06	0.03
SiO_2	52.57	53.28	53.46	53.53	53.94	37.83	53.05	52.43	53.12
TiO_2	0.16	0.17	0.22	0.16	0.12		0.18	0.34	0.23
V_2O_3		0.06			0.04		0.02	0.04	0.01
ZnO		0.03		0.02	0.01		0.01	0.05	0.03
En	74.5	73.8	74.0	72.7	72.8	99.6	72.4	73.2	69.8
Fs	24.0	24.5	24.2	26.1	25.9		26.1	24.2	28.6
Wo	1.5	1.7	1.8	1.2	1.3	0.4	1.5	2.6	1.5

Continued on next page

Table B.7 *Continued from previous page*

Sample no.	191855	191855	191855	191855	191855	191855	191856	191856	191856
Analysis no.	px_12_12	px_13_13	px_14_14	px_15_15	px_16_16	px_17_17	px_1_1	px_2_2	px_7_7
Al_2O_3	1.49	1.35	1.38	1.41	1.42	1.50	1.03	1.12	1.08
CaO	1.09	1.32	0.86	0.58	1.00	0.93	1.31	0.71	1.04
Cr_2O_3	0.04	0.03	0.04	0.05	0.02	0.01	0.04		0.01
FeO	15.25	15.52	17.29	16.09	16.67	16.95	22.58	22.19	19.71
Fe_2O_3	3.39	2.98	1.75	2.66	2.03	2.30	2.13	2.18	3.82
K_2O	0.01	0.01	0.01		0.01	0.01		0.02	0.38
MgO	25.80	25.93	25.33	26.30	25.45	25.31	21.22	21.67	21.73
MnO	0.40	0.36	0.34	0.38	0.35	0.39	0.43	0.46	0.42
Na_2O	0.04	0.02	0.03		0.04	0.01	0.03	0.03	0.08
Nb_2O_5	0.06	0.03	0.01		0.04	0.04	0.02	0.09	0.02
NiO	0.03	0.03	0.06	0.06	0.02	0.09	0.05	0.03	0.04
SiO_2	52.71	53.22	53.51	53.58	53.19	53.13	52.19	52.00	51.50
TiO_2	0.32	0.30	0.23	0.15	0.28	0.25	0.27	0.16	0.28
V_2O_3	0.01				0.03		0.04	0.10	0.02
ZnO	0.09		0.10	0.04	0.02			0.03	0.09
En	73.4	72.9	71.1	73.6	71.6	71.3	60.9	62.6	64.8
Fs	24.3	24.5	27.2	25.3	26.3	26.8	36.4	35.9	33.0
Wo	2.2	2.7	1.7	1.2	2.0	1.9	2.7	1.5	2.2

Continued on next page

Table B.7 *Continued from previous page*

Sample no.	191856	191858	191858	191859	191859	191859	191859	191859	191862
Analysis no.	px_8_8	px_28_28	px_29_29	px_22_22	px_25_25	px_26_26	px_28_28	px_30_30	px_12_12
Al_2O_3	0.97	1.83	1.40	1.33	1.36	1.12	1.61	1.28	1.44
CaO	0.80	1.47	0.90	0.85	0.88	0.79	0.78	0.74	0.87
Cr_2O_3		0.04	0.08	0.01	0.01	0.01		0.02	0.03
FeO	20.27	18.65	18.68	15.33	18.06	16.74	17.67	16.95	16.76
Fe_2O_3	3.45	1.32	1.35	3.68	2.36	2.29	2.73	2.72	2.53
K_2O	0.01	0.02	0.02	0.01				0.02	
MgO	22.32	24.00	24.28	25.56	24.26	25.65	24.25	24.83	25.64
MnO	0.43	0.41	0.39	0.40	0.36	0.41	0.40	0.36	0.38
Na_2O	0.05	0.03	0.03	0.04	0.03	0.02		0.02	0.04
Nb_2O_5		0.03	0.06	0.01			0.05		
NiO	0.03	0.07	0.03	0.05	0.07	0.07	0.01		0.02
SiO_2	51.57	53.49	53.08	52.18	52.54	53.42	51.98	52.22	53.47
TiO_2	0.16	0.01	0.22	0.24	0.26	0.20	0.18	0.22	0.24
V_2O_3		0.04	0.06	0.05			0.03	0.01	0.02
ZnO	0.02	0.01	0.01		0.06		0.05		0.03
En	65.1	67.6	68.6	73.5	69.3	72.0	69.8	71.2	71.9
Fs	33.2	29.5	29.6	24.7	28.9	26.4	28.5	27.3	26.4
Wo	1.7	3.0	1.8	1.8	1.8	1.6	1.6	1.5	1.7

Continued on next page

Table B.7 *Continued from previous page*

Sample no.	191862	191863	191863	191863	191864	191864	191865	191865	191865
Analysis no.	px_9_9	px_24_24	px_30_30	px_32_32	px_13_13	px_19_19	px_37_1	px_8_8	px_9_9
Al_2O_3	1.34	1.34	0.91	1.31	1.20	1.88	0.54	0.76	0.71
CaO	1.05	0.96	0.41	0.56	0.53	0.84	0.34	0.40	0.36
Cr_2O_3	0.01	0.04		0.04	0.03	0.06		0.01	
FeO	16.39	18.16	13.82	14.81	15.29	17.09	18.28	17.49	17.31
Fe_2O_3	3.16	3.59	4.80	3.17	3.03	3.03	1.78	5.04	2.53
K_2O	0.01						0.02	0.01	0.02
MgO	25.37	23.03	26.37	26.42	26.04	24.32	24.56	24.12	25.30
MnO	0.40	0.42	0.32	0.34	0.38	0.43	0.39	0.38	0.44
Na_2O	0.01	0.02	0.02	0.01	0.02	0.02	0.06	0.02	0.03
Nb_2O_5			0.02	0.10		0.03			
NiO	0.04			0.01	0.01	0.07	0.04	0.02	
SiO_2	52.84	50.87	51.64	52.60	52.52	51.80	52.93	51.45	53.10
TiO_2	0.30	0.23		0.16	0.09	0.26	0.01	0.02	0.01
V_2O_3	0.04	0.04			0.03	0.01	0.02		
ZnO		0.06		0.12	0.03	0.11	0.07		
En	71.8	67.9	76.6	75.2	74.4	70.5	70.1	70.5	71.7
Fs	26.0	30.1	22.5	23.7	24.5	27.8	29.3	28.7	27.5
Wo	2.1	2.0	0.9	1.1	1.1	1.8	0.7	0.8	0.7

Continued on next page

Table B.7 *Continued from previous page*

Sample no.	191870	191870	191870	191870	191870
Analysis no.	px_11_11	px_13_13	px_15_15	px_18_18	px_21_21
Al_2O_3	0.49	0.37	0.29	0.32	0.44
CaO	1.36	1.44	1.47	0.52	1.52
Cr_2O_3				0.02	0.01
FeO	34.41	34.22	34.94	35.21	33.06
Fe_2O_3	1.65	1.89	1.65	1.86	2.63
K_2O	0.01	0.01			
MgO	11.81	12.23	11.73	12.17	12.46
MnO	0.67	0.69	0.79	0.68	0.67
Na_2O	0.04	0.02	0.01		0.02
Nb_2O_5	0.02	0.04	0.06		0.04
NiO		0.01	0.06	0.01	0.01
SiO_2	48.41	48.99	48.93	48.71	48.34
TiO_2	0.23	0.14	0.15	0.03	0.19
V_2O_3	0.01	0.01	0.01		0.02
ZnO	0.05	0.07	0.09		0.02
En	36.8	37.7	36.2	37.7	38.8
Fs	60.2	59.1	60.5	61.2	57.8
Wo	3.0	3.2	3.3	1.2	3.4

Table B.8 Olivine major and minor element compositions (see description of analytical method in sections 2.3 and 4.3.1).

Sample no.	191836	191836	191836	191836	191836	191836	191836	191836	191836
Analysis no.	ol_1_1	ol_10_1	ol_11_1	ol_12_1	ol_13_1	ol_14_1	ol_15_1	ol_16_1	ol_17_1
Al_2O_3									0.03
CaO	0.01			0.01	0.01		0.01	0.01	0.01
Cr_2O_3			0.01		0.01				0.01
FeO	33.25	33.82	33.37	33.36	33.29	33.81	33.67	33.58	33.65
K_2O	0.01	0.01	0.01					0.01	
MgO	30.24	29.32	30.28	30.39	30.27	30.30	30.11	30.64	29.96
MnO	0.40	0.43	0.41	0.39	0.41	0.46	0.40	0.37	0.41
Na_2O	0.01	0.01	0.02			0.01	0.02		0.01
Nb_2O_5		0.03		0.01		0.03			
NiO	0.16	0.17	0.12	0.12	0.14	0.12	0.10	0.14	0.12
SiO_2	35.50	36.10	35.71	35.65	35.61	35.67	35.74	35.61	35.82
TiO_2		0.01						0.02	
V_2O_3		0.02						0.01	
ZnO	0.06	0.03		0.07	0.07	0.01			0.01
Fa	38.2	39.3	38.2	38.1	38.2	38.5	38.6	38.1	38.7
Fo	61.8	60.7	61.8	61.9	61.8	61.5	61.4	61.9	61.3

Continued on next page

Table B.8 *Continued from previous page*

Sample no.	191836	191836	191836	191836	191836	191836	191836	191836	191836
Analysis no.	ol_18_1	ol_19_1	ol_2_1	ol_20_1	ol_21_1	ol_22_1	ol_23_1	ol_24_1	ol_25_1
Al_2O_3			0.01	0.01	0.01	0.01			
CaO			0.01	0.01			0.01	0.01	0.01
Cr_2O_3		0.01		0.04	0.01			0.02	
FeO	33.87	33.77	33.98	33.95	33.69	33.67	33.73	33.42	33.73
K_2O							0.01		
MgO	29.83	29.83	29.72	30.07	30.00	30.14	29.47	29.71	30.61
MnO	0.39	0.34	0.39	0.46	0.36	0.44	0.40	0.42	0.38
Na_2O	0.01				0.01				0.01
Nb_2O_5						0.04		0.02	0.09
NiO	0.17	0.15	0.14	0.14	0.12	0.10	0.17	0.14	0.16
SiO_2	35.71	35.67	35.48	35.81	35.82	35.37	35.96	35.64	35.25
TiO_2		0.02			0.03				
V_2O_3				0.03	0.02				
ZnO		0.01			0.05	0.01	0.01		
Fa	38.9	38.8	39.1	38.8	38.7	38.5	39.1	38.7	38.2
Fo	61.1	61.2	60.9	61.2	61.3	61.5	60.9	61.3	61.8

Continued on next page

Table B.8 *Continued from previous page*

Sample no.	191836	191836	191836	191836	191836	191836	191836	191838	191838
Analysis no.	ol_3_1	ol_4_1	ol_5_1	ol_6_1	ol_7_1	ol_8_1	ol_9_1	ol_1_1	ol_10_1
Al_2O_3		0.01			0.01			0.01	
CaO		0.02	0.01	0.01	0.01	0.02	0.02	0.01	0.01
Cr_2O_3			0.01	0.03			0.01		
FeO	33.15	33.09	33.55	33.36	33.83	33.76	35.49	34.10	33.43
K_2O			0.01	0.02					
MgO	30.17	30.41	30.02	29.97	29.95	29.50	28.59	29.37	29.80
MnO	0.46	0.42	0.40	0.37	0.40	0.37	0.41	0.41	0.42
Na_2O				0.01	0.02	0.01			
Nb_2O_5	0.02					0.01			
NiO	0.16	0.14	0.13	0.15	0.16	0.08	0.15	0.12	0.18
SiO_2	35.79	35.33	35.52	35.80	35.39	35.55	35.65	35.57	35.95
TiO_2	0.02						0.02		
V_2O_3		0.01					0.01		
ZnO		0.12		0.02	0.02			0.05	0.07
Fa	38.1	37.9	38.5	38.4	38.8	39.1	41.0	39.4	38.6
Fo	61.9	62.1	61.5	61.6	61.2	60.9	59.0	60.6	61.4

Continued on next page

Table B.8 *Continued from previous page*

Sample no.	191838	191838	191838	191838	191838	191838	191838	191838	191838
Analysis no.	ol_11_1	ol_12_1	ol_13_1	ol_14_1	ol_15_1	ol_16_1	ol_17_1	ol_19_1	ol_2_1
Al_2O_3	0.01		0.01	0.01		0.01	0.01		
CaO	0.01	0.02		0.02		0.02	0.01	0.01	0.01
Cr_2O_3			0.02			0.01			
FeO	33.27	33.56	33.63	34.10	33.39	33.96	33.92	33.87	33.92
K_2O		0.02	0.01		0.01	0.01		0.01	
MgO	29.45	29.96	30.21	29.45	29.83	29.97	29.96	30.21	29.56
MnO	0.45	0.43	0.38	0.44	0.42	0.42	0.43	0.34	0.46
Na_2O	0.04	0.03				0.02	0.02	0.01	0.01
Nb_2O_5	0.01		0.01				0.02	0.01	0.01
NiO	0.15	0.25	0.16	0.20	0.16	0.19	0.18	0.16	0.19
SiO_2	35.94	35.95	36.06	36.05	36.27	35.69	36.06	35.73	35.85
TiO_2			0.01	0.01	0.02		0.01		
V_2O_3	0.04	0.01		0.01					0.01
ZnO	0.06	0.09	0.06		0.19	0.03	0.04	0.04	
Fa	38.8	38.6	38.4	39.4	38.6	38.9	38.9	38.6	39.2
Fo	61.2	61.4	61.6	60.6	61.4	61.1	61.2	61.4	60.8

Continued on next page

Table B.8 *Continued from previous page*

Sample no.	191838	191838	191838	191838	191838	191838	191838	191840	191840
Analysis no.	ol_20_1	ol_4_1	ol_5_1	ol_6_1	ol_7_1	ol_8_1	ol_9_1	ol_11_11	ol_12_12
Al_2O_3		0.01	0.01		0.01			0.02	
CaO		0.01	0.02						0.02
Cr_2O_3			0.01		0.01				
FeO	34.18	33.32	33.15	33.27	34.05	33.90	34.03	36.51	34.53
K_2O			0.01					0.01	
MgO	29.52	30.87	30.17	30.26	29.72	30.08	30.14	27.99	29.42
MnO	0.43	0.41	0.42	0.45	0.42	0.45	0.44	0.43	0.35
Na_2O	0.02			0.01	0.01	0.01	0.03		
Nb_2O_5				0.04			0.02	0.03	
NiO	0.16	0.14	0.24	0.16	0.07	0.12	0.17	0.16	0.18
SiO_2	35.84	35.69	36.23	35.61	35.55	35.73	35.55	35.44	35.00
TiO_2	0.02					0.01			
V_2O_3	0.03	0.01				0.03	0.03		0.02
ZnO		0.01	0.04		0.07	0.05	0.04	0.04	
Fa	39.4	37.7	38.1	38.2	39.1	38.7	38.8	42.3	39.7
Fo	60.6	62.3	61.9	61.8	60.9	61.3	61.2	57.7	60.3

Continued on next page

Table B.8 *Continued from previous page*

Sample no.	191840	191840	191840	191840	191840	191840	191840	191840	191842
Analysis no.	ol_13_13	ol_14_14	ol_15_15	ol_16_16	ol_17_17	ol_18_18	ol_19_19	ol_20_20	ol_1_1
Al_2O_3	0.01				0.01				
CaO	0.02			0.01			0.01	0.01	0.02
Cr_2O_3			0.01	0.01				0.02	
FeO	34.89	35.04	37.02	34.34	35.09	35.55	34.99	34.21	35.74
K_2O	0.01		0.01		0.01	0.01			0.01
MgO	29.18	29.31	27.52	29.66	28.92	28.60	28.80	29.79	27.62
MnO	0.40	0.42	0.45	0.39	0.44	0.39	0.42	0.44	0.36
Na_2O		0.03		0.02	0.02	0.03	0.01	0.02	0.02
Nb_2O_5	0.02	0.03	0.05		0.02	0.03	0.02	0.02	
NiO	0.20	0.21	0.22	0.17	0.14	0.16	0.16	0.14	0.16
SiO_2	35.79	35.16	35.30	35.58	35.32	35.26	35.62	35.21	35.21
TiO_2	0.01	0.03	0.01	0.01		0.01			
V_2O_3		0.03	0.03				0.01		
ZnO	0.05		0.06		0.04	0.05	0.10		0.08
Fa	40.2	40.1	43.0	39.4	40.5	41.1	40.5	39.2	42.1
Fo	59.8	59.9	57.0	60.6	59.5	58.9	59.5	60.8	57.9

Continued on next page

Table B.8 *Continued from previous page*

Sample no.	191842	191842	191842	191842	191842	191842	191842	191842	191842
Analysis no.	ol_11_1	ol_12_1	ol_13_1	ol_14_1	ol_15_1	ol_16_1	ol_17_1	ol_18_1	ol_19_1
Al_2O_3	0.01		0.01	0.01				0.01	
CaO	0.01	0.01	0.01						0.02
Cr_2O_3	0.01					0.01		0.01	0.01
FeO	35.92	35.87	36.20	36.39	35.84	36.36	36.64	36.41	35.94
K_2O	0.02								
MgO	27.37	27.91	27.67	27.50	27.71	27.29	27.30	26.85	28.09
MnO	0.43	0.46	0.41	0.47	0.40	0.39	0.46	0.39	0.41
Na_2O	0.01	0.01						0.02	0.02
Nb_2O_5				0.01		0.01	0.05		0.01
NiO	0.16	0.11	0.13	0.11	0.13	0.17	0.15	0.16	0.15
SiO_2	35.37	35.17	35.15	34.79	35.45	35.46	35.26	35.14	35.00
TiO_2	0.01	0.01	0.01	0.03			0.01	0.01	0.02
V_2O_3		0.03	0.03			0.04		0.02	
ZnO	0.03	0.04			0.06	0.04			0.05
Fa	42.4	41.9	42.3	42.6	42.1	42.8	43.0	43.2	41.8
Fo	57.6	58.1	57.7	57.4	57.9	57.2	57.0	56.8	58.2

Continued on next page

Table B.8 *Continued from previous page*

Sample no.	191842	191842	191842	191842	191842	191842	191842	191842	191842
Analysis no.	ol_20_1	ol_4_1	ol_5_1	ol_6_1	ol_7_1	ol_8_1	ol_2_1	ol_9_1	ol_10_1
Al_2O_3								0.01	0.03
CaO	0.02	0.02	0.01	0.01	0.02	0.01	0.02	0.01	0.03
Cr_2O_3	0.02	0.02				0.02			
FeO	36.15	35.72	36.12	36.20	35.37	36.75	35.07	36.53	36.52
K_2O									
MgO	27.69	27.66	28.08	27.96	28.18	27.69	28.31	27.55	27.86
MnO	0.46	0.46	0.42	0.37	0.46	0.43	0.38	0.45	0.42
Na_2O	0.02				0.01				
Nb_2O_5					0.02				
NiO	0.15	0.09	0.12	0.10	0.10	0.16	0.13	0.11	0.09
SiO_2	35.31	35.12	35.07	34.67	35.30	34.97	35.19	35.12	34.90
TiO_2	0.03			0.01					0.03
V_2O_3		0.02	0.01					0.04	
ZnO	0.06		0.03			0.03	0.08		0.01
Fa	42.3	42.0	41.9	42.1	41.3	42.7	41.0	42.7	42.4
Fo	57.7	58.0	58.1	57.9	58.7	57.3	59.0	57.3	57.6

Continued on next page

Table B.8 *Continued from previous page*

Sample no.	191842	191843	191843	191843	191843	191843	191843	191843	191843
Analysis no.	ol_3_1	ol_1_1	ol_10_1	ol_2_1	ol_3_1	ol_4_1	ol_5_1	ol_6_1	ol_7_1
Al_2O_3	0.01	0.01	0.01	0.01		0.01	0.01		
CaO	0.01	0.01	0.01	0.01	0.02	0.02		0.01	
Cr_2O_3	0.02		0.03		0.03				0.02
FeO	35.99	31.58	33.11	32.05	32.86	32.22	32.17	31.10	31.89
K_2O		0.01					0.01		
MgO	27.49	31.40	30.24	30.68	30.16	31.09	31.29	31.67	31.03
MnO	0.42	0.32	0.33	0.35	0.39	0.31	0.35	0.37	0.40
Na_2O	0.03		0.01			0.01	0.02		0.01
Nb_2O_5	0.02	0.01							
NiO	0.12	0.17	0.16	0.16	0.13	0.20	0.18	0.11	0.20
SiO_2	35.31	35.98	35.56	35.82	35.47	35.27	35.97	35.82	35.84
TiO_2	0.02		0.01		0.01	0.01	0.01		0.01
V_2O_3	0.02				0.01		0.01	0.02	
ZnO	0.08	0.02	0.04	0.07	0.01	0.01			
Fa	42.4	36.1	38.1	37.0	37.9	36.8	36.6	35.5	36.6
Fo	57.6	63.9	61.9	63.0	62.1	63.2	63.4	64.5	63.4

Continued on next page

Table B.8 *Continued from previous page*

Sample no.	191843	191843	191845	191845	191845	191845	191845	191845	191845
Analysis no.	ol_8_1	ol_9_1	ol_1_1	ol_10_1	ol_11_1	ol_12_1	ol_13_1	ol_14_1	ol_15_1
Al_2O_3				0.01			0.01		
CaO		0.01	0.02	0.01		0.01			
Cr_2O_3								0.03	
FeO	31.19	32.19	34.27	34.50	33.58	34.02	34.10	34.06	34.01
K_2O							0.01	0.01	
MgO	31.63	30.54	30.01	29.35	29.77	29.45	29.91	29.86	29.43
MnO	0.44	0.35	0.42	0.40	0.43	0.43	0.44	0.36	0.39
Na_2O			0.01	0.02	0.01	0.02	0.01	0.02	0.01
Nb_2O_5					0.01	0.03			
NiO	0.16	0.17	0.15	0.17	0.13	0.11	0.12	0.18	0.14
SiO_2	36.25	35.99	34.98	34.99	35.59	35.31	35.07	35.34	35.59
TiO_2	0.02			0.01		0.01	0.01	0.02	0.02
V_2O_3	0.02	0.01	0.01	0.04					0.04
ZnO		0.04	0.02		0.04	0.06	0.03	0.01	0.08
Fa	35.6	37.2	39.0	39.7	38.8	39.3	39.0	39.0	39.3
Fo	64.4	62.8	61.0	60.3	61.2	60.7	61.0	61.0	60.7

Continued on next page

Table B.8 *Continued from previous page*

Sample no.	191845	191845	191845	191845	191845	191845	191845	191845	191845
Analysis no.	ol_16_1	ol_17_1	ol_18_1	ol_19_1	ol_2_1	ol_20_1	ol_3_1	ol_4_1	ol_5_1
Al_2O_3		0.02					0.01		0.01
CaO	0.01	0.01	0.01		0.01			0.02	
Cr_2O_3		0.02				0.03	0.02	0.01	
FeO	34.14	32.86	32.58	31.99	33.89	33.61	34.86	34.22	34.04
K_2O				0.01	0.01		0.01		
MgO	29.71	30.43	30.61	31.96	29.83	29.97	28.96	29.37	29.85
MnO	0.39	0.43	0.41	0.44	0.39	0.45	0.37	0.45	0.42
Na_2O		0.01	0.03	0.02		0.01		0.03	0.01
Nb_2O_5	0.01				0.05		0.01		0.06
NiO	0.16	0.13	0.12	0.13	0.12	0.14	0.13	0.13	0.15
SiO_2	35.35	36.06	36.01	35.14	35.56	35.65	35.52	34.96	35.45
TiO_2			0.02	0.01	0.02		0.01		
V_2O_3	0.01				0.02				0.04
ZnO			0.09	0.03			0.05		
Fa	39.2	37.7	37.4	36.0	38.9	38.6	40.3	39.5	39.0
Fo	60.8	62.3	62.6	64.0	61.1	61.4	59.7	60.5	61.0

Continued on next page

Table B.8 *Continued from previous page*

Sample no.	191845	191845	191845	191845	191847	191847	191847	191847	191847
Analysis no.	ol_6_1	ol_7_1	ol_8_1	ol_9_1	ol_12_12	ol_13_13	ol_14_14	ol_15_15	ol_16_16
Al_2O_3		0.01	0.02	0.02	0.02				
CaO			0.01	0.01	0.01	0.01		0.01	0.01
Cr_2O_3			0.01		0.02				0.03
FeO	34.21	35.29	33.82	34.25	32.30	33.84	33.29	33.35	33.15
K_2O	0.01				0.01				
MgO	29.55	29.13	30.03	29.41	31.99	30.08	30.83	30.99	31.03
MnO	0.46	0.43	0.38	0.47	0.41	0.46	0.40	0.40	0.43
Na_2O			0.01	0.02		0.02			
Nb_2O_5	0.02	0.06	0.09	0.01	0.03			0.02	
NiO	0.12	0.14	0.18	0.14	0.18	0.14	0.13	0.14	0.11
SiO_2	35.53	35.02	35.08	35.36	36.42	36.22	36.01	36.07	36.02
TiO_2		0.01				0.01		0.02	
V_2O_3	0.01				0.02		0.04	0.01	0.01
ZnO	0.02	0.07		0.04	0.01	0.03	0.01		0.03
Fa	39.4	40.5	38.7	39.5	36.2	38.7	37.7	37.6	37.5
Fo	60.6	59.5	61.3	60.5	63.8	61.3	62.3	62.4	62.5

Continued on next page

Table B.8 *Continued from previous page*

Sample no.	191847	191847	191847	191847	191848	191848	191848	191848	191848
Analysis no.	ol_17_17	ol_18_18	ol_19_19	ol_20_20	ol_1_1	ol_10_1	ol_11_1	ol_12_1	ol_13_1
Al_2O_3		0.01	0.02			0.01			0.01
CaO	0.01		0.02		0.01	0.01	0.01	0.01	0.03
Cr_2O_3			0.02		0.03	0.06	0.01		0.02
FeO	33.36	32.86	33.02	33.51	32.89	33.36	32.86	32.97	32.73
K_2O								0.02	0.01
MgO	31.00	31.23	30.75	30.53	30.26	30.58	30.80	30.92	30.76
MnO	0.39	0.39	0.42	0.40	0.36	0.40	0.36	0.39	0.38
Na_2O						0.01	0.01	0.03	0.03
Nb_2O_5			0.07		0.05	0.03	0.01		0.01
NiO	0.19	0.18	0.17	0.12	0.14	0.16	0.16	0.13	0.14
SiO_2	35.73	35.84	35.93	35.89	35.51	35.13	35.12	35.23	35.29
TiO_2			0.01	0.01				0.01	0.01
V_2O_3				0.01		0.02		0.04	
ZnO		0.09		0.04	0.03	0.06		0.04	0.02
Fa	37.6	37.1	37.6	38.1	37.9	38.0	37.4	37.4	37.4
Fo	62.4	62.9	62.4	61.9	62.1	62.0	62.6	62.6	62.6

Continued on next page

Table B.8 *Continued from previous page*

Sample no.	191848	191848	191848	191848	191848	191848	191848	191848	191848
Analysis no.	ol_14_1	ol_15_1	ol_16_1	ol_17_1	ol_18_1	ol_19_1	ol_2_1	ol_20_1	ol_3_1
Al_2O_3		0.02	0.02	0.02	0.01	0.02			
CaO		0.01	0.02		0.01	0.03		0.01	0.02
Cr_2O_3				0.02		0.01		0.04	
FeO	33.23	33.31	32.94	32.56	33.03	33.19	33.47	32.89	33.60
K_2O							0.01		0.01
MgO	30.76	30.84	30.72	31.58	30.66	30.86	30.35	30.99	30.29
MnO	0.40	0.42	0.40	0.40	0.44	0.45	0.38	0.44	0.42
Na_2O	0.01			0.01		0.02		0.02	0.01
Nb_2O_5		0.07	0.01	0.02	0.06		0.08	0.04	
NiO	0.12	0.13	0.14	0.08	0.12	0.14	0.13	0.13	0.10
SiO_2	35.25	35.31	35.42	34.75	35.40	35.65	35.32	35.69	35.09
TiO_2			0.02			0.01	0.02		
V_2O_3		0.03	0.03	0.02		0.02		0.01	0.02
ZnO	0.03	0.01	0.08	0.07	0.05			0.03	0.03
Fa	37.7	37.7	37.6	36.7	37.7	37.6	38.2	37.3	38.4
Fo	62.3	62.3	62.4	63.3	62.3	62.4	61.8	62.7	61.6

Continued on next page

Table B.8 *Continued from previous page*

Sample no.	191848	191848	191848	191848	191848	191848	191850	191850	191850
Analysis no.	ol_4_1	ol_5_1	ol_6_1	ol_7_1	ol_8_1	ol_9_1	ol_1_1	ol_10_1	ol_11_1
Al_2O_3									0.01
CaO	0.01	0.02	0.01	0.01	0.02	0.01	0.01	0.02	0.02
Cr_2O_3				0.01	0.01	0.03			
FeO	33.68	33.44	32.88	33.31	33.09	32.67	29.34	30.97	30.99
K_2O		0.01					0.01		0.01
MgO	30.33	30.34	30.80	30.88	30.39	31.25	33.67	32.24	32.03
MnO	0.43	0.44	0.41	0.40	0.49	0.42	0.34	0.37	0.37
Na_2O			0.02	0.03	0.01		0.01	0.01	0.03
Nb_2O_5			0.02			0.02			0.09
NiO	0.12	0.16	0.18	0.11	0.08	0.13	0.15	0.14	0.14
SiO_2	35.25	35.13	35.46	35.02	35.31	35.30	36.54	36.40	36.08
TiO_2	0.01				0.01			0.01	
V_2O_3	0.04	0.01			0.02				
ZnO		0.04	0.11	0.03	0.09	0.06		0.08	0.05
Fa	38.4	38.2	37.5	37.7	37.9	37.0	32.8	35.0	35.2
Fo	61.6	61.8	62.5	62.3	62.1	63.0	67.2	65.0	64.8

Continued on next page

Table B.8 *Continued from previous page*

Sample no.	191850	191850	191850	191850	191850	191850	191850	191850	191850
Analysis no.	ol_12_1	ol_13_1	ol_14_1	ol_15_1	ol_16_1	ol_17_1	ol_18_1	ol_19_1	ol_2_1
Al_2O_3				0.01	0.03	0.01			0.01
CaO	0.01	0.01	0.01	0.01	0.01	0.01	0.02	0.02	
Cr_2O_3	0.02	0.02			0.03				0.03
FeO	31.30	31.58	31.12	30.97	30.99	30.79	29.70	31.67	28.99
K_2O						0.01	0.01	0.02	
MgO	31.88	31.94	32.19	32.09	32.32	32.28	33.02	31.19	34.01
MnO	0.40	0.37	0.40	0.35	0.40	0.37	0.38	0.42	0.33
Na_2O			0.02		0.03	0.02			
Nb_2O_5		0.01		0.02				0.03	
NiO	0.16	0.19	0.14	0.21	0.12	0.22	0.18	0.16	0.22
SiO_2	36.39	36.16	36.38	36.56	36.25	36.49	36.48	36.45	36.45
TiO_2			0.01			0.03	0.01	0.03	
V_2O_3	0.03	0.03	0.03	0.04	0.02	0.01		0.04	
ZnO		0.02	0.03			0.04			0.01
Fa	35.5	35.7	35.2	35.1	35.0	34.9	33.5	36.3	32.4
Fo	64.5	64.3	64.8	64.9	65.0	65.1	66.5	63.7	67.6

Continued on next page

Table B.8 *Continued from previous page*

Sample no.	191850	191850	191850	191850	191850	191850	191850	191850	191851
Analysis no.	ol_20_1	ol_3_1	ol_4_1	ol_5_1	ol_6_1	ol_7_1	ol_8_1	ol_9_1	ol_11_11
Al_2O_3			0.01	0.01	0.02		0.01		0.01
CaO	0.02	0.01	0.02	0.01	0.01	0.01	0.02	0.02	0.01
Cr_2O_3					0.04			0.01	
FeO	30.75	29.55	30.49	30.33	31.22	30.96	30.59	30.77	30.36
K_2O									
MgO	32.46	33.63	33.20	32.78	32.12	32.21	33.07	32.36	33.17
MnO	0.36	0.39	0.30	0.35	0.41	0.33	0.38	0.37	0.42
Na_2O			0.01	0.01			0.01	0.01	0.03
Nb_2O_5			0.03			0.02	0.07		0.05
NiO	0.19	0.18	0.15	0.20	0.16	0.17	0.17	0.16	0.18
SiO_2	36.26	36.87	36.18	36.52	36.31	36.56	36.17	36.61	36.42
TiO_2	0.01		0.04			0.01	0.02		
V_2O_3						0.01	0.02	0.01	
ZnO		0.04				0.04	0.01	0.04	
Fa	34.7	33.0	34.0	34.2	35.3	35.0	34.2	34.8	33.9
Fo	65.3	67.0	66.0	65.8	64.7	65.0	65.8	65.2	66.1

Continued on next page

Table B.8 *Continued from previous page*

Sample no.	191851	191851	191851	191851	191851	191851	191851	191851	191851
Analysis no.	ol_12_12	ol_13_13	ol_14_14	ol_15_15	ol_16_16	ol_17_17	ol_18_18	ol_19_19	ol_20_20
Al_2O_3									
CaO	0.01	0.03		0.02	0.01		0.02		0.01
Cr_2O_3			0.02	0.01	0.02	0.01			0.02
FeO	31.30	31.58	30.92	30.88	30.57	31.38	31.72	31.00	32.25
K_2O		0.01	0.01			0.01			
MgO	32.73	32.17	32.88	32.85	32.90	32.17	32.15	32.79	31.95
MnO	0.43	0.44	0.43	0.41	0.40	0.44	0.41	0.42	0.38
Na_2O	0.03	0.01	0.01	0.02			0.01	0.01	0.02
Nb_2O_5		0.01	0.02					0.03	
NiO	0.12	0.24	0.17	0.20	0.22	0.21	0.18	0.17	0.25
SiO_2	36.28	36.43	36.72	36.62	36.02	35.90	36.71	36.50	35.98
TiO_2		0.01	0.02	0.01			0.01		0.01
V_2O_3	0.06								0.02
ZnO	0.05		0.02		0.02				
Fa	34.9	35.5	34.5	34.5	34.3	35.4	35.6	34.7	36.2
Fo	65.1	64.5	65.5	65.5	65.7	64.6	64.4	65.3	63.8

Continued on next page

Table B.8 *Continued from previous page*

Sample no.	191852	191852	191852	191852	191852	191852	191852	191852	191852
Analysis no.	ol_10_1	ol_11_1	ol_12_1	ol_13_1	ol_14_1	ol_15_1	ol_2_1	ol_3_1	ol_4_1
Al_2O_3	0.01		0.02			0.02	0.03	0.02	
CaO	0.01	0.01				0.01			
Cr_2O_3		0.01			0.02	0.01			
FeO	33.04	33.11	33.02	33.00	34.10	33.06	33.21	33.27	33.35
K_2O	0.01	0.01	0.01		0.01	0.02		0.01	0.01
MgO	29.59	30.39	29.89	30.40	29.63	30.06	30.14	29.98	29.95
MnO	0.39	0.39	0.41	0.40	0.40	0.41	0.43	0.40	0.39
Na_2O	0.02		0.01	0.01		0.01			0.02
Nb_2O_5			0.01						
NiO	0.19	0.15	0.16	0.19	0.17	0.16	0.19	0.19	0.24
SiO_2	36.04	35.48	35.94	35.47	35.55	35.88	35.55	35.88	35.53
TiO_2		0.01	0.01			0.02	0.01		0.01
V_2O_3					0.02				
ZnO	0.06				0.01		0.03		
Fa	38.5	37.9	38.3	37.9	39.2	38.2	38.2	38.4	38.4
Fo	61.5	62.1	61.7	62.1	60.8	61.8	61.8	61.6	61.6

Continued on next page

Table B.8 *Continued from previous page*

Sample no.	191852	191852	191852	191852	191852	191854	191854	191854	191854
Analysis no.	ol_5_1	ol_6_1	ol_7_1	ol_8_1	ol_9_1	ol_1_1	ol_2_1	ol_3_1	ol_4_1
Al_2O_3			0.01		0.02		0.03	0.02	0.09
CaO		0.01	0.01		0.01	0.04	0.10	0.02	0.18
Cr_2O_3			0.01			0.04		0.03	
FeO	33.14	32.51	33.68	33.96	33.61	35.33	31.68	32.44	24.52
K_2O							0.01	0.01	
MgO	29.78	30.88	29.74	29.74	30.19	28.66	31.90	31.05	36.97
MnO	0.42	0.37	0.36	0.40	0.43	0.45	0.40	0.44	0.30
Na_2O	0.03	0.01	0.02		0.04	0.02			0.02
Nb_2O_5	0.02			0.06		0.04	0.01		0.01
NiO	0.21	0.21	0.18	0.17	0.19	0.18	0.14	0.14	0.17
SiO_2	35.68	35.28	35.81	35.23	35.58	35.35	35.84	36.09	37.65
TiO_2		0.01	0.01	0.01	0.01	0.02	0.01	0.02	0.01
V_2O_3		0.01			0.01		0.02		
ZnO	0.06		0.04	0.01	0.03	0.04	0.02		0.04
Fa	38.4	37.1	38.9	39.1	38.4	40.9	35.8	37.0	27.1
Fo	61.6	62.9	61.1	60.9	61.6	59.1	64.2	63.0	72.9

Continued on next page

Table B.8 *Continued from previous page*

Sample no.	191854	191855	191855	191855	191855	191855	191855	191855	191855
Analysis no.	ol_5_1	ol_1_1	ol_10_1	ol_11_1	ol_12_1	ol_13_1	ol_14_1	ol_15_1	ol_2_1
Al_2O_3	0.09	0.01							0.01
CaO	0.02	0.01	0.03	0.02	0.02	0.01	0.02	0.02	0.04
Cr_2O_3	0.03	0.03	0.03			0.03			0.02
FeO	24.69	31.48	31.93	31.31	30.93	30.93	31.30	30.55	31.30
K_2O	0.01	0.01			0.01				0.01
MgO	36.88	31.43	31.40	31.90	32.05	32.29	31.94	31.96	31.74
MnO	0.33	0.41	0.36	0.42	0.40	0.40	0.42	0.36	0.36
Na_2O	0.02	0.03	0.01		0.02	0.02	0.01	0.02	0.01
Nb_2O_5	0.02			0.03		0.05			
NiO	0.27	0.22	0.19	0.20	0.18	0.19	0.17	0.20	0.16
SiO_2	37.71	36.31	36.58	36.38	36.18	36.39	36.30	36.78	36.38
TiO_2			0.01	0.02		0.01	0.02		
V_2O_3		0.02		0.03		0.01	0.03	0.02	
ZnO	0.04				0.12			0.01	
Fa	27.3	36.0	36.3	35.5	35.1	35.0	35.5	34.9	35.6
Fo	72.7	64.0	63.7	64.5	64.9	65.0	64.5	65.1	64.4

Continued on next page

Table B.8 *Continued from previous page*

Sample no.	191855	191855	191855	191855	191855	191855	191855	191856	191856
Analysis no.	ol_3_1	ol_4_1	ol_5_1	ol_6_1	ol_7_1	ol_8_1	ol_9_1	ol_12_1	ol_13_1
Al_2O_3	0.02		0.02						0.02
CaO	0.02	0.01	0.02	0.03	0.02	0.01		0.02	0.03
Cr_2O_3			0.04		0.03				0.02
FeO	30.95	31.50	31.27	31.31	31.03	31.51	32.02	41.05	41.37
K_2O									
MgO	31.57	31.39	31.78	32.58	32.20	31.71	31.53	23.92	23.62
MnO	0.30	0.45	0.39	0.41	0.38	0.40	0.38	0.50	0.46
Na_2O	0.01	0.05	0.03	0.02	0.01	0.03	0.03		0.02
Nb_2O_5	0.04	0.08		0.04	0.06				0.05
NiO	0.18	0.19	0.19	0.19	0.14	0.23	0.21	0.06	0.11
SiO_2	36.51	36.33	36.62	36.07	36.36	36.19	35.90	33.85	34.49
TiO_2	0.03				0.02		0.03		0.01
V_2O_3						0.02		0.01	0.01
ZnO	0.04	0.01					0.06	0.02	0.03
Fa	35.5	36.0	35.6	35.0	35.1	35.8	36.3	49.1	49.6
Fo	64.5	64.0	64.4	65.0	64.9	64.2	63.7	50.9	50.4

Continued on next page

Table B.8 *Continued from previous page*

Sample no.	191856	191856	191856	191856	191856	191856	191856	191856	191856
Analysis no.	ol_14_1	ol_15_1	ol_3_1	ol_4_1	ol_5_1	ol_6_1	ol_7_1	ol_8_1	ol_9_1
Al_2O_3				0.01	0.02			0.01	
CaO	0.03	0.02	0.01	0.02	0.03	0.01	0.01	0.02	0.03
Cr_2O_3			0.01		0.01	0.03	0.01		
FeO	41.66	39.73	42.67	41.24	40.74	40.23	41.39	41.09	40.96
K_2O	0.01		0.01			0.01		0.01	
MgO	23.47	24.98	22.91	23.98	24.07	24.19	23.37	23.48	23.80
MnO	0.46	0.48	0.50	0.45	0.46	0.46	0.49	0.45	0.51
Na_2O				0.03		0.01	0.01	0.04	0.01
Nb_2O_5		0.03		0.05					
NiO	0.13	0.10	0.12	0.05	0.14	0.07	0.07	0.16	0.10
SiO_2	34.81	34.56	34.11	34.19	34.77	34.67	34.62	34.33	34.22
TiO_2		0.01	0.02				0.02	0.01	
V_2O_3		0.02		0.03	0.03			0.01	
ZnO	0.04	0.01	0.06		0.02	0.02	0.02	0.07	
Fa	49.9	47.2	51.1	49.1	48.7	48.3	49.8	49.5	49.1
Fo	50.1	52.8	48.9	50.9	51.3	51.7	50.2	50.5	50.9

Continued on next page

Table B.8 *Continued from previous page*

Sample no.	191856	191856	191856	191856	191858	191858	191858	191858	191858
Analysis no.	ol_1_1	ol_10_1	ol_11_1	ol_2_1	ol_11_11	ol_12_12	ol_13_13	ol_14_14	ol_15_15
Al_2O_3				0.01					
CaO	0.02		0.02	0.02	0.01	0.02	0.02		0.02
Cr_2O_3			0.03					0.03	
FeO	40.89	41.12	41.33	41.28	36.45	35.91	36.30	35.87	35.27
K_2O	0.01	0.01	0.01	0.01	0.01				0.01
MgO	23.75	23.44	23.59	23.07	28.51	29.22	28.81	29.03	29.37
MnO	0.46	0.50	0.45	0.46	0.51	0.46	0.45	0.45	0.46
Na_2O	0.01	0.01	0.01	0.03	0.02	0.03	0.02	0.02	0.02
Nb_2O_5	0.08		0.02	0.13	0.04				
NiO	0.11	0.10	0.08	0.13	0.10	0.12	0.12	0.07	0.15
SiO_2	33.89	34.39	34.06	34.13	35.86	35.97	36.13	36.21	35.93
TiO_2	0.02		0.02	0.02				0.03	0.01
V_2O_3	0.02	0.02	0.02		0.01		0.05		
ZnO	0.05				0.07			0.02	
Fa	49.1	49.6	49.6	50.1	41.8	40.8	41.4	40.9	40.3
Fo	50.9	50.4	50.4	49.9	58.2	59.2	58.6	59.1	59.7

Continued on next page

Table B.8 *Continued from previous page*

Sample no.	191858	191858	191858	191858	191858	191859	191859	191859	191859
Analysis no.	ol_16_16	ol_17_17	ol_18_18	ol_19_19	ol_20_20	ol_12_12	ol_13_13	ol_14_14	ol_15_15
Al_2O_3							0.01	0.02	0.01
CaO	0.02	0.01	0.03	0.02	0.01		0.01	0.01	0.01
Cr_2O_3		0.02		0.01		0.01	0.01		0.02
FeO	35.31	35.86	35.91	35.99	36.55	32.00	31.98	31.23	32.28
K_2O						0.01	0.01	0.01	
MgO	29.32	28.91	29.00	28.79	28.79	31.94	31.67	32.29	31.63
MnO	0.41	0.44	0.46	0.45	0.44	0.36	0.44	0.39	0.36
Na_2O		0.01					0.02		0.01
Nb_2O_5	0.01	0.10							0.02
NiO	0.11	0.09	0.07	0.13	0.12	0.21	0.21	0.24	0.19
SiO_2	35.78	36.20	36.13	36.07	35.97	36.17	36.33	36.30	35.89
TiO_2				0.03	0.01			0.01	0.02
V_2O_3		0.03					0.01		
ZnO			0.06	0.08	0.01	0.03	0.13		0.04
Fa	40.3	41.0	41.0	41.2	41.6	36.0	36.2	35.2	36.4
Fo	59.7	59.0	59.0	58.8	58.4	64.0	63.8	64.8	63.6

Continued on next page

Table B.8 *Continued from previous page*

Sample no.	191859	191859	191859	191859	191859	191860	191860	191860	191860
Analysis no.	ol_16_16	ol_17_17	ol_18_18	ol_19_19	ol_20_20	ol_1_1	ol_10_1	ol_11_1	ol_12_1
Al_2O_3	0.02				0.01		0.01		
CaO	0.02	0.01	0.01	0.01			0.01	0.01	0.01
Cr_2O_3			0.01	0.02				0.02	
FeO	31.87	32.06	32.40	31.80	31.74	31.11	30.60	30.23	30.18
K_2O			0.01	0.01	0.01			0.01	0.01
MgO	31.58	31.90	31.61	32.22	31.63	31.13	32.40	32.90	32.83
MnO	0.42	0.37	0.37	0.41	0.46	0.37	0.36	0.36	0.43
Na_2O					0.02			0.01	0.01
Nb_2O_5					0.06		0.04	0.04	
NiO	0.21	0.20	0.17	0.17	0.14	0.17	0.12	0.19	0.20
SiO_2	35.96	36.02	36.05	35.48	36.03	36.34	36.09	36.08	36.23
TiO_2				0.01				0.05	0.01
V_2O_3					0.01	0.03		0.02	0.01
ZnO		0.05		0.08	0.01	0.03	0.05	0.03	
Fa	36.1	36.1	36.5	35.6	36.0	35.9	34.6	34.0	34.0
Fo	63.9	63.9	63.5	64.4	64.0	64.1	65.4	66.0	66.0

Continued on next page

Table B.8 *Continued from previous page*

Sample no.	191860	191860	191860	191860	191860	191860	191860	191860	191860
Analysis no.	ol_13_1	ol_14_1	ol_15_1	ol_16_1	ol_17_1	ol_18_1	ol_19_1	ol_20_1	ol_3_1
Al_2O_3	0.02			0.01			0.02	0.01	0.01
CaO	0.01		0.01	0.02	0.03	0.01	0.02	0.02	0.01
Cr_2O_3		0.02					0.01		
FeO	30.23	30.26	30.58	30.09	31.01	30.82	30.92	29.93	30.24
K_2O					0.01	0.02			
MgO	32.48	32.29	32.50	32.49	31.85	32.29	32.07	33.00	32.66
MnO	0.38	0.31	0.37	0.37	0.35	0.35	0.37	0.38	0.35
Na_2O	0.01	0.02		0.03		0.02			0.01
Nb_2O_5	0.05					0.01		0.02	0.01
NiO	0.18	0.21	0.14	0.18	0.17	0.15	0.19	0.14	0.21
SiO_2	36.37	36.80	36.31	36.15	36.06	35.97	36.40	36.25	36.59
TiO_2	0.01						0.02	0.01	
V_2O_3				0.02	0.02	0.01			
ZnO		0.03	0.07		0.11	0.02	0.08	0.08	0.08
Fa	34.3	34.5	34.6	34.2	35.3	34.9	35.1	33.7	34.2
Fo	65.7	65.5	65.4	65.8	64.7	65.1	64.9	66.3	65.8

Continued on next page

Table B.8 *Continued from previous page*

Sample no.	191860	191860	191860	191860	191860	191860	191862	191862	191862
Analysis no.	ol_4_1	ol_6_1	ol_8_1	ol_5_1	ol_7_1	ol_9_1	ol_1_1	ol_10_1	ol_11_1
Al_2O_3	0.01		0.01			0.01			
CaO	0.01	0.03	0.02	0.02	0.01		0.02	0.04	0.02
Cr_2O_3		0.02				0.02	0.01		
FeO	29.92	29.94	30.29	29.81	30.09	30.25	32.30	32.24	32.23
K_2O		0.02		0.01			0.01		0.01
MgO	32.58	32.61	32.33	32.58	32.64	32.31	30.64	31.23	31.46
MnO	0.35	0.36	0.41	0.41	0.32	0.41	0.40	0.40	0.39
Na_2O		0.01	0.02			0.01	0.01		
Nb_2O_5			0.01				0.08		
NiO	0.15	0.22	0.18	0.13	0.18	0.15	0.13	0.12	0.12
SiO_2	36.35	36.34	36.32	36.24	36.25	36.13	36.13	36.10	35.43
TiO_2			0.02				0.02	0.02	0.01
V_2O_3			0.02			0.02			
ZnO		0.04	0.06	0.01				0.02	
Fa	34.0	34.0	34.5	33.9	34.1	34.4	37.2	36.7	36.5
Fo	66.0	66.0	65.5	66.1	65.9	65.6	62.8	63.3	63.5

Continued on next page

Table B.8 *Continued from previous page*

Sample no.	191862	191862	191862	191862	191862	191862	191862	191862	191862
Analysis no.	ol_12_1	ol_13_1	ol_14_1	ol_15_1	ol_16_1	ol_17_1	ol_18_1	ol_19_1	ol_2_1
Al_2O_3		0.01	0.01						
CaO	0.02	0.01	0.01			0.02	0.01	0.02	0.02
Cr_2O_3		0.02		0.02	0.02	0.01	0.01		0.02
FeO	32.26	32.21	32.10	32.78	31.90	32.58	32.26	32.18	32.59
K_2O	0.01	0.01			0.01			0.01	0.01
MgO	31.07	31.19	31.79	30.38	31.54	31.25	31.32	31.44	30.68
MnO	0.41	0.38	0.41	0.41	0.29	0.40	0.38	0.38	0.41
Na_2O	0.02	0.03	0.01		0.03				0.02
Nb_2O_5		0.06	0.03	0.02		0.05	0.04		
NiO	0.17	0.12	0.13	0.11	0.14	0.12	0.16	0.13	0.11
SiO_2	35.59	35.46	35.45	35.76	35.57	35.88	35.52	35.54	35.60
TiO_2					0.01	0.02		0.01	0.02
V_2O_3			0.01			0.01	0.02		0.02
ZnO	0.01		0.07	0.02		0.03		0.04	
Fa	36.8	36.7	36.2	37.7	36.2	36.9	36.6	36.5	37.3
Fo	63.2	63.3	63.8	62.3	63.8	63.1	63.4	63.5	62.7

Continued on next page

Table B.8 *Continued from previous page*

Sample no.	191862	191862	191862	191862	191862	191862	191862	191862	191863
Analysis no.	ol_20_1	ol_3_1	ol_4_1	ol_5_1	ol_6_1	ol_7_1	ol_8_1	ol_9_1	ol_11_11
Al_2O_3			0.01						0.03
CaO	0.04	0.01	0.03	0.03	0.02	0.03	0.02	0.02	0.03
Cr_2O_3				0.01			0.01		
FeO	32.41	32.19	32.66	32.03	31.83	32.03	32.06	32.28	31.12
K_2O	0.01				0.01			0.01	0.01
MgO	30.92	30.83	30.91	31.30	30.89	31.42	31.20	31.07	32.18
MnO	0.43	0.42	0.36	0.40	0.40	0.37	0.38	0.36	0.38
Na_2O	0.02	0.01	0.01	0.01			0.01	0.02	0.06
Nb_2O_5	0.01	0.04	0.01	0.02			0.01	0.01	0.02
NiO	0.10	0.13	0.13	0.19	0.13	0.12	0.11	0.12	0.18
SiO_2	35.70	35.88	35.57	35.96	36.05	35.32	36.12	35.88	36.15
TiO_2	0.01			0.01		0.02		0.01	0.01
V_2O_3					0.01	0.04			
ZnO		0.02	0.01			0.05	0.04		
Fa	37.0	36.9	37.2	36.5	36.6	36.4	36.6	36.8	35.2
Fo	63.0	63.1	62.8	63.5	63.4	63.6	63.4	63.2	64.8

Continued on next page

Table B.8 *Continued from previous page*

Sample no.	191863	191863	191863	191863	191863	191863	191863	191863	191863
Analysis no.	ol_12_12	ol_13_13	ol_14_14	ol_15_15	ol_16_16	ol_17_17	ol_18_18	ol_19_19	ol_20_20
Al_2O_3	0.02	0.01							0.01
CaO	0.02		0.01	0.03	0.01	0.01			
Cr_2O_3			0.02			0.01		0.03	
FeO	31.09	30.88	30.43	30.70	30.65	31.09	30.36	30.95	30.87
K_2O					0.02		0.01	0.01	0.01
MgO	32.82	32.46	32.74	32.63	32.75	32.40	32.48	32.74	32.54
MnO	0.37	0.39	0.37	0.35	0.41	0.39	0.39	0.40	0.42
Na_2O	0.01			0.01	0.03	0.01	0.04	0.02	0.04
Nb_2O_5	0.01	0.02						0.04	
NiO	0.15	0.13	0.16	0.13	0.13	0.11	0.14	0.16	0.15
SiO_2	35.65	35.53	35.69	35.74	35.33	35.18	35.29	36.23	35.31
TiO_2	0.01			0.01	0.01	0.01	0.01	0.01	
V_2O_3						0.02			
ZnO	0.06	0.03			0.05	0.07			
Fa	34.7	34.8	34.3	34.5	34.4	35.0	34.4	34.7	34.7
Fo	65.3	65.2	65.7	65.5	65.6	65.0	65.6	65.3	65.3

Continued on next page

Table B.8 *Continued from previous page*

Sample no.	191864	191864	191864	191864	191864	191864	191864	191864	191864
Analysis no.	ol_1_1	ol_10_1	ol_11_1	ol_12_1	ol_13_1	ol_14_1	ol_15_1	ol_16_1	ol_17_1
Al_2O_3	0.01	0.01			0.02	0.02			
CaO		0.02	0.01	0.03	0.01	0.02	0.01	0.01	0.02
Cr_2O_3		0.01							0.04
FeO	31.10	31.51	31.73	30.94	31.09	30.58	31.28	30.84	31.28
K_2O	0.01					0.01		0.01	
MgO	32.35	31.63	32.34	32.53	31.98	32.14	32.32	32.04	32.24
MnO	0.40	0.35	0.41	0.38	0.44	0.39	0.37	0.43	0.38
Na_2O	0.01	0.02		0.01	0.01	0.04			0.02
Nb_2O_5		0.07				0.01	0.09		0.01
NiO	0.17	0.10	0.16	0.17	0.14	0.12	0.12	0.17	0.12
SiO_2	36.21	36.34	35.78	36.22	36.37	36.14	36.13	36.55	36.69
TiO_2		0.01			0.01	0.03	0.02	0.02	
V_2O_3					0.01		0.02		
ZnO	0.03			0.04		0.06	0.04	0.05	0.05
Fa	35.0	35.9	35.5	34.8	35.3	34.8	35.2	35.1	35.2
Fo	65.0	64.1	64.5	65.2	64.7	65.2	64.8	64.9	64.8

Continued on next page

Table B.8 *Continued from previous page*

Sample no.	191864	191864	191864	191864	191864	191864	191864	191864	191864
Analysis no.	ol_18_1	ol_19_1	ol_2_1	ol_20_1	ol_3_1	ol_4_1	ol_5_1	ol_6_1	ol_7_1
Al_2O_3			0.03						
CaO		0.02				0.02	0.01	0.01	0.01
Cr_2O_3			0.04	0.02		0.01	0.01	0.01	
FeO	31.18	31.17	31.00	31.56	30.65	30.91	31.86	31.93	31.17
K_2O				0.01		0.01	0.01		
MgO	32.30	32.67	32.43	32.12	32.90	32.34	31.96	31.94	32.05
MnO	0.43	0.38	0.38	0.40	0.35	0.41	0.43	0.37	0.32
Na_2O	0.03		0.03	0.01	0.01		0.01	0.03	0.04
Nb_2O_5	0.05	0.01			0.02	0.01			
NiO	0.10	0.17	0.13	0.17	0.12	0.16	0.15	0.16	0.11
SiO_2	36.34	36.48	36.11	36.15	36.35	36.47	36.33	35.95	36.43
TiO_2		0.03				0.02		0.02	0.02
V_2O_3		0.03		0.01		0.01	0.01		
ZnO		0.05		0.01					0.07
Fa	35.1	34.9	34.9	35.5	34.3	34.9	35.9	35.9	35.3
Fo	64.9	65.2	65.1	64.5	65.7	65.1	64.1	64.1	64.7

Continued on next page

Table B.8 *Continued from previous page*

Sample no.	191864	191864	191865	191865	191865	191865	191865	191865	191865
Analysis no.	ol_8_1	ol_9_1	ol_10_1	ol_11_1	ol_12_1	ol_17_1	ol_18_1	ol_19_1	ol_20_1
Al_2O_3			0.01	0.01	0.01				
CaO	0.03		0.02	0.02		0.01	0.02	0.01	0.02
Cr_2O_3		0.02	0.01			0.02		0.04	
FeO	31.45	31.62	33.81	33.58	34.47	33.72	34.11	34.49	34.07
K_2O	0.01		0.01					0.01	
MgO	32.09	31.78	29.25	29.75	28.96	29.42	29.12	28.93	29.31
MnO	0.34	0.41	0.44	0.37	0.39	0.42	0.37	0.40	0.45
Na_2O	0.06	0.02	0.01		0.01	0.01			
Nb_2O_5	0.02	0.05				0.05		0.03	
NiO	0.17	0.20	0.16	0.09	0.10	0.14	0.18	0.09	0.10
SiO_2	36.10	36.16	35.61	35.74	35.68	35.76	35.76	35.67	35.70
TiO_2		0.01		0.01	0.01		0.01		0.01
V_2O_3	0.02		0.02	0.03	0.01	0.01	0.01		0.01
ZnO	0.02	0.05	0.01	0.06	0.06	0.05		0.04	0.03
Fa	35.5	35.8	39.3	38.8	40.0	39.1	39.7	40.1	39.5
Fo	64.5	64.2	60.7	61.2	60.0	60.9	60.3	59.9	60.5

Continued on next page

Table B.8 *Continued from previous page*

Sample no.	191865	191865	191865	191865	191865	191865	191865	191865	191865
Analysis no.	ol_22_1	ol_23_1	ol_24_1	ol_25_1	ol_3_1	ol_4_1	ol_5_1	ol_6_1	ol_7_1
Al_2O_3							0.01		
CaO	0.02	0.01	0.01	0.02	0.01		0.02	0.01	
Cr_2O_3	0.02			0.03		0.01	0.01		
FeO	34.79	34.35	34.77	34.51	34.49	34.23	34.38	34.91	33.89
K_2O		0.01	0.01	0.01	0.01				
MgO	29.26	29.31	29.17	28.88	28.90	29.26	29.23	28.34	29.22
MnO	0.37	0.39	0.37	0.41	0.36	0.39	0.44	0.44	0.38
Na_2O	0.01	0.03		0.01	0.02	0.01		0.02	
Nb_2O_5	0.01						0.02	0.10	
NiO	0.07	0.14	0.10	0.12	0.12	0.09	0.15	0.09	0.17
SiO_2	36.02	35.32	35.60	35.87	35.57	35.43	35.30	35.72	35.83
TiO_2	0.01		0.02			0.01			0.03
V_2O_3				0.04		0.04	0.03	0.02	
ZnO	0.02	0.03		0.03		0.02	0.01	0.03	
Fa	40.0	39.7	40.1	40.1	40.1	39.6	39.8	40.9	39.4
Fo	60.0	60.3	59.9	59.9	59.9	60.4	60.2	59.1	60.6

Continued on next page

Table B.8 *Continued from previous page*

Sample no.	191865	191865	191865	191865	191865	191865	191865	191865	191870
Analysis no.	ol_8_1	ol_9_1	ol_1_1	ol_13_1	ol_15_1	ol_14_1	ol_16_1	ol_2_1	ol_16_16
Al_2O_3			0.02						
CaO	0.02	0.01		0.03	0.04	0.01	0.02	0.02	0.01
Cr_2O_3	0.03	0.01			0.04		0.02	0.03	
FeO	34.35	34.40	34.60	33.96	34.90	34.22	34.75	34.93	62.44
K_2O	0.01				0.02				
MgO	28.75	29.13	28.44	29.11	28.61	29.26	28.77	28.17	6.02
MnO	0.37	0.43	0.42	0.43	0.44	0.38	0.39	0.44	0.80
Na_2O	0.02		0.01	0.03	0.02	0.02		0.01	
Nb_2O_5	0.02	0.06	0.02	0.06	0.01		0.02		
NiO	0.11	0.11	0.14	0.13	0.08	0.10	0.08	0.15	0.05
SiO_2	35.29	35.88	35.34	35.65	35.38	36.10	35.53	35.35	30.05
TiO_2	0.59			0.01			0.01		
V_2O_3			0.02	0.01		0.02	0.01	0.01	
ZnO	0.08			0.04					0.04
Fa	40.1	39.9	40.6	39.6	40.6	39.6	40.4	41.0	85.3
Fo	59.9	60.1	59.4	60.4	59.4	60.4	59.6	59.0	14.7

Continued on next page

Table B.8 *Continued from previous page*

Sample no.	191870
Analysis no.	ol_17_17
Al_2O_3	0.01
CaO	0.02
Cr_2O_3	0.01
FeO	62.55
K_2O	
MgO	6.09
MnO	0.87
Na_2O	
Nb_2O_5	
NiO	0.06
SiO_2	29.91
TiO_2	0.01
V_2O_3	0.02
ZnO	0.03
Fa	85.2
Fo	14.8

Table B.9 CIPW normative modal compositions. Norm calculations were carried-out after Pruseth (2009a,b, see also appendix A.3 for further details on the procedure); Afs and Pl were calculated from Ab, An and Or after Le Maitre (1976), Px is total pyroxene (Di + Hyp). Mineral abbreviations in the table are used as listed in (Whitney and Evans 2010, Px for pyroxene not listed).

Sample no.	191 801	191 802	191 803	191 804	191 805	191 806	191 807	191 808	191 809	191 810	191 811
Qz	0.00	0.00	0.00	0.00	0.00	0.00	0.00	0.00	0.00	0.00	0.00
Or	0.24	2.56	2.63	2.27	2.23	1.96	0.71	1.79	1.73	1.48	1.49
Ab	0.14	30.85	28.63	28.89	25.62	25.23	10.63	25.65	25.36	23.28	22.24
An	50.63	49.83	46.80	48.37	43.42	41.61	17.92	51.19	51.13	49.74	45.82
Nph	1.05	0.00	0.00	0.00	0.00	0.00	0.00	0.00	0.00	0.00	0.00
Di	38.66	7.75	4.70	3.98	4.20	4.70	10.44	7.90	3.01	2.70	0.07
Hyp	0.00	2.72	5.83	5.27	6.33	7.22	13.68	4.74	5.80	4.46	7.15
Ol	2.38	0.93	4.45	5.10	10.69	12.65	36.12	4.24	9.29	14.66	18.79
Mag	2.26	2.52	3.72	3.38	4.50	4.41	7.28	2.52	2.75	3.04	3.63
Ilm	4.48	2.75	3.11	2.59	2.76	2.09	3.13	1.82	0.84	0.55	0.71
Ap	0.05	0.07	0.12	0.12	0.17	0.07	0.05	0.07	0.07	0.07	0.10
Py	0.00	0.00	0.00	0.00	0.00	0.00	0.00	0.00	0.00	0.00	0.00
Chr	0.10	0.01	0.03	0.03	0.08	0.06	0.03	0.07	0.01	0.01	0.01
Zrn	0.00	0.00	0.01	0.01	0.01	0.00	0.00	0.00	0.00	0.00	0.00
Afs	0.24	4.07	4.15	3.56	3.48	3.10	1.12	2.66	2.56	2.16	2.19
Pl	50.77	79.17	73.90	75.96	67.79	65.70	28.15	75.97	75.65	72.35	67.36
Px	38.66	10.47	10.53	9.25	10.53	11.92	24.12	12.64	8.81	7.16	7.22

Continued on next page

Table B.9 *Continued from previous page*

Sample no.	191 812	191 813	191 814	191 815	191 816	191 817	191 818	191 819	191 820	191 821	191 822
Qz	0.00	0.00	0.00	0.00	0.00	0.00	0.00	0.00	0.00	0.00	0.00
Or	1.44	1.43	1.01	1.19	1.07	1.43	0.83	1.55	0.18	0.84	0.30
Ab	21.85	22.73	18.86	22.19	19.81	24.72	15.02	21.10	7.53	12.75	11.82
An	45.29	48.58	44.01	47.25	38.67	48.03	32.54	43.28	42.63	42.59	36.48
Nph	0.00	0.00	0.00	0.00	0.00	0.00	0.00	0.00	0.00	0.00	0.00
Di	1.41	3.88	2.88	4.54	7.25	3.81	4.77	6.77	31.11	25.26	30.16
Hyp	6.77	4.48	5.09	7.42	15.20	5.88	11.35	8.32	6.73	9.21	10.72
Ol	18.56	14.45	22.98	13.63	12.39	12.16	29.74	13.28	9.76	6.37	7.25
Mag	3.74	3.27	4.17	3.25	4.44	3.17	5.18	3.91	1.58	2.30	2.62
Ilm	0.85	1.06	0.90	0.50	1.09	0.75	0.50	1.63	0.27	0.52	0.48
Ap	0.05	0.05	0.05	0.02	0.05	0.05	0.05	0.14	0.00	0.05	0.00
Py	0.00	0.02	0.00	0.00	0.00	0.00	0.00	0.00	0.00	0.04	0.04
Chr	0.06	0.06	0.06	0.02	0.01	0.01	0.02	0.02	0.22	0.07	0.12
Zrn	0.00	0.00	0.00	0.00	0.00	0.00	0.00	0.01	0.00	0.00	0.00
Afs	2.11	2.08	1.44	1.73	1.61	2.14	1.21	2.28	0.21	1.08	0.40
Pl	66.46	70.66	62.44	68.90	57.95	72.03	47.18	63.65	50.13	55.10	48.20
Px	8.18	8.36	7.97	11.96	22.45	9.69	16.12	15.09	37.84	34.47	40.88

Continued on next page

Table B.9 *Continued from previous page*

Sample no.	191 823	191 824	191 825	191 826	191 827	191 829	191 830	191 831	191 832	191 834	191 836
Qz	0.00	0.00	0.00	0.00	0.00	0.00	0.00	1.88	0.00	0.00	0.00
Or	0.42	0.30	0.36	0.24	0.30	0.84	1.64	3.41	1.11	1.31	1.19
Ab	9.49	9.33	9.37	8.68	8.93	15.33	20.50	24.24	20.91	19.51	17.71
An	56.17	58.92	46.54	38.84	50.52	33.74	27.49	32.50	38.62	37.63	36.18
Nph	0.00	0.00	0.00	0.00	0.00	0.00	0.00	0.00	0.00	0.00	0.00
Di	20.15	10.77	27.07	33.31	19.42	16.03	20.11	8.35	19.92	4.65	5.68
Hyp	5.25	3.52	7.25	7.56	3.66	17.03	17.73	22.45	9.33	11.55	7.67
Ol	6.76	15.33	7.20	9.17	14.86	8.86	1.65	0.00	5.06	18.92	25.36
Mag	1.24	1.44	1.51	1.76	1.68	4.96	6.36	4.83	3.30	4.87	4.94
Ilm	0.25	0.19	0.29	0.33	0.29	2.48	3.73	2.04	1.53	1.43	1.17
Ap	0.02	0.00	0.00	0.00	0.02	0.65	0.73	0.17	0.11	0.10	0.07
Py	0.02	0.00	0.00	0.00	0.02	0.04	0.04	0.09	0.00	0.02	0.02
Chr	0.23	0.20	0.43	0.12	0.28	0.05	0.00	0.02	0.11	0.01	0.01
Zrn	0.00	0.00	0.00	0.00	0.00	0.01	0.03	0.01	0.00	0.00	0.00
Afs	0.49	0.35	0.43	0.29	0.35	1.22	2.80	5.71	1.69	1.96	1.75
Pl	65.59	68.20	55.83	47.46	59.40	48.70	46.83	54.43	58.95	56.48	53.32
Px	25.40	14.29	34.32	40.87	23.08	33.06	37.84	30.80	29.25	16.20	13.35

Continued on next page

Table B.9 *Continued from previous page*

Sample no.	191 837	191 838	191 839	191 840	191 841	191 842	191 843	191 844	191 845	191 846	191 847
Qz	0.00	0.00	0.00	0.00	0.00	0.00	0.00	0.00	0.00	0.00	0.00
Or	1.67	1.13	1.55	1.31	1.61	1.44	1.20	0.77	1.37	1.43	1.32
Ab	24.12	17.37	18.31	20.87	17.35	23.00	23.37	17.04	24.77	25.37	24.41
An	49.78	41.09	35.12	44.12	32.25	44.83	50.44	37.00	49.88	49.57	50.25
Nph	0.00	0.00	0.00	0.00	0.00	0.00	0.00	0.00	0.00	0.00	0.00
Di	6.80	7.95	13.06	6.56	16.65	6.03	5.33	2.19	5.06	6.10	5.15
Hyp	7.30	12.55	15.92	8.22	12.68	7.33	5.60	7.25	6.91	6.19	7.99
Ol	5.99	14.38	9.52	13.48	12.76	12.35	10.63	30.73	8.84	7.76	7.58
Mag	2.71	4.07	4.36	3.89	4.24	3.73	2.72	4.68	2.70	2.75	2.62
Ilm	1.36	1.38	1.69	1.49	1.86	1.25	0.65	0.31	0.42	0.79	0.62
Ap	0.24	0.05	0.24	0.05	0.24	0.02	0.05	0.02	0.02	0.02	0.05
Py	0.02	0.00	0.13	0.00	0.15	0.00	0.00	0.00	0.00	0.00	0.00
Chr	0.01	0.03	0.08	0.01	0.18	0.01	0.01	0.01	0.01	0.01	0.01
Zrn	0.00	0.00	0.01	0.00	0.01	0.00	0.00	0.00	0.00	0.00	0.00
Afs	2.45	1.59	2.33	1.91	2.44	2.15	1.74	1.12	2.04	2.14	1.94
Pl	73.12	57.99	52.65	64.39	48.77	67.12	73.27	53.69	74.00	74.23	74.04
Px	14.10	20.50	28.98	14.78	29.33	13.36	10.93	9.44	11.97	12.29	13.14

Continued on next page

Table B.9 *Continued from previous page*

Sample no.	191 848	191 849	191 850	191 851	191 852	191 853	191 854	191 855	191 856	191 857	191 858
Qz	0.00	0.00	0.00	0.00	0.00	0.00	0.00	0.00	0.00	0.00	0.00
Or	1.31	0.98	1.07	1.31	1.32	1.61	1.49	1.19	1.96	1.78	1.07
Ab	26.08	22.30	22.96	20.34	24.40	25.77	18.01	20.67	28.27	27.39	17.90
An	51.94	48.50	51.52	48.63	51.20	52.90	34.74	44.93	48.49	47.74	34.25
Nph	0.00	0.00	0.00	0.00	0.00	0.00	0.00	0.00	0.00	0.00	0.00
Di	2.65	2.17	3.24	2.85	2.63	5.19	15.73	9.70	2.86	2.21	0.87
Hyp	4.03	4.66	4.88	5.77	3.89	4.00	15.19	5.74	2.97	2.71	6.33
Ol	10.97	17.91	13.27	16.72	11.90	7.61	8.79	13.39	9.31	12.68	30.85
Mag	2.61	3.17	2.71	3.40	3.19	2.30	4.10	3.34	3.76	3.77	6.50
Ilm	0.36	0.27	0.31	0.84	1.32	0.57	1.53	0.92	2.26	1.57	2.03
Ap	0.05	0.04	0.02	0.07	0.02	0.05	0.22	0.02	0.10	0.05	0.00
Py	0.00	0.00	0.00	0.00	0.00	0.00	0.08	0.00	0.00	0.00	0.00
Chr	0.01	0.01	0.01	0.04	0.12	0.01	0.12	0.09	0.03	0.10	0.21
Zrn	0.00	0.00	0.00	0.00	0.00	0.00	0.01	0.00	0.00	0.00	0.00
Afs	1.94	1.43	1.54	1.85	1.94	2.37	2.23	1.73	3.06	2.77	1.62
Pl	77.38	70.35	74.02	68.44	74.99	77.90	52.01	65.07	75.66	74.15	51.61
Px	6.68	6.83	8.12	8.62	6.52	9.19	30.92	15.44	5.83	4.92	7.20

Continued on next page

Table B.9 *Continued from previous page*

Sample no.	191 859	191 860	191 861	191 862	191 863	191 864	191 865	191 866	191 867	191 868	191 869
Qz	0.00	0.00	0.00	0.00	0.00	0.00	0.00	0.00	0.81	0.93	0.00
Or	1.55	1.07	1.43	1.43	1.13	1.19	1.07	1.92	2.34	2.34	1.17
Ab	24.82	19.66	23.62	24.73	20.21	21.79	17.65	31.39	32.06	31.79	16.73
An	51.22	42.52	49.25	50.68	44.76	44.44	32.87	52.80	54.14	53.04	26.27
Nph	0.00	0.00	0.00	0.00	0.00	0.00	0.00	0.00	0.00	0.00	0.00
Di	2.92	1.67	2.84	2.59	11.07	10.34	1.82	6.39	5.12	5.59	24.76
Hyp	4.49	5.57	2.74	3.56	6.11	4.76	9.75	2.95	2.37	2.70	8.19
Ol	11.73	24.98	16.29	13.30	11.75	13.34	30.33	0.86	0.00	0.00	2.04
Mag	2.72	4.15	3.15	2.92	3.40	3.19	5.88	1.91	1.45	1.63	6.10
Ilm	0.48	0.32	0.57	0.67	1.42	0.84	0.52	1.70	1.62	1.87	14.68
Ap	0.05	0.02	0.05	0.05	0.04	0.05	0.07	0.07	0.07	0.10	0.06
Py	0.00	0.00	0.00	0.00	0.00	0.00	0.00	0.00	0.00	0.00	0.00
Chr	0.01	0.04	0.06	0.05	0.12	0.06	0.06	0.01	0.01	0.01	0.00
Zrn	0.00	0.00	0.00	0.00	0.00	0.00	0.00	0.00	0.00	0.00	0.01
Afs	2.29	1.55	2.10	2.11	1.63	1.76	1.63	3.02	3.66	3.68	1.88
Pl	75.31	61.70	72.20	74.74	64.47	65.66	49.96	83.08	84.88	83.48	42.29
Px	7.41	7.24	5.58	6.15	17.18	15.10	11.57	9.34	7.49	8.29	32.95

Continued on next page

Table B.9 *Continued from previous page*

Sample no.	191 870	191 871	191 872	191 873	191 874	191 875	191 876	191 877	191 878	191 879	191 880
Qz	1.71	1.40	1.64	0.00	0.00	0.00	0.00	0.00	0.00	0.00	0.00
Or	4.36	3.94	3.69	1.42	1.49	1.55	1.13	1.13	1.43	1.84	1.48
Ab	30.03	29.94	29.01	22.93	22.81	23.30	20.47	15.00	21.65	24.60	22.29
An	44.94	45.79	45.52	45.59	46.37	51.15	47.18	34.48	43.71	49.69	46.48
Nph	0.00	0.00	0.00	0.00	0.00	0.00	0.00	0.00	0.00	0.00	0.00
Di	6.23	8.20	8.02	5.65	8.56	4.61	2.47	4.18	6.16	3.23	3.01
Hyp	6.33	4.63	5.27	8.89	8.72	4.99	7.52	9.86	11.90	2.45	5.73
Ol	0.00	0.00	0.00	11.46	7.31	9.18	16.64	29.67	10.47	12.64	16.69
Mag	3.21	2.92	3.17	3.28	3.26	3.11	3.54	5.06	3.43	3.47	3.53
Ilm	2.67	2.75	3.18	0.67	1.38	1.89	0.90	0.50	1.07	1.85	0.71
Ap	0.50	0.41	0.48	0.07	0.10	0.10	0.10	0.07	0.05	0.10	0.06
Py	0.00	0.00	0.00	0.00	0.00	0.04	0.00	0.00	0.00	0.00	0.00
Chr	0.01	0.01	0.01	0.02	0.02	0.09	0.05	0.04	0.13	0.12	0.01
Zrn	0.02	0.02	0.02	0.00	0.00	0.00	0.00	0.01	0.00	0.00	0.00
Afs	7.02	6.32	5.87	2.12	2.19	2.23	1.61	1.61	2.11	2.72	2.17
Pl	72.32	73.36	72.35	67.83	68.47	73.76	67.17	49.01	64.68	73.41	68.08
Px	12.56	12.83	13.29	14.54	17.28	9.60	9.99	14.04	18.06	5.68	8.74

Continued on next page

Table B.9 *Continued from previous page*

Sample no.	191 881	191 882	191 883	191 884	191 885	191 886	191 887	191 888	191 889	191 890	195 161
Qz	0.00	0.00	0.00	0.00	0.00	0.00	0.00	0.00	0.00	0.00	0.00
Or	1.66	1.32	1.13	1.01	1.34	2.63	1.43	1.54	1.48	1.73	0.18
Ab	25.50	21.11	20.69	18.88	23.94	21.70	26.95	26.11	23.34	25.59	10.94
An	53.46	49.24	40.11	39.80	51.98	31.94	61.02	53.96	43.34	47.45	42.24
Nph	0.00	0.00	0.00	0.00	0.00	0.00	0.00	0.00	0.00	0.00	0.00
Di	3.11	10.13	9.76	5.24	1.64	10.01	2.43	5.11	2.15	1.91	29.96
Hyp	5.14	6.53	9.58	7.43	4.12	24.60	1.93	4.37	7.02	4.20	7.14
Ol	7.72	7.71	11.25	22.95	13.63	2.22	4.44	5.25	17.83	13.26	7.74
Mag	2.48	2.75	4.20	4.24	2.77	4.60	1.35	2.31	4.19	4.01	1.34
Ilm	0.84	1.12	3.23	0.36	0.50	1.94	0.38	1.20	0.53	1.68	0.17
Ap	0.07	0.05	0.02	0.05	0.05	0.17	0.05	0.07	0.07	0.07	0.00
Py	0.00	0.00	0.00	0.00	0.00	0.09	0.00	0.00	0.00	0.00	0.00
Chr	0.00	0.05	0.02	0.03	0.04	0.09	0.03	0.06	0.04	0.10	0.28
Zrn	0.00	0.00	0.00	0.00	0.00	0.01	0.00	0.00	0.00	0.00	0.00
Afs	2.43	1.87	1.70	1.48	1.94	4.28	2.04	2.27	2.25	2.63	0.23
Pl	78.19	69.80	60.23	58.22	75.32	51.98	87.35	79.34	65.91	72.14	53.14
Px	8.25	16.66	19.34	12.67	5.76	34.61	4.36	9.48	9.17	6.11	37.10

Continued on next page

Table B.9 *Continued from previous page*

Sample no.	205 265	205 266	205 267	205 268	205 269	205 270	205 271	205 272	205 273	205 274	205 275
Qz	0.00	0.00	0.00	1.12	0.00	0.00	0.77	0.00	0.00	0.00	0.00
Or	0.24	2.09	0.60	0.89	0.12	0.30	0.30	0.30	0.30	0.12	0.12
Ab	9.47	11.63	10.02	17.14	9.21	11.61	8.03	10.23	10.58	2.82	7.68
An	40.35	30.70	31.38	43.50	40.58	39.60	28.10	39.45	39.88	8.64	43.32
Nph	0.00	0.00	0.00	0.00	0.00	0.00	0.00	0.00	0.00	0.00	0.00
Di	31.52	26.51	27.78	16.10	27.88	31.21	27.11	28.62	27.07	62.22	33.14
Hyp	9.61	16.82	11.36	19.07	9.19	14.00	32.84	10.95	15.97	22.10	8.41
Ol	6.65	8.17	15.27	0.00	11.17	1.55	0.00	8.35	4.19	0.79	5.76
Mag	1.56	3.04	2.85	1.86	1.47	1.43	2.42	1.72	1.58	2.07	1.13
Ilm	0.25	0.79	0.54	0.23	0.15	0.23	0.25	0.21	0.23	0.38	0.15
Ap	0.00	0.07	0.00	0.00	0.00	0.00	0.00	0.00	0.00	0.00	0.00
Py	0.00	0.00	0.00	0.00	0.00	0.00	0.00	0.02	0.00	0.00	0.00
Chr	0.36	0.17	0.20	0.10	0.23	0.08	0.18	0.16	0.20	0.85	0.30
Zrn	0.00	0.01	0.00	0.00	0.00	0.00	0.00	0.00	0.00	0.00	0.00
Afs	0.29	2.83	0.79	1.24	0.15	0.38	0.38	0.37	0.38	0.16	0.14
Pl	49.76	41.59	41.21	60.30	49.76	51.12	36.05	49.60	50.38	11.43	50.97
Px	41.13	43.33	39.14	35.17	37.07	45.21	59.95	39.57	43.04	84.32	41.55

Continued on next page

Table B.9 *Continued from previous page*

Sample no.	205 276	205 277	205 278	205 279	205 280	205 281	205 282	205 283	205 284	205 285	205 286
Qz	0.00	0.00	0.00	0.00	0.00	0.00	0.00	0.00	0.00	0.15	0.06
Or	0.12	0.06	0.18	0.18	0.12	0.42	0.18	0.30	0.54	0.06	0.42
Ab	8.97	3.68	9.62	9.74	3.42	10.24	4.95	10.23	8.21	2.99	11.30
An	43.51	12.83	40.50	37.66	11.15	37.50	16.40	40.52	22.44	8.79	21.87
Nph	0.00	0.00	0.00	0.00	0.00	0.00	0.00	0.00	0.00	0.00	0.00
Di	32.95	58.00	33.45	32.39	58.16	28.42	54.24	33.23	27.44	58.74	43.55
Hyp	7.08	20.31	9.57	10.58	21.21	18.82	18.87	8.50	30.52	25.11	19.11
Ol	5.62	2.24	4.82	7.18	2.27	2.47	2.24	4.91	6.23	0.00	0.00
Mag	1.22	2.30	1.40	1.71	2.24	1.66	2.03	1.61	3.90	3.11	2.93
Ilm	0.21	0.40	0.25	0.23	0.46	0.25	0.34	0.31	0.52	0.84	0.71
Ap	0.00	0.00	0.00	0.00	0.00	0.00	0.00	0.00	0.00	0.00	0.00
Py	0.00	0.00	0.00	0.00	0.00	0.00	0.00	0.00	0.02	0.00	0.00
Chr	0.32	0.18	0.21	0.32	0.98	0.22	0.75	0.40	0.18	0.19	0.05
Zrn	0.00	0.00	0.00	0.00	0.00	0.00	0.00	0.00	0.00	0.00	0.00
Afs	0.14	0.08	0.22	0.23	0.16	0.53	0.23	0.37	0.73	0.08	0.63
Pl	52.45	16.49	50.08	47.35	14.54	47.62	21.29	50.67	30.46	11.76	32.96
Px	40.03	78.31	43.02	42.97	79.37	47.24	73.11	41.73	57.96	83.85	62.66

Continued on next page

Table B.9 *Continued from previous page*

Sample no.	205 287	205 288	205 289	205 290	205 291	205 292	205 293	205 294	205 295	205 296	205 297
Qz	2.35	0.00	0.00	1.41	1.03	1.45	0.00	0.00	0.00	0.00	0.00
Or	0.00	0.06	0.77	0.00	6.81	0.12	0.12	0.12	0.06	0.18	0.12
Ab	1.37	3.08	18.49	0.77	24.18	3.77	4.62	3.87	3.68	6.86	4.02
An	8.94	8.76	36.91	10.08	24.60	16.30	18.41	13.32	13.86	28.02	13.93
Nph	0.00	0.00	0.00	0.00	0.00	0.00	0.00	0.00	0.00	0.00	0.00
Di	15.49	56.08	26.50	3.65	12.18	14.79	47.26	50.00	46.89	35.57	47.58
Hyp	66.13	27.14	14.25	78.97	23.54	59.04	24.38	26.30	28.86	23.76	29.41
Ol	0.00	0.42	0.39	0.00	0.00	0.00	1.99	2.64	2.52	2.71	1.16
Mag	4.34	3.37	2.20	4.14	4.88	3.43	2.32	2.53	2.89	2.21	2.57
Ilm	0.63	0.86	0.44	0.46	2.06	0.48	0.48	0.58	0.61	0.38	0.60
Ap	0.00	0.00	0.00	0.00	0.47	0.00	0.00	0.05	0.05	0.00	0.02
Py	0.00	0.00	0.00	0.00	0.16	0.00	0.00	0.00	0.00	0.00	0.00
Chr	0.75	0.23	0.05	0.51	0.06	0.60	0.42	0.60	0.57	0.32	0.58
Zrn	0.00	0.00	0.00	0.00	0.02	0.00	0.00	0.00	0.00	0.00	0.00
Afs	0.00	0.08	1.15	0.00	12.06	0.15	0.15	0.15	0.08	0.22	0.15
Pl	10.31	11.82	55.03	10.86	43.53	20.05	23.01	17.15	17.53	34.83	17.92
Px	81.62	83.22	40.75	82.62	35.72	73.83	71.64	76.30	75.75	59.33	76.99

Continued on next page

Table B.9 *Continued from previous page*

Sample no.	205 298	205 299	205 300	205 301	205 302	205 303	205 304	205 305	205 306	205 307	205 308
Qz	0.96	0.00	0.00	0.00	0.02	0.00	0.00	1.83	0.00	1.20	0.00
Or	1.55	0.24	0.06	0.24	0.00	0.12	0.00	0.06	1.37	0.78	5.18
Ab	22.19	4.38	4.11	9.27	3.01	4.56	3.01	3.44	22.00	19.47	20.73
An	32.61	13.84	13.19	18.60	7.99	15.95	9.06	17.32	32.61	36.56	25.99
Nph	0.00	0.00	0.00	0.00	0.00	0.00	0.00	0.00	0.00	0.00	0.00
Di	19.68	49.04	51.05	43.22	55.06	35.92	58.64	6.26	11.70	2.97	12.83
Hyp	19.21	25.45	26.75	23.38	28.80	38.56	23.18	65.86	23.01	35.69	11.47
Ol	0.00	3.15	1.26	1.03	0.00	0.66	1.39	0.00	2.72	0.00	16.19
Mag	3.23	2.60	2.35	3.43	3.91	3.09	3.39	3.88	4.95	2.98	4.80
Ilm	0.52	0.67	0.40	0.69	1.00	0.52	1.10	0.42	1.53	0.27	2.11
Ap	0.00	0.05	0.02	0.02	0.02	0.00	0.02	0.00	0.02	0.00	0.43
Py	0.00	0.00	0.00	0.00	0.00	0.00	0.00	0.00	0.04	0.00	0.11
Chr	0.05	0.58	0.80	0.11	0.19	0.62	0.19	0.93	0.04	0.09	0.12
Zrn	0.00	0.00	0.00	0.00	0.00	0.00	0.00	0.00	0.00	0.00	0.02
Afs	2.56	0.31	0.08	0.36	0.00	0.15	0.00	0.07	2.26	1.18	8.63
Pl	53.79	18.14	17.27	27.76	10.99	20.48	12.08	20.74	53.72	55.62	43.28
Px	38.89	74.49	77.80	66.60	83.86	74.48	81.82	72.12	34.71	38.66	24.30

Continued on next page

Table B.9 *Continued from previous page*

Sample no.	205 309	205 310	205 311	205 312
Qz	0.00	0.00	0.00	0.12
Or	0.00	0.12	6.19	0.48
Ab	3.19	6.60	23.93	13.77
An	9.34	13.50	22.44	32.94
Nph	0.00	0.00	0.00	0.00
Di	59.83	54.07	14.56	18.30
Hyp	23.42	20.99	11.51	31.09
Ol	0.00	0.31	6.06	0.00
Mag	3.20	3.42	7.10	2.69
Ilm	0.81	0.89	6.63	0.38
Ap	0.02	0.02	1.39	0.02
Py	0.00	0.00	0.13	0.02
Chr	0.18	0.08	0.02	0.19
Zrn	0.00	0.00	0.05	0.00
Afs	0.00	0.18	11.36	0.67
Pl	12.53	20.04	41.20	46.51
Px	83.25	75.06	26.07	49.39

This Report outlines the petrogenesis and emplacement of the Giles Suite and its prospectivity for orthomagmatic Ni–Cu–PGE sulphide ore deposits. Detailed analysis of three large layered mafic-ultramafic intrusions, namely Bell Rock, Lattitude Hills and Wingellina Hills intrusions, are the focus for this study. A combination of both traditional knowledge-driven methods of data analysis and interpretation are used as well as modern data-driven multivariate statistical techniques. The results of this study are used to assess the relative importance of plate- and mantle-dynamics and to constrain the tectonic setting of the Musgrave Province during the Giles Event.

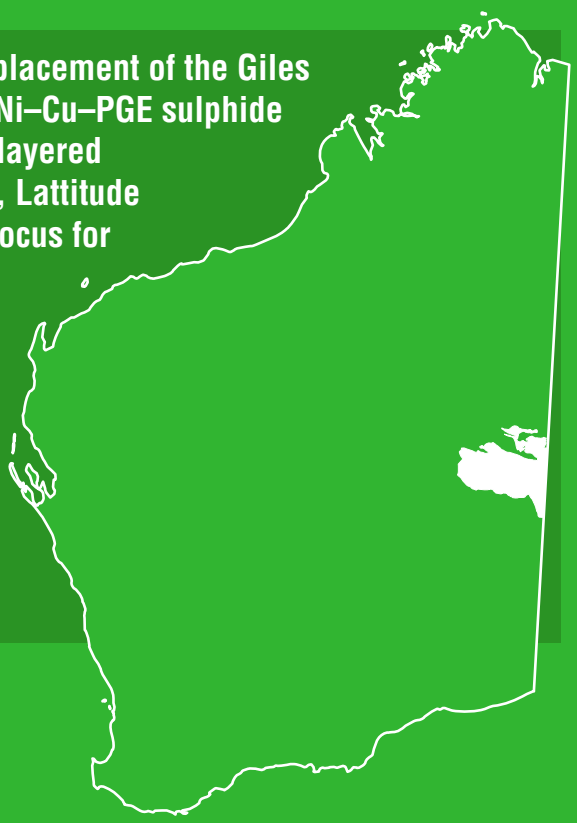

Further details of geological products and maps produced by the Geological Survey of Western Australia are available from:

Information Centre
Department of Mines and Petroleum
100 Plain Street
EAST PERTH WA 6004
Phone: (08) 9222 3459 Fax: (08) 9222 3444

www.dmp.wa.gov.au/GSWApublications

SEUBERT

PETROGENESIS OF THE MAFIC-ULTRAMAFIC INTRUSIONS OF THE MESOPROTEROZOIC GILES EVENT, MUSGRAVE PROVINCE, CENTRAL AUSTRALIA

REPORT 172